Calcium-Aluminium-rich Inclusion Populations and Abundances Within CM Chondritic Lithologies

Pierre-Etienne Michel Clément Martin
B.Sc., M.Sc.

Submitted in fulfilment of the requirements for the degree of

Doctor of Philosophy

School of Geographical and Earth Sciences

College of Science and Engineering

University of Glasgow

December 2024

Abstract

C-type asteroids are considered prime candidates for the delivery of water to Earth in the early stages of the Solar System, due to their high-water and volatile content. Carbonaceous Mighei-like (CM) chondrites are water-rich polymict breccias that are thought to originate from these planetesimals. These carbonaceous meteorites have experienced extensive parent body alteration processes and display a diverse range of degrees of aqueous alteration. Among their components, Calcium-Aluminium-rich Inclusions (CAIs) are the first solids to have formed within the Solar System and accreted early onto these asteroidal parent bodies after migrating from their near-solar forming region. Therefore, these inclusions constitute ideal candidates for recording the aqueous alteration events that affected the CM parent body(-ies).

To this end, CAIs from 21 samples from six CM chondrites spanning a wide range of degrees of aqueous alteration (CM2.0-2.9) were selected for investigation. Using a combination of backscatter electron images and energy dispersive X-ray spectroscopy, CAIs were identified, selected, and measured within Asuka 12236, DNG 06004, Paris, and Winchcombe, and CAIs from DNG 06004, LAP 02239, and Winchcombe were classified according to their mineralogical and morphological features. A singular large altered complex aggregate (CAI) from Winchcombe was further studied using electron probe micro-analysis, transmission electron microscopy, and transmission Kikuchi diffraction to determine the potential role of its unusual pre-accretionary mineralogy on secondary mineralisation processes.

Measurements of CAI modal abundances, combined with data from the literature, reveal a clear correlation: CM CAI modal abundance decreases relative to the increasing aqueous alteration of their host lithology. This is due to the progressive alteration and destruction of CAIs through fluid-mediated replacement reactions. Further petrological and geochemical investigations of the CAI populations within Winchcombe reveal that CAIs have been affected differentially by fluid-mediated replacement reactions. Further evidencing that the CM parent body(-ies) likely underwent heterogeneous aqueous alteration processes. This suggests that the initial distribution of CAIs within the CM parent

body(-ies) was likely homogeneous, and heterogeneity in the CM CAI record was caused by subsequent fluid-driven alteration events.

During the large-scale investigation of CM CAIs, three rare Compound-Chondrule-CAIs (CCCAIs) were identified within Aguas Zarcas and LAP 02239. These objects are described as CAIs enclosed within chondrules and have been previously reported in other major carbonaceous groups (CO, CV, and CH). One CCCAI was subjected to electron backscatter diffraction to test the potential for CAIs to act as nucleation sites for chondrule formation. Additionally, in order to trace the origin of the CCCAI components, oxygen isotopes were measured using secondary ion mass spectrometry. The targets included the CAI and chondrule components of CCCAIs, as well as other CAIs and chondrules from Aguas Zarcas, DNG 06004, LAP 02239, Paris, and Winchcombe for comparison.

Based on the oxygen isotope analysis, the components of the CCCAIs belong to the same CAI and chondrule populations found within the CM lithologies. This led to the proposition of a model for the formation of CCCAIs by the incorporation of CAIs within a precursor ferromagnesian melt during transient heating events in the chondrule forming region. This suggests an early outward migration of near-solar refractory material within 1 Ma after CAI formation (before the formation of a physical barrier, e.g. proto-Jupiter).

The CM CAI populations are diverse in their pre- and post-accretionary histories and can provide invaluable information by constraining the initial and early compositions of the CM parent body(-ies). The methods developed during this thesis could be applied to other carbonaceous groups in order to improve our understanding of early accretion and alteration of asteroidal parent bodies.

Table of Contents

Abstract ii
Table of Contents iv
List of Tables viii
List of Figures x
Acknowledgements xii
Author's Declaration xiii
Conference Abstracts and Journal Articles Related to this Thesis xv
Journal Articles xv
Conference Abstracts xvi
1 Introduction 1
1.1 Background 1
1.1.1 Asteroids 1
1.1.2 Meteorites 2
1.1.3 CM Chondrites 10
1.1.4 Calcium-Aluminium rich Inclusions 14
1.2 Aims and objectives 16
1.3 Overview of Chapters 17
1.3.1 Chapter 2 17
1.3.2 Chapter 3 17
1.3.3 Chapter 4 17
1.4 Methodology and Samples 18
1.4.1 Scanning Electron Microscopy 18
1.4.2 Energy Dispersive X-ray Spectroscopy 19
1.4.3 Electron Probe Micro-Analysis 20
1.4.4 Electron Backscatter Diffraction 21
1.4.5 Transmission Electron Microscopy 22
1.4.6 Transmission Kikuchi Diffraction 24
1.4.7 Secondary Ion Mass Spectrometry 25
1.4.8 Meteorite samples 26
2 The Relationship Between CAI Modal Abundances and the Degree of Aqueous Alteration of CM Chondrites 29
2.1 Introduction 29
2.2 Material and Methods 30
2.2.1 Samples 30
2.2.2 Electron Microscopy 32
2.2.3 CAI Identification 33

2.2.4 CM CAI Classification 34
2.2.5 2D CAI Measurements 36
2.3 Results 43
2.3.1 Petrographic Overview 43
2.3.2 Modal Abundances of CM CAIs 52
2.4 Discussion 60
2.4.1 Progressive Aqueous Alteration of CM CAIs 60
2.4.2 Initial CAI Distribution in CM Lithologies 62
2.4.3 A Potential New Criterion for Quantifying Aqueous Alteration in CM Lithologies 63
2.4.4 Limitations and Future Work 64
2.5 Conclusions 66
2.6 Acknowledgements 67
3 Multiple Aqueous Alteration Events Recorded within the Calcite- and Grossmanite-bearing CAIs of the Winchcombe CM2 Carbonaceous Chondrite 68
3.1 Introduction 68
3.2 Material and Methods 70
3.2.1 Samples 70
3.2.2 Electron Microscopy 71
3.2.3 CAI Identification 72
3.2.4 Electron Probe Micro-Analysis 74
3.2.5 Transmission Electron Microscopy 75
3.2.6 Transmission Kikuchi Diffraction 75
3.3 Results 76
3.3.1 Petrographic Overview of the CAI Populations within the Winchcombe Meteorite 76
3.3.2 Description of the different CAI types in the Winchcombe Meteorite 81
3.3.3 Identification of Grossmanite in Calcitised CAI 85
3.3.4 Transmission Kikuchi Diffraction Observations of a Calcitised CAI .. 93
3.4 Discussion 101
3.4.1 CAI Formation Prior to Incorporation within the CM Parent Body .. 101
3.4.2 CAI Alteration After Incorporation within the CM Parent Body 105
3.5 Conclusions 110
3.6 Acknowledgments 112
4 Origin and Formation of Compound-Chondrule-CAIs (CCCAIs) within CM Chondrites 113
4.1 Introduction 113
4.1.1 Aim of Study 113
4.1.2 Compound-Chondrule-CAIs 115

4.2 Material and Methods 117
4.2.1 Samples 117
4.2.2 Naming Convention for CCCAIs 118
4.2.3 Electron Microscopy 119
4.2.4 Electron Backscatter Diffraction 120
4.2.5 SIMS Oxygen Isotopes 121
4.3 Results 124
4.3.1 Microstructure of CM CCCAIs 124
4.3.2 Oxygen isotopes of CAIs, Chondrules, and CCCAI Components 134
4.4 Discussion 151
4.4.1 Constraining the Thermal Conditions of CCCAI Formation Processes 151
4.4.2 Implications for Understanding Early Solar System Processes 156
4.5 Conclusions 165
4.6 Acknowledgments 166
5 Final Summary 168
5.1 Conclusions 168
5.2 Key Findings 171
6 Future Work 172
6.1 CAI Modal Abundance 172
6.2 CAI Classification 173
6.3 CAI Aqueous Alteration 173
6.4 CCCAI Formation 174
7 Appendices 175
7.1 EBSD Polishing Protocol for CM Chondrites 175
7.2 2D CAI Measurements 176
7.3 CAI Petrographic Descriptions 205
7.4 CAI Types and Mineralogies 213
7.5 EPMA Compositions 215
7.6 Weighted Burger Vectors 218
7.7 Raw Oxygen Isotope SIMS Data 219
7.8 Chondrule Mg# 239
7.8.1 Aguas Zarcas 241
7.8.2 Paris 252
7.8.3 Winchcombe 267
7.9 SIMS Pit Images 270
7.9.1 Aguas Zarcas 271
7.9.2 LAP 02239 283
7.9.3 DNG 06004 288

7.9.4 Paris 291
7.9.5 Winchcombe.....307
List of References 308

List of Tables

Table 1.2. Petrologic subtypes of CM chondrites, adding CM2.8-3.0.. 14
Table 1.3. List of meteorite samples studied in this thesis and their petrological types..... 28
Table 2.1. List of meteorite samples investigated and their reported petrologic type and subtype. 31
Table 2.2. List of meteorite samples mapped using EDS with their image mosaic resolution and pixel size. 33
Table 2.3. Compilation of previous studies of CAI modal abundances in CM chondrites.. 42
Table 2.4. Distribution of CAI types within CM chondritic lithologies. 43
Table 2.5. Modal abundance and size of CAIs within the studied CM lithologies compared to the prototypical CM, Mighei, and other CMs from the literature. . 55
Table 2.6. Modal abundance and size of CAIs within the studied CM lithologies of the Winchcombe meteorite. 56
Table 2.7. Estimated number of CAIs missing from this study.. 59
Table 3.1. List of polished sections investigated in this study with their identified lithologies (A-G; attributed by Suttle et al., 2024), surface area investigated, and degree of aqueous alteration..... 70
Table 3.2. List of the polished sections mapped using EDS with their image mosaic resolution and pixel size.. 71
Table 3.3. Summary of the studied CAIs within the sections of the Winchcombe meteorite. 76
Table 3.4 Description of the CAIs identified within the Winchcombe meteorite.78
Table 3.5. Geometric properties of the CAIs identified within the Winchcombe meteorite. 80
Table 3.6. Mean composition of (*n* = 8) grossmanite grains within CAI 19 obtained using EPMA..... 87
Table 3.7. Average d-spacings for electron diffraction spots from the grossmanite grains within CAI 19 of the Winchcombe meteorite (P30552; lith. A, CM2.2)..... 92
Table 4.1. List of meteorite samples investigated and their reported petrologic type and subtype. 118
Table 4.2. List of meteorite samples mapped using EDS with their image mosaic resolution and pixel size. 120
Table 4.3. EBSD crystallographic axes parameters used to investigate forsterite and diopside grains within the Cockerel's chondrule. 121
Table 4.4. List of objects of interest targeted.....122
Table 4.5. List of objects of interest and mineral phases targeted. 122
Table 4.6. Oxygen-isotope compositions of individual minerals in the CCCAI, CAI, and chondrule populations from the studied CM carbonaceous chondrites.....136
Table 7.1. Protocol for polishing CM chondrite samples for EBSD.....175
Table 7.2. Geometric properties of the CAIs identified within the Asuka 12236 meteorite. 176
Table 7.3. Geometric properties of the CAIs identified within the Paris meteorite. 180
Table 7.4. Measurements and calculated mean size of the CAIs identified within the DNG 06004 meteorite. 202
Table 7.5. Summary of the studied CAIs within the DNG 06004 meteorite. 205
Table 7.6. Description of the CAIs identified within the DNG 06004 meteorite.208
Table 7.7. Mineralogy and type of classified CAIs within CM chondrites. 213

Table 7.8. Oxide compositions (wt%) of targeted spinel grains in CAIs 1 (P30540) and 19 (P30552) of Winchcombe using EPMA. 215
Table 7.9. Oxide compositions (wt%) of targeted perovskite grains in CAIs 15 and 19 of Winchcombe (P30552) using EPMA. 216
Table 7.10. Oxide compositions (wt%) of targeted grossmanite grains in CAI 19 of Winchcombe (P30552) using EPMA. 217
Table 7.11. Unprocessed Oxygen-isotope compositions of individual minerals in the CCCAI, CAI, and chondrule populations from the studied CM carbonaceous chondrites. 219
Table 7.12. Mean Mg# of targeted olivine grains within chondrules and chondrule fragments of the Aguas Zarcas, Paris, and Winchcombe meteorites. 240

List of Figures

Figure 1.1. Schematic diagram of keys objects and phenomena related to meteorites for scientific communication. 2
Figure 1.2. Schematic diagram representing the meteorite classification scheme from Weisberg et al. (2006)..... 4
Figure 1.3. Images of chondrules in three types of chondritic meteorites. 6
Figure 1.4. Three-isotope oxygen diagram for different chondrite groups. 8
Figure 2.1. Selected area of the Paris (B1.5) section during the segmentation process. 38
Figure 2.2. Relative proportions (%) of CAI types for each meteorite. 44
Figure 2.3. Average calculated sizes (μm) of each CAI type for each meteorite. 45
Figure 2.4. CAIs 4, Q, and A12 (respectively), simple inclusions in LAP 02239 (02239,5; CM2.4-2.5)..... 47
Figure 2.5. CAIs F, G, and A18 (respectively), simple aggregates in LAP 02239 (02239,5; CM2.4-2.5)..... 49
Figure 2.6. CAIs 6, T, and B2 (respectively), complex aggregates in LAP 02239 (02239,5; CM2.4-2.5)..... 51
Figure 2.7. Frequency size distribution of CAIs in each meteorite..... 53
Figure 2.8. Modal abundances of CAIs within CM lithologies relative to the degree of aqueous alteration of their host lithologies. 58
Figure 3.1. Schematic diagram representing the structural components of CAIs used for descriptive purposes. 74
Figure 3.2. CAIs 1, 16, and 18 (respectively), simple inclusions in the Winchcombe meteorite (P30540 and P30552; Mx and lith. A). 82
Figure 3.3. CAIs 6, 7, and 8 (respectively), simple aggregates in the Winchcombe meteorite (P30547; Mx). 83
Figure 3.4. CAIs 15 and 9 (respectively), calcitised complex aggregates in the Winchcombe meteorite (P30552 and P30547; lith. A and Mx). 84
Figure 3.5. CAI 19, a calcitised complex aggregate in the Winchcombe meteorite (P30552; lith. A, CM2.2). 86
Figure 3.6. Molar ternary diagram of three prominent cation groups in the M1 site of the clinopyroxenes from CAI 19 of the Winchcombe meteorite. 88
Figure 3.7. Normalised ternary diagram of Ti^{3+}-Sc^{3+}-Al^{3+} proportions inferred from EPMA analyses of the grossmanite grains within CAI 19 of the Winchcombe meteorite. 89
Figure 3.8. BSE image of the locations of the sections selected for TEM and TKD analyses after Pt layering and before FIB extraction within CAI 19 (P30552; lith. A, CM2.2). 90
Figure 3.9. TEM results from grossmanite grains in CAI 19 in the Winchcombe meteorite (P30552; lith. A, CM2.2). 91
Figure 3.10. TKD results from FIB-produced TEM lamella of site 9 within CAI 19 of the Winchcombe meteorite (P30552; lith. A., CM2.2). 94
Figure 3.11. Stereographic projections plotting the poles to the Miller indices of minerals within site 9 of CAI 19 (P30552; lith. A, CM2.2). 95
Figure 3.12. TKD results from FIB-produced TEM lamella of site 12 within CAI 19 of the Winchcombe meteorite (P30552; lith. A., CM2.2)..... 96
Figure 3.13. Stereographic projections plotting the poles to the Miller indices of minerals within site 12 of CAI 19 (P30552; lith. A, CM2.2)..... 98
Figure 3.14. TKD analyses of the twinned perovskite grain in site 12 within CAI 19 of the Winchcombe meteorite (P30552; lith. A., CM2.2)..... 99

Figure 3.15. Upper hemisphere stereographic projection of crystallographic orientations (pole to the Miller indices) of the twins in perovskite in regards to its host grain within site 12 of CAI 19 (P30552; lith. A, CM2.2). 100
Figure 3.16. Schematic diagram of the proposed heterogeneous aqueous alteration sequences that affected the mantles and rims of melilite- and/or anorthite-bearing CAIs according to their type within the lithologies of the Winchcombe meteorite.....110
Figure 4.1. The Cockerel CCCAI (Aguas Zarcas, AZ-P2).....126
Figure 4.2. BSE image of the Cockerel CCCAI (Aguas Zarcas, AZ-P2).....127
Figure 4.3. Disorientation axes figures of the main mineral phases of the Cockerel's chondrule component. 128
Figure 4.4. The Cicero CCCAI (Aguas Zarcas, AZ-03).....130
Figure 4.5. The Capybara CCCAI (LAP 02239, 02239,5).....132
Figure 4.6. BSE image of the Capybara CCCAI (LAP 02239, 02239,5). 133
Figure 4.7. Three-isotope oxygen diagrams of compositions of all analysed phases in chondrules, ARCs, CAIs, and in the CCCAI components from each of the studied CM carbonaceous chondrites. 143
Figure 4.8. Compilation of all oxygen isotope data measurements acquired in this study. 145
Figure 4.9. Three-isotope oxygen diagrams of compositions of individual spot analyses of mineral phases in CAIs and rimmed CAIs from the studied CM carbonaceous chondrites. 146
Figure 4.10. Three-isotope oxygen diagrams of compositions of individual spot analyses of mineral phases in chondrules, ARCs, and ^{16}O-rich forsterite grains from the studied CM carbonaceous chondrites.....147
Figure 4.11. Three-isotope oxygen diagram of compositions of individual spot analyses of mineral phases in the CAI and chondrule components of the Cicero CCCAI and in the proximal chondrule fragments within the same FGR. 150
Figure 4.12. Δ^{17}O values of all the CCCAI components, CAIs, and chondrules from the studied CM carbonaceous chondrites normalised to the TFL.....160
Figure 4.13. Schematic diagram of the proposed CCCAI formation model.....164
Figure 7.1. Weighted Burger Vector diagrams of the main mineral phases of the Cockerel's chondrule component. 218
Figure 7.2. Mean Mg# of targeted olivine grains within chondrules and chondrule fragments of the Aguas Zarcas, Paris, and Winchcombe meteorites. 239

Acknowledgements

First and foremost, I would like to thank my supervisory team for giving me the opportunity to pursue my passion: Prof. Martin Lee and Dr. Luke Daly. Thank you for your invaluable guidance, for supporting me and for being so patient no matter how long it took me to write. And thank you to the College of Science and Engineering for funding this project.

Special thanks to Luke for sitting down with me and listening to/reading the ramblings of “sleep-deprived Pierre”.

Thank you, Ashley, for being so understanding and supportive… and for also listening to my ramblings…

Thank you, Martin, for listening to me “spitball” all my crazy theories all these years.

Thank you to my Glasgow friends (in no particular order, this is not a competition!): Uli, André, Fabi, Issy, Octria, Karlin, Gabriel, Marian, Faith, Alpana, Laura, Faisal, and Jeongha (even Vilte and Judy).

Thank you to my PGR friends for keeping me sane: Matthew, Amanda, Jose, Savanna, Neve, Jahangir, Youssef, Danjuma, Gopikaa, Puja, Robin, Cameron, Fakhri, Kang, Chloe, Careen, Shona, and Beth.

Special thanks to Prof. Michael D. Higgins, Dr. Gilles Christoph, and Prof. Neil Spurway for encouraging me to pursue a career in Planetary Science.

Merci à ma famille pour tout votre amour et soutien, Maman, Papa, et petit blondinet !

Merci à mes amis français pour tout votre soutien dans mes moments les plus noirs (ordre aléatoire): Maxime, J-P, Félix, Louis, Matthieu, Tintin Guillaume et Dan. Et merci aussi à la petite Ambre !

Gracias por todo a mi corazoncito, Ana H. Huembes.

Author's Declaration

I declare that, except where explicit reference is made to the contribution of others, that this dissertation is the result of my own work and has not been submitted for any other degree at the University of Glasgow or any other institution.

Pierre-Etienne Michel Clément MARTIN

*"For dust thou art, and shalt to dust returne."**

-John Milton, *Lost Paradise*, 1667

*John Milton was probably referring to the accretion process through which planets, asteroids, and meteorites originate, and to how they eventually end up being ground into powders on Earth for study by planetary scientists.

Conference Abstracts and Journal Articles Related to this Thesis

Journal Articles

Jenkins, L. E., et al. (2024). Winchcombe: An example of rapid terrestrial alteration of a CM chondrite. *Meteoritics & Planetary Science*, 59 (5), 988–1005. https://doi.org/10.1111/maps.13949

Suttle, M. D., et al. (2024). The Winchcombe meteorite—A regolith breccia from a rubble pile CM chondrite asteroid. *Meteoritics & Planetary Science*, 59 (5), 1043–1067. https://doi.org/10.1111/maps.13938

Daly, L., et al. (2024). Brecciation at the grain scale within the lithologies of the Winchcombe Mighei-like carbonaceous chondrite. *Meteoritics & Planetary Science*, 59 (5), 1068–1100. https://doi.org/10.1111/maps.14164

Noguchi, T., et al. (2023). Mineralogy and petrology of fine-grained samples recovered from the asteroid (162173) Ryugu. *Meteoritics & Planetary Science*, 1–30. https://doi.org/10.1111/maps.14093

Lee, M. R., et al. (2023). Extended timescales of carbonaceous chondrite aqueous alteration evidenced by a xenolith in LaPaz Icefield 02239 (CM2). *Meteoritics & Planetary Science*, 58 (5), 672–687. https://doi.org/10.1111/maps.13978

King, A. J., et al. (2022). The Winchcombe meteorite, a unique and pristine witness from the outer solar system. *Science Advances*, 8 (46), eabq3925. https://doi.org/10.1126/sciadv.abq3925

O'Brien, A. C., et al. (2022). The Winchcombe Meteorite: one year on. *Astronomy and Geophysics*, 63(1), 1.21–1.23. https://doi.org/10.1093/astrogeo/atac009

Lee, M., et al. (2021). CM carbonaceous chondrite falls and their terrestrial alteration. *Meteoritics and Planetary Science*, 56(1), 34–48. https://doi.org/10.1111/maps.13607

Lindgren, P., et al. (2020). Signatures of the post-hydration heating of highly aqueously altered CM carbonaceous chondrites and implications for interpreting asteroid sample returns. *Geochimica et Cosmochimica Acta*, 289, 69–92. https://doi.org/10.1016/j.gca.2020.08.021

Conference Abstracts

Martin, P-E. M. C., et al. (2024). On the Origin of the Compound-Chondrule-CAI Components within CM Chondrites. *LPI* Contributions, 6106.

Martin, P-E. M. C., et al. (2024). Investigating Ca-Al-rich Inclusions (CAIs) and Compound-Chondrule-CAI (CCCAIs) Populations within CM Chondrites using Oxygen Isotopes. *British Planetary Science Conference 2024*, p.7.

Martin, P. E., et al. (2023). Link Between Calcium-Aluminium-Rich Inclusion Abundance and the Degree of Aqueous Alteration of Lithologies Within CM Chondritic Breccias. *LPI Contributions*, *2990*, 6195.

Martin, P. E., & Lee, M. R. (2023). Calcium-Aluminium-Rich Inclusion Abundance and Mineralogy Within CM Carbonaceous Chondrites. *LPI Contributions*, *2806*, 2844.

Martin, P-E., et al. (2023). Chemical and Crystallographic Characterisation of Grossmanite-Bearing Calcium-Aluminium-Rich Inclusion Within the Winchcombe CM2 Carbonaceous Chondrite. *LPI Contributions*, *2806*, 2882.

Martin, P. E., et al. (2022). Calcium-Aluminium-rich Inclusion Populations within the Winchcombe CM2 Meteorite Breccia. *LPI Contributions*, *2695*, 6358.

Martin, P. M. C., et al. (2022). Investigating the Thermal History of a Compound-Chondrule-CAI within the CM2 Breccia Aguas Zarcas. *53rd Lunar and Planetary Science Conference*, *2490*.

Martin, P-E. M. C., & Lee, M. R. (2021). The Conspicuous Compound Chondrule-CAI Conundrum: A Case Study Within the Brecciated CM2.2 Lithology of the Carbonaceous Breccia Aguas Zarcas. *LPI Contributions*, *2609*, 6190.

Martin, P. E., & Lee, M. R. (2021). Clast Populations within the CM2.2 Brecciated Carbonaceous Chondrite Aguas Zarcas: Implications for Understanding Aqueous Alteration on Ryugu. *52nd Lunar and Planetary Science Conference, 2068*.

Martin, P. M. C., & Lee, M. E. (2020). Degree of aqueous alteration of the CM carbonaceous chondrite Aguas Zarcas: Implications for understanding Ryugu and Bennu. *51st Lunar and Planetary Science Conference, 1375*.

1 Introduction

1.1 Background

1.1.1 Asteroids

As with most mysteries in the universe, such as the disappearance of a *pain au chocolat*, it is often most effective to follow the trail of evidence back to its source. Thus, to investigate the formation of terrestrial planets within the early Solar System, it is necessary to examine the remnants of planetary accretion: asteroids. The term ‘asteroid’ originates from the Ancient Greek *ἀστήρ* (*astēr*) meaning 'star’, and later evolved into *ἀστεροειδής* (*asteroeidēs*), meaning ‘star-like’ or ‘planet-like’ (Wall, 2011; Nolan, 2013). Asteroids are small bodies (metric to kilometric in size) made of rock and/or metal orbiting the Sun and are thought to share their composition with the primary building blocks that accreted to form Mercury, Venus, Earth, and Mars. Asteroids that can be observed nowadays are the surviving remnants (the "leftover crumbs") of this early planet formation process, which occurred approximately 4.6 Ga ago (Bottke et al. 2021; Carry 2012; Gaffey 2011). Therefore, they are ideal candidates for investigating the composition and the formation history of the terrestrial planets.

The origin of Earth’s water is one of the most prominent questions in planetary science, and ambitious sample collection missions such as JAXA’s Hayabusa2 and NASA’s OSIRIS-REx sample collection missions aim to help provide answers to this question. In both missions, the targeted asteroids Ryugu and Bennu were water-rich carbonaceous (C-type) asteroids. However, studying asteroids only through sample-return missions is not the most affordable solution. Fortunately, meteorites provide samples of planetary reservoirs and objects formed in the early Solar System. By studying the composition of meteorites, we can better understand the origins of terrestrial planets and the materials from which they may have formed. Planet formation in our Solar System started rapidly after the birth of a central star, the Sun, which constituted the centre of a rotating disk of gas and fine dust grains known as the protoplanetary disk (Chambers, 2004). Within this disk, dust particles collided and grew through accretion, forming planetesimals and eventually planets

(Chambers, 2004). Studying meteorites, the closest to the original materials left from this stage of the protoplanetary disk, thus, allows us to reconstruct the conditions of the environment in which occurred planetary formation and evolution.

1.1.2Meteorites

1.1.2.1 Definitions

Since the terms ‘meteorite’ and ‘meteor’ are often used interchangeably erroneously, it is important to begin with a few definitions (cf. Fig. 1.1).

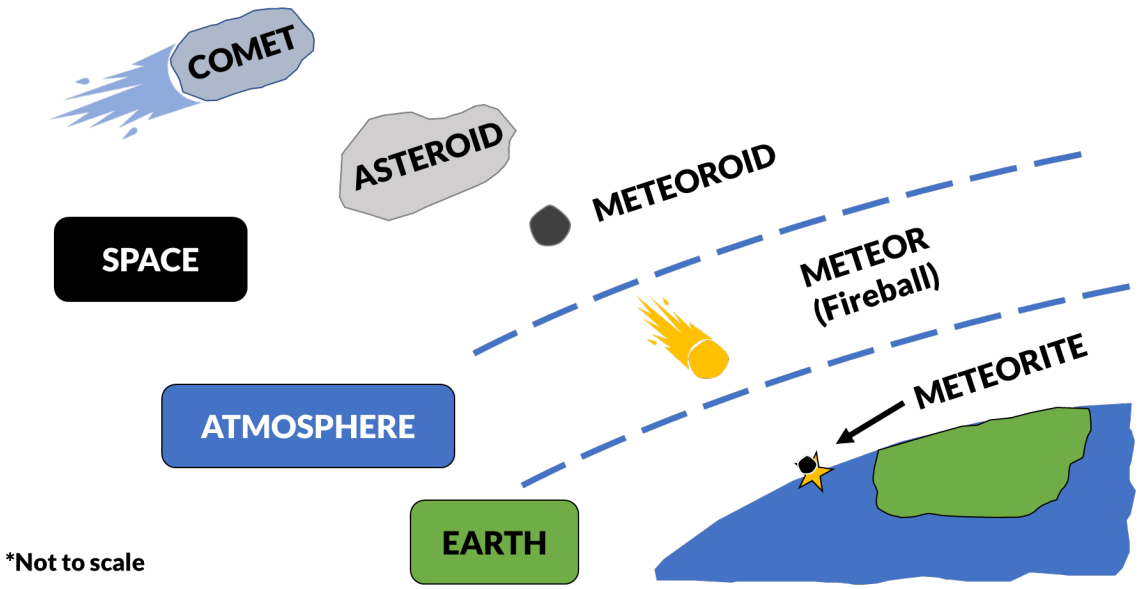

Figure 1.1. Schematic diagram of keys objects and phenomena related to meteorites for scientific communication. Comets (icy bodies composed of rock, dust, and frozen gases that orbit the Sun) are included for context but are not discussed further in this thesis

According to the International Astronomical Union, a ‘meteorite’ is a natural solid object that has survived passage through a gaseous atmosphere and reached the surface of a planetary body. Objects smaller than 1 mm can be referred to as ‘micrometeorites’. A ‘meteor’, by contrast, is not a physical object but a visual phenomenon: it is the light (and the associated heat, shock, and ionisation) that is produced when a solid object from space enters a planetary atmosphere at high velocity. If a meteor is bright enough, it can be referred to as a ‘fireball’.

The object responsible for this display is a ‘meteoroid’. If it survives atmospheric entry and reaches the surface, it then becomes a meteorite. Contrary to popular belief, a meteor itself does not impact the ground. It is in fact the meteoroid passing through the atmosphere, surviving atmospheric ablation, before entering what is known as ‘dark flight’ (in contrast to the brightness of a meteor), that may reach the Earth’s surface, where it will either be patiently waiting to be discovered on land or vanish into the unfathomable depths of our oceans or… in Condover (United Kingdom). The distinction between asteroids and meteoroids is merely a matter of size, with meteoroids generally ranging from centimetres to a few metres in diameter.

In Planetary Science, meteorites are regarded as extraterrestrial solids ejected from a parent body (generally due to impact), before being captured by Earth’s gravity and survive atmospheric entry. These objects exhibit a wide range of compositions and can originate from asteroids, Mars, or even the Moon. As outlined in the introduction, this thesis will focus on C-type asteroids and their associated carbonaceous meteorite groups.

1.1.2.2 Classification

Depending on their origin, meteorites can display a wide array of textures, mineralogies, and chemical and isotopic compositions. They are broadly divided into two categories: chondrites and achondrites, depending on the presence or absence of objects known as ‘chondrules’ within them (cf. Fig. 1.2). The term ‘chondrule’ is derived from the Ancient Greek word *χόνδρος* (*chondros*), meaning ‘grain’, due to their characteristic round shape when they were first described.

Chondrites are stony meteorites that contain chondrules (0-80 vol.%; Weisberg et al., 2006), from which their name is derived. In contrast, achondrites (with the privative prefix *a-*, meaning ‘without’) do not contain chondrules.

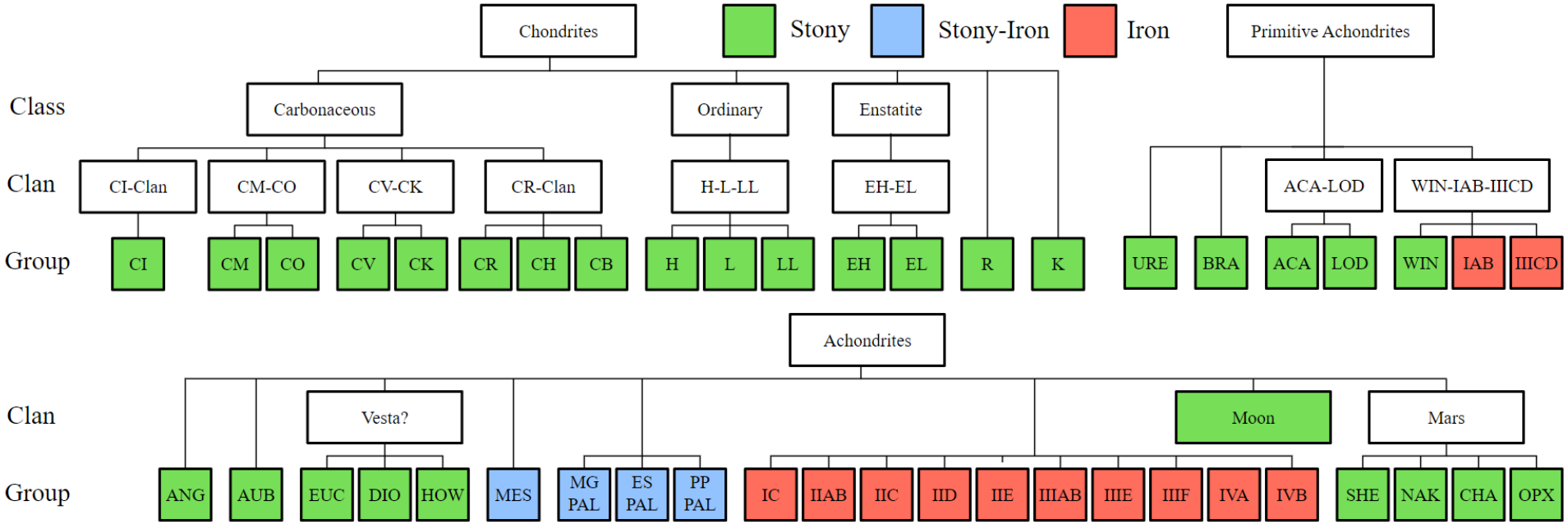

Figure 1.2. Schematic diagram representing the meteorite classification scheme from Weisberg et al. (2006). Groups established after 2006 have not been included (e.g. Martian regolith breccias and CY chondrites).

Achondrites originate from differentiated bodies that have experienced widespread melting. These meteorites resemble igneous rocks and may comprise multiple melt components. They can also be brecciated and originate from a variety of differentiated bodies, including large asteroids, as well as planetary bodies like the Moon and Mars (Weisberg et al., 2006).

Primitive achondrites occupy an intermediate position, in which they also display igneous textures with evidence of melting and recrystallisation but retain some primitive chemical signature similar to that of chondrites (Weisberg et al., 2006).

Chondrites constitute the most common meteorite type found on Earth. They are considered undifferentiated, meaning they have not experienced widespread melting or differentiation on their parent bodies. They are often referred to as ‘cosmic sediments’ due to their sedimentary-like features (e.g. grained components of various sizes, brecciation, clasts). Some chondrites, such as the CI (Ivuna-like) group, contain few or no visible chondrules, but are classified as chondrites due to their solar-like bulk chemical compositions.

Chondrites can be further divided into three main classes: ordinary, carbonaceous, and enstatite (cf. Fig. 1.2 and 1.3). Additionally, K and R correspond to smaller, distinct groups. Chondritic meteorites are also attributed a petrologic type, a number ranging from 1 to 6, based on the scale established by Van Schmus & Wood (1967). These numbers indicate the degree of alteration experienced by the meteorite: type 3 corresponds to a pristine sample (or, at the very least, as pristine as a sample can be); types 3-6 indicate increasing levels of thermal metamorphism; types 1-3 are used to represent aqueous alteration, with type 1 corresponding to a completely aqueously altered sample.

Figure 1.3. Images of chondrules in three types of chondritic meteorites. (a) NWA 8183 (LL3.2), an ordinary chondrite, with a high abundance of chondrules; (b) Allende (CV3), a carbonaceous chondrite, with a high abundance of chondrules and CAIs; (c) Abee (EH4), an enstatite chondrite, with only one visible chondrule. These are personal photographs from previous works (unpublished).

1.1.2.3 Chondrules

Chondrules are generally small (sub-millimetre to millimetre-sized; cf. Fig. 1.3), roughly spherical particles with igneous textures. They are among the primary constituents of chondritic meteorites, comprising up to 80 vol.% of some samples (Weisberg et al., 2006). These objects formed as solidified molten droplets from precursor materials, mainly composed of ferromagnesian silicates (e.g. Olivine: $(Mg,Fe)_2SiO_4$), alongside Fe-Ni metal, minor glass, and other silicates (Hewins 1997; Zanda, 2004). Chondrules are thought to have formed within the first 4 Ma of the Solar System (Bollard et al., 2017; Pape et al., 2019). Due to their abundance in chondrites, chondrules are thought to have been the most abundant objects in the early Solar System and are considered to have been the main building blocks of asteroids and terrestrial planets (Connolly & Jones 2016; Jones et al. 2000; Weisberg et al. 2006). Despite their apparent importance, the precise mechanisms of chondrule formation remain a highly debated topic (Connolly & Jones, 2016).

Chondrules can be classified according to their texture similarly to igneous rocks (e.g. porphyritic, poikilitic). However, they may also be categorised based on the average composition of their olivine components. This composition is defined as the 'Mg number' (Mg#) and is calculated as follows: $Mg\# = [MgO]/[FeO]$, in mol%. Type I chondrules (Mg# > 90) are FeO- and volatile-poor, whereas Type II chondrules (Mg# < 90) are relatively FeO-rich (Hewins, 1997).

1.1.2.4 Oxygen Isotope Systematics

Oxygen isotopes exist in three stable forms: ^{16}O, ^{17}O, and ^{18}O. Isotopic fractionation can occur in two primary ways, depending on the governing processes: mass-dependent or mass-independent.

Mass-dependent fractionation occurs from physical and chemical processes (e.g. evaporation, diffusion) where isotopes are fractioned based on their mass differences. In the case of the evaporation of water (H_2O), for example, lighter isotopes, such as ^{16}O, are preferentially partitioned into the

vapour (due to them requiring less energy to become mobile), while the remaining liquid water becomes relatively more enriched in heavier isotopes, such as ^{18}O.

Mass-independent fractionation occurs from nuclear effects, photochemical reactions, or mixing of reservoirs with distinct isotopic compositions, and do not depend on the mass differences between isotopes. A prime example is the photodissociation of carbon monoxide (CO) in the early solar nebula (self-shielding). This process consisted in separating carbon and oxygen atoms in a non-mass-dependent manner, producing the oxygen isotope anomalies observed in primitive meteorites.

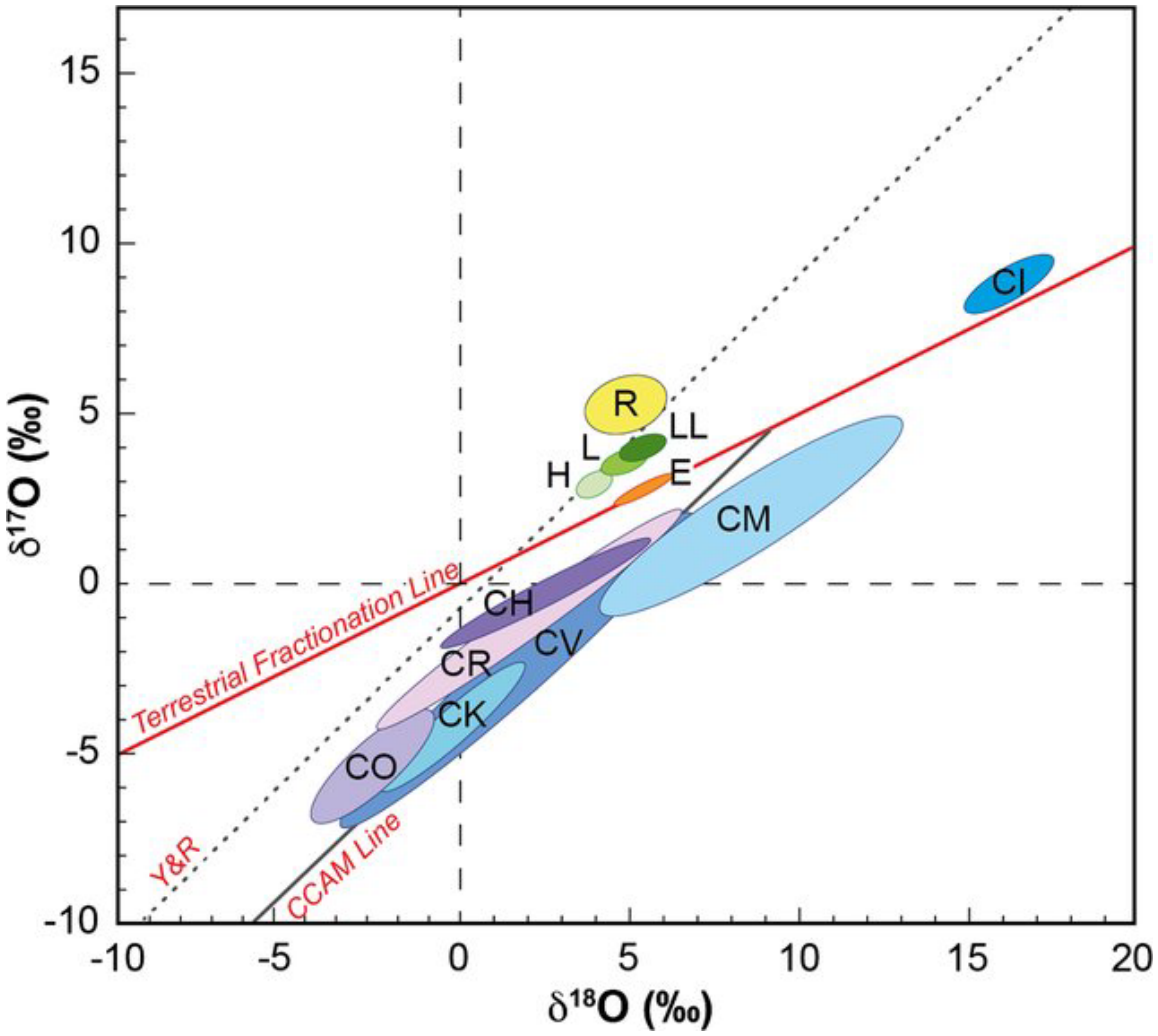

Figure 1.4. Three-isotope oxygen diagram for different chondrite groups. The Terrestrial Fractionation Line (TFL) and the Carbonaceous Chondrite Anhydrous Mineral line (CCAM) are shown here for reference. Oxygen isotope ratios of the carbonaceous groups plot closely or along the CCAM line, with exceptions such as the CI and some CM chondrites. Figure from Ireland et al. (2020).

Isotopic compositions are plotted in what is known as three-isotope diagrams, where variations in $^{17}O/^{16}O$ and $^{18}O/^{16}O$ relative to Standard Mean Ocean Water (SMOW) are expressed in parts per thousand (‰) as $\delta^{17}O$ and $\delta^{18}O$ values. These diagrams help distinguish between mass-dependent and mass-independent processes. More information regarding oxygen isotope calculations can be found in chapter 5.

The discovery that meteorites bear mass-independent and mass-dependent isotopic variations for many elements has been intensively used to fingerprint planetary reservoirs and provide constraints on planetary accretion, differentiation processes, and dynamical models. Oxygen, in particular, presents isotopic variations between chondritic groups and has been used as a diagnostic criterion for meteorite classification due to its ability to retrace the origin of distinct reservoirs from which specific inclusions and chondrules formed (Weisberg et al., 2006; Ireland et al., 2020; cf. Fig. 1.4).

Carbonaceous chondrite groups were each further classified according to their bulk oxygen isotope compositions. This provided a new way of sorting meteorites into more precise categories based on the processes they underwent, in addition to examining their petrographic features (Ireland et al., 2020). Based on these oxygen isotope systematics, two main mass-independent trendlines were defined:

- The Primitive Chondrule Mineral (PCM) line, derived from chondrules and chondrule phenocrysts in carbonaceous chondrites (Ushikubo et al., 2012): $\delta^{17}O = 0.987 \times \delta^{18}O - 2.7$
- The Carbonaceous Chondrite Anhydrous Mineral (CCAM) line, empirically defined from CAIs and anhydrous silicates in carbonaceous chondrites (Clayton et al., 1977; Clayton & Mayeda, 1999): $\delta^{17}O = 0.94 \times \delta^{18}O - 4.2$.

These fractionation lines are typically plotted alongside the Terrestrial Fractionation Line (TFL) for comparison, which was defined using terrestrial material: $\delta^{17}O = 0.52 \times \delta^{18}O$).

It is of utmost importance to understand where extraterrestrial materials plot relative to these lines, as it can provide invaluable information relative to their formation environments, isotopic mixing histories, and the evolution of the solar nebula.

1.1.3 CM Chondrites

1.1.3.1 Origin and Alteration

Carbonaceous Mighei-like (CM; named after its prototypical member) chondrites are amongst the most common carbonaceous (carbon-rich) meteorite samples found on Earth (Suttle et al., 2021) and have a relatively high-water content (~ 9 wt.%; Jarosewich, 1990). They are thought to originate from C-type asteroids (Bates et al., 2020), which formed ~4.6 Ga ago (Bottke et al., 2021; Carry, 2012; Gaffey et al., 2011) through accretion in the outer Solar System (Kallemeyn and Wasson, 1981). However, due to the important petrological variations between the meteorites of this group, certain studies (e.g. (Suttle et al., 2021; Vernazza et al., 2016) have suggested that CM chondrites might have originated from multiple parent bodies.

CM chondrites have been characterised as having been subjected to different degrees of low temperature aqueous alteration (0-240°C; Busemann et al., 2007; Clayton and Mayeda, 1999; Suttle et al., 2021). This alteration is thought to have occurred within the CM parent body(-ies) between 4±2 Myr after the formation of CAIs (Fujiya et al., 2012; Visser et al., 2020) and was caused by the release of frozen water through heating, likely due to the radioactive decay of ^{26}Al contained within most CAIs at that time (Barber, 1981; Bunch and Chang, 1980; Huss et al., 2001; McSween, 1979; Rubin, 2015; Rubin et al., 2007; Tomeoka and Buseck, 1985; Trigo-Rodriguez et al., 2006; Zolensky et al., 1993, 1997).

1.1.3.2 CM Components

Most CM chondrites are polymict breccias (Bischoff et al., 2006; Lentfort et al., 2021; Lindgren et al., 2013; Metzler et al., 1992; Nakamura, 2006; Suttle et al., 2021) composed of chondrules, refractory inclusions (Calcium-Aluminium-rich Inclusions – CAIs – and Ameboid Olivine Aggregates – AOAs), individual

silicate fragments (olivine and pyroxene), sulphides, and minor Fe-Ni metal, supported within a matrix. The amounts of these components can vary greatly depending on the extent of aqueous alteration that affected the CM lithologies. It is also important to note that clasts within the same meteorite may exhibit different degrees of aqueous alteration.

In the most altered samples, for example, the matrix is dominated by serpentine minerals and Tochilinite-Cronstedtite Intergrowths (TCIs; originally PCP: Poorly-Characterised Phase; Rubin et al., 2007), seldom with other alteration phases, such as carbonates (mostly calcite; Rubin, 2007), secondary sulphides, phosphates, oxides, and pyroxene (Howard et al., 2015; Rubin et al., 2007). Most pristine samples can be composed of plagioclase feldspar, amorphous silicates, Glass Embedded Metal and Sulphides (GEMS), and chondrule mesostasis glass (Kimura et al., 2020). Chondrules in CMs are generally type I (Mg-rich, FeO-poor), display porphyritic textures (>95%;(Jones, 2012). They are often surrounded by Fine-Grained Rims (FGRs) which are volatile dust mantles that accreted onto chondrules during transit prior to their incorporation within the CM parent body (Chizmadia and Brearley, 2008; Hua et al., 2002; Lauretta et al., 2000; Metzler et al., 1992; Suttle et al., 2021; Zega and Buseck, 2003; Zolensky et al., 1993).

1.1.3.3 CM Classification

All CM chondrites exhibit signs of fluid-driven parent body alteration and are therefore sub-classified according to the degree to which they are aqueously altered (Kimura et al., 2020). For the purposes of this thesis, the classification scheme defined by Rubin et al., 2007, and expanded in Rubin, 2015 and (Kimura et al., 2020), will be used throughout this study. Rubin's scale relies on a combination of petrographic and geochemical criteria to determine a petrologic subtype, ranging from 2.0 (completely aqueously altered; cf. Table 1.1) to 3.0 (least aqueously altered or pristine; cf. Table 1.2). This classification scheme was originally calibrated from 2.0 to 2.7 according to the extent of large clumps of TCIs within the chondritic matrix and the (un)altered state of mafic silicate phenocrysts in chondrules (cf. Table 1.2). It is important to note that all CM chondrite petrologic subtypes have an error of ±0.1, according to Rubin et al. (2007) and Rubin (2015). This nomenclature was chosen due to its accessibility

and common usage, allowing for an easier comparison with the existing literature.

Other CM classifications exist, such as Howard's scale (Howard et al., 2015), which is referenced only in this thesis for comparative purposes. This classification relies on X-Ray bulk Diffraction (PSD-XRD) measurements to determine the abundance of phyllosilicates relative to anhydrous silicates and scales from petrologic type 1.0 (phyllosilicate fraction >95 vol.%; most altered) to 3.0 (phyllosilicate fraction <5 vol.%; least altered).

Table 1.1. Principal diagnostic characteristics of progressive alteration of CM chondrite petrologic subtypes 2.0-2.7. Table and captions from Rubin (2015)**.**

Petrologic subtype	2.7	2.6	2.5	2.4	2.3	2.2	2.1	2.0
Chondrule mesostases	Phyllosilicate	Phyllosilicate	Phyllosilicate	Phyllosilicate	Phyllosilicate	Phyllosilicate	Phyllosilicate	Phyllosilicate
Matrix phyllosilicates	Abundant	Abundant	Abundant	Abundant	Abundant	Abundant	Abundant	Abundant
Matrix composition: MgO/"FeO"	0.35-0.43	0.35-0.43	0.35-0.43	0.35-0.43	0.50-0.70	0.50-0.70	0.50-0.70	0.50-0.70
Matrix composition: S/SiO_2	0.10-0.18	0.10-0.18	0.10-0.16	0.10-0.16	0.07-0.08	0.07-0.08	0.05-0.07	0.05-0.07
Metallic Fe-Ni (vol.%)	1-2	~1	0.03-0.30	0.03-0.30	0.03-0.30	0.03-0.30	≤0.02	≤0.02
Mafic silicate phenocrysts in chondrules	Unaltered	Unaltered	Unaltered	Unaltered	2-15% altered	15-85% altered	85-99% altered	Completely altered
Large TCI clumps (vol.%)	5-20	15-40	15-40	15-40	15-40	15-40	2-5	2-5
TCI composition: "FeO"/SiO2	4.0-7.0	2.0-3.3	2.0-3.3	1.5-2.0	1.5-2.0	1.0-1.7	1.0-1.7	1.0-1.7
TCI composition: S/SiO_2	0.40-0.60	0.18-0.35	0.18-0.35	0.14-0.20	0.14-0.20	0.05-0.09	0.05-0.09	0.05-0.09
Sulphide	po + pn	Mainly po + pn	Mainly po + pn	po + pn + int	po + pn + int	Mainly pn + int	Mainly pn + int	Mainly pn + int
Carbonate	Ca carbonate	Ca carbonate	Ca carbonate	Ca carbonate	Ca carbonate	Ca carbonate	Ca carbonate and complex carbonate	Ca carbonate and complex carbonate

"FeO" includes FeO in mafic silicates, oxides, and phyllosilicates, Fe^{3+} in cronstedtite and magnetite, Fe^{2+} in sulfides, and small grains of metallic Fe all recalculated as FeO. Subtype 2.6 is distinguishable from 2.5 on the basis of metallic Fe-Ni abundance; subtype 2.1 is distinguishable from 2.0 on the basis of containing rare but identifiable mafic silicate phenocrysts in chondrules.

Table 1.2. Petrologic subtypes of CM chondrites, adding CM2.8-3.0. Truncated table and caption from Kimura et al. (2020).

Petrologic subtype	3.0	2.9	2.8
Chondrule mesostases	Primary meso Rare Phyllo	Primary meso ≈ Phyllo	Phyllo > Primary meso
Matrix phyllosilicates	Rare or no	Rare	Minor
Matrix composition: MgO/"feo"	>0.5	>0.5	>0.5
Matrix composition: S/SiO2	>0.1	>0.1	>0.1
Metallic Fe-Ni (vol.%)	>2	1-2	1-2
Phenocrysts in chondrules	Unaltered	Unaltered	Unaltered
Large TCI clumps (vol.%)	No TCI	No TCI	Minor
TCI composition: "FeO"/SiO2	-	-	-
TCI composition: S/SiO2	-	-	-
Sulphide	Tro > po + pn	Tro > po + pn	Tro > po + pn
Carbonate	No or rare carbonate	No or rare carbonate	Minor

Primary meso: primary feldspar and glass, tro: troilite, po: pyrrhotite, pn: pentlandite, int: sulfide grains with ''intermediate'' Ni/(Fe + Ni) ratios Subtypes 2.7–2.0 are after Rubin (2015).

1.1.4 Calcium-Aluminium rich Inclusions

1.1.4.1 Origin and Composition

CAIs are amongst the oldest solids to have formed within the Solar System (4567.3±0.16 Ma;Amelin et al., 2010; Connelly et al., 2017). They are thought to have formed through condensation of a gas of near-solar composition from within the hot inner protoplanetary disk (>1300 K; (Chaussidon et al., 2006; Gounelle et al., 2013; Krot, 2019; Mckeegan et al., 2000; Mishra and Marhas, 2019; Sossi et al., 2017; Wielandt et al., 2012), over a period of approximately 40,000–400,000 yrs (Kawasaki et al., 2020). They are generally small (μm-cm) and irregular in shape (MacPherson, 2013). They are mostly composed of high-temperature (refractory) minerals, such as spinel ($MgAl_2O_4$), Al-Ti-rich pyroxene ($Ca(Mg,Al,Ti)(Si,Al)_2O_6$), corundum (Al_2O_3), hibonite ($CaAl_{12}O_{19}$), perovskite

($CaTiO_3$), forsterite (Mg_2SiO_4), and melilite ($Ca_2(Al,Mg,Fe)(Al,Si)SiO_7$) (Dunham et al., 2023).

Although melilite is common in unaltered carbonaceous chondrites from other groups, it is a very rare phase in CM CAIs (Armstrong et al., 1982; Fuchs et al., 1973; Greenwood et al., 1994; Macdougall, 1979; Macpherson and Davis, 1994a), and has been thought to have been replaced or destroyed by parent body aqueous alteration processes (Armstrong et al., 1982; Bunch and Chang, 1980; Johnson and Prinz, 1993; Lee and Greenwood, 1994). Studying these refractory inclusions can provide evidence of the earliest thermal and chemical processing, such as CM parent body aqueous alteration processes.

1.1.4.2 Transport Models

CAIs have been observed in both inner (ordinary, enstatite, and Rumuruti chondrites; Kallemeyn and Wasson, 1986) and outer Solar System (carbonaceous chondrites; Kallemeyn and Wasson, 1981) planetesimals. They are thought to have accreted within the asteroidal parent bodies 2.8-4 Ma after their formation (Cournede et al., 2015; Desch et al., 2018; Fujiya et al., 2012; Huss et al., 2001; Sugiura and Fujiya, 2014). This implies that, following their formation near the Sun, CAIs migrated towards the outskirts of the protoplanetary disk.

Although several models have been proposed to explain this transport, only the two most well-established and widely discussed are considered for the purposes of this thesis: (i) turbulent radial diffusion through the protoplanetary disk midplane (diffusion model; e.g. Macpherson et al., 2005; Yang and Ciesla, 2012), and (ii) outward ballistic transport via magnetocentrifugal X-winds above and over the protoplanetary disk plane (X-wind model; e.g. Haugbølle et al., 2019; Shu et al., 1996). These models offer two distinct and testable frameworks for understanding how refractory inclusions were redistributed throughout the protoplanetary disk prior to their incorporation into their respective parent bodies.

1.2 Aims and Objectives

The formation and evolution of water-rich asteroids is of great interest in the search for the origin of Earth's water. CM (Mighei-like) chondrites are among the most common carbonaceous meteorites available and are prime candidates for studying such asteroids. However, their origins and evolution remain poorly understood. Refractory inclusions, such as Calcium-Aluminium-rich Inclusions are the first solids to have formed in the Solar System (4567.3±0.16 Ma; Amelin et al., 2010; Connelly et al., 2017) and have accreted early onto the CM parent body(-ies) (2.8-4 Ma after CAI formation; Cournede et al., 2015; Desch et al., 2018; Fujiya et al., 2012; Huss et al., 2001; Sugiura and Fujiya, 2014), and thus have witnessed the extent of parent body alteration processes (4±2 Ma after CAI formation; (Fujiya et al., 2012; Visser et al., 2020).

Therefore, in order to comprehend the usefulness of CAIs in providing information regarding the origin and evolution of water-rich asteroids, it is necessary to answer these fundamental questions: (1) what was the initial CAI abundance in CM chondrites, (2) how did aqueous alteration affect CAIs, (3) were the CM CAIs distributed homogeneously, and (4) what happened to CAIs prior to their incorporation within the CM parent body?

The questions were grouped into three main axes of investigation: (1) a large-scale report on CAIs within CM chondrites in order to identify any relationship between CAI mineralogy, morphology, abundance, and the degree of aqueous alteration of their host CM lithologies; (2) a case study of the altered CAIs within the Winchcombe meteorite which comprises 12 differentially aqueously altered lithologies, revealing heterogeneities within altered CAI populations within a single meteorite; and (3) the oxygen isotope and crystallographic characterisation of rare Compound-Chondrule-CAIs, which can provide constraints regarding the pre-accretionary histories of CM CAIs.

These investigations are presented in chapters 2, 3, and 4.

1.3 Overview of Chapters

1.3.1 Chapter 2

The focus of this chapter is on reporting CAI mineralogy, morphology, and abundance across a wide range of aqueously altered CM lithologies. This chapter also discusses methods for measuring mean apparent CAI size and area and calculating CAI modal abundance in comparison to existing literature data. Results reveal a homogeneous distribution of CAI types throughout CM chondrites and a clear link between CAI modal abundance and the degree of aqueous alteration of their host CM lithologies.

1.3.2 Chapter 3

This chapter provides insight into fluid-driven parent body alteration processes by investigating the aqueously altered lithologies of the Winchcombe meteorite. In addition, the unusual mineralogy of an altered CAI was investigated using advanced geochemical and crystallographic characterisation techniques in order to characterise and differentiate pre- and post-accretionary mineralisation histories. Results indicate that CM chondrites can host different CAI populations which have experienced significantly different aqueous alteration histories.

1.3.3 Chapter 4

This chapter presents a study on the origin and formation of rare assemblages, designated as Compound-Chondrule-CAIs (CCCAIs), among the CM CAI populations. This study involves the geochemical and crystallographic characterisation of the microstructure of a CCCAI, in an effort to identify potential nucleation patterns for the formation of porphyritic textures within chondrules, and oxygen isotope measurements in order to determine the origin of each component of the CCCAIs in relation to the rest of the CM CAIs and CM chondrules of the investigated samples. Results include a proposed model for the origin and formation of CCCAIs prior to its incorporation within the CM parent body.

1.4 Methodology and Samples

1.4.1 Scanning Electron Microscopy

1.4.1.1 Overview

Scanning Electron Microscopy (SEM) was used throughout this thesis to produce high-resolution images of the sample surfaces. This technique relies on the interaction of a focused electron beam (0.1-30 keV; Goldstein, 2012; Zhou et al., 2007), generated by an electron gun, and the surface of an area of interest within the sample. The beam is focused using a series of lenses and apertures down to a small diameter (≤10 nm; Goldstein, 2012; Zhou et al., 2007). At the point of impact at the surface of the sample, several types of electrons (backscattered, secondary, and auger), X-rays, and cathodoluminescence photons are generated. This allows for specific detectors to be added to an SEM to provide a more specialised role and enable multi-component analyses, such as Electron Dispersive X-ray Spectroscopy (EDS; cf. section 1.4.2). During analysis, samples are kept in a vacuum-sealed holding chamber to avoid collisions between returning electrons and atmospheric molecules, which could result in signal disruption (Goldstein, 2017).

Most SEMs have two detectors: a Back-Scatter Electron (BSE) detector and a Secondary Electron (SE) detector. As the primary electrons from the electron gun penetrate the surface of the sample and lose energy, they are scattered because of the positive attraction of an atom's nucleus deflecting their path. Those scattered back towards the detector are called backscattered. The higher the energy, the fewer the electrons are absorbed within the sample. SEs are electrons liberated from their atomic structure through ionisation by the incident electrons. These produced electrons are of lower energy (3-5 eV; Goldstein, 2012; Zhou et al., 2007) and can therefore only provide surface-level information (~nm penetration), which is useful for high-resolution topographic imaging. In contrast, BSEs tend to have of higher energies (>50 eV) and are used to provide mean atomic number contrast maps. SEM images are produced in greyscale at magnifications up to 300,000 ×, allowing for the characterisation

and analysis of nanometre to micrometre scale objects and features within a sample.

1.4.1.2 Sample Preparation

Samples, comprising of thin sections and polished blocks, were polished using a Buehler Beta Grinder-Polisher. Polishing was done using a 1 μm Al polishing pad initially, followed by the use of a 0.3 μm Al pad, and lubricated using a solution of Al-glycol. The samples were then coated with 20 nm of carbon using a Quorum Q150T ES turbomolecular pumped coater (carbon dispersal from sharpened carbon rods under high vacuum). The quality of the data depends greatly on the quality of the polishing, as well as of the coating, which minimises the charging of the surface of the sample by electrically grounding it to prevent image disruption (due to electrons being deflected).

1.4.1.3 Data Collection and Processing

Unless specified otherwise in the following chapters, all SEM-related datasets were produced using a Carl Zeiss Sigma Variable Pressure field emission gun SEM, operated at 20 kV with a beam current of 1-2 nA at the Geoanalytical Electron Microscopy (GEM) laboratory at the UofG. Data were processed using the AZtec software, either version 5.1 or 6.0, by Oxford Instruments. BSE and SE Images were collected either as single fields, or as series of frames. Maps were generated using the 'auto-montage' feature (with 10% overlap) from the AZtec software and were then manually adjusted.

1.4.2 Energy Dispersive X-ray Spectroscopy

1.4.2.1 Overview

Energy Dispersive X-ray Spectroscopy (EDS) can provide semi-quantitative elemental compositional data of the sample surfaces to supplement the petrographic data provided by BSE imaging. When added to an SEM, an EDS detector can collect X-rays generated from the interaction between the incident electron beam and the surface of the sample (up to ~1 μm penetration). During this process, an incident electron liberates an inner-shell electron from an atom.

The vacancy left in the electron shell is then filled by one of the atom's outer-shell electrons (moving from a higher energy level to a lower energy level). This leads to the emission of an X-ray photon to accommodate for the energy loss. The intensity and wavelength of the generated X-ray depend directly on the element from which it originates. The collected X-rays are displayed as peaks along a spectrum which can then be used to identify existing elements. Quantitative data analysis may also be achieved by calibrating the intensities of the detected X-rays using known standards (Goldstein, 2017).

1.4.2.2 Data Collection and Processing

Unless specified otherwise in the following chapters, all EDS data were acquired using the aforementioned Carl Zeiss Sigma SEM equipped with an 80 mm^2 silicon-drift detector. Sample-wide EDS maps were montaged using the same process as for BSE maps (cf. section 1.4.1.3).

1.4.3 Electron Probe Micro-Analysis

1.4.3.1 Overview

Similar to EDS, Electron Probe Micro-Analysis (EPMA) uses X-rays produced through the interaction with the surface of the sample using an electron beam to determine the chemical composition of a targeted spot (or area when rastering). Specific wavelengths of X-rays corresponding to specific elements are reflected using a curved crystal (e.g. LLIF, TAP) towards a detector and measured separately (contrary to EDS, during which all X-rays are measured at the same time). This method, known as Wavelength-Dispersive X-ray Spectrometry (WDS), is considered more precise than EDS (Reed, 1995).

1.4.3.2 Data Collection and Processing

EPMA data were collected to characterise the compositions of the mineral phases of altered Calcium-Aluminium-rich Inclusions (CAIs) in the Winchcombe meteorite (cf. Chapter 3). The targeted minerals included grossmanite (Ti-rich clinopyroxene; 8 spots), perovskite (10 spots), and spinel (15 spots). These analyses were conducted using a JEOL JXA-8530F electron probe micro-analysis

instrument operated at 10 kV and a beam current of 20 nA in focused beam mode with a 1 μm spot size at the National History Museum (NHM, U.K.). The elemental abundances were determined using Kα lines. The following standards were used for Wavelength Dispersive X-ray Spectrometry (WDS) analysis: fayalite (Si), corundum (Al), wollastonite (Ca), rutile (Ti), forsterite (Mg), vanadinite (V), haematite (Fe), chromium oxide (Cr), nickel oxide (Ni), and jadeite (Na). Detection limits were calculated to be around 100 ppm (SD x 3) for the acquisitions. Only oxide totals comprised within 97 and 102 wt.% were retained for each spot analysis.

1.4.4 Electron Backscatter Diffraction

1.4.4.1 Overview

The technique known as Electron Back-Scatter Diffraction (EBSD) relies on backscattered electrons being diffracted by the crystal lattice of a targeted mineral, to provide crystallographic information regarding the sample. These backscattered electrons are diffracted as cones and project patterns onto a phosphorous screen. These patterns of intersecting bands are known as 'Kikuchi patterns' (Schwarzer et al., 2009), and the bands themselves are referred to as 'Kikuchi bands'. The spacing of the intersections, positions, thicknesses, angles, and intersections of the bands are measured and compared to a Kikuchi pattern database. The software then identifies the best fit for the targeted crystalline structure and extracts its crystallographic information, including phase, grain properties, crystallographic orientation, and deformation features. Therefore, maps of specific areas of interest can be produced from these datasets, displaying mineral phases, Inverse Pole Figures (IPF), Grain Relative Orientation Deviation (GROD) angles, and Kernel Average Misorientation (KAM) angles (cf. Chapter 4). The sample must be tilted at a 70° angle to the incident electron beam (Prior et al., 1999) in order to maximise the strength and quality of the BSE signal to obtain a clear Kikuchi pattern.

1.4.4.2 Sample Preparation

EBSD analysis requires the surface of the sample to be uniformly flat (Halfpenny, 2010; Prior et al., 2009), and thus finer polishing than that required for BSE or SE imaging. A flat surface optimises electron entry and backscatter return angles (Halfpenny et al., 2012). However, CM chondrites have low density, porosity, and a tendency to disaggregate when in contact with water (Suttle et al., 2021). Hence, a new working protocol for polishing water-sensitive extraterrestrial materials for EBSD was developed to avoid destroying the samples while increasing the quality of the data collected. This protocol was developed based on my own experience as well as from Drs. Luke Daly and Sammy Griffin (UofG) and has been shared with researchers at the University of Cambridge and the Open University. This protocol is presented in the form of a checklist in Appendix 7.1. The terminology used refers to the polishing equipment available at the time at the UofG. Interestingly enough, despite the need to avoid water, a minimal amount is still required for rinsing. It is important to note that ethanol should not be used as it forms crystals when in contact with colloidal silica (used for polishing), which are difficult to remove and contaminate the surface of the sample. The samples were then coated with 7 nm of carbon following the procedure described in section 1.4.1.2.

1.4.4.3 Data Collection and Processing

Unless specified otherwise in the following chapters, all EBSD data were acquired using the aforementioned Carl Zeiss Sigma SEM equipped with a NordlysMax2 EBSD detector operated at 20 kV with a 70° sample tilt. Data were collected using the AZtec (v5.1 or v6) software and processed using AZtec Crystal (v2.1) from Oxford Instruments.

1.4.5 Transmission Electron Microscopy

1.4.5.1 Overview

Transmission Electron Microscopy (TEM) relies on a focused beam of accelerated electrons to be transmitted through a sample using electric and magnetic fields. The high-velocity (~200 kV) electrons diffract in a crystalline

material, providing invaluable information regarding the sample's crystallography and mineral orientation (Egerton, 2016). In order to allow for the transmission of electrons, the sample must be thinned to 'electron transparency' (~100 nm; Williams and Carter, 2009). The transmitted electrons are measured using a detector (e.g. semiconductor or scintillator) placed on the opposite side of the sample with respect to the incident electron beam. Diffraction patterns and contrast images can then be produced by controlling the angles of incoming electrons using an objective aperture placed between the sample and detector (Egerton, 2016; Williams and Carter, 2009). This technique was used to generate diffraction contrast images (i.e. bright-field and dark-field) and Selected-Area Electron Diffraction (SAED) patterns.

Bright-field images are produced when the objective aperture (placed directly on the path of the incident electron beam) captures only the most diffracted electrons, while allowing the less diffracted electrons to reach the detector. The generated image displays dark areas, corresponding to highly diffracting crystals, and bright areas, corresponding to amorphous materials (no diffraction) or poorly diffracting crystals. In the case of dark-field images, the objective aperture is placed such that only the most diffracted electrons reach the detector. In these images, highly diffracting crystals appear brighter, whereas amorphous or less diffracting crystals appear darker(Egerton, 2016).

SAED patterns are produced through the introduction of a selected-area aperture, which reduces the analysed area. SAED patterns display an array of spots, each corresponding to electrons diffracted by lattice planes with a specific spacing and orientation. Measurements of these spots can help deduce crystallographic properties, such as the unit cell of a crystal, d-spacing, Miller indices, and axis lengths (Egerton, 2016).

1.4.5.2 Sample Preparation

Preparation of the electron-transparent lamellae was done at the Kelvin Nanocharacterisation Centre (KNC) at the UofG, using a DualBeam Focused Ion Beam (FIB) microscope equipped with a Ga^+ Sidewinder ion column operated at 30 kV. Two areas of interest from a CAI in Winchcombe were coated with a 1

µm-thick layer of Pt (for protection during milling; cf. Chapter 3). The areas were then extracted through milling of the adjacent regions using the FIB, before being welded to a copper support with an in-situ micromanipulator, using Pt and a gas injection system. The lamellae were then milled further down to a thickness of ~100 nm.

1.4.5.3 Data Collection and Processing

Diffraction-contrast images and SAED patterns were collected at the KNC using an FEI T20 TEM operated at 200 kV with the lamellae loaded on a double-tilt goniometer holder.

1.4.6 Transmission Kikuchi Diffraction

1.4.6.1 Overview

Also known as Transmission Electron Backscatter Diffraction (t-EBSD), Transmission Kikuchi Diffraction (TKD) allows for the elemental and crystallographic mapping of a TEM lamella in an SEM on a nanometric scale (cf. Chapter 3). While similar to EBSD, as suggested by its alias, it is capable of achieving a much higher spatial resolution (5–10 nm; Trimby, 2012; Trimby et al., 2014). This higher resolution is the result of TKD having a smaller interaction volume between the scattered electrons and the sample (Sneddon et al., 2016). Diffraction patterns obtained from TKD remain very similar and offer angular resolutions comparable to EBSD, and thus, can be used to produce lamella-wide phase, GROD angle, IPF, and Local Average Misorientation (LAM) maps.

1.4.6.2 Data Collection and Processing

The two TEM lamellae extracted from a CAI in Winchcombe were analysed during three different sessions using a Zeiss Sigma Variable Pressure Analytical SEM operated at 20 kV with a beam current of 1-2 nA, equipped with an S2 Symmetry Electron Backscatter Diffraction (EBSD) detector at a 70° sample tilt at the GEMS centre at UofG. Data were collected using the AZtec (v6) software and processed using AZtec Crystal (v2.1) from Oxford Instruments. Grain boundaries were defined by >10° misorientation, and wild spikes, pseudo-

symmetries, and the most anomalous and mis-indexed data points were manually removed. Zero solution removal was then applied (up to six neighbours). Further details regarding the processing and cleaning of the data are provided in Chapter 3.

1.4.7 Secondary Ion Mass Spectrometry

1.4.7.1 Overview

Secondary Ion Mass Spectrometry (SIMS) enables in-situ measurements of isotopic ratios of small or chemically zoned samples at a micrometric scale (Bouden et al., 2021). Secondary ions are produced by sputtering the surface of a solid sample using a focused primary ion beam (e.g. Cs^+ gas source) from an ion gun (Ireland, 2004). The ejected ions are then accelerated into a mass analyser. The mass/charge ratios of these secondary ions are measured in terms of 'counts', which are obtained through the use of Electron Multipliers (EMs) and Faraday Cups (FC). Whenever secondary ions enter these detectors, they produce a current which is then converted into voltage and recorded (Bouden et al., 2021). The results are expressed in the form of relative count ratios normalised to an analysed standard of known composition (e.g. San Carlos Olivine, Ipanko spinel). Samples are kept in a high-vacuum ($<10^{-4}$ Pa) holding chamber to avoid collisions between secondary ions and atmospheric molecules during analysis, as well as sample surface contamination by the adsorption of atmospheric gases.

In the case of oxygen, three isotopes are measured, ^{16}O, ^{17}O, and ^{18}O, and the following ions are produced: $^{16}O^-$, $^{17}O^-$, and $^{18}O^-$. All O isotopic ratios are expressed in 'delta' notation in relation to the measured ^{16}O counts (cf. Chapter 4). Potential issues during acquisition include isobaric interference (as ^{16}OH and ^{17}O share a similar mass), unconstrained Instrumental Mass Fractionation (IMF; isotopic fractionation occurring between ionisation and analysis), and instrumental drift (constrained though regular analysis of standards). One of the disadvantages of such a complex instrument is the damage that the primary beam can inflict on the surface of the sample (holes ~15 µm in diameter and 1

µm deep), requiring meticulous planning. More details regarding error calculations and processing of the measurements are available in Chapter 4.

1.4.7.2 Sample Preparation

SIMS requires a thin coat (~10 nm) to function properly, and as the samples were previously imaged for target selection using SEM, their previous carbon coat (~20 nm) had to be removed to ensure a precise thickness. Samples were then re-coated in either gold or carbon (10 nm) at the Centre de Recherches Pétrographiques et Géochimiques (CRPG-CNRS, Nancy, France). This allows for better surface conductivity to minimise surface charging effects and optimise image quality during target selection. The nature of the coating (Au or C) has negligible impact on SIMS data acquisition as the coating is sputtered away by the beam at the specified targeted spot before the start of the analysis. The pits resulting from the SIMS analyses are visible in BSE and SE images in Appendix 7.9.

1.4.7.3 Data Collection and Processing

All oxygen isotope compositions were measured using the Cameca IMS 1270 E7 ion microprobe (Bouden et al., 2021) at the Centre de Recherches Pétrographiques et Géochimiques (CRPG-CNRS, Nancy, France) with the help of the Ion Probe Nancy Team (IPNT; TA Facility 9) through the Europlanet2024 Research Infrastructure. A total of 244 successful measurements were acquired for the following target minerals: spinel (99 spots), olivine (139 spots), and diopside (6 spots). More details regarding the acquisition parameters are provided in Chapter 4.

1.4.8 Meteorite samples

This thesis comprises the study of 21 samples from six different CM chondrites (cf. Table 1.3). These meteorites represent a wide range of petrologic subtypes (CM2.0 to CM2.9), as defined by Rubin (2015) and Rubin et al. (2007) and Kimura et al. (2020), to investigate the impact of aqueous alteration on the different CAI populations within CM chondrites.

All investigated samples were identified as breccias. Aguas Zarcas and Winchcombe both display a wide range of aqueously altered lithologies (Kerraouch et al., 2021; Suttle et al., 2024), allowing the investigation of intra-sample heterogeneity as well as the effects of extensive aqueous alteration. D'Angelo Bluff (DNG) 06004 (CM2.4) and LaPaz Icefield (LAP) 02239 (CM2.4-2.5) are both mildly altered CM chondrites which can help visualise transitional patterns and features across the aqueous alteration spectrum. Paris (CM2.7-2.9) and Asuka (A) 12236 (CM2.9) are among the most pristine CM chondrites available for analysis at the time of writing, providing one of the best initial points of reference.

Table 1.3. List of meteorite samples studied in this thesis and their petrological types.

Meteorites	Section ID	Accession number	Petrologic type[a]	Petrologic subtype[b]
A 12236[1]	-	-	-	2.9[c]
Aguas Zarcas[2]	AZ-P1	-	-	
	AZ-P2	-	-	
	AZ-01	-	-	2.2-2.8[d]
	AZ-02	-	-	
	AZ-03	-	-	
DNG 06004[3]	06004,20	-	1.7[e]	2.4[f]
LAP 02239[3]	02239,5	-	1.5[e]	2.4-2.5[g]
Paris[4]	B1.5	-	-	2.7-2.9[h]
Winchcombe[5]	P30423	BM.2022,M1-87		2.2-2.3[j]
	P30424	BM.2022,M3-29		2.1[j]
	P30540	BM.2022,M2-42		2.0-2.1[j]
	P30541	BM.2022,M2-43		2.6[j]
	P30542	BM.2022,M2-44		2.1[j]
	P30545	BM.2022,M2-47	1.1-1.2[i]	2.1[j]
	P30546	BM.2022,M1-103		2.1[j]
	P30547	BM.2022,M1-104		2.1[j]
	P30548	BM.2022,M1-105		2.3[j]
	P30549	BM.2022,M1-106		-
	P30552	BM.2022,M9-14		2.2[j]
	P30555	BM.2022,M9-17		2.2[j]

[1]BSE and EDS data provided by Dr. Y. Marrocchi (Université de Lorraine, Centre National de Recherche Scientifique, Centre de Recherches Pétrographiques et Géochimiques), more details on the sample in Marrocchi et al. (2023). [3]US Antarctic Meteorite Collection. [4]Museum National d'Histoire Naturelle de Paris. [5]Natural History Museum (NHM, U.K.). [a]According to the classification scheme proposed by Howard et al. (2015). [b]According to the classification scheme defined by by Rubin (2015) and Rubin et al. (2007) and Kimura et al. (2020). [c]Kimura et al. (2020). [d]Kerraouch et al. (2021). [e]Howard et al. (2015). [f]Hanna et al. (2020). [g]Lee et al. (2023). [h](Rubin, 2015). [i]King et al. (2022). [j]Suttle et al. (2024).

2 The Relationship Between CAI Modal Abundances and the Degree of Aqueous Alteration of CM Chondrites

2.1 Introduction

CM (Mighei-like) chondrites are amongst the most common carbonaceous meteorite samples and have a relatively high-water content (~9 wt.%; Jaresowich, 1990). They also display a wide range of degrees of aqueous alteration which can vary amongst clasts. Such alteration is thought to have stemmed from a heating event which would have also released frozen water within the CM parent body(-ies) (Barber, 1981; Bunch and Chang, 1980; Huss et al., 2001; McSween, 1979; Rubin, 2015; Rubin et al., 2007; Tomeoka and Buseck, 1985; Trigo-Rodriguez et al., 2006; Zolensky et al., 1993, 1997). The progressive alteration of CM lithologies by these fluid-driven alteration events can be quantified using the classification scheme defined by (Rubin et al., 2007) and expanded in (Rubin, 2015) and (Kimura et al., 2020), which is used throughout this study. Therefore, it is of utmost importance to appreciate the diversity of alteration histories these meteorites might have experienced in order to properly measure, analyse, and evaluate the different populations of components forming CM chondrites.

Components such as Calcium-Aluminium-rich Inclusions (CAIs) are invaluable for understanding the origin and evolution of the early Solar System as they are amongst the oldest solids to have formed within it (4567.3±0.16 Ma;Amelin et al., 2010; Connelly et al., 2017), and thus, can record the alteration events that might have affected, in this case, the CM parent body(-ies). However, despite all previous studies accounting for the diversity and abundance of CAIs, their distribution and concentration throughout CM chondritic lithologies remains poorly constrained. Furthermore, most CM chondrites are polymict breccias (Metzler et al., 1992; Bischoff et al., 2006; Nakamura, 2006; Lindgren et al., 2013; Lentfort et al., 2020; Suttle et al., 2021) and previous studies have not taken their heterogeneous nature into account. Studies such as Hezel et al. (2008) show the difficulty in reporting accurate CAI

modal abundances without sufficient material. Several older CAI classification schemes have been based off CAIs found within CV (Vigarano-like) carbonaceous chondrites and are ill-adapted to CM chondritic lithologies, due to the distinct alteration and thermal histories of their host meteorites. Thus, CAIs from three different CMs were classified using a nomenclature adapted from McPherson & Davis (1994) which focuses on the mineralogical and textural variance within and between the identified CAIs. An effort was made to make this method replicable, accessible, and efficient enough to apply to large quantities of CAIs in a timely manner. This study comprises measuring, characterisation, and description of the diversity of the CAI populations across multiple CM lithologies with different degrees of aqueous alteration from four CM chondrites and was combined with literature data from six additional CM chondrites. Results indicate a clear link between the CAI modal abundance and the degree of aqueous alteration of their host CM lithologies.

Preliminary results from this study were reported in Martin et al. (2023a and 2023c) and the classification and petrographic descriptions of the CAIs from the LaPaz Icefield 02239 meteorite can be found in the supplementary materials of Lee et al. (2023).

2.2 Material and Methods

2.2.1 Samples

CAIs were located and measured within the following meteorites: Asuka 12236 (designated as A 12236 hereafter), D'Angelo Bluff 06004 (designated as DNG 06004 hereafter), LaPaz Icefield 02239 (designated as LAP 02239 hereafter), Paris, and Winchcombe. Details concerning these samples are reported in Table 2.1, including their degree of aqueous alteration, quantified by two different classifications, hereafter designated as Rubin's classification scheme (Rubin et al., 2007; Rubin, 2015; Kimura et al., 2020) and Howard's classification scheme (Howard et al., 2015).

Table 2.1. List of meteorite samples investigated and their reported petrologic type and subtype.

Meteorites	Section ID	Accession number	Sample type	Petrologic type[a]	Petrologic subtype[b]
A 12236[1]	-	-	Thin section	-	2.9[c]
DNG 06004[2]	06004,20	-	Polished block	1.7[d]	2.4[e]
LAP 02239[2]	02239,5	-	Polished block	1.5[d]	2.4-2.5[f]
Paris[3]	B1.5	-	Polished block	-	2.7-2.9[g]
Winchcombe[4]	P30423	BM.2022,M1-87	Polished block	1.1-1.2[h]	2.2-2.3[i]
	P30424	BM.2022,M3-29	Polished block		2.1[i]
	P30540	BM.2022,M2-42	Polished block		2.0-2.1[i]
	P30541	BM.2022,M2-43	Polished block		2.6[i]
	P30542	BM.2022,M2-44	Polished block		2.1[i]
	P30545	BM.2022,M2-47	Polished block		2.1[i]
	P30546	BM.2022,M1-103	Polished block		2.1[i]
	P30547	BM.2022,M1-104	Polished block		2.1[i]
	P30548	BM.2022,M1-105	Polished block		2.3[i]
	P30549	BM.2022,M1-106	Polished block		-
	P30552	BM.2022,M9-14	Polished block		2.2[i]
	P30555	BM.2022,M9-17	Polished block		2.2[i]

[1]BSE and EDS data provided by Dr. Y. Marrocchi (Université de Lorraine, Centre National de Recherche Scientifique, Centre de Recherches Pétrographiques et Géochimiques), more details on the sample in Marrocchi et al. (2023). [2]US Antarctic Meteorite Collection. [3]Museum National d'Histoire Naturelle de Paris. [4]Natural History Museum (NHM, U.K.). [a]According to the classification scheme defined by Howard et al. (2015). [b]According to the classification scheme defined by Rubin et al. (2007) and expanded in Rubin (2015) and Kimura et al. (2020). [c]Kimura et al. (2020). [d]Howard et al. (2015). [e]Hanna et al. (2020). [f]Lee et al. (2023). [g]Rubin et al. (2015). [h]King et al. (2022). [i]Suttle et al. (2024)

The petrologic subtype of each sample analysed within this study was determined using SEM and EDS using Rubin's classification scheme (Rubin et al., 2007; Rubin, 2015; Kimura et al., 2020). Samples evidencing areas (e.g. clasts or lithologies) of differing degrees of aqueous alteration were classified individually. Only CM2.7 lithologies (most altered in Paris; Rubin, 2015) were identified within the sample of the Paris meteorite and it will therefore be referred to as a CM2.7. Each of the polished sections of the brecciated Winchcombe meteorite comprise one or multiple of specific lithologies (A-G) attributed by Suttle et al. (2024), which are further detailed in Chapter 3. For the purposes of this study, the lithologies of the Winchcombe meteorite will be referred to as their denomination (A-G; Suttle et al., 2024) and not by their NHM

section ID. CAIs not found within classifiable aqueously altered CM lithologies, such as the cataclastic matrix (Mx; Suttle et al., 2024; cf. Chapter 3) and fusion crust (FC; Suttle et al., 2024; cf. Chapter 4) of Winchcombe and the xenolith from LAP 02239 (Lee et al., 2023), were excluded from this study.

2.2.2 Electron Microscopy

CAIs were identified using large area Energy Dispersive X-ray Spectroscopy (EDS) maps and Backscattered Electron (BSE) images, collected using a Carl Zeiss Sigma Variable Pressure field emission gun analytical Scanning Electron Microscope (SEM) with an accelerating voltage of 20 keV and a 1-2 nA primary beam current at the Geoanalytical Electron Microscopy & Spectroscopy centre (GEMS) at the University of Glasgow (UofG). Sample preparation comprised fine polishing and carbon coating of ~20 nm thickness. All data were collected and processed using the AZtec v6 software from Oxford Instruments. BSE and EDS sample-wide maps of a thin section of A 12236 were provided by Dr. Y. Marrocchi (CRPG-CNRS). They were obtained originally using a JEOL JSM-6510 equipped with an EDX Genesis X-ray detector using a 3 nA primary beam accelerated at 15 kV (Marrocchi et al., 2023) at the CRPG (Nancy, France). The resolutions and pixel sizes of all montaged mosaic images used in this study are listed in Table 2.2.

Table 2.2. List of meteorite samples mapped using EDS with their image mosaic resolution and pixel size.

Meteorites	Section ID	Accession #	Resolution (pixel)	Pixel size (µm)
A 12236[1]	-	-	3434 x 4520	1.29310
DNG 06004	06004,20	-	7055 x 5553	1.50150
LAP 02239	02239,5	-	6986 x 5727	1.83234
Paris	B1.5	-	7076 x 7874	2.32371
Winchcombe	P30423	BM.2022,M1-87	8553 x 6355	1.10375
	P30424	BM.2022,M3-29	8558 x 5690	0.54885
	P30540	BM.2022,M2-42	6666 x 6564	0.60241
	P30541	BM.2022,M2-43	6508 x 5216	0.75188
	P30542	BM.2022,M2-44	9398 x 5856	0.50050
	P30545	BM.2022,M2-47	7687 x 6510	0.75188
	P30546	BM.2022,M1-103	5922 x 5450	0.75188
	P30547	BM.2022,M1-104	7423 x 6031	0.75188
	P30548	BM.2022,M1-105	8218 x 6634	0.50050
	P30549	BM.2022,M1-106	7809 x 5279	0.75188
	P30552	BM.2022,M9-14	5969 x 7987	0.60241
	P30555	BM.2022,M9-17	8608 x 6640	0.50050

[1]BSE and EDS data provided by Dr. Y. Marrocchi (Université de Lorraine, CNRS, CRPG), more details on the sample in Marrocchi et al. (2023)

2.2.3 CAI Identification

Sample-wide layered RGB colour-coded elemental maps combining Mg (red), Ca (green), and Al (blue) Kα X-ray lines with BSE images were produced in order to generate identifiable Ca-Al-Mg-rich irregularly shaped pixel clusters, potentially corresponding to CAIs through visually scanning at high magnification. CAI candidates were marked across three consecutive passes, and EDS point and area analyses were used to confirm the refractory nature of the targets. An estimation of the potential human error during this process is detailed in section 2.3.2.3. The polishing procedure involved using an Al-rich powder (corundum), which has been observed to accumulate in the fractures and small pores of the polished resin blocks and are visible as deep blue clumps within EDS maps. These features are considered artifacts and were disregarded. The high-spatial resolution (0.50-2.3 µm/pixel; cf. Table 2.2) of the obtained

BSE and EDS maps allowed for identification of CAIs as small as 5 μm in apparent length.

Amoeboid olivine aggregates (AOAs) and Al-Rich Chondrules (ARCs) were excluded from this study due to them having different thermal histories and susceptibility to aqueous alteration compared to CAIs. For the purpose of this study, ARCs have been defined as rounded chondrules composed mostly of ferromagnesian silicates with small amounts of an Al-rich mineral phase (MacPherson and Huss, 2005a; Zhang et al., 2014, 2024, 2020a). CAIs rimmed with ferromagnesian silicates were studied thoroughly as they could have been potential Compound-Chondrule-CAIs (CCCAIs). These assemblages were excluded from this study due to their particularly exotic pre-accretionary history and are the object of a different study (cf. Chapter 4). Due to their paucity in the refractory inclusion record and relatively small sizes, the impact of their exclusion is minimal within the CAI counting process.

It is important to note that only objects containing spinel or diverse assemblages of spinel, hibonite, perovskite, and pyroxene were considered. Very few pyroxene and pyroxene-olivine inclusions were included in this study as proving their identity required more advanced geochemical characterisation techniques (e.g. Electron Probe Micro-Analysis). This decision implies the acceptance of a relatively small bias within the final CAI count in favour of facilitating the exclusion of AOAs and ARCs from the study.

2.2.4CM CAI Classification

CAIs within carbonaceous chondrites are very diverse objects and a universal nomenclature has yet to be defined. Existing classification schemes for CAIs rely on different sets of parameters, including textures, mineralogy, bulk major and trace elements, and isotopic compositions (e.g. MacPherson & Davis, 1994; MacPherson, 2013). Typical classifications of CAIs from other chondritic groups do not port well in the case of CMs due to their degree of alteration. CAIs in CVs are divided into three main categories, depending on their mineralogy, shape, and major element bulk chemical compositions (Krot, 2019; MacPherson and Huss, 2005b; Stolper, 1982): (i) Type A CAIs are fine-grained and composed

mainly of Al-rich melilite and spinel; (ii) Type B CAIs are coarse-grained and consist mainly of melilite, Al-Ti pyroxene, anorthite, and spinel (there are also forsterite-bearing Type B CAIs); and (iii) Type C CAIs are coarse-grained and consist mainly of anorthite, Al-Ti pyroxene, melilite, and spinel. In addition, Type A CAIs can either be spheroidal in shape (compact; CTA) due to melting, or irregularly shaped (fluffy; FTA) due to a lack of melting (Beckett and Stolper, 1994; Macpherson and Grossman', 1984). In CM chondrites, CAIs are generally classified according to their dominant minerals, e.g. spinel-pyroxene, spinel-pyroxene-olivine, hibonite-bearing, etc. Although, according to Brearley and Jones (1998) most CAIs from the less altered CM lithologies are considered to be of Type A.

However, these classifications do not take into account the tumultuous origin of the CAIs, which can be difficult to properly investigate on a large scale in a timely manner in the case of CMs, due to the extent of parent body alteration processes that affected them. A classification relying on observable mineralogy and textures is therefore more useful in order to precisely categorise and group these inclusions. CAIs were therefore classified using a simple but efficient mineralogy- and morphology-dependent nomenclature adapted from the classification scheme used by Macpherson and Davis (1994) to describe the CAIs found within Mighei, the prototypical CM meteorite. This scheme divides the inclusions into three different groups depending on structural criteria: (i) simple inclusions, inclusion fragments, and single crystals; (ii) simple aggregates; and (iii) complex aggregates.

For the purpose of this study, these three main categories were modified in order to render them more transparent while maintaining their main selection criteria. Thus, the following are defined:

1) Simple inclusions (simple monomineralic inclusions, small inclusion fragments, and single crystals): these objects are constituted of a single, generally homogeneous, core region which can be in direct contact with the matrix or seldom enclosed within a rim. In some

cases, the cores may have slight mineralogical variations with micrometric grains of accessory phases.

2) Simple aggregates (simple polymineralic inclusions): diverse objects that can be identified as loosely connected and porous clustered cores or as distended elongated chain-like structures.

3) Complex aggregates (heterogeneous polymineralic aggregates): these CAIs are defined either as disjointed regions of irregularly shaped clustered cores displaying various textures enclosed within a common rim, or as a single heterogeneous assemblage comprising multiple core regions of varied mineralogical textures.

This study encompasses whole inclusions, fragments, and single crystals. Fragments that were too small to be categorised properly were classified as simple inclusions. Objects are considered fragments if they display any sharp distinct discontinuities in the core/mantle/rim structure (if present) or appear to consist of <50% of the original inclusion. Images of CAIs corresponding to each category can be found within sections 2.3.1.2 (simple inclusions), 2.3.1.3 (simple aggregates), and 2.3.1.4 (complex aggregates) of this chapter.

2.2.5 2D CAI Measurements

2.2.5.1 Image Analysis

Composite RGB maps (cf. Fig. 2.1a) and sample-wide BSE images were imported into the CorelDraw X7 software and layered onto one another for each of the samples from A 12236, Paris, and Winchcombe. The outline of each confirmed CAI was drawn manually (segmentation) based on the petrographical information provided by each map (cf. Fig. 2.1b). The boundary between an inclusion and the matrix was defined at the point at which the mineralogy and texture distinctively changed. This means that the outline of an inclusion was drawn either at the boundary between the object's rim (if present) and the matrix, or between the core region and the matrix (in the case of single crystals; cf. section 2.2.4). Holes within the CAIs were excluded when possible. In order

to reduce bias from human perception, segmentation was conducted three times for each EDS sample-wide map a few months apart by a single person (yours truly) to ensure consistency. Disparities in the areas outlined were in the order of a few square pixels per object and were regarded as negligible in the final calculations. Despite these tests for assessing internal consistency, subjectivity remains a potential source for error during segmentation and needs to be taken into account not only in this study, but in all research involving this type of method and is intrinsic to Natural Sciences in general.

The majority of the inclusions in this study are surrounded by a Fine-Grained Rims (FGR). While these are generally similar in composition to the bulk matrix, they are distinguishable by their distinctive texture and slight compositional contrasts to the surrounding matrix (Bland et al., 2011; Hanna and Ketcham, 2018; Macpherson' et al., 1985; Metzler, 1996), e.g. globular sulfides forming a circle around the inclusions (examples of FGRs surrounding objects in CMs are in Chapters 3 and 4). It is important to note that Fine-Grained Rims (FGR) were intentionally excluded and were considered as matrix during segmentation, as they require a separate dedicated study. Disjointed objects enclosed within a singular FGR were considered as a single object (commonly observed in the case of simple and complex aggregates; cf. section 2.2.4) and their masks were combined into a single entity. The produced masks were still disjointed, as to not incur any additional bias in the measurements of the areas.

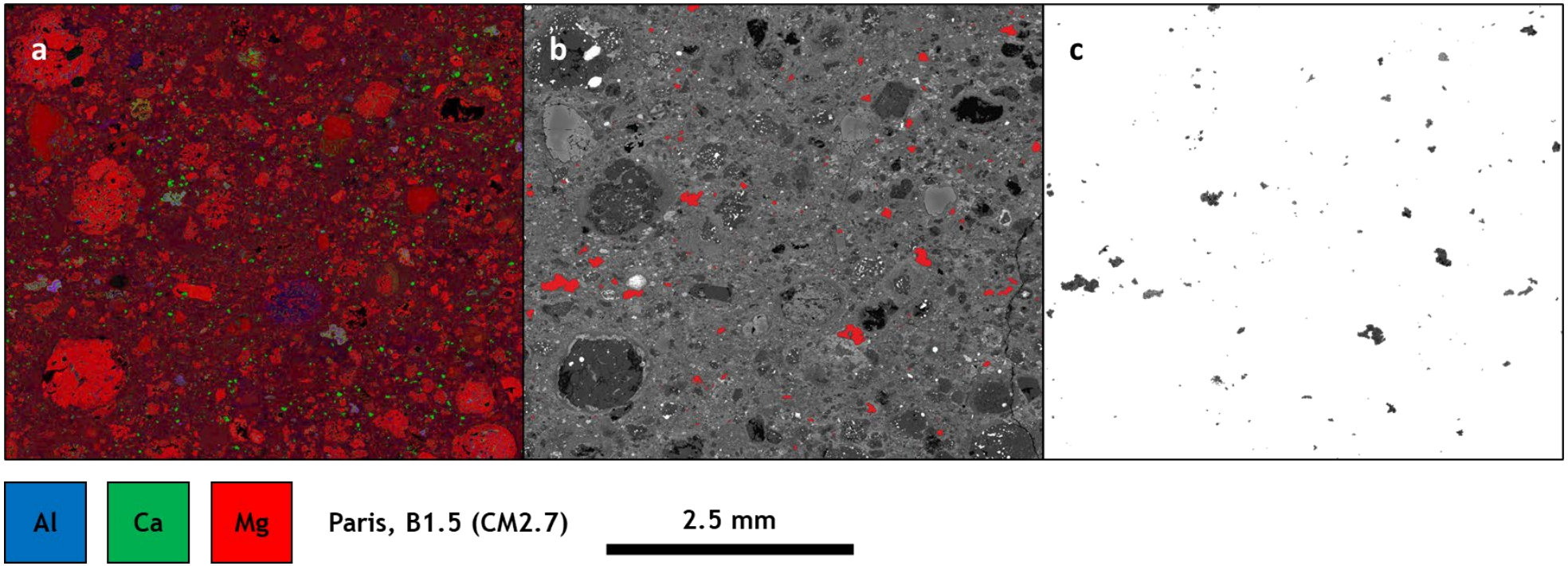

Figure 2.1. Selected area of the Paris (B1.5) section during the segmentation process. (a) Ca-Al-Mg X-ray maps. (b) BSE image with the overlayed confirmed CAI masks in red. (c) Extracted CAI masks from BSE image.

The CAI outlines were then extracted from the maps as masks (areas covering the entirety of the CAI) and combined into a single tif file (cf. Fig. 2.1c) for each mapped section of the meteorite samples. The resulting files were exported unedited (maintaining original resolution and no anti-aliased) at a resolution of 96 dots per inch (dpi). These mask files were then imported into the ImageJ software (v. 1.53a) and thresholded, binarising the images (black CAI masks within a white matrix background). After setting the scale (defined by the original resolution of the associated image mosaic), the thresholded images were analysed (using the 'analyse particles' feature) to produce the following measurements for each individually segmented CAI per section of sample: area, perimeter, major and minor axes (longest dimension and longest dimension perpendicular to it, determined by automated best fit ellipse), circularity (0-1; 1 being a perfect circle), aspect ratio (between major axis length and minor axis length), roundness (inverse of the aspect ratio), and solidity (ratio between area and convex area). Only area, major and minor axes measurements are used in this study, but the additional data can be found in Appendix 7.2. Each sample section was also outlined to measure precisely the total investigated area for each selected meteorite; however, holes were included in this measurement, so investigated areas of each meteorite should be considered upper limits.

2.2.5.2 CAI Modal Abundance Measurements

The method used in this study allows for the precise measurement of outlined apparent CAI surfaces in square pixels (calibrated to square microns), while previous studies (e.g. Rubin et al., 2007; Rubin et al., 2015; Lee et al., 2023; cf. Table 2.3) quantified CAI areas by measuring and multiplying the major and minor axes of the inclusions (cf. Eq. 2.1), effectively approximating them as rectangular objects. The terms "true" (measurement of the apparent 2D surface of the CAI) and "calculated" (approximations using Eq. 2.1 and Eq. 2.2) are used throughout this study to distinguish the two methods. Measurements provided by Prof. M. R. Lee (UofG) for CAIs in DNG 06004 and LAP 02239 were measured manually. Therefore, CAI areas were also calculated to be made comparable with existing literature as follows:

$$area_{CAI\ calc.} = L \times S \qquad \text{(Eq. 2.1)}$$

Where L corresponds to the length of the major axis and S corresponds to the length of the minor axis of a CAI measured using the ImageJ software (v. 1.53a). L and S are perpendicular to one another.

These studies have also reported CAIs sizes as the average of the length of their major and minor axes, which were calculated as follows:

$$\mathrm{d_{CAI\ calc.}} = \frac{\mathrm{L \times S}}{2} \qquad \text{(Eq. 2.2)}$$

While others (e.g.Fendrich and Ebel, 2021; Hezel et al., 2008; cf. Table 2.3) have reported CAI sizes as the apparent diameters (d) calculated from the "true" area as follows:

$$d_{CAI\ true} = 2 \times \sqrt{\frac{area_{CAI\ true}}{\pi}} \qquad \text{(Eq. 2.3)}$$

All CAI abundances ("true" and "calculated") reported in this study are expressed as modal abundances in area% and were calculated using the measured total investigated areas for each meteorite section, as described by Hezel et al. (2008):

$$A_{CAI} = \frac{\sum area_{CAIs}}{\sum area_{samples}} \qquad \text{(Eq. 2.4)}$$

It is important to note that when discussing sizes and areas of inclusions, it is implied that these are apparent sizes as this study comprises only 2D measurements of the surfaces of the sections. As stated by Hezel et al. (2008), there appears to be a certain confusion in the literature when reporting CAI modal abundances. Certain studies expressed abundances as vol.% (cf. Table 2.3), in which the term was used erroneously to extrapolate from measured areas to volumes with the assumption that area% are approximately, if not exactly, equal to vol.%. Data from the literature were converted accordingly to

area% when compared to results from this study. CAI measurements from the literature had to be verified if they could be compared to the results from this study before being included. Works that did not report CAI modal abundances but had datasets that included CAI size measurements and total investigated areas were used to calculate modal abundances for comparison purposes. This is due to the paucity of comparable CAI data in the current literature for CM chondrites. The investigation of the CAIs of the CM2 Murchison meteorite by Fendrich & Ebel (2021) is the closest equivalent to this study (cf. Table 2.3).

Table 2.3. Compilation of previous studies of CAI modal abundances in CM chondrites in order of increasing petrologic subtype (from more to less aqueously altered).

Meteorites	Petrologic subtype	*n* CAIs	Investigated area (mm^2)	Method for CAI		Abundance estimation	Expressed as	Study
				Identification[a]	Measurement			
Nogoya	2.2	6	6	X-ray maps	Area	"True"	area%	Hezel et al. (2008)
Mighei	2.3	35	-	BSE[b]	L x S	Calculated	-	MacPherson & Davis (1994)
LAP 02239	2.4-2.5	70	75.53	X-ray maps	L x S	Calculated	area%	Lee et al. (2023)
Murray	2.4-2.5	-	115.2	X-ray maps	Area (ImageJ)	"True"	vol.%	Norton & McSween (2007)
	2.4-2.5	85	115.6	X-ray maps	L x S	-	-	Lee & Greenwood (1994)
Murchison	2.5	201	34	X-ray maps	Area	"True"	Area%	Hezel et al. (2008)
	2.5	327	40.14	X-ray maps	Area (ImageJ)	"True"	vol.%	Fendrich & Ebel (2021)
QUE 97990	2.6	40	50	X-ray maps[c]	L x S	Calculated	vol.%	Rubin (2007)
Paris	2.7	18	108	X-ray maps[c]	L x S	Calculated	vol.%	Rubin (2015)
Total	2.0-2.9	782						

[a]CAI identification using X-ray maps involved CAI selection through thorough visual scanning. [b]Method was supplemented by geochemical quantitative analyses using wavelength-dispersive techniques. [c]CAIs were marked and identified using point-counting by layering a section of an X-ray map over a grid.

2.3 Results

2.3.1 Petrographic Overview

2.3.1.1 CAI Type Distribution

189 CAIs from Winchcombe, DNG 06004, and LAP 02239 were described and classified according to the nomenclature defined in section 2.2.4. Geometric measurements, as well as short mineralogical and textural descriptions of the CAIs are available in Chapter 3 for Winchcombe, in Appendix 7.3 for DNG 06004, and in the supplementary material of Lee et al. (2023) for LAP 02239.

This study was supplemented with the dataset (35 CAIs) from MacPherson & Davis (1994) recording the CAI types found within the prototypical CM chondrite, Mighei (cf. Table 2.4). One inclusion within MacPherson & Davis (1994) is described as an aggregate without further categorisation and was categorised as a simple aggregate based on its description for the purposes of this study. All CM lithologies within each meteorite were grouped together. CAIs found within the Mx and FC of Winchcombe were exceptionally included in this part of the study, as they are components of CM2 lithologies. However, CAIs identified within the xenolith of LAP 02239 (02239,5), described by Lee et al. (2023) remained excluded from this study.

Table 2.4. Distribution of CAI types within CM chondritic lithologies. SD corresponds to standard deviation.

CAI types	Winchcombe (CM2.0-2.6)		Mighei[a] (CM2.3)		DNG 06004 (CM2.4)		LAP 02239[b] (CM2.4-2.5)		Average	
	CAIs	%	CAIs	%	CAIs	%	CAIs	%	%	SD
Simple incl.	12	57.1	19	54.3	51	52.0	42	60	55.9	3.5
Simple agg.	6	28.6	12	34.3	42	42.9	21	30	33.9	6.4
Complex agg.	3	14.3	4	11.4	5	5.1	7	10	10.2	3.8
Total	21		35		98		70		100.0	

[a]MacPherson & Davis (1994). [b]Lee et al. (2023).

All observed CAIs appear to follow a simple distribution pattern ~60%/~30%/~10% (cf. Table 2.4 and Fig. 2.2) across the three distinct major texturally- and mineralogically-dependant categories: simple inclusions, simple aggregates, and complex aggregates, respectively. Despite the slight discrepancies within Winchcombe (14.3% of complex aggregates) and DNG 06004 (42.9% of simple aggregates), the proportions of each CAI type remain similar across the different degrees of aqueous alteration that affected the studied CM lithologies. A table compiling all primary mineralogies percentages (i.e. excluding any secondary phases that might be the product of aqueous alteration) of all 224 classified CAIs per meteorite and per CAI type is in Appendix 7.4. The most abundant inclusions consist mainly of spinel-pyroxene (28%), followed by spinel-pyroxene-perovskite (21%), spinel (12%), spinel-perovskite (8%), spinel-perovskite-hibonite ± (6%), spinel-pyroxene-hibonite ± perovskite (6%), hibonite ± spinel ± perovskite (6%), and spinel-pyroxene-olivine ± perovskite (5%), spinel-olivine (3%) and pyroxene (1%), along other minor diverse assemblages.

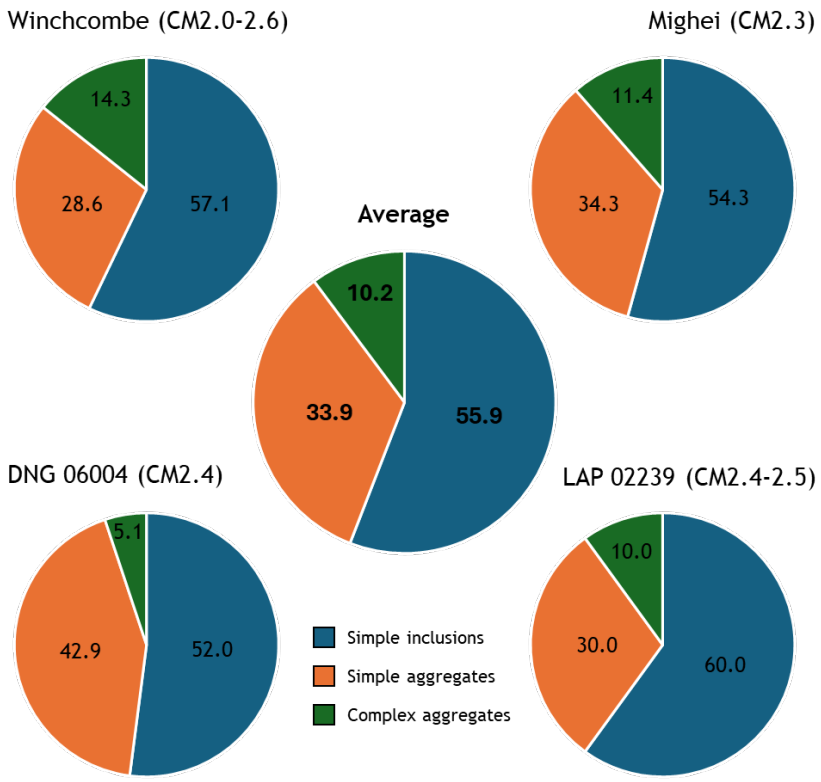

Figure 2.2. Relative proportions (%) of CAI types for each meteorite. The middle diagram represents the mean average of the four CM samples. Mighei CAI data is from MacPherson & Davis (1994) and LAP 02239 CAI data is from Lee et al. (2023). SD of the average values are indicated in Table 2.4.

The average size distribution of CAI types shows that complex aggregates generally comprise larger inclusions then simple aggregates, which in turn are larger than simple inclusions (cf. Fig. 2.3). This is the case for each of the studied meteorites, except for Winchcombe, where the average calculated size of simple aggregates is lower (average: 68.9 µm; cf. Fig. 2.3) than that of simple inclusions (average: 82.9 µm; cf. Fig. 2.3). In the case of DNG 06004, the average sizes of both CAI aggregate types are sensibly the same and within error range (74.6 and 76.4 for simple and complex aggregates respectively; cf. Fig. 2.3), with the simple inclusions still representing the smallest CAIs.

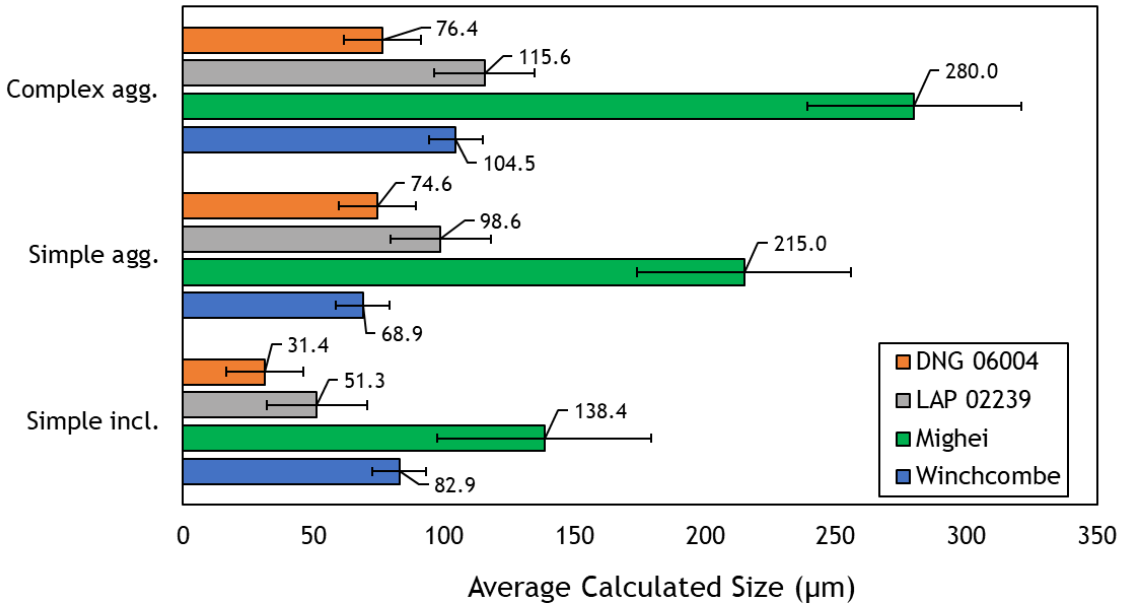

Figure 2.3. Average calculated sizes (µm) of each CAI type for each meteorite. CAI size data for Winchcombe is provided in Table 3.5; data for DNG 06004 is available in Appendix 7.2. LAP 02239 and Mighei CAI data are sourced from Lee et al. (2023) and MacPherson & Davis (1994), respectively. Error bars represent the standard deviation of the average size for each CAI type category in each meteorite.

2.3.1.2 Simple Inclusions

These inclusions are the most abundant type of CAI observed within the studied CM samples (average: 55.9±3.5%, SD; cf. Table 2.4 and Fig. 2.2). The specimens generally display a core region mainly composed of spinel (cf. Fig. 2.4). Perovskite and hibonite can occur as mineral accessories alongside or within the spinel (cf. Fig. 2.4). Most simple inclusions are either rimmed by pyroxene (generally diopside) or by Fe-rich phyllosilicates (mostly in Mighei and DNG 06004; MacPherson & Davis, 1994; Martin et al., 2023). Some inclusions can be in direct contact with the matrix (no rim-like structure). Out of the 124 investigated simple inclusions, their most common mineralogies are spinel-pyroxene inclusions (31%), spinel-pyroxene-perovskite inclusions (18%), spinel inclusions (11%), and spinel-perovskite-hibonite (9%) (for the rest cf. Appendix 7.4).

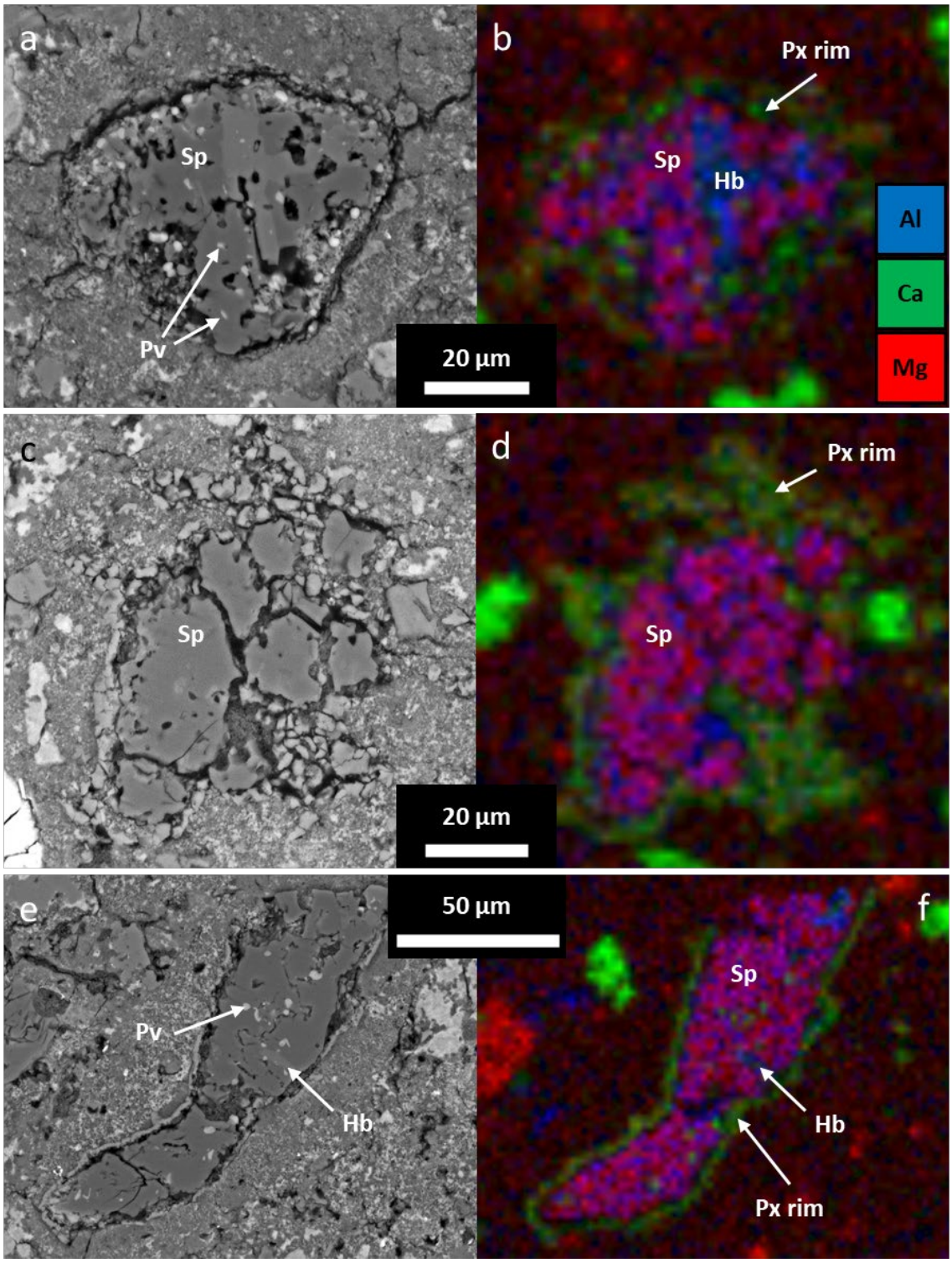

Figure 2.4. CAIs 4, Q, and A12 (respectively), simple inclusions in LAP 02239 (02239,5; CM2.4-2.5). The cores are mostly composed of spinel (Sp), seldom alongside hibonite (Hb) and perovskite (Pv) grains, within a pyroxene (Px) rim. (a, c, e) BSE images. (b, d, f) Ca-Al-Mg X-ray maps. Spinel is purple in the EDS maps, while hibonite appears as dark blue and pyroxene is green.

2.3.1.3 Simple Aggregates

These are the second most abundant type of CAI observed within the studied CM samples (average: 33.9±6.4%, SD; cf. Table 2.4 and Fig. 2.2). The inclusions are observable as loosely connected and porous clusters of spinel grains (hibonite can occur as a mineral accessory within the spinel) or as distended elongated chain-like structures within a rim of pyroxene (generally diopside; cf. Fig. 2.5), olivine, or phyllosilicates. Phyllosilicate rims within these inclusions appeared to be more frequent in Mighei (MacPherson & Davis, 1994) and DNG 06004 (Martin et al. 2023c). In the case of LAP 02239, many of these inclusions have pyroxene rims with 120° triple-junction grain boundaries (Martin et al. 2023c; Lee et al, 2023). The most common mineralogies for these inclusions are spinel-pyroxene (26%), spinel-pyroxene-perovskite (23%), followed by spinel (10%) and spinel perovskite (10%) (for the rest cf. Appendix 7.4).

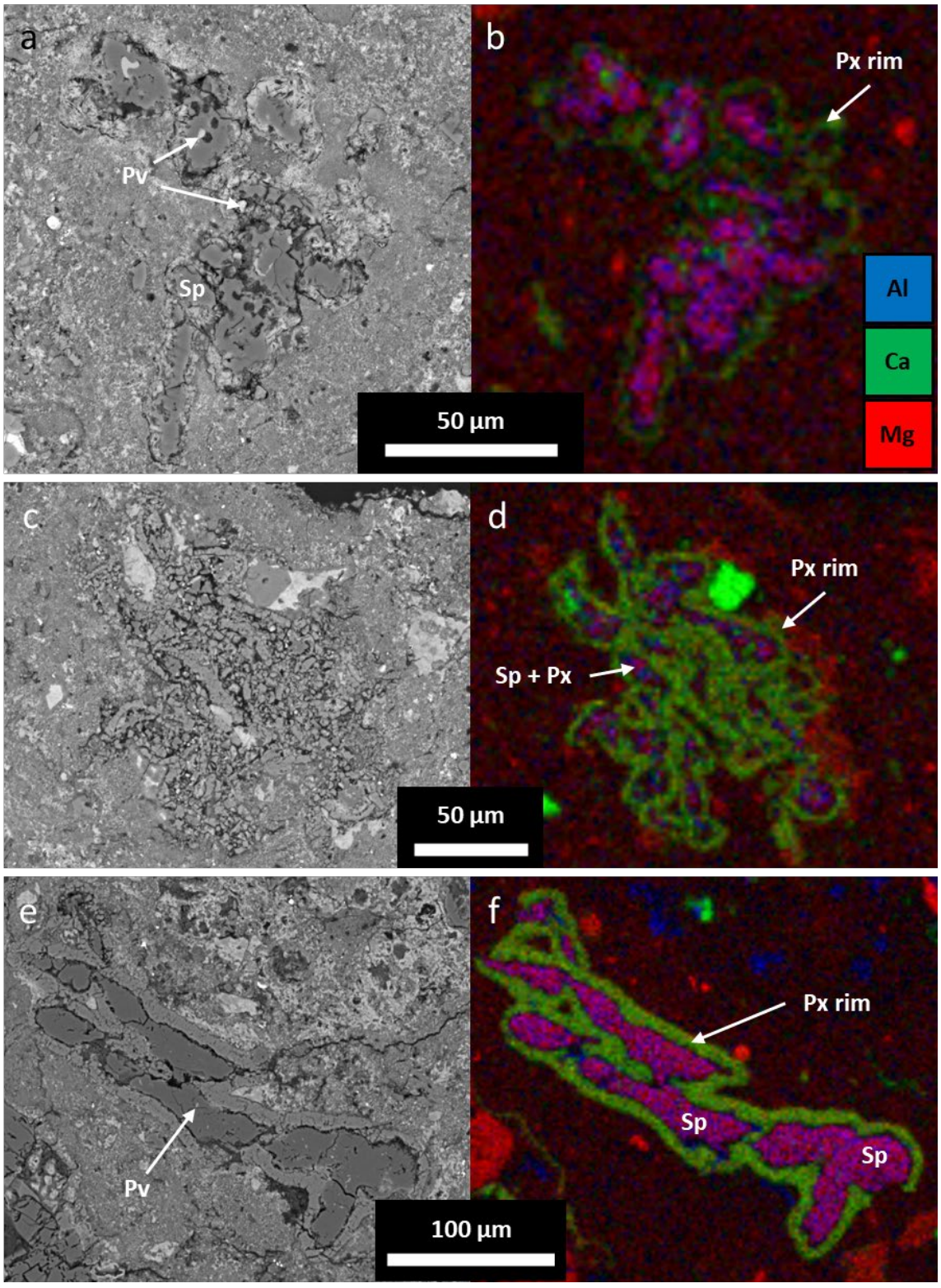

Figure 2.5. CAIs F, G, and A18 (respectively), simple aggregates in LAP 02239 (02239,5; CM2.4-2.5). The cores are mostly composed of disjoined spinel (Sp) clusters and seldom contain micrometric perovskite (Pv) grains, within a pyroxene (Px) rim. (a, c, e) BSE images. (b, d, f) Ca-Al-Mg X-ray maps. Spinel is purple in the EDS maps, while pyroxene is green.

2.3.1.4 Complex Aggregates

They are the least abundant type of CAI among the studied CM lithologies (average: 10.2±3.8%, SD; cf. Table 2.4 and Fig. 2.2). Disjointed core regions of irregularly shaped mineral clusters (generally polymineralic but mostly composed of spinel; cf. Fig. 2.6) with varied igneous and alteration textures, often mantled by calcite or Fe-rich phyllosilicates, and enclosed within a common rim of pyroxene (seldom olivine). Contrary to simple aggregates, these complex aggregates do not display any textures related destabilisation or melting. Based on observation of their primary refractory mineralogy, they mostly constitute spinel-pyroxene-perovskite inclusions (37%), spinel inclusions (16%), spinel-pyroxene inclusions (16%) and spinel-pyroxene-olivine-perovskite inclusions (11%) (for the rest cf. Appendix 7.4). However, many are dominated by either by calcite (in Winchcombe and Mighei; Martin et al., 2022, 2023); MacPherson & Davis, 1994; cf. Chapter 3), or Fe-rich phyllosilicates (in DNG 06004 and LAP 02239; Lee et al., 2023; cf. Appendix 7.3). Calcite-dominated complex aggregates within the Winchcombe meteorite are further studied in Chapter 3.

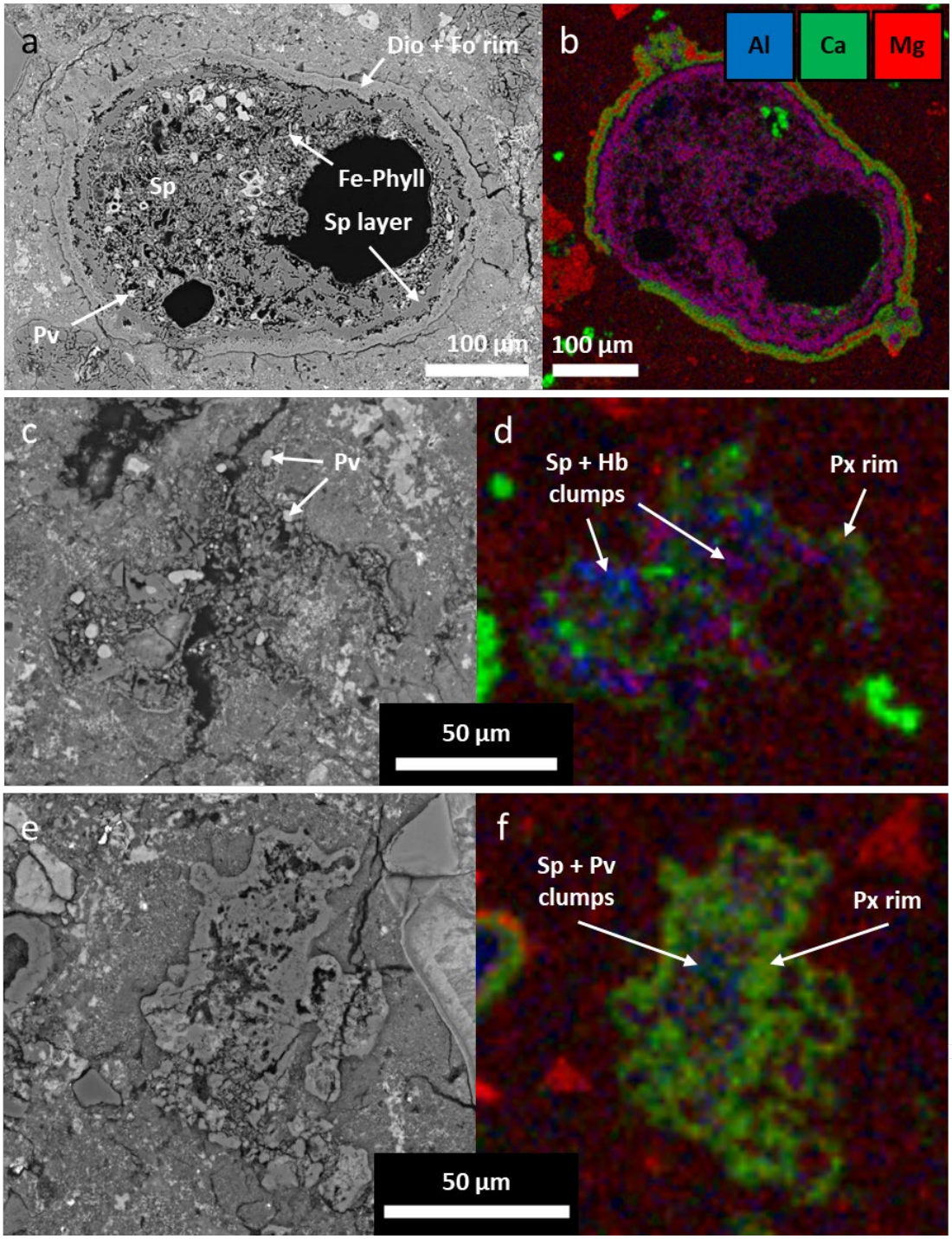

Figure 2.6. CAIs 6, T, and B2 (respectively), complex aggregates in LAP 02239 (02239,5; CM2.4-2.5). These CAIs display disjointed and irregularly shaped polymineralic clusters with varied textures, within a pyroxene (Px) rim. Inner clusters mostly comprise spinel (Sp), seldom alongside hibonite (Hb), perovskite (Pv), and patches Fe-rich phyllosilicates (Phyll). CAI 6 (a and b) has a complex polymineralic rim, composed of diopside (Dio) with an inner layer of forsterite (Fo). (a, c, e) BSE images. (b, d, f) Ca-Al-Mg X-ray maps. Spinel is purple in the EDS maps, while hibonite is dark blue, pyroxene is green, and forsterite appears as red within the rim of CAI 6 (in b).

2.3.2 Modal Abundances of CM CAIs

2.3.2.1 Comparison of CM CAI Metrics in the Literature

A total of 1144 CAIs were identified and 1027 outlined within a total investigated area of 287.7 mm^2 across four CM chondrites. All compatible CM CAI data from the literature available at the time of writing were compiled into Table 2.5 and comprises the degrees of aqueous alteration of the host CM lithologies, number of CAIs identified, total area investigated, CAI densities (CAIs/mm^2), CAI size measurements, and CAI modal abundances.

Measurements from the literature were separated according to their methods used to determine the CAI modal abundances in their respective studies (cf. Table 2.3). This study comprises both methods and can provide an estimate as to the accuracy of the rectangular approximation of the "calculated" method relative to "true" measurements. In this study, the "calculated" method was found to consistently overestimate the CAI modal abundances by 20±3.4% (SD; calculated average cf. Table 2.5 and 2.6). This factor needs to be taken into account before any comparison is to be made between values of both categories. Mean CAI sizes, however, remain quite sensibly similar despite the method used (cf. Table 2.5) and appear to vary substantially from 14 µm (Nogoya, CM2.2) to 181±206 (Mighei, CM2.3).

CAI size distributions within CMs will be the object of a future study, however, preliminary data for the studied meteorites indicate that the mildly aqueously altered CM lithologies (CM2.0-2.6) predominantly comprise smaller inclusions (<50 µm; 945 out of 1200 CAIs; cf. Fig. 2.7), with a sharp decrease in frequency beyond 100 µm and only rare occurrences larger than 200 µm. This trend is especially evident in the most pristine sample in this study, A 12236 (CM2.9), which is overwhelmingly dominated by inclusions smaller than 100 µm.

CAI densities do not appear to follow a simple distribution and range from ~0.10 CAIs/mm^2 to 10 CAIs/mm^2 (a factor of 100). However, it is important to note that the reported minimum CAI sizes do not necessarily correspond to the cut-off value of a study but to the smallest mean CAI size identified. This is

highly dependent on the type of CAI identification method employed. Studies involving point-counting, which consists in determining CAI density by counting CAIs within a grid overlayed with an X-ray map, tend to have a more difficulty in identifying objects smaller than the grid size (cf. Table 2.3 and 2.5) and appear to be biased towards larger inclusions.

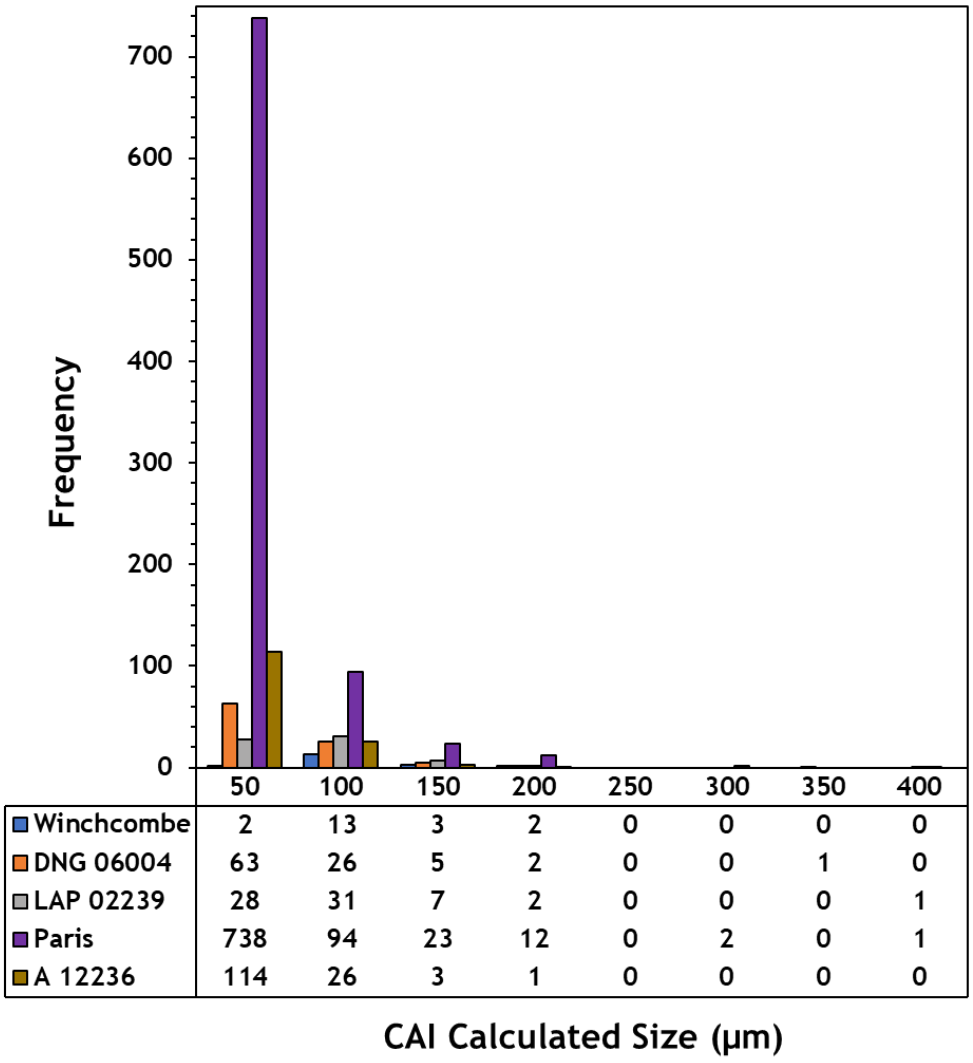

	50	100	150	200	250	300	350	400
Winchcombe	2	13	3	2	0	0	0	0
DNG 06004	63	26	5	2	0	0	1	0
LAP 02239	28	31	7	2	0	0	0	1
Paris	738	94	23	12	0	2	0	1
A 12236	114	26	3	1	0	0	0	0

Figure 2.7. Frequency size distribution of CAIs in each meteorite. CAI sizes are grouped into bins of 50 μm increments (0-50, 51-100, …, 351-400). The table below the x-axis shows the number of CAIs in each bin for each meteorite. CAI size data for Winchcombe is provided in Table 3.5; data for DNG 06004 is available in Appendix 7.2. LAP 02239 CAI data is sourced from Lee et al. (2023).

The principle of using modal abundances has the advantage of taking into account the surface analysed of each sample which makes comparisons between studies more reliable as "nugget effects" (biased values due to heterogeneous distribution) can be identified and excluded rapidly. This is particularly relevant in the context of brecciated lithologies that have undergone different degrees of aqueous alteration (Vacher et al., 2018; Verdier-Paoletti et al., 2017). Data from each lithology studied in Winchcombe (cf. Table 2.6) reveal a high discrepancy in the CAI inventory of the meteorite. Studies that do not take into account the brecciated nature of their CM samples introduce an additional bias when extrapolating from smaller areas of investigation. This could explain the large discrepancy between the CAI modal abundance of Paris of this study and of Rubin (2015). This is also likely the case for the low CAI modal abundance of lithology D (cf. Table 2.6) in Winchcombe which is very likely biased due to a small area of investigation.

Table 2.5. Modal abundance and size of CAIs within the studied CM lithologies compared to the prototypical CM, Mighei, and other CMs from the literature. Only compatible studies are reported here. CAI measurements were sorted as "true" and "calculated" according to the method applied in their respective studies. CAI measurements comprise whole inclusions, fragments, and single crystals.

Meteorites	Petrologic subtype	*n* CAIs	Investigated area (mm^2)	CAIs/mm^2	CAI size range (µm)		Mean CAI size (µm)		CAI abundance (area%)	
					"True"	Calculated	"True"	Calculated	"True"	Calculated
Winchcombe*[a]	2.0-2.6	11	125.5	0.09±0.15	50-189	48-199	93±45	95±48	0.10±0.17	0.12±0.21
Nogoya[b]	2.2	6	6	1.00	10-26	-	14	-	0.02	-
Mighei[c]	2.3	35	-	~0.10	-	25-1150	-	181±206	-	-
DNG 06004[a]	2.4	98	47.21	2.08	-	12-317	-	52±44	-	0.84
LAP 02239[d]	2.4-2.5	70	75.53	0.93	-	14-352	-	72±59	-	0.72
Murray[e]	2.4-2.5	-	115.2	-	-	-	-	-	1.6±1.3	-
[f]	2.4-2.5	85	115.6	0.74±0.23	-	<30-1380	-	-	-	-
Murchison[b]	2.5	201	34	5.91	12-360	-	46	-	0.97	-
[g]	2.5	327	40.14	8.15	0-176	-	36±24	-	1.2	-
QUE 97990[h]	2.6	40	50	0.80	-	30-530	-	130±90	-	1.80
Paris[i]	2.7-2.9	37	108	0.34	-	30-450	-	130±80	-	0.76
[a]	2.7	871	101	8.62	5-301	5-366	31 ±32	32±37	1.30	1.66
A 12236[a]	2.9	145	14	10	8-147	9-152	34 ±25	36±26	1.40	1.80
Total	2.0-2.9	1926	832.18							

*Mean values across all seven investigated lithologies (A-G, excluding Mx and FC). [a]This study. [b]Hezel et al. (2008). [c]MacPherson & Davis (1994). [d]Lee et al. (2023). [e]Norton & McSween (2007). [f]Lee & Greenwood (1994). [g]Fendrich & Ebel (2021). [h]Rubin (2007). [i]Rubin (2015). ± represents standard deviation.

Table 2.6. Modal abundance and size of CAIs within the studied CM lithologies of the Winchcombe meteorite. CAI count comprises whole inclusions, fragments, and single crystals.

Winchcombe lithology	Petrologic subtype	*n* CAIs	Investigated area (mm^2)	CAIs/mm^2	CAI size range (μm)		Mean CAI size (μm)		CAI abundance (area%)	
					"True"	Calculated	"True"	Calculated	"True"	Calculated
A	2.2	7	18.9	0.37	50-167	48-172	85±40	88±42	0.25	0.32
B	2.1	2	42.8	0.05	71-80	69-78	76±6	74±6	0.02	0.02
C	2.2-2.3	0	40.2	0.00	-	-	-	-	0.00	0.00
D	2.6	0	10.2	0.00	-	-	-	-	0.00	0.00
E	2.3	2	8.2	0.24	87-189	89-199	138±72	144±78	0.41	0.53
F	2.0	0	3.9	0.00	-	-	-	-	0.00	0.00
G	2.1	0	1.3	0.00	-	-	-	-	0.00	0.00
Total	2.0-2.6	11	125.5							

Lithologies Mx and FC were excluded. ± represents standard deviation.

2.3.2.2 Correlation Between CAI Modal Abundance and Degree of Aqueous Alteration of CM Host Lithologies

CAI Modal abundances range from 0 to 1.40 area% ("true") and 0 to 1.80 area% (calculated) in the studied CM samples (cf. Tables 2.5 and 2.6). There is a clear correlation between CAI modal abundances and the degree of aqueous alteration ($r^2 > 0.55$ for both "true" and calculated plots; cf. Fig. 2.8), with highly aqueously altered samples (CM2.0-2.3) having the lowest modal abundances while the more pristine samples (CM2.6-2.9) have the highest modal abundances. The correlation appears to be stronger between calculated values compared to "true" (cf. Fig. 2.8). However, the correlation persists and is significant ($r^2 > 0.55$), no matter the type of method used.

Differences in CAI modal abundances for same meteorites can be explained by sample heterogeneity. As mentioned previously, brecciation is an important feature of CM chondrites (Metzler et al., 1992; Bischoff et al., 2006; Nakamura, 2006; Lindgren et al., 2013; Lentfort et al., 2020; Suttle et al., 2021) which is not systematically reported. Therefore, it is expected for data from the same meteorite to differ if the concerned studies considered their own samples as being homogeneous when selecting and measuring CAIs (cf. Fig. 2.8).

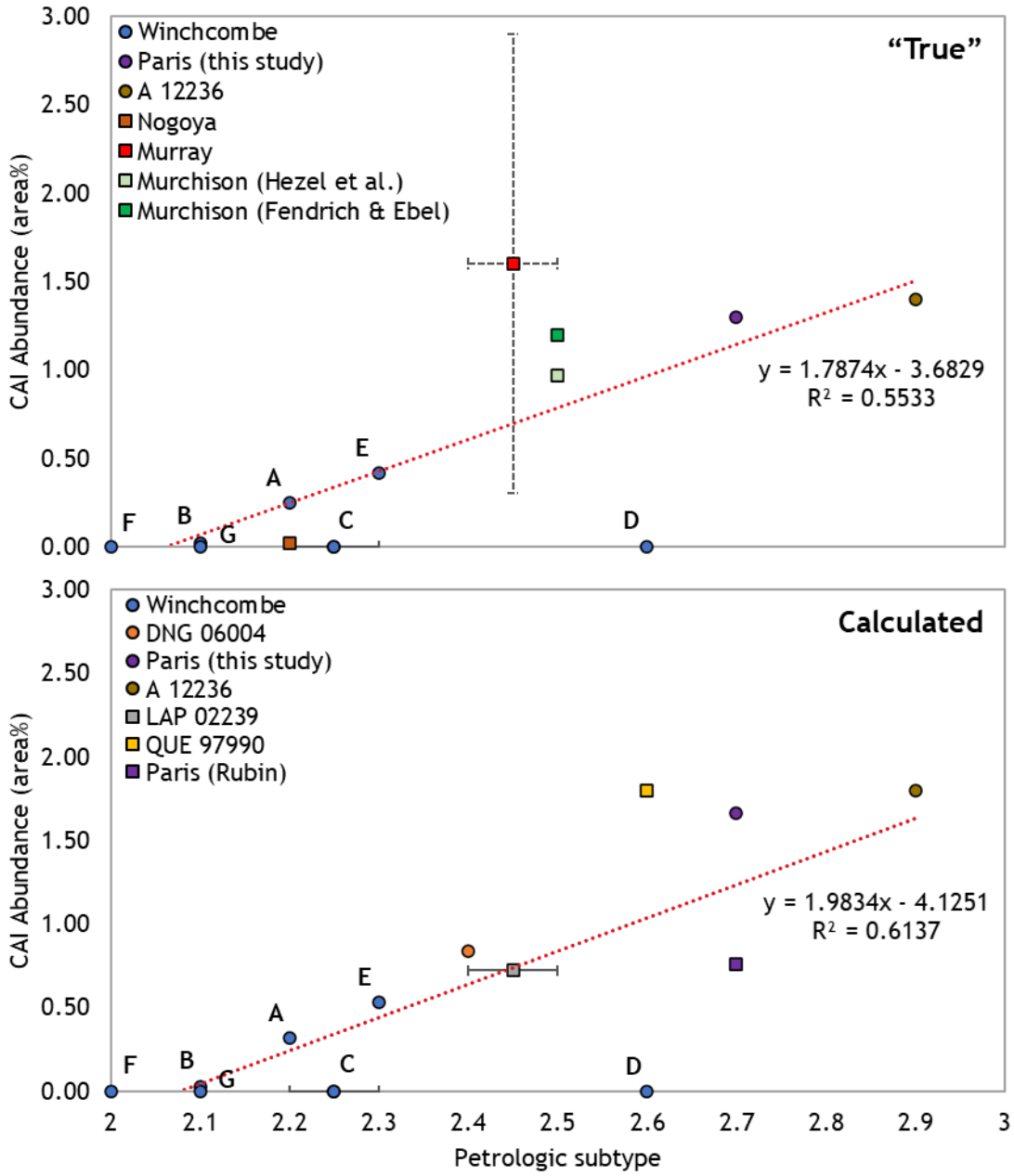

Figure 2.8. Modal abundances of CAIs within CM lithologies relative to the degree of aqueous alteration of their host lithologies. Top plot comprises only "true" values and bottom plot only calculated values. Round data points correspond to data produced in this study and square data points represent data from the literature: Nogoya (Hezel et al., 2008), Murray (Norton & MsSween, 2007), Murchison (Hezel et al., 2008; Fendrich & Ebel, 2021), LAP 02239 (Lee et al., 2023), QUE 97990 (Rubin et al., 2007), and Paris (Rubin, 2015). Each equation is associated with the red dotted trendlines, shown here for reference. Error along the x-axis correspond to overlapping criteria when defining the petrologic subtype (i.e. lithology C of Winchcombe is defined as CM2.2-2.3 and LAP 02239 is defined as a CM2.4-2.5), whereas error along the y-axis corresponds to standard deviation between the CAI modal abundances of different samples of the same meteorite.

2.3.2.3 Accuracy and Precision of Measurements and Calculations

During the mineralogical and geochemical verification of the candidates, false-positive CAIs such as Al-rich chondrules (which can contain minor amounts of spinel; Zhang et al. 2020) and porous areas filled with Al-rich polishing compounds were removed. Each sample section was perused thrice and in order to quantify the potential human error during CAI identification, the number of CAIs were recorded after each pass of the Paris (B1.5) section as an example (cf. Table 2.7). In the case of the section of Paris, only one false-positive CAI was identified and removed from the study, which is the equivalent of a relative error of 0.1% on the CAI identification.

Table 2.7. Estimated number of CAIs missing from this study. Measurements were made during the CAI identification and sectioning processes for Paris (B1.5).

Pass number	Total CAIs identified after each pass	Increase	
		CAIs	%
1	766	766	-
2	859	93	12.1
3	871	12	12.9
Estimated missing		2	0.18
Estimated total (including missing)		873	

Following the increasing trend in Table 2.7, the potential number of CAIs missing from the study can be estimated to ~1.5 CAIs per section (12.9% of 12). These potentially missing CAIs would logically be amongst the smallest and hardest to perceive despite the high-resolution of the maps analysed. Therefore, an absolute error of the total calculated CAI areas can be estimated as: $n_{missing\ CAIs} \times A_{smallest\ CAI}$, which equates to 50 μm^2, corresponding to a relative error of 0.001% for the “true” and “calculated” CAI modal abundances of the Paris section (cf. Table 2.5). Therefore, errors have been considered negligible.

2.4 Discussion

2.4.1 Progressive Aqueous Alteration of CM CAIs

Rubin et al. (2007) and Rubin (2015) have shown that lower CM petrological subtypes (CM2.2-2.7) display higher proportions of carbonates (with increasing complexity in CM2.0-2.1 lithologies) and phyllosilicates (CM2.2-2.6) in the matrix directly linked to the effects of fluid-driven alteration. Low temperature metasomatic alteration effects have been shown to affect primary phases within CAIs (e.g. pyroxene, olivine, plagioclase; Rubin et al. 2007; Rubin, 2015) within the most altered CM samples. Within this study, several large CAIs (>50 μm^2) were found to display evidence of fluid driven mineral alteration and replacement (cf. Chapter 3; Lee et al., 2014, 2012; Lee and Greenwood, 1994; Russell et al., 1998). This was observed extensively in the form of calcite-dominated CAIs within the more aqueously altered samples (CM2.0-2.3; Winchcombe and Mighei; MacPherson & Davis, 1994; cf. Chapter 3). The effects of aqueous alteration in CAIs are more visible in complex aggregates due to them having larger and more complex internal structures (cf. section 2.3.1.4; e.g. potentially multiple core regions, and a mantle, enclosed within a rim structure). Within the lower CM petrological subtypes, the mantle structures are dominated by secondary minerals (phyllosilicates and calcite). These are considered products of aqueous alteration (Rubin, 2015; Rubin et al., 2007; Lee et al., 1994; Russell et al, 1997; Lee et al., 2012; Lee et al., 2014; Tomeoka & Busek, 1985; Suttle et al., 2024; Daly et al., 2024). Within lithology A (CM2.2) of Winchcombe, these complex aggregates are dominated by calcite (Martin et al., 2022, 2023); cf. Chapter 3), whereas in mildly altered samples (CM2.3-2.6), CAI aggregates (simple and complex) are dominated by phyllosilicates (Rubin, 2007; Lee et al, 2023), and Mighei (CM2.3) having both calcite- and phyllosilicate-bearing complex aggregates (MacPherson & Davis, 1994). This is further evidenced by the fact that these phases within complex aggregates do not display evidence of destabilisation, nor melting, indicating that the calcite and phyllosilicates are very likely replacive within these CAIs and stem from a later stage of CAI incorporation within the CM parent body(-ies). Sufficient alteration of CAIs may therefore lead to complete mineral replacement and lead to lower reported modal abundances for lower petrological CM subtypes. In addition, previous studies (e.g. Armstrong et al., 1982; Rubin 2007) have discussed the

process of fragmentation and disintegration of refractory inclusions due to parent body aqueous processes. The most abundant CAI type within highly to mildly aqueously altered lithologies (CM2.0-2.6) are smaller simple inclusions which include all CAI fragments identified in this study (< 50 μm; cf. Fig. 2.2, 2.3, and 2.7). This concurs with previous observations regarding fragmentation of altered refractory inclusions in carbonaceous chondrites (e.g. Rubin, 2007). Therefore, the decrease in CAI modal abundance with increasing degree of aqueous alteration within CMs (cf. Fig. 2.8) is likely due to the progressive alteration (e.g. mineral replacement by phyllosilicates or calcite) and destruction of CAIs during fluid-driven parent body processes.

In a broader context, Dunham et al. (2023) have conducted a comprehensive compilation of systematic CAI searches and studies in most carbonaceous chondrite (CC) groups: CK (Karoonda-like), CV (Vigarano-like), CO (Ornans-like), CR (Renazzo-like), and CM. They reported a mean CAI modal abundance is $2.4^{+14.0}_{-2.3}$ area% (max; min) for CCs. Compared to the CAI modal abundances reported in this study (cf. Tables 2.5, 2.6, and Fig. 2.3), CMs lie on the lower end of the CAI modal abundance spectrum, surpassing only CRs, with an average of $0.3^{+0.5}_{-0.2}$ area% (max; min) (Dunham et al., 2023). This is a particular case as CR chondrites have experienced relatively low degrees of aqueous alteration (Lee et al., 2025), and their low CAI modal abundance likely reflects a low initial CAI budget (< 1 vol.%; Aléon et al., 2002). Therefore, the low CAI modal abundances observed in CM lithologies highlights the destructive impact of extensive aqueous alteration on CAIs populations.

An alternative interpretation of this relationship is that CAI modal abundances may follow a bimodal distribution, with more aqueously altered (CM2.0–2.5) and less altered (CM2.6–2.9) CM lithologies are shaped by distinct secondary processes. Lower petrologic subtypes appear to have undergone extensive fluid-driven alteration on the parent body(-ies), leading to the destruction of smaller inclusions and the fragmentation of larger CAI aggregates. In contrast, higher subtypes may have experienced less intensive alteration, affecting both inclusions and aggregates to a lesser extent. If so, the CAI modal abundances observed in these more pristine CM lithologies could be closer to the

original CAI abundance of the CM parent body(-ies). However, this interpretation requires substantial further investigation.

2.4.2 Initial CAI Distribution in CM Lithologies

Since aqueous alteration has been shown to lead to the alteration and destruction of CAIs (e.g. Armstrong et al., 1982; Rubin, 2007), this leads to two hypotheses regarding the initial distribution of CAIs within the CM parent body(-ies):

1) Initial CAI distribution was heterogeneous. The more pristine CM lithologies would have had a higher abundance of simpler (mineralogically and structurally, i.e. no mantle) and larger CAIs, which would have better survived the effects of ubiquitous parent body aqueous alteration events.

2) Initial CAI distribution was homogeneous. More CAIs were altered and destroyed within the lithologies that were the most subjected to extensive fluid-driven alteration processes regardless of CAI type. This scenario implies that fluid-driven alteration events affected the parent body heterogeneously and were probably localised (Pignatelli et al., 2016; Suttle et al., 2024; Daly et al., 2024).

However, the current predominance of smaller simple inclusions in the studied samples indicates that either extensive fragmentation or fluid-driven secondary processing of the larger CAIs occurred or that the initial CAI distribution of CAIs within the CM parent body(-ies) was biased towards smaller simpler inclusions (< 50 μm; cf. Fig. 2.7). Therefore, it is very unlikely that initial CAI distribution was heterogeneous as the proportions of different CAI types remain equal across the highly and mildly aqueously altered (CM2.0-2.6) lithologies (cf. Table 2.4 and Fig. 2.2), implying that all CAI types were affected by aqueous alteration equally in proportion.

Studies (e.g. Vernazza et al., 2016; Suttle et al., 2021) have suggested that CM chondrites might have originated from multiple parent bodies. This would imply a homogeneous CAI distribution in the carbonaceous asteroid

accretion region of the proto-planetary disk (homogeneous distribution of CAIs within multiple parent bodies) and heterogeneity within the CAI modal abundances would have stemmed from differences in the extent of aqueous alteration that affected each parent body homogeneously. A likely scenario would be that CM chondrites are derived from a singular parent body (homogeneous CAI distribution) that was then fragmented through impact into multiple bodies (through catastrophic impact events; Suttle et al., 2021), which is evidenced but the clastic nature of the CM breccias (Metzler et al., 1992; Bischoff et al., 2006; Nakamura, 2006; Lindgren et al., 2013; Lentfort et al., 2020; Suttle et al., 2021). While the alternative of the multiple parent bodies having different initial CAI distributions is very unlikely (no clear correlation would be observed), results from this study are unable to discredit the possibility of multiple parent bodies.

In any case, results seem to indicate that the initial distribution of CAIs within the CM parent body(-ies) was homogeneous and heterogeneity in the CAI modal abundances of CM lithologies stems from later occurring fluid-driven alteration events.

2.4.3 A Potential New Criterion for Quantifying Aqueous Alteration in CM Lithologies

The results of this study combined with the datasets from the literature reveal a clear correlation (r^2 ~0.6; cf. Fig. 2.8) between the CAI modal abundances and the degree of aqueous alteration of their host CM lithologies: CAI modal abundances in CMs decrease the more aqueously altered the host CM lithology. The degree of aqueous alteration of a lithology could therefore be inferred by the extent to which CAIs within are preserved. It is also interesting to note that should outlying data points be removed on the grounds of being too imprecise (i.e. Murray; Norton and Mcsween, 2007) or for being an outlier (possibly an artefact), likely due to an area of investigation too small (i.e. lithology D of Winchcombe; cf. Fig. 2.8), the correlation factor (r^2) would increase to ~0.8, which represents a strong correlation. This demonstrates the potential of this relationship to become a powerful asset when combined with Rubin's classification scheme for any meteoriticist willing to section CAIs in CM chondrites.

It is important to note, however, that this criterion does not function properly with bulk CM meteorite measurements and requires a thorough investigation and identification of potential clasts within the studied CM samples. Modal abundances of CAIs should be investigated alongside mineralogical, geochemical, and isotopic observations and measurements as their susceptibility to aqueous alteration depends greatly on their primary mineralogy (Rubin, 2015; Rubin et al., 2007). In addition, some CAIs have undergone different pre-accretionary thermal processes which might render their reaction to aqueous alteration difficult to predict without any preliminary study (Grossman et al., 2008; Hu et al., 2021; Krot, 2019; Richter et al., 2007, 2002; Shahar and Young, 2007). This is also the reason why FGRs should not be taken into account when measuring CAI surfaces.

2.4.4 Limitations and Future Work

Although reporting an average value for all CM lithologies can seem nonsensical, for the sake of comparison, the average values are: 0.55±0.64 area% ("true") and 0.65±0.70 area% (calculated). In comparison, Hezel et al. (2008) investigated and compiled CAI modal abundances from different studies within CMs and reported an average of $1.21^{+1.0}_{-0.5}$ area% (2SD) with a total investigation area of 156 mm^2. Dunham et al. (2023) also reported an average CAI modal abundance of $1.3^{+2.5}_{-0.8}$ area% (max; min) for CMs also from the compilation of previous works from the literature (with different criteria for data selection). Despite this seemingly wide discrepancy, it is important to note that both of these studies were not focused on CM CAIs and did not take into account the degree of aqueous alteration of the samples. This study comprises more data from lower petrological subtypes which, as shown previously, lower the average CAI modal abundance value.

When selecting comparable studies and datasets, options were quite limited. Some studies did not separate data per type refractory inclusions (AOAs and CAIs were combined), were not transparent in their method for CAI selection and measurement, or simply did not provide the total area investigated (making it impossible to convert results to modal abundances). Studies involving point counting were also avoided unless the method for obtaining measurements was

clearly described and compatible with other sources from the literature (i.e. Rubin 2007; Rubin 2015).

Discrepancies in the CAI modal abundances reported by previous studies investigating the same meteorite can be explained by the heterogeneous nature of the samples. Low modal abundance in Paris (Rubin 2015; cf. Table 3.4 and Fig 2.8) might result from clast differences or from sampling bias. Low modal abundance might also result from clast differences within the same meteorite or from sampling bias (minimal mean CAI size cut-off value higher than present study). This highlights the differing histories of each clast within the CM chondrites and further evidences localised fluid-driven alteration within the CM parent body(-ies). Another potential explanation would be a sampling bias due to the more aqueously altered CAIs being mis-categorised as false-negatives due to the difficulty of identifying them properly. However, several studies show that replacement of Al-rich refractory phases leaves high enough concentrations of Al (mobility of Al low in these conditions; Lee & Greenwood, 1994; cf. Chapter 3) within the emplacement of the replacing mineral, thus, unaffecting the method used in this study relying on Ca-Al-Mg EDS maps.

However, although this relationship appears to be promising, it needs to be supplemented by data. According to Hezel et al. (2008), CAIs follow a Poisson distribution, meaning that data can only be representative if large areas are studied (1000-2000 mm^2). This estimate is based upon multiple simulations of CAIs within fictitious carbonaceous lithologies and does not take into account heterogeneity within CMs (e.g. brecciation, localised fluid alteration). This renders the task to accumulate sufficient areas of study for precise lithological alteration grading significantly more difficult. To give a point of reference, the total investigated area of CM lithologies used to evidence this relationship amounts to 716.6 mm^2 (cf. Fig. 2.8), while including ten different CM meteorites (Mighei was excluded from plot due to the original study missing data for determination of CAI modal abundance measurement). Nevertheless, this only proves that this relation is worthy of being studied further and added upon. To this end, future work will focus on increasing the surface area and diversity of petrologic types of CM lithologies studied in order to investigate the multiple parent body origins of CM chondritic breccias (Suttle et al., 2021). Future work

will also involve the study of CAI size distributions as shown in Hezel et al. (2008).

2.5 Conclusions

Petrographic observations and geochemical data indicate that the most abundant refractory inclusions within four studied CM chondrites are spinel-pyroxene (28%), followed by spinel-pyroxene-perovskite (21%), spinel (12%), spinel-perovskite (8%), spinel-perovskite-hibonite ± (6%), spinel-pyroxene-hibonite ± perovskite (6%), hibonite ± spinel ± perovskite (6%), and spinel-pyroxene-olivine ± perovskite (5%), spinel-olivine (3%) and pyroxene (1%), and other various minor assemblages. The most common type of CAI, categorised mineralogically and morphologically, within CMs are simple inclusions (55.9±3.5%, SD), followed by simple aggregates (33.9±6.4%, SD), and complex aggregates (10.2±3.8%, SD). This distribution seems consistent in four different meteorites (Winchcombe, Mighei, DNG 06004, and LAP 02239), from highly (CM2.0) to mildly (CM2.6) aqueously altered lithologies. Further results from this study combined with data from the literature show that CM CAI modal abundance decreases relative to the increasing aqueous alteration, due to the alteration and destruction of CAIs through fluid-mediated replacement reactions. This suggests that a homogeneous initial distribution of CAIs within the CM parent body, with heterogeneity within CM lithologies being driven by aqueous alteration. Although more data is required, this correlation (r^2 ~0.6) could prove useful for future efforts in quantifying the degree of aqueous alteration within CM lithologies.

It is, therefore, of utmost importance for future studies to record the total investigated area of the samples, and to provide details regarding CAI area measurements (either individual or total), as well as the mean CAI size cut-off value (minimal mean diameter at which CAIs were excluded from the study due to their size). This will aid in the effort to establish a definite relationship between CAI modal abundance and the degree of aqueous alteration within the CM brecciated lithologies. Future work will focus on increasing the area of investigation of CM lithologies in order to obtain a more representative CAI modal abundance across the different degrees of aqueously altered CM lithologies.

2.6 Acknowledgements

P-E. M. would like to thank Antarctic Search for Meteorites (ANSMET), the NHM and the Muséum National d'Histoire Naturelle (MNHN, Paris) for the loan of the meteorite samples in this study. Prof. M. R. Lee (UofG) is acknowledged for providing measurements of CAIs in DNG 06004 and LAP 02239. Dr. Y. Marrocchi (CRPG-CNRS) is acknowledged for providing BSE and EDS maps of the Asuka 12236 meteorite.

3 Multiple Aqueous Alteration Events Recorded within the Calcite- and Grossmanite-bearing CAIs of the Winchcombe CM2 Carbonaceous Chondrite

3.1 Introduction

The Winchcombe meteorite is a CM2 (Mighei-like) carbonaceous chondrite breccia composed of eight main CM lithologies within a cataclastic matrix (Suttle et al., 2024). These lithologies display a wide range of aqueous alteration states, from near-completely aqueously altered (2.0; Suttle et al., 2024) according to Rubin's scale (Rubin, 2015; Rubin et al., 2007; Kimura et al., 2020) to moderately aqueously altered (up to 2.6; Suttle et al., 2024). They bear testament of the variety of geological and aqueous alteration events that have occurred on the meteorite's parent body. Aqueous alteration within the CM parent body is thought to have occurred between 4±2 Myr after the formation of CAIs (Fujiya et al., 2012; Visser et al., 2020). Studying CM chondrites is challenging owing to the degree of brecciation and heterogeneity of the lithologies sampled by the meteorites. In addition to this, the CM parent body (or bodies) has (or have) been affected by aqueous alteration, with some CM chondrites displaying signs of post-hydration thermal metamorphism (Nakamura et al., 2005; Suttle et al., 2021). The aqueous alteration history of these bodies can be qualified and quantified through multiple mineralogical, petrographical, and geochemical techniques, and the required information lies within the residues of secondary mineralisation processes.

Refractory inclusions such as CAIs were the first solids to condense from within the hot inner protoplanetary disk. As such, they can provide evidence of the earliest thermal and chemical processing. Their shape and textures vary from irregular structures suggestive of gaseous condensates (i.e. fine-grained and porous, with individual grains <5 μm; Scott and Krot, 2014), to more compact and rounded structures with igneous textures, that may have derived from melts or partial melts that slowly cooled over a period of days (i.e. coarse-grained, grain size >10 μm). However, while CAIs in CVs (Vigarano-like) have been studied extensively, CM CAIs and their aqueous alteration still requires further investigation (Suttle et al., 2021). Because the Winchcombe meteorite is a veritable cornucopia of a variety of CM carbonaceous chondrite lithologies with

eight distinct textures identified so far (Suttle et al., 2024), this meteorite is the ideal candidate for studying the potential of aqueously altered CM CAIs for providing new insights into the origin and evolution of the CM parent body(-ies) within the early Solar System.

Among the 21 simple inclusions, simple aggregates, and complex aggregates (CAI types; cf. Chapter 2) identified in this study, 12 bear signs of fluid-driven alteration processes. In these 12 CAIs fluid-driven aqueous alteration exhibits itself in several different ways. The secondary minerals produced by aqueous alteration processes are particularly evident in complex aggregates – larger inclusions which display noticeable internal textural and mineralogical variations (e.g. replacement by calcite, spinel-free core regions, absence of primitive refractory phases). However, as secondary mineralisation is controlled by primary mineralisation, the mineralogical heterogeneity within these complex aggregate CAIs might have been inherited from solar nebular processes, which would influence the fidelity of these refractory inclusions as records for parent body fluid-driven alteration events. Thus, it is important to determine which features reflect primary condensation/igneous processes in the nebula and which are a consequence of secondary fluid-driven alteration. Most of the CAIs in the Winchcombe meteorite are composed of a spinel-bearing core, however, a heated calcite-bearing altered inclusion (designated as CAI 19), displays a particularly complex and unusual mineralogy: the absence of spinel in its core region and the presence of Ti-rich pyroxenes. This led to a more in-depth investigation of CAI 19, in an effort to separate its thermal history prior to its incorporation within the CM parent body, from its parent body aqueous alteration history. This was done in addition to the thorough description of the various CAI populations found within the Winchcombe lithologies with regards to the diverse aqueous alteration histories of each host lithology.

Preliminary results of this study have been reported in Martin et al. (2022, 2023).

3.2 Material and Methods

3.2.1 Samples

In total, 12 polished sections were investigated amongst the 16 polished sections of the Winchcombe meteorite produced at the Natural History Museum (NHM), London in the mineral preparation laboratory, and described by Suttle et al. (2024). This represents a total investigated surface of 154.7 mm^2 (cf. Table 3.1).

Table 3.1. List of polished sections investigated in this study with their identified lithologies (A-G; attributed by Suttle et al., 2024), surface area investigated, and degree of aqueous alteration. The abbreviations 'Mx' and 'FC' correspond to the cataclastic matrix and the fusion crust, respectively.

Section ID	Area (mm^2)	Lithology	Subtype
P30423	40.2	C	2.2-2.3
P30424	6.2	B	2.1
	1.3	Mx	-
P30540	1.3	G	2.1
	0.7	Mx	-
	3.9	F	2.0
P30541	10.2	D	2.6
	2.0	Mx	-
P30542	7.8	B	2.1
P30545	16.6	B	2.1
	2.3	Mx	-
P30546	11.5	B	2.1
	0.7	Mx	-
P30547	0.7	B	2.1
	13.2	Mx	-
P30548	8.2	E	2.3
P30549	9.0	FC	-
P30552	9.8	A	2.2
P30555	9.1	A	2.2
Total	154.7		

The Winchcombe meteorite is a breccia comprised of eight main lithologies labelled A, B, C, D, E, F, G, H, alongside a cataclastic matrix (Mx), and the fusion crust (FC). In-depth descriptions of lithological units A-G are in Suttle et al. (2024). As indicated throughout the previous Chapter 2, the aqueous

alteration scale described by Rubin (2015) and Rubin et al. (2007), and supplemented by Kimura et al., (2020), is used to quantify the degree of aqueous alteration within the CM lithologies in this study, as it is based on multiple supporting petrographical and geochemical criteria (e.g. alteration of chondrule mineralogy, abundance of Fe-Ni metal, types of carbonates present, etc.). The Winchcombe meteorite displays different degrees of aqueous alteration ranging from 2.0 to 2.6 (Suttle et al., 2024) and 1.1 to 1.2 (King et al., 2022) according to Howard's classification scheme (Howard et al., 2015).

3.2.2 Electron Microscopy

Calcium-Aluminium-rich Inclusions (CAIs) were investigated within each of the studied sections, using large-area Backscattered Secondary Electron (BSE) imaging and geochemical maps obtained using Energy Dispersive X-ray Spectroscopy (EDS). The samples were initially mapped by Scanning Electron Microscopy (SEM) using a Zeiss EVO LS15 operating at 20 kV, with a beam current of 3 nA, and with a live frame time of 270s at the NHM (Suttle et al., 2024), where sample preparation was carried out, consisting in fine polishing and carbon coating of ~20 nm thickness. The resolutions and pixel sizes of the montaged mosaic images are in Table 3.2.

Table 3.2. List of the polished sections mapped using EDS with their image mosaic resolution and pixel size. A more detailed overview of the acquisition and collection of each sample is in Suttle et al. (2024).

Section ID	Accession number	Resolution (pixel)	Pixel size (μm)
P30423	BM.2022,M1-87	8553 x 6355	1.10375
P30424	BM.2022,M3-29	8558 x 5690	0.54885
P30540	BM.2022,M2-42	6666 x 6564	0.60241
P30541	BM.2022,M2-43	6508 x 5216	0.75188
P30542	BM.2022,M2-44	9398 x 5856	0.50050
P30545	BM.2022,M2-47	7687 x 6510	0.75188
P30546	BM.2022,M1-103	5922 x 5450	0.75188
P30547	BM.2022,M1-104	7423 x 6031	0.75188
P30548	BM.2022,M1-105	8218 x 6634	0.50050
P30549	BM.2022,M1-106	7809 x 5279	0.75188
P30552	BM.2022,M9-14	5969 x 7987	0.60241
P30555	BM.2022,M9-17	8608 x 6640	0.50050

Sections P30540, P30548, and P30552 were further studied to confirm the mineralogy of the phases within the CAIs using a Carl Zeiss Sigma Variable Pressure field emission gun analytical SEM, with an accelerating voltage of 20 kV and a beam current of 1-2 nA at the Geoanalytical Electron Microscopy & Spectroscopy centre (GEMS) at the UofG, where further BSE images and EDS maps were collected. Data were processed using the AZtec v6 software from Oxford Instruments. A CAI (designated as number 2; cf. Table 3.3) within section P30542 was also further analysed using a Hitachi S3400 SEM (20 kV/20 nA) and an Oxford Instrument X-Max SSD Energy Dispersive X-Ray Spectrometer at the University of Kent.

Layered RGB colour-coded elemental maps combining Mg, Ca, and Al Kα X-ray lines were combined in order to produce identifiable clusters potentially corresponding to CAIs. Semi-quantitative analyses inferred from EDS spectra of refractory phases were used to prove the refractory nature of the CAIs candidates. It is also important to note that the samples were polished using an Al-rich powder (corundum), which has accumulated in the fractures and small pores of the polished resin blocks and are visible as deep blue clumps. These features are considered artifacts and were disregarded. The high-spatial resolution (0.50-1.1 μm/pixel; cf. Table 3.2) of the obtained BSE and EDS maps allowed for identification of smaller CAIs, with the smallest one in this study having an apparent size of 33 μm in length.

3.2.3 CAI Identification

The method for identifying CAIs within the sections of the Winchcombe meteorite was the same as detailed in Chapter 2. This process relies on four separate steps:

1) Identifying the objects of interests, i.e. the potential CAIs, by locating the regions or objects enriched in Ca, Al, and Mg, in overlayed EDS elemental maps for each section.

2) Using EDS point and area analysis to confirm mineralogy of the targeted CAI candidates. This step was seldom complemented using Electron Probe

Micro-Analysis (EPMA; cf. Section 3.2.4) in order to confirm the refractory nature of the phases of the targeted objects.

3) Individually drawing around the confirmed CAIs using the CorelDRAW X7 software. The resulting bitmap contains the EDS maps of the sections with the outlined CAIs, which are then converted into masks and extracted using the ImageJ software (v. 1.53a) to produce quantifiable measurements of the objects: area size, major and minor axes, perimeter, circularity, aspect ratio, roundness, and solidity (cf. Table 3.5).

4) Description of the CAIs using a simple but efficient mineralogy-dependent classification scheme (cf. Chapter 2), adapted from Macpherson's and Davis's (1994) nomenclature used for the categorisation of Mighei (CM2) CAIs.

It is important to note that Fine-Grained Rims (FGR) were excluded when measuring CAI areas, as their presence and integrity depend on multiple factors that intervened prior to the incorporation (especially in the case of multiple accretion episodes) of these objects within the CM parent body(-ies), although their presence and the completeness of the FGR were recorded for future reference.

The description of the CAIs considers three main structural components: core, mantle, and rim (cf. Fig. 3.1). The core region is generally within the centroid of the inclusion. The mantle envelops the core region and can be up to ~50 μm thick (generally thicker than the rim). The rim is a relatively thin (1-20 μm) outer-layer encircling the core region (and the mantle if present) and can either be in contact with an FGR or the matrix. Not all studied inclusions have a mantle, but all within the Winchcombe meteorite have a rim (cf. Table 3.4).

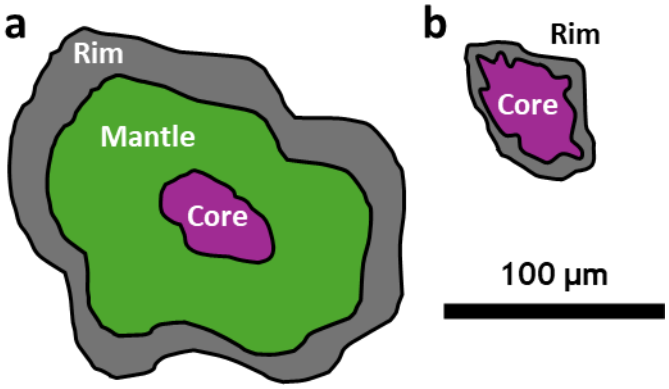

Figure 3.1. Schematic diagram representing the structural components of CAIs used for descriptive purposes.

Among the refractory inclusions that can be found within CM chondrites, Amoeboid olivine aggregates (AOAs) were not included in this study due to their different thermal history and susceptibility to aqueous alteration processes relative to CAIs.

3.2.4 Electron Probe Micro-Analysis

Several sparse elongated Ti-rich clinopyroxenes were identified within CAI 19 (cf. Table 3.3) in section P30552 of the Winchcombe meteorite. Due to their unusual Ti-rich composition, quantitative analyses using EPMA were conducted on these grains and adjacent mineral phases within CAI 19. Data were collected using a JEOL JXA-8530F electron probe micro-analysis instrument (10 kV/20 nA) in focused beam mode with a 1 µm spot size at the NHM. Compositions of oxides within targeted spinel and perovskite grains are located in Appendix 7.5, whereas the average composition of eight individual analyses from Ti-rich clinopyroxene grains is displayed in Table 3.6.

The following standards were used for Wavelength Dispersive X-ray Spectrometry (WDS) analysis: fayalite (Si), corundum (Al), wollastonite (Ca), rutile (Ti), forsterite (Mg), vanadinite (V), haematite (Fe), chromium oxide (Cr), nickel oxide (Ni), and jadeite (Na). Elemental abundances were determined using Kα lines. The detection limits have been calculated to be around 100 ppm (SD x 3) for the acquisitions.

3.2.5 Transmission Electron Microscopy

Two areas of interest (sites 9 and 12 within CAI 19 of section P30552; cf. Fig. 3.8) containing the Ti-rich clinopyroxenes in contact with perovskite and calcite were selected and coated in a 1 µm thick layer of Pt using a gas injection system to protect them from ion beam damage. The Pt layer was first deposited using the electron beam following the deposition of a thicker Pt layer with the io beam. Preparation of the electron transparent lamellae was undertaken at the Kelvin Nano-characterisation Centre (KNC) at UofG using a DualBeam Focused Ion Beam (FIB) microscope equipped with a Ga^+ sidewinder ion column operated at 30 kV at variable beam currents. Milling and extraction of the ~100 nm thick lamellae was done using the FIB and an in-situ micromanipulator before welding to a copper support grid. Diffraction-contrast images and Selected Area Electron Diffraction (SAED) patterns were collected at the KNC using an FEI T20 TEM operated at 200 kV with a double-tilt goniometer holder.

3.2.6 Transmission Kikuchi Diffraction

The two FIB wafers extracted from sites 9 and 12 (CAI 19 of section P30552) were analysed during three different sessions using Transmission Kikuchi Diffraction (TKD) on a Zeiss Sigma Variable Pressure Analytical SEM (20 kV/1-2 nA) equipped with an S2 Symmetry Electron Backscatter Diffraction (EBSD) detector at a 70° sample tilt at the GEMS centre at UofG. The first session was focused on the FIB section of site 9, with a raster size of 324 x 123 pixels and a step size of 0.03 µm, while the second session was focused on the FIB section of site 12, with a raster size 515 x 266 pixels and a step size of 0.02 µm. The third and last session was solely focused on the perovskite grain within site 12 in order to investigate its twinning, with raster size 555 x 205 and a step size of 0.005 µm. All crystallographic data were collected using the Aztec v5.1 software and processed using AZtec Crystal v2.1 from Oxford Instruments. Grain boundaries were defined by >10° misorientation, and wild spikes, pseudo-symmetries, as well as most anomalous and mis-indexed data points were manually removed. Zero solution removal was then applied (up to six neighbours). Furthermore, in order to make the twins within the perovskite grain more visible, the area was isolated as a subset and pseudo-symmetrical indexing was removed.

3.3 Results

3.3.1 Petrographic Overview of the CAI Populations within the Winchcombe Meteorite

A total of 21 refractory inclusions within eight sections of the Winchcombe meteorite were identified and studied. A summary of the location and mineralogy of each inclusion is in Table 3.3, with a brief petrological and mineralogical description for each in Table 3.4, and their geometrical dimensions are in Table 3.5. CAIs have then been sorted following the classification scheme described in Chapter 2 (i.e. simple inclusion, simple aggregate, or complex aggregate).

Table 3.3. Summary of the studied CAIs within the sections of the Winchcombe meteorite. Each inclusion has been attributed a type (i.e. simple inclusion, simple aggregate, or complex aggregate), and the integrity of the FGR, as well as their mineralogy (from most abundant mineral phase to least abundant, in terms of area%) has been recorded.

#	Section ID	Lithology	Type	Mineralogy	FGR
1	P30540	Mx	Simple incl.	Sp-Phyll	Complete
2	P30542	B	Simple incl.	Ol-Sp-Pv-Phyll	Incomplete
3	P30545	Mx	Simple incl.	Sp-Px-Pv	Complete
4	P30545	Mx	Simple incl.	Sp-Px	Incomplete
5	P30545	B	Simple incl.	Sp-Ol	Complete
6	P30547	Mx	Simple agg.	Sp-Ol	Incomplete
7	P30547	Mx	Simple agg.	Px-Sp	Complete
8	P30547	Mx	Simple agg.	Sp-Ol-Hb-Pv	Absent
9	P30547	Mx	Complex agg.	Cal-Sp-Px-Ol-Pv	Complete
10	P30547	Mx	Simple incl.	Ol-Phyll-Sp-Pv	Incomplete
11	P30548	E	Simple incl.	Phyll-Sp	Complete
12	P30548	E	Simple agg.	Sp-Px-Phyll	Incomplete
13	P30549	FC	Simple agg.	Ol-Px-Sp-Pv	Absent
14	P30549	FC	Simple agg.	Ol-Px-Sp-Pv	Absent
15	P30552	A	Complex agg.	Cal-Px-Pv	Incomplete
16	P30552	A	Simple incl.	Sp-Px-Ol	Complete
17	P30552	A	Simple incl.	Cal-Px-Ol-Sp	Complete
18	P30552	A	Simple incl.	Cal-Ol-Sp	Incomplete
19	P30552	A	Complex agg.	Cal-Px-Sp-Pv-Gro	Complete
20	P30555	A	Simple incl.	Cal-Sp-Px-Arg	Complete
21	P30555	A	Simple incl.	Cal-Pv-Sp-Px	Complete

Abbreviations: Arg – aragonite; Cal - calcite; FC – Fusion Crust; FGR - Fine-Grained Rim; Gro - grossmanite; Hb - hibonite; Mx – cataclastic matrix; Ol - olivine; Phyll - phyllosilicate; Pv - perovskite; Px - pyroxene; Sp - spinel.

The Winchcombe meteorite lithologies have a diverse population of CAIs. These inclusions display a wide range of aqueous alteration states from near-completely altered (e.g. extensive signs of mineral replacement) to well preserved with a quasi-spherical intact pyroxene rim (cf. Tables 3.3 and 3.4). They are generally enclosed, either completely or incompletely, by an FGR. Most of the identified CAIs have a core containing spinel and/or perovskite, alongside olivine and/or pyroxene. They mostly fall within three main mineralogical groups: (1) those with spinel-rich cores enclosed within a relatively-well preserved pyroxene rim (spinel-pyroxene inclusions; Greenwood et al., 1994; MacPherson & Davis, 1994; Rubin et al., 2007; Rubin, 2015), (2) those with a forsterite-dominated core comprising ~2 μm rounded grains of perovskite (spinel-pyroxene-olivine inclusions; Greenwood et al., 1994; MacPherson & Davis, 1994; Rubin et al., 2007; Rubin, 2015), and (3) Calcite-dominated inclusions with core regions comprising sparse micrometric spinel and/or perovskite grains (spinel inclusions; Greenwood et al., 1994; MacPherson & Davis, 1994; Rubin et al., 2007; Rubin, 2015).

A large portion of the observed CAIs seem to have undergone some form of alteration, which has identified through the presence of modified textures and structures, and epitaxial mineral replacement features (Daly et al., 2024; Suttle et al., 2024). Calcite-bearing inclusions are referred to as “calcitised” in Fig. 3.4, as to set this particular type of alteration apart. Among the 21 identified CAIs, the complex polymineralic CAI aggregates appear to all have been subjected to this calcite replacement. However, there does not seem to be any relationship between the degree of aqueous alteration of their host lithologies and the type of alteration they have undergone.

Table 3.4 Description of the CAIs identified within the Winchcombe meteorite.

Inclusion #	Type	Description
1	Simple incl.	Small altered CAI, Sp core with void spaces within a Fe-rich Phyll rim of variable thickness (1-5 μm).
2	Simple incl.	Altered CAI with a thin fragmented TCI rim enclosing clumps of Sp and Fo, and a submicrometric Pv grain. The assemblage is encircled by an incomplete FGR.
3	Simple incl.	Rounded porous cluster of micrometric Sp, Px, and Pv grains, enclosed within a continuous Px rim (~5 μm thickness).
4	Simple incl.	Oblong Sp cluster within fragmented continuous Px rim. FGR is discontinuous and partially missing. CAI is bordered by a large (~50 μm long) fragmented Ol grain.
5	Simple incl.	Rounded CAI containing an irregularly shaped Sp cluster enclosed within a heavily fragmented and incomplete Fo rim.
6	Simple agg.	Loosely connected chain of Sp grains, rimmed by Mg-rich Ol (~5 μm thickness).
7	Simple agg.	Globular disjointed Sp clusters within a discontinuous Dio rim. FGR is of variable thickness (1-10 μm).
8	Simple agg.	Sp-Hb core comprising a few sparse micrometric grains of Pv, within an incomplete rim of Mg-rich Ol (~2 μm thickness).
9	Complex agg.	Calcitised CAI, mainly composed of Cal, with a few sparse micrometric grains of Sp and Pv, alongside disjoined Ol clusters. The whole assemblage is comprised within a continuous irregularly shaped bimineralic rim (inner: Sp, outer: Dio), with 1-2 μm thick layers.
10	Simple incl.	Altered CAI, with sparse micrometric Sp and Pv grains within long distended vein-like Fe-rich Phyll clusters. The whole assemblage is within an incomplete Ol rim.
11	Simple incl.	Fragment of a heavily altered CAI with a continuous but incomplete layered rim structure: 1-2 μm thin layer of Serp enclosing an altered (and containing several void spaces) irregularly shaped Sp rim. The core part of the CAI has been replaced by Fe-rich Phyll.
12	Simple agg.	Fragment of porous Sp and Px cluster with Fe-rich Phyll-rimmed grains, enclosed within an incomplete FGR.

Abbreviations: Arg - aragonite; Cal - calcite; Dio - diopside; FGR - Fine-Grained Rim; Fo - forsterite; Gro - grossmanite; Hb - hibonite; Ol - olivine; Phyll - phyllosilicate; Pv - perovskite; Px - pyroxene; Serp - serpentine; Sp - spinel; TCI - Tochilinite Cronstedtite Intergrowth.

Table 3.4. (cont.) Description of the CAIs identified within the Winchcombe meteorite.

Inclusion #	Type	Description
13	Simple agg.	V-shaped chain of Ol containing disjoined clusters of micrometric Sp and euhedral Pv grains, comprised within a continuous rim of Dio (1-2 μm thickness). Maximum thickness of the chain is 20 μm.
14	Simple agg.	Disjoined clusters of Sp and a few sparse micrometric Pv grains enclosed in Ol, within an incomplete rim of Dio.
15	Complex agg.	Calcitised CAI, with sparse micrometric Pv grains within Cal surrounded by an irregularly shaped rim (with several void spaces) of Px of variable thickness (1-10 μm), enclosed within an incomplete FGR.
16	Simple incl.	Central core cluster of Sp containing a surrounded by shapeless clumps of Ol, within a continuous irregularly shaped rim of Dio.
17	Simple incl.	Altered CAI, with an irregularly shaped discontinuous Cal rim of variable thickness (1-10 μm) with sparse Px grains enclosing an altered Sp core with void spaces.
18	Simple incl.	Altered CAI, with an irregularly shaped and incomplete Cal rim of variable thickness (1-20 μm) containing a Sp core with void spaces surrounded by Ol.
19	Complex agg.	Calcitised CAI, mainly composed of Cal with a few sparse round micrometric (~10 μm) Sp grains spread throughout surrounded by an incomplete rim of Px (up to ~10 μm thick). The core region is composed of sparse micrometric clusters of small (1-5 μm) grains of Pv and Gro.
20	Simple incl.	Calcitised CAI, with a Dio rim enclosing a Cal matrix with Mg-Al Sp grains and minor Arg.
21	Simple incl.	Calcitised CAI, with discontinuous rim of Dio enclosing a Cal matrix with Mg-Al Sp and numerous Ti-Ca-rich Pv grains spread throughout.

Abbreviations: Arg - aragonite; Cal - calcite; Dio - diopside; FGR - Fine-Grained Rim; Fo - forsterite; Gro - grossmanite; Hb - hibonite; Ol - olivine; Phyll - phyllosilicate; Pv - perovskite; Px - pyroxene; Serp - serpentine; Sp - spinel; TCI - Tochilinite Cronstedtite Intergrowth.

Table 3.5. Geometric properties of the CAIs identified within the Winchcombe meteorite.

Inclusion #	Area (μm^2)	Major (μm)	Minor (μm)	Perimeter (μm)	Circularity (0-1)	Aspect Ratio	Roundness (0-1)	Solidity (0-1)
1	1000	56	27	155	0.63	2.08	0.48	0.91
2	4000	83	54	319	0.44	1.55	0.65	0.84
3	2000	53	51	174	0.88	1.04	0.96	0.97
4	2000	69	35	228	0.46	1.97	0.51	0.82
5	5000	86	70	266	0.85	1.22	0.82	0.97
6	1000	76	25	214	0.41	3.06	0.33	0.82
7	3000	92	48	393	0.28	1.93	0.52	0.72
8	450	33	17	95	0.63	1.91	0.52	0.89
9	4000	78	63	290	0.58	1.23	0.81	0.87
10	13000	152	112	531	0.60	1.36	0.74	0.93
11	28000	258	139	1897	0.10	1.86	0.54	0.60
12	6000	99	78	449	0.38	1.27	0.79	0.81
13	3000	71	55	349	0.32	1.29	0.77	0.79
14	10000	133	100	493	0.54	1.33	0.75	0.83
15	4000	95	47	310	0.46	2.04	0.49	0.80
16	2000	59	36	227	0.40	1.65	0.61	0.81
17	2000	67	39	237	0.45	1.72	0.58	0.87
18	4000	94	59	320	0.53	1.60	0.63	0.80
19	22000	206	138	739	0.51	1.49	0.67	0.86
20	7000	130	73	426	0.52	1.78	0.56	0.85
21	6000	134	54	495	0.29	2.50	0.40	0.78

3.3.2 Description of the different CAI types in the Winchcombe Meteorite

Most of the identified CAIs in this study are simple inclusions as described in Chapter 2 (cf. Tables 3.3 and 3.4), in common with refractory inclusions within the Mighei CM2 chondrite (MacPherson & Davis, 1994). The cores of these specimens are mainly composed of spinel. These simple inclusions are seldom enclosed within a relatively well-preserved pyroxene rim (generally diopside) or mantled by Fe-rich phyllosilicates (cf. Fig. 3.2). Perovskite and hibonite can occur as accessory minerals alongside but seldom within the spinel. Not all of these CAIs are surrounded by an FGR (either complete or discontinuous) and some are in direct contact with the matrix. No aqueous alteration reaction textures have been observed at the boundaries of simple inclusions and the matrix.

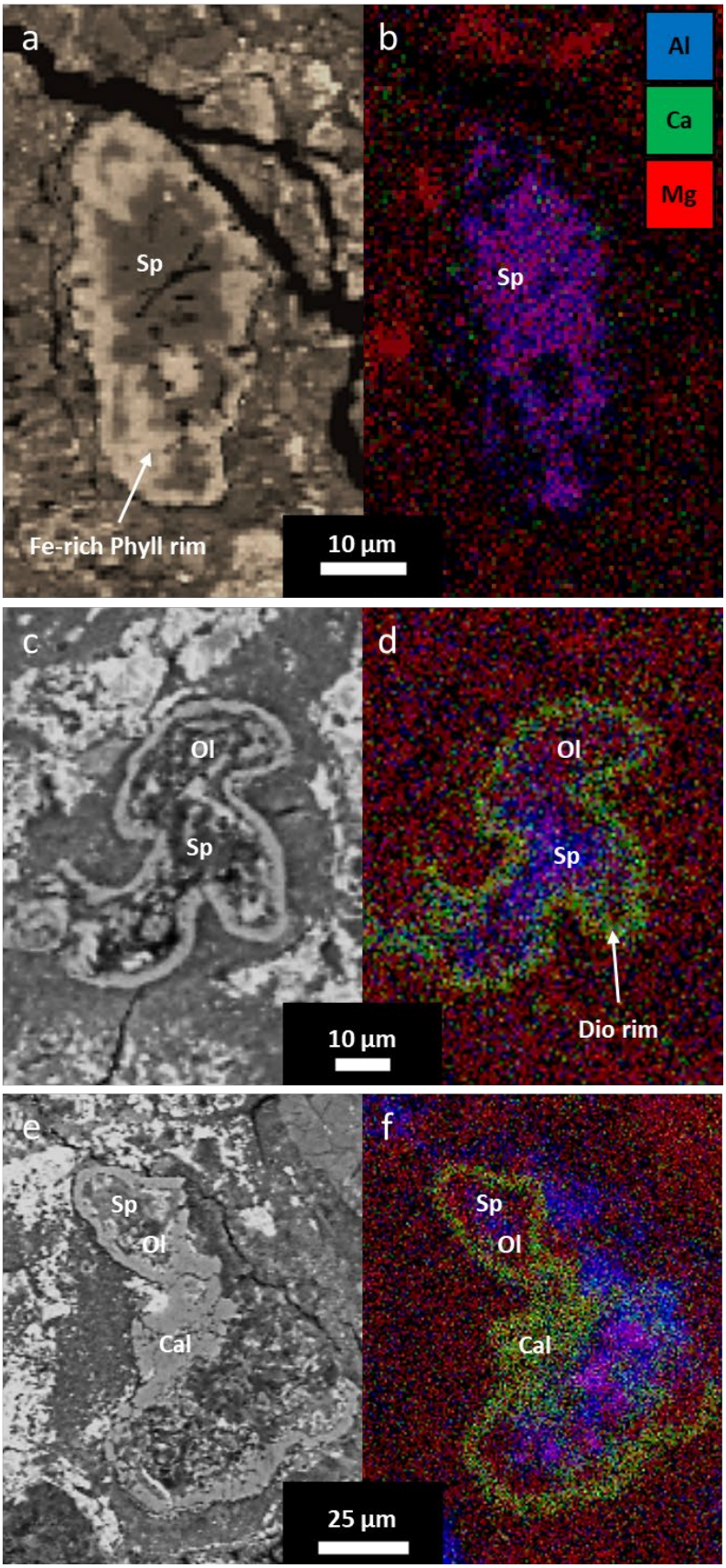

Figure 3.2. CAIs 1, 16, and 18 (respectively), simple inclusions in the Winchcombe meteorite (P30540 and P30552; Mx and lith. A). (a, c, e) BSE images. (b, d, f) Ca-Al-Mg X-ray maps. The core of CAI 1 is composed of spinel (Sp) and is rimmed by Fe-rich phyllosilicates (Phyll). The cores of CAIs 16 and 18 are mostly composed of spinel (Sp), alongside olivine (Ol). CAI 16 is rimmed by diopside (Dio), whereas CAI 18 is altered and rimmed by calcite (Cal). Spinel is dark purple in the EDS maps.

The simple aggregates (cf. Chapter 2) constitute the second most abundant type of CAI observed within the Winchcombe meteorite (cf. Tables 3.3 and 3.4). Their cores mostly consist of spinel grains (associated with perovskite or hibonite as an accessory mineral in some cases) and appear as loosely connected and porous clusters, or as distended chain-like structures, either rimmed with pyroxene (generally diopside), olivine (forsterite; cf. Fig. 3.3), or phyllosilicates.

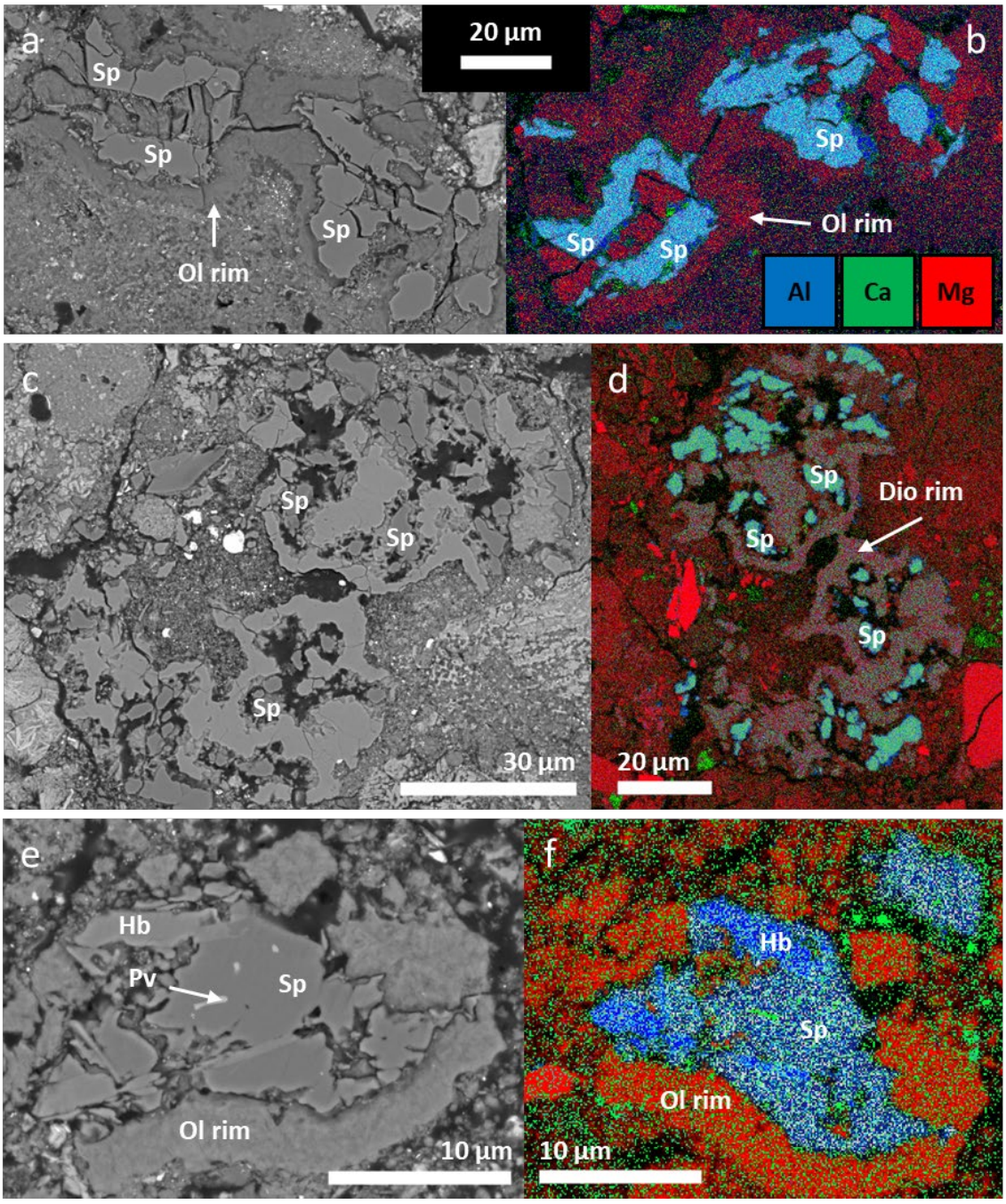

Figure 3.3. CAIs 6, 7, and 8 (respectively), simple aggregates in the Winchcombe meteorite (P30547; Mx). (a, c, e) BSE images. (b, d, f) Ca-Al-Mg X-ray maps. CAI 6 constitutes a loosely

connected chain of spinel (Sp) grains within an olivine (Ol) rim. CAI 7 comprises globular disjointed spinel clusters within a discontinuous diopside (Dio) rim. The core of CAI 8 is composed of spinel and hibonite (Hb), alongside a few sparse micrometric grains of perovskite (Pv), within an incomplete rim of Mg-rich olivine. Spinel is light blue to turquoise in the EDS maps, while small granular patches of dark blue correspond to corundum (Al-rich) polishing powder that accumulated within fractures (apart from f). Images courtesy of Dr. C. Harrison (NHM).

Three complex aggregates were identified within the Winchcombe meteorite. These CAIs are mostly composed of calcite, with irregularly shaped and disjointed regions comprising few sparse micrometric grains of spinel and perovskite displaying various textures. The spinel grains do not appear to be part of a core region. These assemblages are rimmed by pyroxene, as well as spinel in the case of CAI 9 (cf. Table 3.4 and Fig. 3.4). CAI 19, however, contains a distinctive core region, apart from the rest of the spinel grains within its calcite mantle, composed of sparse micrometric grains of perovskite and Ti-rich pyroxene, identified as grossmanite (Ma and Rossman, 2009; Martin et al., 2023) using EPMA (cf. section 3.3.3).

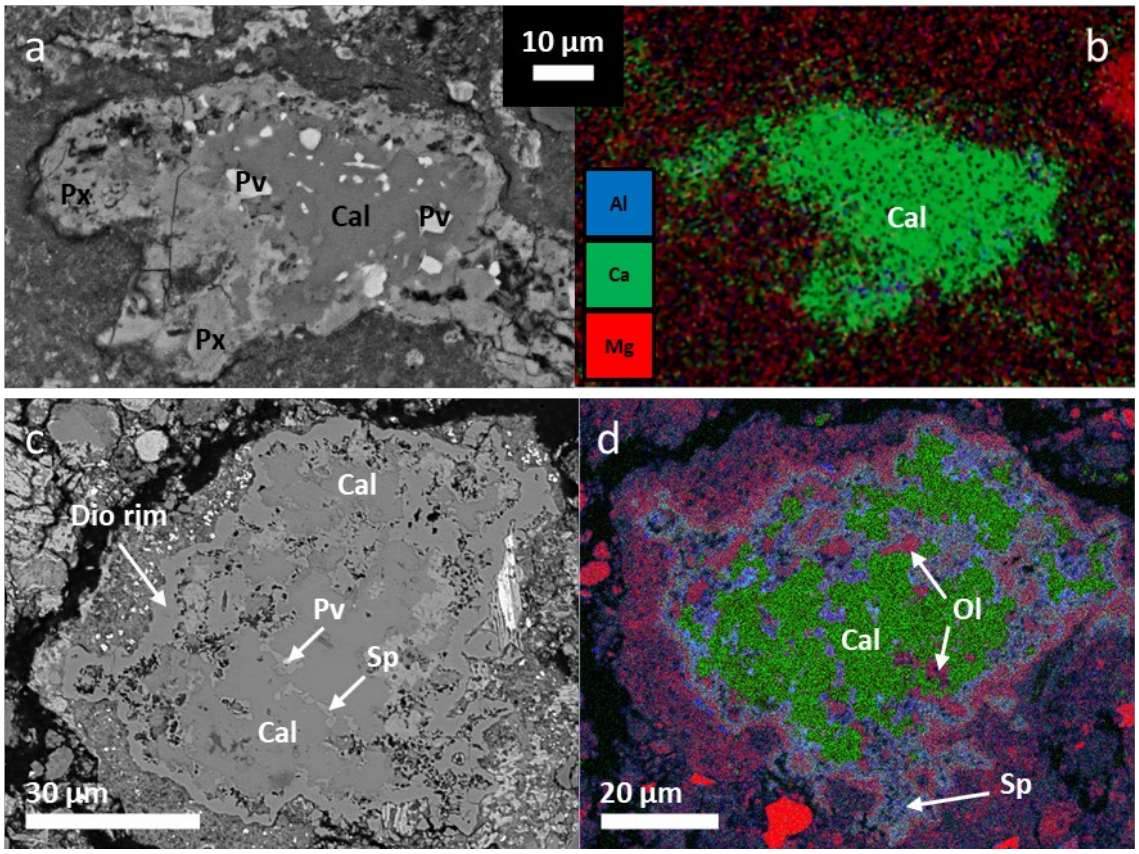

Figure 3.4. CAIs 15 and 9 (respectively), calcitised complex aggregates in the Winchcombe meteorite (P30552 and P30547; lith. A and Mx). (a, c, e) BSE images. (b, d, f) Ca-Al-Mg X-ray maps. CAI 15 is entirely rimmed by pyroxene (Px) and is dominated by calcite (Cal) and contains several disjointed perovskite (Pv) grains. The core of CAI 9 is mainly composed of calcite, with a few sparse micrometric grains of spinel (Sp) and perovskite (Pv), alongside

disjoined olivine (Ol) clusters, rimmed by spinel and diopside (Dio). Calcite is green in the EDS map. Images courtesy of Dr. C. Harrison (NHM).

3.3.3 Identification of Grossmanite in Calcitised CAI

3.3.3.1 Geochemical Characterisation of Grossmanite

CAI 19 within section P30552 (cf. Fig. 3.5) was selected for further geochemical characterisation due to the presence of an unusually Ti-rich clinopyroxene, grossmanite ($Ca(Ti^{3+},Mg,Ti^{4+})AlSiO_6$). Grossmanite has been previously referred to as "fassaite" in the literature, which is now considered an obsolete term, discredited officially by the Commission on New Minerals, Nomenclature and Classification of the International Mineralogical Association (CNMNC-IMA; Morimoto, 1988; Ma & Rossman, 2009). Although previous works (e.g. Brearley and Jones, 1998; Dowty and Clark, 1973; Krot et al., 2021) described particularly Ti-rich fassaite in the CV3 Allende meteorite, the present study constitutes the first mention of grossmanite within a CAI in a CM chondrite (Martin et al., 2023).

The CAI itself constitutes a heavily calcitised object and is mainly composed of calcite with a partial pyroxene rim structure comprising a few sparse globular micrometric (~10 μm) spinel grains spread alongside its inner edges (cf. Fig. 3.5a and 3.5b). The core region of the CAI is composed of sparse micrometric clusters of small (1-5 μm) grains of perovskite and elongated grossmanite grains (cf. Fig. 3.5b). The dimensions of the CAI are 138 x 206 μm in the section plane and is surrounded by an incomplete FGR (up to ~20 μm thick; cf. Fig. 3.5).

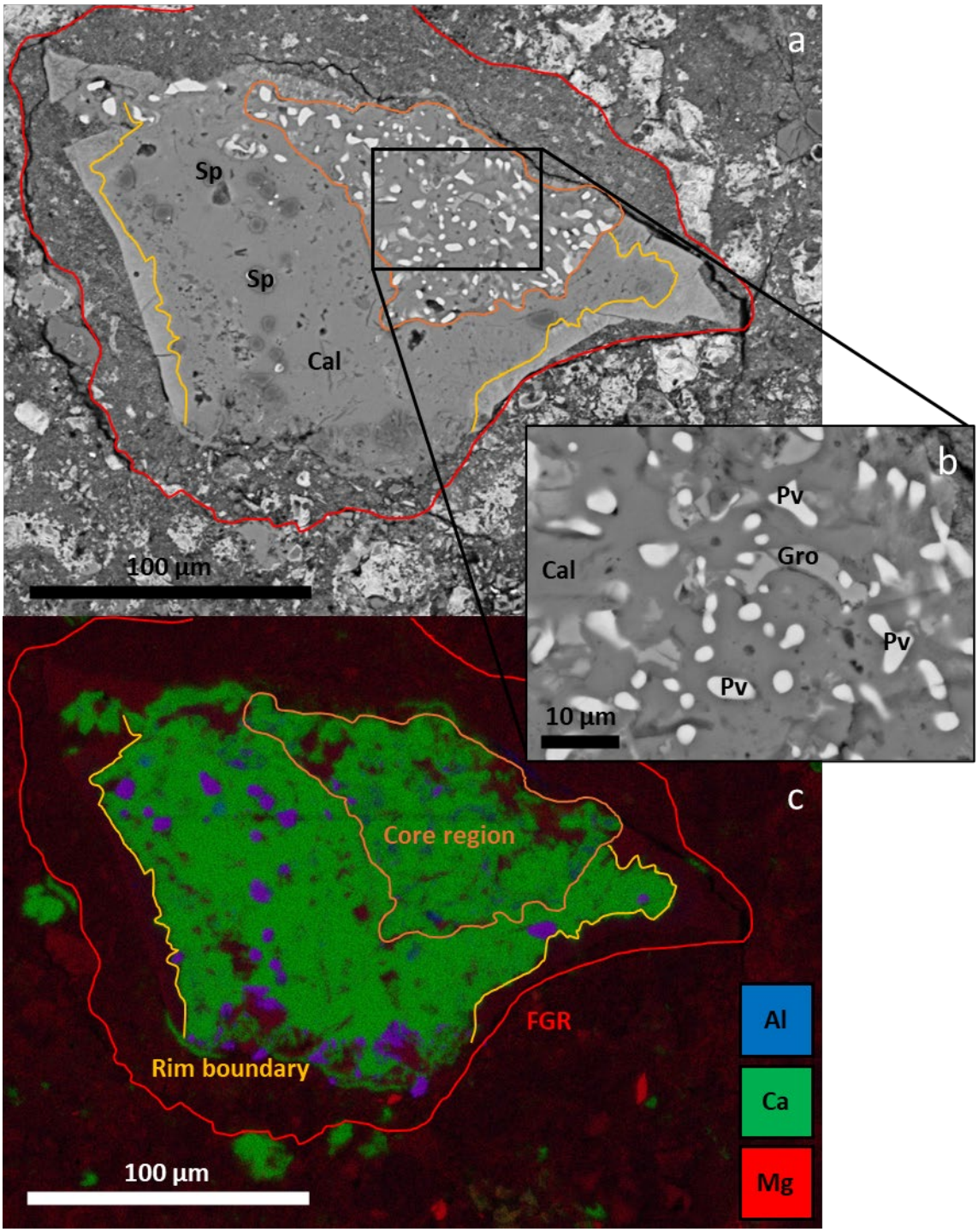

Figure 3.5. CAI 19, a calcitised complex aggregate in the Winchcombe meteorite (P30552; lith. A, CM2.2). (a) BSE image. (b) Close-up BSE map of a portion of the core region of CAI 19. (c) Ca-Al-Mg X-ray maps. The CAI is dominated by calcite (Cal) and contains several spinel (Sp) grains spread around a core region (outlined in orange). This core region is composed of sparse micrometric clusters of small grains of perovskite (Pv) and grossmanite (Gro). The calcite mantle is partially rimmed (boundary highlighted in yellow) by pyroxene (Px) and the assemblage is enclosed within an incomplete FGR (outlined in red). Spinel is purple and calcite green in the EDS map.

In order to quantitatively determine the composition of these Ti-rich clinopyroxenes, the grains were characterised using EPMA and the average composition of eight individual analyses is displayed in Table 3.6 (only

measurements with 97-101 wt.% oxide totals were considered). Specific compositions and formulae inferred from for each analysis are in Appendix 7.5. Results concur with the composition of grossmanite defined by Chi & Rossman (2009).

Table 3.6. Mean composition of (*n* = 8) grossmanite grains within CAI 19 obtained using EPMA. TiO_2* corresponds to the total Ti content (no differentiation between Ti^{3+} and Ti^{4+}). Mean EMPA results of eight individual analyses from Ma & Rossman (2009) are also presented for comparison.

	This study				Ma & Rossman (2009)	
	wt.%	Range		SD	wt.%	SD
		min.	max.			
SiO_2	28.61	25.84	29.89	1.38	27.99	0.32
Al_2O_3	22.96	21.92	23.76	0.61	24.71	0.30
CaO	25.22	24.56	26.36	0.61	24.58	0.18
TiO_2*	15.90	14.34	18.64	1.27	18.80	0.21
MgO	4.87	4.23	5.42	0.42	4.45	0.15
V_2O_3	0.91	0.74	1.46	0.23	0.19	0.02
FeO	0.22	0.05	0.46	0.11	0.08	0.05
Cr_2O_3	0.17	<dt	0.25	0.08	0.03	0.02
NiO	0.15	<dt	0.18	0.02	-	-
Na_2O	0.07	<dt	0.07	<dt	-	-
Total	99.09				100.83	

Grossmanite is a member of the Ca-clinopyroxenes (diopside group) and is defined as being Ti^{3+} dominant in the M1 site (cf. Fig.3.5 and 3.6) with an end-member formula $CaTi^{3+}AlSiO_6$ and a general formula $Ca(Ti^{3+},Mg,Ti^{4+})AlSiO_6$. Determination of the Ti^{3+} and Ti^{4+} proportions for each analysis was done with the assumption of perfect stoichiometry for 4 cations and 6 oxygen atoms. Using this, it is possible to determine the associated valence ratio in regards to the total Ti content and deduce the formula for each point of analysis (cf. Fig. 3.6, 3.7, and Appendix 7.5). Therefore, the following mean empirical formula of grossmanite is obtained (based on 6 O atoms per formula unit):

$$Ca_{1.000}[(Ti^{3+}_{0.235}Al_{0.162}V_{0.028}Cr_{0.005})(Mg_{0.282}Ca_{0.051}Fe_{0.007})Ti^{4+}_{0.229}](Si_{1.111}Al_{0.889})O_6$$

Calculated Ti^{3+}/Ti^{4+} ratios were obtained from charge balance based on cation norms from EPMA data, corresponding to a mean Ti^{3+}/Ti^{4+} valence ratio of 1.026.

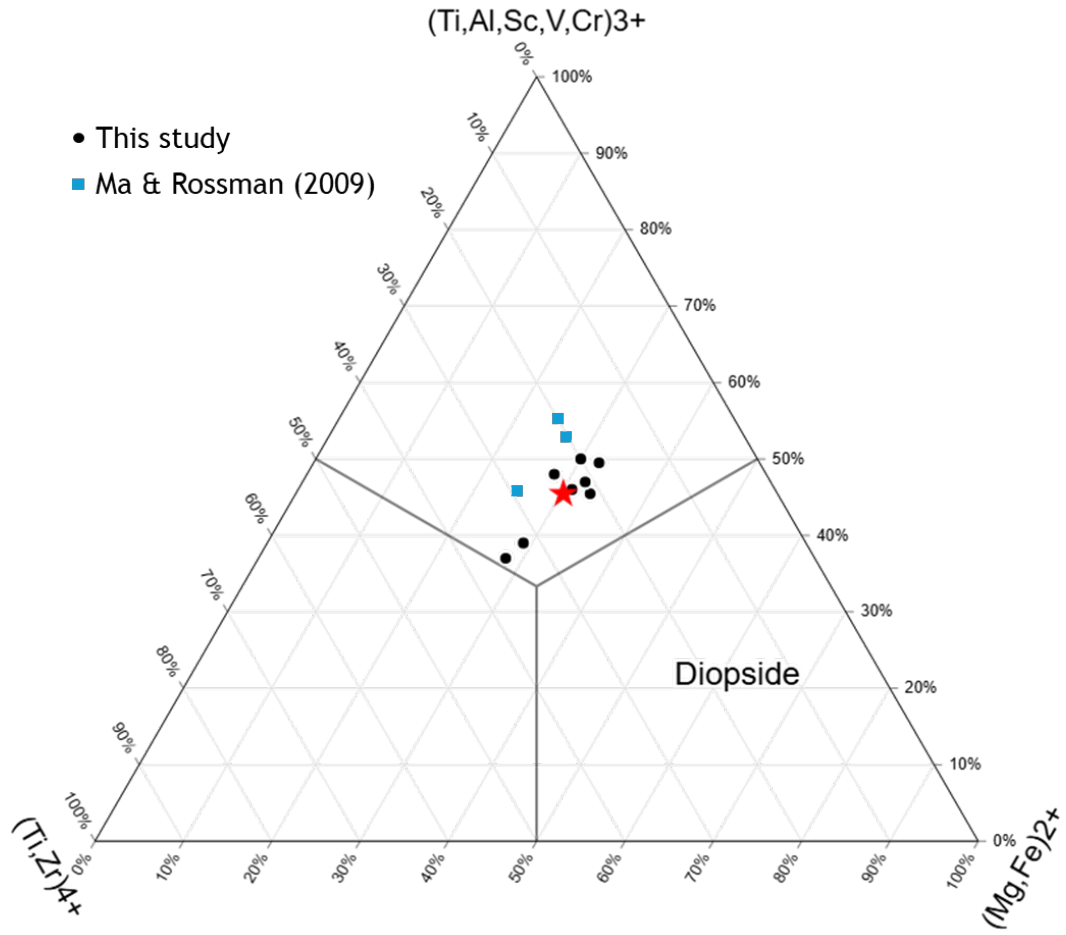

Figure 3.6. Molar ternary diagram of three prominent cation groups in the M1 site of the clinopyroxenes from CAI 19 of the Winchcombe meteorite. The red star represents the average value of all eight analyses in this study. Analyses of grossmanite from Ma & Rossman (2009) were included for comparison (light blue squares). This diagram was designed following the method developed by Ma & Rossman (2009) and Ma & Rossman (2009b).

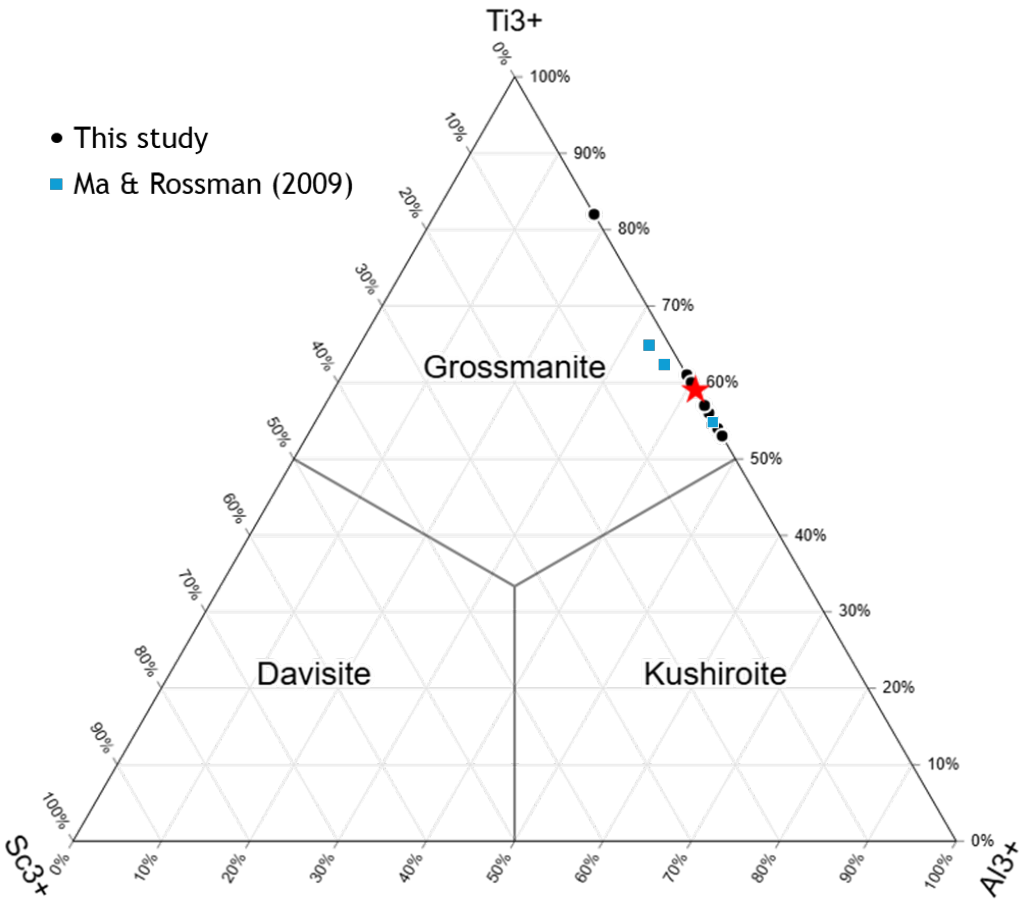

Figure 3.7. Normalised ternary diagram of Ti^{3+}-Sc^{3+}-Al^{3+} proportions inferred from EPMA analyses of the grossmanite grains within CAI 19 of the Winchcombe meteorite. Grossmanite is the Ti^{3+} end-member with the following formula: $CaTi^{3+}AlSiO_6$. The red star represents the average value of all eight analyses in this study. Analyses of grossmanite from Ma & Rossman (2009) were included for comparison (light blue squares). This diagram was designed following the method developed by Ma & Rossman (2009) and Ma & Rossman (2009b).

The oxidation state of Ti within the most refractory mineral phases of the CAIs in the Winchcombe meteorite can provide insights into the formation conditions of these objects (Dyl et al., 2011; Macpherson et al., 2005; Simon et al., 2007). Unfortunately, EPMA of the perovskites embedded within grossmanite and those of spinel grains outside the core region of the CAI yielded no identifiable Ti^{3+}/Ti^{4+} ratios (producing negative Ti valence values). This is due to the low content of TiO_2* (total Ti content, no Ti^{3+} and Ti^{4+} partition) of the spinel grains (<4 wt.% oxide; Simon et al., 2007), and the probable non-negligible and undetermined cation contribution from Fe^{3+} in the mass balance calculations due to the necessary assumption of perfect stoichiometry (Young et al., 2012). Other geochemical techniques would be required in order to accurately measure the

Ti^{3+}/Ti^{4+} ratio in those phases grains directly, such as X-ray Absorption Near-Edge Structure (XANES) analysis (Simon et al., 2007).

3.3.3.2 Crystallographic Characterisation of Grossmanite

As defined by Ma & Rossman (2009), grossmanite has a monoclinic structure and belongs to the C2/c space group. The unit cell parameters of grossmanite are as follows: a = 9.80 Å, b = 8.85 Å, c = 5.36 Å, with β = 105.62°, V = 447.70 $Å^3$, and Z = 4. The average d-spacings of each reflection set (cf. Fig. 3.9) are reported in table 3.7 in regards to the "fassaite" described by Dowty & Clark (1973). TEM analysis was performed on FIB sections extracted from sites 9 and 12 within the core region of CAI 19 (P30552; lith. A, CM2.2) as seen in Fig.3.8.

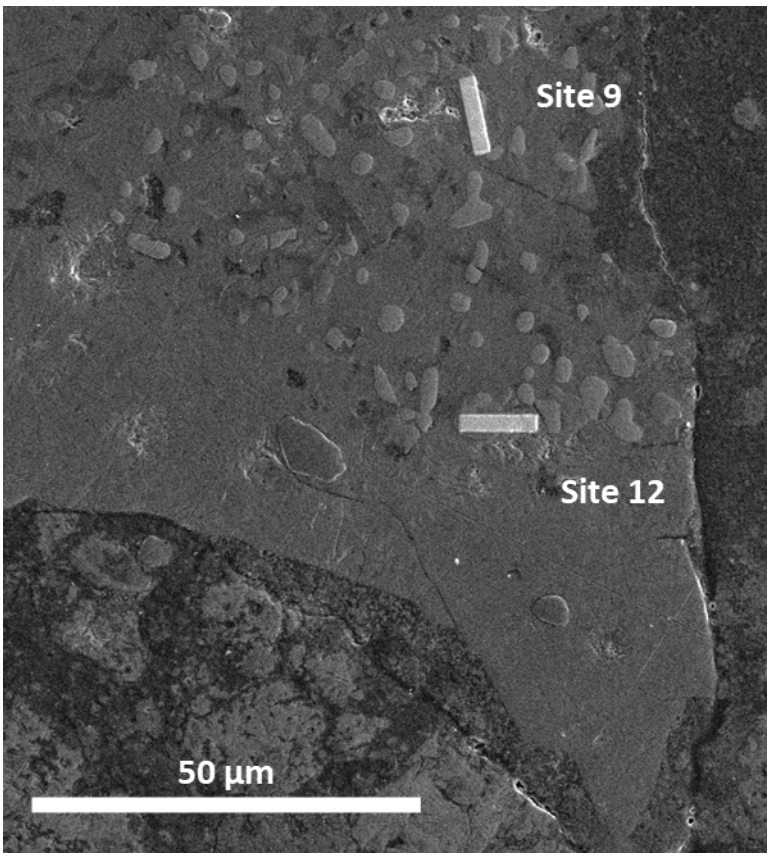

Figure 3.8. BSE image of the locations of the sections selected for TEM and TKD analyses after Pt layering and before FIB extraction within CAI 19 (P30552; lith. A, CM2.2).

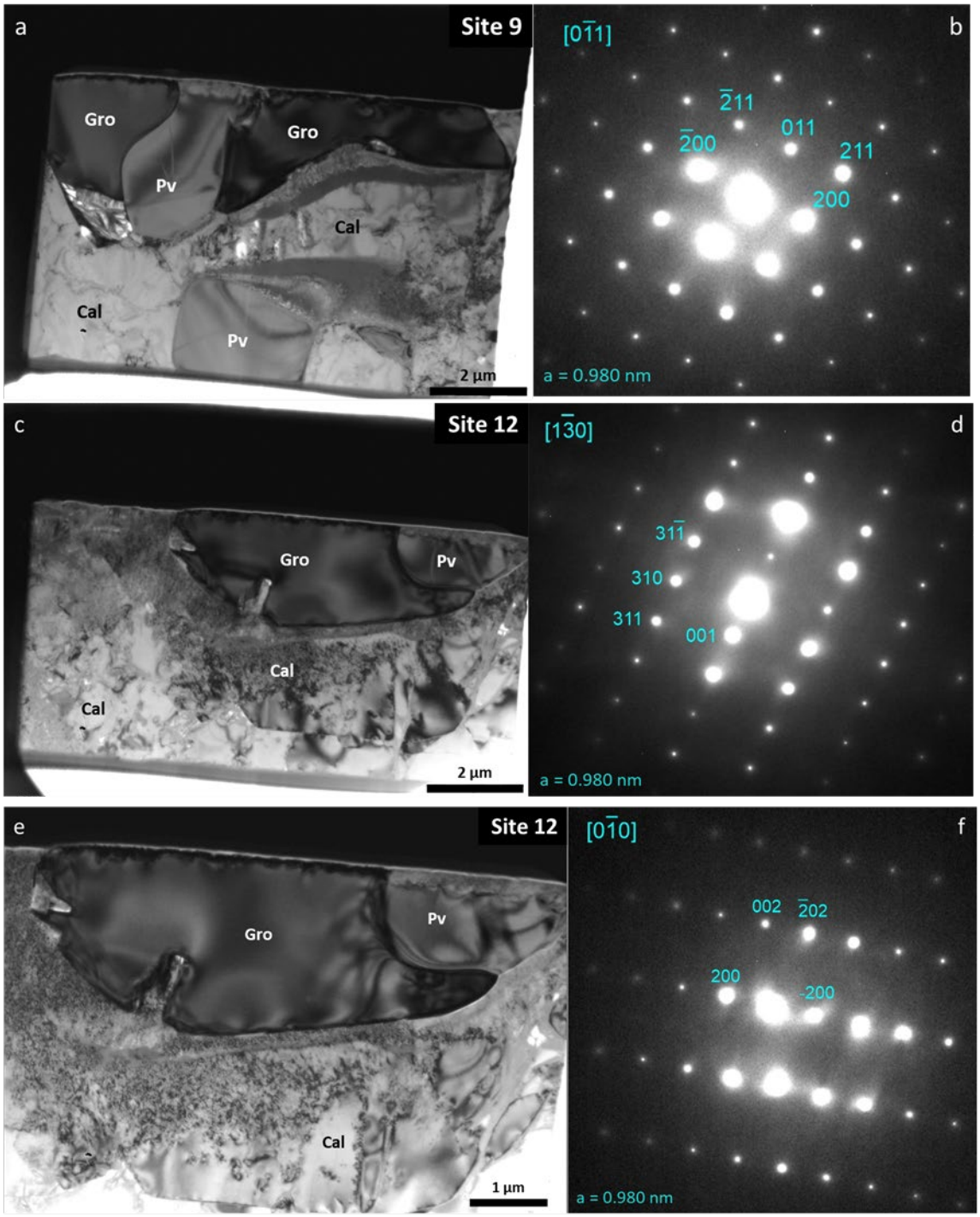

Figure 3.9. TEM results from grossmanite grains in CAI 19 in the Winchcombe meteorite (P30552; lith. A, CM2.2). (a) Bright-field image of site 9. (b) SAED pattern of grossmanite in site 9. (c) Bright-field image of site 12 (orientation 1: A = -1.5°, B = 0.4°). (d) SAED pattern of grossmanite in site 12 (orientation 1). (e) Close-up bright-field image of site 12 (orientation 2: A = -20.1°, B = 9.3°). (f) SAED pattern of grossmanite in site 12 (orientation 2). The d-spacings of the diffraction spots are: a = 9.80±0.01 Å, b = 8.85±0.01 Å, c = 5.36±0.005 Å, β = 105°37'±0.10', Z = 4, and are consistent with the unit-cell parameters of the "fassaite" from Dowty & Clark (1973). In these FIB sections, perovskite (Pv) occurs in contact with grossmanite (Gro) grains, surrounded by a mantle of calcite (Cal). Miller indices of the selected diffraction spots are annotated in turquoise in the images, with the corresponding zone axis in square brackets.

The bright-field images (cf. Fig. 3.9a and 3.9c) reveal several sub-grains of calcite and some patches of amorphous material (fibrous texture; serpentine?) and some well-defined quasi-rectilinear contacts between the calcite sub-grains.

The SAED patterns (cf. Fig. 3.9b, 3.9d, and 3.9f) concur with those obtained for "fassaite" by Dowty & Clark (1973), which corresponds to grossmanite according to Ma & Rossman (2009), as seen in Table 3.7.

Table 3.7. Average d-spacings for electron diffraction spots from the grossmanite grains within CAI 19 of the Winchcombe meteorite (P30552; lith. A, CM2.2) compared to the mineral described as "fassaite" by Dowty & Clark (1973), which corresponds to grossmanite, according to Ma & Rossman (2009).

Dowty & Clark (1973)		Grossmanite (this study)		
hkl	d (Å)	$[0\bar{1}1]$ zone axis d (Å)	$[1\bar{3}0]$ zone axis d (Å)	$[0\bar{1}0]$ zone axis d (Å)
001	5.16	-	5.14	-
200	4.72	4.65	-	4.66
011	4.46	4.41	-	-
-211	3.70	3.72	-	-
310	2.96	-	2.93	-
211	2.92	2.84	-	-
31-1	2.91	-	2.90	-
-202	2.58	-	-	2.57
002	2.58	-	-	2.58
311	2.33	-	2.30	-
202	2.05	-	-	2.02

Grossmanite d-spacings internally calibrated using FIB-deposited platinum. Error ±~1.5%.

The obtained EPMA and TEM results from this study are consistent with previously established measurements for grossmanite, confirming the mineralogy of these Ti-rich clinopyroxenes.

3.3.4 Transmission Kikuchi Diffraction Observations of a Calcitised CAI

3.3.4.1 Microstructural overview

The FIB-produced TEM lamella of CAI 19, referred to as site 9, comprises a small globular micrometric perovskite grain embedded within an elongated grossmanite grain (cf. Fig. 3.9a). These grains display a 120° triple-junction grain boundary between themselves and the calcite mantle. A dark patch is wedged between the grossmanite and the perovskite grain, and the calcite mantle; this resembles serpentine due to its fibrous texture observed in TEM (cf. Fig. 3.9a).

The Grain Relative Orientation Deviation (GROD) angle map shows relatively low to no deformation within the perovskite grain, with slightly more deformation in the grossmanite grain (~2°; cf. Fig. 3.10b). However, despite the calcite mantle displaying no internal deformation in its majority, a ~0.5 µm-wide area along its border with the grossmanite grain shows continuous lattice bending up to 9.16° (extensive internal misorientation).

The Inverse Pole Figure |Z| (IPF) map does not reveal any shared orientations, nor any particular crystallographic relationships between the studied minerals (cf. Fig. 3.10c).

The stereographic projections of crystallographic orientations of perovskite, grossmanite and calcite of site 9 do not indicate any Crystallographic Orientation Relationships (CORs) relative to each other (cf. Fig. 3.11).

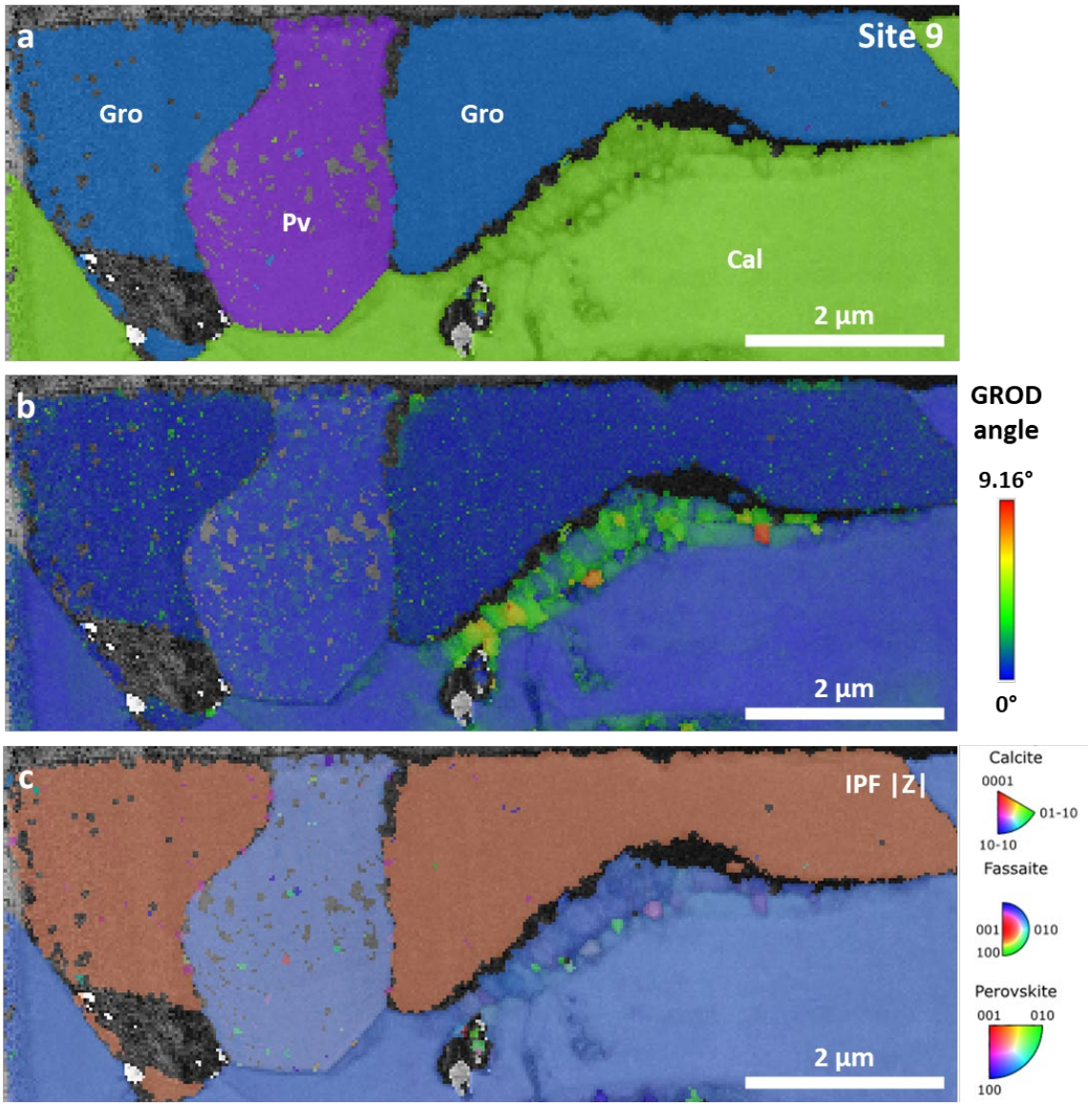

Figure 3.10. TKD results from FIB-produced TEM lamella of site 9 within CAI 19 of the Winchcombe meteorite (P30552; lith. A., CM2.2). (a) TKD phase map. The lamella contains a perovskite (Pv) grain embedded within a grossmanite (Gro) grain, mantled by calcite (Cal). (b) TKD Grain Reference Orientation Deviation (GROD) angle map (grain boundary threshold angle of 10°). (c) Inverse Pole Figure |Z| (IPF) map. Dark areas correspond to non-indexed regions (amorphous phases). Grossmanite was indexed as "fassaite" by the AZtec processing software. Data were collected at an image raster size of 324 x 123 pixels, with a step size 0.03 µm.

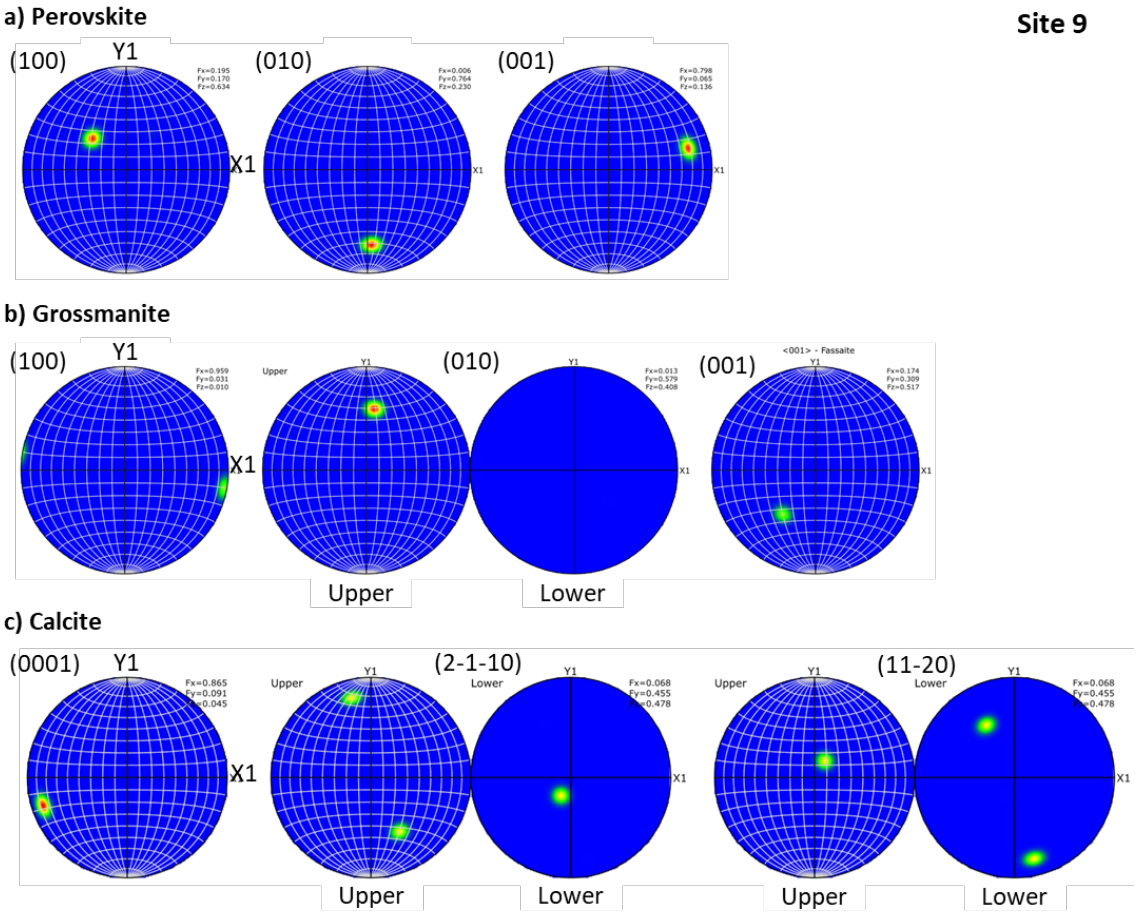

Figure 3.11. Stereographic projections plotting the poles to the Miller indices of minerals within site 9 of CAI 19 (P30552; lith. A, CM2.2). Axes represent crystal coordinates using an equal area projection (triclinic sample symmetry, XY, with Y1 corresponding to the bottom of the sample; cf. Fig. 3.9c) with a half width of 10.0°. (a) Upper hemisphere stereographic projection of crystallographic orientations of the perovskite. (b) Upper and lower hemisphere stereographic projection of crystallographic orientations of the grossmanite. (c) Upper and lower hemisphere stereographic projection of crystallographic orientations of the calcite. No Crystallographic Orientation Relationships (CORs) between the studied mineral phases can be observed.

In the case of the region corresponding to site 12, the lamella comprises a small globular micrometric twinned perovskite grain in contact with an elongated grossmanite grain (cf. Fig. 3.12a) and a polycrystalline calcite mantle. These grains display a 120° triple-junction boundary between themselves and the upper calcite grain.

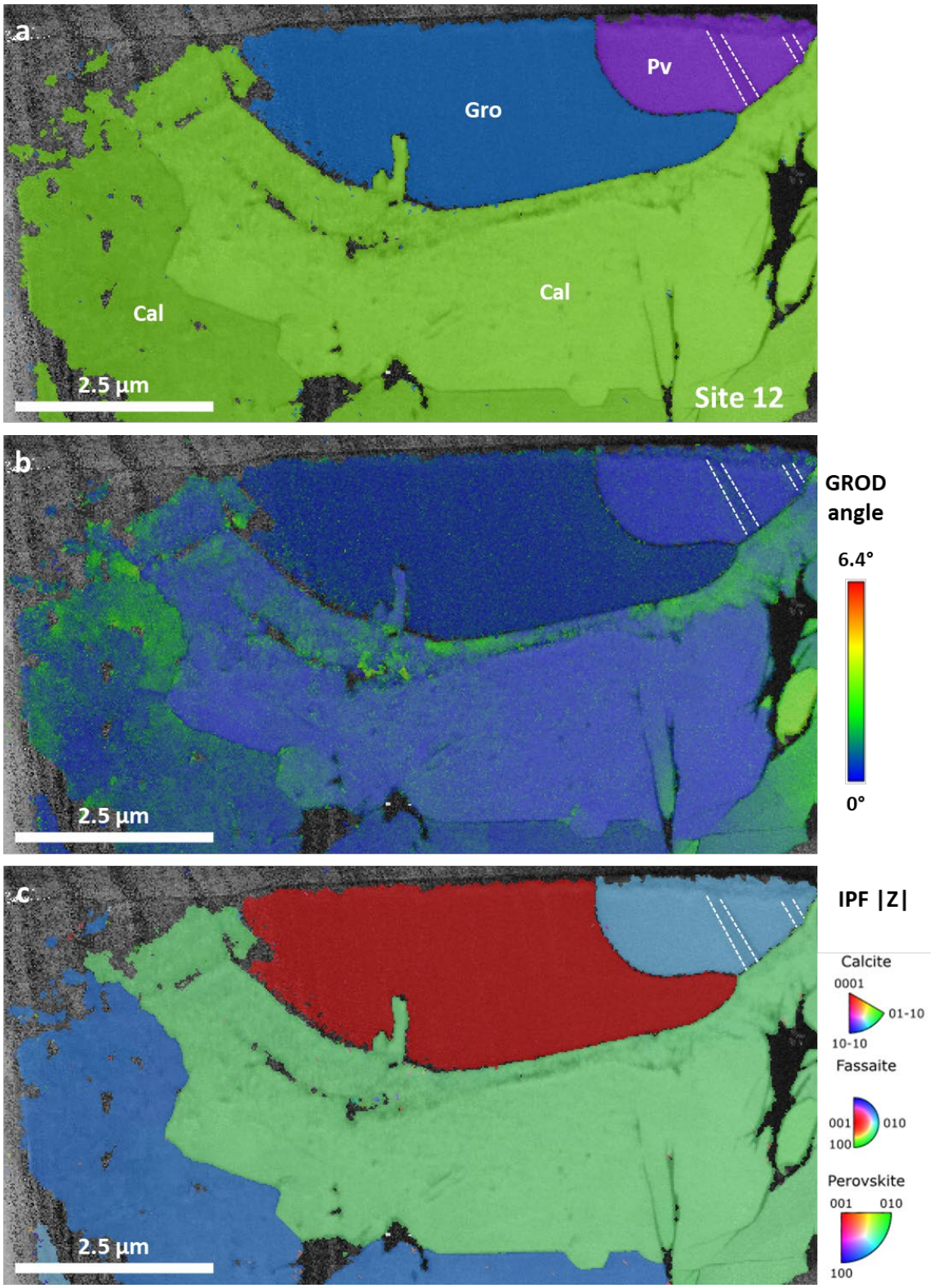

Figure 3.12. TKD results from FIB-produced TEM lamella of site 12 within CAI 19 of the Winchcombe meteorite (P30552; lith. A., CM2.2). (a) TKD phase map. The lamella contains a perovskite (Pv) grain in contact with a grossmanite (Gro) grain, within a mantle composed of two calcite (Cal) sub-grains (hereafter referred to as upper and lower). (b) TKD GROD angle map (grain boundary threshold angle of 10°). (c) IPF |Z| map. Dark areas correspond to non-indexed regions (amorphous phases). Grossmanite was indexed as "fassaite" by the AZtec processing software. The two twins identified in the perovskite grain are indicated with white dashed lines in the GROD angle and IPF maps. Data were collected at an image raster size of 515 x 266 pixels, with a step size 0.002 µm.

The GROD angle map shows minimal to no internal deformation within the perovskite and grossmanite grains (<2°; cf. Fig. 3.12b). However, deformation is more well-developed within the calcite sub-grains: the upper grain is relatively uniform and undeformed apart from the areas within ~0.5 μm of its contact with the grossmanite and perovskite grains (<3° internal misorientation; cf. Fig. 3.12b), whereas the lower calcite grain displays heterogeneous deformation (up to 3° internal misorientation; cf. Fig. 3.12b), along its contact with the upper calcite grain and the edges of the lamella.

The IPF |Z| map does not reveal any shared orientations, nor any particular crystallographic relationships between the grains (cf. Fig. 3.12c). The calcite mantle, however, is divided, along a contact presenting quasi-rectilinear segments, into two sub-grains of different orientations.

The stereographic projections of crystallographic orientations of perovskite, grossmanite and calcite of site 12 do not indicate any CORs relative to each other (cf. Fig. 3.13).

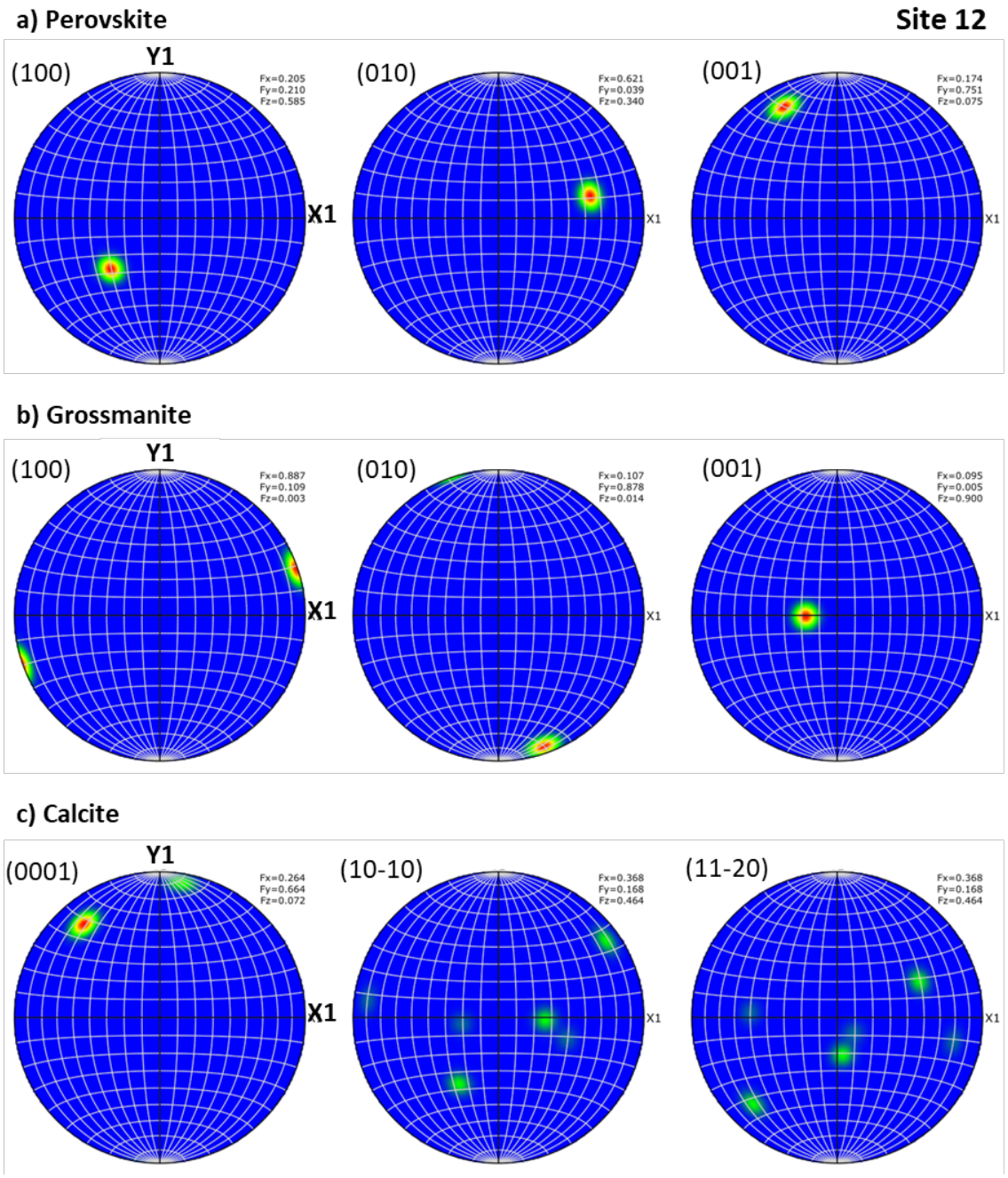

Figure 3.13. Stereographic projections plotting the poles to the Miller indices of minerals within site 12 of CAI 19 (P30552; lith. A, CM2.2). Axes represent crystal coordinates using an equal area projection (triclinic sample symmetry, XY, with Y1 corresponding to the bottom of the sample; cf. Fig. 3.11c) with a half width of 10.0°. (a) Upper hemisphere stereographic projection of crystallographic orientations of the perovskite. (b) Upper hemisphere stereographic projection of crystallographic orientations of the grossmanite. (c) Upper hemisphere stereographic projection of crystallographic orientations of the calcite grains. No CORs between the studied mineral phases can be observed.

3.3.4.2 Twinning in perovskite grain

Two submicrometric twins were identified within the perovskite grain of CAI 19 (P30552; lith. A., CM2.2). Despite being visible in band contrast images, and the Kikuchi patterns being distinct, the resolution of the TKD Kikuchi pattern analysis of site 12 was too low for the AZtec software to index and separate the orientation of the twins from the host grain (cf. Fig. 3.14a). Therefore, the FIB-produced TEM lamella of site 12 was re-analysed at a higher resolution and lower step size (cf. Fig. 3.14).

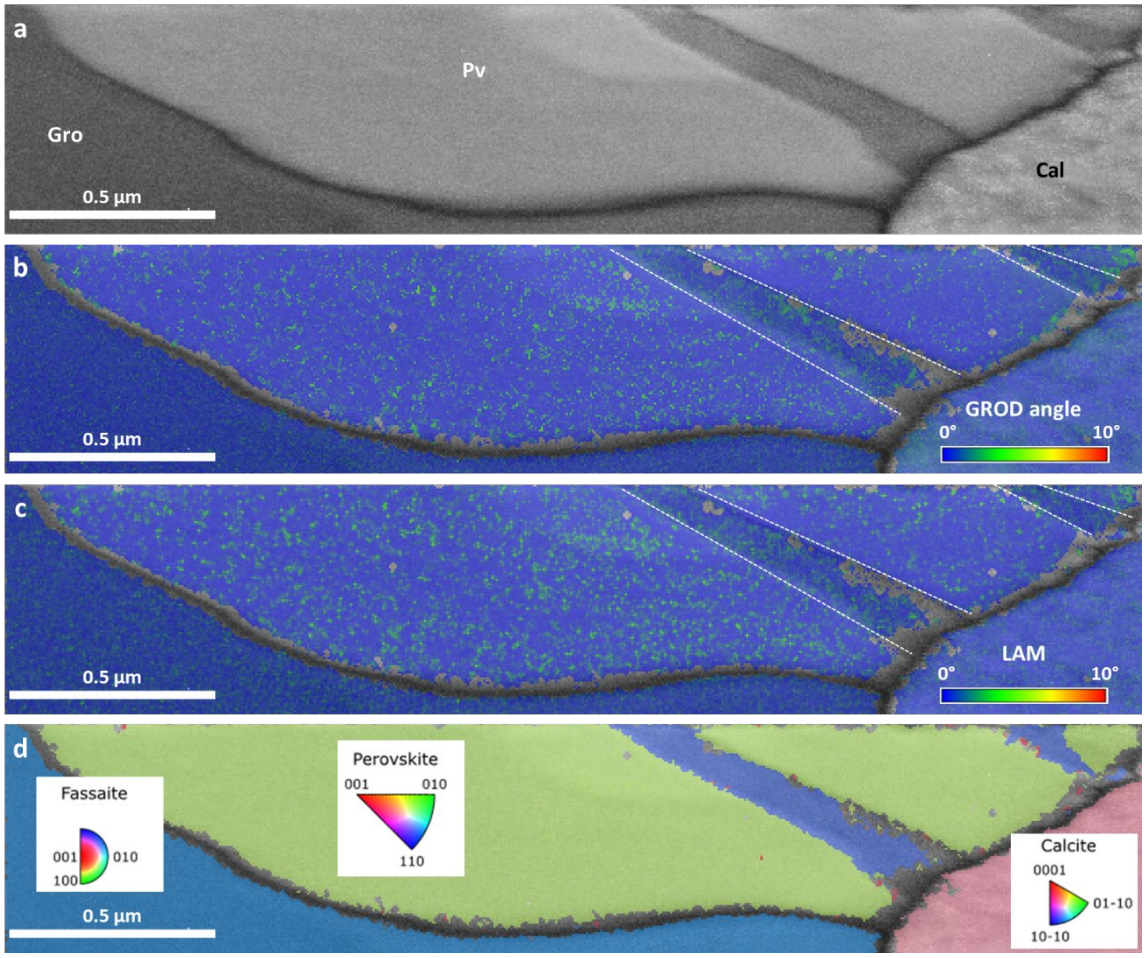

Figure 3.14. TKD analyses of the twinned perovskite grain in site 12 within CAI 19 of the Winchcombe meteorite (P30552; lith. A., CM2.2). (a) Band contrast image. The perovskite (Pv) grain contains two visible twins and is in contact with a grossmanite (Gro) grain and a calcite (Cal) grain. (b) TKD GROD angle map (grain boundary threshold angle of 10°). (c) TKD Local Average Misorientation (LAM) map. (d) IPF |Z| map. Grossmanite was indexed as "fassaite" by the AZtec processing software. The two twins identified in the perovskite grain are indicated with white dashed lines in the GROD angle and LAM maps. Several data points can be seen as differently coloured pixels within the perovskite and non-indexed grey areas remain in the GROD, LAM, and IPF |Z| maps; those artefacts are due to systematic mis-indexing by the AZtec software. Data were collected at an image raster size of 555 x 205 pixels, with a step size 0.005 µm.

The higher resolution band contrast images reveal a ~130 nm spacing between the twin planes (cf. Fig. 3.14a).

The higher resolution GROD angle map and LAM angle map of this site concur with the very low deformation observed within the perovskite grain (0-2°; cf. Fig. 3.12b, 3.14b, and 3.14c).

The higher resolution IPF |Z| map does not reveal any shared orientations, nor any particular crystallographic relationships between the grains (cf. Fig. 3.14d), although twinning within the perovskite is more easily observed.

Upper hemisphere stereographic projections of the crystallographic orientations of the perovskite twins relative to their host grain indicate rotations of ~60° around the [111] axis (cf. Fig. 3.15).

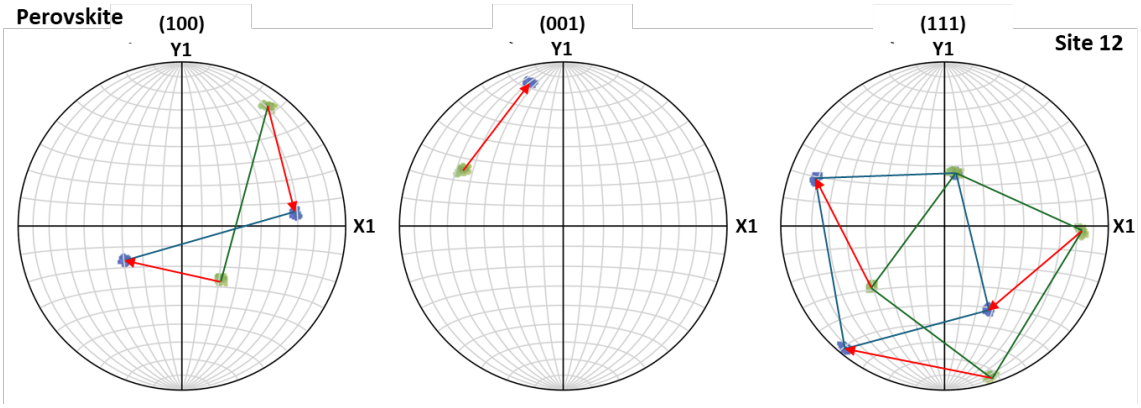

Figure 3.15. Upper hemisphere stereographic projection of crystallographic orientations (pole to the Miller indices) of the twins in perovskite in regards to its host grain within site 12 of CAI 19 (P30552; lith. A, CM2.2). Axes represent crystal coordinates using an equal area projection (triclinic sample symmetry, XY, with Y1 corresponding to the bottom of the sample; cf. Fig. 4.13d) with a half width of 10.0°. Blue points correspond to the crystallographic orientations of the perovskite twins, while green points correspond the crystallographic orientation of the host grain, as seen in the IPF |Z| map in figure 3.13d. The red arrows indicate a ~60°rotation around the [111] axis.

3.4 Discussion

3.4.1 CAI Formation Prior to Incorporation within the CM Parent Body

3.4.1.1 Crystallisation Sequence Revealed by CAI Microstructure

Complex aggregates within the Winchcombe meteorite are mineralogically heterogeneous, dominated by calcite, and among the largest of the CAIs studied. Thus, they constitute the perfect candidates to study the extent of the calcitisation of CAIs. However, the origin of this mineralogical heterogeneity remains elusive. Because these secondary replacement phases do not display any signs of destabilisation, melting, or re-equilibration (cf. Fig. 3.10 and 3.12), it is likely that part of the heterogeneity of these objects is due to parent body alteration processes. However, mineral heterogeneity could also have been partially inherited from solar nebular processes. The potential drivers of this mineralogical heterogeneity will be discussed as highlighted by the following study of the pre-accretionary thermal history of the large and mineralogically exotic CAI 19.

EDS, TKD phase and crystal orientation maps (cf. Fig. 3.5, 3.10 and 3.12) of CAI 19 reveal igneous textures and a clear mineralogical formation sequence between the spinel, perovskite, grossmanite, calcite, and pyroxene grains:

- Spinel grains within CAI 19 are globular and larger (~10 µm) than the rest of the refractory phases within the CAI (cf. Fig. 3.5a and 3.5c). This suggests that the spinel grains were among the first to form as they had more space available for crystal growth.

- Perovskite grains are also globular but smaller and appear to be embedded within larger elongated grossmanite grains (cf. Fig 3.5b, 3.10, and 3.12). This could suggest that grossmanite formed later or potentially simultaneously from two immiscible fluids (fractional crystallisation?).

- Grossmanite is inferred to have formed after spinel and perovskite, as the grains appear to have formed from their contact with the perovskite grains (cf. Fig. 3.5b, 3.10 and 3.12).

- The mantle would then have crystallised enveloping the solid refractory phases. TKD maps reveals 120° triple-junctions between the grossmanite, perovskite, and calcite grains (cf. Fig. 3.10 and 3.12), which is a definite sign for annealing. The calcite was almost certainly not there at the time of annealing as the rectilinear contact between calcite sub-grains is not annealed (cf. Fig. 3.12), and as will be discussed, temperatures associated with annealing of grossmanite and perovskite would have resulted in the thermal decomposition of calcite (cf. section 3.4.1.2). Pole figures show no relationship between calcite and other phases which concurs with our assessment that the calcite is secondary and not one of the original phases of the CAI (cf. Fig. 3.11 and 3.13).

- The CAI is then enveloped by pyroxene forming a rim. This concurs with nebular condensation sequences described by Ebel (2021)

By principle of inclusion, it is likely that the perovskite grains formed before the grossmanite, and for the spinel, perovskite, and grossmanite grains to have formed before the calcite-precursor mantle and the pyroxene rim. The low Ti valence (Ti^{3+}/Ti^{4+} = 1.026; cf. section 3.3.3.1) of grossmanite indicates that the mineral formed in a reduced environment (Beckett, 1986). This means that despite grossmanite forming after spinel and perovskite, it is still a result of high-temperature condensation within the solar nebula. These mineralogical observations, paired with crystallographic data lead to the following crystallisation sequence:

perovskite → spinel → grossmanite → calcite-precursor → pyroxene (rim)

This is consistent with conclusions made by Ma & Rossman (2009) regarding a grossmanite-bearing CAI from the Allende meteorite (CV3) in which the Ti-rich pyroxene is inferred to have formed after spinel and perovskite but

before the crystallisation of melilite ($Ca_2Al_2SiO_7$; a potential precursor for the calcite mantle; cf. section 3.4.2.1).

3.4.1.2 Thermodynamic Conditions of CAI Formation Constrained by Perovskite Twinning

Twinning in the sample has been identified using a band contrast imaging and confirmed by comparing the Kikuchi patterns of the twins in regards to those of the hosting perovskite grain. Using the identified twinning within the perovskite grain, it is possible to estimate or at least constrain the last recorded thermal event (Keller and Busek, 1994) and thus, contribute to reconstructing the thermal history of the CAI before its incorporation with the CM parent body and its subsequent endogenous aqueous alteration events.

Ideal perovskite is cubic and transitions to an orthorhombic structure at room temperature (i.e. terrestrial conditions; Keller and Busek, 1994). Meteoritic perovskite has been observed to follow three twinning laws: (1) a 90° rotation around [101], (2) a 180° rotation around [101], and (3) a rotation around [121]. However, twinning observed in this study corresponds to a 60° rotation around [111] according to the pole figures (cf. Fig. 3.15). Even though previous studies have shown that twinning in perovskite might result from mechanical deformation processes, the obtained twins are predominantly (101) twins(Doukhan and Doukhan, 1986; Keller and Busek, 1994; Wang et al., 1992). This suggests that the observed twins are unlikely to be the result of mechanical deformation, which concurs with the observed low GROD and LAM angles (cf. Fig. 3.14). This conclusion leads to two potential explanations: (1) either this twinning has not been observed previously, or (2) the anomalous rotation angle is due to mis-indexing by the software:

1) <u>Thermodynamic conditions of the system permitted perovskite to remain close to a cubic system while undergoing short-lived high-temperature metamorphism.</u> A rotation of 60° around [111] is a common twin in cubic systems (commonly observed in metals, alloys, and minerals; Li et al., 2023; Gröger et al., 2023) and therefore should not be unexpected. While cooling, perovskite undergoes a displacive phase transition from a high symmetry cubic system to a lower symmetry orthorhombic system (Keller

& Busek, 1994). This particular twinning would suggest that the CAI was formed at temperatures (~1650-1500 K; Grossman and Larimer, 1974) above the cubic-orthorhombic transition temperature before undergoing cooling slow enough to generate the observed 120° triple-junctions between the phases (cf. Fig. 3.10, 3.12, and 3.14), but not slow enough to destroy the (111) twins by annealing (<10^6s; Stolper and Paque, 1986).

2) Thermodynamic conditions of the system led to a phase transition from cubic to orthorhombic followed by a rapid cooling. Keller and Busek (1994) found that meteoritic perovskite predominantly comprises (121) twins, in contrast to terrestrial perovskites, which commonly have more (101) twinning. It is difficult to distinguish a three-fold 60° rotation (3 x 60 = 180°) around (121) [pseudocubic (111)] from a single 60° rotation around [111] in a high symmetry cubic system. The reported (111) twins could therefore be the product of mis-indexing of the twinning of a 180° rotation around (121) from the AZtec software. According to experimentations by Keller and Busek (1994) on synthetic perovskite cooling rates, twinning on (121) only occurs during rapid cooling (≥50°C/min) during the cubic-orthorhombic phase transition, as slower cooling rates (≤50°C/min) correlate with more prevalent (101) twins. This would imply that the CAI system would have been heated to temperatures above the cubic-orthorhombic phase transition (>1573 K; Keller & Busek, 1994) before being subjected to a sudden temperature drop (from ~1650-1500 K; Grossman & Larimer, 1974), possibly during nebula transition.

In any case, it is important to note that annealing could have occurred within three distinct regions: (i) in the proto-planetary nebula (following condensation sequence of refractory mineral phases), (ii) through transient heating during outward migration of the CAIs throughout the chondrule forming region (diffusion model; MacPherson et al., 2005; Ciesla, 2012), and (iii) upon entering the chondrule forming region within the carbonaceous asteroid reservoir following X-wind transport (CAIs being accelerated by magnetic field lines; Haugbølle et al., 2019; Shu et al., 1996). In this last case, annealing within the CAI is very unlikely to have occurred during transport as thermal processes are minimal outside of protoplanetary disk (MacPherson, 2005). However, the

temperatures the system might have undergone in these regions would never have exceeded that of the perovskite cubic-orthorhombic crystal system transition, as the observed twins would have been destroyed by slow-rate annealing. In both detailed scenarios, any primary calcite would have been thermally decomposed due to the CAI being subjected to these annealing temperatures, further evidencing that the calcite within the mantle of the CAI is very likely due to secondary mineralisation.

3.4.2 CAI Alteration After Incorporation within the CM Parent Body

3.4.2.1 Mantle Replacement in Calcitised CAIs

Previous studies (Rubin, 2015; Rubin et al., 2007; Lee et al., 1994; Russell et al., 1998; Lee et al., 2012; Lee et al., 2014) have shown that carbonate replacement is one of the most prominent fluid-driven secondary mineralisation processes to have occurred on the CM parent body(-ies). Primary phases within CAIs (e.g. pyroxene, olivine, plagioclase) have been shown to have undergone low temperature metasomatic alteration within the most aqueously altered CM lithologies (Rubin, 2015; Rubin et al., 2007). Calcitisation only affected simple inclusions and complex aggregates within lithology A (CM2.2) and Mx within the brecciated Winchcombe meteorite (cf. Table 3.2, 3.4, and 3.5). The affected CAIs in this study can be identified by the presence of a mantle dominated by calcite (cf. Fig. 3.4 and 3.5).

TKD analyses of a cross section of the core region of a CAI affected by such alteration reveal two adjacent calcite sub-grains with different crystallographic orientations (cf. Fig. 3.12c). This suggests that the grains formed from separate nucleation points. Deviation of internal grain orientation from the mean grain orientation of the calcite mantle of CAI 19 show extensive internal crystal plastic deformation (up to 9.16°; cf. Fig. 3.10b) along its contact with grossmanite. In site 12 (cf. Fig. 3.12b), this deformation is observable along the edges of the borders of the calcite sub-grains, as well as near the contacts with grossmanite and perovskite. This plastic deformation was very likely caused by crystal growth pressure. The absence of internal deformation within the grossmanite and perovskite grains in both sites confirms that they both formed prior to the calcite, as they were not subjected to the pressure incurred by its

growth (cf. Fig. 3.10b and 3.12b). It is therefore very likely that the two calcite sub-grains formed simultaneously due to there being deformation features within both grains along their common border (cf. Fig. 3.12b). This is reinforced by the fact that their contact is well defined and rectilinear (cf. Fig. 3.12c), albeit lacking annealing features. Thus, an argument can be made that calcite was replacing a more primitive phase through epitaxial replacement. This would explain why the 120° triple-junctions between the original mantle, grossmanite and perovskite were conserved. Furthermore, deformation structures in calcite display no systematic evidence for dislocation control, suggesting that the formation of calcite is the result of low-temperature parent body processes.

The mineralogy of the secondary assemblages depends on the composition of the primary element being replaced and components introduced by the altering aqueous fluid (Krot et al., 2021). According to Brearley & Jones (1998), CAIs in CMs are typically type A, which are melilite-rich, fine-grained, and generally irregularly shaped. Although there is a lack of melilite occurrence in the CM chondrite record, this paucity is generally attributed to extensive aqueous alteration (Greenwood et al., 1994; Rubin, 2007; Rubin et al., 2007; Rubin, 2015; Lee et al., 2019b), but could also be the result of solar nebular processes (MacPherson and Davis 1994; Simon et al., 2006; Marrocchi et al., 2014). In any case, melilite can be found in CAIs from less altered CM lithologies (> CM2.5; Rubin, 2015; Rubin et al., 2007; Rubin, 2007b; Kimura et al., 2020) and is frequently considered a potential calcite precursor (Bunch & Chang, 1980; Johnson & Prinz, 1993; Lee et al., 1994).

Another potential candidate for calcite replacement is anorthite ($CaAl_2Si_2O_8$), which has been found to replace melilite through metasomatism (Krot et al., 2021) during the reprocessing of CAIs during chondrule formation (Krot et al., 2017b; Krot et al., 2018). This reaction would have released Ca into the aqueous solution which would eventually become calcite saturated. Any secondary anorthite produced would have been subsequently replaced by calcite during extensive aqueous alteration events (Krot et al., 2021), potentially resulting in the mineralogy observed in this study.

3.4.2.2 Multiple Secondary Mineralisation Events Recorded in CAIs

According to Tyra et al. (2012, 2007), calcite in CM chondrites can be divided into type 1 and type 2. Lee et al. (2014) further divides these types into four sub-categories: (i) type 1a which occurs as subhedral or anhedral nanoporous grains seldom rimmed with tochilinite/serpentine; (ii) type 1b which is similar to type 1a, without the porosity and rims, and instead, contains Fe-sulphides or Fe-Ni sulphide intergrowths. In contrast, type 2 calcite is finely polycrystalline and microporous, and lacks tochilinite/serpentine rims: (iii) type 2a contains micrometric sized Fe-Ni sulphide inclusions, while (iv) type 2b is similar to type 2a, but lacks sulphides.

Tochilinite-Cronstedtite-Intergrowth-like (TCI) objects and Mg-Fe serpentine have been reported to replace Ca-carbonates in the matrix of the lithologies of the Winchcombe meteorite (Suttle et al., 2024; Daly et al., 2024), including what corresponds to type 1 calcite. However, no calcite within the observed CAIs can be seen being replaced or rimmed by TCI/serpentine (cf. Table 3.3 and 3.4). Therefore, the calcite in the calcitised CAIs of the Winchcombe meteorite is likely type 2b, as it is polycrystalline, presents microporosities, and is not rimmed by tochilinite/serpentine. This suggests that type 2 calcite precipitated after the formation of TCI/serpentine as there is no calcite replacement by TCI/serpentine in the CAIs observed. This implies that the CAIs recorded different fluid-driven alteration events on their parent body(-ies) depending on their mineralogical and morphological properties (i.e. CAI type; cf. Chapter 2) and concurs with similar observations by Lee et al. (2012, 2014) within other samples from extensively aqueously altered CM chondrites.

However, certain simple inclusions and aggregates within lithologies B (CM2.1), E (CM 2.3) and Mx (cf. Table 3.1, 3.3, and 3.4) comprise a mantle/rim composed of a Fe-rich phyllosilicates. Therefore, a potential explanation would be that these CAIs contained type 1 calcite which was then replaced by Fe-rich phyllosilicates (probably TCI/serpentine; Tomeoka & Busek, 1985; Suttle et al., 2024; Daly et al., 2024), while the calcitised simple inclusions and complex aggregates had their original mantle replaced by type 2 calcite during a subsequent parent body aqueous alteration event. Lee & Greenwood (1994) and Greenwood et al. (1994) have also shown that melilite could be a potential

precursor of the Fe-rich phyllosilicates in simple inclusions and simple aggregates. However, since Al remains relatively immobile during low-temperature aqueous alteration (Lee & Greenwood, 1994) this would require the phyllosilicate mantles/rims to be more enriched in Al than the matrix, which is not what has been observed within the altered CAIs (e.g. Fig. 3.2a and 3.2b).

Following previous works on the evolution and chemical variations of an alteration fluid (Lee et al., 2012; Lindgren et al., 2017; Oelkers et al., 2018; Pignatelli et al., 2016), this study implies the potential for multiple generations of chemically distinct fluids affected specific phases through dissolution and replacement over short periods of time (Daly et al., 2024). Under the assumption that all the now-altered CAIs originated from the same initial population of melilite- or anorthite-bearing CAIs, the CAI populations of the Winchcombe meteorite can be divided into three groups depending on the mineralogy resulting from their altered state, following the proposed aqueous alteration sequences (cf. Fig.3.15):

1) Simple inclusions and aggregates from lith. E, along with a few simple inclusions from lith. B and Mx, that experienced an early fluid-driven replacement of melilite/anorthite by type 1 calcite, before undergoing a second alteration event, leading to the replacement of said-calcite with Fe-rich phyllosilicates.

2) Complex aggregates and several simple inclusions from lith. A, along complex aggregates from Mx that underwent a later alteration event, replacing their melilite/anorthite mantles/rims with type 2 calcite.

3) The rest of the simple inclusions and aggregates from lithologies A, B, FC, and Mx that did not visibly experience the described alteration events.

This does not necessarily indicate that CAIs from the third category did not undergo aqueous alteration; they are not likely pristine as none of them are composed of melilite or anorthite. Among the affected lithologies, simple inclusions from lith. A, and simple aggregates and a few simple inclusions from Mx do not display effects of the described aqueous alteration events. This

suggests that they have either undergone a different type of fluid-driven alteration or that the few of them that exhibit mantle structures did not originally have a mantle or rim of melilite and/or anorthite. This could be evidence of nebular heterogeneity producing diverse populations of CAIs (McKeegan et al., 1998).

These observations provide further evidence to the hypothesis that the CM parent body experienced heterogeneous aqueous alteration processes (Pignatelli et al., 2016; Suttle et al., 2024; Daly et al., 2024), as the first metasomatism event has only apparently affected CAIs from specific lithologies (e.g. lith. B, lith. E, and Mx; cf. Fig. 3.16). However, the heterogeneity of the extent of these aqueous alteration events might also be explained by differences of pervasiveness of clasts (e.g. anisotropic permeability; Bland et al., 2009; Hanna et al., 2015, 2022; Lindgren et al., 2015; Zhang, 2013) or by different matrix compositions (Hanowski and Brearley, 2001) producing microchemical environments that influenced the composition of the altering fluid. It is also important to note that heterogeneity within CM lithological clasts themselves was also evidenced by multiple studies (Bischoff, 1998; Brearley, 2006; Leroux et al., 2015; Metzler et al., 1992; Zolensky et al., 1997). In any case, these hypotheses require further investigation.

According to age data of carbonates from recent works, (Fujiya et al., 2012; Visser et al., 2020), CMs have an alteration age of $4{,}563.4^{+0.4}_{-0.5}$ Myr. These studies further suggest that all carbonates formed due to multiple low-temperature hydrothermal aqueous alteration events (e.g. calcite replacement within the CAIs) during a relatively brief period of time ranging from 2-6 Ma after the formation of CV (Vigarano-like) CAIs. Although, it is important to note that these inferences are made from small sample sizes and that the CAIs within the Winchcombe meteorite are not homogeneous in mineralogy, nor in morphology (cf. Tables 3.3 and 3.4).

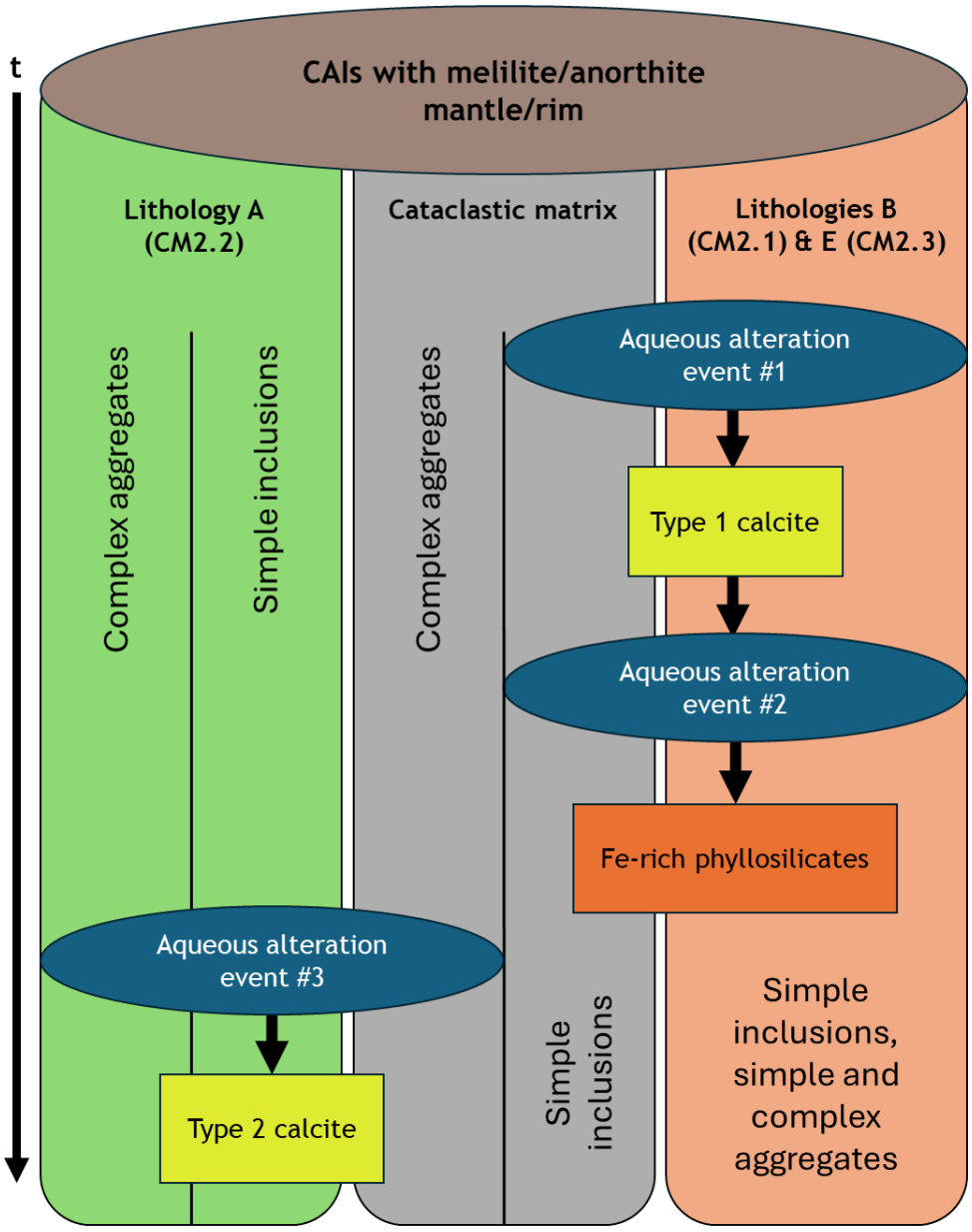

Figure 3.16. Schematic diagram of the proposed heterogeneous aqueous alteration sequences that affected the mantles and rims of melilite- and/or anorthite-bearing CAIs according to their type within the lithologies of the Winchcombe meteorite.

3.5 Conclusions

CM carbonaceous chondrites witnessed extensive fluid-driven alteration processes within their parent body(-ies) which greatly affected their original components (e.g. Fuchs et al., 1973; Bunch and Chang, 1980; Tomeoka and Buseck, 1985; Brearley, 2006a; Suttle et al. 2021; Suttle et al., 2024; Daly et al., 2024; Rubin, 2015; Rubin et al., 2007; Kimura et al., 2020). CAIs, which are amongst the first assemblages to have formed from the early solar nebula, have recorded these aqueous processes after their incorporation within their parent

body(-ies). The Winchcombe meteorite, being an amalgam of multiple CM lithologies of a wide range of degrees of aqueous alteration, constitutes an ideal candidate for investigating the effects of such processes.

The investigated sections of the Winchcombe meteorite comprise 21 CAIs, with 12 of them presenting signs of alteration. After investigation of the thermal history of the primary components of a calcitised CAI through the petrological, geochemical, and crystallographic characterisations of its microstructure, at least two episodes of metasomatism were evidenced. Results led to the categorisation of three observable CAI populations within the Winchcombe meteorite, comprising: (i) some that experienced an early fluid-driven replacement of melilite/anorthite by type 1 calcite, before undergoing a second alteration event, replacing the calcite with Fe-rich phyllosilicates, (ii) others that had their melilite/anorthite mantles/rims replaced by type 2 calcite due to a later fluid-driven alteration event, (iii) and the rest of the CAIs that did not experience any visible extensive mineral alteration. In any case, this calcite-forming process would have had to occur early as these specimens are visible even in lithologies with lower degrees of aqueous alteration (Lee et al., 2014; Rubin, 2015; Rubin et al., 2007; Kimura et al., 2020). However, further investigation is required to determine the exact nature of precursor of the calcite within CAIs and its potential relationship to the carbonates within the matrix.

Heterogeneity of the aqueous alteration records could also stem from the diverse thermal histories of the CAIs, as highlighted by the study of the thermal processing of CAI 19 in this study. In-depth investigation of CAI 19 proved that despite undergoing aqueous alteration, the CAI could still provide answers regarding pre-accretionary thermal metamorphism. Future work should include oxygen-isotope measurements to determine the location of the annealing event that affected CAI 19: (i) CAI forming region, near-solar environment (should the perovskite and grossmanite grains be ^{16}O-rich), or (ii) within the chondrule forming region, indicating solid-state annealing through gas-solid equilibrium. Furthermore, oxygen isotope measurements could also be used to compare the composition of carbonates within the matrix in regards to those found within the

altered CAIs in an effort to constrain the extent and types of aqueous alteration within the CM lithologies.

3.6 Acknowledgments

P-E. M. acknowledges support from the Winchcombe fine-grained team (consortium organised by the UK Fireball Alliance) in providing locations of potential CAIs within the meteorite. The Natural History Museum (NHM, London) is acknowledged for the loan of the samples of the Winchcombe meteorite. Dr. L. Daly (UofG) is acknowledged for supporting TKD data acquisition and processing. Prof. M. R. Lee (UofG) is acknowledged for assisting in TEM data collection. Dr. C. Ma (Caltech, USA) is acknowledged for providing EPMA parameters for acquiring measurements of grossmanite and aiding in the associated stoichiometric calculations. Dr. A. J. King (NHM, London) and M. J. Spratt (NHM, London) are acknowledged for supporting and assisting in operating the electron probe at the NHM. Dr. C. Harrison (NHM, London) is acknowledged for collecting close-up EDS maps of CAIs in Winchcombe (P30549). The Scottish Alliance for Geoscience, Environment & Society (SAGES) is acknowledged for providing funding.

4 Origin and Formation of Compound-Chondrule-CAIs (CCCAIs) within CM Chondrites

4.1 Introduction

4.1.1 Aim of Study

Refractory inclusions, such as Calcium-Aluminium-rich Inclusions (CAIs), are the first solids to have formed in the Solar System and some have witnessed thermal alteration (e.g. melting, annealing, partial vaporisation) prior to their incorporation within chondritic parent bodies (Richter et al., 2002; Shahar & Young, 2007; Richter et al., 2007; Grossman et al., 2008; Krot, 2019; Hu et al., 2021). In the case of most of the CM (Mighei-like) parent body(-ies), these inclusions have also undergone low temperature fluid alteration events after accretion (e.g. 0-240°C; Clayton & Mayeda 1999; Busemann et al. 2007; Suttle et al., 2021). Thus, CAIs constitute valuable records of some of the Solar System's earliest events and can provide key constraints on the evolution of the protoplanetary disk (Russell et al., 2005).

Among these inclusions, rare occurrences defined as Compound-Chondrule-CAIs (CCCAIs) have been reported sporadically within most major carbonaceous groups (CO: Grossman et al., 2006; CV: Jacquet and Marrocchi, 2017; CH: Krot et al., 2006). These assemblages were also identified within CM lithologies that have undergone different degrees of aqueous alteration: Aguas Zarcas (Martin and Lee, 2021, 2020) and Paris (Rubin et al., 2015). These rare objects have been described as either CAIs, partially or entirely, enclosed within a chondrule, or as a chondrule enclosed within a CAI, either partially or in its entirety (Itoh and Yurimoto, 2003; Ivanova et al., 2015, 2012; Krot, 2019; Krot et al., 2017, 2005; Misawa and Fujita, 1994; Rubin, 2015; Russell et al., 2017; Wakaki et al., 2013; Young and Russell, 1998; Martin et al., 2024). Nevertheless, CAIs and CCCAIs have yet to be studied intensively in CM chondrites.

CAIs and chondrules are thought to have remained separate until their accretion into mutual parent bodies (Amelin et al., 2002; Krot et al., 2005; Russell et al., 2005; Connelly et al., 2017). However, the existence of CCCAIs suggests that chondrules and CAIs have interacted prior to their incorporation

within the CM parent body(-ies). These interactions could have occurred in high particle density environments of the protoplanetary disk. Since CAIs are more refractory than chondrules, some CAIs or mineral components may have survived the chondrule forming region and can thus provide additional constraints on the thermal conditions under which chondrules formed. These formation conditions remain an open question even to this day (Cashion et al., 2025; Herbst and Greenwood, 2024; Marrocchi et al., 2024). Consequently, CCCAIs could provide a new way of understanding the chondrule forming environment and elucidating the potential role of CAIs in the formation and evolution of chondrules.

The primary objective of this study is therefore twofold: (i) to identify potential genetic links between the CAI and chondrule components of the CCCAIs, and (ii) to determine if the CCCAI components share the same origin as the other individual CAIs and/or chondrules found within the CM samples.

The intra-specific interactions (nature of the relationship between the CCCAI components) were investigated using Electron Backscatter Diffraction (EBSD). The Cockerel, a CCCAI within Aguas Zarcas that is composed of a CAI enclosed within a chondrule, has been selected as the target of the advanced crystallographic characterisation technique to determine its mineralogy and infer its thermal history.

The inter-specific interactions (nature of the relationship between CCCAI components and their CM counterparts) were studied by performing Secondary Ion Mass Spectrometry (SIMS) oxygen isotope measurements of the CCCAI components of the three CCCAIs identified and the minerals within individual CAIs and chondrules within the CM samples.

The preliminary results of this study have been reported in Martin et al. (2021b, 2022a, 2024a, 2024b).

4.1.2 Compound-Chondrule-CAIs

The existence of these CCCAI assemblages evidences the presence of CAIs within a high-density chondrule-forming environment. Since the trajectory and method of travel of CAIs within the protoplanetary disk remains elusive, the study of such objects can not only reveal many clues as to the thermal and alteration history of the material from whence it came but provide invaluable insight into the migration of primitive refractory material throughout the early Solar System. This study is primarily focused on CCCAIs found within CM chondrites and specifically on the potential of these assemblages as witnesses to alteration processes that have occurred prior to and before their incorporation into the CM parent body(-ies).

In this study, two such objects were identified within Aguas Zarcas (cf. Fig. 4.1, 4.2, and 4.4), and one within LAP 02239 (cf. Fig. 4.5 and 4.6). Two other CCCAIs have been described previously in the Paris meteorite (Rubin, 2015). However, the interactions between these refractory inclusions within Paris and their associated chondrules differ from the CCCAIs studied here. In Paris, Rubin (2015) reported chondrules within CAIs, whereas the opposite has been observed in the present study within Aguas Zarcas and LAP 02239.

As its name suggests, a CCCAI is composed of two main components: the chondrule and the CAI. This study defines the following list of criteria in order for an object to be defined as a CCCAI and should be referenced as such:

- The CAI must constitute a simple or complex aggregate (cf. Chapter 2 on the classification of CAIs), i.e. have a core composed of refractory mineral phases (spinel, perovskite, pyroxene), a mantle (more or less preserved), and a rim (either complete or incomplete, but distinguishable).
- The refractory phases of the CAI must have ^{16}O-rich isotopic compositions similar to that reported previously in CM CAIs ($\Delta^{17}O$ ~ -24‰; e.g.Hiyagon and Hashimoto, 1999; Ito et al., 2004; Makide et al., 2009).
- The chondrule component must be a coarse aggregate composed mainly of olivine, pyroxene, glass (including replacive secondary phases), and Fe-Ni metal (Gooding and Keil, 1981; Scott & Krot, 2003).

- The chondrule's mineral phases must have an oxygen isotope composition close to terrestrial (depleted in ^{16}O) similar to that reported previously in CM chondrules ($\Delta^{17}O$ = -7‰ to -4‰; e.g. (Chaumard et al., 2021, 2018; Fukuda et al., 2022).

The term "Compound-chondrule-CAI" is a purely descriptive designation to which this study attempts to link attributes, regarding composition, crystallography, thermal history, and alteration processes. These assemblages are distinct from other objects that can be found in CM chondrites with which they might bear similarities, such as rimmed CAIs, Al-Rich Chondrules (ARCs), and Amoeboid Olivine Aggregates (AOAs).

Some CAIs in CMs are enveloped within a singular rim of olivine or pyroxene. These CAIs, however, are simple inclusions (as described in Chapter 2), and their rim is generally composed of a singular olivine or pyroxene grain that does not display any resemblance to a chondrule: lack of textures, polycrystallinity, no traces of mesostasis, etc. These objects formed following the condensation sequence described in (Ebel, 2006 and 2021); thus, their rims display near-solar compositions.

ARCs are defined by their high aluminium content (Al_2O_3 >10 wt.% oxide) and display similar igneous textures (i.e. porphyritic, sub-ophitic, and barred olivine) and mineral assemblages as ferromagnesian chondrules (Zhang et al., 2020b). They have been described in most chondritic groups (ordinary, carbonaceous, enstatite, and Rumuruti; Bischoff & Keil, 1983; Bischoff & Keil, 1984; Bischoff et al., 1989; Sheng et al., 1991b; Russell et al., 1996; Maruyama et al., 1999; Russell et al., 2000; Krot et al., 2002; Krot & Keil, 2002; Krot et al., 2004a; MacPherson and Huss, 2005; Guan et al., 2006; Akaki et al., 2007; Ma et al., 2008; Rout et al., 2010; Wakaki et al., 2013; Zhang et al., 2014; Wang et al., 2016; Krot et al., 2018) and have intermediate compositions between ferromagnesian chondrules and plagioclase-rich CAIs (MacPherson & Huss, 2005). Thus, they are thought to have formed either from the melting of AOAs and/or CAI precursors ($\Delta^{17}O$ is a mix between solar and chondrule, due to reprocessing of the CAI component) or by the melting of the same precursor material as ferromagnesian chondrules with incorporation of refractory phases in the chondrule forming region ($\Delta^{17}O$-like CM chondrule values; Zhang et al., 2020). It

is within ARCs that relict CAI have been found in CR, CH, and CV carbonaceous chondrite (CC) groups (Krot & Keil, 2002; Krot et al., 2002) which strengthens the argument that CAIs have played a role in the formation of chondrules.

AOAs are the most common type of refractory inclusions within carbonaceous chondrites (Krot et al., 2004; Torrano et al., 2024). They are usually millimetric in size and are characterised by their distinct amoeboid shape and by their fine-grained forsterite composition. They mainly differ from chondrules in their formation process as they are not thought to have formed from the melting of precursor dust but directly from the condensation of vapours in a near-solar environment. Thus, they display ^{16}O-enriched isotope signatures ($\Delta^{17}O$ = -23.7±0.4‰, 2SD; Chaumard et al., 2021; Hiyagon & Hashimoto, 1999; Krot et al., 2004). Some chondrules in CMs may also display similar ^{16}O-rich isotope signatures but have been found to result from the melting of their AOA precursors (Marrocchi et al., 2019). Due to some of them having a core-like structure within the olivine, composed of (Al-rich) anorthite, spinel, and augite, seldom with a diopside rim-like component, there are arguments to be made that AOAs might be transitional between CAIs and chondrules.

4.2 Material and Methods

4.2.1 Samples

The search for CCCAIs in this study used five different meteorites: Aguas Zarcas, D'Angelo Bluff 06004 (designated as DNG 06004 hereafter), LaPaz Icefield 02239 (designated as LAP 02239 hereafter), Paris, and Winchcombe. A more detailed view of the sample selection is listed in Table 4.1 and includes the degree of aqueous alteration that affected the meteorites, quantified using two classification schemes denoted hereafter as Rubin's classification scheme (Rubin et al., 2007; Rubin, 2015; Kimura et al., 2020) and Howard's classification scheme (Howard et al., 2015).

Table 4.1. List of meteorite samples investigated and their reported petrologic type and subtype.

Meteorites	Section ID	Sample type	Petrologic type[a]	Petrologic subtype[b]
	AZ-P1	Polished block		
	AZ-P2	Polished block		
Aguas Zarcas[1]	AZ-01	Thin section	-	2.2-2.8[c]
	AZ-02	Thin section		
	AZ-03	Thin section		
DNG 06004[2]	06004,20	Polished block	1.7[d]	2.4[e]
LAP 02239[2]	02239,5	Polished block	1.5[d]	2.4-2.5[f]
Paris[3]	B1.5	Polished block	-	2.7-2.9[g]
Winchcombe[4]	B.2022, M9-14 (P30552)	Polished block	1.1-1.2[h]	2.0-2.6[i]

[1]Commercially obtained. [2]US Antarctic Meteorite Collection. [3]Museum National d'Histoire Naturelle de Paris. [4]Natural History Museum (U.K.). [a]According to the classification scheme defined by Howard et al. (2015). [b]According to the classification scheme defined by Rubin et al. (2007) and expanded in Rubin (2015) and Kimura et al. (2020). [c]Kerraouch et al. (2021). [d]Howard et al. (2015). [e]Hanna et al. (2020). [f]Lee et al. (2023). [g]Rubin et al. (2015). [h]King et al. (2022). [i]Suttle et al. (2024).

The three CCCAIs reported in this study were identified within CM clasts in the investigated brecciated samples: CM2.2-2.3 (Aguas Zarcas) and CM2.4-2.5 (LAP02239). The Aguas Zarcas sections all sample the same CM brecciated lithology of subtype CM2.2-2.3 (Martin et al., 2020a, 2021a). Their measurements have therefore been grouped together for the purpose of this study.

4.2.2 Naming Convention for CCCAIs

Due to the paucity of CCCAIs within the CM meteorite record, a strict and unique method to identify and differentiate these conspicuous objects has been devised:

- Step 1: Locate the CCCAI-candidate and verify its nature to the best of your capabilities as explained in section 4.1.2 of this chapter.

- Step 2: Delicately trace the outline of the CCCAI using the graphics software of your predilection (do not include the Fine-Grained Rims – FGR - as they are not part of the object themselves and were formed through the rapid accretion of residual dust from the chondrule forming region

after the formation of the CCCAI, prior to the assemblage's incorporation within the CM parent body).

- Step 3: Compare the minutely drawn sketch to a familiar beast, whose species starts with the third letter of the Roman alphabet, i.e. 'C' (pronounced "see"). This happens to also be the third letter of the English alphabet.

- Step 4: Study thoroughly the newly designated object and share your findings, while showcasing your creativity in choosing a name, with the Planetary Science community.

In the unfortunate event you find yourself unable to correlate the shape of the CCCAI to the likeliness of an animal, then refer to step 1 while only using the outline of the CCCAI's CAI component. If all else fails, unbridled creativity is encouraged.

4.2.3 Electron Microscopy

The CCCAIs were identified using sample-wide Backscattered Electron (BSE) images combined with multi-elemental Energy-Dispersive X-ray Spectroscopy (EDS) maps. Sample preparation comprised fine polishing and carbon coating of ~20 nm thickness at the University of Glasgow (UofG).

The maps were produced using a Carl Zeiss Sigma Variable Pressure field emission gun analytical Scanning Electron Microscope (SEM) with an accelerating voltage of 20 kV and beam current of 1-2 nA at the Geoanalytical Electron Microscopy & Spectroscopy centre (GEMS) at the UofG. All data were collected and processed using the AZtec v5.1 software from Oxford Instruments.

Magnesium, calcium, and aluminium Kα elemental maps were combined according to an RGB-colour scheme with Mg in red, Ca in green, and Al in blue, to visually identify clusters corresponding to potential CAIs. Pixel resolutions and sizes for each studied section are indicated within table 4.2. The high-resolution of the obtained maps allowed for identification of CAIs with an apparent size as small as ~10 μm in length.

Table 4.2. List of meteorite samples mapped using EDS with their image mosaic resolution and pixel size.

Meteorites	Section ID	Resolution (pixel)	Pixel size (µm)
Aguas Zarcas	AZ-P1	4888 x 5021	1.00307
	AZ-P2	7778 x 5748	1.00307
	AZ-01	6720 x 8677	1.20368
	AZ-02	5695 x 5537	1.20368
	AZ-03	7556 x 5608	1.20368
DNG 06004	06004,20	7055 x 5553	1.50150
LAP 02239	02239,5	6986 x 5727	1.83234
Paris	B1.5 (both chips)	7076 x 7874	2.32371
	B1.5 (small chip)	5625 x 3805	2.40736
Winchcombe	B.2022, M9-14 (P30552)	5969 x 7987	0.60241

CAIs surrounded by ferromagnesian silicates were given special attention as they could potentially be identified as CCCAIs. Amongst the CAIs selected for this study, a few with a complete and uniform forsterite rim were identified. These objects are defined as ‘rimmed CAIs’ throughout this study. Chondrules composed mostly of ferromagnesian silicates but with an Al-rich mineral phase were defined as ARCs (McPherson et al., 2005; Zhang et al., 2014, 2020, 2024). Mineralogy of the studied objects was inferred from EDS spectra area analysis.

4.2.4 Electron Backscatter Diffraction

The polished section (AZ-P2) of Aguas Zarcas, containing the CCCAI designated as the ‘Cockerel’, was selected for further crystallographic characterisation by EBSD. Sample preparation was carried out at the UofG and consisted in carbon coat removal using 0.3 alumina before undergoing a finer polish using colloidal silica (for the full EBSD polishing protocol, cf. Appendix 7.1), and finally sputter coated with 7 nm of carbon.

EBSD data were acquired using a Carl Zeiss Sigma Variable Pressure analytical SEM (20 kV/1-2 nA) equipped with an NordlysMax2 EBSD detector with a step size of 0.3 µm and a 70° sample tilt. All data were collected using the AZtec v5.1 software and processed using AZtec Crystal v2.1 from Oxford Instruments.

Table 4.3. EBSD crystallographic axes parameters used to investigate forsterite and diopside grains within the Cockerel's chondrule.

	Measurement count	Grain count	Laue group	Lattice dimensions (Å)		
				a	b	c
Diopside	2001	170	Monoclinic (2/m)	9.75	8.99	5.25
Forsterite	152	47	Orthorhombic (mmm)	4.76	10.21	5.98

Disorientation axes diagrams were also generated in order to identify how potential deformation is expressed within the crystal structure of the mineral phases of the CCCAI's chondrule component using Aztec Crystal v2.1. The parameters used for these projections are displayed in Table 4.3 for diopside ($CaMgSi_2O_6$) and forsterite (Mg_2SiO_4) as indexed by the software. Grains under 50 μm^2 in area size were excluded as smaller areas generally constitute artefacts (e.g. small portions of divided fractured grains mis-indexed by the software as being different grains). In the case of diopside, 180° rotation twins (on {100} and {001}) were also accounted for as to mitigate any mis-indexing from the software.

4.2.5 SIMS Oxygen Isotopes

In-situ triple oxygen isotope (^{16}O, ^{17}O, and ^{18}O) Secondary-Ion Mass Spectrometry (SIMS) analyses were conducted on mineral phases within CAIs and chondrules within the following meteorite samples (cf. Table 4.4): Aguas Zarcas (AZ-P2 and AZ-03), DNG 06004 (06004,20), LAP 02239 (02239,5), Paris (B1.5), and Winchcombe (B.2022, M9-14 P30552). All oxygen isotope compositions were measured using the Cameca IMS 1270 E7 ion microprobe (Bouden et al., 2021) at the Centre de Recherches Pétrographiques et Géochimiques (CRPG-CNRS, Nancy, France) with the help of the Ion Probe Nancy Team (IPNT; TA Facility 9) through the Europlanet2024 Research Infrastructure. Sample preparation included coating removal and coating, whether in gold or carbon (10 nm) depending on which coating instrument was available at the time (effects on acquisition are negligible) at the CRPG-CNRS.

Table 4.4. List of objects of interest targeted. The petrologic subtype of each CM lithology investigated is characterised according to Rubin's classification (Rubin et al., 2007; Rubin, 2015; Kimura et al., 2020).

Meteorites	Petrologic subtype of lithology[1]	*n* CAIs	*n* chondrules	*n* CCCAIs
Aguas Zarcas	2.2-2.3[a]	7	21	2
DNG 06004	2.4[b]	7	0	0
LAP 02239	2.4-2.5[c]	5	0	1
Paris	2.7[d]	14	25	0
Winchcombe	2.2[e]	0	3	0
Total		33	49	3

[a]Martin et al. LPSC (2020, 2021). [b]Hanna et al. (2020). [c]Lee et al. (2023). [d]Rubin et al. (2015). [e]Sample P30552 is within lithology A of Winchcombe, which has been characterised as being CM2.2 according to Suttle et al. (2024).

Table 4.5 lists the targets of the analysis which include the CAI component within the CCCAIs (spinel), the chondrule component of CCCAIs (olivine and diopside), CAIs within the matrix (spinel, olivine), and chondrules (spinel, olivine, and diopside) from the different CM lithologies. Rimmed CAIs are within the CM CAI category and ARCs are included within the CM chondrule category. Targeted areas within the minerals were selected considering 10 µm SIMS analysis spot size to avoid overlapping and heating effects from the beam.

Table 4.5. List of objects of interest and mineral phases targeted.

Targeted phases	Measurements
CCCAIs (*n* = 3)	
CAI component	
spinel	6
Chondrule component	
olivine	30
diopside	3
CM CAIs (*n* = 33)	
spinel	85
olivine	3
CM chondrules (*n* = 49)	
spinel	8
olivine	106
diopside	3
Total	244

All measurements were controlled using the sample standard bracketing procedure to correct for instrumental drift over time. Data were corrected using the following standards: olivine (San Carlos Olivine; SCOL), and spinel (Mg-spinel Ipanko). Diopside measurements were corrected using SCOL (bias is relatively small, up to ~1.2‰, according to Zhang et al., 2022). Values displaying low counts or originating from mistargeting were rejected.

$^{16}O^-$, $^{17}O^-$, and $^{18}O^-$ ions were produced by a Cs^+ primary ion beam (~5 µm, 0.2 nA) and measured in multi-collection mode using an off-axis Faraday cup for $^{16}O^-$, an off-axis Electron Multiplier (EM) for $^{18}O^-$, as well as an axial EM for $^{17}O^-$. Entrance and exit slits of the central EM were adjusted to a Mass Resolving Power (MRP = M/ΔM) of 7,000 for $^{17}O^-$ to ensure the removal of ^{16}OH isobaric interference on the $^{17}O^-$ peak. Although the OH contribution was not calculated, it is considered negligible (<0.1 %), as the mass resolution was high enough, the ^{16}OH interference was well resolved, and only anhydrous minerals were targeted. Exit slit 1 for multi-collection was set at MRP = 2500. Total measurement duration per spot was set to 330 s, comprising 30s of pre-sputtering followed by 60 cycles of 5s measurements. The instrumental Mass Fractionation (IMF) line for the three oxygen isotopes was defined using three terrestrial standard materials (SCOL, Ipanko, and Rockport fayalite), to alleviate any matrix effects in olivine. The SCOL standard was reanalysed twice a day to monitor instrumental drift and maintain precision. Instrumental drift was then considered linear and rectified according to the signals recorded by the EMs.

All oxygen isotope compositions are expressed as follows, in per mil units (‰):

$$\delta^{n/16}O = \left[\frac{\left(^{n}O/^{16}O\right)_{sample}}{\left(^{n}O/^{16}O\right)_{V-SMOW}} - 1\right] \times 1000 \qquad \text{(Eq. 4.1)}$$

Where n corresponds to the atomic number of the studied oxygen isotope: 17 or 18, and V-SMOW refers to the Vienna Standard Mean Ocean Water (V-SMOW) terrestrial reference (Lodders & Fegley, 1998).

The Terrestrial Fractionation Line (TFL) was defined by samples linked by mass-dependent fractionation in regard to the V-SMOW composition plot along a slope of 0.52 (Miller, 2002; Rumble et al., 2007).

Mass independent variations, representing vertical deviations from the TFL in a triple-oxygen isotope diagram, are expressed as follows, in per mil units (‰):

$$\Delta^{17}O = \delta^{17/16}O - 0.52 \times \delta^{18/16}O \quad \text{(Eq. 4.2)}$$

Measurement error was determined using the two-Standard Error of the mean (±2SE) as follows:

$$2 \times SE = 2 \times SD/\sqrt{n} \quad \text{(Eq. 4.3)}$$

Where n is the number of cycles per spot and 2SD is the two-standard deviation (corresponding to 95% of the Gaussian distribution) of all the measurements performed during the cycles per spot.

Typical uncertainties consider the external reproducibility of the standards and internal errors on each measurement. They are estimated to be ~0.67‰ for $\delta^{17}O$, ~0.35‰ for $\delta^{18}O$, and 0.70‰ for $\Delta^{17}O$ (error calculated through quadratic summation of errors on $\delta^{17}O$ and $\delta^{18}O$).

Verification of the targeted locations (beam spot laser ablated hole) was done using a FEI Quanta 200F Environmental SEM at the GEMS centre at the UofG. All SIMS analytical spots were checked and any that were not fully on the designated target or included a mixture of different mineral phases were excluded from the data set. The produced BSE and secondary electron images of the targets can be found in the supplementary materials related to this chapter.

4.3 Results

4.3.1 Microstructure of CM CCCAIs

4.3.1.1 The Cockerel

Aguas Zarcas is a polymict carbonaceous breccia composed of five main lithologies (two metal-rich ones, a brecciated CM, and two distinct carbonaceous ones; Kerraouch et al., 2021). All samples in this study are contained within an extensively aqueously altered and brecciated CM lithology (mainly CM2.2; Martin et al. LPSC 2020, Martin et al. LPSC 2021). The CCCAI was found within a clast

that is less aqueously altered (CM2.2-2.3) than the rest of the main lithology of Aguas Zarcas and named after the characteristic shape of its CAI component, resembling a cockerel (cf. Section 4.2.2 and cf. Fig. 4.1a and 4.2). The Cockerel is composed of a quasi-circular chondrule (outlined in yellow; cf. Fig. 4.1a) enclosing a CAI, comprised of a cluster of spinel crystals (outlined in white; cf. Fig. 4.1) mantled by calcite. The entire assemblage is surrounded by an irregular (~8 µm to 25 µm thick) but complete FGR (outlined in red; cf. Fig. 4.1a) composed of very fine sub-micrometre-sized grains of olivine as well as Fe-Ni sulphides (e.g. pentlandite and phyllosilicates), as are most larger objects within the CM brecciated lithology of Aguas Zarcas.

The core of the CAI within the Cockerel is a simple aggregate composed of multiple spinel grains (indexed as chromite by EBSD; <5 µm in size). These grains are randomly orientated with 120° triple-junction boundaries between them. The spinel cluster is enveloped by calcite (most of which was lost during polishing; Fig. 4.1b to 4.1e).

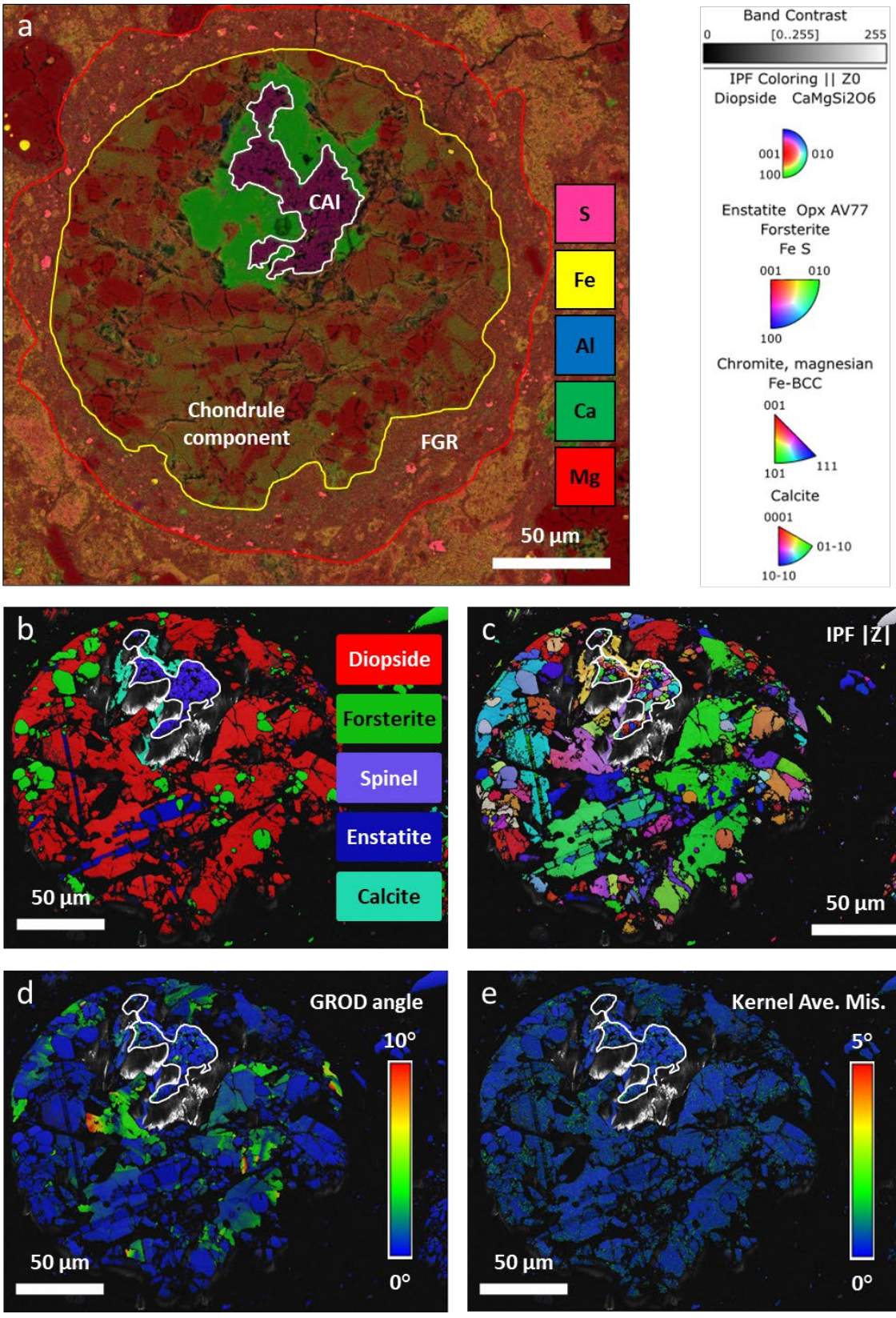

Figure 4.1. The Cockerel CCCAI (Aguas Zarcas, AZ-P2). (a) Element X-ray maps. (b) EBSD phase map. (c) Inverse Pole Figure |Z| (IPF) map (see key above). (d) Grain Relative Orientation Deviation (GROD) angle map. (e) Kernel Average Misorientation (KAM). The CAI component (outlined in white in all panels) is mantled by calcite (green in the EDS map). The surrounding chondrule component (outlined in yellow) is mostly composed of diopside and forsterite (with minor enstatite). The entire assemblage is enclosed within a complete FGR (outlined in red).

The Inverse Pole Figure |Z| (IPF) map (cf. Fig. 4.1c) of the CAI component reveals that the cluster of spinel grains are randomly orientated and display 120° triple-junction grain boundaries. The calcite mantle appears to be a single crystal with a uniform orientation.

The chondrule part of the CCCAI is characteristic of a Type I Porphyritic Olivine-Pyroxene chondrule (POP-chondrule; Fig. 4.1b), composed mainly of globular forsterite (~3-15 μm) and tabular diopside (~50-80 μm), with minor amounts lamellar enstatite crystals (~50 μm; cf. Fig. 4.1b).

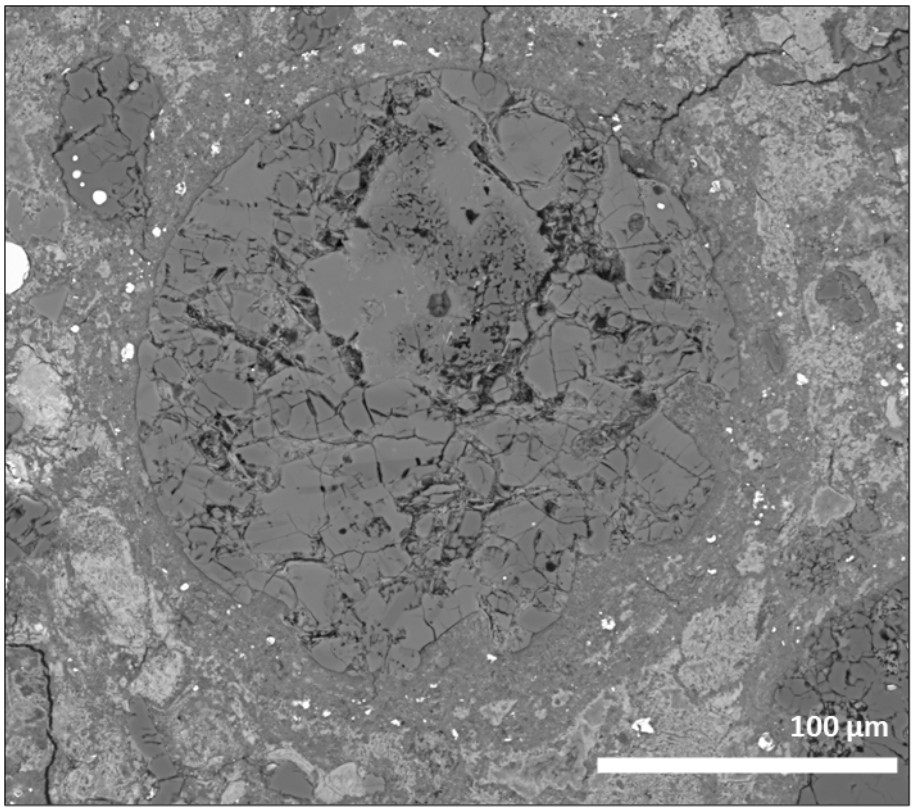

Figure 4.2. BSE image of the Cockerel CCCAI (Aguas Zarcas, AZ-P2).

The IPF |Z| map (cf. Fig. 4.1c) reveals that the olivine, diopside, and enstatite grains are all randomly oriented and do not display any preferential orientations relative to themselves or other minerals. Investigations of the crystallographic orientations of the spinel cluster, the calcite mantle, and neighbouring olivine and pyroxenes do not exhibit any crystallographic orientation relationships.

The Grain Relative Orientation Deviation (GROD) angle map shows relatively low to no deformation within the olivine and pyroxene component of the CCCAI as evidenced by the blue coloration (cf. Fig. 4.1d). However, some diopside grains display continuous lattice bending (internal misorientation) shown as a blue to red-coloured gradient (up to 10°; cf. Fig. 4.1d).

The GROD angle and Kernel Average Misorientation (KAM) maps show minimal (<2°; cf. Figs 4.1d & 4.1e) to no internal deformation within the spinel cluster, nor within the calcite mantle. The KAM map reveals minimal pixel to pixel misorientation (<2°; cf. Fig. 4.1e). In addition, this deformation appears to be homogeneous throughout the chondrule grains as opposed to being concentrated along linear low-angle boundaries.

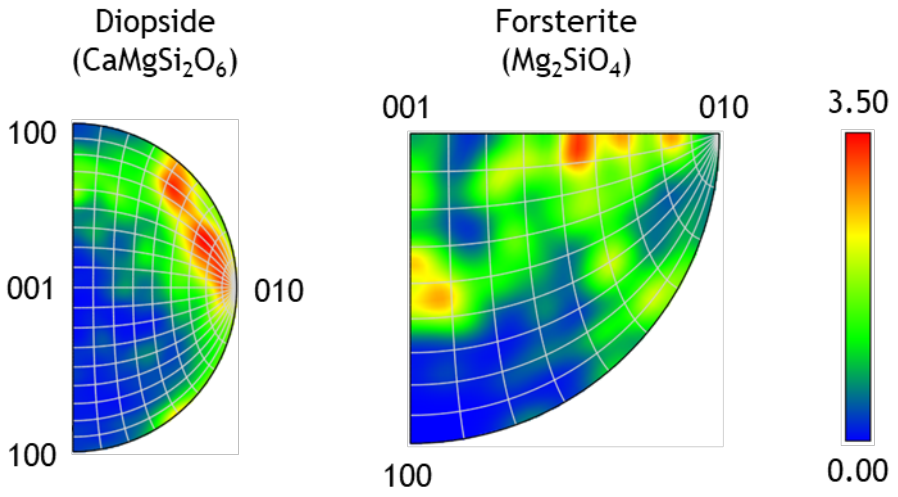

Figure 4.3. Disorientation axes figures of the main mineral phases of the Cockerel's chondrule component. Axes represent crystal coordinates using an equal area projection with a half width of 10.0°, with disorientation angles ranging from 2 to 10°.

Deformation is minor within the Cockerel's chondrule. Nonetheless, evaluation of the disorientation axes diagrams (cf. Fig. 4.3) shows that the deformation within the diopside grains is predominantly accommodated by a rotation around the (010) axis with a slight inclination towards (100). The disorientation axes diagram for forsterite (cf. Fig. 4.3) shows that deformation is accommodated by a rotation around the (001) and (010) axes. Weighted Burger Vector (WBV) diagrams of diopside and forsterite are in Appendix 7.6. It is

important to note that these diagrams are calibrated to terrestrial mantle conditions.

4.3.1.2 Cicero

This object was also found within an extensively aqueously altered (CM2.2-2.3) clast of Aguas Zarcas. Initially named CCRO (Compound-Chondrule-Refractory-Object), its appellation then became ‘Cicero’ to conform to the strict naming convention described in section 4.2.2. Cicero is a complex object; it is composed of a CAI, comprising a cluster of spinel crystals rimmed by diopside (outlined in white; cf. Fig. 4.4), which is enclosed within a forsteritic chondrule (outlined in yellow; cf. Fig. 4.4). A large euhedral calcite grain juxtaposes said chondrule. The entire assemblage is within a singular incomplete FGR of variable thickness (up to ~200 μm; outlined in red; cf. Fig. 4.4) and contains four other chondrule fragments: three forsteritic (outlined in orange; cf. Fig. 4.4) and one fayalitic (outlined in gold; cf. Fig. 4.4). These forsterite-rich chondrules also contain some diopside grains and traces of secondary Fe-Ni sulphides.

Cicero’s CAI component is a simple aggregate (cf. Fig. 4.4) composed of multiple spinel grains (<5 μm in size) within a continuous irregular but complete micrometric rim of diopside (<5 μm in size). The chondrule part of the CCCAI is characteristic of a Type I POP-chondrule (Fig. 4.4) and is composed mainly of globular forsterite (~1-20 μm) and diopside grains (<5 μm).

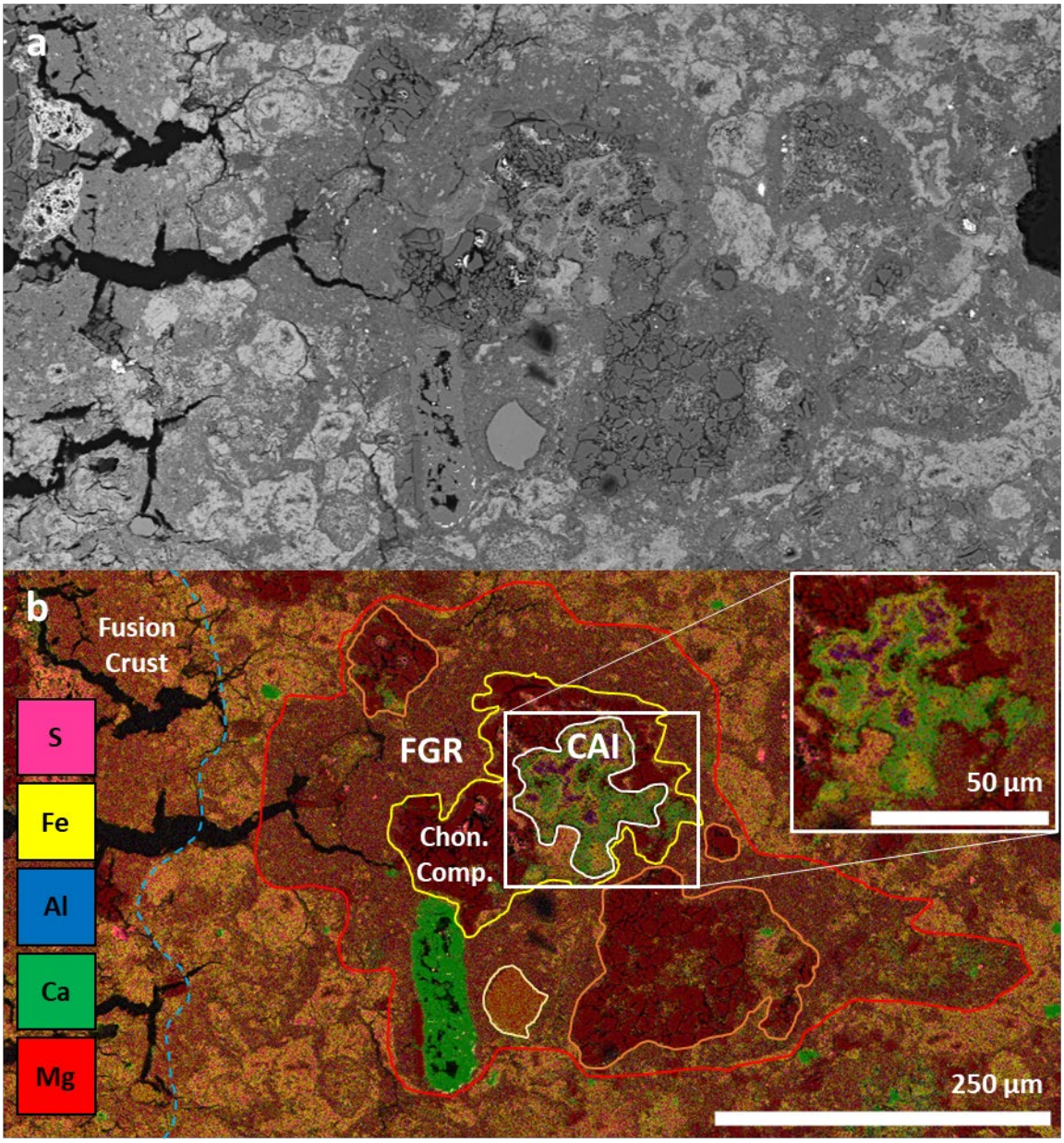

Figure 4.4. The Cicero CCCAI (Aguas Zarcas, AZ-03). (a) BSE image of the CCCAI named 'Cicero'. (b) Element X-ray maps of the CCCAI (modified from Martin et al., 2020). The dark sub-mm fractures on the left-hand side are characteristic of the fusion crust (outlined in light blue dashed line) of the meteorite sample. The CAI component (outlined in white) is enclosed within a chondrule component (Chon. Comp.; outlined in yellow) mostly composed of forsterite (with minor Fe-sulphides). The entire assemblage and four other chondrule fragments (three forsteritic, outlined in orange; one fayalitic, outlined in gold) are enclosed within a complete FGR (outlined in red).

4.3.1.3 The Capybara

This object was found within LAP 02239 (CM2.4-2.5). It was named as such due to the elongated shape of its chondrule component loosely resembling the majestic animal that is the capybara (cf. Fig. 4.5 and 4.6). The Capybara comprises a CAI, composed of a cluster of spinel grains with minor interstitial forsterite (outlined in white; cf. Fig. 4.5), within an elongated Type I POP-chondrule (outlined in yellow; cf. Fig. 4.5). Some secondary minerals can also be observed within the interstices of the spinel cluster: Fe-phyllosilicates, and within the chondrule: Fe-sulphides. The entire assemblage is surrounded by a heavily fractured complete but irregular layered FGR (~35-138 μm thick; outlined in red; cf. Fig. 4.5), with a complete inner-layer enriched in Mg (~10-60 μm thick; outlined with a red dashed line; cf. Fig. 4.5), compared to an incomplete outer-layer enriched in Fe (up to 93 μm thick).

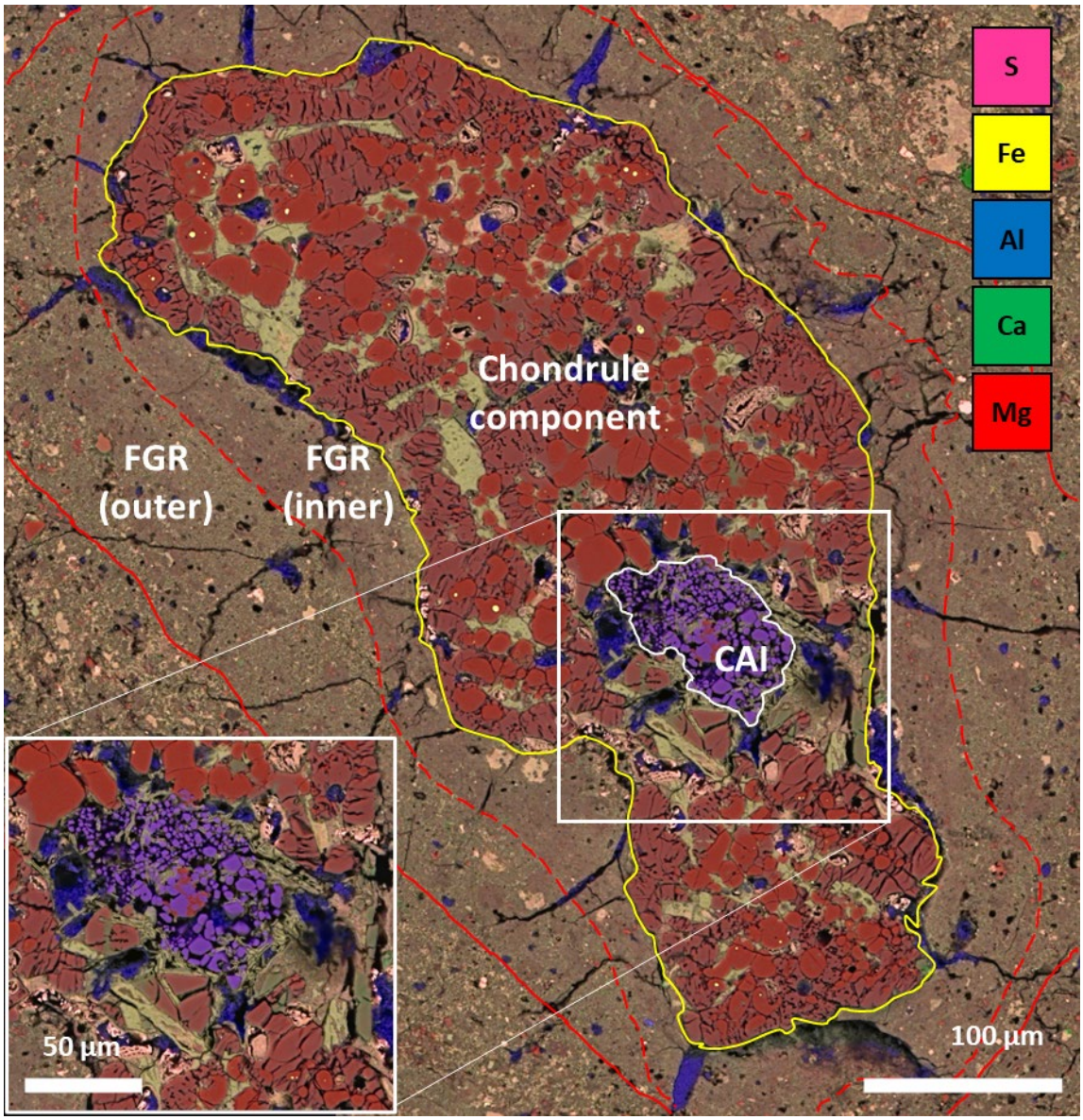

Figure 4.5. The Capybara CCCAI (LAP 02239, 02239,5). Element X-ray maps of the assemblage named the 'Capybara' due to its obvious resemblance to the mammalian species. The deep blue sub-mm veins cross-cutting the FGR are the result of the accumulation of Al-rich polishing powder (corundum) in the fractures and small pores of the polished resin block; these features are to be considered as artifacts and be disregarded. The CAI component (outlined in white) is surrounding by a chondrule component (outlined in yellow) mostly composed of forsterite and enstatite (with minor diopside). The entire assemblage is enclosed within a layered FGR (inner, outlined in red solid line; outer, outlined in red dashed line).

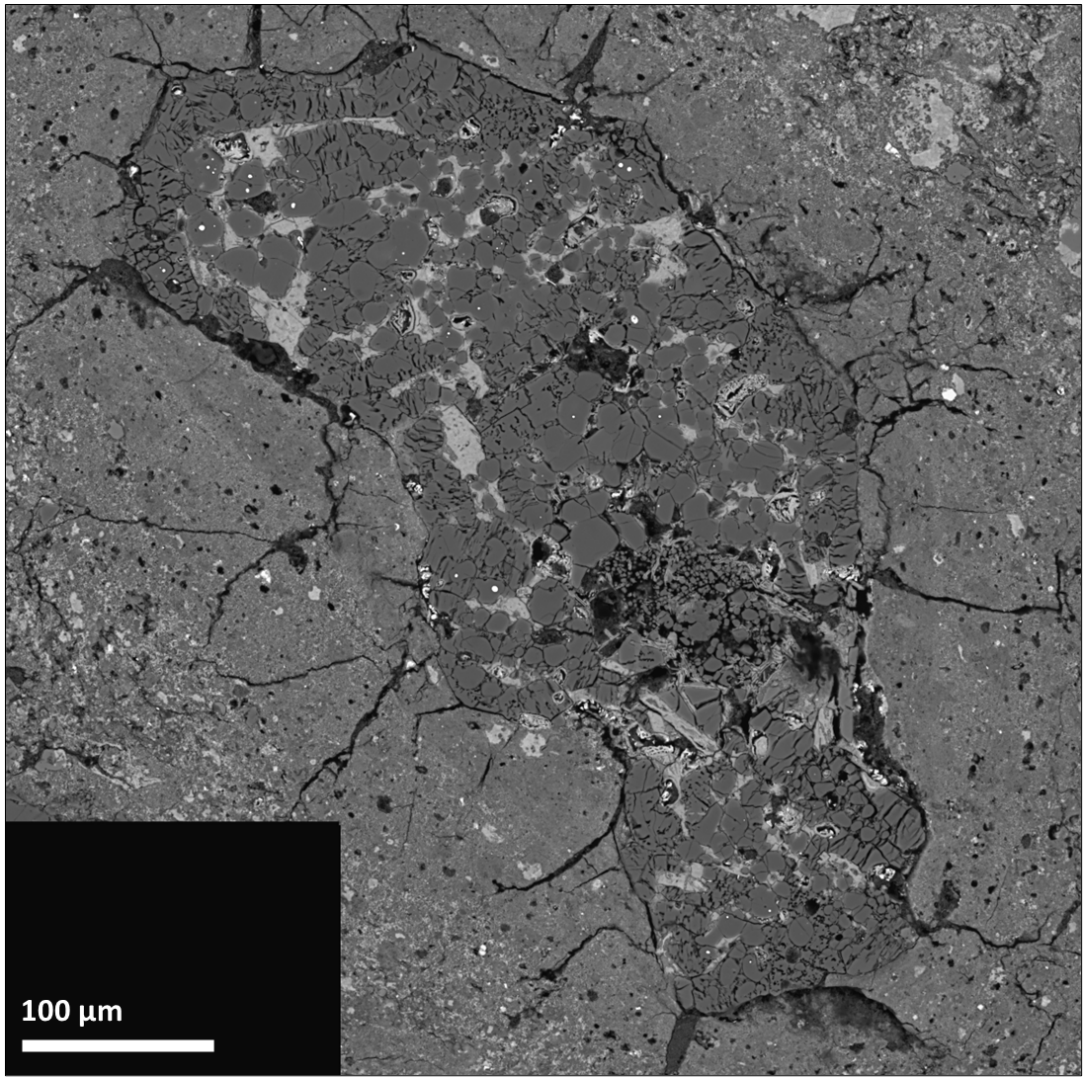

Figure 4.6. BSE image of the Capybara CCCAI (LAP 02239, 02239,5).

The Capybara's CAI component is a simple aggregate composed of a cluster of globular spinel grains (most <5 µm, up to 10 µm in size) with interstitial forsterite at the centre (cf. Fig. 4.5). The spinel core is adjacent to lamellar euhedral diopside crystals (up to 30 µm).

The chondrule component of the CCCAI is composed of globular forsterite (up to 30 µm; cf. Fig. 4.5), fractured tabular enstatite (~50 µm), and lamellar diopside grains (~10 µm) with interstitial olivine (up to 30 µm). Some Fe-Ni nuggets (up to ~3 µm) can be observed within certain forsterite grains. The chondrule has an incomplete and irregular rim (up to 30 µm thick) of fractured tabular enstatite (~50 µm long grains).

4.3.2 Oxygen isotopes of CAIs, Chondrules, and CCCAI Components

4.3.2.1 Oxygen Isotope Signatures of CM CAIs and CM Chondrules by Meteorite

The CAIs observed in this study are generally simple aggregates, comprising a core of spinel grains surrounded by a rim of diopside. Other targeted CAIs are simple inclusions composed of spinel or spinel-hibonite. No complex aggregates were targeted within this study. Unprocessed "raw" oxygen isotope measurements are shown in Appendix 7.7, while the processed data is summarised in Table 4.6.

All oxygen isotope compositions are presented relative to the Vienna Standard Mean Ocean Water (V-SMOW) reference (Lodders & Fegley, 1998). The error bars in the three-isotope oxygen diagrams ($\delta^{17}O$ vs. $\delta^{18}O$) represent the standard error (±2SE) and are smaller than the symbol sizes. The Terrestrial Fractionation Line (TFL), the Primitive Chondrule Minerals (PCM; Ushikubo et al., 2012), and the Carbonaceous Chondrite Anhydrous Mineral line (CCAM; Clayton et al., 1977; Clayton & Mayeda, 1999) are shown for reference, with the following equations: TFL: $\delta^{17}O = 0.52 \times \delta^{18}O$; PCM: $\delta^{17}O = 0.987 \times \delta^{18}O - 2.7$; CCAM: $\delta^{17}O = 0.94 \times \delta^{18}O - 4.2$.

Most measurements excluded from this study were removed due to low hydrogen counts (indicating low measurement reliability) or electron gun failure. Spinel, olivine, and pyroxene measurements were also discarded in cases of mistargeting, which is defined as hitting the wrong mineral phase (or overlapping multiple phases) due to the difficult-to-predict curvature of the analytical beam (especially for targets located near the edges of the polished sections) or misidentification of an object during the target selection process. In cases where hibonite, perovskite, calcite, or FGRs were targeted, the corresponding data points were excluded due to the absence of appropriate standards. However, if spinel, diopside, or olivine was mistakenly targeted instead, the analysis was retained, reclassified, and corrected using the appropriate standards for use in this study (cf. Appendix 7.9).

The chondrules observed in this study are generally type I PO (FeO-poor and volatile poor; Porphyritic Olivine) or POP comprising generally forsterite

olivine and diopside compositions. 12 of the targeted olivine grains are from type II (FeO-rich, Mg# <90) chondrules (Hewins, 1997). It is to be noted that chondrule targets in this study include fragments. No internal oxygen isotope zoning has been observed within the targeted chondrule minerals in this study, suggesting that these objects are isotopically homogeneous in oxygen. Olivine compositions were initially determined using semi-quantitative EDS analysis. Within this study, 27 type I chondrules have an estimated Mg# >91.35±0.24 (SD) and 11 type II chondrules have an estimated Mg# ranging from 49.65 to 83.28 (cf. Appendix 7.8).

However, previous studies of individual chondrules from CCs have shown that their oxygen isotope ratios vary against their Mg# (Nakashima et al., 2010, 2011; Ushikubo et al., 2012; Schrader et al., 2013, 2014, 2017a; Tenner et al., 2013, 2015, 2017; Hertwig et al., 2017, 2018). In addition, an oxygen isotopic study of chondrules in the Murchison (CM2.5) chondrite by Chaumard et al. (2018) showed that lower $\Delta^{17}O$ values of individual chondrules correspond to higher Mg# values, up to a difference of approximately $\Delta^{17}O$ = -2.5‰ between chondrules with Mg# >98.5 (~-5‰) and chondrules with Mg# <96 (~-2.5‰). To account for this discrepancy, accurate Mg# values will be acquired in a future study through more precise quantitative techniques, such as Electron Probe Micro-Analysis (EPMA). The Mg# of 38 targeted olivine grains in chondrules and chondrule fragments in the Aguas Zarcas, Paris, and Winchcombe meteorites are in shown in Appendix 7.8, which also presents details regarding calculations and estimates.

Table 4.6. Oxygen-isotope compositions of individual minerals in the CCCAI, CAI, and chondrule populations from the studied CM carbonaceous chondrites.

Chondrite	Object	Mineral	$\partial^{17}O$	2SE	$\partial^{18}O$	2SE	$\Delta^{17}O$	2SE
CCCAI CAIs								
Aguas Zarcas	Cicero	Spinel	-36.26	0.63	-33.46	0.40	-18.86	0.67
		Spinel	-34.94	0.53	-32.84	0.36	-17.87	0.57
		Spinel	-36.67	0.70	-32.98	0.33	-19.52	0.72
	Cockerel	Spinel	-31.91	0.74	-28.56	0.39	-17.06	0.77
LAP 02239	Capybara	Spinel	-29.59	0.85	-29.84	0.59	-14.07	0.90
		Spinel	-20.32	0.74	-16.10	0.41	-11.94	0.77
CCCAI chondrules								
Aguas Zarcas	Cicero-chon	Forsterite	-44.13	0.80	-39.77	0.49	-23.45	0.84
		Forsterite	-44.47	0.68	-39.73	0.34	-23.81	0.70
		Forsterite	-47.63	0.59	-43.75	0.35	-24.88	0.62
		Forsterite	-47.10	0.71	-44.26	0.30	-24.09	0.73
		Forsterite	-48.57	0.76	-46.05	0.35	-24.63	0.78
		Forsterite	-45.03	0.89	-41.46	0.76	-23.48	0.98
	Cicero-Ol-1	Forsterite	-6.56	0.67	-3.08	0.25	-4.96	0.69
	Cicero-Ol-2	Fayalite	-1.58	0.63	1.78	0.24	-2.51	0.64
		Fayalite	-1.83	0.61	1.08	0.30	-2.39	0.63
	Cockerel-chon	Forsterite	-2.35	0.68	1.93	0.23	-3.35	0.69
		Forsterite	-1.81	0.64	2.17	0.25	-2.93	0.66
		Forsterite	-3.57	0.64	-1.83	0.26	-2.62	0.65
		Forsterite	-1.91	0.54	1.37	0.25	-2.62	0.55
		Forsterite	-1.32	0.50	2.74	0.28	-2.74	0.52
		Diopside	-1.32	0.74	3.88	0.30	-3.33	0.76
		Diopside	-1.74	0.63	2.29	0.23	-2.93	0.64
		Diopside	-1.63	0.59	2.02	0.25	-2.68	0.61
LAP 02239	Capybara-chon	Forsterite	-11.80	0.64	-5.19	0.36	-9.10	0.67
		Forsterite	-10.29	0.73	-3.22	0.33	-8.62	0.75
		Forsterite	-10.61	0.67	-2.55	0.28	-9.28	0.69
		Forsterite	-10.05	0.66	-2.71	0.25	-8.64	0.67
		Forsterite	-10.14	0.58	-3.56	0.31	-8.29	0.60
		Forsterite	-10.14	0.58	-7.99	0.31	-5.99	0.60
		Forsterite	-11.18	0.67	-6.67	0.30	-7.71	0.68
		Forsterite	-7.71	0.70	-4.47	0.39	-5.39	0.72
		Forsterite	-10.51	0.63	-7.39	0.33	-6.67	0.65
		Forsterite	-12.41	0.62	-10.41	0.37	-7.00	0.65
		Forsterite	-11.44	0.69	-7.98	0.30	-7.29	0.70
		Forsterite	-11.84	0.65	-8.76	0.33	-7.29	0.68

Chondrite	Object	Mineral	∂^{17}O	2SE	∂^{18}O	2SE	Δ^{17}O	2SE
		Forsterite	-10.40	0.77	-6.89	0.31	-6.81	0.78
		Forsterite	-10.73	0.72	-7.05	0.29	-7.06	0.73
		Forsterite	-9.15	0.62	-5.56	0.33	-6.25	0.64
		Forsterite	-11.09	0.72	-7.28	0.26	-7.30	0.73
CAIs								
Aguas Zarcas	6	Spinel	-49.32	0.72	-46.41	0.33	-25.18	0.74
		Spinel	-47.31	0.75	-44.05	0.33	-24.41	0.77
		Spinel	-48.61	0.82	-45.56	0.35	-24.92	0.84
	17	Spinel	-48.24	0.85	-44.25	0.36	-25.23	0.87
		Spinel	-35.61	0.78	-32.08	0.35	-18.92	0.80
		Spinel	-24.28	0.75	-19.38	0.35	-14.20	0.77
		Spinel	-40.70	0.81	-36.97	0.35	-21.47	0.83
		Spinel	-23.15	0.82	-18.52	0.34	-13.52	0.84
		Spinel	-16.52	0.59	-11.78	0.33	-10.39	0.61
	19	Spinel	-35.34	0.73	-31.16	0.38	-19.13	0.75
		Spinel	-46.86	0.78	-43.02	0.45	-24.49	0.81
		Spinel	-34.37	0.78	-29.02	0.59	-19.27	0.84
	25	Spinel	-39.81	0.60	-35.96	0.35	-21.11	0.62
		Spinel	-41.26	0.79	-38.31	0.35	-21.34	0.81
	3	Spinel	-42.88	0.55	-40.00	0.32	-22.08	0.58
	7	Spinel	-27.55	0.76	-25.23	0.27	-14.43	0.77
		Spinel	-31.34	0.62	-29.57	0.33	-15.96	0.64
	11	Spinel	-41.27	0.62	-38.48	0.32	-21.26	0.64
		Spinel	-43.52	0.57	-41.28	0.30	-22.05	0.59
DNG 06004	64	Spinel	-44.36	0.66	-42.18	0.34	-22.43	0.69
		Spinel	-37.77	0.66	-35.54	0.34	-19.29	0.68
		Spinel	-41.87	0.63	-40.25	0.35	-20.94	0.65
		Spinel	-41.26	0.75	-38.37	0.28	-21.31	0.76
		Spinel	-41.85	0.56	-38.81	0.31	-21.67	0.58
	65	Spinel	-27.46	0.69	-24.78	0.37	-14.57	0.71
		Spinel	-42.05	0.62	-39.45	0.37	-21.53	0.65
	61	Spinel	-47.55	0.69	-44.87	0.40	-24.22	0.72
	60	Spinel	-41.44	0.75	-35.78	0.32	-22.83	0.77
	51	Spinel	-47.21	0.73	-45.19	0.38	-23.71	0.76
	29	Spinel	-47.27	0.65	-45.10	0.40	-23.82	0.68
		Spinel	-46.69	0.79	-44.22	0.34	-23.70	0.81
		Spinel	-37.14	0.69	-33.51	0.33	-19.72	0.71
		Spinel	-43.99	0.71	-39.74	0.33	-23.32	0.73
		Spinel	-43.62	0.72	-39.86	0.48	-22.90	0.76
		Spinel	-37.61	0.84	-34.30	0.53	-19.77	0.88

Chondrite	Object	Mineral	$\partial^{17}O$	2SE	$\partial^{18}O$	2SE	$\Delta^{17}O$	2SE
		Spinel	-45.69	0.77	-43.38	0.39	-23.13	0.80
		Spinel	-47.83	0.79	-44.43	0.32	-24.73	0.80
	25b	Spinel	-41.66	0.83	-38.99	0.46	-21.39	0.86
		Spinel	-40.88	1.01	-39.30	0.51	-20.45	1.04
		Spinel	-31.29	0.68	-30.01	0.34	-15.68	0.70
		Spinel	-37.59	0.55	-34.67	0.35	-19.57	0.58
		Spinel	-36.36	0.72	-33.63	0.35	-18.87	0.74
LAP 02239	A14	Spinel	-19.45	0.79	-17.50	0.38	-10.35	0.81
		Spinel	-21.88	0.69	-20.93	0.43	-11.00	0.73
	A7	Spinel	-44.35	0.71	-40.93	0.34	-23.06	0.73
		Spinel	-39.89	0.64	-36.90	0.36	-20.70	0.67
	E7	Spinel	-44.67	0.79	-40.73	0.34	-23.49	0.81
	E6	Spinel	-30.46	0.75	-27.64	0.46	-16.09	0.79
	A21	Spinel	-23.13	0.58	-21.11	0.40	-12.16	0.61
Paris	68	Spinel	-38.82	0.76	-37.79	0.35	-19.17	0.79
		Spinel	-34.48	0.76	-32.49	0.34	-17.59	0.78
		Spinel	-31.73	0.59	-29.26	0.33	-16.52	0.62
	55	Spinel	-53.88	0.78	-61.01	0.44	-22.15	0.82
		Spinel	-43.20	0.90	-47.54	0.37	-18.48	0.92
		Spinel	-45.57	0.81	-51.17	0.36	-18.96	0.83
	53	Spinel	-44.88	0.80	-43.69	0.33	-22.17	0.82
		Spinel	-45.34	0.80	-44.73	0.40	-22.09	0.82
	52	Spinel	-21.37	0.68	-18.70	0.35	-11.65	0.71
	49	Spinel	-40.32	0.92	-40.23	0.37	-19.40	0.94
	38	Spinel	-45.57	0.55	-43.37	0.35	-23.02	0.58
		Spinel	-41.27	0.62	-40.10	0.40	-20.41	0.66
	81	Spinel	-36.12	0.93	-35.77	0.53	-17.52	0.97
	82	Spinel	-42.33	0.61	-41.47	0.34	-20.77	0.64
		Spinel	-42.33	0.69	-39.92	0.33	-21.57	0.71
	84	Spinel	-45.20	0.84	-43.54	0.36	-22.56	0.86
	91	Spinel	-38.84	0.66	-35.99	0.32	-20.13	0.68
		Spinel	-39.66	0.75	-38.69	0.40	-19.54	0.78
	104	Spinel	-46.31	0.72	-43.32	0.31	-23.79	0.73
	119	Spinel	-48.11	0.86	-46.11	0.39	-24.13	0.88
		Spinel	-42.15	0.88	-39.60	0.48	-21.56	0.91
	157	Spinel	-46.99	0.65	-45.44	0.38	-23.36	0.68
		Spinel	-45.01	0.65	-42.08	0.32	-23.13	0.67
	74	Spinel	-46.59	0.70	-45.29	0.33	-23.03	0.72
		Spinel	-48.16	0.77	-46.03	0.37	-24.23	0.79
		Spinel	-47.10	0.69	-44.58	0.37	-23.92	0.72

Chondrite	Object	Mineral	$\partial^{17}O$	2SE	$\partial^{18}O$	2SE	$\Delta^{17}O$	2SE
		Spinel	-47.64	0.77	-45.51	0.36	-23.97	0.79
Chondrules								
Aguas Zarcas	Ol-06-1	Forsterite	-6.86	0.75	-2.31	0.33	-5.66	0.77
		Forsterite	-6.86	0.70	-2.25	0.32	-5.70	0.72
	Ol-06-2	Forsterite	-9.07	0.84	-4.50	0.28	-6.73	0.85
	Rfay-1	Fayalite	-0.78	0.60	2.43	0.27	-2.04	0.62
	Rfay-2	Fayalite	-0.35	0.58	1.90	0.23	-1.34	0.59
	Rfay-3	Fayalite	-0.23	0.53	3.48	0.27	-2.04	0.55
	Rol-01	Fayalite	-0.59	0.61	1.44	0.24	-1.34	0.62
		Fayalite	-1.66	0.57	0.61	0.26	-1.97	0.58
		Fayalite	-1.22	0.55	0.07	0.28	-1.25	0.57
	Rol-02	Forsterite	-2.97	0.59	0.19	0.30	-3.07	0.61
		Forsterite	-1.48	0.66	1.22	0.32	-2.12	0.68
	Rol-03	Forsterite	-0.72	0.50	3.48	0.30	-2.53	0.53
	Rol-04	Forsterite	-9.27	0.61	-4.34	0.30	-7.02	0.63
	Rol-05	Forsterite	-7.12	0.71	-3.78	0.32	-5.16	0.72
		Forsterite	-7.43	0.73	-3.53	0.26	-5.59	0.75
		Forsterite	-6.89	0.73	-1.36	0.30	-6.18	0.75
		Forsterite	-7.77	0.60	-2.85	0.25	-6.29	0.62
	Rol-06	Forsterite	-6.16	0.63	0.23	0.25	-6.29	0.64
		Forsterite	-4.10	0.57	-2.14	0.22	-2.99	0.58
		Forsterite	-6.27	0.75	-5.26	0.45	-3.53	0.79
	Rol-07	Forsterite	1.85	0.69	3.51	0.28	0.02	0.71
		Forsterite	2.57	0.50	4.96	0.28	-0.01	0.53
		Forsterite	1.64	0.58	3.53	0.28	-0.19	0.60
		Forsterite	1.98	0.65	3.28	0.27	0.28	0.67
	Rol-08	Forsterite	-3.33	0.79	0.76	0.29	-3.73	0.81
		Forsterite	-3.16	0.67	-0.93	0.25	-2.68	0.68
	Rol-09	Forsterite	-1.18	0.51	2.98	0.23	-2.73	0.53
		Forsterite	-0.46	0.64	2.80	0.28	-1.91	0.66
		Forsterite	-1.12	0.48	4.35	0.28	-3.38	0.50
	Rol-10	Forsterite	-7.46	0.65	-3.80	0.29	-5.49	0.67
		Forsterite	-7.13	0.66	-3.15	0.26	-5.49	0.68
	Rol-11	Fayalite	-1.44	0.52	-0.33	0.25	-1.27	0.54
	Rol-12	Forsterite	-7.56	0.55	-5.70	0.29	-4.60	0.57
		Forsterite	-7.27	0.67	-4.17	0.30	-5.10	0.69
	Shard-ol-1	Forsterite	-1.74	0.58	1.14	0.31	-2.33	0.61
	Shard-ol-2	Forsterite	-6.16	0.66	-1.53	0.30	-5.36	0.68
	Shard-ol-3	Forsterite	-5.40	0.65	-2.03	0.29	-4.34	0.67
		Forsterite	-2.85	0.54	-1.41	0.30	-2.12	0.56
	Shard-ol-4	Forsterite	-5.50	0.70	-1.84	0.31	-4.54	0.72

Chondrite	Object	Mineral	$\partial^{17}O$	2SE	$\partial^{18}O$	2SE	$\Delta^{17}O$	2SE
Paris	78	Forsterite	-11.73	0.62	-14.20	0.31	-4.34	0.64
		Forsterite	-11.42	0.76	-13.11	0.27	-4.61	0.77
		Forsterite	-11.65	0.62	-12.94	0.24	-4.92	0.63
	91	Forsterite	-2.87	0.64	-0.34	0.29	-2.69	0.66
	119-1	Forsterite	-0.81	0.59	1.59	0.34	-1.63	0.62
	119-2	Forsterite	-1.57	0.66	-0.32	0.41	-1.40	0.70
	Rol-01	Forsterite	-9.45	0.82	-6.04	0.29	-6.31	0.84
		Forsterite	-8.81	0.63	-4.49	0.32	-6.48	0.66
		Forsterite	-7.43	0.70	-4.40	0.27	-5.14	0.71
	Rol-02	Forsterite	-3.23	0.62	-1.00	0.31	-2.72	0.64
		Forsterite	-3.54	0.65	-1.29	0.31	-2.87	0.67
	Rol-03	Fayalite	-2.30	0.70	-1.88	0.29	-1.32	0.71
		Fayalite	-2.30	0.62	-1.06	0.26	-1.74	0.63
		Fayalite	-2.49	0.67	-1.77	0.26	-1.58	0.69
		Fayalite	-2.01	0.65	-0.84	0.31	-1.57	0.66
	Rol-04-1	Fayalite	-0.93	0.52	-0.37	0.28	-0.73	0.54
	Rol-04-2	Fayalite	-0.66	0.45	-0.27	0.30	-0.52	0.47
	Rol-05	Fayalite	4.50	0.55	10.03	0.29	-0.72	0.57
	Rol-06	Forsterite	-0.39	0.64	2.49	0.30	-1.69	0.66
		Forsterite	-2.14	0.59	0.38	0.34	-2.34	0.62
	Rol-07	Forsterite	-5.30	0.71	-2.00	0.28	-4.26	0.73
		Forsterite	-5.35	0.73	-2.06	0.24	-4.28	0.75
	Rol-08	Forsterite	-0.13	0.62	2.49	0.30	-1.43	0.64
		Forsterite	-5.41	0.62	-2.12	0.30	-4.30	0.64
	Rol-09	Forsterite	-7.64	0.73	-3.81	0.35	-5.66	0.75
	Rol-10	Forsterite	-4.94	0.76	-1.29	0.32	-4.27	0.77
	Rol-11	Fayalite	-0.84	0.60	1.51	0.31	-1.62	0.62
	Rol-12	Forsterite	-5.08	0.66	-3.09	0.36	-3.48	0.68
		Forsterite	-5.75	0.66	-2.73	0.35	-4.33	0.68
		Forsterite	-6.72	0.66	-2.83	0.31	-5.25	0.68
	Rol-13	Forsterite	-6.92	0.66	-3.64	0.34	-5.03	0.68
		Forsterite	-7.08	0.67	-5.16	0.30	-4.40	0.69
	Rol-14	Forsterite	-6.36	0.62	-3.52	0.28	-4.53	0.64
		Forsterite	-6.58	0.69	-3.36	0.24	-4.83	0.70
		Forsterite	-6.96	0.68	-3.39	0.25	-5.20	0.70
		Forsterite	-6.78	0.67	-3.42	0.24	-5.00	0.68
		Forsterite	-7.99	0.66	-3.90	0.30	-5.97	0.68
		Forsterite	-6.67	0.66	-3.15	0.32	-5.03	0.68
		Forsterite	-8.02	0.68	-5.39	0.27	-5.22	0.70
	Rol-15	Forsterite	-7.54	0.56	-4.30	0.30	-5.30	0.59
	Rol-16	Forsterite	-6.77	0.67	-2.74	0.34	-5.35	0.69

Chondrite	Object	Mineral	∂^{17}O	2SE	∂^{18}O	2SE	Δ^{17}O	2SE
		Forsterite	-7.87	0.72	-3.51	0.30	-6.05	0.74
	Rol-17	Fayalite	-1.44	0.65	0.81	0.31	-1.87	0.67
		Fayalite	-0.97	0.68	1.38	0.28	-1.69	0.70
		Fayalite	-0.72	0.65	1.40	0.25	-1.45	0.66
		Fayalite	-1.34	0.67	-0.26	0.25	-1.21	0.69
	Rol-18	Forsterite	-7.49	0.69	-4.14	0.27	-5.34	0.71
		Forsterite	-4.27	0.68	-1.43	0.31	-3.53	0.70
	Rol-19	Forsterite	-6.02	0.59	-2.97	0.30	-4.48	0.61
	154	Diopside	-5.31	0.80	-2.10	0.31	-4.21	0.81
Winchcombe	Ol-01	Forsterite	-6.33	0.65	-2.94	0.25	-4.80	0.67
		Forsterite	-6.41	0.65	-2.98	0.23	-4.86	0.66
	Ol-06	Forsterite	-6.74	0.62	-3.03	0.32	-5.17	0.64
		Forsterite	-8.38	0.70	-3.40	0.29	-6.62	0.71
	Ol-02	Forsterite	-6.66	0.74	-1.61	0.31	-5.82	0.76
		Forsterite	-5.65	0.67	-1.50	0.27	-4.87	0.69
		Forsterite	-6.19	0.70	-1.82	0.29	-5.24	0.71
		Forsterite	-6.14	0.70	-1.82	0.26	-5.20	0.71
Rimmed CAIs (core)								
Paris	66	Spinel	-26.18	0.73	-28.55	0.46	-11.33	0.77
	79	Spinel	-42.90	0.68	-40.95	0.29	-21.61	0.69
		Spinel	-44.03	0.64	-42.35	0.36	-22.01	0.67
		Spinel	-43.01	0.81	-40.56	0.34	-21.92	0.83
	128	Spinel	-46.18	0.69	-44.96	0.41	-22.80	0.72
		Spinel	-46.37	0.73	-46.59	0.39	-22.15	0.76
	161	Spinel	-46.66	0.73	-45.64	0.39	-22.93	0.76
		Spinel	-45.88	0.71	-44.95	0.37	-22.51	0.74
		Spinel	-45.70	0.73	-43.70	0.40	-22.98	0.76
Rimmed CAIs (rim)								
Paris	66	Forsterite	-39.33	0.58	-41.38	0.31	-17.82	0.60
	89	Forsterite	-45.17	0.84	-46.06	0.30	-21.22	0.85
		Forsterite	-43.86	0.68	-45.89	0.31	-20.00	0.70
Al-rich chondrules								
Paris	56	Spinel	-12.90	0.74	-12.28	0.36	-6.51	0.76
		Spinel	-12.30	0.78	-10.42	0.38	-6.88	0.80
		Forsterite	-11.79	0.74	-10.11	0.30	-6.53	0.75
		Forsterite	-16.03	0.74	-18.23	0.37	-6.55	0.77
		Forsterite	-14.90	0.72	-15.58	0.30	-6.80	0.74
		Forsterite	-11.75	0.77	-16.37	0.34	-3.24	0.79

Chondrite	Object	Mineral	$\partial^{17}O$	2SE	$\partial^{18}O$	2SE	$\Delta^{17}O$	2SE
		Forsterite	-11.12	0.79	-14.12	0.29	-3.77	0.80
	64	Forsterite	-7.57	0.67	-10.39	0.30	-2.17	0.69
		Forsterite	-7.53	0.73	-10.22	0.24	-2.22	0.74
		Forsterite	-8.00	0.66	-9.88	0.29	-2.86	0.68
		Diopside	-7.50	0.50	-9.65	0.28	-2.48	0.53
		Diopside	-7.72	0.79	-9.65	0.34	-2.70	0.81
	160	Spinel	-1.16	0.77	-0.15	0.36	-1.09	0.79
		Spinel	-1.38	0.87	-0.42	0.45	-1.16	0.90
		Spinel	-0.92	0.67	0.16	0.36	-1.01	0.70
		Spinel	-1.26	0.79	-0.58	0.29	-0.96	0.81
		Spinel	-1.84	0.80	-0.48	0.40	-1.59	0.82
		Spinel	-0.65	0.74	0.00	0.35	-0.66	0.76
^{16}O-rich forsterites								
Aguas Zarcas	Ol-07	Forsterite	-44.88	0.60	-42.81	0.24	-22.62	0.61
Paris	55-1	Forsterite	-45.28	0.73	-57.48	0.32	-15.39	0.75

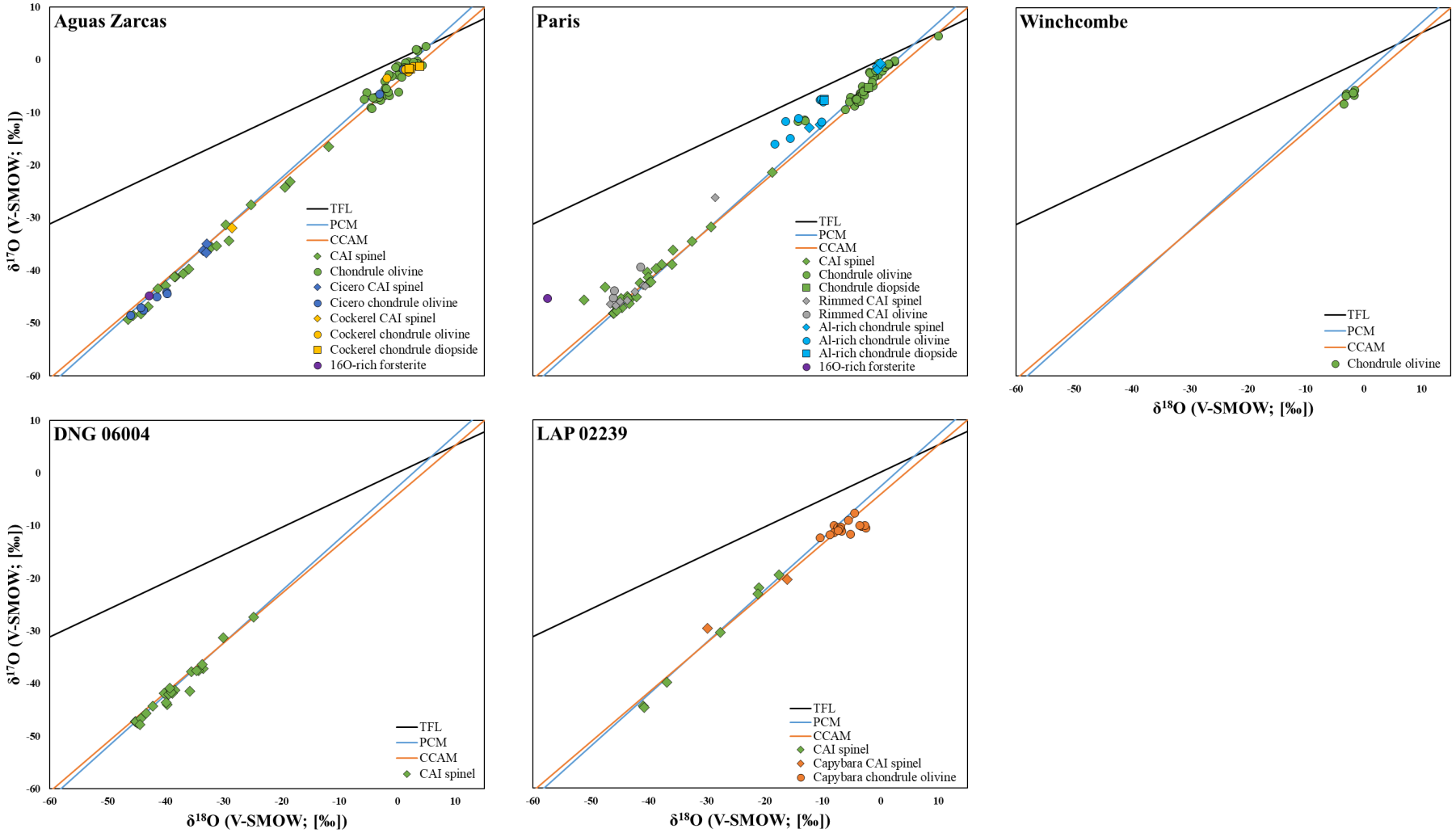

Figure 4.7. Three-isotope oxygen diagrams of compositions of all analysed phases in chondrules, ARCs, CAIs, and in the CCCAI components from each of the studied CM carbonaceous chondrites. The error bars, corresponding to the standard error (±2SE), are smaller than the symbol sizes.

As seen in figure 4.7, despite having targeted CAI and chondrule populations from all samples, only samples from Aguas Zarcas and Paris comprise both measurements from CAIs and chondrules, while DNG 06004 and LAP 02239 only include CAI measurements, and only measurements from chondrules from Winchcombe were successful. This is unfortunately due to either mistargeting, mixing, or low-count values during SIMS data acquisition (cf. Appendix 7.9).

Components from the targeted CCCAIs are reported within the plots of their host meteorites. The Paris sample was found to contain rimmed CAIs and ARCs, whose measurements are reported in figure 4.7 in regards to the other CAI and chondrule populations. The $\Delta^{17}O$ values of all the studied objects are plotted in figure 4.8 relative to their $\delta^{18}O$ values.

The studied CAIs have ^{16}O-rich compositions and plot mostly along the PCM line within three-isotope oxygen diagrams (cf. Fig. 4.9; apart from two outliers in the Paris meteorite that plot slightly to the left of the line, which might be the result of improper correction for IMF effects). Their $\delta^{17}O/\delta^{18}O$ compositions are spread within a wide range along the fractionation line (cf. Fig. 4.9) and their $\Delta^{17}O$ falls within -25.18‰ and -10.35‰ (cf. Fig. 4.8), with an average value of -20.40±0.75‰ (2SE). CAI measurements in Paris and DNG 06004 are more clustered than in the Aguas Zarcas and LAP 02239 samples, which are more spread. The more intermediate compositions may reflect slight ion probe spot overlap with neighbouring ^{16}O-poor phases (cf. Appendix 7.9). Oxygen isotope compositions for targeted CAIs concur with other CAIs found in weakly metamorphosed carbonaceous chondrites (petrologic types ≤3), which have relatively isotopically uniform ^{16}O-rich compositions ($\Delta^{17}O$ ~ -24‰; e.g. Hiyagon & Hashimoto, 1999; Itoh et al., 2004; Makide et al., 2009).

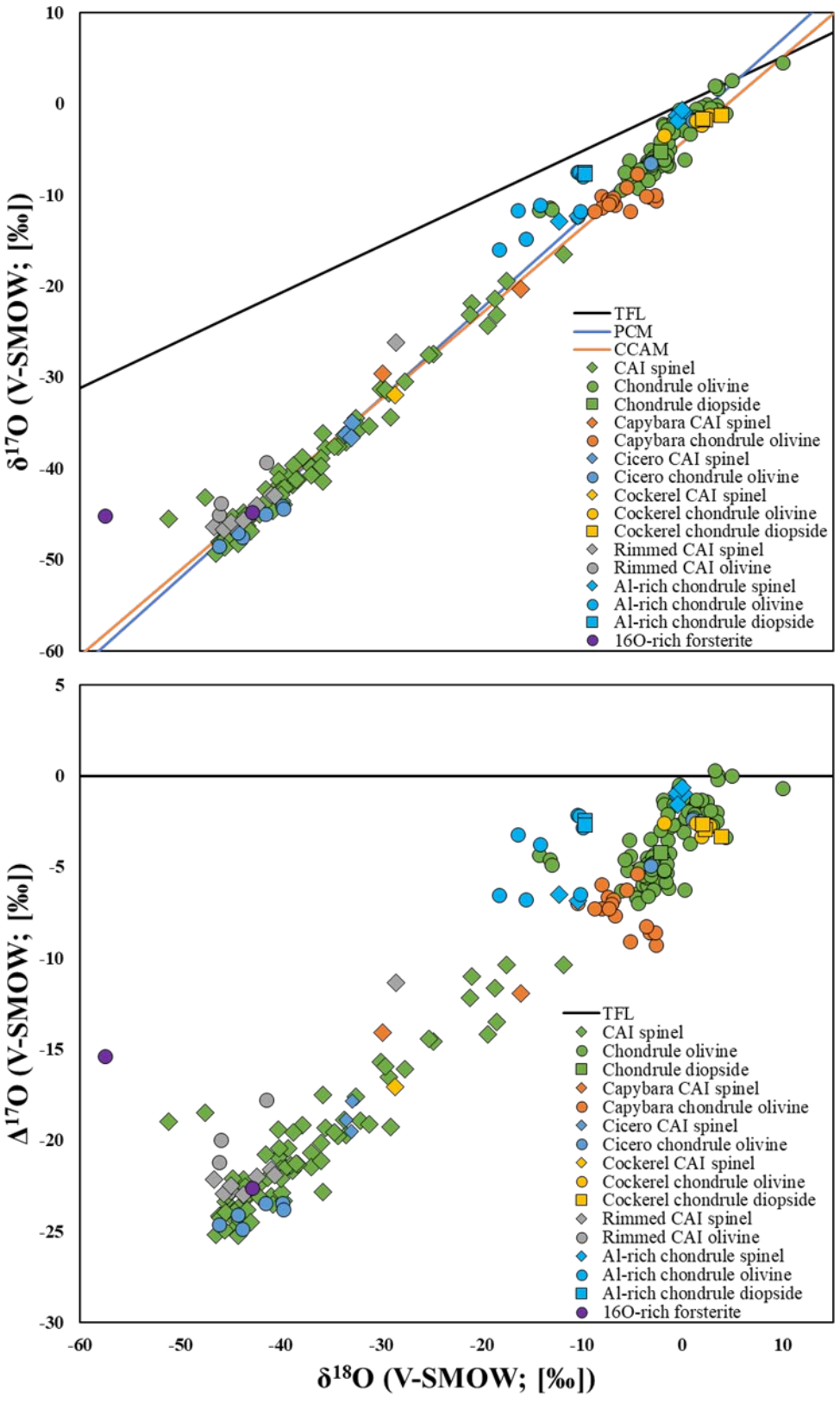

Figure 4.8. Compilation of all oxygen isotope data measurements acquired in this study. (top) Three-isotope oxygen diagram of compositions of individual spot analyses of mineral phases in CCCAIs, CAIs, and chondrules from the studied CM carbonaceous chondrites. (bottom) $\Delta^{17}O$ values vs. $\delta^{18}O$ of all the CCCAI components, CAIs, and chondrules from the

studied CM carbonaceous chondrites. The error bars, corresponding to the standard error (±2SE), are smaller than the symbol sizes.

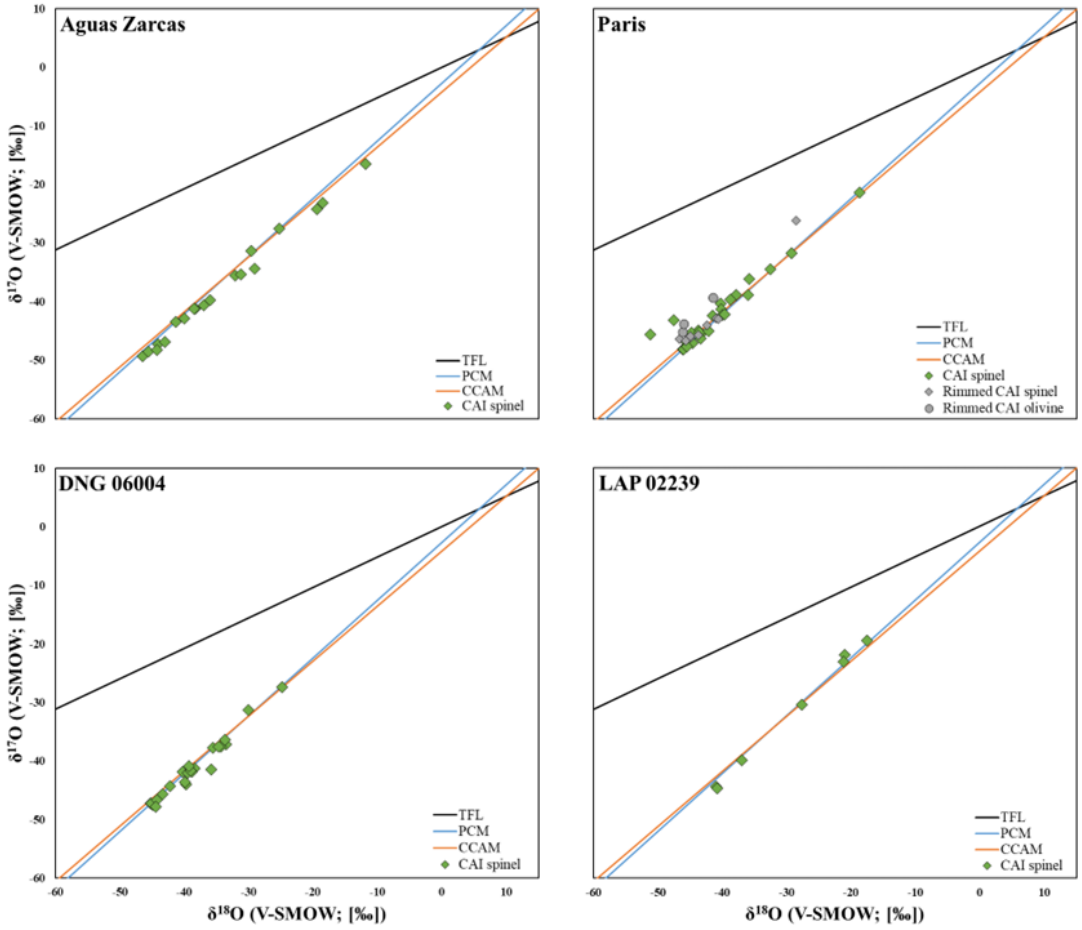

Figure 4.9. Three-isotope oxygen diagrams of compositions of individual spot analyses of mineral phases in CAIs and rimmed CAIs from the studied CM carbonaceous chondrites. The error bars, corresponding to the standard error (±2SE), are smaller than the symbol sizes.

The observed rimmed CAIs are composed of a core of spinel within a continuous and multilayered rim of diopside (inner layer) and forsterite (outer layer). All three mineral phases show homogeneous oxygen isotope compositions enriched in ^{16}O. Oxygen isotope measurements from the spinel in the cores of rimmed CAI within the Paris meteorite plot similarly to the rest of the CAIs from other studied CMs (cf. Fig. 4.9). Their compositions are clustered towards a ^{16}O-rich composition with a mean $\Delta^{17}O$ value of -21.14±0.74‰ (2SE; cf. Fig. 4.8). Apart from a single outlier within the Paris meteorite, whose composition may have resulted from a slight ion probe spot overlap with neighbouring ^{16}O-poor phases with a $\Delta^{17}O$ value of -11.33±0.77‰ (2SE; cf. Fig. 4.8 and Appendix 7.9). The rimmed CAI measurements plot slightly to the left of the PCM line but appear to follow its slope. The oxygen isotope compositions of the olivine

(forsterite) rims plot similarly to the cores of the rimmed CAIs with a mean $\Delta^{17}O$ value of -19.68±0.72‰ (2SE; cf. Fig. 4.8), although they are slightly displaced to the left of the PCM line (cf. Fig. 4.9).

The oxygen isotope compositions of olivine within the studied chondrules are ^{16}O-poor and their $\Delta^{17}O$ values range from -7.02‰ to 0.02‰ (cf. Fig. 4.10), which agrees literature data on mineral phases in CM2 chondrules ($\Delta^{17}O$ = -7‰ to -4‰; e.g. Chaumard et al., 2018, 2021; Fukuda et al., 2022). Three-oxygen isotope measurements of olivine within the main CM chondrule population follow the PCM line (cf. Fig. 4.10).

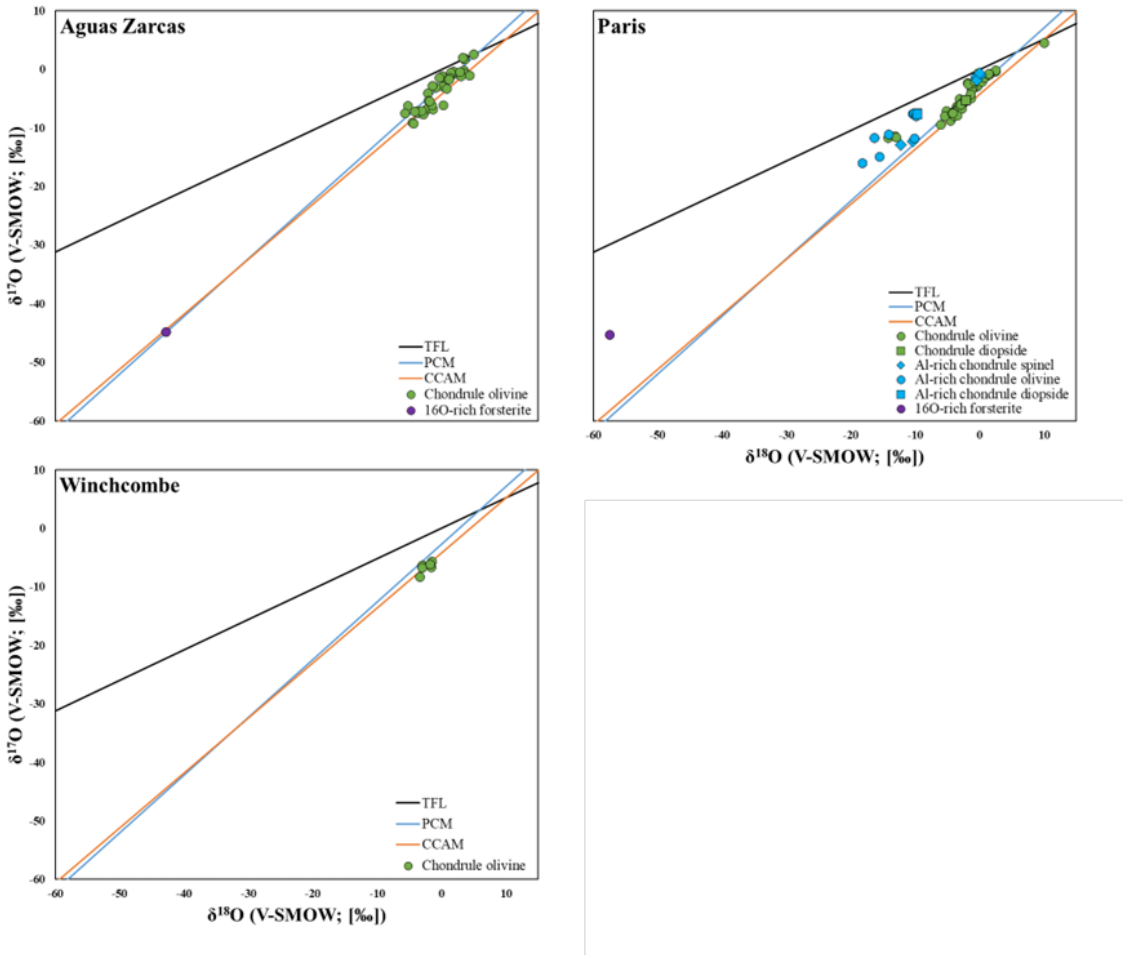

Figure 4.10. Three-isotope oxygen diagrams of compositions of individual spot analyses of mineral phases in chondrules, ARCs, and ^{16}O-rich forsterite grains from the studied CM carbonaceous chondrites. The error bars, corresponding to the standard error (±2SE), are smaller than the symbol sizes.

The three observed ARC specimens have porphyritic textures and are composed of spinel, forsterite, and diopside. The targeted mineral phases have CM chondrule-like oxygen isotope compositions, albeit on the heavier end of the range, with an average $\Delta^{17}O$ value of all targeted phases of -3.29±0.76‰ (2SE; cf. Fig. 4.7 and 4.8). However, their compositions do not seem to follow the PCM line and plot slightly to the left on three-isotope diagrams (cf. Fig. 4.10). The majority of their measurements appear to cluster above the more commonly observed CM chondrule oxygen isotope compositions ($\delta^{17}O$ ARCs < $\delta^{17}O$ rest of the chondrules). The displacement from the mass-dependent fractionation line is unlikely to be caused by improper correction for the IMF effects as these results were acquired for different mineral phases, during multiple analytical sessions, and coincide with previous observations regarding O isotope data from Na-, Al-rich chondrules ($\Delta^{17}O$ = −5.2±1.7‰, 2SD; Zhang et al., 2020).

Spinel measurements from two ARCs plot the closest to the PCM line but differ noticeably from each other (cf. Fig. 4.10). Spinel within object designated as ‘56’ (cf. Table 4.6) has a lighter oxygen isotope composition, with an average $\Delta^{17}O$ of -6.70±0.78‰ (2SE; cf. Fig. 4.8), compared to object ‘160’ which has a mean $\Delta^{17}O$ of -1.08±0.80‰ (2SE; cf. Fig. 4.8). This lighter oxygen isotope composition is also observed in olivine measurements from objects ‘56’ and ‘64’, with a mean $\Delta^{17}O$ of -4.27±0.75‰ (2SE; cf. Fig. 4.8). However, diopside measurements from object ‘64’ do not follow this trend and have a mean $\Delta^{17}O$ of -2.59±0.67‰ (2SE; cf. Fig. 4.8). Three-oxygen isotope compositions of olivine and diopside grains from ARCs plot the furthest away from the PCM line. Olivine and diopside measurements from these two ARCs appear to be more enriched in ^{16}O than the rest of the CM chondrules in this study. Two populations of ARCs can therefore be inferred from these figures (cf. Fig. 4.8 and 4.10): those with intermediate mineral oxygen isotope signatures and those with more chondrule-like oxygen compositions.

Two objects, designated as ‘Ol-07’ and ‘55-1’ in Aguas Zarcas and Paris, respectively (cf. Table 4.6), and corresponding to two forsterite grains fragments (potentially chondrule fragments) with^{16}O-rich compositions (cf. Fig. 4.10), with a mean $\Delta^{17}O$ value of -19.01±0.68‰ (2SE; cf. Fig. 4.8), set themselves apart from the rest of the main CM chondrule population. Object

‘55-1’, however, plots completely to the left away from the PCM line in a three-oxygen isotope diagram (cf. Fig. 4.10), with a $\delta^{18}O$ value of -57.48±0.32‰ (2SE; cf. Fig. 4.10). The displacement of the measurement is likely due to mistargeting (cf. Appendix 7.9), as the area hit comprised a large portion of the FGR surrounding the initial target, and correction for IMF effects for FGR mineral phases (mostly olivine, phyllosilicates, Fe-sulfides and carbonates) was not conducted. The measurement, however, was not removed from the study as the oxygen isotope composition remains considerably ^{16}O-rich even while considering the major overlap with neighbouring ^{16}O-depleted FGR material. These two ^{16}O-rich forsterites are heavier in composition than previously observed AOAs within CM2 meteorites, and do not share any textural similarities ($\Delta^{17}O$ = -23.7±0.4‰, 2SD; Chaumard et al., 2021; Hiyagon & Hashimoto, 1999; Krot et al., 2004).

4.3.2.2 Comparison of Oxygen Isotope Signatures Between CCCAI Components and their CM Counterparts

The CAI components from CCCAIs have ^{16}O-rich compositions that plot close to the PCM line (cf. Fig. 4.8). The spinel from CCCAI CAI components from Cicero and the Cockerel have similar $\Delta^{17}O$ values averaging -18.33±0.68‰ (2SE; cf. Fig. 4.7 and 4.8), whereas the Capybara’s CAI spinel has a heavier oxygen isotope composition with $\Delta^{17}O$ = -13.01±0.84‰ (2SE; cf. Fig. 4.8). The mean oxygen isotope compositions of the spinel clusters from the CAI components of the CCCAIs are similar to the composition of the spinel grains from the targeted CM CAIs (-25.18‰ < $\Delta^{17}O$ < -10.35‰; cf. Fig. 4.8), which have an average $\Delta^{17}O$ of -20.40±0.75‰ (2SE).

The oxygen isotope composition of the olivine and diopside from the chondrule components of the Cockerel and the Capybara correspond to the oxygen isotope signatures of the chondrules of the studied CM lithologies, with an average $\Delta^{17}O$ value of -5.91±0.67‰ (2SE; cf. Fig. 4.7 and 4.8). It is to be noted, however, that the Capybara’s chondrule component is on the lighter side or the compositional range than the Cockerel’s chondrule and other chondrules in this study, with an average $\Delta^{17}O$ value of -7.42±0.68‰ (2SE; cf. Fig. 4.7 and 4.8).

In the case of Cicero, however, we can observe a slight discrepancy between the oxygen isotope composition of the forsterite cluster directly adjacent to the CAI component of the CCCAI in regards to the other three chondrule fragments in close proximity within the assemblage (cf. Fig. 4.4 and 4.11). The enclosing chondrule's oxygen isotope's signature is ^{16}O-rich (mean Δ^{17}O = -24.05±0.77‰, 2SE; cf. Fig. 4.8) similar to CAI oxygen compositions (Δ^{17}O ~ -24‰; e.g. Hiyagon & Hashimoto, 1999; Itoh et al., 2004; Makide et al., 2009) or AOAs observed within CM2 meteorites (Δ^{17}O = -23.7±0.4‰, 2SD; Chaumard et al., 2021; Hiyagon & Hashimoto, 1999; Krot et al., 2004). In contrast, the olivine measurements from the three remaining fragments' oxygen isotope compositions plot within the range defined by the rest of the observed CM chondrules, with an Δ^{17}O value of -3.29±0.65‰ (2SE; cf. Fig. 4.8).

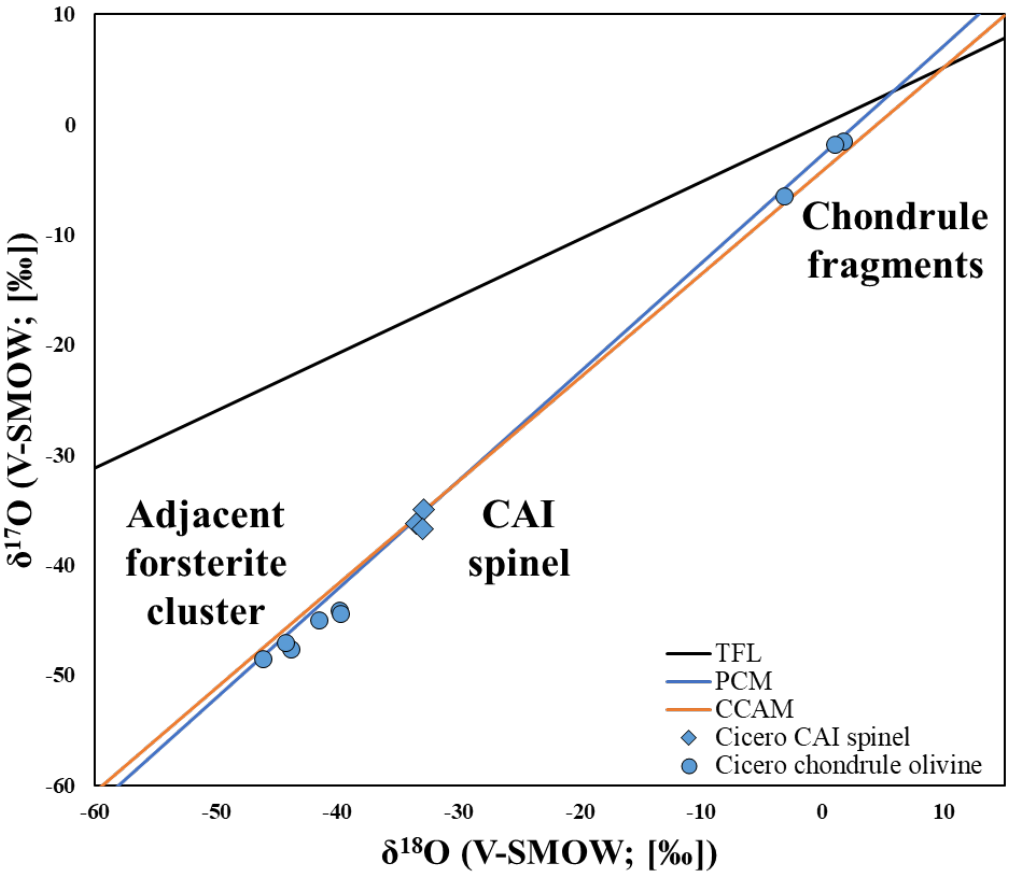

Figure 4.11. Three-isotope oxygen diagram of compositions of individual spot analyses of mineral phases in the CAI and chondrule components of the Cicero CCCAI and in the proximal chondrule fragments within the same FGR. The error bars, corresponding to the standard error (±2SE), are smaller than the symbol sizes.

4.4 Discussion

4.4.1 Constraining the Thermal Conditions of CCCAI Formation Processes

4.4.1.1 Recrystallisation of Spinel in CCCAIs within the Chondrule Forming Environment

The CAI components of the studied CCCAIs are mainly composed of clusters of fine spinel grains. They display signs of recrystallisation in the form of 120° triple-junctions and annealing textures. These features coincide with the finely grained diopside found (partially) surrounding the core spinel clusters of the CAI components of Cicero and the Capybara.

During the process of annealing (recovery, recrystallisation, and grain growth), recovery occurs first, and excess vacuities (such as pores) anneal out. At high temperatures, dislocations are eliminated and rearrange themselves, leading to polygonisation. This is observed as triple-junctions between the spinel grains of the CAI components of the studied CCCAIs. Recovery and recrystallisation decrease the dislocation density which coincides with the low deformation observed in the GROD and KAM angle maps (cf. Fig. 4.1d and 4.1e) produced for the mineral phases found within the Cockerel's chondrule component, which do not display extensive misorientation between the grains.

The annealing process culminates in grain growth if thermal conditions are sustained for a longer period of time and is intensified at higher temperatures. This means that due to the fine-grained nature of the spinel clusters of the CCCAIs, they were very likely subjected to high temperatures for a short period of time (inferior to ~10s of minutes; Libourel & Portail, 2018), with the recovery and recrystallisation of spinel grains being complete, while stunting the grain growth stage of the process. Complete annealing implies a slow cooling rate (~10 K/h; Libourel & Portail, 2018) and no phase transformation, hence the spinel clusters within the CAIs of CCCAIs can be considered pristine. It is therefore possible to establish a coarse thermometer for the formation of CCCAIs within the chondrule forming region.

The chondrule forming environment has been constrained through mineralogical observations, correlated with furnace experiments and thermodynamic modelling, and has been shown to reach peak temperatures within the range of 1700-2100 K (Jones et al., 2003; Hewins, et al., 2005; Joham & Dorfi, 2012), with the liquidus of ferromagnesian chondrules being within 1600-1900 K (the temperature at which the chondrule is entirely melted; Jones et al., 2018; Marrocchi et al., 2024). According to petrological experiments, spinel can remain solid and stable up to ~1820 K (Stolper, 1982). This establishes upper and lower temperature limits to this system, with the Cockerel defining a temperature range from 1820 K (destabilisation and melting of spinel; Stolper, 1982) to 1300 K (crystallisation of olivine and enstatite; Ebel et al., 2006 and 2021) during the melting, cooling and formation of the CCCAI prior to its incorporation within the CM parent body(-ies).

However, the CAI component could not have been completely melted as there is no evidence of mixing between the CCCAI components as they have very distinct oxygen isotope compositions from each other, cf. Table 4.6, and Fig. 4.7 and 4.8. If both CCCAI components were completely melted in the chondrule forming region, then mixing would have occurred, which would have translated to an intermediate ^{16}O signature for the components, i.e. lighter chondrule signature and heavier CAI signature. This is not what has been observed (cf. Fig. 4.7 and 4.8). This also implies that both the CAI component and chondrule precursor were heated separately before accretion and formation of the CCCAI in the chondrule forming region (Russel et al., 2017). Consequently, this leads to two possible scenarios for the formation of CCCAIs: (1) by the incorporation of a CAI within a ferromagnesian melt, or (2) with the CAI serving as an accretion nucleus for the formation of a chondrule.

4.4.1.2 Evaluating the Potential for CAIs as Nucleation Sites for Chondrule Formation

Chondrule texture depends on the availability of nucleation sites for crystal growth within the chondrule melt during cooling. The chondrule components of CCCAIs within this study display porphyritic textures which require numerous nucleation sites for the growth of the larger crystals (Lofgren and Russell, 1986; Radomsky and Hewins, 1990; Lofgren, 1996; Hewins et al., 2005; Desch et al., 2012; Jones et al., 2018). The survivability of the nuclei requires an incomplete melting of the chondrule precursor, which implies that the precursor material remained at conditions below or towards the lower end of the chondrule liquidus (in addition to several other factors such as grain size within the chondrule precursor aggregate and heating time; e.g. Connolly et al., 1998). In contrast, heating at temperatures above the chondrule liquidus decreases the likelihood of nuclei survivability and leads to the formation of radial textures within chondrules (Lofgren and Russell, 1986; Radomsky & Hewins, 1990; Lofgren, 1996; Jones et al., 2018).

The crystal orientation map (IPF; cf. Fig. 4.1c) generated from EBSD shows that the Cockerel's chondrule mineral phase crystallised in random orientations, in accord with crystallisation within a low-gravity environment in space. No Crystallographic Preferred Orientation (CPO) within the CCCAI-mineral phases, nor between them and the CCCAI-hosted minerals (cf. Fig. 4.1c) can be observed. Deviation of internal grain orientation from the mean grain orientation of the CCCAI-hosted chondrule's mineral phases (GROD map; cf. Fig. 4.1d) show crystal plastic deformation within the diopside grains whereas the forsterite and enstatite grains are relatively undeformed. Such plastic deformation is very likely the result of crystal growth pressure and the KAM map (cf. Fig. 4.1e), displaying the local grain misorientation, indicates that the crystal boundaries have not fully recovered from said plastic deformation (relatively low average misorientation of <2°). Thus, the environment in which the assemblage evolved was not at a high enough temperature for long enough time for the boundaries to reform and overprint the deformation signature.

Misorientation within crystallographic slip-systems can be inferred from disorientation axes diagrams. They allow representation of plastic deformation

defined by a crystallographic plane and direction (Barber et al., 2010). These slip-systems depend on a variety of factors such as temperature, pressure, strain, water content, crystal orientation, etc. (Karato et al., 2008; Paul Raterron & Jaoul, 1991; Tielke et al., 2019). To envision these systems, disorientation axes figures can highlight the planes and orientations around which the crystals accommodate for deformation. In the case of the diopside grains within the chondrule component of the Cockerel, the disorientation axes (cf. Fig. 4.3) hint towards a high temperature system (from 600 K to 1200 K; Avé Lallemant, 1978; Kollé & Blacic, 1982; Raleigh, 1967), due to an inclination towards (100). This is confirmed by the disorientation axes diagram of the forsterite grains which displays an inclination towards (010) which indicates deformation caused by a high temperature system (up to 1773.15 K; Katayama et al., 2004), in regard to terrestrial mantle conditions. No strong evidence for shock deformation can be inferred from the produced crystallographic data, and so it is very likely that shock deformation is little to none, which is consistent with the low shock stages (S1) experienced by CMs (<5 GPa of shock pressure; Scott et al. 1992; Stöffler et al. 1991; Stöffler et al. 2018). It is to be noted, however, that further investigation is required as, due to the paucity of the data points, any inference made concerning the slip-systems would not be robust enough. This remains quite a difficult endeavour due to the rarity of CCCAIs in the CM meteorite record, coupled with the difficulties of sample preparation for EBSD analysis.

Petrographic observations (cf. Fig. 4.1a and 4.1b) show well-formed diopside, globular forsterite, and lamellar enstatite. This provides further evidence for the chondrule melt being a slow cooling system. The chondrule component of the Cockerel therefore must have formed within the chondrule forming region during which it cooled slowly after a short high temperature heating event. However, since recrystallisation during annealing removes internal stress features caused by plastic deformation, this does not necessarily invalidate the hypothesis that the CAI component might have served as a nucleation point for the now surrounding chondrule.

4.4.1.3 Accretion of Ferromagnesian Material to a Partially Molten CAI

Chondrules are thought to have formed from the melting of a chondrule precursor assemblage under the high temperatures of the chondrule forming region. The chondrule components of the CCCAIs display porphyritic textures. These textures are formed when peak temperature is below the liquidus, allowing for increased nuclei survivability, followed by a slow cooling (Lofgren and Russell, 1986; Radomsky and Hewins, 1990; Lofgren, 1996; Hewins et al., 2005; Desch et al., 2012; Jones et al., 2018). The hypothesis for the formation of CCCAIs proposed in this study is that ferromagnesian material originating from precursor chondrule aggregates melted under chondrule forming conditions and accreted to the partially molten CAI. The process of incorporating the CAI into the molten chondrule requires the two soon-to-be components to be immiscible. This means that the chondrule precursor was very likely melted before the incorporation of the CAI component, as mixing would have incurred oxygen isotopic exchange between the CAI and chondrule components of the CCCAIs. Thus, the temperature at which the components combined must have been on the lower end of the chondrule liquidus range (within 1600-1820 K as constrained previously), allowing for nuclei survivability for the formation of porphyritic chondrule textures.

Another possible model for the formation of porphyritic textures in chondrules is the epitaxial growth model from surviving nuclei in the chondrule forming region. This model, originally proposed by Libourel & Portail (2018), suggests a slow cooling rate (a few K/h) at temperatures above the chondrule liquidus allowing for the survival of Fe-Ni nuggets, metal beads which serve as crystal nucleation points for larger crystals within the melt under the conditions of the chondrule forming region (temperature of approximately 1800 K). Following this slow crystallisation, the model suggests a sudden and rapid cooling (>1000 K/h), stopping the crystallisation process. It is important to note that no signs of epitaxial growth have been observed through EBSD within the grains of the porphyritic chondrule of the Cockerel. However, a few forsterite grains in the Capybara's chondrule component have very fine Fe-Ni grains within their centres. This implies that the Capybara's chondrule might not have been completely melted and that the formation of the larger observed crystals might depend on the presence of surviving crystals from the high temperatures of the

chondrule liquidus. The presence of material of more primitive origin is further evidenced by the lower $\Delta^{17}O$ value ($\Delta^{17}O$ = -7.42±0.68‰, 2SE; cf. Table 4.6) of the chondrule component of the Capybara in regards to the rest of the CM chondrules. Unfortunately, due to the lack of oxygen isotope measurements from chondrules in LAP 02239, it is not possible to make any inferences regarding the fact that CMs might sample different chondrule populations in this study.

These observations coupled with previous models reinforce the idea that CCCAIs formed due to one or several transient short-lived heating events leading to the incorporation of partially melted CAIs within melted ferromagnesian precursor aggregate material before a sudden slow cooling (allowing for larger crystals to form) leading to the formation porphyritic chondrule textures.

4.4.2 Implications for Understanding Early Solar System Processes

4.4.2.1 Early Outward Migration of CAIs Through the Chondrule Forming region

Oxygen isotope analysis of the spinel clusters of the CAI components of the CCCAIs indicates that they were formed within the same near-solar environment as individual CAIs found within the CM lithologies (^{16}O-rich oxygen isotope compositions; cf. Fig. 4.8 and 4.9). Oxygen isotope analysis of the mineral phases within the chondrule components of the Cockerel and the Capybara shows a similar trend, with CCCAI-chondrules and CM chondrules both originating from the chondrule forming region (^{16}O-depleted isotope compositions; cf. Fig. 4.8 and 4.10). There is no evidence for different CAI populations, nor different chondrule populations, within the CCCAIs as there are no indications that they sampled different O isotope reservoirs. There is also no evidence of isotope fractionation through ^{16}O diffusion from the CAI component to the chondrule component of CCCAIs. This indicates that the studied CCCAIs would have formed through the interaction of CAIs derived from a common region of origin as CM CAIs (^{16}O-rich) with chondrules sourced from a common region of origin as CM chondrules (^{16}O-depleted).

However, in the case of Cicero, the mineral phases within its chondrule component display a different oxygen isotope composition that is enriched in ^{16}O ($\Delta^{17}O$ = -24.05±0.77‰, 2SE; cf. Fig. 4.7 and Table 4.6). This composition is in contrast to the other three chondrule fragments enclosed within its singular FGR, whose oxygen isotope compositions are consistent with CM chondrules found within the rest of the CM lithologies as well as in the chondrule components of the rest of the studied CCCAIs. Previous studies show that chondrule precursor aggregates were isotopically diverse and heterogeneous and may have contained CAI-like material (Wakaki et al., 2013; Krot et al., 2017; Yap & Tissot, 2023), AOAs (Nagashima et al., 2015, Zhang et al., 2020), and even early formed chondrule fragments from ^{16}O-rich reservoirs (Marrocchi et al. 2019). This suggests that Cicero's chondrule component formed from the recycling of near-solar (^{16}O-rich) material. Other ^{16}O rich forsterites were found within the Aguas Zarcas meteorite (objects 'Ol-07' and '55-1'; cf. Table 4.6) which further evidences this claim. Furthermore, it is of importance to note that neither Cicero's chondrule component nor do these forsterites display AOA-like textures (fine-grained olivine grains in the shape of an ameboid) despite having a similar ^{16}O-rich oxygen isotope composition (cf. Fig. 4.7 and 4.8).

Since the CAIs formed through the condensation of a high-temperature solar nebular gas, and chondrules are thought to have formed by the melting of precursor material within a few astronomical units (AU) from the protosun (Russell et al., 2005; Lauretta et al., 2006; MacPherson, 2013; Scott and Krot, 2014; Russell et al., 2018), CCCAIs provides tangible evidence of outward transportation of refractory material during chondrule formation. These assemblages give temporal and locational information to the migration of CAI material from a near-solar environment, throughout the chondrule forming region, prior to its incorporation within the CM parent body(-ies). The envelopment of the studied CCCAIs by FGRs reveals a simple chronological relationship through cross-cutting: CCCAI formation (after accretion, heating, and melting) is followed by episodes of dust mantle accretion. Multiple layers, such as in the case of the Capybara, show multiple distinct episodes of accretion. The layers of the Capybara having different compositions (cf. Fig. 4.5) is very likely due to the changes of gas and dust conditions in the nebula during the evolution of the protoplanetary disk. And in the case of Cicero, ^{16}O-depleted

chondrule fragments (cf. Fig. 4.4 and 4.12) can be observed enclosed within the same FGR as the ^{16}O-rich CCCAI, which further evidences the frequency of multiple accretion events within a dense chondrule-rich environment. According to the EDS elemental maps generated, the FGRs of the CCCAIs and the CM matrix appear to share a similar mineralogy which implies that the dust originated from the chondrule forming region. Spot overlapping during SIMS analysis suggests that the mineral phases within the CM matrix and FGRs are ^{16}O-depleted like the CM chondrules providing further evidence to this claim. However, a more rigorous study should be conducted in the future to definitively prove this last point.

The presence of CCCAIs in carbonaceous chondrites therefore suggests that the outward transport of inner Solar System CAI material must have occurred before the formation of a physical barrier, such as that proposed by the early formation of proto-Jupiter or other disk gap models, within ~1 Ma after CAI formation (Kruijer et al., 2017; Desch et al., 2018; Brasser & Mojzsis, 2020; Jongejan et al., 2023; Fukuda et al., 2024). This timing concurs with the formation of chondrules from carbonaceous chondrites, which are thought to have formed over a period of 1 to 3 Ma after CAI formation (Amelin, 2002; Krot et al., 2005; Connelly et al., 2017) and the formation of carbonaceous C-type asteroids, which accreted within 4±2 Ma after CAI formation (parent body fluid alteration dating; Fujiya et al., 2012; Visser et al., 2020).

4.4.2.2 Relationship Between CCCAIs, Rimmed CAIs, and Al-rich Chondrules

CAIs and chondrules have long been thought of as independent objects, having formed in different environments. However, the existence of CCCAIs and ARCs suggests the existence of a genetic link between CAIs and chondrules (Bischoff and Keil, 1983; Bischoff and Keil, 1984; Bischoff et al., 1989; Sheng et al., 1991b; Russell et al., 1996; Maruyama et al., 1999; Russell et al., 2000; Krot et al., 2002; Krot and Keil, 2002; Krot et al., 2004a; MacPherson and Huss, 2005; Guan et al., 2006; Akaki et al., 2007; Ma et al., 2008; Rout et al., 2010; Wakaki et al., 2013; Zhang et al., 2014; Wang et al., 2016; Krot et al., 2018). There also exists refractory objects such as rimmed CAIs, which are CAIs with a forsterite rim (cf. section 4.2.3). While these assemblages might appear similar to CCCAIs petrographically (in spite of textural differences), both the CAI component and

the rim present a common ^{16}O-rich oxygen isotope composition ($\Delta^{17}O$ = −21.14±0.74‰, 2SE for the CAI cores, and $\Delta^{17}O$ = −19.68±0.72‰, 2SE for the rims; cf. Fig. 4.12 and Table 4.6). The observed rimmed CAIs appear to have acquired their rim in a near-solar ^{16}O-rich environment and were preserved during one or several transient heating events throughout the protoplanetary disk until their incorporation within the CM parent body(-ies). Because their forsteritic rims display condensation and annealing textures, it is likely that these objects were never subjected fully to the thermal conditions of the chondrule forming environment, and, therefore, have distinct transport and thermal histories from those of CCCAIs. However, ARCs display igneous textures and show mineralogical and isotopic evidence (cf. section 4.2.3) that their precursors could have contained a small amount of refractory material, such as CAIs or AOAs, and melted in the chondrule forming region through the same transient heating events. This suggestion concurs with previously obtained oxygen isotopic data ($\Delta^{17}O$ = −5.2±1.7‰, 2SD; Zhang et al., 2020) and the mean measurements within this study ($\Delta^{17}O$ = −3.29±0.76‰, 2SE; cf. Table 4.6).

The ARCs observed in this study represent an isotopically heterogeneous category, and display evidence for having processed CAI material either completely or partially. Oxygen isotope compositions are intermediate (as low as $\Delta^{17}O$ = −6.70±0.78‰, 2SE for object 56; cf. Fig. 4.12 and Table 4.6) due to mixing of both components, melted CAI remnant material and chondrule melt, homogenising their oxygen isotope compositions. The resulting object resembles a chondrule with an anomalous enrichment in recrystallised Al-rich phases, such as the spinel grains observed in the ARCs found in Paris. According to Zhang et al. (2020), ARCs can be divided into two categories: (i) those isotopically lighter in oxygen having formed from the melting and complete reprocessing of CAI material within the chondrule forming region, and (ii) those isotopically heavier and chondrule-like having formed solely within the chondrule forming region with crystallisation sequences depending on their bulk composition. In the first case, the ^{16}O-depleted spinel grains most likely experienced melting and isotope exchange within a ^{16}O-depleted environment in the chondrule forming region. During this process, spinel with a ferromagnesian melt which in turn became slightly ^{16}O-enriched. The enrichment of olivine and pyroxene relative to the depletion of the spinel, of these latter objects, is due to the incomplete mixing

of the ^{16}O-depleted ferromagnesian melt with ^{16}O-enriched CAI material. Whereas in the second case, the ^{16}O-poor spinel grains most likely experienced melting and isotope exchange within a ^{16}O-depleted environment before being reprocessed and recrystallised (igneous melting textures) within a ^{16}O-depleted ferromagnesian melt.

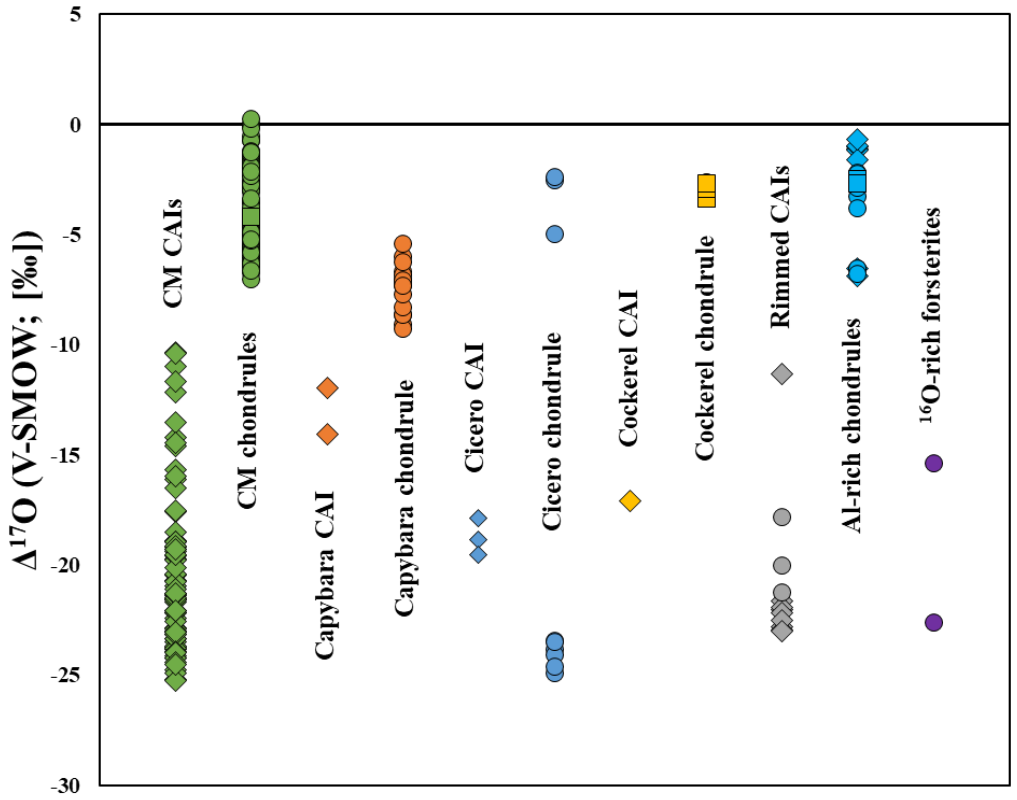

Figure 4.12. $\Delta^{17}O$ values of all the CCCAI components, CAIs, and chondrules from the studied CM carbonaceous chondrites normalised to the TFL. The TFL is represented by a straight horizontal black line, lozenges represent spinel, squares represent diopside, and circles represent olivine measurements. The error bars, corresponding to the standard error (±2SE), are smaller than the symbol sizes.

The observations made in this study can be compiled into a spectrum defined by a melting and reprocessing gradient of CAI material: spanning from ARCs formed from completely melted ^{16}O-poor chondrule precursor material, to ARCs formed from reprocessed incompletely melted CAIs (which had retained partially their slightly ^{16}O-rich composition due to only partial exchange), to finally CCCAIs with texturally preserved CAIs which have not undergone isotope

exchange within a ^{16}O-depleted environment, nor with the ferromagnesian melt they have been incorporated within.

The relatively low abundance of these CCCAIs within carbonaceous chondrites remains difficult to understand as interactions between CAIs and chondrules within a high-density particle environment should result in a non-negligible presence of such objects in the records of the most studied type of meteorites. There are three possible explanations for this discrepancy: (i) that such objects have not been systematically studied nor dutifully reported during petrological and mineralogical CM chondrite overview reports; (ii) CCCAIs are far more common than realised but are simply in different forms, resulting in a more troublesome identification process depending on the degree of preservation of the CAI component; (iii) the paucity of CCCAIs could be explained by the low survivability of CAIs within the higher temperature conditions of the chondrule forming region (temperatures >1820 K; Russel & Howard, 2013). In any case, ARCs with partially processed CAIs could be the missing link to understanding the interactions between CAIs and chondrules in the early Solar System.

4.4.2.3 A Proposed Unified Model for CM CCCAI Formation

Considering these assumptions, the results obtained within this study, and correlating with published crystallisation experiments and condensation models, it is possible to produce the following model, represented schematically in figure 4.13, detailing the chronology for the formation of CCCAIs:

1) <u>CAI formation through condensation</u>
   CAIs formed from the condensation of refractory material from the solar nebula about 4567.30±0.16 Ma ago (Amelin et al., 2010; Connelly et al., 2017). CAIs formed in a near-solar environment (^{16}O-rich reservoir) as fine-grained condensates from a high temperature nebular gas (>1300 K; McKeegan et al., 2000; Chaussidon et al., 2006; Wielandt et al., 2012; Gounelle et al., 2013; Sossi et al., 2017; Mishra & Marhas, 2019). The CAI is represented by a simple aggregate in figure 4.12: a spinel core (purple) within a mantle (yellow). Chondrule precursor aggregates were isotopically heterogeneous and may have contained material originating

from either ^{16}O-rich or ^{16}O-depleted reservoirs (e.g. Wakaki et al., 2013; Krot et al., 2017; Yap & Tissot, 2023; Nagashima et al., 2015, Zhang et al., 2020; Marrocchi et al. 2019). Since chondrules are thought to have formed over a period of ~1 to 3 Ma after CAI formation (Amelin, 2002; Krot et al., 2005; Connelly et al., 2017), the chondrule precursor aggregate (grey spotted pattern in figure 4.13) must have started undergoing rapid melting within the chondrule forming region within that time period, following an early outward migration.

2) Accretion of ferromagnesian material around partially molten CAI

The migrating CAI is then partially melted upon experiencing high temperatures of the chondrule forming environment, up to 1820 K (temperature of destabilisation of spinel; Stolper, 1982). At these high temperatures, the CAI's mantle (yellow in figure 4.13) melts and the spinel grains (purple lozenges in figure 4.13) of the CAI's core undergo an annealing process and recrystallise. The chondrule precursor aggregate entered the region, melted due to being within chondrule liquidus conditions, resulting in the accretion of molten ferromagnesian material (dark grey in figure 4.13) onto the partially molten CAI. The enrichment in ^{16}O of the ferromagnesian melt depends on the origin of the chondrule precursor's material. Isotope exchange does not occur as O isotopes are immobile in forsterite in those conditions and no mixing has occurred due to immiscibility between the components.

3) Formation of CCCAI

Following this heating event, the temperature of the newly formed partially melted assemblage rapidly decreases (~1000 K/h; Libourel & Portail, 2018), stunting the crystal growth step of the annealing process within the CAI. As the temperature decreases, the surviving fine grains of spinel clump together towards the centroid of the object, forming a cluster enveloped within the residual CAI melt. The cooling rate slows down to a few K/h, allowing for the formation of larger crystals of pyroxene and olivine (e.g. diopside, enstatite, and forsterite; green and blue euhedral, and green globular crystals respectively in figure 4.13) at a temperature of at least 1300 K (Ebel et al., 2006 and 2021) within the

ferromagnesian melt, leading to the formation of a porphyritic chondrule, and, ultimately, to the final form of the CCCAI.

4) Dust mantle accretion

Residual dust from chondrule formation (mostly forsterite; ^{16}O-depleted) accreted quickly around the CCCAI, forming what is known as an FGR (brown spotted pattern in figure 4.13). Due to the presence of Fe-sulfides within the FGR, it is very likely that this dust formed at temperatures below 650 K (Rubin et al., 1993; Desch et al., 2012). Multiple dust mantle accretion episodes may occur as observed within the Capybara (cf. Fig. 4.5). The temperature of the system continues to decrease the farther the assemblage migrates from the heat source of chondrule formation.

5) Incorporation within the CM parent body

The CCCAI reached the end of its journey when entering the accretion radius of a C-type asteroid destined to become the CM parent body (single parent body model is assumed for the sake of simplicity). The increase of pressure on the asteroid lead to compaction, which created mineral alignments (such as with the Fe-sulfides in the Cockerel) within the FGR. Subsequent aqueous alteration events within the CM chondrite body would then lead to the formation of type II replacive calcite within the CAI components of the CCCAI (as observed within the Cockerel and Cicero). This type of calcite within CMs has been observed as the result of the replacement of melilite or anorthite due to extensive fluid alteration (e.g. Bunch & Chang, 1980; Johnson & Prinz, 1993; Lee et al., 1994). Most CAIs within CMs are considered to be type A (melilite bearing; Brearley & Jones, 1998); this is what is observed in more pristine samples of CMs (CM2.5 and above; Rubin, 2015; Rubin et al., 2007; Kimura et al., 2020). Any other assumptions as to the original mineralogy of the CAI component of CCCAIs would be purely speculative. Recent studies have established that chondritic asteroids have accreted 2.8 to 4 Ma after CAI formation (e.g. Huss et al. 2001; Cournede et al., 2015; Fujiya et al., 2012, 2013; Sugiura and Fujiya, 2014; Doyle et al., 2015; Jogo et al., 2017; Blackburn et al., 2017;

Edwards and Blackburn, 2020; Anand & Mezger 2023) over 2.8 AU from the protosun (Walsh et al. 2011; Walsh et al. 2012), which means that this entire process remained quite early as to not have been affected by physical barriers (e.g. proto-Jupiter; Kruijer et al., 2017; Desch et al., 2018; Brasser & Mojzsis, 2020; Jongejan et al., 2023).

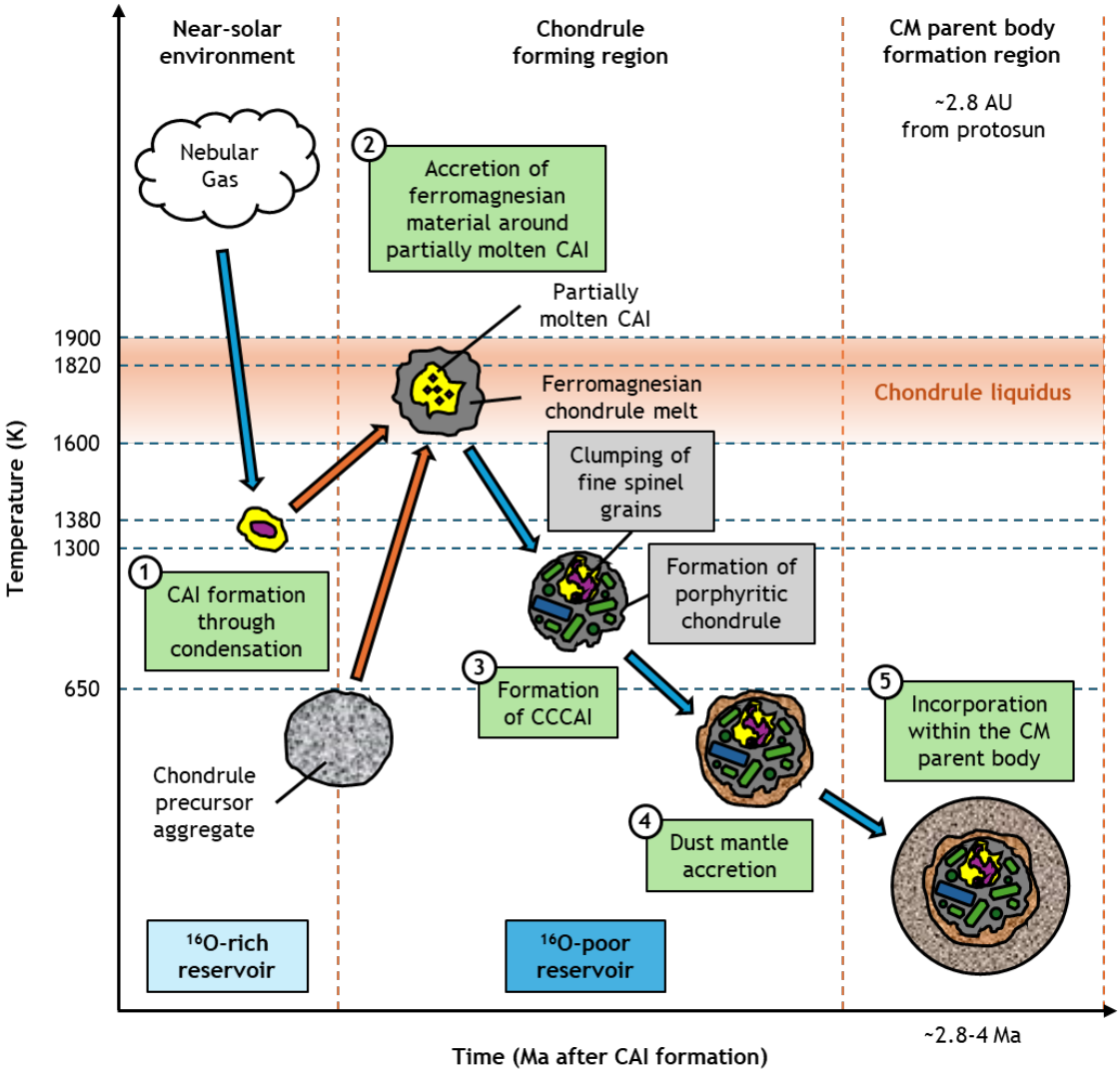

Figure 4.13. Schematic diagram of the proposed CCCAI formation model.

Considering that CAIs formed in a near-solar environment, this model assumes an early outward migration of CAIs (≤ 1 Ma) through the protoplanetary disk (radial transport) and into the chondrule forming region (an overview of the models for CAI material migration throughout the protoplanetary disk can be found in Chapter 1). Temperatures used in designing this model were determined by following the condensation sequence highlighted and compiled by Ebel et al. (2006 and 2021) through experimentation and simulation at a

pressure of 10^{-4} bars (sufficiently low to be representative of the early conditions of the chondrule forming environment). Thermal variations within the system are considered to be spatially driven. This may imply migration processes involving leaving the protoplanetary disk, inducing a sudden decrease in temperature before entering the chondrule forming environment. It is also important to note that oxygen isotope measurements cannot be used to infer chronology and any derived time constraints would only remain speculative.

Concerning temperature and time constraints regarding the chondrule precursor, previous studies, such as Rubin et al. (1993) and Desch et al. (2012), have established that the precursor aggregate formed at a temperature below 650 K in order to allow the condensation of troilite (FeS). These temperatures can be attained if mechanisms are considered for leaving the hot and dense regions of the protoplanetary disk before re-entering it further from the Sun towards the CM parent body accretion region.

4.5 Conclusions

CCCAIs constitute polymineralic CAIs within porphyritic chondrules. CAIs and chondrules are among the most important components in chondrites which are thought to have formed separately within the first 2-5 Ma of the Solar System (Amelin, 2002; Krot et al., 2005; Connelly et al., 2017). Considering CAIs formed in a near-solar environment and chondrules are thought to have formed by the melting of precursors a few AUs from the protosun, the mere existence of CCCAIs challenges our perceptions of early transport and mixing of refractory material and isotopic reservoirs during the early stages of the formation and evolution of the Solar System.

Results show that CCCAIs are heterogeneous objects, with the CAI components being ^{16}O-rich compared to their ^{16}O-depleted chondrule hosts. Based on oxygen isotope analysis, the CAI components of the CCCAIs belong to the same CAI population as the CAIs within the CM lithologies. The same conclusion can be made for the CCCAI chondrule components being part of the same chondrule population as the rest of the ferromagnesian chondrules within the CM lithologies. The observations made indicate that the chondrule component of the CCCAIs crystallised from ^{16}O-poor melts during chondrule

formation, whereas the CAI components formed in a near-solar ^{16}O-rich environment. Formation of these CCCAIs would have occurred by incorporating the CAIs within the precursor ferromagnesian melt during transient heating events that would later become the chondrule component of such assemblages. The initial hypothesis for CCCAI formation was that the CAI component might have served as a nucleation point for the formation of porphyritic textures within the chondrule melt. However, no evidence within this study supports this hypothesis at this stage.

CCCAIs can be used as thermometer to constrain thermal alteration even after aqueous alteration occurred after their incorporation within the CM parent body(-ies). This allows to provide further constraints regarding ferromagnesian material processing within the chondrule forming region. Thus, studying CCCAIs can help us retrace the migration of CAI material throughout the protoplanetary disk and evidences an early outward migration of near-solar refractory material within 1 Ma after CAI formation (before proto-Jupiter formed a barrier; Kruijer et al., 2017; Desch et al., 2018; Brasser & Mojzsis, 2020; Jongejan et al., 2023).

Future investigations should focus on increasing sample sizes, as well as sample diversity (wider range of aqueously altered CM lithologies). Further enquiries are required to determine how parent body fluid alteration affects CCCAI mineralogy and comparing these alteration effect on CCCAIs across endmembers of the CM aqueous alteration spectrum might reveal some important discrepancies, which could possibly even challenge the current single parent body model for the origin of the CM chondrites (McSween, 1979; Lee et al., 2019).

4.6 Acknowledgments

P-E. M. acknowledges receiving funding from the Europlanet2024 Research Infrastructure (RI). Europlanet2024 RI has received funding from the European Union's Horizon 2020 research and innovation programme under grant agreement No 871149. Prof. M. R. Lee (UofG) is acknowledged for his support and for pointing out that the ‘Cockerel’ resembles a ‘rooster’. Drs. L. Daly (UofG) and S. Griffin (UofG) are acknowledged for assisting in EBSD data acquisition and

analysis. Drs. J. Villeneuve (CRPG-CNRS) and Y. Marrocchi (CRPG-CNRS) are acknowledged for assisting in SIMS data acquisition and analysis.

5 Final Summary

5.1 Conclusions

This thesis aimed to investigate the origin and evolution of the CM parent body(-ies) by studying the pre- and post-accretionary histories of CAI populations across a wide range of aqueously altered CM chondrites. CAIs constitute invaluable witnesses to both early Solar System processes and subsequent parent body alteration and are therefore key to understanding the formation and evolution of C-type, water-rich asteroids, and, thus, the origin of Earth's water.

To this end, 21 samples from six CM chondrites spanning the full range of petrologic subtypes (CM2.0-2.9) were investigated in order to characterise the petrography, mineralogy, and abundance of the different CAI populations in relation to the degree of aqueous alteration of their host lithologies. CAIs were identified, measured, and segmented in A 12236, Paris, and Winchcombe. These measurements, combined with compatible data from the literature, revealed that modal abundance of CAIs decreases with increasing aqueous alteration of their host lithologies. This trend evidences the destructive effect of fluid-driven parent body alteration processes on CAIs and presents CAI modal abundance as a potential supporting criterion for assessing CM petrologic subtypes.

Petrological observations of CAIs from DNG 06004, LAP 02236, and Winchcombe show that progressive aqueous alteration affects CAIs regardless of their mineralogical and textural complexity (simple inclusion or aggregates), in the form of extensive mineral replacement and destruction. In the Winchcombe meteorite, petrographic and geochemical investigations of 21 CAIs from 12 distinct lithologies (CM2.0-2.6) revealed that CAIs have been affected differentially by fluid-mediated replacement reactions, with some having experienced potentially multiple mineral replacement reactions. Further investigation of CAI 19, a large complex aggregate, using EPMA, TEM, and TKD, suggests that its pre-accretionary mineralogy directly influenced the secondary mineralisation processes it experienced.

Oxygen isotope analysis of the components of three CCCAIs in relation to that of CM CAIs and CM chondrules revealed a common origin for chondrules and

CAIs of both groups. EBSD characterisation of the microstructure of a CCCAI revealed a clear formation sequence from which a model for its pre-accretionary history was inferred. The existence of CCCAIs further evidences early transport and mixing of refractory material during the early stages of the formation and evolution of the Solar System.

These investigations lead to the following key answers to the original research questions:

1) What was the initial CAI abundance in CM chondrites?
   The initial distribution of CAIs within the CM parent body(-ies) was likely homogeneous. Current observable variations in CAI modal abundances stem from post-accretionary destruction linked to aqueous alteration rather than initial heterogeneity within CM lithologies.

2) How did aqueous alteration affect CAIs?
   Fluid-driven parent body processes progressively altered and destroyed CAIs through mineral replacement reactions, affecting all inclusion types, regardless of their original mineralogical and/or textural complexity.

3) Were CM CAIs distributed homogeneously?
   Large-scale investigations revealed important mineralogical and textural variability within the CM CAI populations. Heterogeneity of the CAI record was driven by post-accretionary alteration processes within the CM lithologies, and current observations do not reflect initial CAI abundances. Findings point towards a more uniform initial CAI distribution prior to parent body alteration processes.

4) What happened to CAIs prior to their incorporation within the CM parent body?
   Isotopic and microstructural analyses revealed that CM CAIs have diverse pre-accretionary thermal histories. The presence of CCCAIs provides direct evidence of an early outward migration of near-solar refractory material (pre-proto-Jupiter) and high-temperature reprocessing of CAIs within the chondrule and CM parent body(-ies) forming regions.

In fine, this work demonstrates that CAIs in CM lithologies are capable of preserving pre-accretionary and post-accretionary histories. Through the combination of large-scale petrographic surveys, precise geochemical and crystallographic studies, and advanced isotopic analyses, this thesis contributes to a better understanding of how water-rich, carbonaceous asteroids formed and evolved in the early Solar System before potentially delivering water to Earth.

5.2 Key Findings

- CM CAI modal abundance decreases relative to increasing aqueous alteration due to the alteration and destruction of CAIs through fluid-mediated replacement reactions. This correlation may serve as an additional criterion for determining the degree of aqueous alteration in CM chondritic lithologies.

- Reported CM CAI modal abundances are substantially lower than those of previous studies and should be considered independently for each petrological subtype.

- There exists a consistent distribution of mineralogically and morphologically distinct CAI types: approximately 60% of simple inclusions, 30% of simple aggregates, and 10% of complex aggregates within CM chondrites.

- Initial distribution of CAIs within the CM parent body(-ies) was likely homogeneous, and heterogeneity in the CAI record was caused by subsequent occurring fluid-driven alteration events.

- Lithological heterogeneity within CM samples must be considered, as the CM parent body(-ies) likely underwent heterogeneous aqueous alteration.

- CM CAIs recorded different parent body alteration processes depending on their mineralogy and morphology, with certain populations having undergone multiple fluid-driven alteration events.

- CCCAIs are rare objects within CM chondrites and are formed by the incorporation of CAIs within a precursor ferromagnesian melt during transient heating events in the chondrule forming region.

- The existence of CCCAIs evidences an early outward migration of near-solar refractory material within 1 Ma after CAI formation (before the formation of a physical barrier, e.g. proto-Jupiter).

6 Future Work

6.1 CAI Modal Abundance

The systematic study of CAIs within CM chondrites revealed a clear correlation between their modal abundance and the degree of aqueous alteration within their host lithologies. However, as indicated by Hezel et al. (2008), the total investigated surface area for each petrologic subtype should be increased (up to 1000-2000 mm^2) to better constrain this relationship.

Future studies of CM CAIs should report the total investigated area of their samples and provide details regarding CAI mean apparent size and area measurements, as well as the precise methodology used for CAI identification and selection. As demonstrated throughout this thesis, extrapolation from smaller areas or sample sizes does not yield representative values, and large-scale studies should be prioritised. These studies should also consider investigating the brecciated nature of their samples, which can exhibit various degrees of aqueous alteration and, consequently, very disparate CAI modal abundances, as observed within the 12 lithologies of the Winchcombe meteorite. In the absence of a consensus on CAI measurement methods, it is recommended to use “true” size and area measurements obtained with the support of an image processing programme, as this approach requires fewer assumptions and reduces potential biases.

Another promising avenue for future research is the use of micro-X-ray Computed Tomography (μXCT) to generate 3D volumetric spatial analyses of CMs in order to segment and measure CAIs. This approach would allow for more accurate estimates of CAI abundances compared to traditional 2D methods. Additionally, μXCT would help reduce the risk of misclassifying CAI types due to the infamous “2D cutting effect” (discrepancy between apparent surface area and volume).

6.2 CAI Classification

A unified CAI classification scheme is yet to be accepted, and a comprehensive nomenclature across all meteorite groups is unlikely to be established. This is due to the distinctive nature of pre- and post-accretionary histories of CM CAIs. Since all known CM chondrites have experienced various degrees of aqueous alteration (Rubin et al., 2007; Rubin, 2015; Kimura et al., 2020), only altered surviving CAIs are available for study. Thus, common nomenclatures used in other meteorite groups are not as applicable. A classification combining both mineralogical and morphological criteria is therefore more useful in this case, as it can provide information on igneous and mineral replacement textures pertaining to the pre- and post-accretionary histories of CM CAIs. Classification and description of CM CAIs using the nomenclature (adapted from MacPherson & Davis, 1994) revealed a uniform distribution of the different CAI types across four CM chondrites: ~60% of simple inclusions, ~30% of simple aggregates, and ~10% of complex aggregates.

Subsequent research will involve classifying and measuring CAIs in less altered CM lithologies (CM2.6-2.9) to verify whether this trend persists within higher petrological subtypes and investigate CAI size distributions relative to their CAI type and mineralogies. A Poisson distribution is expected (Hezel et al., 2008); however, this could provide insight into potential preferential alteration and destruction of CAIs during progressive aqueous alteration processes.

6.3 CAI Aqueous Alteration

Mineral replacement of CAI mantles and rims was the most frequently observed effect of aqueous alteration in this thesis. The mineralogy of these secondary assemblages depends on the composition of the replaced primary phases and altering fluid (Krot et al., 2021). Therefore, an interesting project would be to compare the elemental and oxygen isotope compositions of carbonates within the matrix and those within the altered CAIs of aqueously altered and pristine CM lithologies. This would further constrain the extent and composition of altering fluids that affected the host CM lithologies and potentially reveal multiple new events.

6.4 CCCAI Formation

The current model for CM CCCAI formation suggests the incorporation of a CAI within a molten precursor ferromagnesian melt during transient heating events within the high density chondrule forming region. However, the question of whether the CAI component might have served as a nucleation point for the formation of porphyritic textures within the chondrule melt remains. Understanding the origin of these porphyritic textures in the chondrule components of CCCAIs is critical for constraining their formation processes and merits further investigation.

Future research will involve advanced crystallographic characterisation techniques, such as TKD, to examine potential nucleation patterns at the nanometre scale within cross-sections of these assemblages. In addition, nano-XCT scanning could provide 3D visualisation of CCCAIs, helping to resolve the chondrule envelope surrounding the hosted CAIs. This would aid in identifying growth patterns related to nucleation sites and clarify whether CAIs may have served as nuclei for chondrule formation.

Such insights would be invaluable for understanding the mechanisms CAI material incorporation into chondrules and, by extension, the formation of CCCAIs. This work could provide new constraints on the thermodynamic conditions of the early chondrule forming environment and better our understanding of the origin and evolution of the early Solar System.

7 Appendices

7.1 EBSD Polishing Protocol for CM Chondrites

Table 7.1. Protocol for polishing CM chondrite samples for EBSD.

Name:	**Type**	**Date**
Sample:		

Removing Carbon coating (up to ≃ 20 nm thick)	**Time**	**Done**
Take a clean **polishing plate** (**0.3 µm**) and place it on a **mat** (**60 RPM**).	-	
Add **Aluminium+Glycol** (**0.3 µm**) polishing mix (a few mL/squirts).	-	
Gently push and **move** sample in a **non-repetitive motion** (Figure of 8 or side to side across the rotating mat).	≤ 1 min	
Rinse sample briefly with **tap water** (no ethanol!).	2 s	
Dab sample with **Kimwipe** to **dry** without scratching it.	-	
Rinse polishing **plate** with **tap water** before putting it on drying rack.	-	

EBSD Polishing Protocol for <u>CM chondrites</u>	**Time**	**Done**
Take clean **diamond polishing plate** (**0.1 µm**) and place on the **vibromat** (set-up needs to be unscrewed in order to place the plate, also make sure the tongue of the tape on one part of the plate is accessible to aid removal of the plate after polishing).	-	
Place the **metal ring** onto the **polishing plate**. **Screw down** the **circular metal ring** by hand using the bolts provided until it is tight.		
Add **colloidal silica+De-Ionized Water** (**0.1 µm**) polishing mix (enough to cover slightly the whole plate; **≤ 1 mm height**). When pouring, **wrap hand around the opening of the bottle** to avoid getting rogue crystals on plate.	-	
Set **vibromat** on **low speed** (min. 0.5 and **NEVER MORE THAN 3!**).	-	
Mount sample on holder (this will provide weight during polishing).	-	
Place sample face down on **vibromat** (If sample stops, nudge it gently; increase the speed slightly or add weight if stopping persists).	30 min	
Unmount sample and **rinse briefly** with **tap water** (no ethanol!).	2 s	
Add a **drop of (fairy) dishwashing soap** on sample (it helps get rid of the colloidal silica) and **dab gently** with a **Kimwipe**.	-	
Place sample in a **small beaker** with **distilled water** and place in **ultrasonic bath**.	1 min	
Rinse sample **briefly** with **tap water** and **dab** with **Kimwipe** until dry.	-	
Wash the **vibromat's circular ring and polishing plate** with warm tap water before putting them on the drying rack.	-	
Use the absorbing towel to **remove the colloidal silica solution** from the vibromat and rinse it with hot water (this may take several tries).	-	

7.2 2D CAI Measurements

Table 7.2. Geometric properties of the CAIs identified within the Asuka 12236 meteorite.

#	Area (μm^2)	Major (μm)	Minor (μm)	Perimeter (μm)	Circularity (0-1)	Aspect Ratio	Roundness (0-1)	Solidity (0-1)
1	342	72	25	17	0.82	1.48	0.68	0.89
2	6000	534	122	61	0.26	2.01	0.50	0.69
3	6000	372	113	69	0.56	1.65	0.61	0.87
4	329	66	22	19	0.95	1.16	0.86	0.93
5	897	135	50	23	0.61	2.20	0.45	0.81
6	543	123	43	16	0.45	2.62	0.38	0.78
7	2000	263	73	38	0.40	1.92	0.52	0.73
8	3000	393	78	55	0.28	1.40	0.71	0.69
9	158	55	20	10	0.66	2.08	0.48	0.83
10	2000	175	52	46	0.78	1.13	0.88	0.94
11	88	35	13	9	0.90	1.43	0.70	0.86
12	1000	144	54	30	0.76	1.82	0.55	0.93
13	258	72	27	12	0.62	2.29	0.44	0.85
14	363	85	31	15	0.64	2.12	0.47	0.85
15	82	34	13	8	0.90	1.59	0.63	0.90
16	308	76	23	17	0.68	1.33	0.75	0.87
17	788	113	38	27	0.78	1.42	0.71	0.90
18	834	133	44	24	0.59	1.85	0.54	0.83
19	347	68	22	20	0.93	1.08	0.93	0.93
20	375	88	24	20	0.61	1.25	0.80	0.78
21	128	43	14	12	0.89	1.23	0.81	0.91
22	3000	272	77	51	0.53	1.50	0.67	0.82
23	417	103	28	19	0.49	1.43	0.70	0.76
24	315	75	28	14	0.71	2.01	0.50	0.89
25	1000	165	51	26	0.49	1.94	0.52	0.81
26	1000	169	60	26	0.55	2.29	0.44	0.84
27	5000	469	118	54	0.28	2.20	0.46	0.69
28	464	94	34	17	0.65	1.95	0.51	0.87
29	7000	517	114	82	0.35	1.40	0.72	0.84
30	3000	447	79	56	0.22	1.40	0.72	0.65
31	182	58	18	13	0.69	1.33	0.75	0.82
32	818	123	34	30	0.68	1.13	0.88	0.86
33	3000	284	81	49	0.48	1.65	0.61	0.82
34	461	85	31	19	0.81	1.65	0.61	0.90
35	291	64	23	16	0.88	1.40	0.71	0.95
36	666	120	39	22	0.59	1.76	0.57	0.83
37	673	134	35	25	0.47	1.40	0.72	0.75
38	165	52	17	12	0.76	1.43	0.70	0.86

#	Area (μm^2)	Major (μm)	Minor (μm)	Perimeter (μm)	Circularity (0-1)	Aspect Ratio	Roundness (0-1)	Solidity (0-1)
39	555	124	41	17	0.45	2.32	0.43	0.77
40	843	118	39	28	0.76	1.41	0.71	0.88
41	1000	157	53	30	0.64	1.75	0.57	0.86
42	11000	494	132	109	0.58	1.20	0.83	0.86
43	477	85	30	20	0.82	1.49	0.67	0.92
44	391	86	24	21	0.67	1.12	0.89	0.87
45	324	79	28	15	0.65	1.84	0.54	0.80
46	2000	218	72	36	0.55	2.00	0.50	0.86
47	1000	170	44	30	0.45	1.47	0.68	0.78
48	235	67	24	13	0.67	1.90	0.53	0.86
49	2000	240	57	45	0.45	1.25	0.80	0.82
50	8000	538	112	86	0.33	1.30	0.77	0.67
51	3000	250	79	51	0.64	1.54	0.65	0.89
52	349	71	24	18	0.86	1.33	0.76	0.90
53	117	42	15	10	0.83	1.48	0.67	0.92
54	93	35	13	9	0.98	1.33	0.75	0.93
55	371	83	30	16	0.67	1.95	0.51	0.87
56	832	148	52	20	0.48	2.53	0.40	0.79
57	128	43	16	10	0.88	1.63	0.61	0.91
58	82	37	15	7	0.75	2.21	0.45	0.85
59	1000	168	45	31	0.50	1.46	0.69	0.79
60	529	91	32	21	0.81	1.49	0.67	0.90
61	443	128	46	12	0.34	3.81	0.26	0.68
62	2000	267	62	42	0.36	1.45	0.69	0.79
63	5000	304	89	76	0.72	1.17	0.86	0.93
64	1000	190	73	25	0.50	2.93	0.34	0.83
65	2000	209	56	38	0.49	1.46	0.69	0.80
66	200	57	19	14	0.78	1.39	0.72	0.88
67	2000	175	46	44	0.66	1.05	0.95	0.87
68	343	84	32	14	0.61	2.29	0.44	0.84
69	261	58	19	18	0.97	1.06	0.94	0.94
70	273	72	28	13	0.67	2.20	0.45	0.89
71	119	42	17	9	0.83	2.00	0.50	0.84
72	98	38	14	9	0.87	1.57	0.64	0.89
73	420	97	30	18	0.56	1.66	0.60	0.76
74	2000	219	70	32	0.46	2.18	0.46	0.78
75	275	67	24	15	0.76	1.59	0.63	0.89
76	17000	699	190	114	0.44	1.67	0.60	0.79
77	3000	385	112	38	0.28	2.95	0.34	0.71
78	116	42	14	10	0.81	1.40	0.71	0.87
79	804	128	36	28	0.62	1.30	0.77	0.78

#	Area (μm^2)	Major (μm)	Minor (μm)	Perimeter (μm)	Circularity (0-1)	Aspect Ratio	Roundness (0-1)	Solidity (0-1)
80	231	71	24	12	0.58	2.03	0.49	0.77
81	1000	175	55	25	0.44	2.26	0.44	0.78
82	263	68	22	15	0.72	1.44	0.69	0.87
83	2000	171	54	44	0.81	1.22	0.82	0.92
84	109	39	14	10	0.91	1.40	0.72	0.87
85	280	62	21	17	0.93	1.23	0.81	0.91
86	224	60	25	12	0.77	2.15	0.47	0.89
87	524	85	29	23	0.90	1.28	0.78	0.95
88	147	46	16	12	0.86	1.31	0.76	0.92
89	636	143	44	18	0.39	2.39	0.42	0.72
90	3000	213	73	45	0.71	1.61	0.62	0.91
91	77	32	12	8	0.92	1.41	0.71	0.97
92	198	58	23	11	0.73	2.05	0.49	0.87
93	3000	249	80	48	0.62	1.65	0.61	0.86
94	422	83	24	22	0.76	1.10	0.91	0.85
95	2000	220	65	49	0.65	1.32	0.76	0.89
96	6000	317	101	70	0.69	1.45	0.69	0.90
97	1000	154	47	37	0.73	1.29	0.77	0.89
98	555	126	42	17	0.44	2.51	0.40	0.65
99	2000	232	72	40	0.53	1.79	0.56	0.80
100	1000	173	50	37	0.61	1.36	0.74	0.84
101	473	89	28	21	0.75	1.33	0.75	0.91
102	403	80	25	20	0.80	1.24	0.81	0.93
103	147	46	18	11	0.89	1.67	0.60	0.93
104	86	34	13	9	0.96	1.46	0.69	0.95
105	3000	281	95	43	0.51	2.21	0.45	0.83
106	823	119	39	27	0.73	1.46	0.69	0.89
107	443	82	28	20	0.83	1.41	0.71	0.90
108	75	33	12	8	0.88	1.39	0.72	0.90
109	1000	161	54	27	0.55	2.04	0.49	0.83
110	2000	156	46	41	0.78	1.12	0.89	0.90
111	660	115	36	23	0.63	1.52	0.66	0.86
112	2000	232	71	31	0.40	2.32	0.43	0.79
113	201	62	23	11	0.67	2.03	0.49	0.79
114	4000	258	77	62	0.71	1.24	0.81	0.90
115	12000	564	169	91	0.48	1.86	0.54	0.85
116	145	47	17	11	0.83	1.53	0.66	0.88
117	2000	233	54	39	0.39	1.38	0.72	0.73
118	336	75	23	19	0.76	1.25	0.80	0.84
119	3000	251	65	58	0.59	1.13	0.89	0.83
120	471	90	28	21	0.73	1.32	0.76	0.90

#	Area (μm^2)	Major (µm)	Minor (µm)	Perimeter (µm)	Circularity (0-1)	Aspect Ratio	Roundness (0-1)	Solidity (0-1)
121	904	136	43	27	0.61	1.63	0.61	0.84
122	564	102	36	20	0.68	1.83	0.55	0.85
123	914	139	44	27	0.60	1.66	0.60	0.85
124	7000	443	144	60	0.44	2.40	0.42	0.76
125	81	32	10	10	1.00	1.05	0.95	0.97
126	68	29	9	9	1.00	1.02	0.98	0.91
127	447	106	29	19	0.50	1.50	0.67	0.75
128	1000	145	47	37	0.83	1.26	0.79	0.92
129	603	108	41	18	0.65	2.24	0.45	0.86
130	56	28	10	7	0.89	1.52	0.66	0.90
131	503	115	36	18	0.48	2.08	0.48	0.76
132	74	32	12	8	0.89	1.42	0.70	0.85
133	75	35	14	7	0.76	2.16	0.46	0.90
134	1000	159	50	29	0.58	1.70	0.59	0.83
135	95	37	15	8	0.86	1.75	0.57	0.93
136	110	39	13	11	0.92	1.21	0.83	0.96
137	611	122	47	17	0.52	2.84	0.35	0.82
138	65	28	10	8	1.00	1.23	0.81	0.94
139	219	60	18	15	0.76	1.22	0.82	0.85
140	1000	136	47	27	0.68	1.74	0.58	0.89
141	928	126	41	29	0.74	1.40	0.72	0.90
142	203	57	21	12	0.78	1.67	0.60	0.90
143	997	132	46	28	0.72	1.68	0.60	0.89
144	114	42	16	9	0.82	1.72	0.58	0.89
145	228	58	22	13	0.86	1.65	0.61	0.90

Table 7.3. Geometric properties of the CAIs identified within the Paris meteorite.

#	Area (μm^2)	Major (μm)	Minor (μm)	Perimeter (μm)	Circularity (0-1)	Aspect Ratio	Roundness (0-1)	Solidity (0-1)
1	1000	61	25	153	0.64	2.46	0.41	0.91
2	393	42	12	94	0.56	3.50	0.29	0.87
3	207	18	15	52	0.97	1.23	0.82	0.91
4	57	10	7	25	1.00	1.37	0.73	0.96
5	72	13	7	30	0.99	1.70	0.59	0.85
6	14000	164	105	548	0.57	1.56	0.64	0.87
7	233	22	13	58	0.87	1.68	0.60	0.92
8	31	8	5	17	1.00	1.50	0.67	1.00
9	1000	44	30	129	0.79	1.44	0.70	0.88
10	140	14	13	41	1.00	1.09	0.92	0.89
11	605	31	25	94	0.87	1.21	0.83	0.90
12	466	30	20	81	0.88	1.49	0.67	0.91
13	683	41	21	113	0.67	1.91	0.52	0.83
14	140	18	10	46	0.84	1.83	0.55	0.83
15	129	14	12	39	1.00	1.21	0.83	0.93
16	4000	109	49	333	0.47	2.24	0.45	0.82
17	155	16	13	48	0.86	1.24	0.80	0.81
18	62	10	8	27	1.00	1.33	0.75	1.00
19	135	14	12	43	0.93	1.23	0.82	0.87
20	1000	58	25	143	0.68	2.35	0.43	0.89
21	5000	89	66	317	0.57	1.35	0.74	0.85
22	652	38	22	134	0.46	1.72	0.58	0.74
23	104	13	10	36	1.00	1.25	0.80	1.00
24	254	24	14	63	0.80	1.74	0.57	0.83
25	78	11	9	30	1.00	1.13	0.89	0.86
26	864	42	26	116	0.80	1.63	0.61	0.88
27	98	12	11	37	0.92	1.12	0.89	0.81
28	450	37	15	91	0.69	2.43	0.41	0.91
29	62	10	8	27	1.00	1.33	0.75	1.00
30	492	32	19	84	0.87	1.68	0.60	0.95
31	580	44	17	105	0.66	2.58	0.39	0.86
32	192	18	13	51	0.93	1.38	0.73	0.86
33	11000	158	92	516	0.54	1.71	0.59	0.82
34	1000	49	27	135	0.73	1.80	0.56	0.89
35	316	27	15	68	0.86	1.75	0.57	0.87
36	311	26	15	70	0.80	1.72	0.58	0.90
37	171	18	12	52	0.79	1.47	0.68	0.84
38	2000	50	42	154	0.87	1.20	0.83	0.91
39	295	22	17	63	0.93	1.34	0.75	0.87
40	549	31	22	100	0.69	1.40	0.72	0.79

#	Area (μm^2)	Major (µm)	Minor (µm)	Perimeter (µm)	Circularity (0-1)	Aspect Ratio	Roundness (0-1)	Solidity (0-1)
41	2000	65	46	199	0.74	1.43	0.70	0.87
42	2000	55	37	189	0.57	1.49	0.67	0.81
43	62000	382	206	1377	0.41	1.85	0.54	0.84
44	274	20	18	75	0.62	1.13	0.89	0.79
45	186	19	12	52	0.88	1.59	0.63	0.89
46	83	14	7	33	0.96	1.93	0.52	0.94
47	1000	54	30	156	0.66	1.81	0.55	0.82
48	109	15	9	39	0.91	1.68	0.60	0.93
49	62	10	8	28	0.97	1.18	0.85	0.86
50	62	12	7	28	0.97	1.76	0.57	0.89
51	2000	83	35	206	0.69	2.33	0.43	0.91
52	109	16	9	39	0.88	1.77	0.57	0.86
53	41	8	7	21	1.00	1.23	0.81	0.94
54	119	15	10	39	0.99	1.50	0.67	0.98
55	7000	108	85	370	0.66	1.27	0.79	0.92
56	145	15	12	43	0.97	1.21	0.83	0.97
57	176	16	14	50	0.87	1.13	0.88	0.86
58	838	42	25	131	0.62	1.67	0.60	0.81
59	704	37	24	101	0.87	1.53	0.66	0.92
60	3000	84	51	265	0.61	1.63	0.61	0.85
61	1000	45	34	147	0.70	1.33	0.75	0.86
62	6000	103	73	307	0.79	1.41	0.71	0.93
63	388	31	16	81	0.75	1.91	0.53	0.81
64	41	8	7	21	1.00	1.23	0.81	0.94
65	1000	60	27	175	0.53	2.24	0.45	0.83
66	637	35	23	101	0.79	1.48	0.68	0.86
67	2000	56	39	171	0.74	1.46	0.69	0.86
68	119	19	8	44	0.78	2.36	0.42	0.87
69	160	19	11	47	0.91	1.79	0.56	0.90
70	2000	65	39	212	0.56	1.65	0.61	0.81
71	16000	185	112	760	0.36	1.65	0.61	0.75
72	590	35	21	101	0.73	1.65	0.61	0.85
73	745	38	25	114	0.73	1.53	0.65	0.85
74	668	35	24	127	0.52	1.47	0.68	0.79
75	3000	82	41	327	0.31	2.01	0.50	0.68
76	52	10	7	24	1.00	1.55	0.65	0.91
77	72	11	8	28	1.00	1.32	0.76	0.93
78	254	23	14	61	0.86	1.67	0.60	0.93
79	104	17	8	39	0.86	2.30	0.44	0.98
80	119	17	9	41	0.88	1.99	0.50	0.84
81	890	40	29	121	0.77	1.39	0.72	0.87

#	Area (μm^2)	Major (µm)	Minor (µm)	Perimeter (µm)	Circularity (0-1)	Aspect Ratio	Roundness (0-1)	Solidity (0-1)
82	47	8	8	22	1.00	1.00	1.00	1.00
83	574	30	25	95	0.80	1.21	0.83	0.91
84	3000	73	47	237	0.61	1.57	0.64	0.86
85	233	19	15	55	0.95	1.24	0.81	0.88
86	802	47	22	122	0.68	2.17	0.46	0.85
87	3000	77	43	223	0.66	1.78	0.56	0.87
88	223	25	11	59	0.79	2.15	0.47	0.88
89	1000	61	30	163	0.69	2.03	0.49	0.86
90	285	23	16	70	0.73	1.50	0.67	0.79
91	543	29	24	96	0.74	1.20	0.84	0.86
92	119	15	10	38	1.00	1.47	0.68	0.90
93	6000	145	53	445	0.39	2.74	0.37	0.77
94	5000	99	66	380	0.44	1.51	0.66	0.86
95	119	15	10	39	0.96	1.49	0.67	0.89
96	1000	43	37	157	0.65	1.16	0.86	0.86
97	135	17	10	42	0.96	1.73	0.58	0.96
98	2000	58	36	183	0.62	1.63	0.62	0.86
99	52	10	7	24	1.00	1.38	0.72	0.91
100	114	13	11	40	0.90	1.25	0.80	0.83
101	605	33	24	94	0.86	1.38	0.73	0.88
102	471	27	22	83	0.85	1.23	0.82	0.90
103	140	14	13	41	1.00	1.05	0.95	0.87
104	564	28	26	90	0.87	1.06	0.94	0.88
105	41	8	7	21	1.00	1.23	0.81	0.94
106	207	21	13	55	0.86	1.62	0.62	0.88
107	533	32	22	94	0.77	1.46	0.68	0.86
108	2000	64	37	171	0.80	1.71	0.59	0.91
109	114	15	10	39	0.95	1.57	0.64	0.96
110	119	18	8	43	0.82	2.11	0.48	0.85
111	88	12	9	32	1.00	1.26	0.79	0.92
112	626	46	17	115	0.59	2.71	0.37	0.85
113	83	11	9	30	1.00	1.21	0.83	0.89
114	6000	119	68	376	0.57	1.74	0.57	0.83
115	119	15	10	39	0.99	1.50	0.67	0.98
116	1000	41	32	130	0.76	1.27	0.79	0.87
117	5000	95	64	323	0.58	1.49	0.67	0.83
118	72	11	9	30	1.00	1.24	0.81	0.93
119	197	18	14	50	0.97	1.33	0.75	0.91
120	212	20	14	54	0.93	1.48	0.68	0.88
121	186	19	13	52	0.86	1.51	0.66	0.84
122	321	36	11	82	0.60	3.13	0.32	0.81

#	Area (μm^2)	Major (μm)	Minor (μm)	Perimeter (μm)	Circularity (0-1)	Aspect Ratio	Roundness (0-1)	Solidity (0-1)
123	766	39	25	127	0.59	1.56	0.64	0.81
124	849	41	27	114	0.82	1.54	0.65	0.91
125	83	12	9	32	1.00	1.31	0.76	0.91
126	466	28	21	81	0.88	1.37	0.73	0.93
127	2000	52	38	152	0.84	1.40	0.72	0.93
128	202	19	14	52	0.95	1.41	0.71	0.91
129	243	23	13	58	0.90	1.74	0.58	0.90
130	8000	125	83	489	0.43	1.50	0.67	0.79
131	1000	47	31	151	0.63	1.54	0.65	0.82
132	9000	117	103	516	0.45	1.14	0.88	0.78
133	238	22	14	58	0.89	1.65	0.61	0.89
134	31	8	5	17	1.00	1.50	0.67	1.00
135	554	35	20	90	0.86	1.71	0.59	0.92
136	2000	69	33	202	0.55	2.08	0.48	0.79
137	155	17	12	46	0.93	1.47	0.68	0.85
138	57	9	8	27	0.98	1.22	0.82	0.82
139	1000	49	32	137	0.82	1.55	0.65	0.92
140	2000	51	44	181	0.66	1.16	0.86	0.83
141	160	17	12	45	0.98	1.44	0.69	0.94
142	1000	52	34	171	0.60	1.52	0.66	0.82
143	248	22	14	58	0.92	1.55	0.65	0.91
144	7000	110	85	348	0.76	1.30	0.77	0.91
145	114	14	10	37	1.00	1.36	0.74	0.88
146	192	18	14	49	1.00	1.32	0.76	0.89
147	4000	82	66	281	0.67	1.24	0.80	0.87
148	4000	112	41	353	0.36	2.75	0.36	0.80
149	300	27	14	67	0.83	1.94	0.52	0.91
150	3000	86	46	249	0.64	1.86	0.54	0.87
151	279	22	16	66	0.80	1.42	0.70	0.84
152	1000	62	27	172	0.55	2.32	0.43	0.79
153	311	23	17	63	0.98	1.36	0.74	0.90
154	1000	59	28	158	0.64	2.11	0.47	0.86
155	2000	56	50	197	0.71	1.13	0.89	0.87
156	963	46	26	131	0.70	1.75	0.57	0.85
157	424	35	16	86	0.73	2.24	0.45	0.84
158	642	35	24	119	0.57	1.47	0.68	0.80
159	430	31	18	81	0.81	1.75	0.57	0.89
160	486	29	21	81	0.94	1.38	0.73	0.90
161	1000	46	29	144	0.63	1.62	0.62	0.84
162	761	33	29	106	0.85	1.16	0.87	0.91
163	2000	61	42	218	0.54	1.44	0.69	0.81

#	Area (μm^2)	Major (µm)	Minor (µm)	Perimeter (µm)	Circularity (0-1)	Aspect Ratio	Roundness (0-1)	Solidity (0-1)
164	254	20	16	59	0.90	1.20	0.83	0.90
165	947	53	23	139	0.62	2.37	0.42	0.84
166	600	36	21	94	0.85	1.68	0.60	0.90
167	109	12	12	35	1.00	1.00	1.00	0.91
168	590	33	23	99	0.75	1.47	0.68	0.83
169	1000	47	33	135	0.85	1.42	0.71	0.90
170	186	18	13	50	0.94	1.43	0.70	0.94
171	414	37	14	109	0.44	2.58	0.39	0.70
172	15000	272	72	682	0.42	3.76	0.27	0.79
173	331	24	18	78	0.68	1.37	0.73	0.82
174	802	42	24	123	0.67	1.72	0.58	0.85
175	1000	39	34	134	0.73	1.13	0.88	0.89
176	642	37	22	99	0.82	1.66	0.60	0.88
177	424	26	21	76	0.92	1.21	0.82	0.93
178	621	37	21	101	0.77	1.74	0.57	0.86
179	155	17	12	43	1.00	1.41	0.71	0.92
180	518	32	21	91	0.78	1.52	0.66	0.86
181	166	19	11	49	0.87	1.65	0.61	0.85
182	140	18	10	47	0.79	1.75	0.57	0.82
183	104	14	9	38	0.93	1.59	0.63	0.91
184	3000	69	60	225	0.80	1.14	0.88	0.91
185	83	14	8	33	0.96	1.87	0.53	0.94
186	176	17	13	48	0.94	1.25	0.80	0.91
187	1000	56	27	151	0.66	2.05	0.49	0.84
188	62	9	9	26	1.00	1.00	1.00	0.86
189	336	25	17	72	0.82	1.44	0.69	0.88
190	4000	81	56	274	0.59	1.45	0.69	0.81
191	166	18	12	47	0.94	1.51	0.66	0.89
192	2000	58	45	175	0.85	1.28	0.78	0.93
193	336	22	19	67	0.94	1.18	0.85	0.92
194	357	31	15	78	0.74	2.13	0.47	0.81
195	357	24	19	69	0.94	1.31	0.77	0.90
196	243	20	15	61	0.81	1.32	0.76	0.86
197	1000	49	30	145	0.68	1.66	0.60	0.85
198	792	43	23	113	0.78	1.87	0.54	0.91
199	207	22	12	73	0.49	1.78	0.56	0.74
200	492	26	24	85	0.86	1.11	0.90	0.91
201	67	10	9	28	1.00	1.15	0.87	0.90
202	4000	75	64	253	0.75	1.17	0.86	0.88
203	22000	208	135	961	0.30	1.54	0.65	0.74
204	228	20	15	68	0.62	1.37	0.73	0.77

#	Area (μm^2)	Major (µm)	Minor (µm)	Perimeter (µm)	Circularity (0-1)	Aspect Ratio	Roundness (0-1)	Solidity (0-1)
205	248	21	15	57	0.97	1.43	0.70	0.90
206	1000	52	27	154	0.59	1.89	0.53	0.80
207	5000	89	71	314	0.63	1.26	0.79	0.88
208	29000	226	163	821	0.54	1.39	0.72	0.85
209	2000	47	40	147	0.88	1.18	0.85	0.92
210	1000	53	32	148	0.75	1.67	0.60	0.88
211	362	30	15	82	0.68	2.00	0.50	0.82
212	171	19	12	48	0.91	1.61	0.62	0.92
213	124	17	9	48	0.66	1.84	0.54	0.79
214	8000	108	91	395	0.62	1.20	0.84	0.88
215	926	43	27	119	0.82	1.59	0.63	0.91
216	393	35	14	84	0.70	2.43	0.41	0.88
217	2000	65	44	197	0.72	1.49	0.67	0.89
218	714	36	25	135	0.49	1.43	0.70	0.81
219	342	26	17	70	0.87	1.55	0.65	0.89
220	93	12	10	33	1.00	1.25	0.80	0.95
221	295	21	18	64	0.91	1.14	0.88	0.87
222	93	12	10	34	1.00	1.25	0.80	0.95
223	171	18	12	47	0.97	1.52	0.66	0.92
224	171	21	10	50	0.85	2.04	0.49	0.86
225	1000	46	30	126	0.86	1.50	0.67	0.92
226	2000	53	41	228	0.41	1.28	0.78	0.77
227	2000	59	42	196	0.64	1.41	0.71	0.86
228	4000	88	53	332	0.42	1.66	0.60	0.71
229	5000	94	61	336	0.50	1.53	0.65	0.82
230	2000	58	51	267	0.41	1.14	0.87	0.69
231	274	38	9	83	0.51	4.06	0.25	0.74
232	155	16	12	45	0.95	1.38	0.73	0.92
233	2000	55	36	170	0.67	1.53	0.65	0.85
234	3000	67	50	208	0.76	1.34	0.74	0.88
235	52	10	7	24	1.00	1.38	0.72	0.91
236	192	21	11	55	0.78	1.89	0.53	0.81
237	98	13	10	35	1.00	1.38	0.73	0.88
238	109	14	10	36	1.00	1.40	0.71	0.93
239	228	25	12	62	0.75	2.11	0.48	0.80
240	693	37	24	101	0.85	1.54	0.65	0.92
241	104	13	10	36	1.00	1.25	0.80	1.00
242	10000	140	90	453	0.61	1.55	0.65	0.86
243	4000	120	44	395	0.33	2.75	0.36	0.73
244	7000	165	53	632	0.22	3.11	0.32	0.72
245	424	40	14	89	0.68	2.93	0.34	0.92

#	Area (μm^2)	Major (µm)	Minor (µm)	Perimeter (µm)	Circularity (0-1)	Aspect Ratio	Roundness (0-1)	Solidity (0-1)
246	129	14	12	39	1.00	1.15	0.87	0.91
247	20000	216	120	705	0.52	1.79	0.56	0.84
248	455	28	21	82	0.85	1.31	0.77	0.88
249	357	29	16	79	0.71	1.85	0.54	0.82
250	393	35	14	87	0.66	2.50	0.40	0.81
251	761	47	21	125	0.61	2.25	0.44	0.80
252	1000	53	36	194	0.49	1.47	0.68	0.75
253	124	15	11	39	1.00	1.38	0.72	0.91
254	1000	54	35	155	0.78	1.57	0.64	0.92
255	11000	143	98	528	0.50	1.47	0.68	0.81
256	83	12	9	32	1.00	1.45	0.69	0.82
257	233	22	13	59	0.85	1.70	0.59	0.85
258	430	27	20	78	0.88	1.32	0.76	0.91
259	124	17	9	43	0.86	1.77	0.57	0.87
260	78	12	8	30	1.00	1.44	0.70	0.88
261	564	36	20	103	0.66	1.84	0.54	0.80
262	62	11	7	28	0.97	1.48	0.68	0.86
263	2000	56	41	200	0.57	1.37	0.73	0.81
264	4000	90	59	267	0.73	1.52	0.66	0.90
265	342	27	16	90	0.53	1.66	0.60	0.75
266	217	26	11	63	0.68	2.38	0.42	0.83
267	88	14	8	35	0.91	1.66	0.60	0.85
268	41000	364	145	1304	0.31	2.52	0.40	0.73
269	166	18	12	49	0.87	1.53	0.66	0.82
270	202	22	12	58	0.75	1.85	0.54	0.81
271	4000	105	44	347	0.38	2.38	0.42	0.73
272	3000	70	52	216	0.77	1.34	0.75	0.91
273	98	12	10	34	1.00	1.16	0.86	0.88
274	233	21	14	58	0.88	1.56	0.64	0.92
275	347	24	19	69	0.93	1.29	0.78	0.94
276	109	14	10	38	0.97	1.51	0.66	0.93
277	2000	85	37	251	0.49	2.32	0.43	0.78
278	124	16	10	41	0.94	1.59	0.63	0.91
279	279	27	13	68	0.76	2.03	0.49	0.85
280	916	45	26	127	0.72	1.73	0.58	0.88
281	186	20	12	48	1.00	1.61	0.62	0.95
282	1000	49	29	151	0.62	1.65	0.61	0.83
283	114	14	10	39	0.92	1.42	0.70	0.86
284	7000	164	54	457	0.42	3.05	0.33	0.78
285	254	22	14	61	0.87	1.55	0.64	0.85
286	150	14	13	44	0.98	1.07	0.94	0.91

#	Area (μm^2)	Major (μm)	Minor (μm)	Perimeter (μm)	Circularity (0-1)	Aspect Ratio	Roundness (0-1)	Solidity (0-1)
287	14000	218	80	618	0.45	2.73	0.37	0.80
288	5000	109	56	328	0.56	1.95	0.51	0.84
289	880	61	18	152	0.48	3.29	0.30	0.75
290	254	20	16	62	0.83	1.30	0.77	0.85
291	668	44	20	109	0.71	2.23	0.45	0.86
292	254	20	16	58	0.94	1.25	0.80	0.92
293	414	25	21	74	0.94	1.17	0.85	0.90
294	145	18	10	44	0.92	1.75	0.57	0.85
295	98	13	10	37	0.92	1.37	0.73	0.81
296	155	15	13	44	1.00	1.10	0.91	0.92
297	104	14	9	36	0.99	1.46	0.68	0.91
298	642	38	21	102	0.77	1.79	0.56	0.87
299	171	16	13	47	0.97	1.21	0.83	0.89
300	98	14	9	35	1.00	1.50	0.67	0.91
301	238	23	13	63	0.75	1.80	0.55	0.87
302	911	50	23	127	0.71	2.20	0.46	0.88
303	683	36	24	102	0.82	1.47	0.68	0.88
304	207	20	13	52	0.95	1.50	0.67	0.88
305	295	24	16	65	0.87	1.48	0.68	0.91
306	5000	88	68	324	0.56	1.30	0.77	0.79
307	129	14	11	41	0.98	1.27	0.79	0.93
308	828	36	30	117	0.76	1.21	0.83	0.86
309	683	44	20	119	0.60	2.23	0.45	0.79
310	574	35	21	93	0.84	1.69	0.59	0.91
311	166	18	11	48	0.89	1.61	0.62	0.93
312	781	38	26	108	0.85	1.49	0.67	0.88
313	129	18	9	44	0.84	1.97	0.51	0.91
314	1000	44	33	129	0.86	1.34	0.75	0.92
315	109	14	10	38	0.97	1.33	0.75	0.91
316	12000	136	112	662	0.34	1.22	0.82	0.80
317	83	11	9	30	1.00	1.21	0.83	0.89
318	171	25	9	56	0.68	2.77	0.36	0.85
319	29000	244	154	1204	0.26	1.59	0.63	0.74
320	238	29	10	64	0.74	2.78	0.36	0.86
321	435	33	17	99	0.56	1.92	0.52	0.76
322	678	56	15	129	0.51	3.66	0.27	0.85
323	4000	97	48	265	0.66	2.01	0.50	0.88
324	476	32	19	91	0.72	1.73	0.58	0.87
325	600	33	24	93	0.87	1.38	0.72	0.90
326	900	44	26	144	0.55	1.67	0.60	0.74
327	52	9	7	24	1.00	1.33	0.75	0.91

#	Area (μm^2)	Major (µm)	Minor (µm)	Perimeter (µm)	Circularity (0-1)	Aspect Ratio	Roundness (0-1)	Solidity (0-1)
328	207	26	10	64	0.64	2.62	0.38	0.85
329	197	19	13	52	0.92	1.51	0.66	0.92
330	528	28	24	86	0.90	1.20	0.83	0.90
331	166	16	13	46	0.99	1.18	0.85	0.91
332	3000	75	47	262	0.51	1.60	0.63	0.78
333	2000	66	34	188	0.63	1.93	0.52	0.83
334	135	19	9	44	0.88	2.04	0.49	0.91
335	124	19	8	44	0.81	2.19	0.46	0.89
336	155	18	11	50	0.77	1.70	0.59	0.79
337	129	15	11	40	1.00	1.33	0.75	0.86
338	2000	67	32	185	0.62	2.12	0.47	0.86
339	295	22	17	66	0.85	1.35	0.74	0.90
340	47	8	8	22	1.00	1.00	1.00	1.00
341	3000	80	48	251	0.61	1.68	0.60	0.86
342	88	12	9	35	0.91	1.30	0.77	0.85
343	569	31	23	102	0.69	1.37	0.73	0.83
344	590	36	21	112	0.59	1.75	0.57	0.79
345	88	13	8	36	0.85	1.59	0.63	0.83
346	223	27	11	68	0.61	2.56	0.39	0.74
347	119	19	8	46	0.71	2.40	0.42	0.74
348	109	14	10	36	1.00	1.48	0.68	0.93
349	36	9	5	19	1.00	1.60	0.63	0.88
350	243	30	10	67	0.68	2.96	0.34	0.83
351	2000	74	38	199	0.69	1.97	0.51	0.87
352	2000	74	38	244	0.47	1.93	0.52	0.79
353	72	13	7	32	0.91	1.86	0.54	0.85
354	6000	103	71	540	0.25	1.45	0.69	0.70
355	62	10	8	27	1.00	1.28	0.78	0.86
356	316	27	15	68	0.86	1.76	0.57	0.87
357	181	18	13	47	1.00	1.33	0.75	0.92
358	507	33	20	111	0.52	1.67	0.60	0.76
359	62	10	8	27	1.00	1.33	0.75	1.00
360	88	13	8	36	0.85	1.59	0.63	0.85
361	471	26	23	92	0.69	1.14	0.88	0.88
362	192	25	10	68	0.52	2.56	0.39	0.71
363	331	23	19	67	0.92	1.23	0.82	0.91
364	336	23	19	67	0.94	1.24	0.81	0.91
365	771	41	24	136	0.53	1.74	0.58	0.76
366	668	38	23	99	0.85	1.68	0.60	0.89
367	119	15	10	39	0.99	1.50	0.67	0.98
368	1000	48	36	168	0.61	1.33	0.75	0.79

#	Area (μm^2)	Major (µm)	Minor (µm)	Perimeter (µm)	Circularity (0-1)	Aspect Ratio	Roundness (0-1)	Solidity (0-1)
369	217	22	12	56	0.88	1.81	0.55	0.97
370	140	18	10	43	0.93	1.74	0.57	0.98
371	3000	109	32	275	0.46	3.35	0.30	0.86
372	595	36	21	96	0.81	1.73	0.58	0.88
373	580	35	21	102	0.71	1.69	0.59	0.82
374	181	18	13	50	0.90	1.44	0.70	0.88
375	129	13	12	41	0.95	1.08	0.92	0.83
376	378	28	17	74	0.86	1.60	0.63	0.89
377	72	12	7	30	1.00	1.66	0.60	0.97
378	6000	111	71	435	0.41	1.58	0.63	0.71
379	704	42	21	111	0.72	1.96	0.51	0.84
380	942	44	27	133	0.67	1.60	0.63	0.85
381	3000	85	48	320	0.40	1.77	0.57	0.74
382	1000	56	34	159	0.74	1.68	0.60	0.88
383	300	22	17	63	0.94	1.27	0.79	0.89
384	104	13	10	35	1.00	1.20	0.83	0.85
385	823	48	22	122	0.69	2.16	0.46	0.82
386	295	28	14	74	0.68	2.05	0.49	0.78
387	41	9	6	24	0.91	1.44	0.70	0.84
388	264	26	13	68	0.72	2.05	0.49	0.81
389	207	20	13	55	0.85	1.57	0.64	0.85
390	104	14	9	36	0.99	1.49	0.67	0.93
391	88	12	9	32	1.00	1.26	0.79	0.92
392	21	5	5	13	1.00	1.00	1.00	1.00
393	440	32	18	90	0.69	1.77	0.56	0.81
394	71000	574	157	2937	0.10	3.65	0.27	0.59
395	657	31	27	105	0.75	1.13	0.89	0.87
396	1000	60	30	169	0.62	2.01	0.50	0.84
397	378	33	15	80	0.75	2.23	0.45	0.89
398	419	28	19	90	0.65	1.50	0.67	0.78
399	83	10	10	31	1.00	1.00	1.00	1.00
400	430	28	19	82	0.80	1.48	0.68	0.88
401	171	16	14	47	0.99	1.18	0.85	0.97
402	1000	40	32	149	0.58	1.24	0.81	0.83
403	21	5	5	13	1.00	1.00	1.00	1.00
404	631	32	25	92	0.93	1.27	0.79	0.94
405	83	12	9	32	1.00	1.26	0.79	0.89
406	52	9	7	24	1.00	1.33	0.75	0.91
407	31	8	5	17	1.00	1.50	0.67	1.00
408	290	26	14	68	0.79	1.88	0.53	0.82
409	88	15	8	34	0.94	1.98	0.51	0.97

#	Area (μm^2)	Major (μm)	Minor (μm)	Perimeter (μm)	Circularity (0-1)	Aspect Ratio	Roundness (0-1)	Solidity (0-1)
410	3000	65	58	256	0.56	1.12	0.89	0.83
411	2000	52	40	170	0.72	1.29	0.78	0.87
412	2000	69	30	193	0.56	2.28	0.44	0.80
413	124	17	9	43	0.86	1.94	0.52	0.84
414	523	39	17	111	0.53	2.23	0.45	0.75
415	124	13	12	39	1.00	1.11	0.90	0.91
416	109	12	12	36	1.00	1.03	0.97	0.91
417	678	39	22	111	0.69	1.80	0.56	0.84
418	450	27	21	89	0.71	1.25	0.80	0.80
419	88	12	9	32	1.00	1.26	0.79	0.92
420	26000	269	125	1256	0.21	2.16	0.46	0.69
421	52	10	7	24	1.00	1.55	0.65	0.91
422	1000	47	33	154	0.66	1.41	0.71	0.83
423	98	12	10	36	0.94	1.15	0.87	0.86
424	983	47	27	130	0.73	1.78	0.56	0.91
425	135	15	11	41	0.99	1.33	0.76	0.87
426	140	15	12	41	1.00	1.28	0.78	0.90
427	574	33	22	99	0.73	1.51	0.66	0.83
428	83	12	9	32	1.00	1.26	0.79	0.89
429	135	18	9	44	0.85	1.97	0.51	0.85
430	166	15	14	44	1.00	1.03	0.97	0.94
431	197	18	14	58	0.73	1.31	0.77	0.83
432	1000	47	32	145	0.70	1.48	0.68	0.85
433	311	26	15	71	0.77	1.76	0.57	0.81
434	166	20	11	49	0.87	1.83	0.55	0.87
435	67	12	7	30	0.96	1.80	0.56	0.93
436	145	15	12	42	1.00	1.20	0.83	0.97
437	6000	112	73	332	0.73	1.54	0.65	0.92
438	2000	76	40	262	0.44	1.90	0.53	0.78
439	171	22	10	55	0.71	2.16	0.46	0.86
440	792	47	21	122	0.67	2.21	0.45	0.87
441	3000	76	51	263	0.55	1.48	0.68	0.80
442	10000	144	86	459	0.58	1.67	0.60	0.85
443	93	13	9	33	1.00	1.36	0.73	0.95
444	150	21	9	49	0.78	2.31	0.43	0.82
445	248	23	14	59	0.88	1.66	0.60	0.91
446	83	12	9	32	1.00	1.29	0.77	0.89
447	492	28	22	87	0.83	1.29	0.78	0.86
448	1000	81	18	234	0.26	4.44	0.23	0.64
449	1000	54	27	158	0.58	1.96	0.51	0.80
450	4000	81	60	358	0.37	1.36	0.74	0.80

#	Area (μm^2)	Major (µm)	Minor (µm)	Perimeter (µm)	Circularity (0-1)	Aspect Ratio	Roundness (0-1)	Solidity (0-1)
451	62	10	8	27	1.00	1.33	0.75	1.00
452	207	21	12	54	0.88	1.71	0.59	0.95
453	129	17	10	43	0.90	1.79	0.56	0.86
454	1000	49	37	156	0.74	1.31	0.76	0.91
455	12000	163	91	515	0.55	1.80	0.56	0.85
456	2000	69	39	183	0.79	1.79	0.56	0.91
457	290	25	15	70	0.73	1.66	0.60	0.84
458	207	20	13	57	0.81	1.51	0.66	0.82
459	1000	48	31	144	0.72	1.53	0.65	0.83
460	367	35	13	95	0.51	2.63	0.38	0.73
461	1000	53	35	212	0.41	1.53	0.65	0.72
462	140	17	10	44	0.91	1.67	0.60	0.89
463	9000	158	71	450	0.55	2.23	0.45	0.83
464	2000	86	29	220	0.51	2.92	0.34	0.80
465	6000	117	66	389	0.50	1.78	0.56	0.83
466	3000	74	52	268	0.53	1.42	0.71	0.85
467	1000	48	35	156	0.67	1.39	0.72	0.86
468	559	43	17	109	0.59	2.59	0.39	0.86
469	238	21	15	55	0.97	1.42	0.70	0.88
470	14000	171	108	606	0.50	1.58	0.63	0.85
471	155	18	11	49	0.81	1.63	0.61	0.79
472	1000	52	26	162	0.52	2.01	0.50	0.79
473	88	12	9	32	1.00	1.26	0.79	0.92
474	2000	50	46	180	0.70	1.08	0.93	0.88
475	326	28	15	74	0.76	1.93	0.52	0.85
476	181	19	12	50	0.90	1.56	0.64	0.86
477	23000	245	119	826	0.42	2.06	0.49	0.79
478	93	14	9	35	0.97	1.62	0.62	0.86
479	155	22	9	52	0.73	2.47	0.41	0.81
480	1000	50	38	148	0.86	1.32	0.76	0.93
481	119	15	10	43	0.82	1.57	0.64	0.81
482	41	8	7	21	1.00	1.23	0.81	0.94
483	305	24	16	65	0.92	1.49	0.67	0.89
484	4000	78	58	320	0.44	1.34	0.74	0.76
485	1000	49	28	147	0.63	1.77	0.56	0.81
486	119	20	8	44	0.78	2.56	0.39	0.84
487	197	25	10	56	0.80	2.46	0.41	0.97
488	559	36	20	110	0.58	1.78	0.56	0.82
489	719	47	19	156	0.37	2.42	0.41	0.70
490	331	27	16	76	0.73	1.74	0.58	0.79
491	1000	43	32	131	0.79	1.33	0.75	0.88

#	Area (μm^2)	Major (µm)	Minor (µm)	Perimeter (µm)	Circularity (0-1)	Aspect Ratio	Roundness (0-1)	Solidity (0-1)
492	207	18	15	53	0.93	1.25	0.80	0.92
493	2000	91	33	277	0.38	2.77	0.36	0.74
494	202	25	10	59	0.72	2.50	0.40	0.84
495	756	35	27	111	0.77	1.30	0.77	0.88
496	921	44	26	117	0.85	1.68	0.60	0.93
497	590	34	22	92	0.87	1.54	0.65	0.91
498	533	34	20	94	0.75	1.69	0.59	0.86
499	2000	71	34	276	0.31	2.10	0.48	0.66
500	502	30	21	96	0.68	1.39	0.72	0.80
501	119	17	9	42	0.85	1.97	0.51	0.92
502	57	10	7	25	1.00	1.37	0.73	0.96
503	533	29	23	92	0.79	1.28	0.78	0.85
504	963	36	34	119	0.85	1.04	0.96	0.89
505	72	13	7	30	0.99	1.88	0.53	0.85
506	166	17	13	47	0.94	1.32	0.76	0.88
507	233	19	15	55	0.95	1.26	0.79	0.88
508	533	37	18	105	0.60	2.00	0.50	0.78
509	1000	66	19	165	0.47	3.41	0.29	0.74
510	409	23	22	77	0.86	1.06	0.95	0.84
511	31	8	5	17	1.00	1.50	0.67	1.00
512	47	8	8	22	1.00	1.00	1.00	1.00
513	1000	60	22	140	0.67	2.67	0.38	0.87
514	528	42	16	105	0.60	2.58	0.39	0.85
515	259	19	18	63	0.83	1.07	0.93	0.86
516	119	13	12	39	0.96	1.14	0.88	0.87
517	93	12	10	37	0.87	1.25	0.80	0.77
518	186	20	12	54	0.82	1.66	0.60	0.87
519	21	5	5	13	1.00	1.00	1.00	1.00
520	78	11	9	30	1.00	1.14	0.88	0.97
521	57	10	7	25	1.00	1.37	0.73	0.96
522	2000	59	38	185	0.64	1.58	0.64	0.85
523	2000	79	38	227	0.57	2.07	0.48	0.84
524	212	21	13	58	0.80	1.70	0.59	0.87
525	414	30	17	88	0.67	1.74	0.57	0.81
526	3000	133	31	314	0.42	4.24	0.24	0.88
527	21	5	5	13	1.00	1.00	1.00	1.00
528	248	19	16	59	0.91	1.17	0.86	0.87
529	47	8	8	22	1.00	1.00	1.00	1.00
530	202	17	15	50	1.00	1.17	0.85	0.96
531	900	43	27	120	0.79	1.62	0.62	0.88
532	88	13	9	34	0.94	1.48	0.67	0.92

#	Area (μm^2)	Major (μm)	Minor (μm)	Perimeter (μm)	Circularity (0-1)	Aspect Ratio	Roundness (0-1)	Solidity (0-1)
533	181	27	9	70	0.47	3.17	0.32	0.67
534	52	9	7	24	1.00	1.33	0.75	0.91
535	72	11	8	28	1.00	1.32	0.76	0.93
536	404	23	22	76	0.89	1.03	0.97	0.87
537	285	27	13	69	0.76	2.05	0.49	0.88
538	41	10	5	22	1.00	2.00	0.50	1.00
539	72	10	10	28	1.00	1.02	0.98	0.93
540	83	12	9	32	1.00	1.39	0.72	0.89
541	83	14	7	33	0.96	1.93	0.52	0.94
542	62	10	8	27	1.00	1.33	0.75	1.00
543	11000	159	91	518	0.53	1.75	0.57	0.84
544	217	18	15	55	0.91	1.22	0.82	0.89
545	647	40	20	107	0.72	1.97	0.51	0.87
546	802	38	27	132	0.58	1.39	0.72	0.81
547	393	25	20	81	0.76	1.25	0.80	0.80
548	109	15	9	38	0.94	1.57	0.64	0.88
549	114	15	10	38	0.99	1.58	0.63	0.88
550	300	24	16	70	0.76	1.55	0.65	0.87
551	114	15	10	38	1.00	1.54	0.65	0.96
552	595	32	24	94	0.84	1.32	0.76	0.91
553	7000	116	74	433	0.45	1.56	0.64	0.79
554	52	9	7	25	1.00	1.24	0.81	0.91
555	22000	182	153	725	0.52	1.19	0.84	0.86
556	1000	50	28	133	0.80	1.76	0.57	0.91
557	461	28	21	84	0.82	1.30	0.77	0.85
558	171	18	12	50	0.87	1.54	0.65	0.92
559	114	13	12	38	1.00	1.08	0.92	0.94
560	233	18	17	58	0.88	1.09	0.92	0.91
561	238	22	14	63	0.75	1.58	0.63	0.77
562	114	14	11	37	1.00	1.29	0.77	0.86
563	176	17	13	50	0.87	1.34	0.75	0.83
564	223	20	14	60	0.78	1.47	0.68	0.86
565	52	9	7	24	1.00	1.33	0.75	0.91
566	109	15	9	38	0.97	1.54	0.65	0.96
567	192	24	10	63	0.60	2.35	0.43	0.80
568	171	19	12	52	0.80	1.64	0.61	0.85
569	497	30	21	87	0.83	1.40	0.72	0.87
570	4000	93	49	259	0.68	1.89	0.53	0.92
571	611	38	21	98	0.80	1.85	0.54	0.87
572	83	13	8	33	0.96	1.52	0.66	0.91
573	78	12	8	30	1.00	1.39	0.72	0.88

#	Area (μm^2)	Major (µm)	Minor (µm)	Perimeter (µm)	Circularity (0-1)	Aspect Ratio	Roundness (0-1)	Solidity (0-1)
574	2000	62	44	242	0.46	1.43	0.70	0.73
575	212	30	9	66	0.61	3.41	0.29	0.92
576	2000	62	41	178	0.79	1.53	0.65	0.89
577	62	10	8	27	1.00	1.28	0.78	0.86
578	554	31	23	91	0.84	1.35	0.74	0.86
579	41	9	6	23	1.00	1.55	0.64	0.80
580	2000	67	38	206	0.60	1.75	0.57	0.81
581	15000	219	90	677	0.42	2.45	0.41	0.79
582	202	17	15	52	0.93	1.18	0.85	0.88
583	647	34	24	111	0.66	1.41	0.71	0.84
584	52	10	7	24	1.00	1.38	0.72	0.91
585	202	17	15	49	1.00	1.17	0.86	0.92
586	47	8	8	22	1.00	1.00	1.00	1.00
587	41	8	7	21	1.00	1.23	0.81	0.94
588	683	43	20	114	0.66	2.12	0.47	0.84
589	895	41	28	119	0.80	1.49	0.67	0.91
590	797	37	27	111	0.81	1.38	0.73	0.87
591	72	12	7	30	1.00	1.66	0.60	0.97
592	492	33	19	93	0.72	1.74	0.57	0.83
593	430	25	21	79	0.87	1.19	0.84	0.88
594	9000	121	92	569	0.34	1.31	0.76	0.76
595	450	34	17	85	0.79	2.04	0.49	0.88
596	83	13	8	35	0.86	1.70	0.59	0.84
597	31	8	5	17	1.00	1.50	0.67	1.00
598	140	17	10	45	0.86	1.66	0.60	0.90
599	393	29	17	84	0.70	1.65	0.61	0.85
600	1000	40	35	121	0.93	1.14	0.88	0.92
601	93	13	9	33	1.00	1.36	0.73	0.95
602	18000	182	127	1144	0.17	1.43	0.70	0.61
603	761	49	20	115	0.72	2.46	0.41	0.90
604	688	44	20	121	0.59	2.17	0.46	0.82
605	1000	53	29	174	0.49	1.82	0.55	0.73
606	999	54	23	141	0.63	2.31	0.43	0.85
607	357	27	17	74	0.82	1.59	0.63	0.86
608	67	12	7	30	0.96	1.55	0.65	0.93
609	352	24	19	66	1.00	1.25	0.80	0.94
610	67	11	8	28	1.00	1.37	0.73	0.93
611	104	14	9	36	0.99	1.50	0.67	0.91
612	186	21	11	57	0.73	1.83	0.55	0.82
613	461	25	23	88	0.74	1.09	0.92	0.85
614	342	23	19	66	0.99	1.22	0.82	0.93

#	Area (μm^2)	Major (μm)	Minor (μm)	Perimeter (μm)	Circularity (0-1)	Aspect Ratio	Roundness (0-1)	Solidity (0-1)
615	176	18	12	51	0.85	1.45	0.69	0.82
616	104	14	9	38	0.93	1.59	0.63	0.91
617	900	43	27	120	0.79	1.58	0.63	0.89
618	47	8	8	22	1.00	1.00	1.00	1.00
619	1000	46	34	147	0.71	1.37	0.73	0.85
620	20000	195	133	1000	0.26	1.46	0.68	0.77
621	238	21	14	61	0.81	1.45	0.69	0.87
622	88	13	8	34	0.99	1.61	0.62	0.85
623	186	22	11	59	0.66	1.98	0.50	0.79
624	2000	54	39	201	0.51	1.41	0.71	0.79
625	600	40	19	104	0.70	2.13	0.47	0.85
626	83	12	9	32	1.00	1.45	0.69	0.82
627	166	19	11	50	0.82	1.79	0.56	0.85
628	72	10	10	28	1.00	1.02	0.98	0.93
629	7000	124	67	420	0.46	1.86	0.54	0.78
630	347	29	15	72	0.85	1.87	0.54	0.92
631	31	8	5	17	1.00	1.50	0.67	1.00
632	10000	127	96	420	0.69	1.32	0.76	0.88
633	52	10	7	24	1.00	1.55	0.65	0.91
634	228	21	14	58	0.85	1.55	0.64	0.87
635	98	13	10	35	1.00	1.38	0.73	0.88
636	2000	62	41	199	0.64	1.50	0.67	0.85
637	2000	65	42	227	0.52	1.56	0.64	0.78
638	393	26	19	73	0.93	1.40	0.72	0.89
639	404	29	18	87	0.67	1.60	0.62	0.79
640	8000	144	68	468	0.45	2.11	0.47	0.81
641	2000	58	42	209	0.56	1.38	0.73	0.83
642	9000	145	76	492	0.45	1.91	0.52	0.83
643	181	20	11	51	0.87	1.74	0.57	0.93
644	202	25	10	58	0.75	2.45	0.41	0.88
645	124	16	10	41	0.94	1.55	0.65	0.91
646	166	20	10	52	0.78	1.92	0.52	0.87
647	166	18	11	47	0.94	1.62	0.62	0.90
648	719	38	24	107	0.78	1.58	0.63	0.91
649	2000	79	35	227	0.53	2.23	0.45	0.83
650	1000	60	22	155	0.54	2.72	0.37	0.81
651	3000	84	44	336	0.33	1.91	0.52	0.63
652	735	43	22	113	0.73	1.95	0.51	0.89
653	160	19	11	47	0.91	1.68	0.60	0.90
654	83	13	8	33	0.96	1.52	0.66	0.91
655	1000	48	28	131	0.76	1.74	0.57	0.91

#	Area (μm^2)	Major (µm)	Minor (µm)	Perimeter (µm)	Circularity (0-1)	Aspect Ratio	Roundness (0-1)	Solidity (0-1)
656	150	17	12	44	0.98	1.43	0.70	0.91
657	523	28	24	85	0.91	1.14	0.88	0.89
658	21	5	5	13	1.00	1.00	1.00	1.00
659	223	19	15	55	0.91	1.24	0.81	0.89
660	756	35	28	108	0.82	1.27	0.79	0.88
661	714	35	26	99	0.92	1.34	0.75	0.92
662	140	20	9	47	0.81	2.16	0.46	0.93
663	21	5	5	13	1.00	1.00	1.00	1.00
664	373	27	17	74	0.86	1.56	0.64	0.91
665	1000	54	32	190	0.47	1.70	0.59	0.79
666	316	28	14	74	0.72	1.97	0.51	0.85
667	1000	50	36	147	0.82	1.41	0.71	0.89
668	2000	58	47	219	0.55	1.24	0.81	0.82
669	212	22	12	57	0.83	1.73	0.58	0.84
670	523	30	22	87	0.88	1.35	0.74	0.90
671	2000	56	39	211	0.49	1.41	0.71	0.78
672	2000	56	39	175	0.70	1.46	0.69	0.85
673	1000	54	24	147	0.59	2.23	0.45	0.86
674	492	28	22	88	0.79	1.25	0.80	0.86
675	4000	86	56	258	0.72	1.54	0.65	0.91
676	93	12	10	33	1.00	1.25	0.80	0.95
677	124	16	10	41	0.94	1.71	0.59	0.94
678	399	28	18	76	0.86	1.55	0.65	0.91
679	430	35	15	93	0.62	2.28	0.44	0.77
680	31	8	5	17	1.00	1.50	0.67	1.00
681	440	24	23	88	0.72	1.02	0.98	0.84
682	5000	100	59	417	0.34	1.69	0.59	0.68
683	3000	81	45	272	0.49	1.78	0.56	0.74
684	129	17	10	44	0.84	1.75	0.57	0.85
685	1000	52	30	144	0.75	1.71	0.58	0.87
686	243	26	12	63	0.76	2.21	0.45	0.81
687	119	14	11	38	1.00	1.25	0.80	0.87
688	114	14	11	39	0.92	1.29	0.78	0.85
689	430	32	17	91	0.65	1.85	0.54	0.81
690	197	18	14	52	0.92	1.23	0.82	0.91
691	41	8	7	21	1.00	1.23	0.81	0.94
692	109	14	10	36	1.00	1.40	0.71	0.93
693	3000	101	37	266	0.52	2.73	0.37	0.85
694	72	11	8	30	0.99	1.42	0.70	0.82
695	52	10	7	25	1.00	1.56	0.64	0.91
696	248	27	12	64	0.76	2.35	0.43	0.89

#	Area (μm^2)	Major (µm)	Minor (µm)	Perimeter (µm)	Circularity (0-1)	Aspect Ratio	Roundness (0-1)	Solidity (0-1)
697	57	10	7	25	1.00	1.37	0.73	0.96
698	52	10	7	24	1.00	1.55	0.65	0.91
699	709	38	24	111	0.72	1.61	0.62	0.88
700	10000	140	87	459	0.57	1.60	0.63	0.86
701	295	25	15	71	0.74	1.70	0.59	0.85
702	98	14	9	35	1.00	1.49	0.67	0.88
703	31	8	5	17	1.00	1.50	0.67	1.00
704	176	20	11	50	0.87	1.80	0.56	0.87
705	274	30	12	68	0.74	2.59	0.39	0.85
706	93	12	10	34	1.00	1.26	0.80	0.86
707	47	8	8	22	1.00	1.00	1.00	1.00
708	119	14	11	39	0.96	1.34	0.75	0.89
709	124	15	11	39	1.00	1.34	0.75	0.91
710	600	40	19	98	0.78	2.11	0.47	0.89
711	518	32	21	88	0.84	1.54	0.65	0.88
712	559	37	19	97	0.75	1.89	0.53	0.90
713	98	15	9	36	0.94	1.70	0.59	0.88
714	52	9	7	27	0.89	1.33	0.75	0.80
715	502	31	20	96	0.69	1.55	0.65	0.81
716	52	9	7	24	1.00	1.33	0.75	0.91
717	217	18	15	55	0.91	1.19	0.84	0.91
718	98	12	11	36	0.94	1.13	0.89	0.88
719	109	16	9	38	0.94	1.86	0.54	0.86
720	285	27	13	71	0.71	2.07	0.48	0.80
721	119	15	10	39	0.99	1.50	0.67	0.98
722	83	12	9	32	1.00	1.39	0.72	0.89
723	435	30	19	83	0.79	1.58	0.63	0.86
724	31	8	5	17	1.00	1.50	0.67	1.00
725	186	19	12	50	0.92	1.58	0.64	0.87
726	21	5	5	13	1.00	1.00	1.00	1.00
727	833	35	30	111	0.86	1.14	0.88	0.92
728	57	10	7	25	1.00	1.37	0.73	0.96
729	279	24	15	61	0.95	1.63	0.61	0.96
730	228	19	16	57	0.89	1.20	0.84	0.90
731	735	44	21	129	0.56	2.08	0.48	0.83
732	518	33	20	88	0.84	1.70	0.59	0.89
733	2000	65	42	203	0.66	1.53	0.66	0.86
734	254	27	12	69	0.67	2.32	0.43	0.84
735	72	12	7	30	1.00	1.66	0.60	0.97
736	109	16	9	38	0.94	1.89	0.53	0.89
737	98	13	10	34	1.00	1.27	0.79	0.97

#	Area (μm^2)	Major (µm)	Minor (µm)	Perimeter (µm)	Circularity (0-1)	Aspect Ratio	Roundness (0-1)	Solidity (0-1)
738	31	8	5	17	1.00	1.50	0.67	1.00
739	114	15	10	38	1.00	1.48	0.67	0.96
740	93	14	9	35	0.97	1.63	0.61	0.86
741	688	34	25	102	0.83	1.35	0.74	0.87
742	269	28	12	69	0.71	2.37	0.42	0.80
743	797	48	21	174	0.33	2.30	0.43	0.63
744	23000	193	152	768	0.49	1.27	0.79	0.86
745	761	37	26	107	0.84	1.43	0.70	0.91
746	2000	55	54	219	0.62	1.02	0.98	0.82
747	342	30	14	83	0.62	2.13	0.47	0.77
748	4000	86	53	282	0.56	1.64	0.61	0.84
749	528	37	18	96	0.72	2.05	0.49	0.86
750	166	17	13	46	0.99	1.33	0.75	0.88
751	926	40	30	128	0.71	1.33	0.75	0.84
752	160	19	11	48	0.89	1.81	0.55	0.85
753	98	11	11	35	1.00	1.04	0.96	0.88
754	3000	70	47	233	0.59	1.49	0.67	0.83
755	5000	86	67	314	0.58	1.29	0.78	0.81
756	647	37	23	103	0.76	1.63	0.62	0.85
757	88	15	8	34	0.94	1.98	0.51	0.97
758	2000	57	34	170	0.66	1.70	0.59	0.86
759	7000	108	78	411	0.49	1.39	0.72	0.79
760	129	15	11	41	0.95	1.42	0.71	0.85
761	316	26	16	68	0.86	1.62	0.62	0.89
762	11000	135	103	465	0.63	1.31	0.76	0.87
763	109	14	10	38	0.97	1.50	0.67	0.93
764	1000	41	34	125	0.88	1.19	0.84	0.94
765	83	17	6	38	0.74	2.81	0.36	0.87
766	1000	73	25	191	0.50	2.87	0.35	0.81
767	238	25	12	61	0.80	2.12	0.47	0.88
768	228	20	15	55	0.95	1.32	0.76	0.91
769	274	22	16	59	0.98	1.40	0.71	0.93
770	331	24	18	69	0.87	1.37	0.73	0.88
771	93	13	9	34	1.00	1.37	0.73	0.95
772	166	16	13	47	0.94	1.24	0.81	0.88
773	47	8	8	22	1.00	1.00	1.00	1.00
774	83	13	8	32	1.00	1.57	0.64	0.91
775	135	16	11	41	0.99	1.47	0.68	0.87
776	2000	70	28	213	0.43	2.47	0.41	0.72
777	2000	60	41	233	0.45	1.44	0.69	0.79
778	72	10	10	28	1.00	1.02	0.98	0.93

#	Area (μm^2)	Major (μm)	Minor (μm)	Perimeter (μm)	Circularity (0-1)	Aspect Ratio	Roundness (0-1)	Solidity (0-1)
779	88	14	8	35	0.88	1.84	0.54	0.79
780	150	16	12	44	0.98	1.31	0.77	0.91
781	533	26	26	91	0.82	1.02	0.98	0.87
782	352	23	20	72	0.86	1.16	0.87	0.91
783	31	8	5	17	1.00	1.50	0.67	1.00
784	124	18	9	48	0.69	2.08	0.48	0.73
785	88	13	8	34	0.99	1.61	0.62	0.85
786	2000	51	38	178	0.61	1.33	0.75	0.84
787	1000	41	37	140	0.77	1.09	0.92	0.88
788	6000	109	71	350	0.62	1.53	0.65	0.88
789	404	32	16	88	0.66	1.95	0.51	0.80
790	1000	40	36	133	0.81	1.09	0.92	0.90
791	88	12	9	33	1.00	1.34	0.75	0.92
792	72	10	9	28	1.00	1.13	0.89	0.93
793	336	26	17	69	0.89	1.53	0.65	0.88
794	223	23	12	59	0.81	1.91	0.52	0.84
795	657	47	18	116	0.61	2.66	0.38	0.84
796	269	21	17	58	1.00	1.23	0.81	0.93
797	202	24	11	58	0.75	2.19	0.46	0.88
798	238	21	15	68	0.65	1.42	0.70	0.83
799	797	43	24	135	0.55	1.81	0.55	0.77
800	497	35	18	107	0.54	1.94	0.52	0.73
801	135	13	13	41	0.99	1.04	0.96	0.87
802	248	20	16	62	0.81	1.30	0.77	0.93
803	186	18	13	49	0.97	1.35	0.74	0.88
804	554	33	21	92	0.82	1.56	0.64	0.87
805	336	25	17	69	0.89	1.48	0.68	0.90
806	93	12	10	33	1.00	1.25	0.80	0.95
807	217	19	14	54	0.92	1.35	0.74	0.93
808	864	43	26	115	0.82	1.64	0.61	0.89
809	414	27	20	80	0.81	1.35	0.74	0.85
810	357	24	19	72	0.87	1.23	0.81	0.90
811	47	8	8	22	1.00	1.00	1.00	1.00
812	31	8	5	17	1.00	1.50	0.67	1.00
813	114	17	9	42	0.81	1.88	0.53	0.88
814	212	25	11	60	0.74	2.36	0.42	0.85
815	414	32	17	91	0.63	1.93	0.52	0.77
816	5000	89	65	306	0.61	1.36	0.74	0.84
817	347	25	18	68	0.95	1.40	0.72	0.92
818	4000	91	51	272	0.62	1.78	0.56	0.86
819	228	28	10	65	0.69	2.77	0.36	0.86

#	Area (μm^2)	Major (µm)	Minor (µm)	Perimeter (µm)	Circularity (0-1)	Aspect Ratio	Roundness (0-1)	Solidity (0-1)
820	430	28	20	77	0.91	1.41	0.71	0.91
821	78	12	8	30	1.00	1.44	0.70	0.88
822	145	21	9	53	0.65	2.35	0.43	0.72
823	362	23	20	76	0.80	1.13	0.89	0.86
824	129	16	11	41	0.95	1.48	0.68	0.85
825	792	39	26	108	0.85	1.48	0.68	0.90
826	72	10	10	28	1.00	1.02	0.98	0.93
827	279	23	16	60	0.98	1.46	0.69	0.90
828	771	37	26	103	0.91	1.40	0.71	0.93
829	336	27	16	75	0.75	1.71	0.59	0.84
830	662	31	27	98	0.86	1.14	0.88	0.89
831	78	11	9	30	1.00	1.14	0.88	0.97
832	1000	59	26	155	0.64	2.26	0.44	0.85
833	1000	58	33	149	0.84	1.76	0.57	0.94
834	549	37	19	96	0.74	1.91	0.52	0.91
835	1000	56	27	147	0.68	2.12	0.47	0.84
836	383	33	15	83	0.70	2.23	0.45	0.86
837	88	15	8	35	0.91	1.89	0.53	0.83
838	155	17	12	44	0.99	1.46	0.69	0.88
839	52	10	7	25	1.00	1.56	0.64	0.91
840	709	38	24	113	0.70	1.61	0.62	0.87
841	41	8	7	21	1.00	1.23	0.81	0.94
842	14000	201	89	633	0.44	2.25	0.44	0.83
843	430	29	19	80	0.84	1.50	0.67	0.88
844	88	12	10	32	1.00	1.19	0.84	0.92
845	1000	43	31	127	0.81	1.38	0.73	0.92
846	2000	75	36	248	0.43	2.11	0.47	0.79
847	730	38	24	105	0.83	1.59	0.63	0.90
848	347	23	19	67	0.96	1.20	0.83	0.94
849	274	20	18	72	0.67	1.11	0.91	0.83
850	1000	45	41	149	0.82	1.09	0.92	0.90
851	41	8	7	21	1.00	1.23	0.81	0.94
852	176	20	11	51	0.85	1.72	0.58	0.80
853	5000	81	71	313	0.58	1.15	0.87	0.81
854	41	8	7	21	1.00	1.23	0.81	0.94
855	388	33	15	86	0.66	2.19	0.46	0.81
856	802	39	26	112	0.81	1.52	0.66	0.89
857	248	26	12	68	0.67	2.15	0.47	0.82
858	197	20	13	52	0.92	1.52	0.66	0.91
859	57	10	7	25	1.00	1.37	0.73	0.96
860	2000	52	49	233	0.46	1.06	0.94	0.73

#	Area (μm^2)	Major (µm)	Minor (µm)	Perimeter (µm)	Circularity (0-1)	Aspect Ratio	Roundness (0-1)	Solidity (0-1)
861	5000	93	72	512	0.25	1.29	0.77	0.74
862	497	41	15	98	0.65	2.68	0.37	0.84
863	574	36	20	98	0.75	1.75	0.57	0.87
864	983	38	33	126	0.78	1.18	0.85	0.87
865	57	10	7	25	1.00	1.37	0.73	0.96
866	135	22	8	48	0.74	2.95	0.34	0.98
867	31	8	5	17	1.00	1.50	0.67	1.00
868	378	27	18	83	0.68	1.50	0.67	0.82
869	57	10	7	25	1.00	1.37	0.73	0.96
870	31	8	5	17	1.00	1.50	0.67	1.00
871	471	28	22	82	0.88	1.27	0.79	0.87

Table 7.4. Measurements and calculated mean size of the CAIs identified within the DNG 06004 meteorite. Mean CAI size was calculated using equation 3.2. Measurements provided by Prof. M. R. Lee (UofG).

#	Long axis (μm)	Short axis (μm)	Mean size (μm)
1	15	11	13
2	23	12	17
4	34	9	21
5	25	11	18
6	16	14	15
7	95	29	62
8	43	39	41
9	48	36	42
10	35	18	26
11	85	41	63
12	44	9	27
13a	40	20	30
13b	99	40	70
14	90	60	75
15	26	22	24
16	73	26	50
17	31	28	30
18	28	15	21
19	19	12	16
20	74	50	62
21	93	43	68
22	41	16	29
23a	21	12	17
23b	84	64	74
24	32	23	27
25a	93	74	83
25b	273	112	192
26	130	46	88
27	22	13	17
28	162	36	99
29	195	83	139
30	30	15	23
31	57	28	42
32	87	44	65
33	26	24	25
34	33	32	33
35	38	35	36
36	23	22	23
37	37	28	32

#	Long axis (μm)	Short axis (μm)	Mean size (μm)
38	49	41	45
39a	64	21	43
39b	225	138	181
40	72	22	47
41	35	4	20
42	54	26	40
43	63	21	42
44	61	50	56
45	44	16	30
46	40	12	26
47	60	23	41
48	24	11	17
49a	76	18	47
49b	40	24	32
50	54	25	40
51	231	63	147
52	42	16	29
53	55	20	37
54	81	59	70
55	64	57	61
56	132	53	92
57	39	37	38
58	33	21	27
59	15	10	12
60	87	50	69
61	35	20	27
62	64	23	43
63	38	37	38
64	402	231	317
65	146	49	97
67	95	77	86
69	139	32	85
70	62	32	47
71a	24	22	23
71b	161	93	127
72	68	47	57
73	35	9	22
74	95	21	58
74a	76	46	61
75	30	21	25
76	87	56	71
78	91	66	79

#	Long axis (μm)	Short axis (μm)	Mean size (μm)
79	51	24	38
80	51	31	41
81	133	81	107
81a	42	30	36
82	57	17	37
83	22	19	20
84	30	17	24
86	20	12	16
87	152	57	105
88	33	32	33
89	26	17	22
91	50	21	36
92	36	31	33
94	57	24	40
96	23	13	18
97	82	46	64
98	85	29	57

7.3 CAI Petrographic Descriptions

Table 7.5. Summary of the studied CAIs within the DNG 06004 meteorite. Each inclusion has been attributed a type (i.e. simple inclusion, simple aggregate, or complex aggregate), and the integrity of the FGR, as well as their mineralogy (from most abundant mineral phase to least abundant, in terms of area%) has been recorded.

#	Type	Mineralogy	FGR
1	Simple incl.	Sp-Phyll-Px	Absent
2	Simple incl.	Hb	Incomplete
4	Simple incl.	Sp-Pv	Absent
5	Simple incl.	Sp-Pv-Hb	Incomplete
6	Simple incl.	Hb	Absent
7	Simple agg.	Sp-Px-Ol	Complete
8	Simple agg.	Hb-Sp-Phyll	Complete
9	Simple agg.	Al-Mg-Ca silicate-Px	Complete
10	Simple agg.	Sp-Pv-Phyll	Complete
11	Simple agg.	Al-Mg silicate	Complete
12	Simple incl.	Sp-Hb	Complete
13a	Simple agg.	Sp-Phyll-Px	Complete
13b	Simple agg.	Sp-Px	Incomplete
14	Simple agg.	Sp-Px-Ol	Complete
15	Simple agg.	Sp-Pv-Hb-Phyll-Px	Complete
16	Simple incl.	Pv-Hb-Phyll	Complete
17	Simple agg.	Sp-Px	Incomplete
18	Simple agg.	Sp-Pv-Phyll-Px	Complete
19	Simple incl.	Sp	Absent
20	Simple incl.	Sp-Phyll-Px	Complete
21	Simple incl.	Px-Sp-Phyll	Incomplete
22	Simple incl.	Px-Al-Mg-Ca silicate-Pv	Incomplete
23a	Simple incl.	Sp-Pv-Phyll-Px	Complete
23b	Simple agg.	Phyll-Px-Pv-Sp	Complete
24	Simple incl.	Px-Sp	Complete
25a	Complex agg.	Phyll-Sp-Pv-Px	Incomplete
25b	Simple agg.	Sp-Pv-Phyll-Px	Incomplete
26	Simple agg.	Sp-Phyll-Pv	Incomplete
27	Simple incl.	Sp-Phyll-Px	Incomplete
28	Simple agg.	Px-Ol-Sp	Incomplete
29	Simple agg.	Sp-Px-Ol-Pv	Complete
30	Simple incl.	Sp-Hb	Complete
31	Simple incl.	Sp-Px	Complete
32	Simple agg.	Px-Sp-Mg-Al-Ca silicate	Complete
33	Simple incl.	Sp-Px-Pv	Complete

#	Type	Mineralogy	FGR
34	Simple incl.	Sp-Phyll-Px-Pv	Complete
35	Simple incl.	Px-Ol-Sp	Incomplete
36	Simple incl.	Ol-Sp	Complete
37	Simple incl.	Sp-Phyll-Pv-Px	Complete
38	Simple incl.	Px-Phyll-Sp-Pv	Complete
39a	Simple agg.	Sp-Px-Phyll-Pv	Complete
39b	Simple agg.	Ol-Sp	Complete
40	Simple incl.	Sp-Px	Complete
41	Simple incl.	Hb	Incomplete
42	Simple incl.	Sp-Px	Incomplete
43	Simple agg.	Sp-Phyll-Pv	Complete
44	Simple agg.	Sp-Px-Phyll-Pv	Complete
45	Simple agg.	Sp-Px-Ol	Complete
46	Simple incl.	Sp-Phyll-Px	Incomplete
47	Simple incl.	Sp-Phyll-Px-Pv	Complete
48	Simple incl.	Sp-Phyll-Px	Incomplete
49a	Simple agg.	Sp-Pv-Phyll	Complete
49b	Simple agg.	Phyll-Px-Sp	Incomplete
50	Simple incl.	Hb-Pv	Incomplete
51	Simple agg.	Sp-Px-Phyll-Pv	Complete
52	Simple incl.	Sp-Phyll-Px-Hb	Complete
53	Simple agg.	Phyll-Px-Sp-Pv	Incomplete
54	Simple agg.	Px-Phyll-Sp	Complete
55	Simple agg.	Phyll-Sp-Px-Pv	Complete
56	Complex agg.	Phyll-Sp-Pv-Px	Complete
57	Simple incl.	Phyll-Hb-Px	Complete
58	Simple incl.	Px-Phyll-Sp	Incomplete
59	Simple incl.	Sp-Pv	Complete
60	Simple agg.	Sp-Px-Phyll	Complete
61	Simple incl.	Sp-Px-Pv	Incomplete
62	Simple incl.	Sp-Px	Incomplete
63	Simple incl.	Sp-Px	Complete
64	Simple agg.	Px-Sp-Pv	Complete
65	Simple agg.	Phyll-Sp-Pv	Complete
67	Simple incl.	Phyll-Sp-Pv-Px	Complete
69	Complex agg.	Sp-Pv-Px-Phyll	Complete
70	Simple incl.	Sp-Hb	Incomplete
71a	Simple incl.	Sp-Px-Phyll	Complete
71b	Simple agg.	Sp-Phyll-Px-Pv-Hb	Complete
72	Simple agg.	Sp-Phyll-Px-Pv	Incomplete
73	Simple incl.	Hb-Sp	Complete
74	Simple incl.	Sp-Px-Phyll-Pv	Complete

#	Type	Mineralogy	FGR
74a	Simple agg.	Sp-Phyll-Px-Pv	Complete
75	Simple incl.	Sp-Phyll-Px-Pv	Incomplete
76	Simple agg.	Phyll-Sp-Pv	Incomplete
78	Simple agg.	Sp-Phyll	Complete
79	Simple agg.	Sp-Px	Incomplete
80	Simple agg.	Sp-Px-Hb	Complete
81	Simple agg.	Phyll-Sp-Pv-Px	Complete
81a	Simple incl.	Phyll-Pv	Incomplete
82	Simple incl.	Sp-Phyll-Px	Complete
83	Simple incl.	Sp-Px-Pv	Complete
84	Simple incl.	Sp-Px-Pv-Hb	Complete
86	Simple incl.	Sp-Phyll-Pv-Px	Complete
87	Simple agg.	Px-Sp-Pv	Complete
88	Simple incl.	Phyll-Sp-Pv-Px	Complete
89	Simple incl.	Sp-Phyll-Px	Complete
91	Simple agg.	Sp-Phyll	Incomplete
92	Simple incl.	Phyll-Sp-Pv-Px	Complete
94	Simple agg.	Sp-Px-Pv-Phyll	Complete
96	Simple incl.	Sp-Px	Incomplete
97	Complex agg.	Px-Phyll-Sp	Complete
98	Complex agg.	Phyll-Pv-Px-Sp	Complete

Abbreviations: FGR - Fine-Grained Rim; Hb - hibonite; Ol - olivine; Phyll - phyllosilicate; Pv - perovskite; Px - pyroxene; Sp - spinel.

Table 7.6. Description of the CAIs identified within the DNG 06004 meteorite.

#	Description
1	Sp core with a few Px grains surrounded by a Phyll rim of (~1 μm thickness).
2	Two disjoined Hb grains (up to ~10 μm long) adjacent to a few patches of FGR, within matrix.
4	Two disjoined Sp-Pv cores within matrix.
5	Sp-Hb-Pv cluster partially surrounded by a FGR (< 1 μm thickness), within matrix.
6	Disjoined Hb clusters within matrix.
7	Cluster of Sp grains with void spaces surrounded by a broken and incomplete Px-Ol rim (~5 μm thickness).
8	Circular object containing globular micrometric Sp and Hb grains within a Phyll mantle.
9	Irregularly shaped cluster of Al-Mg-Ca silicate and Px within matrix.
10	Elongated Sp core within a broken and incomplete Phyll mantle (5~10 μm thickness), containing a few globular Pv grains.
11	Distended cluster of Al-Mg silicate grains surround by a FGR.
12	Distended Sp-Hb core with void spaces.
13a	Sp core within a Phyll mantle, surrounded by an almost intact Px rim (~1 μm thickness).
13b	Core made of clustered Sp grains with void spaces, surrounded by a fragmented Px rim (~5 μm thickness).
14	Sp core with large void spaces surrounded by a Px rim, adjacent to a cluster of Ol also rimmed by Px.
15	Sp-Hb-Pv core within a Phyll mantle comprising multiple void spaces. The entire assemblage is partially rimmed by Px (~1 μm thickness).
16	Disjoined Hb-Pv clusters adjacent to a large void space (up to ~60 μm in length), alongside patches of Phyll.
17	Sp core within a broken Px rim (~1 μm thickness) adjacent to multiple large void spaces.
18	Sp core with a few globular grains of Pv, mantled by Phyll. The whole assemblage is completely rimmed by Px (~1 μm thickness).
19	Cluster of Sp grains with round edges within FGR.
20	Multiple irregularly shaped Sp grains within a Phyll mantle with void spaces. The entire assemblage is rimmed by Px.
21	Disjoined Sp grains alongside a few patches of Phyll, separated by void spaces. The object is adjacent to a thick broken Px rim (~10 μm thickness).
22	Al-Mg-Ca silicate core with a few globular Pv grains, within an incomplete rim of Px.

#	Description
23a	Sp-Pv core mantled by Phyll with void spaces and rimmed by Px.
23b	Distended chain-like object comprising multiple Sp-Pv clusters, each mantled by Phyll and rimmed by Px.
24	Large Sp cluster with a few void spaces, rimmed by Px.
25a	Sp-Pv core mantled by Phyll with large void spaces and partially rimmed by Px.
25b	Distended chain-like object comprising Sp-Pv clusters mantled by Phyll and rimmed by Px.
26	Sp-Pv core within Phyll mantle with void spaces.
27	Sp core mantled by Phyll (with void spaces), within an incomplete Px rim.
28	Core made of clustered Sp grains with large void spaces, partially surrounded by a fragmented Px-Ol rim (5~10 μm thickness).
29	Oblong Sp-Pv core with a multiple rims-like structure: complete inner rim of Px with a partial outer rim of Ol.
30	Multiple disjoined grains of Sp and Hb within FGR.
31	Sp core partially surrounded by fragmented Px rim with void spaces.
32	Core made of Sp and Mg-Al-Ca silicate grains with void spaces surrounded by an incomplete and fragmented rim of Px.
33	Sp-Pv core alongside a fragment of Px rim.
34	Fragmented Sp-Pv core, partially mantled by Phyll, within an incomplete Px rim.
35	Sp core mantled by Px with patches of Ol on the exterior edges.
36	Sp core mantled by Ol.
37	Sp-Pv core mantled by Phyll (with large void spaces), within an incomplete Px rim.
38	Sp-Pv core mantled by Phyll (with void spaces), rimmed by Px.
39a	Disjoined Sp-Pv cores mantled by Phyll (with void spaces), within a singular rim of Px.
39b	Multiple disjoined Sp grains alongside patches of Ol and void spaces.
40	Sp core alongside a large void space (~20 μm in length) within broken and incomplete Px rim.
41	Cluster of acicular Hb grains (10~20 μm long).
42	Sp core alongside a large void space, partially surrounded by a Px rim.
43	Multiple disjoined Sp-Pv clusters partially connected by Phyll patches.

#	Description
44	Three Sp-Pv clusters, each mantled by Phyll and completely rimmed by Px (~4 μm thickness). The Px rims of of the disjoined clusters are connected.
45	Sp core with large void space adjacent to a cluster of Px grains (fragmented rim) and a large Ol grain (~10 μm long).
46	Sp cluster mantled by Phyll and partially rimmed by Px (~1 μm thickness).
47	Disjoined Sp-Pv clusters within a single Phyll mantle, surrounded by a Px rim (~1 μm thickness).
48	Sp core mantled by Phyll and Px.
49a	Distended chain-like object comprising four Sp-Pv clusters connected by a singular Phyll mantle.
49b	Sp clusters mantled by Phyll (and multiple void spaces) within a Px rim.
50	Hb-Pv cluster partially surrounded by an FGR.
51	Sp-Pv core, mantled by Phyll with large void spaces, rimmed by Px (~10 μm thickness).
52	Sp-Hb core mantled by Phyll and partially rimmed by Px.
53	Disjoined Sp-Pv clusters, each mantled by Phyll, all within a singular Px rim (~1 μm thickness).
54	Sp clusters mantled by Phyll (and multiple void spaces) within a Px rim (~5 μm thickness).
55	Sp-Pv clusters within a single Phyll mantle (with void spaces), rimmed by Px.
56	Multiple disjoined Sp-Pv clusters within a single Phyll mantle (alongside large void spaces), rimmed by Px. One cluster is separated from the rest, and is partially surrounded by a broken Px rim.
57	Two Hb cores within a single Phyll mantle, rimmed by Px.
58	Sp core mantled by Phyll (with void spaces) and partially rimmed by Px.
59	Sp-Pv cluster surrounded by a FGR.
60	Disjoined Sp clusters, each mantled by patches of Phyll (and void spaces) and rimmed by Px.
61	Large Sp core (~25 μm long) with small globular Pv grains (~1 μm), alongside a fragment of a Px rim and a large void space.
62	Multiple disjoined Sp clusters, each with their own incomplete Px rim, apart from two which are surrounded by void space.
63	Multiple disjoined Sp clusters alongside void spaces and a long fragmented chain of Px grains (rim remnant).
64	Large aggregate of Sp-Pv clusters with patches of Phyll.
65	Multiple disjoined Sp clusters with several amongst them connected by a Phyll mantle containing a few globular Pv grains.

#	Description
67	Distended chain-like Sp-Pv cluster within a single Phyll mantle, partially rimmed by Px.
69	Multiple disjoined clusters of Sp-Pv. Two such clusters are mantled by patches of Phyll, whereas the main distended chain of Sp-Pv clusters is within a singular rim of Px.
70	Disjoined grains of Sp and hb surrounded by an incomplete FGR.
71a	Sp core mantled by Phyll and partially rimmed by Px.
71b	Multiple disjoined Sp-Hb-Pv clusters, all within a Phyll mantle and rimmed by Px.
72	Sp-Pv cluster mantled by Phyll and rimmed by Px.
73	Sp-Hb cluster surrounded by an FGR.
74	Oblong Sp core with a few sporadic globular Pv grains (~1 μm), within a thin Phyll mantle. The assemblage is entirely comprised within a Px rim.
74a	Multiple disjoined Sp clusters, some alongside globular Pv grains. Three are comprised within a singular Phyll mantle and share a Px rim, while one is separated, nearby a Phyll patch and a fragmented Px rim.
75	Sp-Pv cluster mantled by Phyll and partially rimmed by Px.
76	Disjoined Sp clusters alongside a large patch of Phyll containing several globular Pv grains and void spaces.
78	Multiple disjoined Sp clusters within a mantle of Phyll. Some Sp clusters are outside of the Phyll mantle.
79	Sp cluster alongside an incomplete and fragmented Px rim.
80	Disjoined Sp and Hb grains alongside Px grains, with a nearby chain-like structure composed of Px grains (remnant rim).
81	Multiple Sp-Pv clusters within a single Phyll mantle and rimmed by Px.
81a	Multiple sporadic globular Pv grains (1~5 μm), within a single Phyll mantle.
82	Oblong Sp core within a Phyll mantle, entirely rimmed by Px.
83	Sp-Pv cluster rimmed by Px.
84	Sp-Hb-Pv cluster completely rimmed by Px.
86	Sp-Pv cluster alongside a patch of Phyll, partially rimmed by Px.
87	Multiple disjoined Sp clusters (with a few sporadic Pv grains), all partially rimmed by Px.
88	Sp-Pv cluster mantled by Phyll and completely rimmed by Px.

#	Description
89	Sp core enclosed within a thin mantle of Phyll and entirely rimmed by Px.
91	Multiple disjoined Sp clusters with some partially mantled by Phyll.
92	Sp core containing an elongated Pv grain (~10 μm) within a singular mantle of Phyll, comprising a few disjoined Sp and Pv grains. The entire assemblage is enclosed within a thin Px rim (~1 μm thickness).
94	Distended chain-like structure comprising multiple Sp-Pv clusters alongside a few patches of Phyll and void spaces, all within a single rim of Px.
96	Sp cluster surrounded by void space, enclosed within an incomplete fragmented Px rim.
97	Irregularly shaped object comprising multiple void spaces and Sp clusters entirely rimmed by Px. The clusters within the lower section are enclosed within a Phyll mantle.
98	Irregularly shaped object comprising multiple small and large globular Pv grains (1~10 μm) within an incomplete Phyll mantle. The assemblage is partially rimmed by Px.

Abbreviations: FGR - Fine-Grained Rim; Hb - hibonite; Ol - olivine; Phyll - phyllosilicate; Pv - perovskite; Px - pyroxene; Sp - spinel.

7.4 CAI Types and Mineralogies

Table 7.7. Mineralogy and type of classified CAIs within CM chondrites. CAIs were grouped by apparent primary mineralogy (not by order of abundance). Secondary mineralogies are not reported in this table but can be accessed in Chapter 4, for Winchcombe, and Lee et al. (2023), for LAP 02239.

	Winchcombe (CM2.0-2.6)			Mighei (CM2.3)			DNG 06004 (CM2.4)			LAP 02239 (CM2.4-2.5)		
Mineralogy	S. I.	S. A.	C. A.	S. I.	S. A.	C. A.	S. I.	S. A.	C. A.	S. I.	S. A.	C. A.
Sp	2			9	6	3	1	2		2	2	
Sp-Px	5	2				1	17	8	1	17	11	1
Sp-Px-Ol	1	2					1	4				
Sp-Px-Pv			1				14	14	4	8	5	2
Sp-Px-Pv-Hb							1	1		6	1	1
Sp-Px-Hb							1	1		2		
Sp-Px-Ol-Pv			1					1				1
Sp-Ol	4	1					1	1				
Sp-Ol-Hb		1										
Sp-Ol-Rt												1
Sp-Pv				3	4		2	6		2		
Sp-Pv-Hb				6	1		1	1		4	1	
Sp-Hb					1		4	1			1	
Px							1	2				
Px-Ol												1
Px-Pv			1									
Px-Hb							1					
Pv							1					

	Winchcombe			Mighei			DNG 06004			LAP 02239		
Pv-Hb							2					
Hb				1			3			1		
Totals	12	6	3	19	12	4	51	42	5	42	21	7

Abbreviations: S. I. – Simple Inclusion; S. A. – Simple Aggregate; C. A. – Complex Aggregate.

7.5 EPMA Compositions

Table 7.8. Oxide compositions (wt%) of targeted spinel grains in CAIs 1 (P30540) and 19 (P30552) of Winchcombe using EPMA.

CAI #	Target #	SiO_2	Al_2O_3	CaO	TiO_2*	MgO	V_2O_3	FeO	Cr_2O_3	NiO	Na_2O	Total
1	1	<dt	67.78	1.09	1.31	27.25	0.87	1.04	0.14	<dt	<dt	99.48
1	2	<dt	69.98	<dt	0.32	28.00	0.78	1.47	0.15	0.13	<dt	100.83
1	3	<dt	69.29	0.08	0.45	28.36	0.82	1.08	0.19	<dt	<dt	100.27
1	4	<dt	70.18	0.14	0.52	28.66	0.89	1.02	0.14	<dt	0.06	101.62
1	5	<dt	69.58	0.06	0.40	28.65	0.90	1.16	0.14	<dt	0.08	100.98
1	6	<dt	71.00	0.06	0.35	28.20	0.68	1.17	0.15	0.06	0.14	101.80
1	7	<dt	69.67	<dt	0.34	28.49	0.83	1.18	0.12	<dt	<dt	100.63
1	8	<dt	70.51	0.07	0.40	28.96	0.77	1.00	0.15	<dt	<dt	101.86
19	9	<dt	70.58	0.54	0.40	28.52	0.57	0.20	0.21	<dt	<dt	101.01
19	10	<dt	69.49	0.50	0.35	27.89	0.64	0.11	0.16	<dt	<dt	99.14
19	11	<dt	70.44	0.49	0.37	28.45	0.68	0.33	0.14	<dt	<dt	100.91
19	12	<dt	65.55	5.85	0.47	26.41	0.61	0.29	0.11	<dt	<dt	99.29
19	13	<dt	69.93	0.52	0.41	28.61	0.68	0.27	0.16	<dt	<dt	100.57
19	14	<dt	70.31	0.44	0.38	28.30	0.45	0.33	0.17	<dt	<dt	100.39
19	15	<dt	70.09	0.54	0.43	28.54	0.76	0.17	0.16	<dt	<dt	100.69

TiO_2* corresponds to the total Ti content (no differentiation between Ti^{3+} and Ti^{4+}) and dt corresponds to the detection limit.

Table 7.9. Oxide compositions (wt%) of targeted perovskite grains in CAIs 15 and 19 of Winchcombe (P30552) using EPMA.

CAI #	Target #	SiO_2	Al_2O_3	CaO	TiO_2*	MgO	V_2O_3	FeO	Cr_2O_3	NiO	Na_2O	Total
15	1	<dt	0.29	41.32	55.69	<dt	0.24	0.84	<dt	<dt	<dt	98.52
15	2	<dt	0.38	40.92	56.77	<dt	0.25	0.64	0.07	<dt	<dt	99.02
15	3	0.39	1.00	38.30	56.74	0.37	0.49	1.51	<dt	<dt	<dt	98.82
15	4	<dt	0.31	39.94	57.64	<dt	0.32	1.00	<dt	<dt	<dt	99.23
15	5	<dt	0.29	40.66	59.10	<dt	0.29	0.98	0.06	<dt	<dt	101.38
15	6	<dt	0.31	40.15	57.79	<dt	0.34	0.91	<dt	<dt	<dt	99.49
19	7	<dt	0.24	40.08	57.37	<dt	0.21	0.48	<dt	<dt	<dt	98.38
19	8	<dt	0.26	39.42	56.03	<dt	0.42	0.63	0.05	0.18	<dt	97.00
19	9	<dt	0.28	40.19	55.77	<dt	0.09	0.65	<dt	<dt	<dt	96.98
19	10	<dt	0.31	39.72	56.47	<dt	0.32	0.79	<dt	<dt	<dt	97.61
19	11	<dt	1.49	39.96	56.59	<dt	0.18	0.21	0.07	<dt	<dt	98.50

TiO_2* corresponds to the total Ti content (no differentiation between Ti^{3+} and Ti^{4+}) and dt corresponds to the detection limit.

Table 7.10. Oxide compositions (wt%) of targeted grossmanite grains in CAI 19 of Winchcombe (P30552) using EPMA.

#	SiO_2	Al_2O_3	CaO	TiO_2*	MgO	V_2O_3	FeO	Cr_2O_3	NiO	Na_2O	Total	Final Formula
1	25.84	21.92	25.67	18.64	4.23	1.12	0.05	0.22	<dt	<dt	97.69	$Ca_{1.000}[(Ti^{3+}_{0.237}Al_{0.053}V_{0.036}Cr_{0.007})(Mg_{0.251}Ca_{0.094}Fe_{0.002})Ti^{4+}_{0.320}](Si_{1.027}Al_{0.973})O_6$
2	29.51	23.57	25.13	15.52	4.93	0.74	0.22	0.25	<dt	<dt	99.86	$Ca_{1.000}[(Ti^{3+}_{0.257}Al_{0.198}V_{0.023}Cr_{0.008})(Mg_{0.282}Ca_{0.034}Fe_{0.007})Ti^{4+}_{0.191}](Si_{1.132}Al_{0.868})O_6$
3	27.78	22.71	26.36	16.11	4.43	1.20	0.24	0.15	<dt	<dt	98.98	$Ca_{1.000}[(Ti^{3+}_{0.187}Al_{0.122}V_{0.037}Cr_{0.005})(Mg_{0.257}Ca_{0.100}Fe_{0.008})Ti^{4+}_{0.284}](Si_{1.080}Al_{0.920})O_6$
4	29.38	23.31	25.56	15.81	5.02	0.61	0.21	0.25	0.18	0.07	100.40	$Ca_{1.000}[(Ti^{3+}_{0.237}Al_{0.176}V_{0.019}Cr_{0.008})(Mg_{0.287}Ca_{0.049}Fe_{0.007})Ti^{4+}_{0.218}](Si_{1.124}Al_{0.876})O_6$
5	29.89	23.14	25.01	14.95	5.42	0.65	0.46	0.07	<dt	<dt	99.59	$Ca_{1.000}[(Ti^{3+}_{0.224}Al_{0.193}V_{0.020}Cr_{0.002})(Mg_{0.310}Ca_{0.029}Fe_{0.015})Ti^{4+}_{0.208}](Si_{1.146}Al_{0.854})O_6$
6	27.84	23.76	24.84	16.27	4.58	1.08	0.22	<dt	<dt	<dt	98.59	$Ca_{1.000}[(Ti^{3+}_{0.250}Al_{0.177}V_{0.034}Cr_{0.000})(Mg_{0.266}Ca_{0.039}Fe_{0.007})Ti^{4+}_{0.227}](Si_{1.085}Al_{0.915})O_6$
7	28.90	22.39	24.64	15.54	5.07	0.85	0.18	<dt	0.13	<dt	97.70	$Ca_{1.000}[(Ti^{3+}_{0.253}Al_{0.172}V_{0.027}Cr_{0.000})(Mg_{0.297}Ca_{0.038}Fe_{0.006})Ti^{4+}_{0.206}](Si_{1.135}Al_{0.865})O_6$
8	29.75	22.90	24.56	14.34	5.27	1.02	0.20	0.06	<dt	<dt	98.10	$Ca_{1.000}[(Ti^{3+}_{0.240}Al_{0.208}V_{0.032}Cr_{0.002})(Mg_{0.306}Ca_{0.025}Fe_{0.007})Ti^{4+}_{0.180}](Si_{1.158}Al_{0.842})O_6$

TiO_2* corresponds to the total Ti content (no differentiation between Ti^{3+} and Ti^{4+}).

7.6 Weighted Burger Vectors

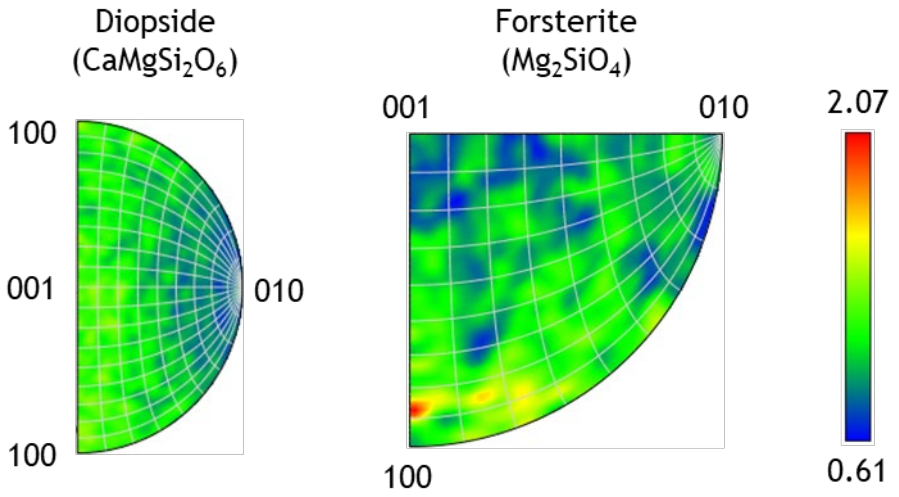

Figure 7.1. Weighted Burger Vector diagrams of the main mineral phases of the Cockerel's chondrule component. These display the magnitude and axial direction of lattice distortions resulting from dislocations in crystal lattices. Diagrams are calibrated to terrestrial mantle conditions.

7.7 Raw Oxygen Isotope SIMS Data

Table 7.11. Unprocessed Oxygen-isotope compositions of individual minerals in the CCCAI, CAI, and chondrule populations from the studied CM carbonaceous chondrites.

Date	Hour	Analysis Name	X	Y	Chamber Pressure	Primary Intensity	^{16}O	^{17}O	^{18}O	$^{18}O/^{16}O$	Error	$^{17}O/^{16}O$	Error	nb cycles
24-Apr-23<	11:54	Ipanko@1	1129	-1982	5.11E-09	2.48E-10	70855712.91	26833.73	141084.66	2.01E-03	3.23E-07	3.81E-04	1.05E-07	60
24-Apr-23<	12:04	Ipanko@2	1129	-2002	5.04E-09	2.48E-10	70524583.99	26708.44	140672.36	2.01E-03	2.51E-07	3.81E-04	1.29E-07	60
24-Apr-23<	12:14	Ipanko@3	1129	-2022	5.08E-09	2.46E-10	69934256.71	26503.1	139688.34	2.01E-03	2.21E-07	3.81E-04	1.22E-07	60
24-Apr-23<	12:24	Ipanko@4	1129	-2042	5.02E-09	2.44E-10	69295417.51	26249.4	138495.92	2.02E-03	2.41E-07	3.81E-04	1.63E-07	60
24-Apr-23<	12:34	Ipanko@5	1129	-2062	4.96E-09	2.45E-10	69474024.77	26329.28	138987.7	2.02E-03	2.72E-07	3.81E-04	1.21E-07	60
24-Apr-23<	12:44	Ipanko@6	1129	-2082	4.97E-09	2.44E-10	68961680.22	26141.95	138047.04	2.02E-03	2.50E-07	3.81E-04	1.11E-07	60
24-Apr-23<	12:54	SCOL@1	1830	2562	4.91E-09	2.43E-10	83326625.78	31284.7	163906.9	1.99E-03	2.87E-07	3.78E-04	1.00E-07	60
24-Apr-23<	13:04	SCOL@2	1830	2542	4.92E-09	2.44E-10	84202864.55	31630.65	165783.89	1.99E-03	2.78E-07	3.78E-04	1.40E-07	60
24-Apr-23<	13:14	SCOL@3	1830	2522	4.86E-09	2.45E-10	83760433.79	31487.84	164940.73	1.99E-03	2.74E-07	3.78E-04	9.87E-08	60
24-Apr-23<	13:24	SCOL@4	1830	2502	4.88E-09	2.43E-10	82881698.17	31146.62	163280.03	1.99E-03	2.42E-07	3.78E-04	1.00E-07	60
24-Apr-23<	13:34	SCOL@5	1830	2482	4.86E-09	2.44E-10	83311729.71	31303.11	164184.64	1.99E-03	2.32E-07	3.78E-04	1.15E-07	60
24-Apr-23<	13:44	SCOL@6	1830	2462	4.81E-09	2.44E-10	83185569.61	31244.36	163954.14	1.99E-03	2.51E-07	3.78E-04	1.23E-07	60
24-Apr-23<	14:09	Ipanko@7	1094	-2038	4.73E-09	2.44E-10	71459685	27109.17	143185.42	2.02E-03	2.86E-07	3.82E-04	1.08E-07	60
24-Apr-23<	14:19	Ipanko@8	1094	-2058	4.78E-09	2.43E-10	68135994.71	25831.26	136546.57	2.02E-03	2.37E-07	3.81E-04	1.21E-07	60
24-Apr-23<	14:29	Rockport@1	4726	-4389	4.77E-09	2.42E-10	93963154.48	35137.35	183156.74	1.97E-03	2.71E-07	3.76E-04	9.34E-08	60
24-Apr-23<	14:39	Rockport@2	4706	-4389	4.72E-09	2.43E-10	94482322.38	35320.18	184196.5	1.97E-03	2.00E-07	3.76E-04	1.19E-07	60
24-Apr-23<	14:48	Rockport@3	4686	-4389	4.77E-09	2.43E-10	94065672.92	35170.6	183399.91	1.97E-03	2.29E-07	3.76E-04	1.10E-07	60
24-Apr-23<	14:58	Rockport@4	4666	-4389	4.76E-09	2.41E-10	92801769.73	34708.9	181049.13	1.97E-03	2.40E-07	3.77E-04	1.28E-07	60
24-Apr-23<	15:08	Rockport@5	4646	-4389	4.68E-09	2.42E-10	93379126.98	34924.43	182124.88	1.97E-03	2.60E-07	3.77E-04	9.49E-08	60
24-Apr-23<	15:18	Rockport@6	4606	-4389	4.71E-09	2.42E-10	93088119.73	34806.41	181604.77	1.97E-03	2.86E-07	3.76E-04	1.10E-07	60

Date	Hour	Analysis Name	X	Y	Chamber Pressure	Primary Intensity	^{16}O	^{17}O	^{18}O	$^{18}O/^{16}O$	Error	$^{17}O/^{16}O$	Error	nb cycles
24-Apr-23<	17:05	Ipanko@9	1094	-2078	4.54E-09	2.40E-10	67604397.35	25620.7	135595.7	2.02E-03	2.90E-07	3.81E-04	1.27E-07	60
24-Apr-23<	19:06	CAI-A16-Fo@1	-5021	-4350	1.53E-08	2.33E-10	67032215.26	24847.26	128926.64	1.94E-03	3.42E-07	3.73E-04	1.17E-07	60
24-Apr-23<	19:16	CAI-A16-Fo@2	-5081	-4338	1.47E-08	2.33E-10	70061611.37	26006.3	135013.03	1.94E-03	3.09E-07	3.73E-04	1.34E-07	60
24-Apr-23<	19:26	CAI-A16-Fo@3	-5107	-4340	1.46E-08	2.34E-10	71721892.44	26612.93	138267.54	1.94E-03	2.64E-07	3.73E-04	1.24E-07	60
24-Apr-23<	19:36	CAI-A16-Fo@04	-5190	-4232	1.44E-08	2.32E-10	70937904.95	26330.68	136747.66	1.94E-03	2.27E-07	3.73E-04	1.21E-07	60
24-Apr-23<	19:46	CAI-A16-Fo@05	-5138	-4263	1.42E-08	2.31E-10	75748066.19	28109.37	145886.64	1.94E-03	2.95E-07	3.73E-04	1.06E-07	60
24-Apr-23<	19:46	CAI-A16-Fo@05	-5138	-4263	1.42E-08	2.31E-10	75748066.19	28109.37	145886.64	1.93E-03	2.93E-07	3.73E-04	1.06E-07	60
24-Apr-23<	19:56	CAI-A16-Fo@06	-5095	-4390	1.41E-08	2.33E-10	69008118.67	25592.62	133068.56	1.94E-03	2.81E-07	3.73E-04	1.22E-07	60
24-Apr-23<	20:06	CAI-A16-Fo@07	-5040	-4436	1.40E-08	2.32E-10	55090298.94	20238.81	105209.82	1.92E-03	3.56E-07	3.69E-04	1.33E-07	60
24-Apr-23<	20:16	CAI-A16-Fo@08	-5040	-4474	1.38E-08	2.31E-10	62298743.91	23181.92	120407.15	1.94E-03	3.65E-07	3.74E-04	1.28E-07	60
24-Apr-23<	20:26	CAI-A16-Fo@09	-5022	-4536	1.36E-08	2.32E-10	67753756.84	25142.67	130581.26	1.94E-03	3.05E-07	3.73E-04	1.16E-07	60
24-Apr-23<	20:36	CAI-A16-Fo@10	-5001	-4506	1.36E-08	2.32E-10	68590134.78	25396.67	131799.25	1.93E-03	3.50E-07	3.73E-04	1.14E-07	60
24-Apr-23<	20:46	CAI-A16-Fo@11	-5006	-4560	1.37E-08	2.30E-10	66182562.98	24541.39	127488.63	1.93E-03	2.77E-07	3.73E-04	1.26E-07	60
24-Apr-23<	20:56	CAI-A16-Fo@12	-5010	-4582	1.33E-08	2.32E-10	64203771.45	23797.39	123587	1.93E-03	3.13E-07	3.73E-04	1.20E-07	60
24-Apr-23<	21:06	CAI-A16-Fo@13	-5024	-4592	1.33E-08	2.32E-10	66529867.58	24689.3	128324.62	1.94E-03	2.90E-07	3.73E-04	1.42E-07	60
24-Apr-23<	21:16	CAI-A16-Fo@14	-5123	-4425	1.31E-08	2.30E-10	66050806.22	24509.03	127377.28	1.94E-03	2.64E-07	3.73E-04	1.32E-07	60
24-Apr-23<	21:26	CAI-A16-Fo@15	-5036	-4385	1.31E-08	2.31E-10	68668087.27	25511.72	132631.74	1.94E-03	3.10E-07	3.74E-04	1.13E-07	60
24-Apr-23<	21:36	CAI-A16-Sp@1	-5093	-4425	1.30E-08	2.31E-10	29008771.95	10854.85	56210.65	1.94E-03	4.80E-07	3.76E-04	1.68E-07	60
24-Apr-23<	21:46	CAI-A16-Sp@2	-5052	-4409	1.29E-08	2.29E-10	50154537.07	18258.43	94542.14	1.89E-03	5.37E-07	3.66E-04	1.53E-07	60
24-Apr-23<	21:56	CAI-A16-Sp@3	-5068	-4471	1.29E-08	2.29E-10	75628899.55	28242.56	146701.58	1.95E-03	2.98E-07	3.76E-04	1.20E-07	60
24-Apr-23<	22:06	CAI-A16-Sp@4	-4984	-4486	1.27E-08	2.30E-10	82034733.64	30916.45	160803.57	1.97E-03	2.80E-07	3.79E-04	1.24E-07	60
24-Apr-23<	22:16	CAI-A16-Sp@5	-5039	-4523	1.28E-08	2.26E-10	73842208.88	27564.14	143333.76	1.95E-03	3.04E-07	3.76E-04	1.36E-07	60
24-Apr-23<	22:26	CAI-A16-Sp@6	-5033	-4570	1.26E-08	2.25E-10	65220389.73	24185.97	125805.34	1.94E-03	2.40E-07	3.73E-04	1.33E-07	60
24-Apr-23<	22:36	CAI-A16-Sp@7	-5011	-4455	1.26E-08	2.26E-10	64571823.94	24170.07	125706.62	1.96E-03	3.69E-07	3.76E-04	1.29E-07	60

Date	Hour	Analysis Name	X	Y	Chamber Pressure	Primary Intensity	^{16}O	^{17}O	^{18}O	$^{18}O/^{16}O$	Error	$^{17}O/^{16}O$	Error	nb cycles
24-Apr-23<	22:46	CAI-A16-Sp@8	-4976	-4462	1.26E-08	2.25E-10	58405969.43	21969.49	114313.43	1.97E-03	2.90E-07	3.78E-04	1.30E-07	60
24-Apr-23<	22:56	CAI-A14-Sp@1	-3466	-4327	1.26E-08	2.24E-10	66681007.56	24508.63	127242.81	1.92E-03	3.25E-07	3.70E-04	1.43E-07	60
24-Apr-23<	23:06	CAI-A14-Sp@2	-3488	-4336	1.26E-08	2.25E-10	52231817.28	19161.05	99357.33	1.91E-03	3.80E-07	3.69E-04	1.25E-07	60
24-Apr-23<	23:16	CAI-A14-Sp@3	-3500	-4361	1.26E-08	2.24E-10	67842645.58	25371.02	131871.76	1.95E-03	3.06E-07	3.76E-04	1.31E-07	60
24-Apr-23<	23:26	CAI-A7-Sp@1	-1875	-4422	1.27E-08	2.23E-10	68117276.81	25241.49	131305.24	1.94E-03	6.62E-07	3.73E-04	1.43E-07	60
24-Apr-23<	23:36	CAI-A7-Sp@2	-1792	-4438	1.25E-08	2.24E-10	66137725.46	24119.56	125246.76	1.90E-03	4.90E-07	3.67E-04	1.39E-07	60
24-Apr-23<	23:46	CAI-A7-Sp@3	-1831	-4514	1.26E-08	2.23E-10	64512389	23131.17	120296.95	1.87E-03	2.80E-07	3.61E-04	1.24E-07	60
24-Apr-23<	23:56	CAI-A7-Sp@4	-1841	-4558	1.25E-08	2.22E-10	63184588.29	22764.73	118291.11	1.88E-03	3.01E-07	3.62E-04	1.13E-07	60
25-Apr-23<	00:07	CAI-A7-Sp@5	-1868	-4505	1.23E-08	2.23E-10	59002762.83	21488.89	111816.03	1.90E-03	3.40E-07	3.66E-04	1.44E-07	60
25-Apr-23<	00:17	CAI-E7-Sp@1	-1723	-5115	1.24E-08	2.22E-10	64375857.79	23080.24	120069.97	1.87E-03	2.83E-07	3.61E-04	1.39E-07	60
25-Apr-23<	00:27	CAI-E6-Sp@1	-1095	-5131	1.24E-08	2.21E-10	73422372.67	27573.04	143795.49	1.97E-03	3.69E-07	3.78E-04	1.05E-07	60
25-Apr-23<	00:37	CAI-E6-Sp@2	-1078	-5142	1.24E-08	2.22E-10	68172942.85	24779.16	128831.15	1.90E-03	4.10E-07	3.66E-04	1.33E-07	60
25-Apr-23<	00:47	CAI-A11-Sp@1	-869	-4840	1.25E-08	2.23E-10	70678430.63	25815.32	134240.68	1.91E-03	3.76E-07	3.67E-04	1.51E-07	60
25-Apr-23<	00:57	CAI-A11-Sp@2	-891	-4866	1.25E-08	2.21E-10	67610816.21	25149.1	131057.34	1.95E-03	2.86E-07	3.74E-04	1.03E-07	60
25-Apr-23<	01:17	CAI-A22-Sp@2	-249	-2235	1.25E-08	2.23E-10	57349000.8	21391.29	111598	1.95E-03	3.76E-07	3.75E-04	1.39E-07	60
25-Apr-23<	01:17	CAI-A22-Sp@2	-249	-2235	1.25E-08	2.23E-10	57349000.8	21391.29	111598	1.95E-03	3.76E-07	3.75E-04	1.39E-07	60
25-Apr-23<	01:27	CAI-A21-Sp@1	-1422	-1566	1.23E-08	2.22E-10	75713452.35	27724.08	144052.59	1.91E-03	3.52E-07	3.68E-04	1.02E-07	60
25-Apr-23<	01:37	CAI-A23-Sp@1	-38	-910	1.25E-08	2.22E-10	67777708.49	25424.42	132316.83	1.96E-03	3.23E-07	3.77E-04	1.11E-07	60
25-Apr-23<	01:47	CAI-A23-Sp@2	-65	-938	1.24E-08	2.22E-10	63619524.7	23671.03	123309.08	1.95E-03	3.06E-07	3.74E-04	1.39E-07	60
25-Apr-23<	01:57	CAI-A23-Sp@3	-64	-916	1.24E-08	2.20E-10	67641250.99	25228.36	131330.81	1.95E-03	3.40E-07	3.75E-04	1.22E-07	60
25-Apr-23<	02:07	CAI-A24-Sp@1	744	-929	1.24E-08	2.20E-10	55639980.99	20884.8	108862.22	1.96E-03	4.24E-07	3.77E-04	1.60E-07	60
25-Apr-23<	02:17	CAI-A24-Sp@2	711	-921	1.24E-08	2.21E-10	58328472.46	21458.24	111740.82	1.92E-03	4.62E-07	3.70E-04	1.28E-07	60
25-Apr-23<	02:27	CAI-S-Sp@1	1726	-660	1.26E-08	2.19E-10	73502931.64	27604.76	143874.69	1.97E-03	3.10E-07	3.78E-04	1.55E-07	60
25-Apr-23<	02:37	CAI-S-Sp@2	1701	-638	1.25E-08	2.17E-10	49841593.03	17901.62	92999.54	1.87E-03	2.67E-07	3.61E-04	1.36E-07	60

Date	Hour	Analysis Name	X	Y	Chamber Pressure	Primary Intensity	^{16}O	^{17}O	^{18}O	$^{18}O/^{16}O$	Error	$^{17}O/^{16}O$	Error	nb cycles
25-Apr-23<	02:47	CAI-S-Sp@3	1700	-674	1.23E-08	2.18E-10	64999955.91	24463.82	127567	1.97E-03	3.21E-07	3.79E-04	1.13E-07	60
25-Apr-23<	02:57	CAI-B1-Sp@1	-1078	1004	1.24E-08	2.17E-10	61907406.98	23243.8	121252.51	1.97E-03	2.82E-07	3.78E-04	1.67E-07	60
25-Apr-23<	08:36	Ipanko@10	1054	-1406	7.84E-09	2.07E-10	59193640.78	22458.28	117678.98	2.00E-03	3.15E-07	3.82E-04	1.35E-07	60
25-Apr-23<	08:46	Ipanko@11	1054	-1426	7.66E-09	2.07E-10	59437045.26	22549.45	118178.77	2.00E-03	3.34E-07	3.82E-04	1.17E-07	60
25-Apr-23<	08:56	Ipanko@12	1054	-1446	7.42E-09	2.06E-10	59439863.44	22539.52	118280.23	2.00E-03	3.16E-07	3.81E-04	1.33E-07	60
25-Apr-23<	09:06	Ipanko@13	1054	-1466	7.26E-09	2.05E-10	58234763.9	22082.5	115918.66	2.00E-03	3.11E-07	3.82E-04	1.34E-07	60
25-Apr-23<	09:16	SCOL@7	1876	2698	7.06E-09	2.06E-10	71402843.3	26851.11	139621.29	1.96E-03	2.25E-07	3.78E-04	1.20E-07	60
25-Apr-23<	09:26	SCOL@8	1876	2678	6.97E-09	2.05E-10	71026519.63	26701.57	138887.17	1.96E-03	3.51E-07	3.78E-04	1.34E-07	60
25-Apr-23<	09:36	SCOL@9	1876	2658	6.87E-09	2.03E-10	69954278.79	26314.23	136853.25	1.96E-03	2.38E-07	3.78E-04	1.22E-07	60
25-Apr-23<	09:46	SCOL@10	1876	2638	6.82E-09	2.04E-10	70237861.65	26423.9	137522.68	1.97E-03	2.68E-07	3.79E-04	1.16E-07	60
25-Apr-23<	09:56	Rockport@7	4713	-4415	6.63E-09	2.04E-10	79526537.31	29748.64	154212.26	1.95E-03	2.57E-07	3.77E-04	1.10E-07	60
25-Apr-23<	10:06	Rockport@8	4693	-4415	6.50E-09	2.02E-10	78268011.53	29286.03	151778.32	1.95E-03	2.69E-07	3.77E-04	9.54E-08	60
25-Apr-23<	10:16	Rockport@9	4673	-4415	6.47E-09	2.02E-10	78396942.56	29350.33	152025.51	1.95E-03	2.88E-07	3.77E-04	1.28E-07	60
25-Apr-23<	10:26	Rockport@10	4653	-4415	6.44E-09	2.03E-10	78745082.59	29467.33	152688.16	1.95E-03	2.62E-07	3.77E-04	1.12E-07	60
25-Apr-23<	11:50	CAI-64-Sp@1	-568	-1592	9.41E-09	2.26E-10	68612774.68	24590.43	127940.15	1.87E-03	2.81E-07	3.61E-04	1.16E-07	60
25-Apr-23<	12:00	CAI-64-Sp@2	-406	-1534	9.38E-09	2.27E-10	72762991.6	26259.53	136562.21	1.89E-03	2.79E-07	3.63E-04	1.16E-07	60
25-Apr-23<	12:10	CAI-64-Sp@3	-498	-1601	9.28E-09	2.25E-10	69860887.77	25107.64	130526.83	1.88E-03	2.86E-07	3.62E-04	1.10E-07	60
25-Apr-23<	12:20	CAI-64-Sp@4	-411	-1600	9.27E-09	2.24E-10	70583342.28	25380.33	132130.05	1.88E-03	2.10E-07	3.62E-04	1.33E-07	60
25-Apr-23<	12:30	CAI-64-Sp@5	-546	-1557	9.27E-09	2.26E-10	70624722.76	25378.47	132131.04	1.88E-03	2.49E-07	3.62E-04	9.73E-08	60
25-Apr-23<	12:40	CAI-65-Sp@1	-344	-1909	9.28E-09	2.26E-10	75811580.03	27630.08	143852.6	1.91E-03	3.15E-07	3.67E-04	1.22E-07	60
25-Apr-23<	12:50	CAI-65-Sp@2	-362	-1907	9.28E-09	2.25E-10	65357867.89	23483.77	122231.91	1.88E-03	3.08E-07	3.61E-04	1.09E-07	60
25-Apr-23<	13:00	CAI-61-Sp@1	331	-1734	9.28E-09	2.24E-10	63280186.97	22621.37	117712.48	1.87E-03	3.36E-07	3.59E-04	1.20E-07	60
25-Apr-23<	13:10	CAI-60-Sp@1	596	-1700	9.31E-09	2.23E-10	68408431.5	24590	128418.61	1.89E-03	2.59E-07	3.62E-04	1.32E-07	60
25-Apr-23<	13:20	CAI-57-Sp@1	888	-1876	9.31E-09	2.21E-10	81717310.01	30404.88	158428.32	1.95E-03	2.73E-07	3.74E-04	1.28E-07	60

Date	Hour	Analysis Name	X	Y	Chamber Pressure	Primary Intensity	^{16}O	^{17}O	^{18}O	$^{18}O/^{16}O$	Error	$^{17}O/^{16}O$	Error	nb cycles
25-Apr-23<	13:30	CAI-57-Sp@2	897	-1892	9.32E-09	2.22E-10	78365473.88	29315.93	152925.69	1.96E-03	2.32E-07	3.76E-04	1.23E-07	60
25-Apr-23<	13:40	CAI-63-Sp@1	776	-2370	9.31E-09	2.22E-10	73562005.57	27510.54	143370.59	1.96E-03	3.16E-07	3.76E-04	1.33E-07	60
25-Apr-23<	13:50	CAI-63-Sp@2	775	-2400	9.38E-09	2.21E-10	71497268.22	26778.93	139574.77	1.96E-03	3.04E-07	3.77E-04	1.18E-07	60
25-Apr-23<	14:00	CAI-51-Sp@1	1369	-631	9.26E-09	2.21E-10	63273511.06	22615.94	117694.48	1.87E-03	3.15E-07	3.60E-04	1.28E-07	60
25-Apr-23<	14:10	CAI-51-Sp@2	1388	-579	9.35E-09	2.21E-10	71929910.03	26025.1	135469.83	1.89E-03	2.56E-07	3.64E-04	1.32E-07	60
25-Apr-23<	14:20	CAI-51-Dio@1	1330	-496	9.35E-09	2.20E-10	58778531.76	22017.35	114534.03	1.96E-03	3.22E-07	3.77E-04	1.38E-07	60
25-Apr-23<	14:30	CAI-51-Dio@2	1376	-510	9.36E-09	2.20E-10	76079754.59	28574.3	149033.41	1.97E-03	4.44E-07	3.78E-04	1.06E-07	60
25-Apr-23<	14:40	CAI-51-Dio@3	1382	-476	9.43E-09	2.20E-10	70293930.28	25291.16	131765.8	1.88E-03	2.94E-07	3.62E-04	1.17E-07	60
25-Apr-23<	14:50	CAI-29-Sp@1	2468	-249	9.37E-09	2.19E-10	63242891.05	22609.28	117672.89	1.87E-03	3.37E-07	3.60E-04	1.13E-07	60
25-Apr-23<	15:00	CAI-29-Sp@2	2468	-238	9.46E-09	2.19E-10	64338960.68	23013.61	119803.49	1.87E-03	2.79E-07	3.60E-04	1.39E-07	60
25-Apr-23<	15:10	CAI-29-Sp@3	2465	-220	9.41E-09	2.19E-10	70468587.18	25441.06	132641.02	1.89E-03	2.66E-07	3.63E-04	1.22E-07	60
25-Apr-23<	15:20	CAI-29-Sp@4	2461	-196	9.41E-09	2.18E-10	68641937.41	24615.53	128382.25	1.88E-03	2.66E-07	3.61E-04	1.25E-07	60
25-Apr-23<	15:30	CAI-29-Sp@5	2463	-170	9.42E-09	2.18E-10	69560369.41	24952.69	130077.47	1.88E-03	4.26E-07	3.61E-04	1.26E-07	60
25-Apr-23<	15:40	CAI-29-Sp@6	2464	-136	9.41E-09	2.19E-10	78434155.32	28084.51	146182.49	1.87E-03	2.50E-07	3.60E-04	1.10E-07	60
25-Apr-23<	15:50	CAI-29-Sp@7	2462	-107	9.41E-09	2.18E-10	70583003.94	25478.64	132767.95	1.89E-03	4.77E-07	3.63E-04	1.49E-07	60
25-Apr-23<	16:00	CAI-29-Sp@8	2490	-137	9.35E-09	2.17E-10	62900137.87	22524.75	117254.77	1.87E-03	3.35E-07	3.60E-04	1.36E-07	60
25-Apr-23<	16:10	CAI-29-Sp@9	2500	-156	9.41E-09	2.17E-10	61057578.92	21814.48	113704.32	1.87E-03	2.52E-07	3.59E-04	1.38E-07	60
25-Apr-23<	16:20	CAI-25b-Sp@1	3901	-106	9.36E-09	2.16E-10	65127437.21	23417.84	121961.54	1.88E-03	4.03E-07	3.62E-04	1.47E-07	60
25-Apr-23<	16:29	CAI-25b-Sp@2	3881	-115	9.52E-09	2.15E-10	66460611.76	23896.76	124348.66	1.88E-03	4.58E-07	3.62E-04	1.80E-07	27
25-Apr-23<	16:39	CAI-25b-Sp@3	3856	-113	9.46E-09	2.16E-10	73686810.45	26756.41	139210.71	1.90E-03	2.86E-07	3.65E-04	1.21E-07	60
25-Apr-23<	16:49	CAI-25b-Sp@4	3860	-132	9.53E-09	2.16E-10	89072989.97	32889.48	171574.34	1.93E-03	3.50E-07	3.72E-04	1.13E-07	60
25-Apr-23<	16:59	CAI-25b-Sp@5	3853	-214	9.39E-09	2.14E-10	70281578.32	25370.8	132186.82	1.89E-03	2.93E-07	3.63E-04	9.53E-08	60
25-Apr-23<	17:09	CAI-25b-Sp@6	3888	-244	9.46E-09	2.15E-10	67379837.4	24347.81	126861.75	1.89E-03	2.88E-07	3.64E-04	1.28E-07	60
25-Apr-23<	17:30	SCOL@11	1854	2561	8.12E-09	2.42E-10	83725740.57	31473.25	163988.31	1.97E-03	2.88E-07	3.78E-04	1.13E-07	60

Date	Hour	Analysis Name	X	Y	Chamber Pressure	Primary Intensity	^{16}O	^{17}O	^{18}O	$^{18}O/^{16}O$	Error	$^{17}O/^{16}O$	Error	nb cycles
25-Apr-23<	17:40	SCOL@12	1854	2541	7.66E-09	2.45E-10	84439526.96	31757.15	165389.55	1.97E-03	2.32E-07	3.79E-04	1.09E-07	60
25-Apr-23<	17:51	SCOL@13	1854	2521	7.45E-09	2.46E-10	84922045.36	31922.33	166341.85	1.97E-03	2.93E-07	3.78E-04	9.85E-08	60
25-Apr-23<	19:20	CAI-78-Fo@1	1998	3836	2.74E-08	2.44E-10	79004507.77	29273.21	151748.86	1.93E-03	2.92E-07	3.73E-04	1.14E-07	60
25-Apr-23<	19:30	CAI-78-Fo@2	1895	3441	2.69E-08	2.43E-10	77696046.8	28788.2	149402.28	1.93E-03	2.48E-07	3.73E-04	1.40E-07	60
25-Apr-23<	19:40	CAI-78-Fo@3	1643	3578	2.64E-08	2.42E-10	78161402.87	28957.1	150334.35	1.93E-03	2.20E-07	3.73E-04	1.14E-07	60
25-Apr-23<	19:50	CAI-66-Fo@1	2848	5224	2.65E-08	2.43E-10	76529615.42	27588.36	143082.15	1.88E-03	2.78E-07	3.63E-04	1.03E-07	60
25-Apr-23<	20:00	CAI-66-Sp@1	2901	5187	2.60E-08	2.42E-10	78413552.96	28609.85	148415.43	1.90E-03	4.10E-07	3.67E-04	1.30E-07	60
25-Apr-23<	20:10	CAI-69-Sp@1	2546	5343	2.57E-08	2.41E-10	84522435.36	31291.02	162454.25	1.93E-03	2.57E-07	3.73E-04	1.42E-07	60
25-Apr-23<	20:20	CAI-69-Sp@2	2524	5345	2.52E-08	2.42E-10	70008128.43	25894.7	133501.51	1.92E-03	4.60E-07	3.72E-04	1.18E-07	60
26-Apr-23<	07:32	CAI-68-Sp@2	2666	5055	1.63E-08	2.24E-10	67935369.39	24980.01	130001.29	1.92E-03	2.40E-07	3.70E-04	1.56E-07	60
26-Apr-23<	07:42	CAI-68-Sp@3	2699	5096	1.62E-08	2.25E-10	80171880.43	29961.81	156290.72	1.96E-03	2.22E-07	3.76E-04	1.22E-07	60
26-Apr-23<	07:52	CAI-56-Fo@1	4398	6228	1.63E-08	2.26E-10	67782441.36	25059.9	130278.16	1.93E-03	2.97E-07	3.72E-04	1.14E-07	60
26-Apr-23<	08:02	CAI-56-Fo@2	4442	6416	1.63E-08	2.25E-10	66190509.06	24427.93	126776.2	1.92E-03	2.69E-07	3.71E-04	1.27E-07	60
26-Apr-23<	08:12	CAI-56-Fo@3	4697	6417	1.62E-08	2.25E-10	50152558.11	18323.21	94199.22	1.89E-03	3.13E-07	3.67E-04	1.35E-07	60
26-Apr-23<	08:22	CAI-56-Sp@1	4602	6459	1.61E-08	2.25E-10	44866110.22	16241.39	82826.27	1.85E-03	4.05E-07	3.64E-04	1.29E-07	60
26-Apr-23<	08:32	CAI-56-Sp@2	4457	6377	1.62E-08	2.24E-10	58403465.02	21390.82	110415.09	1.90E-03	3.25E-07	3.68E-04	1.40E-07	60
26-Apr-23<	08:42	CAI-56-Sp@3	4519	6408	1.62E-08	2.23E-10	59839653	22048.04	114320.81	1.92E-03	2.70E-07	3.71E-04	1.48E-07	60
26-Apr-23<	08:52	CAI-56-Sp@4	4347	6299	1.60E-08	2.24E-10	60168821.86	22204.88	115152.03	1.92E-03	2.82E-07	3.71E-04	1.23E-07	60
26-Apr-23<	09:02	CAI-55-Sp@1	4399	6669	1.60E-08	2.23E-10	47341304.98	16969.03	87334.79	1.85E-03	4.80E-07	3.60E-04	1.70E-07	60
26-Apr-23<	09:12	CAI-55-Sp@2	4417	6720	1.59E-08	2.22E-10	51483679.77	18887.21	96426.26	1.88E-03	5.18E-07	3.69E-04	1.13E-07	60
26-Apr-23<	09:22	CAI-55-Sp@3	4513	6784	1.59E-08	2.23E-10	50969344.92	18186.67	92977.29	1.83E-03	3.47E-07	3.59E-04	1.30E-07	60
26-Apr-23<	09:59	Ipanko@14	1166	-1964	1.09E-08	2.22E-10	63513275.17	24072.07	126683.72	2.00E-03	3.12E-07	3.81E-04	1.28E-07	60
26-Apr-23<	10:09	Ipanko@15	1166	-1984	9.95E-09	2.21E-10	62929536.85	23868.14	125505.04	2.00E-03	3.04E-07	3.82E-04	1.21E-07	60
26-Apr-23<	10:19	Ipanko@16	1166	-2004	9.40E-09	2.20E-10	62483051.78	23695.21	124727.27	2.00E-03	2.98E-07	3.81E-04	1.34E-07	60

Date	Hour	Analysis Name	X	Y	Chamber Pressure	Primary Intensity	^{16}O	^{17}O	^{18}O	$^{18}O/^{16}O$	Error	$^{17}O/^{16}O$	Error	nb cycles
26-Apr-23<	10:29	Ipanko@17	1166	-2024	9.02E-09	2.21E-10	62682023.24	23763	125072.35	2.00E-03	3.44E-07	3.81E-04	1.36E-07	60
26-Apr-23<	10:39	SCOL@14	1803	2457	8.59E-09	2.20E-10	75663507.72	28453.68	148377.46	1.97E-03	2.39E-07	3.78E-04	1.23E-07	60
26-Apr-23<	10:50	SCOL@15	1803	2437	8.53E-09	2.19E-10	74853572.61	28129.15	146806.23	1.97E-03	2.56E-07	3.78E-04	1.02E-07	60
26-Apr-23<	11:00	SCOL@16	1803	2417	8.26E-09	2.19E-10	74615537.96	28053.6	146255.85	1.97E-03	2.67E-07	3.78E-04	1.17E-07	60
26-Apr-23<	11:10	SCOL@17	1803	2397	7.90E-09	2.18E-10	74541539.61	28016.99	146193.19	1.97E-03	2.69E-07	3.78E-04	1.22E-07	60
26-Apr-23<	11:20	Rockport@11	4613	-4433	7.93E-09	2.17E-10	83021501.19	31033.76	161248.97	1.95E-03	2.77E-07	3.76E-04	9.94E-08	60
26-Apr-23<	11:30	Rockport@12	4593	-4433	7.79E-09	2.17E-10	83035340.67	31062.41	161307.33	1.95E-03	2.52E-07	3.77E-04	9.58E-08	60
26-Apr-23<	11:40	Rockport@13	4573	-4433	7.62E-09	2.18E-10	82944070.37	31021.23	161092.87	1.95E-03	2.83E-07	3.76E-04	1.06E-07	60
26-Apr-23<	11:50	Rockport@14	4553	-4433	7.56E-09	2.16E-10	82171429.3	30725.29	159630.19	1.95E-03	2.23E-07	3.76E-04	9.24E-08	60
26-Apr-23<	12:23	CAI-68-Sp@1	2673	5051	1.47E-08	2.14E-10	62573694.57	22557.91	117445.89	1.89E-03	2.87E-07	3.63E-04	1.35E-07	60
26-Apr-23<	12:33	CAI-68-Sp@2	2660	5059	1.49E-08	2.14E-10	66795698.38	24177.49	126034.07	1.90E-03	2.86E-07	3.64E-04	1.36E-07	60
26-Apr-23<	12:43	CAI-68-Sp@3	2693	5099	1.50E-08	2.14E-10	64763616.71	23508.22	122606.52	1.90E-03	2.66E-07	3.65E-04	1.04E-07	60
26-Apr-23<	12:53	CAI-56-Fo@1	4412	6219	1.51E-08	2.13E-10	62787977.91	23266.38	121222.53	1.94E-03	2.76E-07	3.73E-04	1.36E-07	60
26-Apr-23<	13:03	CAI-56-Fo@2	4455	6410	1.52E-08	2.12E-10	58706162.7	21667.59	112446.37	1.92E-03	3.47E-07	3.71E-04	1.36E-07	60
26-Apr-23<	13:13	CAI-56-Fo@3	4709	6406	1.48E-08	2.13E-10	59827040.2	22108.38	114904.27	1.93E-03	2.76E-07	3.72E-04	1.33E-07	60
26-Apr-23<	13:23	CAI-56-Sp@1	4597	6458	1.51E-08	2.11E-10	59159299.11	21890.48	113942.81	1.93E-03	3.09E-07	3.72E-04	1.35E-07	60
26-Apr-23<	13:33	CAI-56-Sp@2	4459	6374	1.49E-08	2.10E-10	61722532.07	22879.47	119246.66	1.94E-03	3.22E-07	3.73E-04	1.42E-07	60
26-Apr-23<	13:43	CAI-56-Sp@3	4521	6405	1.48E-08	2.10E-10	57415570.96	21254.37	110798.39	1.94E-03	3.34E-07	3.72E-04	1.41E-07	60
26-Apr-23<	13:53	CAI-56-Sp@4	4359	6290	1.49E-08	2.09E-10	63275849.14	23464.69	122481.78	1.94E-03	2.71E-07	3.73E-04	1.45E-07	60
26-Apr-23<	14:03	CAI-55-Sp@1	4393	6666	1.47E-08	2.08E-10	46843771.44	16648.02	85960.84	1.84E-03	3.74E-07	3.57E-04	1.37E-07	60
26-Apr-23<	14:13	CAI-55-Sp@2	4414	6685	1.46E-08	2.09E-10	51551047.57	18483.74	95561.3	1.86E-03	2.88E-07	3.60E-04	1.30E-07	60
26-Apr-23<	14:23	CAI-55-Sp@3	4514	6786	1.47E-08	2.09E-10	57753430.61	20729.35	107381.54	1.87E-03	3.07E-07	3.61E-04	1.60E-07	60
26-Apr-23<	14:33	CAI-55-Sp@4	4450	6720	1.48E-08	2.08E-10	57678921.93	20657.48	106859.97	1.86E-03	2.94E-07	3.60E-04	1.43E-07	60
26-Apr-23<	14:52	SCOL@18	1935	2585	1.05E-08	2.08E-10	71099956.62	26713.26	139477.51	1.97E-03	2.52E-07	3.78E-04	1.16E-07	60

Date	Hour	Analysis Name	X	Y	Chamber Pressure	Primary Intensity	^{16}O	^{17}O	^{18}O	$^{18}O/^{16}O$	Error	$^{17}O/^{16}O$	Error	nb cycles
26-Apr-23<	15:02	SCOL@19	1935	2565	9.56E-09	2.07E-10	70118413.38	26350.25	137497.21	1.97E-03	2.91E-07	3.78E-04	1.09E-07	60
26-Apr-23<	15:12	SCOL@20	1935	2545	9.10E-09	2.07E-10	70395271.17	26459.6	138096.23	1.97E-03	3.15E-07	3.78E-04	1.32E-07	60
26-Apr-23<	17:13	CAI-53-Sp@1	3901	6119	1.40E-08	2.01E-10	3338225.95	1243.71	6440.73	1.91E-03	1.17E-06	3.70E-04	6.67E-07	60
26-Apr-23<	17:23	CAI-53-Sp@2	3923	6113	1.41E-08	2.03E-10	4052796.75	1510.11	7833.4	1.92E-03	1.17E-06	3.70E-04	4.97E-07	60
26-Apr-23<	17:33	CAI-53-Sp@3	3894	6082	1.40E-08	2.02E-10	58383579.03	20918.57	108999.86	1.87E-03	2.63E-07	3.60E-04	1.41E-07	60
26-Apr-23<	17:43	CAI-53-Sp@4	3955	6085	1.39E-08	2.01E-10	60326673.67	21603.56	112512.32	1.87E-03	3.43E-07	3.60E-04	1.40E-07	60
26-Apr-23<	17:53	CAI-52-Sp@1	3720	5920	1.39E-08	2.01E-10	72868307.41	26715.18	139487.34	1.92E-03	2.94E-07	3.69E-04	1.23E-07	60
26-Apr-23<	18:03	CAI-49-Sp@1	3493	5905	1.39E-08	2.01E-10	59638420.96	21468.19	111736.53	1.88E-03	3.09E-07	3.62E-04	1.65E-07	60
26-Apr-23<	18:13	CAI-49-Sp@2	3489	5921	1.39E-08	1.99E-10	60607629.25	22455.42	117143.16	1.94E-03	4.05E-07	3.73E-04	1.48E-07	60
26-Apr-23<	18:23	CAI-49-Sp@3	3502	5922	1.41E-08	1.99E-10	62897387.74	22896	119215.18	1.90E-03	2.67E-07	3.66E-04	1.31E-07	60
26-Apr-23<	18:33	CAI-38-Sp@1	2075	6667	1.38E-08	2.00E-10	57190334.35	20477.84	106826.51	1.88E-03	2.90E-07	3.60E-04	9.49E-08	60
26-Apr-23<	18:43	CAI-38-Sp@2	2102	6709	1.36E-08	1.98E-10	59843295.27	21511.15	112140.87	1.88E-03	3.48E-07	3.62E-04	1.09E-07	60
26-Apr-23<	18:53	CAI-64-Sp@1	3910	3034	1.36E-08	2.00E-10	69821635.57	25974.55	135536.39	1.95E-03	2.81E-07	3.74E-04	1.24E-07	60
26-Apr-23<	19:03	CAI-64-Sp@2	3955	3092	1.37E-08	2.00E-10	69921243.21	26008.58	135823.71	1.95E-03	2.65E-07	3.74E-04	9.20E-08	60
26-Apr-23<	19:13	CAI-64-Sp@3	3994	3144	1.36E-08	1.99E-10	68799942.32	25590.16	133562.32	1.95E-03	2.21E-07	3.74E-04	1.35E-07	60
26-Apr-23<	19:23	CAI-64-Sp@4	4103	3139	1.36E-08	1.99E-10	68681004.38	25542.42	133378.26	1.95E-03	2.69E-07	3.74E-04	1.22E-07	60
26-Apr-23<	19:33	CAI-64-Sp@5	3632	3160	1.36E-08	2.00E-10	63622163.31	23670.01	123583.85	1.95E-03	3.17E-07	3.74E-04	1.46E-07	60
26-Apr-23<	19:43	CAI-64-Sp@6	3727	3130	1.37E-08	1.99E-10	38834789.06	14500.85	75944.26	1.96E-03	3.72E-07	3.75E-04	1.33E-07	60
26-Apr-23<	19:53	CAI-79-Sp@1	5806	2871	1.37E-08	1.99E-10	66176686.58	23744.6	123916.85	1.88E-03	2.27E-07	3.61E-04	1.19E-07	60
26-Apr-23<	20:03	CAI-79-Sp@2	5842	2857	1.38E-08	2.00E-10	65291343.09	23402.98	122080.06	1.88E-03	3.01E-07	3.61E-04	1.12E-07	60
26-Apr-23<	20:14	CAI-79-Sp@3	5784	2837	1.37E-08	1.99E-10	64687512.76	23215.34	121184.68	1.88E-03	2.77E-07	3.61E-04	1.43E-07	60
26-Apr-23<	20:24	CAI-81-Sp@1	2528	709	1.35E-08	1.99E-10	58196636.32	21026.15	109561.75	1.89E-03	4.80E-07	3.63E-04	1.67E-07	60
26-Apr-23<	20:34	CAI-81-Sp@2	2499	704	1.34E-08	2.00E-10	74469633.63	27916.27	146222.67	1.97E-03	4.61E-07	3.77E-04	1.19E-07	60
26-Apr-23<	20:44	CAI-81-Sp@3	2417	736	1.33E-08	1.99E-10	68466172.89	25180.74	131299.75	1.93E-03	6.33E-07	3.70E-04	1.56E-07	60

Date	Hour	Analysis Name	X	Y	Chamber Pressure	Primary Intensity	^{16}O	^{17}O	^{18}O	$^{18}O/^{16}O$	Error	$^{17}O/^{16}O$	Error	nb cycles
26-Apr-23<	20:54	CAI-81-Sp@4	2458	765	1.34E-08	1.99E-10	75239585.06	27960.94	146055.22	1.95E-03	2.68E-07	3.74E-04	1.13E-07	60
26-Apr-23<	21:04	CAI-81-Sp@5	2583	678	1.32E-08	2.00E-10	67889123.73	25032.6	130776.14	1.93E-03	3.75E-07	3.71E-04	1.35E-07	60
26-Apr-23<	21:14	CAI-81-Sp@6	2504	680	1.33E-08	1.99E-10	73683026.43	27458.01	143378.05	1.95E-03	3.52E-07	3.75E-04	1.13E-07	60
26-Apr-23<	21:24	CAI-82-Sp@1	2243	872	1.32E-08	1.98E-10	61517126.64	22090.36	115171.78	1.88E-03	2.80E-07	3.61E-04	1.07E-07	60
26-Apr-23<	21:34	CAI-82-Sp@2	2226	882	1.32E-08	1.99E-10	67826042.74	24350.81	127153.91	1.88E-03	2.65E-07	3.61E-04	1.21E-07	60
26-Apr-23<	21:44	CAI-82-Sp@3	2226	809	1.31E-08	1.99E-10	72268941.56	26374.67	137662.04	1.91E-03	2.41E-07	3.67E-04	1.34E-07	60
26-Apr-23<	21:54	CAI-84-Sp@1	2760	882	1.32E-08	1.98E-10	60088083.33	21520.94	112255.56	1.88E-03	2.98E-07	3.60E-04	1.49E-07	60
26-Apr-23<	22:14	CAI-89-Fo@2	474	2191	1.29E-08	1.99E-10	66878079.44	23964.68	125145.17	1.88E-03	2.75E-07	3.60E-04	1.49E-07	60
26-Apr-23<	22:24	CAI-89-Fo@3	432	2150	1.29E-08	1.98E-10	65893712.35	23636.63	123337.39	1.88E-03	2.78E-07	3.61E-04	1.21E-07	60
26-Apr-23<	22:34	CAI-91-Sp@1	-1533	3681	1.28E-08	1.99E-10	62679590.65	22591.66	117980.97	1.89E-03	2.63E-07	3.62E-04	1.15E-07	60
26-Apr-23<	22:44	CAI-91-Sp@2	-1499	3549	1.29E-08	1.99E-10	62717325.08	22574.46	117741.99	1.89E-03	3.42E-07	3.62E-04	1.32E-07	60
26-Apr-23<	22:54	CAI-91-Sp@3	-1433	3615	1.27E-08	1.98E-10	61991424.88	22929.02	119721.34	1.94E-03	8.09E-07	3.72E-04	1.62E-07	60
26-Apr-23<	23:04	CAI-91-Fo@1	-1382	3610	1.28E-08	1.98E-10	64199274.85	24002.02	125308.18	1.96E-03	2.72E-07	3.76E-04	1.19E-07	60
26-Apr-23<	23:14	CAI-104-Sp@1	-759	100	1.28E-08	1.99E-10	61452376.66	21981.2	114826.78	1.88E-03	2.45E-07	3.60E-04	1.26E-07	60
26-Apr-23<	23:24	CAI-104-Sp@2	-697	58	1.26E-08	1.97E-10	41186704.27	14868.73	77721.34	1.89E-03	3.56E-07	3.63E-04	1.66E-07	60
26-Apr-23<	23:34	CAI-104-Sp@3	-720	122	1.26E-08	1.97E-10	80815323.98	30075.5	157082.59	1.95E-03	2.68E-07	3.75E-04	1.04E-07	60
26-Apr-23<	23:44	CAI-104-Sp@4	-669	86	1.27E-08	1.98E-10	84280864.29	31490.82	164592.99	1.96E-03	2.46E-07	3.76E-04	1.22E-07	60
26-Apr-23<	23:54	CAI-112-Sp@1	-6132	-3134	1.25E-08	1.97E-10	1445780.96	555.82	2956.57	1.99E-03	1.93E-06	3.74E-04	1.03E-06	60
27-Apr-23<	00:04	CAI-112-Sp@2	-6111	-3113	1.23E-08	1.96E-10	771135.25	295.01	1557.59	1.91E-03	2.38E-06	3.63E-04	1.13E-06	60
27-Apr-23<	00:14	CAI-112-Sp@3	-6128	-3086	1.21E-08	1.97E-10	56135.39	39.18	205.8	2.02E-03	8.91E-06	3.86E-04	2.80E-06	60
27-Apr-23<	00:24	CAI-116@Sp1	-6092	-4182	1.21E-08	1.97E-10	-46263.96	0.13	0.63	3.14E-04	2.28E-04	1.08E-04	8.05E-05	60
27-Apr-23<	00:35	CAI-117-Sp@1	-6064	-4380	1.21E-08	1.96E-10	-46275.3	0.13	0.6	5.77E-05	3.50E-04	7.27E-05	3.45E-05	60
27-Apr-23<	00:45	CAI-135-Sp@1	5377	-6996	1.25E-08	1.96E-10	59769746.77	21419.22	110218.15	1.85E-03	3.08E-07	3.60E-04	1.12E-07	60
27-Apr-23<	00:55	CAI-135-Sp@2	5389	-7044	1.29E-08	1.95E-10	73757775.16	27086.71	140720.96	1.92E-03	2.48E-07	3.69E-04	1.32E-07	60

Date	Hour	Analysis Name	X	Y	Chamber Pressure	Primary Intensity	^{16}O	^{17}O	^{18}O	$^{18}O/^{16}O$	Error	$^{17}O/^{16}O$	Error	nb cycles
27-Apr-23<	01:05	CAI-135-Sp@3	5446	-7046	1.30E-08	1.94E-10	13785390.7	5113.27	26841.87	1.95E-03	7.12E-07	3.72E-04	2.39E-07	60
27-Apr-23<	01:15	CAI-128-Sp@1	1649	-7128	1.27E-08	1.95E-10	63434655.46	22690.7	118361.02	1.87E-03	3.47E-07	3.60E-04	1.20E-07	60
27-Apr-23<	01:25	CAI-128-Sp@2	1634	-7117	1.25E-08	1.95E-10	65092575.77	23270.59	121263.42	1.87E-03	3.33E-07	3.60E-04	1.28E-07	60
27-Apr-23<	01:35	CAI-128-Sp@3	1627	-7101	1.25E-08	1.94E-10	72091457.03	27178.93	142277.57	1.98E-03	2.17E-07	3.79E-04	1.06E-07	60
27-Apr-23<	01:45	CAI-125-Sp@1	514	-7178	1.25E-08	1.95E-10	72427982.25	27188.68	141667	1.96E-03	2.90E-07	3.78E-04	1.17E-07	60
27-Apr-23<	01:55	CAI-125-Sp@2	480	-7140	1.24E-08	1.95E-10	65967576.5	24411.45	127384.8	1.94E-03	2.81E-07	3.72E-04	1.13E-07	60
27-Apr-23<	02:05	CAI-125-Sp@3	535	-7211	1.25E-08	1.93E-10	67720089.95	25248.28	131814.18	1.95E-03	2.80E-07	3.75E-04	1.39E-07	60
27-Apr-23<	02:15	CAI-125-Dio@1	474	-7217	1.24E-08	1.94E-10	69089991.28	25876.28	135280.28	1.97E-03	3.37E-07	3.77E-04	1.29E-07	60
27-Apr-23<	02:25	CAI-123-Sp@1	-75	-8887	1.23E-08	1.95E-10	22217180.58	8475.15	45321.4	2.05E-03	5.55E-07	3.83E-04	2.24E-07	60
27-Apr-23<	02:35	CAI-123-Sp@2	-106	-8842	1.23E-08	1.95E-10	32612964.2	12038.25	64280.33	1.98E-03	4.02E-07	3.71E-04	1.78E-07	60
27-Apr-23<	02:45	CAI-123-Sp@3	-60	-8821	1.23E-08	1.95E-10	21136698.8	7739.91	41362.92	1.96E-03	5.58E-07	3.68E-04	2.02E-07	60
27-Apr-23<	02:55	CAI-123-Sp@4	-32	-8809	1.23E-08	1.95E-10	40202524.31	14635.36	77998.28	1.95E-03	3.73E-07	3.66E-04	1.46E-07	60
27-Apr-23<	03:05	CAI-123-Sp@5	12	-8820	1.22E-08	1.94E-10	31302970.34	11520.29	61838.87	1.98E-03	4.89E-07	3.70E-04	1.74E-07	60
27-Apr-23<	03:15	CAI-123-Sp@6	28	-8838	1.22E-08	1.94E-10	16715181.06	6124.47	32672.53	1.96E-03	5.23E-07	3.68E-04	2.84E-07	60
27-Apr-23<	03:25	CAI-123-Sp@7	100	-8879	1.22E-08	1.92E-10	18450288.35	6804.1	36385.48	1.98E-03	5.13E-07	3.70E-04	2.26E-07	60
27-Apr-23<	03:35	CAI-123-Sp@8	10	-8755	1.22E-08	1.90E-10	45076465.89	16892.77	89899.95	2.00E-03	3.71E-07	3.77E-04	1.66E-07	60
27-Apr-23<	03:45	CAI-123-Sp@9	-70	-8733	1.21E-08	1.90E-10	49973223.15	18619.01	98882.43	1.99E-03	8.03E-07	3.74E-04	2.15E-07	60
27-Apr-23<	03:55	CAI-122-Sp@1	-485	-8600	1.22E-08	1.91E-10	29876783.01	10951.92	58538.08	1.97E-03	4.84E-07	3.68E-04	2.07E-07	60
27-Apr-23<	04:05	CAI-122-Sp@2	-450	-8576	1.20E-08	1.90E-10	41726750.48	15169.06	80210.79	1.93E-03	3.37E-07	3.65E-04	1.49E-07	60
27-Apr-23<	04:16	CAI-122-Sp@3	-425	-8526	1.21E-08	1.89E-10	29359953.19	10761.96	57399.68	1.96E-03	4.65E-07	3.68E-04	1.61E-07	60
27-Apr-23<	04:26	CAI-122-Sp@4	-466	-8478	1.22E-08	1.90E-10	39625843.72	14403.04	76501.27	1.94E-03	3.91E-07	3.65E-04	1.59E-07	60
27-Apr-23<	04:36	CAI-119-Sp@1	-1298	-6481	1.20E-08	1.90E-10	54981138.61	19630.04	102511.29	1.87E-03	3.29E-07	3.59E-04	1.51E-07	60
27-Apr-23<	04:46	CAI-119-Sp@2	-1330	-6480	1.20E-08	1.89E-10	53162863.97	19091.97	99776.46	1.88E-03	4.28E-07	3.61E-04	1.56E-07	60
27-Apr-23<	04:56	CAI-119-Sp@3	-1355	-6483	1.20E-08	1.90E-10	64035408.67	23944.7	124886.56	1.96E-03	2.70E-07	3.76E-04	1.32E-07	60

Date	Hour	Analysis Name	X	Y	Chamber Pressure	Primary Intensity	^{16}O	^{17}O	^{18}O	$^{18}O/^{16}O$	Error	$^{17}O/^{16}O$	Error	nb cycles
27-Apr-23<	05:06	CAI-119-Fo@1	-1375	-6426	1.19E-08	1.90E-10	64758736.41	24244.13	126698.44	1.97E-03	3.25E-07	3.77E-04	1.09E-07	60
27-Apr-23<	05:16	CAI-119-Fo@2	-1344	-6309	1.19E-08	1.89E-10	62147310.96	23253.47	121357.31	1.96E-03	3.96E-07	3.76E-04	1.23E-07	60
27-Apr-23<	05:26	CAI-118-Sp@1	-2157	-6128	1.21E-08	1.89E-10	58475172.54	21589.49	112815.61	1.94E-03	6.02E-07	3.71E-04	1.72E-07	60
27-Apr-23<	05:36	CAI-118-Sp@2	-2029	-6066	1.19E-08	1.90E-10	64723580.1	24548.73	129465.77	2.01E-03	2.79E-07	3.81E-04	1.33E-07	60
27-Apr-23<	05:46	CAI-161	-896	-4810	1.20E-08	1.88E-10	56820293.45	20314.56	105986.68	1.87E-03	3.31E-07	3.59E-04	1.28E-07	60
27-Apr-23<	05:56	CAI-161@0	-931	-4797	1.20E-08	1.89E-10	58231119.74	20823.09	108712.36	1.87E-03	3.05E-07	3.60E-04	1.25E-07	60
27-Apr-23<	06:06	CAI-161@1	-935	-4840	1.19E-08	1.89E-10	58959429.85	21092.58	110194.03	1.88E-03	3.45E-07	3.60E-04	1.29E-07	60
27-Apr-23<	06:16	CAI-160-Sp@1	52	-4123	1.18E-08	1.88E-10	56973183.68	21310.16	111212.57	1.96E-03	3.11E-07	3.76E-04	1.41E-07	60
27-Apr-23<	06:26	CAI-160-Sp@2	43	-4098	1.19E-08	1.89E-10	57809378.28	21618.75	112835.04	1.96E-03	4.12E-07	3.76E-04	1.61E-07	60
27-Apr-23<	06:36	CAI-160-Sp@3	52	-4074	1.19E-08	1.89E-10	58886094.93	22031.08	115009.41	1.96E-03	3.09E-07	3.76E-04	1.22E-07	60
27-Apr-23<	06:46	CAI-160-Sp@4	80	-4083	1.20E-08	1.88E-10	58333970.83	21819.4	113854.3	1.96E-03	2.27E-07	3.76E-04	1.46E-07	60
27-Apr-23<	06:56	CAI-160-Sp@5	74	-4116	1.19E-08	1.88E-10	57410809.74	21461.46	112041.91	1.96E-03	3.53E-07	3.76E-04	1.47E-07	60
27-Apr-23<	07:06	CAI-160-Sp@6	62	-4096	1.19E-08	1.89E-10	58796206.31	21995.56	114798.25	1.96E-03	3.03E-07	3.76E-04	1.36E-07	60
27-Apr-23<	07:39	Ipanko@18	432	-1720	9.48E-09	1.88E-10	52635583.66	19945.01	105195.69	2.01E-03	2.98E-07	3.81E-04	1.27E-07	60
27-Apr-23<	07:49	Ipanko@19	432	-1740	8.84E-09	1.87E-10	51799084.75	19629.35	103559.46	2.01E-03	3.76E-07	3.81E-04	1.21E-07	60
27-Apr-23<	07:59	Ipanko@20	432	-1760	8.53E-09	1.87E-10	51824242.3	19636.78	103602.19	2.01E-03	3.16E-07	3.81E-04	1.08E-07	60
27-Apr-23<	08:09	Ipanko@21	432	-1780	8.20E-09	1.87E-10	51981483.6	19699.17	103924.42	2.01E-03	2.80E-07	3.81E-04	1.32E-07	60
27-Apr-23<	08:19	SCOL@21	1887	2766	7.98E-09	1.86E-10	62079039.69	23309.87	121958.06	1.97E-03	3.16E-07	3.78E-04	1.43E-07	60
27-Apr-23<	08:29	SCOL@22	1887	2786	7.84E-09	1.86E-10	61579468.59	23136.05	120984.04	1.97E-03	2.85E-07	3.78E-04	9.86E-08	60
27-Apr-23<	08:39	SCOL@23	1887	2806	7.69E-09	1.86E-10	61816743.41	23228.07	121437.86	1.97E-03	3.22E-07	3.78E-04	1.62E-07	60
27-Apr-23<	08:49	SCOL@24	1887	2826	7.49E-09	1.86E-10	61384078.92	23066.94	120610.42	1.97E-03	2.94E-07	3.78E-04	1.25E-07	60
27-Apr-23<	08:59	Rockport@15	4493	-4028	7.36E-09	1.85E-10	68807395.07	25730.4	133869.47	1.95E-03	2.74E-07	3.76E-04	1.11E-07	60
27-Apr-23<	09:09	Rockport@16	4493	-4068	7.26E-09	1.86E-10	69230363.22	25857.93	134691.46	1.95E-03	3.02E-07	3.76E-04	1.23E-07	60
27-Apr-23<	09:19	Rockport@17	4493	-4088	7.09E-09	1.86E-10	68571156.05	25637.99	133411.57	1.95E-03	3.42E-07	3.76E-04	1.49E-07	60

Date	Hour	Analysis Name	X	Y	Chamber Pressure	Primary Intensity	^{16}O	^{17}O	^{18}O	$^{18}O/^{16}O$	Error	$^{17}O/^{16}O$	Error	nb cycles
27-Apr-23<	09:29	Rockport@18	4493	-4108	7.16E-09	1.85E-10	67993127.8	25396.88	132289.52	1.95E-03	3.11E-07	3.76E-04	1.34E-07	60
27-Apr-23<	10:52	CAI-01-Sp@1	186	425	7.19E-09	2.22E-10	65604922.21	23424.45	122650.86	1.88E-03	3.21E-07	3.59E-04	1.04E-07	60
27-Apr-23<	11:02	CAI-01-Sp@2	198	415	7.12E-09	2.20E-10	67781416.91	24212.95	126649.23	1.88E-03	2.72E-07	3.59E-04	1.26E-07	60
27-Apr-23<	11:12	CAI-01-Sp@3	205	437	6.94E-09	2.20E-10	64562379	23033.44	120411.47	1.87E-03	3.20E-07	3.59E-04	1.34E-07	60
27-Apr-23<	11:22	CAI-01-Sp@4	176	399	6.97E-09	2.21E-10	66741018.99	23895.64	125045.21	1.88E-03	7.15E-07	3.60E-04	1.59E-07	60
27-Apr-23<	11:32	CAI-01-Sp@5	155	413	6.85E-09	2.18E-10	67750233.65	24444.44	127870.77	1.90E-03	3.46E-07	3.63E-04	1.11E-07	60
27-Apr-23<	11:42	CAI-01-Sp@6	138	423	6.84E-09	2.18E-10	71396148.49	25789.67	134848.23	1.90E-03	3.08E-07	3.64E-04	9.24E-08	60
27-Apr-23<	11:52	CAI-01-Sp@7	157	440	6.74E-09	2.18E-10	74581457.14	27392.74	143369.17	1.93E-03	2.79E-07	3.70E-04	1.22E-07	60
27-Apr-23<	12:02	CAI-01-Sp@8	174	464	6.73E-09	2.16E-10	66196198.33	23880.86	125011.06	1.90E-03	2.69E-07	3.63E-04	1.24E-07	60
27-Apr-23<	12:12	CAI-01-Fo@1	100	441	6.63E-09	2.15E-10	74337651.94	27548.05	144386.03	1.95E-03	3.15E-07	3.73E-04	1.26E-07	60
27-Apr-23<	12:22	CAI-01-Fo@2	81	427	6.62E-09	2.17E-10	46019409.02	16505.3	86364.64	1.88E-03	4.56E-07	3.60E-04	1.43E-07	60
27-Apr-23<	12:32	CAI-01-Fo@3	85	410	6.54E-09	2.15E-10	52112234.81	18676.85	97780.58	1.88E-03	3.11E-07	3.60E-04	1.21E-07	60
27-Apr-23<	12:52	CAI-01-Fo@5	237	316	6.45E-09	2.15E-10	64700550.83	24065.73	125904	1.95E-03	2.27E-07	3.74E-04	1.24E-07	60
27-Apr-23<	13:02	CAI-01-Ol@1	107	288	6.41E-09	2.14E-10	72847682.38	27232.45	142439.07	1.96E-03	2.16E-07	3.76E-04	1.16E-07	60
27-Apr-23<	13:12	CAI-01-Ol@2	107	274	6.37E-09	2.13E-10	77595216.25	28997.61	151606.55	1.96E-03	2.87E-07	3.76E-04	1.12E-07	60
27-Apr-23<	13:22	CAI-01-Cal@1	52	256	6.38E-09	2.14E-10	89955398.1	33872.99	178247.91	1.99E-03	2.93E-07	3.79E-04	1.16E-07	60
27-Apr-23<	13:32	CAI-01-Cal@2	38	293	6.30E-09	2.14E-10	68713930.34	25888.77	136400.63	1.99E-03	2.68E-07	3.79E-04	1.15E-07	60
27-Apr-23<	13:43	CAI-06-Sp@1	1426	332	6.22E-09	2.12E-10	58711753.68	20920.71	109346.2	1.87E-03	2.64E-07	3.58E-04	1.26E-07	60
27-Apr-23<	13:53	CAI-06-Sp@2	1411	380	6.23E-09	2.13E-10	71810601.63	25626.1	134038.15	1.87E-03	2.70E-07	3.59E-04	1.31E-07	60
27-Apr-23<	14:03	CAI-06-Sp@3	1393	334	6.24E-09	2.13E-10	59877721.98	21343.41	111595.29	1.87E-03	2.88E-07	3.59E-04	1.44E-07	60
27-Apr-23<	14:13	CAI-06-Fo@1	1514	430	6.21E-09	2.10E-10	67040098.97	24934.11	130492.67	1.96E-03	3.08E-07	3.74E-04	1.39E-07	60
27-Apr-23<	14:23	CAI-06-Fo@2	1534	386	6.10E-09	2.11E-10	65696445.79	24419.96	127876.38	1.96E-03	3.01E-07	3.74E-04	1.29E-07	60
27-Apr-23<	14:33	CAI-06-Fo@3	1664	442	6.17E-09	2.12E-10	63975586.24	23743.37	124280.39	1.95E-03	2.60E-07	3.73E-04	1.55E-07	60
27-Apr-23<	14:43	RFay@1	2240	588	6.04E-09	2.09E-10	81553818.07	30488	159476.49	1.96E-03	2.56E-07	3.76E-04	1.11E-07	60

Date	Hour	Analysis Name	X	Y	Chamber Pressure	Primary Intensity	^{16}O	^{17}O	^{18}O	$^{18}O/^{16}O$	Error	$^{17}O/^{16}O$	Error	nb cycles
27-Apr-23<	14:53	RFay@2	2575	466	6.06E-09	2.10E-10	84657671.84	31663.24	165434.22	1.96E-03	2.08E-07	3.77E-04	1.07E-07	60
27-Apr-23<	15:03	RFay@3	3655	669	6.07E-09	2.11E-10	76361071.18	28570.16	149459.56	1.97E-03	2.57E-07	3.77E-04	9.75E-08	60
27-Apr-23<	15:13	CAI-17-Sp@1	4138	749	6.06E-09	2.09E-10	56117188.14	20019.14	104708.55	1.87E-03	2.97E-07	3.59E-04	1.50E-07	60
27-Apr-23<	15:23	CAI-17-Sp@2	4126	737	5.99E-09	2.08E-10	59861727.76	21616.62	113046.2	1.90E-03	2.91E-07	3.63E-04	1.38E-07	60
27-Apr-23<	15:33	CAI-17-Sp@3	4191	664	6.01E-09	2.10E-10	63462572.59	23176.81	121357.75	1.92E-03	2.92E-07	3.67E-04	1.34E-07	60
27-Apr-23<	15:43	CAI-17-Sp@4	3939	665	5.94E-09	2.08E-10	56423492.17	20271.89	106003.46	1.89E-03	2.93E-07	3.61E-04	1.44E-07	60
27-Apr-23<	15:53	CAI-17-Sp@5	3971	608	5.88E-09	2.07E-10	64207820.1	23482.46	122873.36	1.92E-03	2.85E-07	3.68E-04	1.48E-07	60
27-Apr-23<	16:03	CAI-17-Sp@6	4031	792	5.90E-09	2.09E-10	68306625.64	25128.61	131591.26	1.93E-03	2.81E-07	3.70E-04	1.05E-07	60
27-Apr-23<	16:13	CAI-19-Sp@1	3478	-861	5.93E-09	2.08E-10	71775313.01	25916.38	135614.99	1.90E-03	3.25E-07	3.63E-04	1.28E-07	60
27-Apr-23<	16:23	CAI-19-Sp@2	3433	-900	5.86E-09	2.06E-10	60547016.75	21612.52	113061.65	1.88E-03	3.88E-07	3.59E-04	1.37E-07	60
27-Apr-23<	16:33	CAI-19-Sp@3	3470	-930	5.88E-09	2.08E-10	66572569.26	24060.57	126027.83	1.90E-03	5.36E-07	3.64E-04	1.38E-07	60
27-Apr-23<	16:43	CAI-19-Dio@1	3452	-910	5.86E-09	2.09E-10	66620553.83	23779.42	124499.46	1.88E-03	2.59E-07	3.59E-04	1.16E-07	60
27-Apr-23<	16:53	CAI-25-Sp@1	1872	-2851	5.79E-09	2.06E-10	62610173.96	22504.58	117709.71	1.89E-03	2.93E-07	3.62E-04	1.04E-07	60
27-Apr-23<	17:03	CAI-25-Sp@2	1902	-2880	5.90E-09	2.07E-10	59314805.28	21300.93	111257.22	1.88E-03	2.95E-07	3.61E-04	1.39E-07	60
27-Apr-23<	17:34	SCOL@25	1882	2491	5.89E-09	2.31E-10	79642929.25	29879.06	156066.1	1.97E-03	2.44E-07	3.78E-04	1.06E-07	60
27-Apr-23<	17:44	SCOL@26	1882	2471	5.82E-09	2.36E-10	81467084.07	30582.41	159658.95	1.97E-03	2.17E-07	3.78E-04	1.20E-07	60
27-Apr-23<	17:54	SCOL@27	1882	2451	5.73E-09	2.34E-10	80136183.55	30078.54	157054.41	1.97E-03	2.46E-07	3.78E-04	1.02E-07	60
27-Apr-23<	19:13	CAI-04-Sp@1	-1605	-668	8.32E-09	2.35E-10	66758355.21	24179.26	126490.96	1.90E-03	3.34E-07	3.64E-04	1.32E-07	60
27-Apr-23<	19:23	CAI-04-Sp@2	-1584	-686	8.35E-09	2.36E-10	78227175.41	28790.63	150802.94	1.94E-03	3.00E-07	3.70E-04	1.36E-07	60
27-Apr-23<	19:33	CAI-04-Sp@3	-1572	-658	8.32E-09	2.34E-10	80214984.71	29914.74	156427.47	1.96E-03	2.94E-07	3.75E-04	1.21E-07	60
27-Apr-23<	19:43	CAI-04-Fo@1	-1615	-709	8.39E-09	2.34E-10	74803117.64	27954.99	146354.85	1.97E-03	2.85E-07	3.76E-04	1.38E-07	60
27-Apr-23<	19:53	CAI-04-Fo@2	-1635	-653	8.35E-09	2.36E-10	82711246.8	30868.56	161514.53	1.96E-03	2.10E-07	3.76E-04	1.26E-07	60
27-Apr-23<	20:03	CAI-04-Fo@3	-1631	-609	8.35E-09	2.34E-10	83402293.11	31145.07	162878.69	1.96E-03	2.35E-07	3.76E-04	1.19E-07	60
27-Apr-23<	20:13	CAI-04-Fo@4	-1548	-604	8.43E-09	2.34E-10	81461192.55	30413.83	159135.89	1.96E-03	2.15E-07	3.76E-04	1.17E-07	60

Date	Hour	Analysis Name	X	Y	Chamber Pressure	Primary Intensity	^{16}O	^{17}O	^{18}O	$^{18}O/^{16}O$	Error	$^{17}O/^{16}O$	Error	nb cycles
27-Apr-23<	20:24	CAI-04-Fo@5	-1536	-673	8.38E-09	2.36E-10	85665892.29	31930.42	166645.27	1.95E-03	2.41E-07	3.75E-04	1.18E-07	60
27-Apr-23<	20:34	CAI-04-Fo@6	-1551	-582	8.33E-09	2.34E-10	83076859.14	31023.53	162224.12	1.96E-03	2.27E-07	3.76E-04	1.09E-07	60
27-Apr-23<	20:44	CAI-04-Fo@7	-1575	-555	8.39E-09	2.33E-10	82122932.5	30659.9	160249.02	1.96E-03	2.34E-07	3.76E-04	9.88E-08	60
27-Apr-23<	20:54	CAI-04-Fo@8	-1622	-576	8.45E-09	2.35E-10	85438342.16	31914.57	166981.34	1.96E-03	2.63E-07	3.76E-04	9.23E-08	60
27-Apr-23<	21:04	CAI-04-Cal@1	-1559	-676	8.46E-09	2.37E-10	32044312.85	11862.78	61673.12	1.93E-03	5.99E-07	3.72E-04	1.83E-07	60
27-Apr-23<	21:14	CAI-04-Cal@2	-1582	-721	8.40E-09	2.37E-10	52539351.78	19470.61	101945.89	1.95E-03	3.79E-07	3.72E-04	1.16E-07	60
27-Apr-23<	21:24	CAI-03-Sp@1	-1404	-904	8.41E-09	2.40E-10	71508007.91	25620.84	133943	1.88E-03	2.55E-07	3.60E-04	9.51E-08	60
27-Apr-23<	21:34	CAI-03-Sp@2	-1425	-918	8.41E-09	2.40E-10	79886135.28	29225.59	153102.51	1.92E-03	2.78E-07	3.68E-04	1.09E-07	60
27-Apr-23<	21:44	CAI-01-Sp@1	949	-2484	8.49E-09	2.38E-10	91696801.4	34443.53	180672.19	1.98E-03	2.55E-07	3.78E-04	1.05E-07	60
27-Apr-23<	21:54	CAI-01-Sp@2	950	-2555	8.44E-09	2.40E-10	96660385.89	36388.37	191236.28	1.99E-03	2.39E-07	3.79E-04	9.84E-08	60
27-Apr-23<	22:04	CAI-01-Sp@3	926	-2529	8.47E-09	2.40E-10	93091862.17	35054.35	184346.25	1.99E-03	2.34E-07	3.79E-04	1.02E-07	60
27-Apr-23<	22:14	CAI-04-Dio@1	852	-2531	8.48E-09	2.37E-10	71751563.61	25587.21	133535.71	1.87E-03	3.19E-07	3.59E-04	1.03E-07	60
27-Apr-23<	22:24	CAI-04-Dio@2	877	-2701	8.60E-09	2.39E-10	58056442.05	20712.95	107962.46	1.87E-03	3.41E-07	3.59E-04	1.12E-07	60
27-Apr-23<	22:34	CAI-04-Dio@3	930	-2781	8.48E-09	2.39E-10	69812103.67	24878.93	129974.79	1.87E-03	2.70E-07	3.59E-04	1.02E-07	60
27-Apr-23<	22:44	CAI-04-Dio@4	983	-2378	8.55E-09	2.37E-10	85363551.84	32061.41	168321.71	1.98E-03	2.38E-07	3.78E-04	1.11E-07	60
27-Apr-23<	22:54	CAI-04-Dio@5	1024	-2385	8.50E-09	2.38E-10	69820110.24	24871.95	129834.91	1.87E-03	2.60E-07	3.58E-04	1.34E-07	60
27-Apr-23<	23:04	CAI-04-Dio@6	894	-2420	8.49E-09	2.39E-10	68938800.27	24805.25	129500.43	1.89E-03	3.69E-07	3.62E-04	1.01E-07	60
27-Apr-23<	23:14	CAI-01-Cal@1	919	-2411	8.49E-09	2.37E-10	70559473.79	26361.4	137926.8	1.96E-03	3.13E-07	3.76E-04	1.16E-07	60
27-Apr-23<	23:24	CAI-01-Cal@2	962	-2666	8.56E-09	2.37E-10	67382468.45	25037.27	131058.5	1.95E-03	3.92E-07	3.74E-04	1.31E-07	60
27-Apr-23<	23:34	CAI-07-Sp@1	1465	260	8.57E-09	2.39E-10	84321076.68	30654.42	160274.58	1.91E-03	2.03E-07	3.66E-04	1.35E-07	60
27-Apr-23<	23:44	CAI-07-Sp@2	1475	311	8.59E-09	2.37E-10	86081591.02	31174.49	162857	1.90E-03	2.68E-07	3.64E-04	1.08E-07	60
27-Apr-23<	23:54	CAI-11-Sp@1	1118	1112	8.59E-09	2.37E-10	67668523.59	25429.67	133688.18	1.98E-03	3.06E-07	3.78E-04	1.29E-07	60
28-Apr-23<	00:04	CAI-11-Sp@2	1192	1115	8.59E-09	2.38E-10	78826329.57	28266.15	147867.54	1.88E-03	2.61E-07	3.61E-04	1.07E-07	60
28-Apr-23<	00:14	CAI-11-Sp@3	1216	1010	8.74E-09	2.36E-10	73201974.77	26193.29	136915.4	1.88E-03	2.41E-07	3.60E-04	9.85E-08	60

Date	Hour	Analysis Name	X	Y	Chamber Pressure	Primary Intensity	^{16}O	^{17}O	^{18}O	$^{18}O/^{16}O$	Error	$^{17}O/^{16}O$	Error	nb cycles
28-Apr-23<	00:24	ROI-01-Ol@1	2226	-1385	8.54E-09	2.36E-10	84735915.41	31653.86	165378.13	1.96E-03	2.25E-07	3.76E-04	1.12E-07	60
28-Apr-23<	00:34	ROI-01-Ol@2	2236	-1274	8.60E-09	2.37E-10	91538099.03	34169.84	178487.71	1.96E-03	2.37E-07	3.76E-04	1.04E-07	60
28-Apr-23<	00:44	ROI-01-Ol@3	2194	-1210	8.67E-09	2.36E-10	98860932.42	36899.04	192668.36	1.96E-03	2.58E-07	3.76E-04	1.02E-07	60
28-Apr-23<	00:54	Shard-Ol@1	2454	-1211	8.54E-09	2.35E-10	81739692.86	30500.28	159475.06	1.96E-03	2.92E-07	3.76E-04	1.07E-07	60
28-Apr-23<	01:05	Shard-Ol@2	2623	-1100	8.56E-09	2.36E-10	73143027.47	27188.55	142344.96	1.95E-03	2.81E-07	3.74E-04	1.22E-07	60
28-Apr-23<	01:15	Shard-Ol@3	2376	-954	8.62E-09	2.35E-10	78424797.31	29391.97	153889.24	1.97E-03	2.31E-07	3.77E-04	8.79E-08	60
28-Apr-23<	01:25	Shard-Ol@4	2242	-868	8.56E-09	2.34E-10	78653876.55	29243.68	152964.29	1.95E-03	2.74E-07	3.74E-04	1.20E-07	60
28-Apr-23<	01:35	Shard-Ol@5	2178	-859	8.55E-09	2.36E-10	83547944.17	31136.74	162600.92	1.95E-03	2.81E-07	3.75E-04	9.96E-08	60
28-Apr-23<	01:45	Shard-Ol@6	2176	-549	8.55E-09	2.35E-10	78269468.82	29103.04	152260.16	1.95E-03	2.93E-07	3.74E-04	1.29E-07	60
28-Apr-23<	01:55	Shard-Ol@7	1884	-395	8.56E-09	2.33E-10	74642237.85	26684.73	139379.94	1.88E-03	2.08E-07	3.60E-04	1.06E-07	60
28-Apr-23<	02:05	ROI-02-Ol@1	2331	-238	8.62E-09	2.35E-10	82567538.78	30774.31	160950.57	1.96E-03	2.80E-07	3.75E-04	1.08E-07	60
28-Apr-23<	02:15	ROI-02-Ol@2	2371	-318	8.62E-09	2.35E-10	76708940.93	28638.32	149699.22	1.96E-03	3.02E-07	3.76E-04	1.22E-07	60
28-Apr-23<	02:25	ROI-03-Ol@1	2800	-1182	8.57E-09	2.33E-10	85526287.73	31941.88	167242.23	1.96E-03	2.88E-07	3.76E-04	9.21E-08	60
28-Apr-23<	02:35	ROI-04-Ol@1	1368	-1518	8.61E-09	2.35E-10	80151542.7	29697.07	155523.44	1.95E-03	2.81E-07	3.73E-04	1.12E-07	60
28-Apr-23<	02:45	ROI-05-Ol@1	-628	-1261	8.45E-09	2.35E-10	84254262.69	31268.53	163585.04	1.95E-03	3.04E-07	3.74E-04	1.30E-07	60
28-Apr-23<	02:55	ROI-05-Ol@2	-511	-1418	8.53E-09	2.33E-10	74236968.82	27543.6	144174.83	1.95E-03	2.38E-07	3.73E-04	1.35E-07	60
28-Apr-23<	03:05	ROI-05-Ol@3	-738	-1502	8.44E-09	2.35E-10	71799478.25	26658.86	139741.26	1.95E-03	2.86E-07	3.74E-04	1.35E-07	60
28-Apr-23<	03:15	ROI-05-Ol@4	-712	-1353	8.36E-09	2.35E-10	80853402.41	29989.8	157122.84	1.95E-03	2.33E-07	3.73E-04	1.10E-07	60
28-Apr-23<	03:25	ROI-06-Ol@1	-2077	-344	8.47E-09	2.33E-10	74166900.04	27559.93	144585.06	1.96E-03	2.33E-07	3.74E-04	1.15E-07	60
28-Apr-23<	03:35	ROI-06-Ol@2	-2089	-178	8.45E-09	2.34E-10	91412487.07	34017.35	177764.94	1.95E-03	1.94E-07	3.75E-04	1.04E-07	60
28-Apr-23<	03:45	ROI-06-Ol@3	-1942	-349	8.38E-09	2.35E-10	57891674.28	21518.71	112263.61	1.95E-03	4.29E-07	3.74E-04	1.39E-07	60
28-Apr-23<	03:55	ROI-07-Ol@1	-1261	-86	8.36E-09	2.33E-10	81219959.82	30413.27	158844.2	1.96E-03	2.66E-07	3.77E-04	1.29E-07	60
28-Apr-23<	03:55	ROI-07-Ol@1	-1261	-86	8.36E-09	2.33E-10	81219959.82	30413.27	158844.2	1.96E-03	2.66E-07	3.77E-04	1.29E-07	60
28-Apr-23<	04:05	ROI-07-Ol@2	-1315	-125	8.42E-09	2.33E-10	80971794.11	30338.77	158588.61	1.97E-03	2.67E-07	3.77E-04	9.27E-08	60

Date	Hour	Analysis Name	X	Y	Chamber Pressure	Primary Intensity	^{16}O	^{17}O	^{18}O	$^{18}O/^{16}O$	Error	$^{17}O/^{16}O$	Error	nb cycles
28-Apr-23<	04:15	ROI-07-Ol@3	-1341	-86	8.42E-09	2.35E-10	80078621.72	29980.5	156625.98	1.96E-03	2.57E-07	3.77E-04	1.08E-07	60
28-Apr-23<	04:25	ROI-07-Ol@4	-1307	-45	8.35E-09	2.33E-10	85129575.29	31869.52	166425.99	1.96E-03	2.50E-07	3.77E-04	1.21E-07	60
28-Apr-23<	04:35	ROI-08-Ol@1	-1194	100	8.41E-09	2.33E-10	77284476.1	28794.46	150724.45	1.96E-03	2.72E-07	3.75E-04	1.47E-07	60
28-Apr-23<	04:45	ROI-08-Ol@2	-1198	156	8.40E-09	2.34E-10	80188090.14	29863.34	156139.83	1.96E-03	2.30E-07	3.75E-04	1.23E-07	60
28-Apr-23<	04:55	ROI-09-Ol@1	-1960	793	8.40E-09	2.33E-10	82292399.12	30709.49	160845.56	1.96E-03	2.08E-07	3.76E-04	9.38E-08	60
28-Apr-23<	05:05	ROI-09-Ol@2	-1906	749	8.38E-09	2.33E-10	81975831.71	30615.75	160207.03	1.96E-03	2.59E-07	3.76E-04	1.19E-07	60
28-Apr-23<	05:15	ROI-09-Ol@3	-2034	697	8.31E-09	2.34E-10	80069838.31	29888.13	156712.7	1.97E-03	2.67E-07	3.76E-04	8.69E-08	60
28-Apr-23<	05:25	ROI-10-Ol@1	-1066	1202	8.43E-09	2.32E-10	80774748.69	29965.93	156822.71	1.95E-03	2.66E-07	3.73E-04	1.20E-07	60
28-Apr-23<	05:35	ROI-10-Ol@2	-1042	1162	8.39E-09	2.32E-10	79239257.38	29397.67	153922.24	1.95E-03	2.40E-07	3.73E-04	1.22E-07	60
28-Apr-23<	05:45	ROI-11-Ol@1	-537	1046	8.39E-09	2.33E-10	99239516.68	37008.05	193308.73	1.96E-03	2.31E-07	3.76E-04	9.58E-08	60
28-Apr-23<	05:55	ROI-12-Ol@1	-364	1038	8.34E-09	2.32E-10	79971143.6	29658.43	154961.67	1.95E-03	2.70E-07	3.73E-04	9.95E-08	60
28-Apr-23<	06:05	ROI-12-Ol@2	-384	983	8.22E-09	2.31E-10	75408684.99	27980.93	146361.87	1.95E-03	2.85E-07	3.73E-04	1.24E-07	60
28-Apr-23<	06:16	ROI-12-Ol@3	0	0	8.41E-09	2.33E-10	83841423.71	31391.6	164758.45	1.97E-03	2.92E-07	3.77E-04	1.12E-07	60
28-Apr-23<	07:27	Ipanko@22	1123	-1562	7.63E-09	2.31E-10	64550533.59	24393.09	128700.08	2.00E-03	3.08E-07	3.80E-04	1.29E-07	60
28-Apr-23<	07:37	Ipanko@23	1123	-1582	7.30E-09	2.29E-10	64130440.32	24258.32	127948.55	2.00E-03	2.83E-07	3.81E-04	1.18E-07	60
28-Apr-23<	07:47	Ipanko@24	1123	-1602	7.09E-09	2.31E-10	64812905.47	24508.01	129244.35	2.00E-03	2.32E-07	3.80E-04	1.26E-07	60
28-Apr-23<	07:57	Ipanko@25	1123	-1622	6.93E-09	2.30E-10	64509657.77	24391.33	128713.18	2.00E-03	2.54E-07	3.80E-04	1.06E-07	60
28-Apr-23<	08:07	SCOL@28	1968	2631	6.80E-09	2.29E-10	77916113.93	29195.91	152689.97	1.97E-03	2.51E-07	3.77E-04	1.20E-07	60
28-Apr-23<	08:17	SCOL@29	1968	2651	6.63E-09	2.30E-10	78440307.67	29394.59	153653.67	1.97E-03	2.30E-07	3.77E-04	1.11E-07	60
28-Apr-23<	08:27	SCOL@30	1968	2671	6.63E-09	2.30E-10	77717675.49	29116.98	152313.04	1.97E-03	2.85E-07	3.77E-04	9.56E-08	60
28-Apr-23<	08:37	SCOL@31	1968	2691	6.48E-09	2.28E-10	76849760.83	28794.46	150593.85	1.97E-03	3.02E-07	3.77E-04	9.24E-08	60
28-Apr-23<	08:47	Rockport@19	4558	-4080	6.41E-09	2.30E-10	88276676.98	32915.32	171280.83	1.95E-03	2.87E-07	3.75E-04	1.17E-07	60
28-Apr-23<	08:57	Rockport@20	4558	-4100	6.34E-09	2.30E-10	87297967.04	32562.06	169398.48	1.95E-03	2.13E-07	3.75E-04	1.16E-07	60
28-Apr-23<	09:07	Rockport@21	4558	-4120	6.27E-09	2.28E-10	85921412.47	32026.63	166743.01	1.95E-03	2.40E-07	3.75E-04	1.09E-07	60

Date	Hour	Analysis Name	X	Y	Chamber Pressure	Primary Intensity	^{16}O	^{17}O	^{18}O	$^{18}O/^{16}O$	Error	$^{17}O/^{16}O$	Error	nb cycles
28-Apr-23<	09:17	Rockport@22	4558	-4140	6.21E-09	2.29E-10	86605875.48	32279.19	168004.97	1.95E-03	2.53E-07	3.75E-04	9.55E-08	60
28-Apr-23<	10:21	CAI-01-Dio@1	2407	1431	9.65E-09	2.24E-10	72811770.03	27039.12	141784.4	1.96E-03	5.17E-07	3.74E-04	1.26E-07	60
28-Apr-23<	10:31	CAI-01-Dio@2	2386	1434	9.81E-09	2.17E-10	85580154.38	32142.43	168623.92	1.98E-03	2.93E-07	3.78E-04	1.09E-07	60
28-Apr-23<	10:41	CAI-01-Cal@1	2383	1400	9.83E-09	2.15E-10	91189074.42	34587.73	182770.23	2.01E-03	3.48E-07	3.82E-04	8.79E-08	60
28-Apr-23<	10:51	CAI-01-Ol@1	2485	1524	9.89E-09	2.16E-10	77381127.59	28736.86	150353.34	1.95E-03	2.29E-07	3.74E-04	1.20E-07	60
28-Apr-23<	11:01	CAI-01-Ol@2	2555	1526	9.93E-09	2.16E-10	75339729.49	27962.13	146388.89	1.95E-03	2.10E-07	3.74E-04	1.19E-07	60
28-Apr-23<	11:11	CAI-03-Sp@1	3311	-223	9.96E-09	2.14E-10	71790950.01	26893.24	141112.47	1.97E-03	4.13E-07	3.77E-04	1.25E-07	60
28-Apr-23<	11:21	CAI-03-Sp@2	3348	-228	9.98E-09	2.15E-10	68683058.94	25682.94	134975.3	1.97E-03	2.67E-07	3.76E-04	1.26E-07	60
28-Apr-23<	11:31	CAI-06-Sp@1	3381	-1080	9.97E-09	2.16E-10	82050323.39	30698.94	161775.74	1.98E-03	2.71E-07	3.77E-04	1.43E-07	60
28-Apr-23<	11:41	CAI-06-Sp@2	3400	-997	9.97E-09	2.14E-10	88059029.21	33173.48	174875.62	1.99E-03	4.44E-07	3.79E-04	1.13E-07	60
28-Apr-23<	11:51	CAI-06-Sp@3	3425	-1028	9.98E-09	2.15E-10	92457251.18	35008.76	185004.01	2.01E-03	3.78E-07	3.81E-04	7.72E-08	60
28-Apr-23<	12:01	CAI-06-Sp@4	3504	-1009	9.99E-09	2.16E-10	91708285.79	34750.4	183546.68	2.01E-03	4.13E-07	3.82E-04	1.04E-07	60
28-Apr-23<	12:11	CAI-06-Sp@5	3490	-988	9.93E-09	2.14E-10	76083519.71	28744.95	151748.32	2.00E-03	2.85E-07	3.80E-04	9.94E-08	60
28-Apr-23<	12:21	CAI-06-Ol@1	3486	-563	1.00E-08	2.14E-10	68301947.59	25338.28	132715.46	1.95E-03	3.03E-07	3.73E-04	1.13E-07	60
28-Apr-23<	12:31	CAI-06-Ol@2	3463	-604	9.94E-09	2.16E-10	68863522.3	25508.42	133746.97	1.95E-03	2.71E-07	3.73E-04	1.28E-07	60
28-Apr-23<	12:41	Ol-02-Ol@1	2053	-101	9.92E-09	2.13E-10	62889209.17	23342.11	122353.85	1.95E-03	2.92E-07	3.73E-04	1.37E-07	60
28-Apr-23<	12:51	Ol-02-Ol@2	2054	22	9.98E-09	2.13E-10	66434261.33	24675.23	129286.78	1.95E-03	2.48E-07	3.74E-04	1.24E-07	60
28-Apr-23<	13:02	Ol-02-Ol@3	2010	-56	9.97E-09	2.16E-10	67417299.66	25028.69	131150.23	1.95E-03	2.72E-07	3.73E-04	1.28E-07	60
28-Apr-23<	13:12	Ol-02-Ol@4	2031	185	9.96E-09	2.14E-10	68954582.8	25602.61	134131.3	1.95E-03	2.39E-07	3.74E-04	1.28E-07	60
28-Apr-23<	13:37	SCOL@32	1859	2432	8.66E-09	2.16E-10	73842545.32	27668.59	144689.36	1.97E-03	2.78E-07	3.77E-04	1.07E-07	60
28-Apr-23<	13:47	SCOL@33	1859	2412	8.14E-09	2.14E-10	72234805.92	27056.93	141542.04	1.97E-03	2.85E-07	3.77E-04	1.12E-07	60
28-Apr-23<	13:57	SCOL@34	1859	2392	7.78E-09	2.15E-10	72534211	27166.68	142137.19	1.97E-03	2.28E-07	3.77E-04	1.28E-07	60
28-Apr-23<	16:17	CAI-157-Sp@1	1456	-4425	1.06E-08	2.13E-10	11911051.2	4390.71	22957.18	1.93E-03	7.67E-07	3.69E-04	3.60E-07	60
28-Apr-23<	16:27	CAI-157-Sp@2	1419	-4404	1.05E-08	2.10E-10	6509560.92	2404.84	12525.05	1.92E-03	9.69E-07	3.69E-04	4.91E-07	60

Date	Hour	Analysis Name	X	Y	Chamber Pressure	Primary Intensity	^{16}O	^{17}O	^{18}O	$^{18}O/^{16}O$	Error	$^{17}O/^{16}O$	Error	nb cycles
28-Apr-23<	16:37	CAI-157-Sp@3	1596	-4484	1.02E-08	2.11E-10	68777504.65	24492.51	127994.18	1.87E-03	3.22E-07	3.58E-04	1.12E-07	60
28-Apr-23<	16:47	CAI-157-Sp@4	1606	-4514	1.03E-08	2.12E-10	67770792.52	24182.47	126535.97	1.88E-03	2.62E-07	3.59E-04	1.13E-07	60
28-Apr-23<	19:28	CAI-154-Fo@2	3004	-4656	1.02E-08	2.10E-10	69256242.8	25726.42	134675.5	1.95E-03	2.87E-07	3.74E-04	1.48E-07	60
28-Apr-23<	19:38	ROI-01-Fo@1	3904	-4619	1.03E-08	2.08E-10	67386834.64	24930.94	130512.5	1.95E-03	2.73E-07	3.72E-04	1.52E-07	60
28-Apr-23<	19:48	ROI-01-Fo@2	3929	-4521	1.00E-08	2.07E-10	67290319.24	24916.11	130527.1	1.95E-03	2.98E-07	3.72E-04	1.16E-07	60
28-Apr-23<	19:58	ROI-01-Fo@3	3630	-4683	1.00E-08	2.09E-10	69723897.26	25846.93	135253.23	1.95E-03	2.51E-07	3.73E-04	1.29E-07	60
28-Apr-23<	20:08	ROI-02-Fo@1	3814	-4932	1.01E-08	2.07E-10	70004610.9	26058.63	136275.86	1.96E-03	2.89E-07	3.74E-04	1.14E-07	60
28-Apr-23<	20:18	ROI-02-Fo@2	3712	-5003	1.01E-08	2.05E-10	68868882.69	25629.29	134031.03	1.95E-03	2.95E-07	3.74E-04	1.20E-07	60
28-Apr-23<	20:28	ROI-03-Fa@1	4128	-5228	1.01E-08	2.08E-10	84907884.55	31619.27	165108.58	1.95E-03	2.69E-07	3.75E-04	1.29E-07	60
28-Apr-23<	20:38	ROI-03-Fa@2	4254	-5133	1.01E-08	2.08E-10	83227519.02	30992.28	161960.71	1.95E-03	2.42E-07	3.75E-04	1.14E-07	60
28-Apr-23<	20:48	ROI-03-Fa@3	4331	-5061	1.01E-08	2.05E-10	83876746.35	31232.68	163105.3	1.95E-03	2.42E-07	3.75E-04	1.24E-07	60
28-Apr-23<	20:58	ROI-03-Fa@4	4182	-5120	1.00E-08	2.07E-10	83670817.35	31166.75	162855.39	1.96E-03	2.87E-07	3.75E-04	1.19E-07	60
28-Apr-23<	21:08	ROI-04-Fa@1	4707	-5447	1.01E-08	2.08E-10	83375803.03	31087.18	162331.42	1.96E-03	2.61E-07	3.75E-04	9.60E-08	60
28-Apr-23<	21:19	ROI-04-Fa@2	4501	-5549	1.01E-08	2.06E-10	82053563.06	30591.96	159799.62	1.96E-03	2.82E-07	3.75E-04	8.09E-08	60
28-Apr-23<	21:29	ROI-05-Fa@1	2558	-4651	1.01E-08	2.07E-10	78416356.02	29393.61	154292.72	1.98E-03	2.72E-07	3.77E-04	1.02E-07	60
28-Apr-23<	21:39	ROI-06-Fo@1	2627	-4979	9.98E-09	2.09E-10	67945254.74	25354.34	132701.18	1.96E-03	2.78E-07	3.75E-04	1.19E-07	60
28-Apr-23<	21:49	ROI-06-Fo@2	2511	-4819	9.89E-09	2.07E-10	68066595.03	25362.83	132651.94	1.96E-03	3.21E-07	3.75E-04	1.09E-07	60
28-Apr-23<	21:59	ROI-07-Fa@1	-1223	-1909	9.96E-09	2.06E-10	69504661.79	25808.97	135129.61	1.95E-03	2.62E-07	3.74E-04	1.32E-07	60
28-Apr-23<	22:09	ROI-07-Fa@2	-1089	-1789	9.75E-09	2.09E-10	69871827.81	25948.07	135823.23	1.95E-03	2.20E-07	3.74E-04	1.36E-07	60
28-Apr-23<	22:19	ROI-08-Fo@1	-1394	-2139	9.72E-09	2.07E-10	70645209.81	26366.09	137961.28	1.96E-03	2.80E-07	3.76E-04	1.15E-07	60
28-Apr-23<	22:29	ROI-08-Fo@2	-1531	-2196	9.68E-09	2.06E-10	74532179.72	27666.9	144876.78	1.95E-03	2.79E-07	3.74E-04	1.13E-07	60
28-Apr-23<	22:49	ROI-09-Fo@1	-2042	-2038	9.71E-09	2.08E-10	68679802.26	25451.76	133278.03	1.95E-03	3.31E-07	3.73E-04	1.34E-07	60
28-Apr-23<	22:59	ROI-10-Fo@1	-1777	-1794	9.62E-09	2.06E-10	68448403.84	25424.86	133150.64	1.95E-03	3.02E-07	3.74E-04	1.39E-07	60
28-Apr-23<	23:09	ROI-11-Fa@1	-445	559	9.64E-09	2.08E-10	81696705.77	30466.53	159350.01	1.96E-03	2.92E-07	3.75E-04	1.11E-07	60

Date	Hour	Analysis Name	X	Y	Chamber Pressure	Primary Intensity	^{16}O	^{17}O	^{18}O	$^{18}O/^{16}O$	Error	$^{17}O/^{16}O$	Error	nb cycles
28-Apr-23<	23:19	ROI-12-Fo@1	-504	2189	9.76E-09	2.08E-10	68322997.9	25364.49	132673.02	1.95E-03	3.36E-07	3.74E-04	1.21E-07	60
28-Apr-23<	23:29	ROI-12-Fo@2	-458	2251	9.70E-09	2.06E-10	67461469.96	25030.74	131046.51	1.95E-03	3.28E-07	3.73E-04	1.21E-07	60
28-Apr-23<	23:39	ROI-12-Fo@3	-268	2294	9.78E-09	2.07E-10	67402800.52	24991.02	130915.39	1.95E-03	2.89E-07	3.73E-04	1.22E-07	60
28-Apr-23<	23:49	ROI-13-Fo@1	193	2586	9.77E-09	2.08E-10	69274121.48	25679.19	134435.63	1.95E-03	3.24E-07	3.73E-04	1.21E-07	60
28-Apr-23<	23:59	ROI-13-Fo@2	7	2512	9.70E-09	2.06E-10	68747646.37	25476.21	133210.49	1.95E-03	2.80E-07	3.73E-04	1.24E-07	60
29-Apr-23<	00:09	ROI-14-Fo@1	2016	2213	9.81E-09	2.06E-10	69066419.55	25612.5	134052.38	1.95E-03	2.64E-07	3.73E-04	1.14E-07	60
29-Apr-23<	00:19	ROI-14-Fo@2	1998	2083	9.70E-09	2.08E-10	68521434.45	25399.65	132992.43	1.95E-03	2.17E-07	3.73E-04	1.27E-07	60
29-Apr-23<	00:29	ROI-14-Fo@3	2018	2543	1.00E-08	2.06E-10	64942532.06	24076.34	126065.1	1.95E-03	2.34E-07	3.73E-04	1.26E-07	60
29-Apr-23<	00:39	ROI-14-Fo@4	2402	2393	9.87E-09	2.05E-10	1023228.64	392.74	2080.42	1.95E-03	2.02E-06	3.69E-04	9.51E-07	60
29-Apr-23<	00:49	ROI-14-Fo@5	1670	2364	9.87E-09	2.08E-10	68082283.05	25235.44	132130.48	1.95E-03	2.23E-07	3.73E-04	1.23E-07	60
29-Apr-23<	00:59	ROI-14-Fo@6	1535	2457	9.85E-09	2.06E-10	69590639.74	25763.36	134992.34	1.95E-03	2.81E-07	3.72E-04	1.21E-07	60
29-Apr-23<	01:09	ROI-14-Fo@7	2596	2944	9.80E-09	2.05E-10	68364845.24	25340.66	132708.38	1.95E-03	2.97E-07	3.73E-04	1.21E-07	60
29-Apr-23<	01:20	ROI-14-Fo@8	3020	2749	9.83E-09	2.07E-10	70390148.93	26057.39	136349.83	1.95E-03	2.48E-07	3.72E-04	1.26E-07	60
29-Apr-23<	01:30	ROI-15-Fo@1	2934	3180	9.90E-09	2.07E-10	67998336.98	25180.1	131838.31	1.95E-03	2.85E-07	3.73E-04	1.03E-07	60
29-Apr-23<	01:40	ROI-16-Fo@1	2946	3884	9.85E-09	2.05E-10	67529586.25	25030.56	131123.16	1.95E-03	3.19E-07	3.73E-04	1.22E-07	60
29-Apr-23<	01:50	ROI-16-Fo@2	2984	3993	9.86E-09	2.07E-10	68349635.41	25299.9	132619.38	1.95E-03	2.77E-07	3.72E-04	1.33E-07	60
29-Apr-23<	02:00	ROI-17-Fa@1	-878	4984	9.81E-09	2.07E-10	78367692.89	29187.79	152711.79	1.96E-03	2.92E-07	3.75E-04	1.19E-07	60
29-Apr-23<	02:10	ROI-17-Fa@2	-816	5029	9.67E-09	2.05E-10	75929954.71	28293.74	148019.89	1.96E-03	2.65E-07	3.75E-04	1.26E-07	60
29-Apr-23<	02:20	ROI-17-Fa@3	-771	5097	9.78E-09	2.07E-10	75536827.83	28156.11	147257.82	1.96E-03	2.36E-07	3.75E-04	1.19E-07	60
29-Apr-23<	02:30	ROI-17-Fa@4	-676	5124	9.70E-09	2.08E-10	77985466.36	29047.31	151786	1.95E-03	2.30E-07	3.75E-04	1.25E-07	60
29-Apr-23<	02:40	ROI-18-Fo@1	896	4453	9.71E-09	2.06E-10	67932759.13	25155.64	131714.09	1.95E-03	2.45E-07	3.73E-04	1.27E-07	60
29-Apr-23<	02:50	ROI-18-Fo@2	1016	4503	9.80E-09	2.07E-10	67309316.88	25003.78	130842.6	1.95E-03	2.89E-07	3.74E-04	1.26E-07	60
29-Apr-23<	03:00	ROI-19-Fo@1	820	4313	9.65E-09	2.08E-10	68655058.65	25457.84	133261.53	1.95E-03	2.77E-07	3.73E-04	1.08E-07	60
29-Apr-23<	03:10	CAI-74-Sp@1	170	5716	9.72E-09	2.07E-10	64005979.44	22779.49	119022.65	1.87E-03	2.65E-07	3.58E-04	1.23E-07	60

Date	Hour	Analysis Name	X	Y	Chamber Pressure	Primary Intensity	^{16}O	^{17}O	^{18}O	$^{18}O/^{16}O$	Error	$^{17}O/^{16}O$	Error	nb cycles
29-Apr-23<	03:20	CAI-74-Sp@2	177	5700	9.78E-09	2.07E-10	58598353.81	20822.76	108874.01	1.87E-03	3.12E-07	3.57E-04	1.34E-07	60
29-Apr-23<	03:30	CAI-74-Sp@3	198	5694	9.70E-09	2.09E-10	45958095.29	16515.4	86373.29	1.89E-03	3.18E-07	3.61E-04	1.34E-07	60
29-Apr-23<	03:40	CAI-74-Sp@4	193	5651	9.70E-09	2.08E-10	63921075.07	22738.02	118937.24	1.87E-03	3.10E-07	3.58E-04	1.21E-07	60
29-Apr-23<	03:50	CAI-74-Sp@5	166	5674	9.76E-09	2.08E-10	59831130.43	21272.76	111201.47	1.87E-03	3.01E-07	3.58E-04	1.34E-07	60
29-Apr-23<	09:50	Ipanko@26	-13	-1771	2.96E-08	2.08E-10	59289073.13	22339.42	117952.28	2.00E-03	3.56E-07	3.79E-04	1.11E-07	60
29-Apr-23<	10:00	Ipanko@27	-13	-1791	1.41E-08	2.07E-10	58255819.88	21953.87	115947.45	2.00E-03	3.06E-07	3.79E-04	1.30E-07	60
29-Apr-23<	10:10	Ipanko@28	-13	-1811	1.15E-08	2.08E-10	58899516.7	22221.45	117230.66	2.00E-03	2.62E-07	3.79E-04	1.21E-07	60
29-Apr-23<	10:20	Ipanko@29	-13	-1831	1.03E-08	2.08E-10	58837059.45	22195.61	117150.28	2.00E-03	3.21E-07	3.79E-04	1.24E-07	60
29-Apr-23<	10:30	Ipanko@30	-13	-1851	9.64E-09	2.07E-10	58121445.3	21920.71	115721.66	2.00E-03	2.57E-07	3.79E-04	1.16E-07	60
29-Apr-23<	10:40	SCOL@32	1772	2354	9.10E-09	2.07E-10	70155461.69	26231.44	137268.13	1.97E-03	2.45E-07	3.76E-04	1.21E-07	60
29-Apr-23<	10:50	SCOL@33	1772	2334	8.74E-09	2.08E-10	70299150.8	26295.09	137545.33	1.97E-03	2.71E-07	3.76E-04	1.33E-07	60
29-Apr-23<	11:00	SCOL@34	1772	2314	8.44E-09	2.06E-10	69040367.97	25807.72	135104.13	1.97E-03	3.06E-07	3.76E-04	1.39E-07	60
29-Apr-23<	11:10	SCOL@35	1772	2294	8.20E-09	2.06E-10	69267154.49	25900.55	135558.39	1.97E-03	2.87E-07	3.76E-04	1.10E-07	60
29-Apr-23<	11:20	SCOL@36	1772	2274	8.05E-09	2.07E-10	69717665.52	26057.01	136435.19	1.97E-03	2.79E-07	3.76E-04	1.24E-07	60
29-Apr-23<	11:30	Rockport@23	5054	-4151	7.81E-09	2.05E-10	77716713.42	28905.75	150493.1	1.94E-03	2.32E-07	3.74E-04	1.11E-07	60
29-Apr-23<	11:40	Rockport@24	5054	-4131	7.65E-09	2.05E-10	77213029.42	28726.86	149649.29	1.95E-03	2.62E-07	3.74E-04	1.33E-07	60
29-Apr-23<	11:50	Rockport@25	5054	-4111	7.50E-09	2.06E-10	77189032.4	28704.82	149556.58	1.95E-03	2.58E-07	3.74E-04	1.03E-07	60
29-Apr-23<	12:00	Rockport@26	5054	-4091	7.38E-09	2.05E-10	76082134.25	28284.17	147408.22	1.95E-03	2.37E-07	3.74E-04	1.06E-07	60

7.8 Chondrule Mg#

Semi-quantitative EDS areal analyses were performed using the AZtec v6 software from Oxford Instruments on chondrules and chondrule fragments of the Aguas Zarcas, Paris, and Winchcombe meteorites. Target locations (marked by red circles) within the investigated olivine grains, along with their corresponding analytical spectra, are shown in the following BSE images, organised by meteorite. Measurements were conducted in proximity of their corresponding SIMS analysis locations (cf. Appendix 7.9).

Since olivine is the most abundant phase within the targeted chondrule mineral, Mg# values were calculated as the average of the individual measurements per target. Mg# for each data point was determined using the following relation: $Mg\# = [MgO]/[FeO]$ in mol% (Ebel and Grossman, 2000; Tenner et al., 2015; Chaumard et al., 2018), with the assumption of perfect stoichiometry for 3 cations and 4 oxygen atoms, for intermediate mineral compositions between Fe_2SiO_4 and Mg_2SiO_4 (based on 4 O atoms per formula unit). A total of 38 chondrule target Mg# values are plotted in Fig. 7.2 and listed in Table 7.12. Uncertainties are reported as standard deviations (SD); values of 0.00 indicate single measurements.

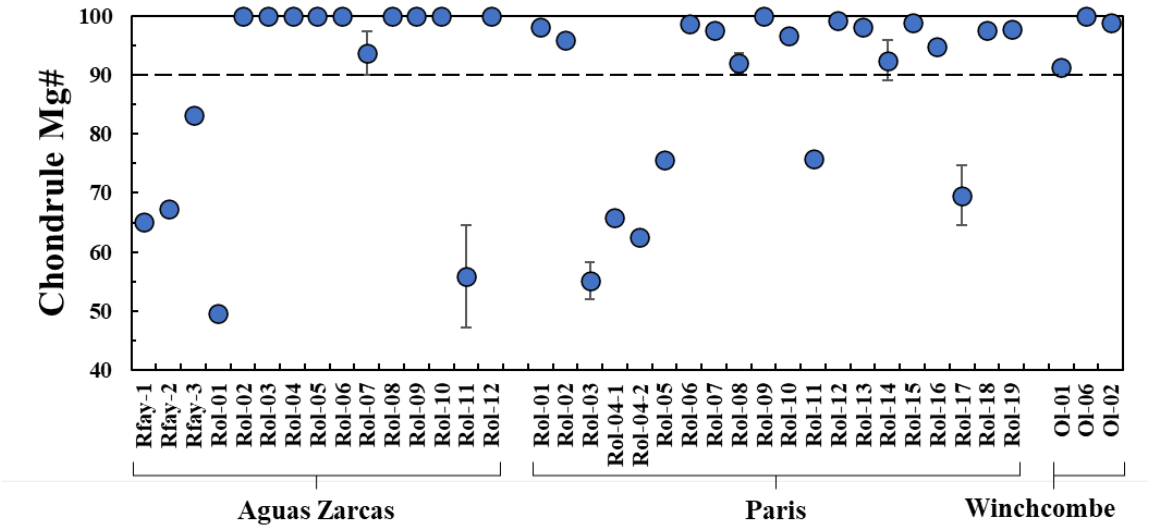

Figure 7.2. Mean Mg# of targeted olivine grains within chondrules and chondrule fragments of the Aguas Zarcas, Paris, and Winchcombe meteorites. The uncertainties correspond to the standard deviation (SD) of the measured values.

Table 7.12. Mean Mg# of targeted olivine grains within chondrules and chondrule fragments of the Aguas Zarcas, Paris, and Winchcombe meteorites.

Chondrite	Object	Mg#	SD
Aguas Zarcas	Rfay-1	65.14	0.00
	Rfay-2	67.35	0.00
	Rfay-3	83.28	0.00
	Rol-01	49.65	0.00
	Rol-02	100.00	0.00
	Rol-03	100.00	0.00
	Rol-04	100.00	0.00
	Rol-05	100.00	0.00
	Rol-06	100.00	0.00
	Rol-07	93.76	3.64
	Rol-08	100.00	0.00
	Rol-09	100.00	0.00
	Rol-10	100.00	0.00
	Rol-11	55.85	8.75
	Rol-12	100.00	0.00
Paris	Rol-01	98.19	0.61
	Rol-02	95.90	0.26
	Rol-03	55.17	3.18
	Rol-04-1	65.89	0.00
	Rol-04-2	62.52	0.00
	Rol-05	75.70	0.00
	Rol-06	98.67	0.19
	Rol-07	97.53	0.48
	Rol-08	92.07	1.61
	Rol-09	100.00	0.00
	Rol-10	96.73	0.00
	Rol-11	75.79	0.00
	Rol-12	99.28	0.12
	Rol-13	98.16	0.42
	Rol-14	92.48	3.41
	Rol-15	98.92	0.00
	Rol-16	94.84	1.13
	Rol-17	69.61	5.15
	Rol-18	97.55	0.13
	Rol-19	97.88	0.00
Winchcombe	Ol-01	91.35	0.24
	Ol-06	100.00	0.00
	Ol-02	98.94	0.78

7.8.1 Aguas Zarcas

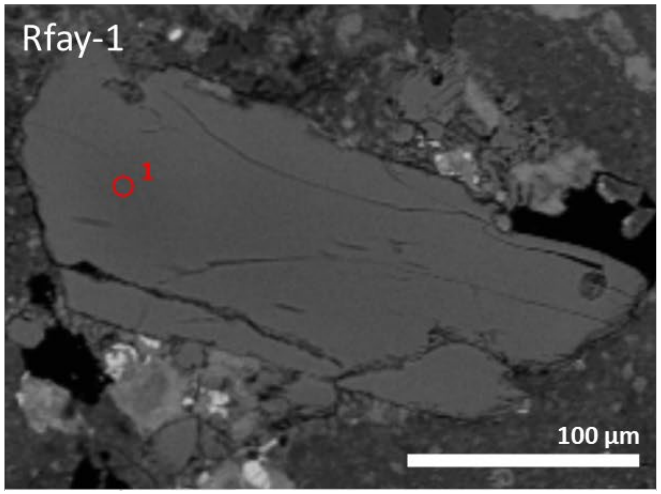

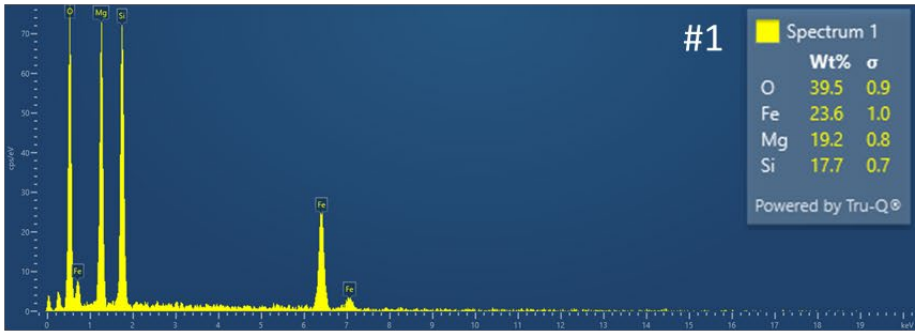

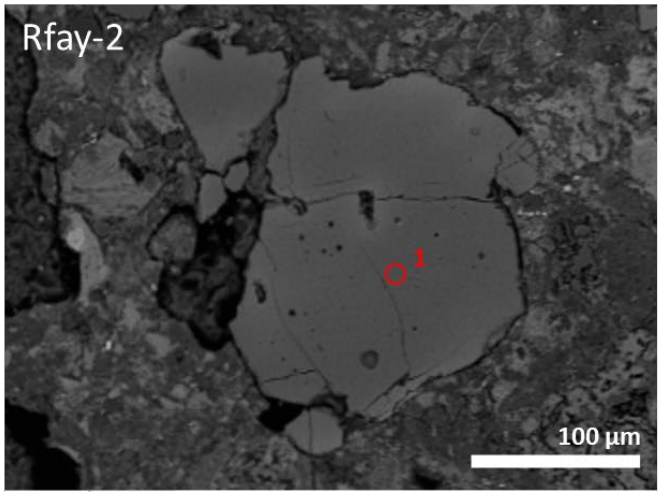

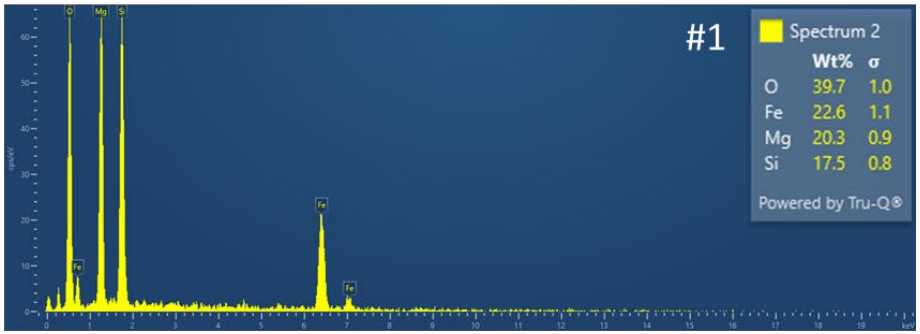

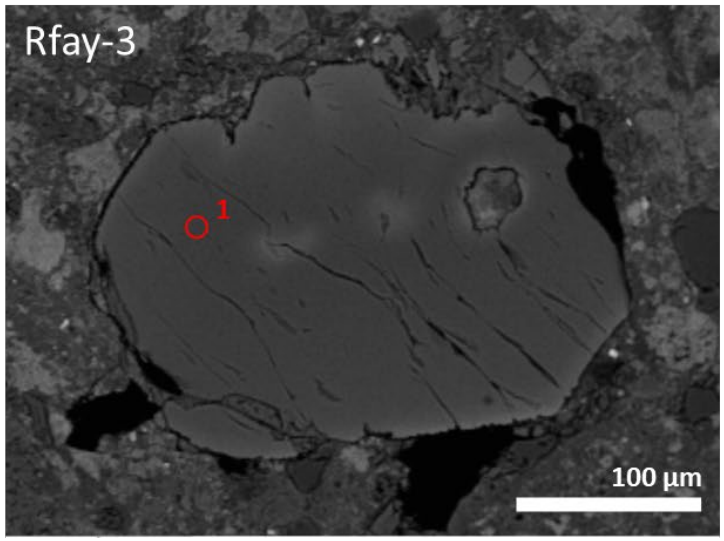
Rfay-3
1
100 µm

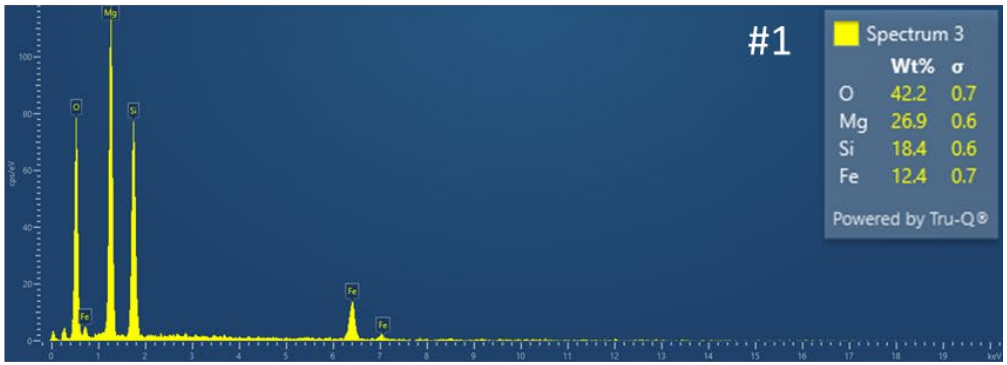
#1
Spectrum 3
Wt% σ
O 42.2 0.7
Mg 26.9 0.6
Si 18.4 0.6
Fe 12.4 0.7
Powered by Tru-Q®

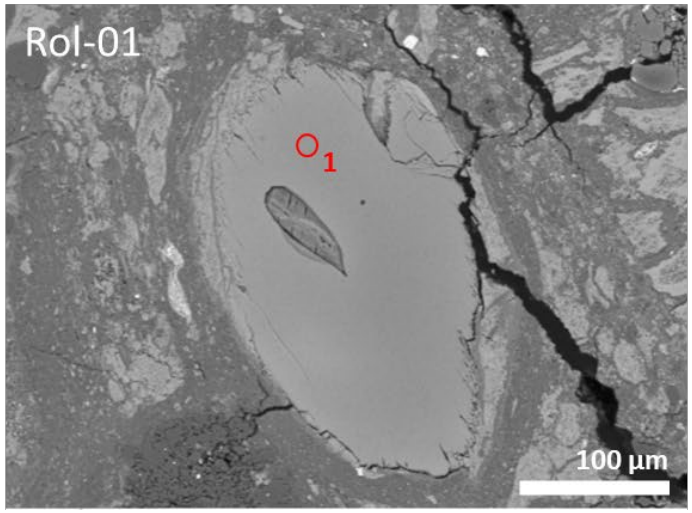
Rol-01
1
100 µm

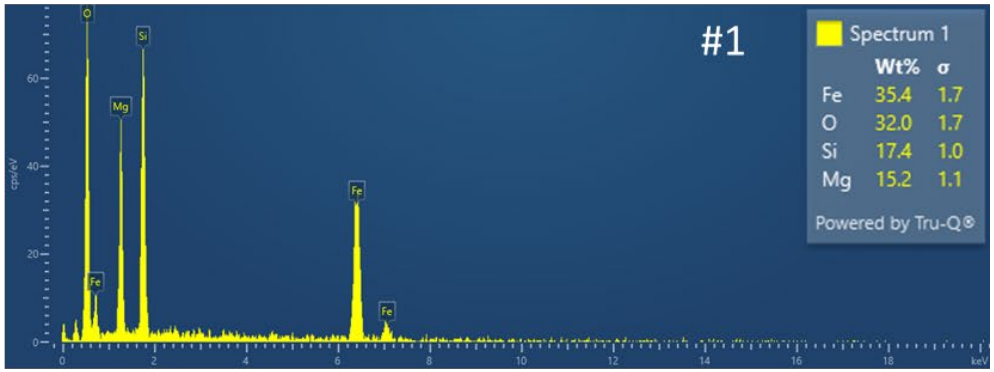
#1
Spectrum 1
Wt% σ
Fe 35.4 1.7
O 32.0 1.7
Si 17.4 1.0
Mg 15.2 1.1
Powered by Tru-Q®

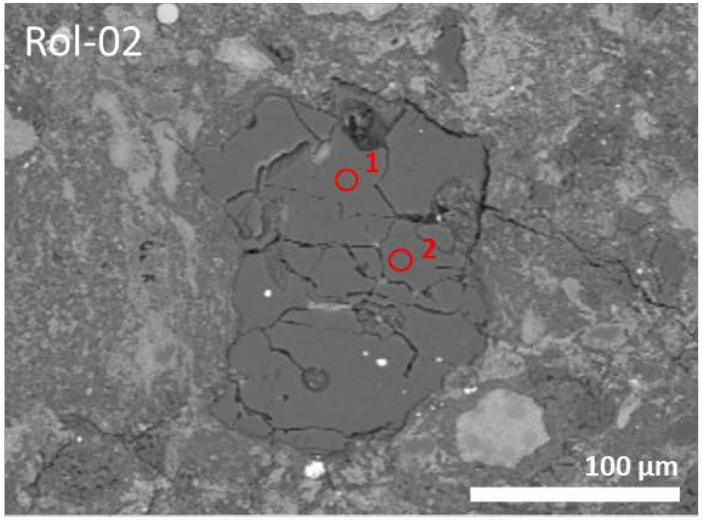
Rol-02
1
2
100 µm


#1
Spectrum 4
Wt% σ
O 46.3 3.2
Si 30.1 2.4
Mg 23.6 2.2
Powered by Tru-Q®
O
Mg
Si
cps/eV
keV


#2
Spectrum 5
Wt% σ
O 44.9 5.0
Si 34.5 4.0
Mg 20.6 3.2
Powered by Tru-Q®
O
Mg
Si
cps/eV
keV

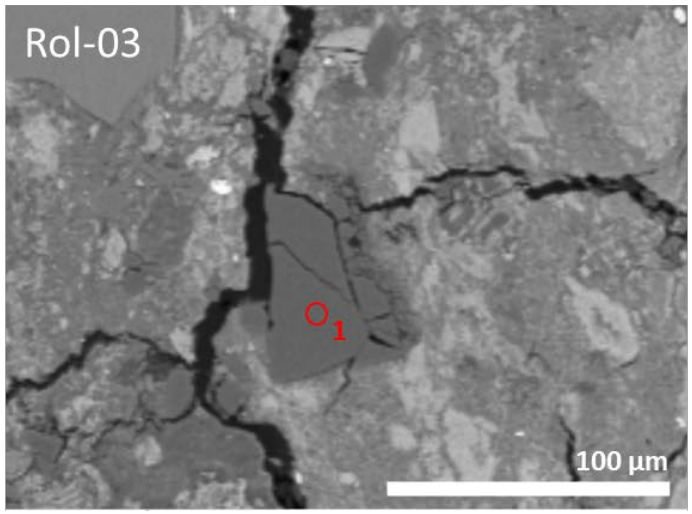
Rol-03
1
100 µm


#1
Spectrum 6
Wt% σ
Mg 39.8 3.2
O 37.3 4.0
Si 22.9 2.7
Powered by Tru-Q®
Mg
O
Si
cps/eV
keV

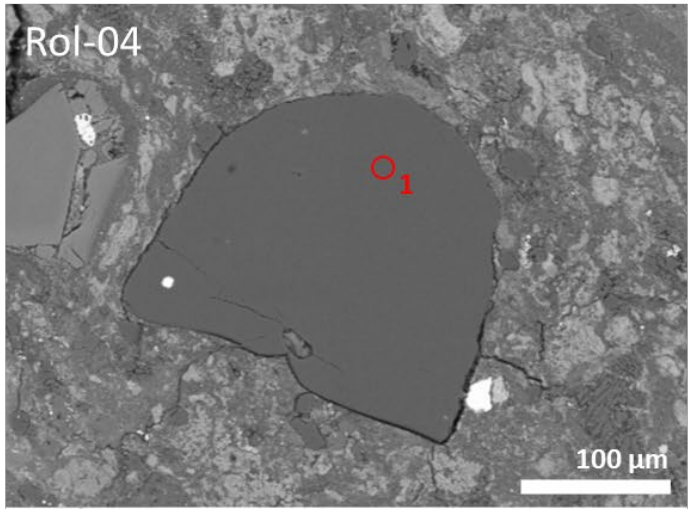
Rol-04
1
100 µm


#1
Spectrum 7
Wt% σ
O 41.3 1.3
Mg 35.6 1.0
Si 23.1 0.9
Powered by Tru-Q®
Mg
O
Si
cps/eV
keV

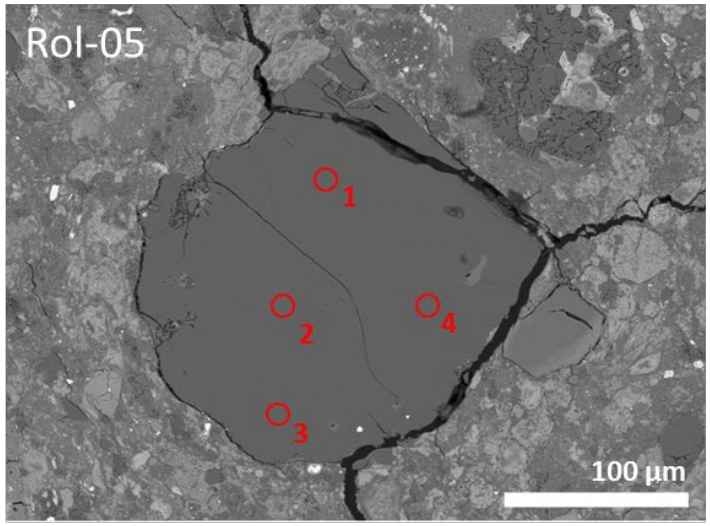
RoI-05
1
2
3
4
100 µm


#1
Spectrum 8
Wt% σ
O 41.5 1.0
Mg 35.5 0.8
Si 23.0 0.7
Powered by Tru-Q®


#2
Spectrum 9
Wt% σ
O 40.9 0.6
Mg 36.7 0.5
Si 22.4 0.4
Powered by Tru-Q®


#3
Spectrum 10
Wt% σ
O 40.2 1.1
Mg 37.8 0.9
Si 22.0 0.8
Powered by Tru-Q®

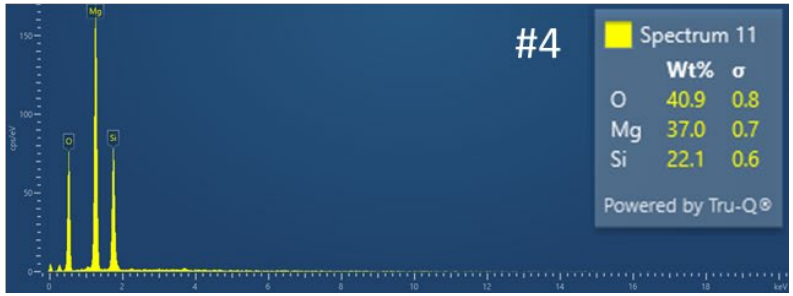
#4
Spectrum 11
Wt% σ
O 40.9 0.8
Mg 37.0 0.7
Si 22.1 0.6
Powered by Tru-Q®

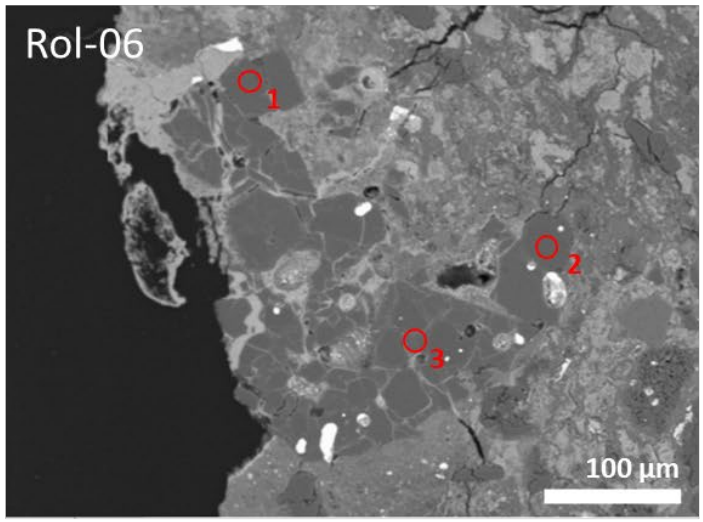
Rol-06
1
2
3
100 µm


#1
Mg
Si
O
cps/eV
keV
Spectrum 12
Wt% σ
O 43.2 2.8
Si 32.2 2.1
Mg 24.6 1.9
Powered by Tru-Q®

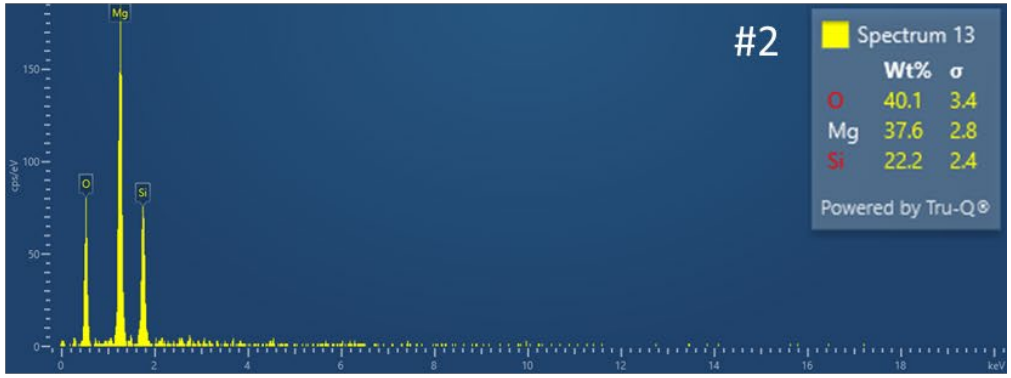
#2
Mg
Si
O
cps/eV
keV
Spectrum 13
Wt% σ
O 40.1 3.4
Mg 37.6 2.8
Si 22.2 2.4
Powered by Tru-Q®

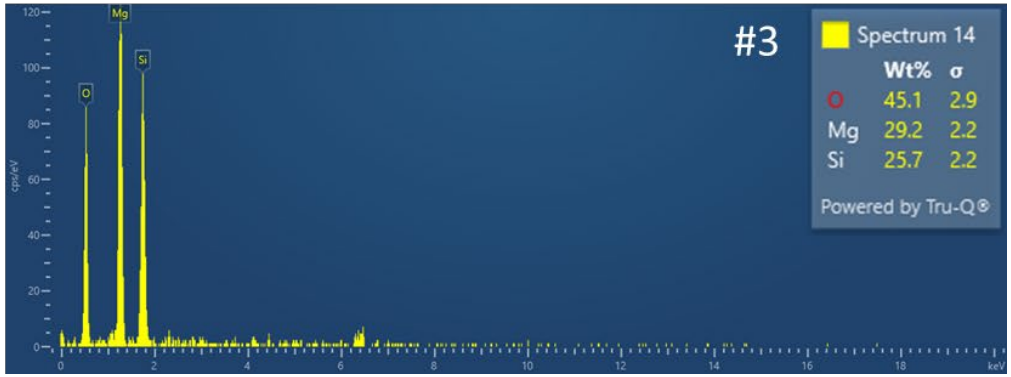
#3
Mg
Si
O
cps/eV
keV
Spectrum 14
Wt% σ
O 45.1 2.9
Mg 29.2 2.2
Si 25.7 2.2
Powered by Tru-Q®

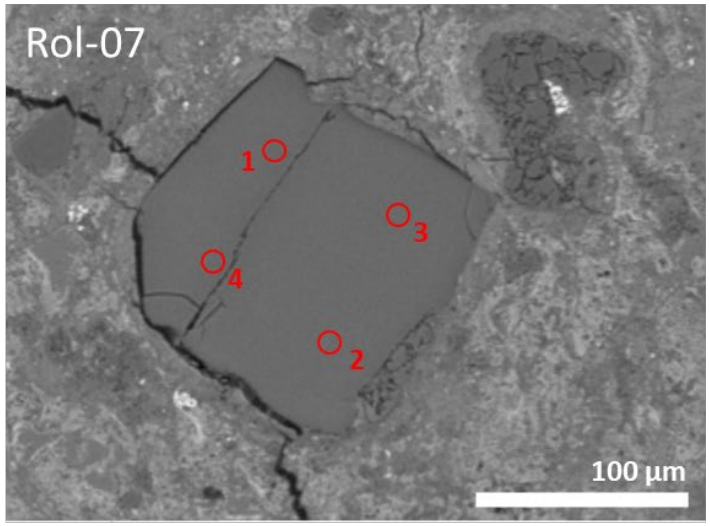
Rol-07
1
2
3
4
100 µm

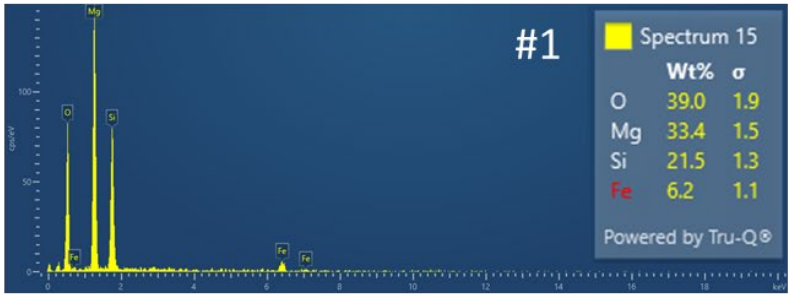
#1
Spectrum 15
Wt% σ
O 39.0 1.9
Mg 33.4 1.5
Si 21.5 1.3
Fe 6.2 1.1
Powered by Tru-Q®

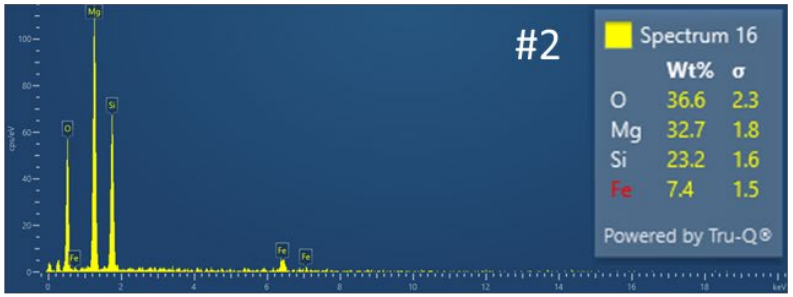
#2
Spectrum 16
Wt% σ
O 36.6 2.3
Mg 32.7 1.8
Si 23.2 1.6
Fe 7.4 1.5
Powered by Tru-Q®

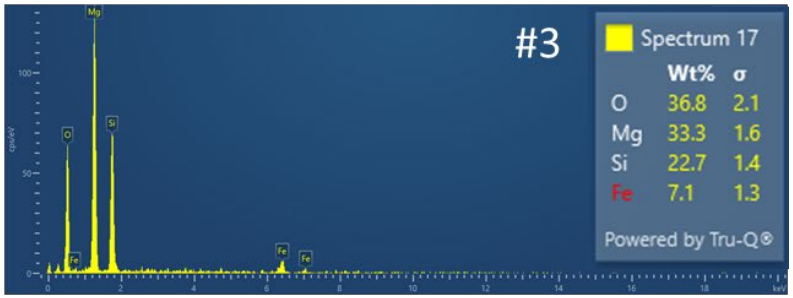
#3
Spectrum 17
Wt% σ
O 36.8 2.1
Mg 33.3 1.6
Si 22.7 1.4
Fe 7.1 1.3
Powered by Tru-Q®


#4
Spectrum 18
Wt% σ
O 42.4 3.0
Mg 35.4 2.4
Si 22.2 2.1
Powered by Tru-Q®

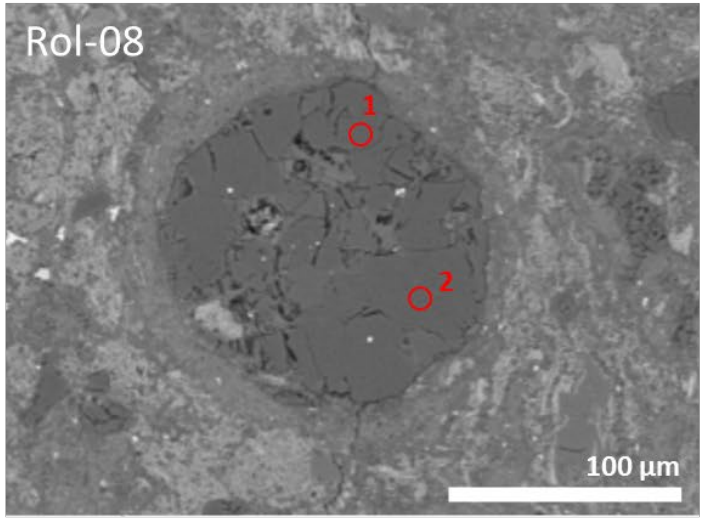
Rol-08
1
2
100 µm


#1
Mg
O
Si
cps/eV
keV
Spectrum 19
Wt% σ
O 38.3 4.2
Mg 37.9 3.3
Si 23.8 2.9
Powered by Tru-Q®

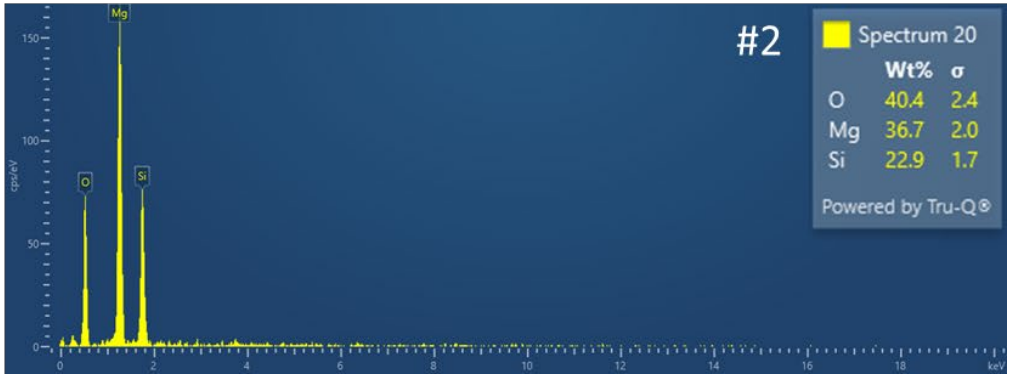
#2
Mg
O
Si
cps/eV
keV
Spectrum 20
Wt% σ
O 40.4 2.4
Mg 36.7 2.0
Si 22.9 1.7
Powered by Tru-Q®

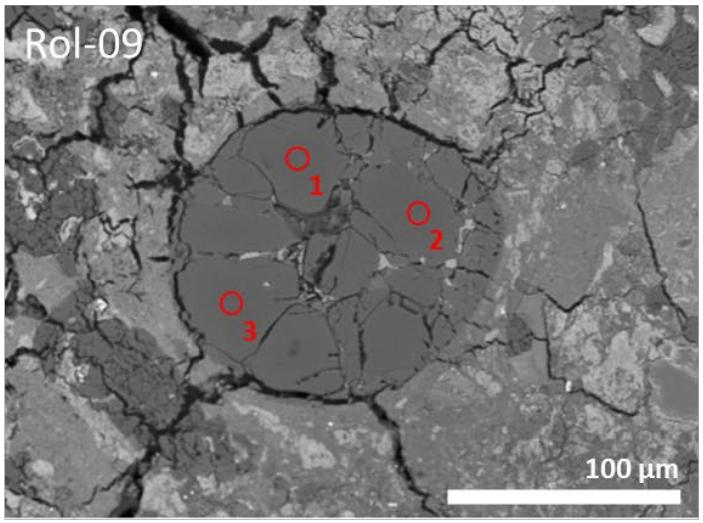
Rol-09
1
2
3
100 µm


#1
Spectrum 21
Wt% σ
O 43.4 2.4
Mg 37.2 2.0
Si 19.3 1.7
Powered by Tru-Q®
Mg
O
Si
cps/eV
keV

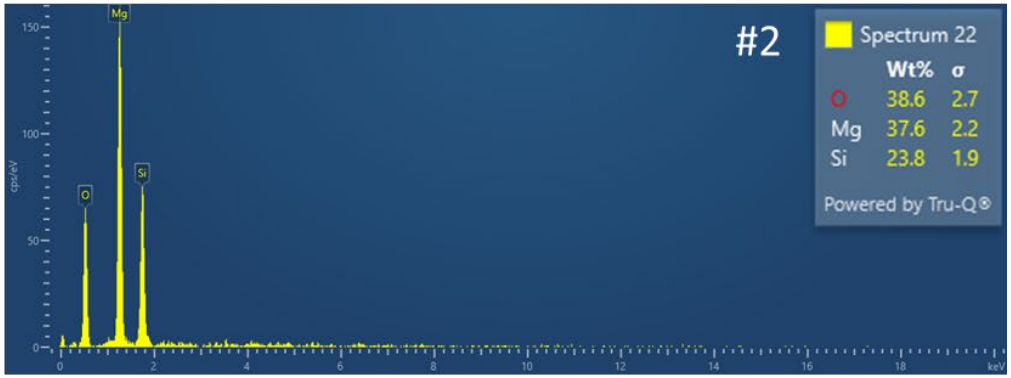
#2
Spectrum 22
Wt% σ
O 38.6 2.7
Mg 37.6 2.2
Si 23.8 1.9
Powered by Tru-Q®
Mg
O
Si
cps/eV
keV


#3
Spectrum 23
Wt% σ
O 42.6 2.4
Mg 33.1 1.9
Si 24.3 1.7
Powered by Tru-Q®
Mg
O
Si
cps/eV
keV

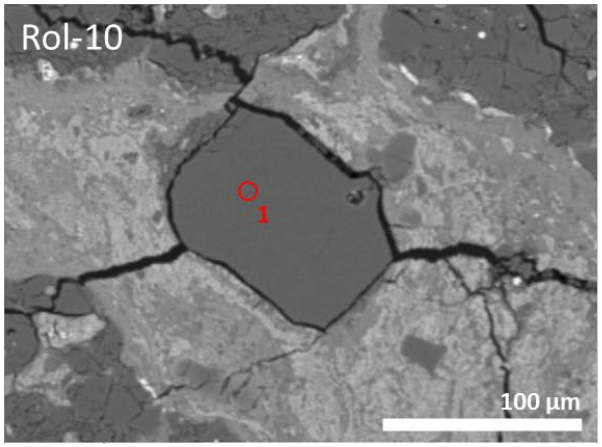
Rol-10
O1
100 µm

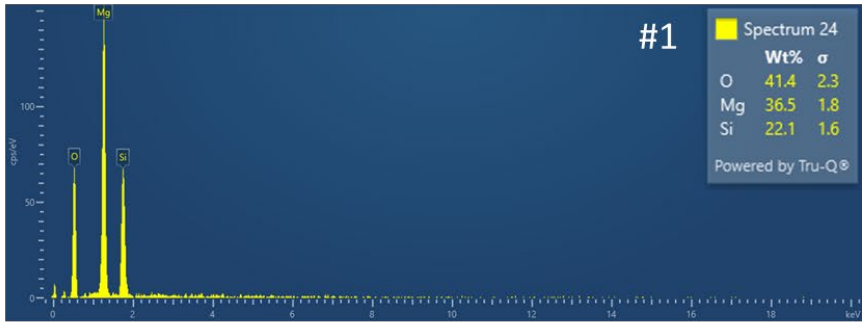
#1
Spectrum 24
Wt% σ
O 41.4 2.3
Mg 36.5 1.8
Si 22.1 1.6
Powered by Tru-Q®

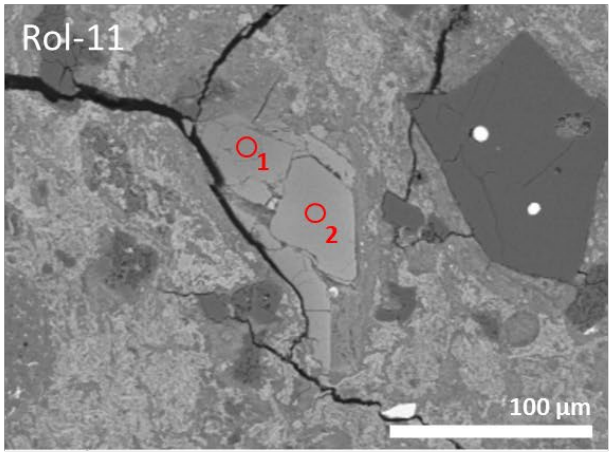
Rol-11
O1
O2
100 µm

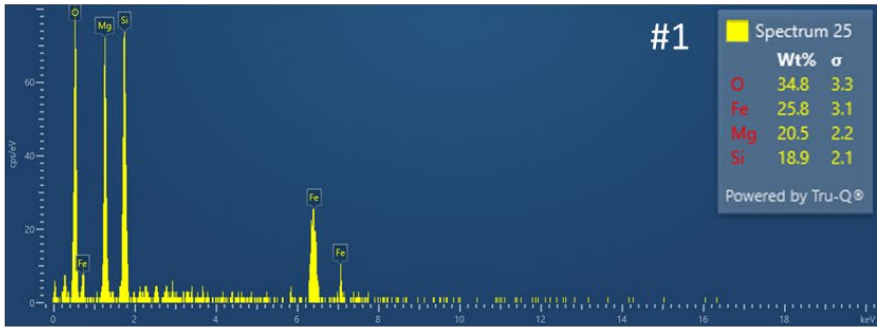
#1
Spectrum 25
Wt% σ
O 34.8 3.3
Fe 25.8 3.1
Mg 20.5 2.2
Si 18.9 2.1
Powered by Tru-Q®

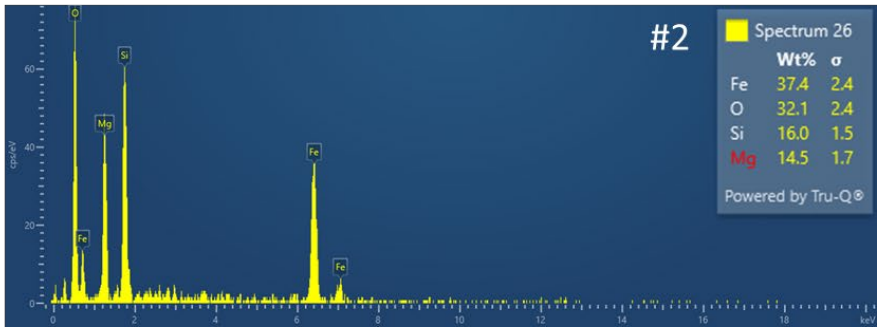
#2
Spectrum 26
Wt% σ
Fe 37.4 2.4
O 32.1 2.4
Si 16.0 1.5
Mg 14.5 1.7
Powered by Tru-Q®

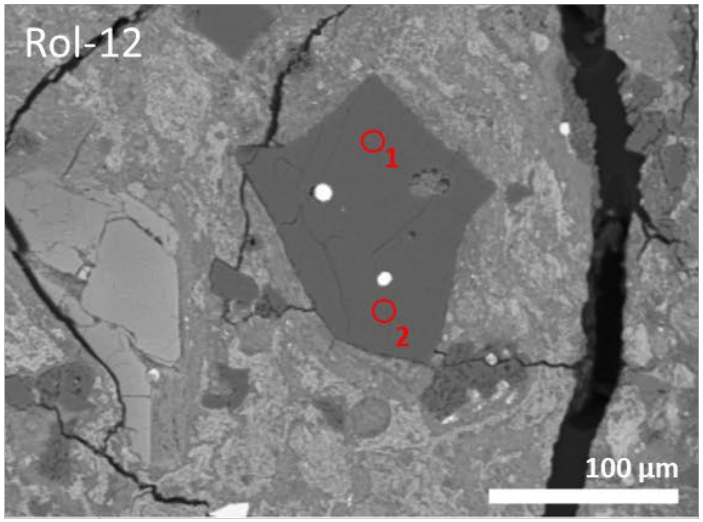
Rol-12
O1
O2
100 µm

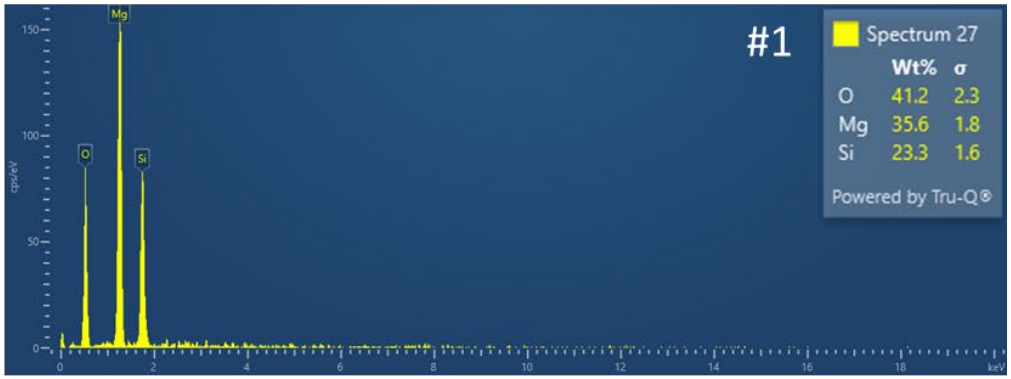
#1
Mg
O
Si
Spectrum 27
Wt% σ
O 41.2 2.3
Mg 35.6 1.8
Si 23.3 1.6
Powered by Tru-Q®
cps/eV
keV

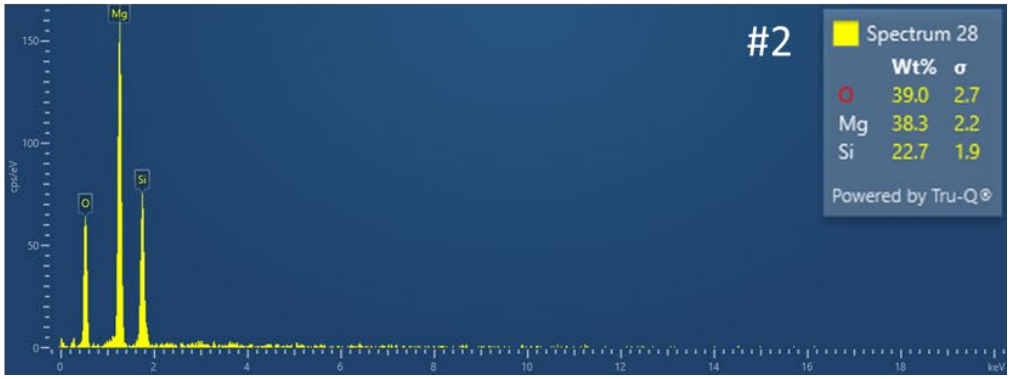
#2
Mg
O
Si
Spectrum 28
Wt% σ
O 39.0 2.7
Mg 38.3 2.2
Si 22.7 1.9
Powered by Tru-Q®
cps/eV
keV

7.8.2 Paris

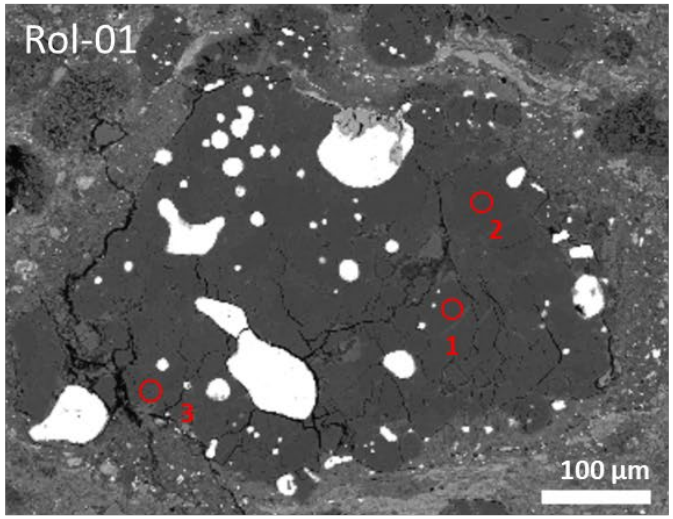
Rol-01
1
2
3
100 µm

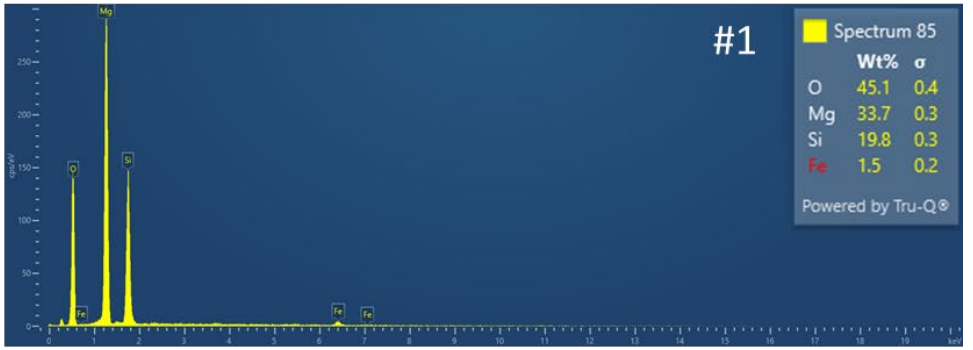
#1
Spectrum 85
Wt% σ
O 45.1 0.4
Mg 33.7 0.3
Si 19.8 0.3
Fe 1.5 0.2
Powered by Tru-Q®

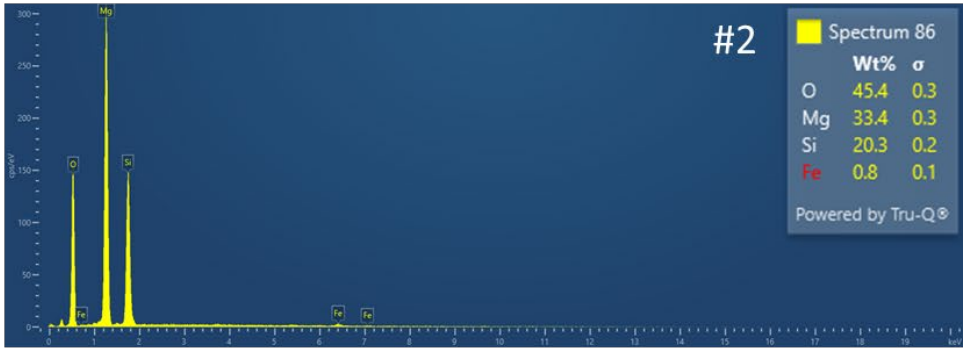
#2
Spectrum 86
Wt% σ
O 45.4 0.3
Mg 33.4 0.3
Si 20.3 0.2
Fe 0.8 0.1
Powered by Tru-Q®

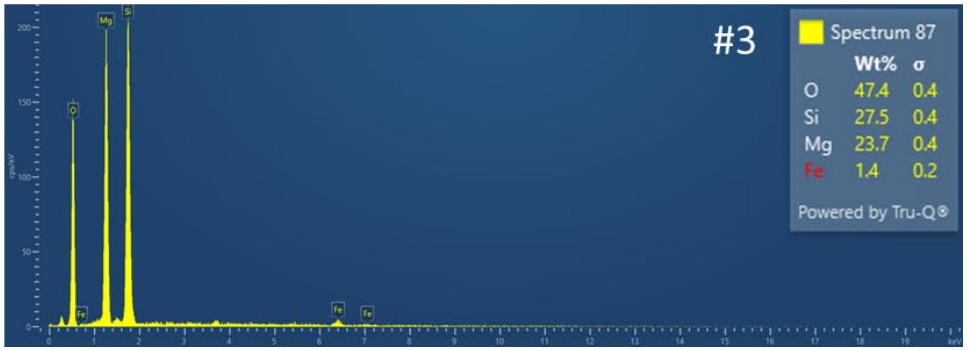
#3
Spectrum 87
Wt% σ
O 47.4 0.4
Si 27.5 0.4
Mg 23.7 0.4
Fe 1.4 0.2
Powered by Tru-Q®

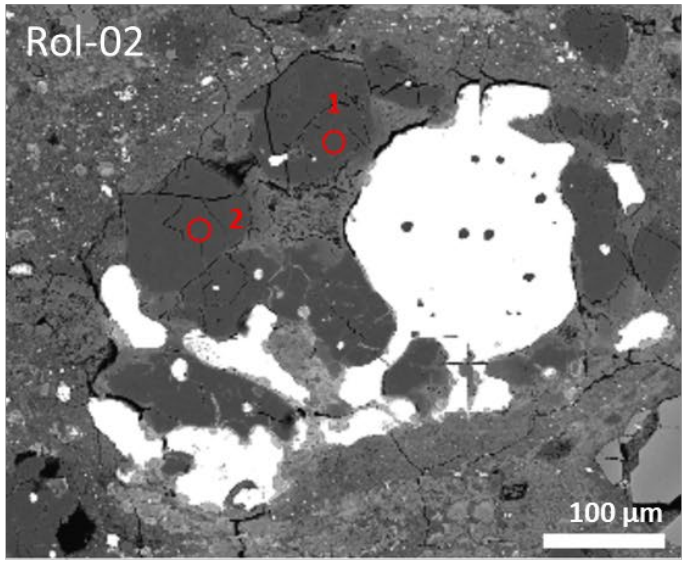
Rol-02
1
2
100 µm

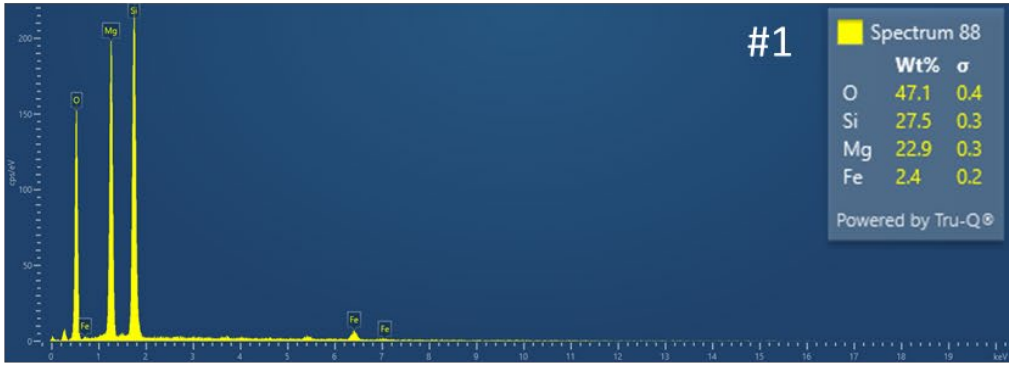
#1
Spectrum 88
Wt% σ
O 47.1 0.4
Si 27.5 0.3
Mg 22.9 0.3
Fe 2.4 0.2
Powered by Tru-Q®

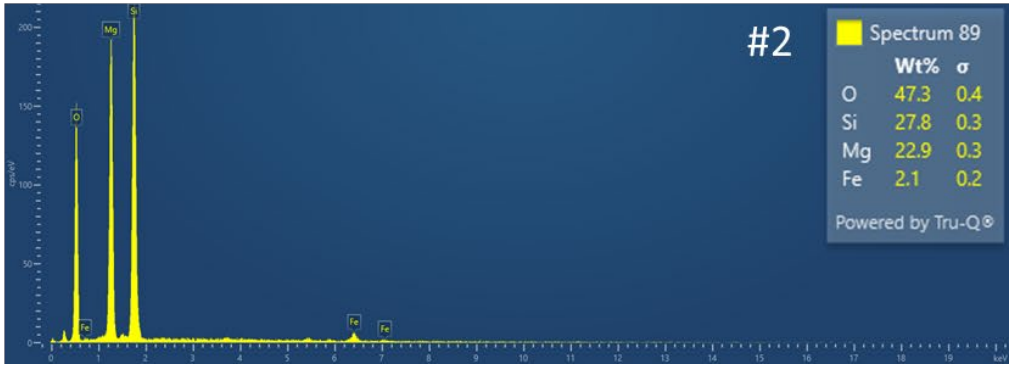
#2
Spectrum 89
Wt% σ
O 47.3 0.4
Si 27.8 0.3
Mg 22.9 0.3
Fe 2.1 0.2
Powered by Tru-Q®

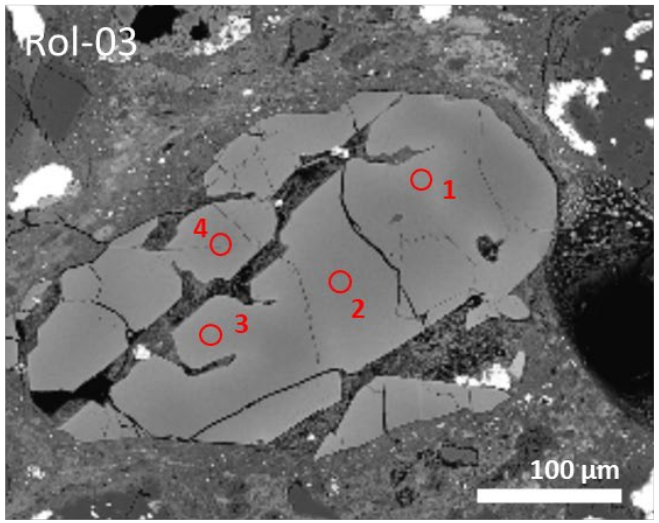
Rol-03
1
2
3
4
100 µm

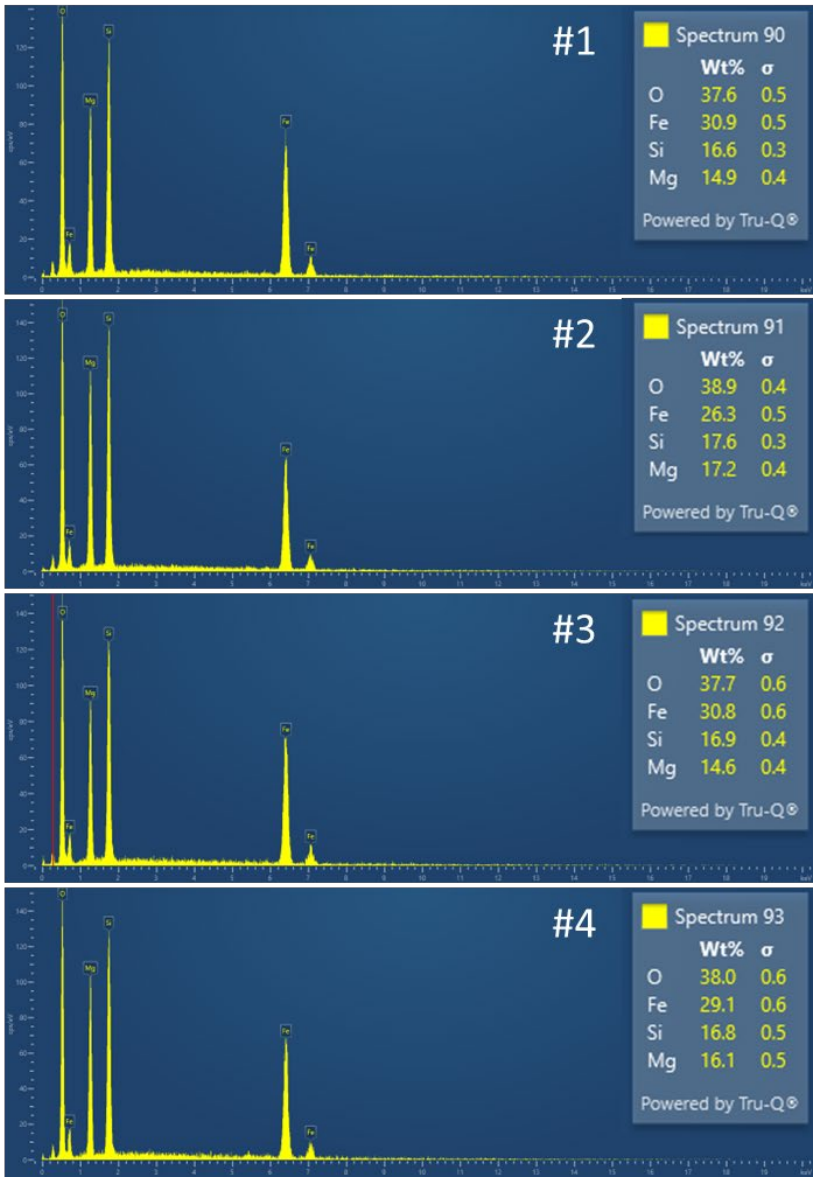
#1
Spectrum 90
Wt% σ
O 37.6 0.5
Fe 30.9 0.5
Si 16.6 0.3
Mg 14.9 0.4
Powered by Tru-Q®
#2
Spectrum 91
Wt% σ
O 38.9 0.4
Fe 26.3 0.5
Si 17.6 0.3
Mg 17.2 0.4
Powered by Tru-Q®
#3
Spectrum 92
Wt% σ
O 37.7 0.6
Fe 30.8 0.6
Si 16.9 0.4
Mg 14.6 0.4
Powered by Tru-Q®
#4
Spectrum 93
Wt% σ
O 38.0 0.6
Fe 29.1 0.6
Si 16.8 0.5
Mg 16.1 0.5
Powered by Tru-Q®

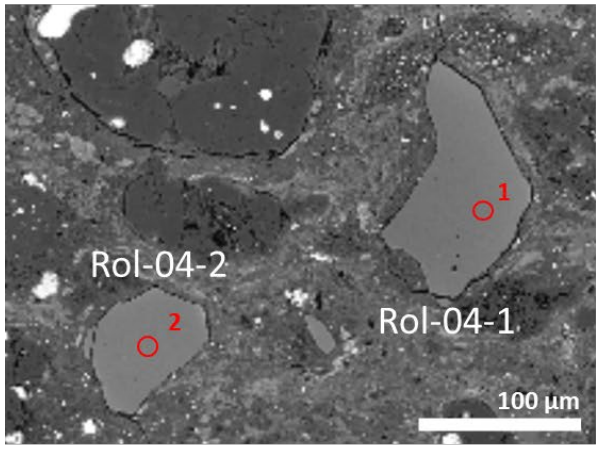
Rol-04-2
Rol-04-1
1
2
100 µm

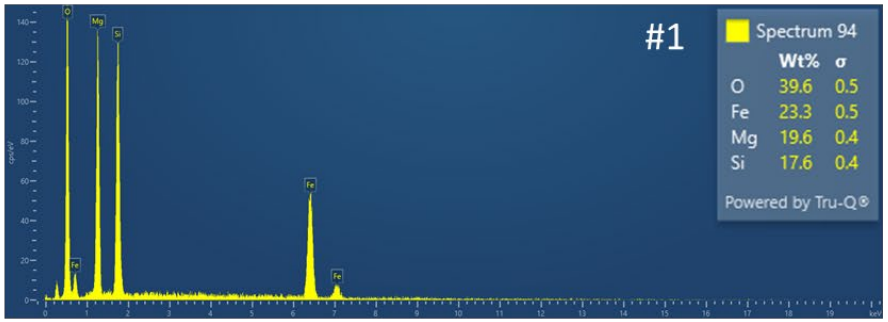
#1
Spectrum 94
Wt% σ
O 39.6 0.5
Fe 23.3 0.5
Mg 19.6 0.4
Si 17.6 0.4
Powered by Tru-Q®

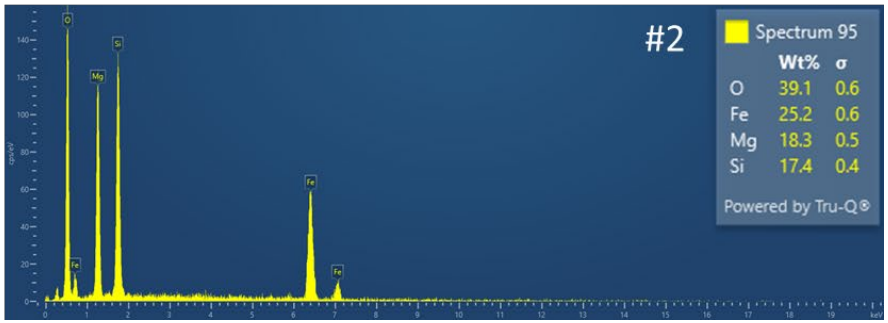
#2
Spectrum 95
Wt% σ
O 39.1 0.6
Fe 25.2 0.6
Mg 18.3 0.5
Si 17.4 0.4
Powered by Tru-Q®

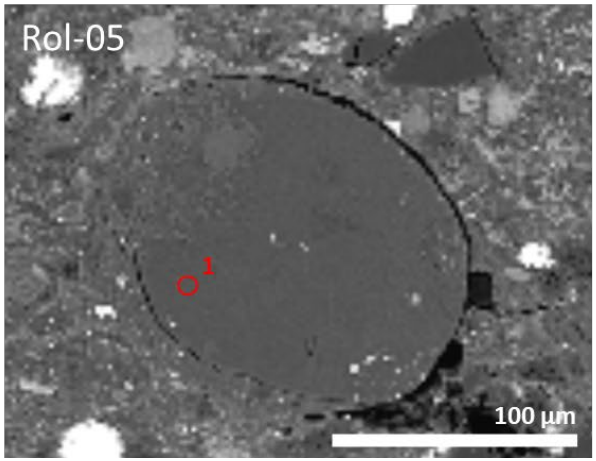
Rol-05
1
100 µm

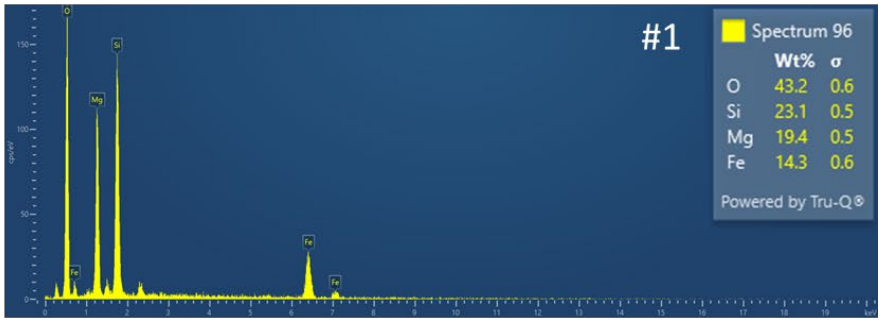
#1
Spectrum 96
Wt% σ
O 43.2 0.6
Si 23.1 0.5
Mg 19.4 0.5
Fe 14.3 0.6
Powered by Tru-Q®

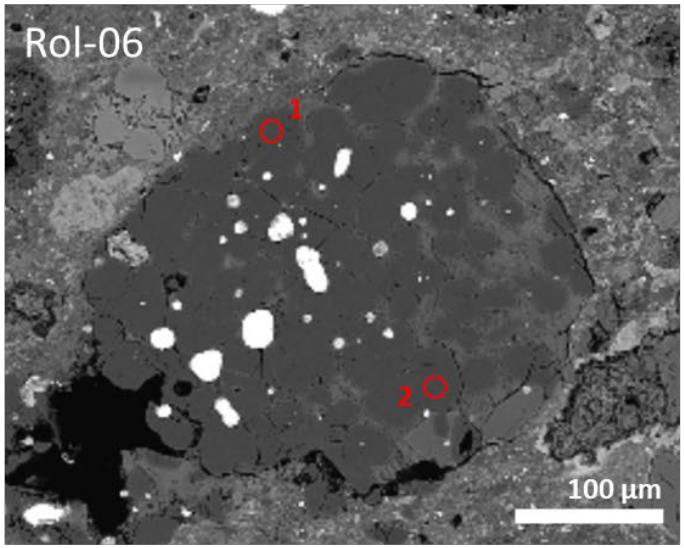
Rol-06
1
2
100 µm

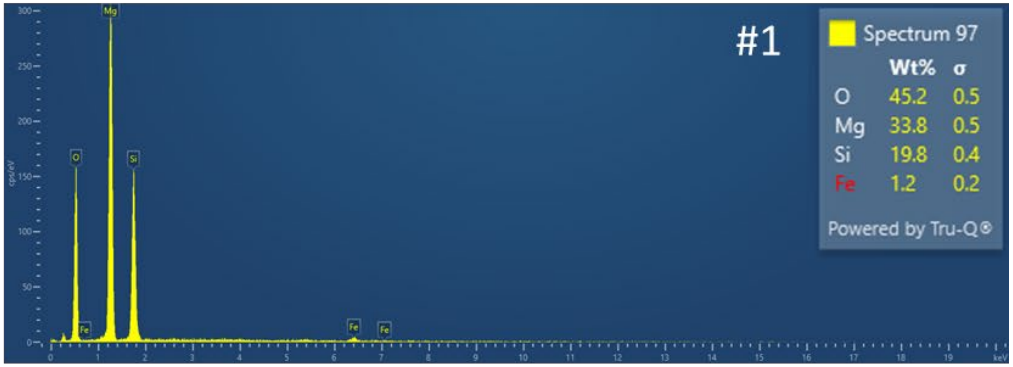
#1
Spectrum 97
Wt% σ
O 45.2 0.5
Mg 33.8 0.5
Si 19.8 0.4
Fe 1.2 0.2
Powered by Tru-Q®

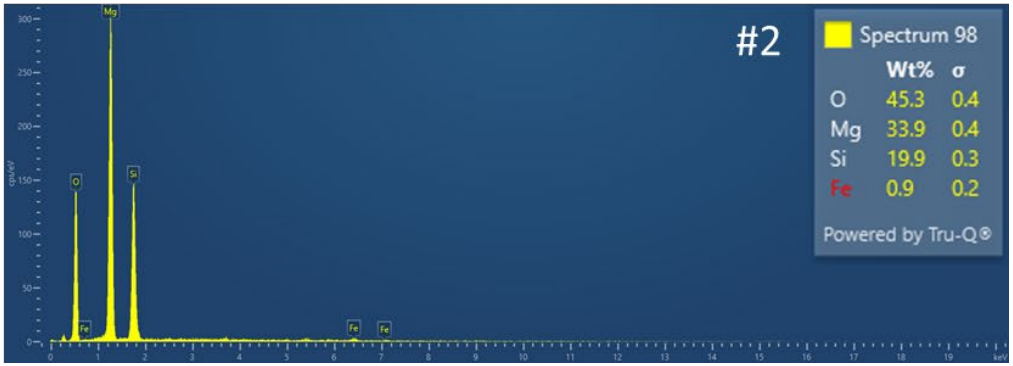
#2
Spectrum 98
Wt% σ
O 45.3 0.4
Mg 33.9 0.4
Si 19.9 0.3
Fe 0.9 0.2
Powered by Tru-Q®

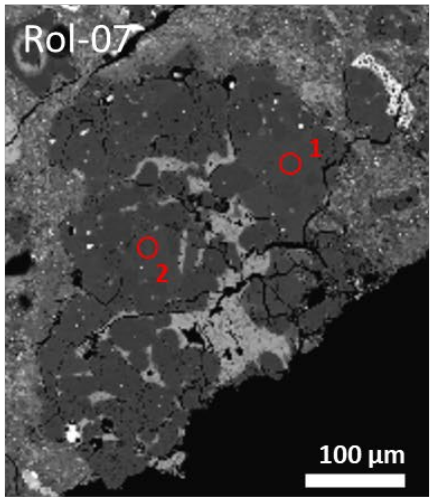
Rol-07
1
2
100 µm

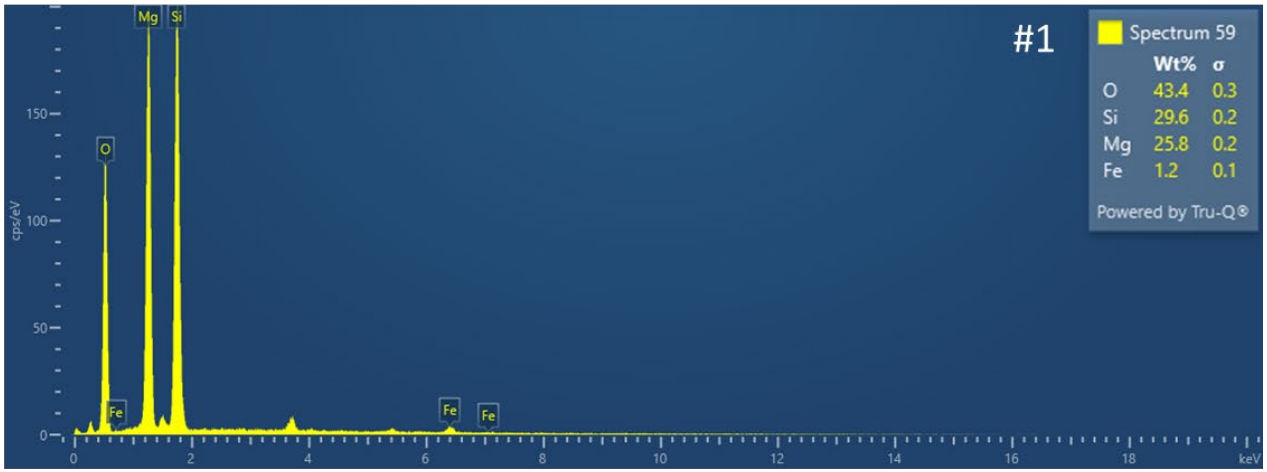
#1
Mg
Si
O
Fe
Fe
Fe
cps/eV
keV
Spectrum 59
Wt% σ
O 43.4 0.3
Si 29.6 0.2
Mg 25.8 0.2
Fe 1.2 0.1
Powered by Tru-Q®

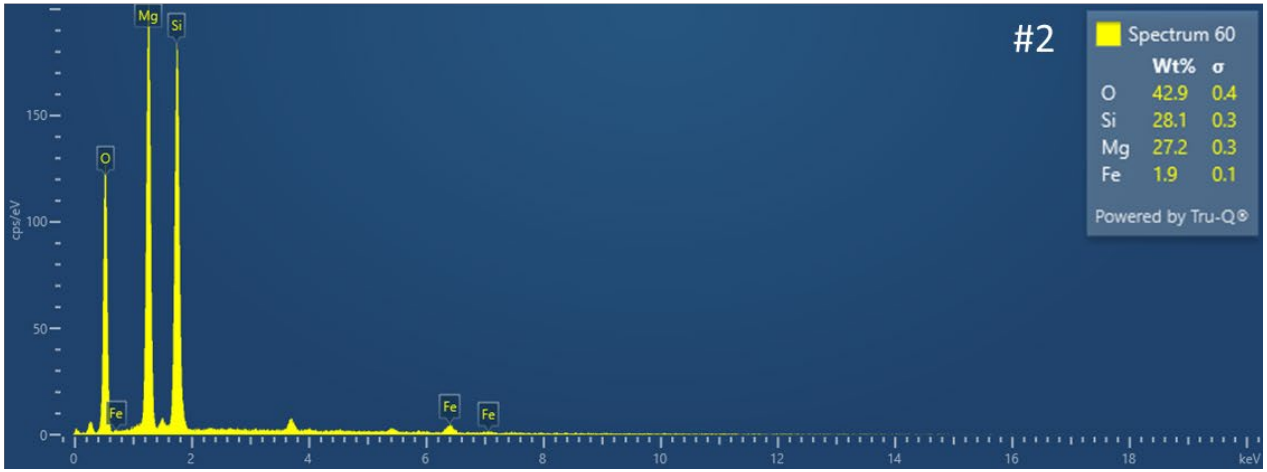
#2
Mg
Si
O
Fe
Fe
Fe
cps/eV
keV
Spectrum 60
Wt% σ
O 42.9 0.4
Si 28.1 0.3
Mg 27.2 0.3
Fe 1.9 0.1
Powered by Tru-Q®

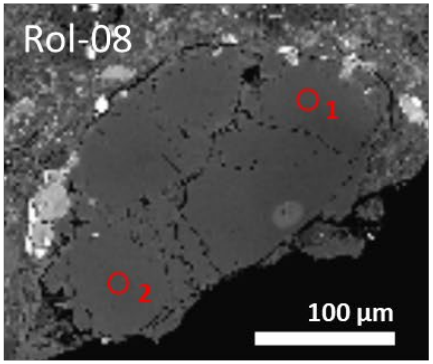
Rol-08
1
2
100 µm

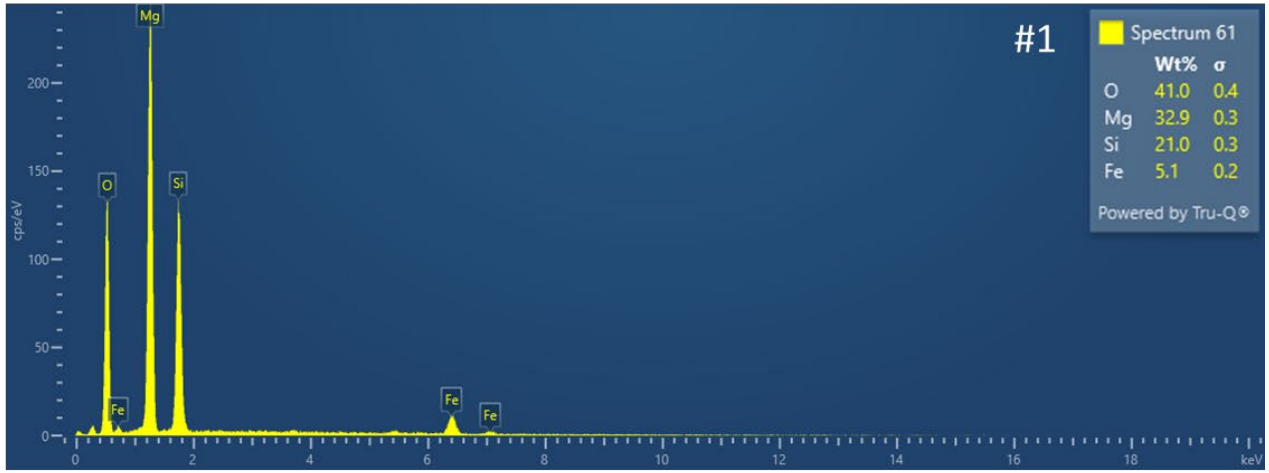
#1
Spectrum 61
Wt% σ
O 41.0 0.4
Mg 32.9 0.3
Si 21.0 0.3
Fe 5.1 0.2
Powered by Tru-Q®
Mg
O
Si
Fe
Fe
Fe
cps/eV
keV

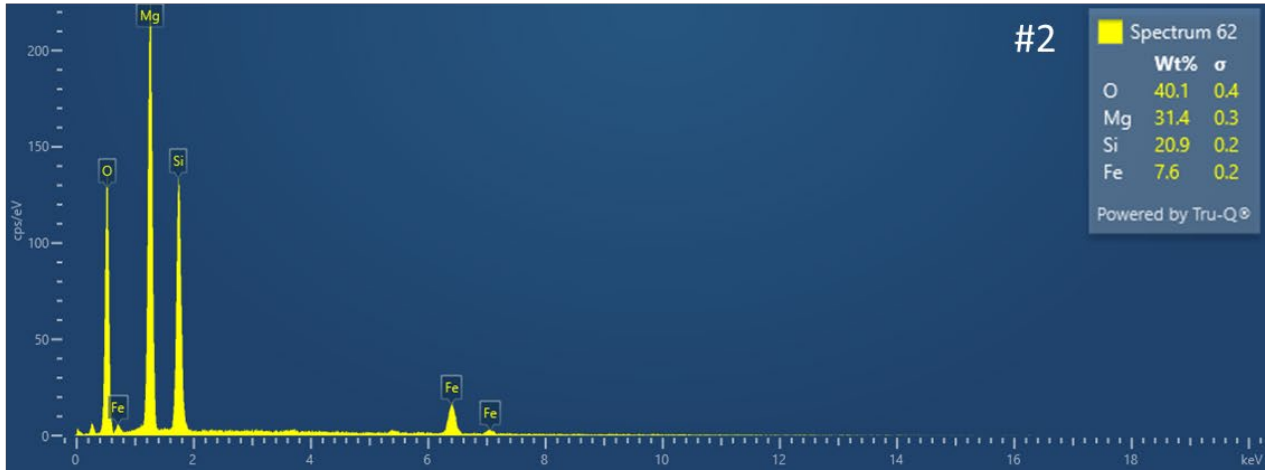
#2
Spectrum 62
Wt% σ
O 40.1 0.4
Mg 31.4 0.3
Si 20.9 0.2
Fe 7.6 0.2
Powered by Tru-Q®
Mg
O
Si
Fe
Fe
Fe
cps/eV
keV

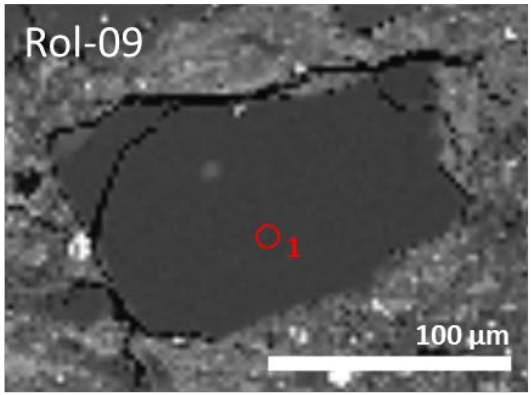
Rol-09
O1
100 µm

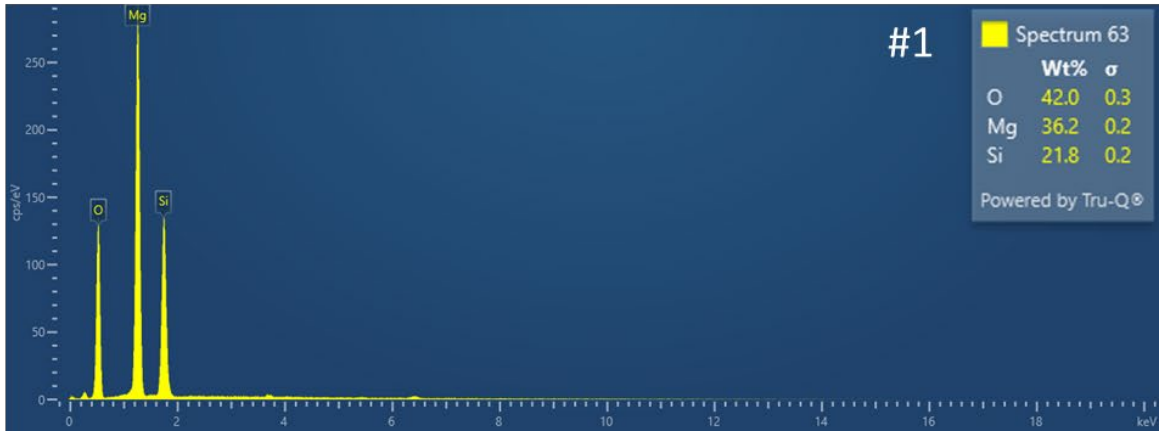
#1
Spectrum 63
Wt% σ
O 42.0 0.3
Mg 36.2 0.2
Si 21.8 0.2
Powered by Tru-Q®
Mg
O
Si
cps/eV
keV

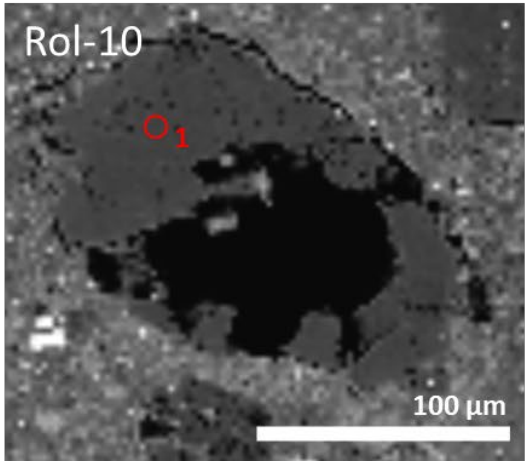
Rol-10
O1
100 µm

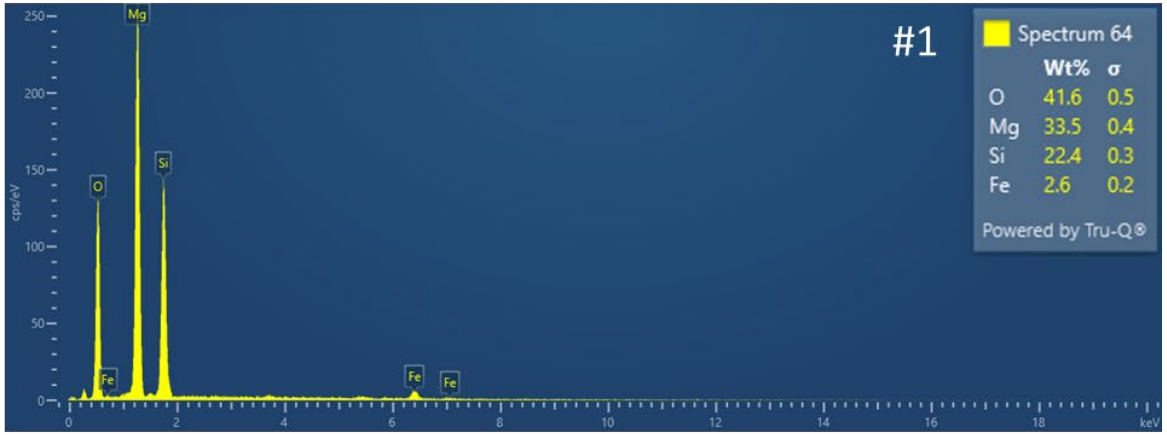
#1
Spectrum 64
Wt% σ
O 41.6 0.5
Mg 33.5 0.4
Si 22.4 0.3
Fe 2.6 0.2
Powered by Tru-Q®
Mg
O
Si
Fe
Fe
Fe
cps/eV
keV

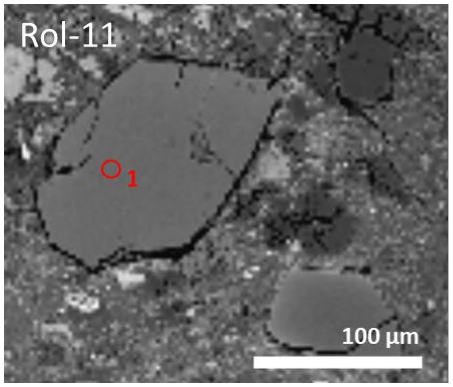
Rol-11
1
100 µm

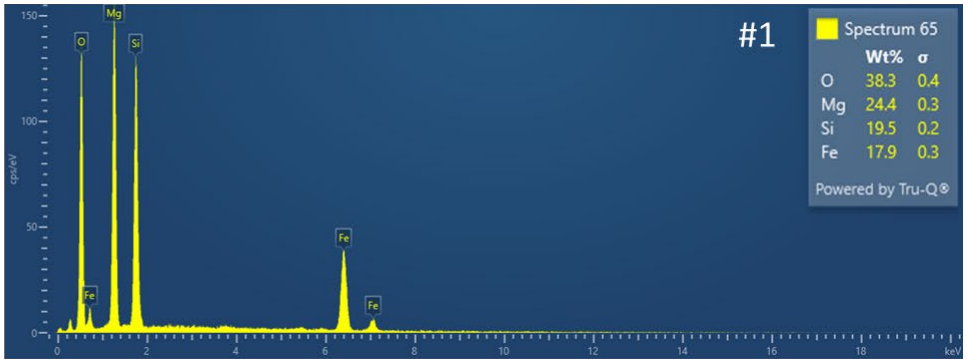
#1
Spectrum 65
Wt% σ
O 38.3 0.4
Mg 24.4 0.3
Si 19.5 0.2
Fe 17.9 0.3
Powered by Tru-Q®

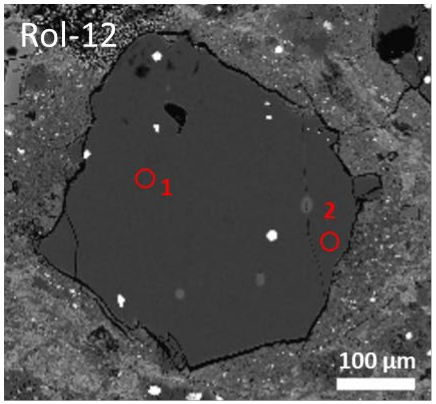
Rol-12
1
2
100 µm

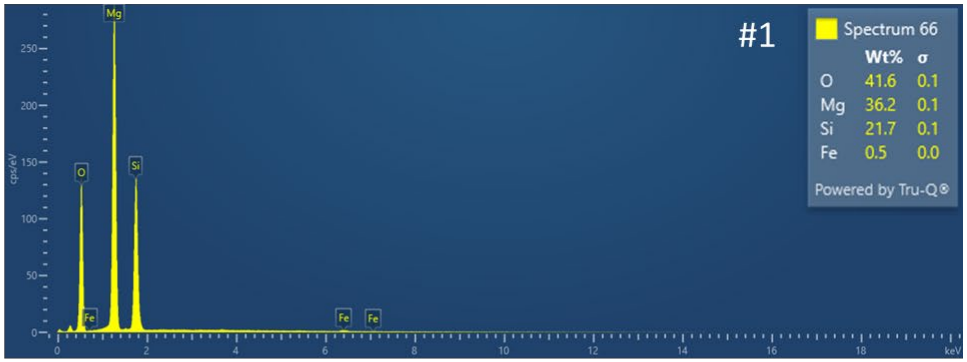
#1
Spectrum 66
Wt% σ
O 41.6 0.1
Mg 36.2 0.1
Si 21.7 0.1
Fe 0.5 0.0
Powered by Tru-Q®

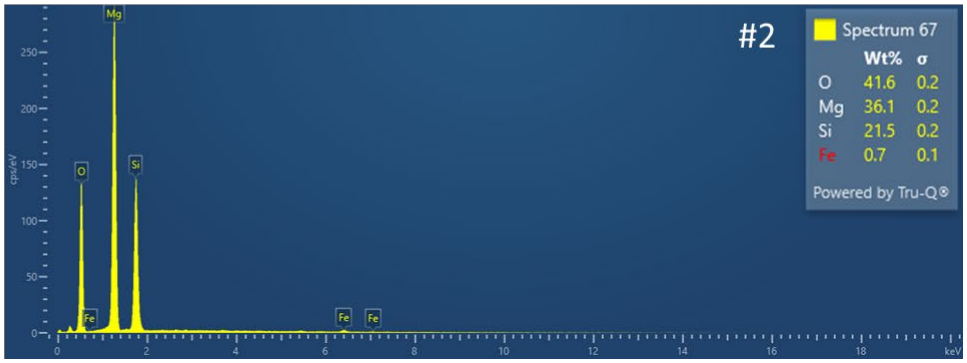
#2
Spectrum 67
Wt% σ
O 41.6 0.2
Mg 36.1 0.2
Si 21.5 0.2
Fe 0.7 0.1
Powered by Tru-Q®

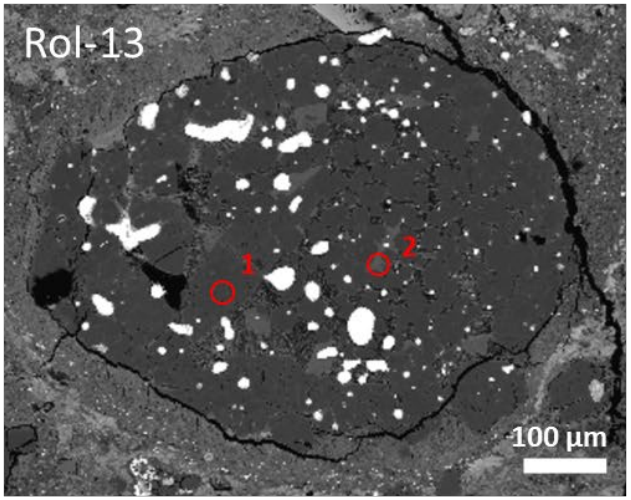
Rol-13
1
2
100 µm

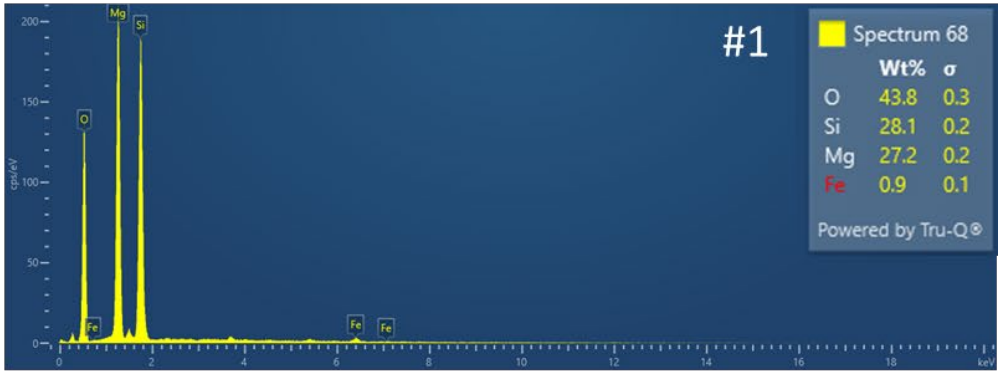
#1
Spectrum 68
Wt% σ
O 43.8 0.3
Si 28.1 0.2
Mg 27.2 0.2
Fe 0.9 0.1
Powered by Tru-Q®
Mg
Si
O
Fe
Fe
Fe
cps/eV
keV

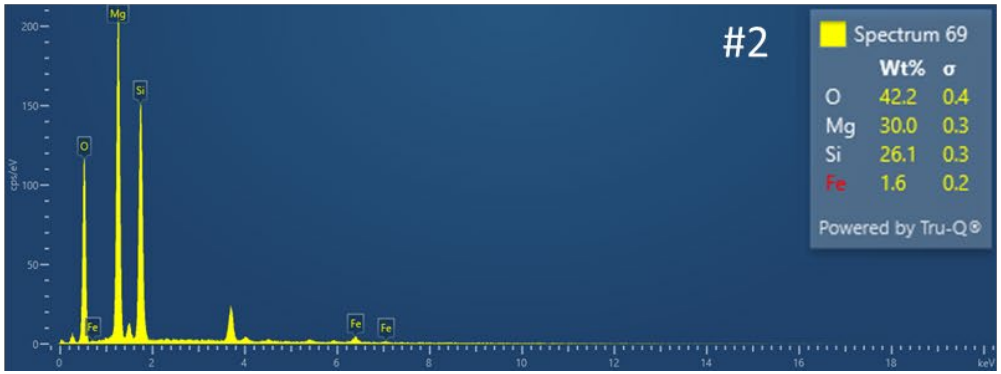
#2
Spectrum 69
Wt% σ
O 42.2 0.4
Mg 30.0 0.3
Si 26.1 0.3
Fe 1.6 0.2
Powered by Tru-Q®
Mg
Si
O
Fe
Fe
Fe
cps/eV
keV

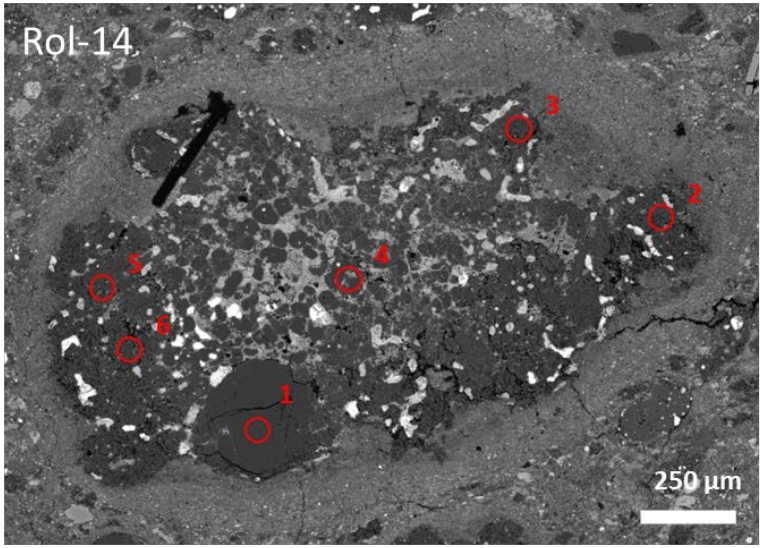
Rol-14
1
2
3
4
5
6
250 µm

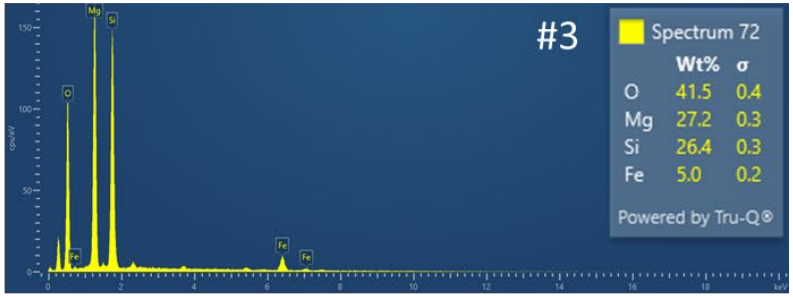
#3
Spectrum 72
Wt% σ
O 41.5 0.4
Mg 27.2 0.3
Si 26.4 0.3
Fe 5.0 0.2
Powered by Tru-Q®

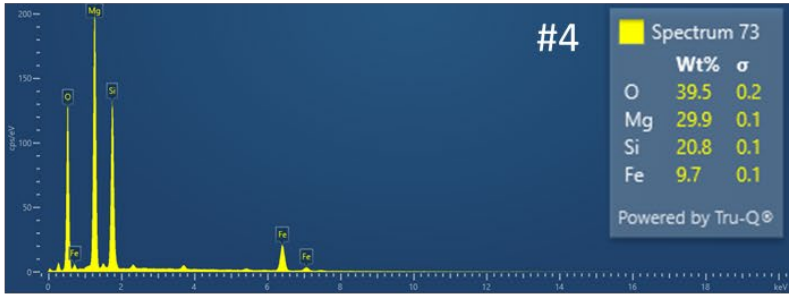
#4
Spectrum 73
Wt% σ
O 39.5 0.2
Mg 29.9 0.1
Si 20.8 0.1
Fe 9.7 0.1
Powered by Tru-Q®


#1
Spectrum 70
Wt% σ
O 41.3 0.1
Mg 36.0 0.1
Si 22.0 0.1
Fe 0.7 0.0
Powered by Tru-Q®

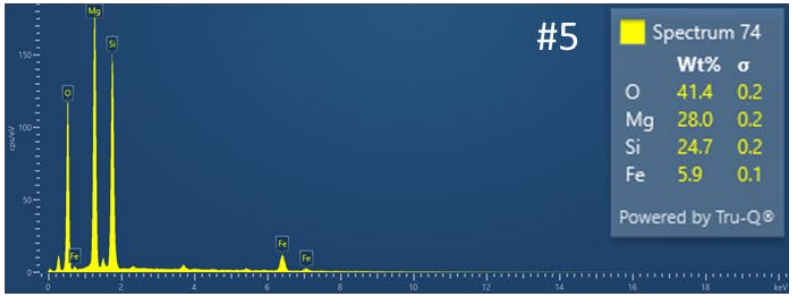
#5
Spectrum 74
Wt% σ
O 41.4 0.2
Mg 28.0 0.2
Si 24.7 0.2
Fe 5.9 0.1
Powered by Tru-Q®

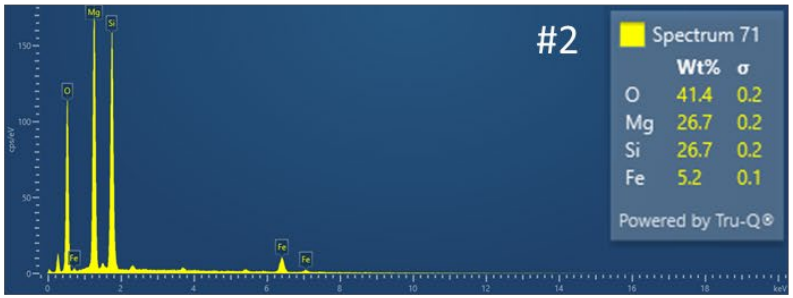
#2
Spectrum 71
Wt% σ
O 41.4 0.2
Mg 26.7 0.2
Si 26.7 0.2
Fe 5.2 0.1
Powered by Tru-Q®

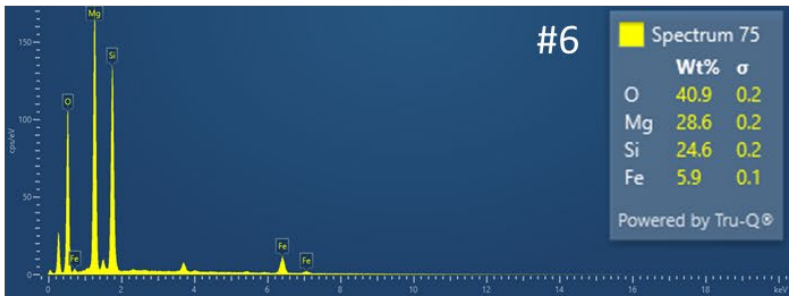
#6
Spectrum 75
Wt% σ
O 40.9 0.2
Mg 28.6 0.2
Si 24.6 0.2
Fe 5.9 0.1
Powered by Tru-Q®

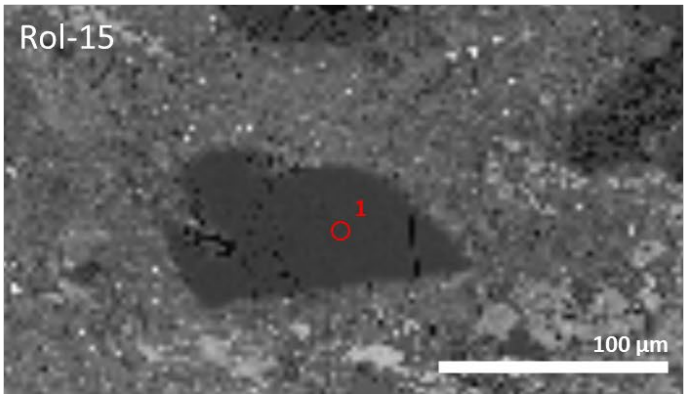
Rol-15
1
100 µm

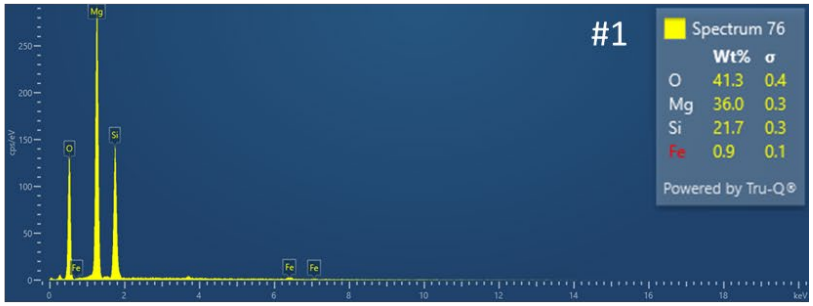
#1
Spectrum 76
Wt% σ
O 41.3 0.4
Mg 36.0 0.3
Si 21.7 0.3
Fe 0.9 0.1
Powered by Tru-Q®

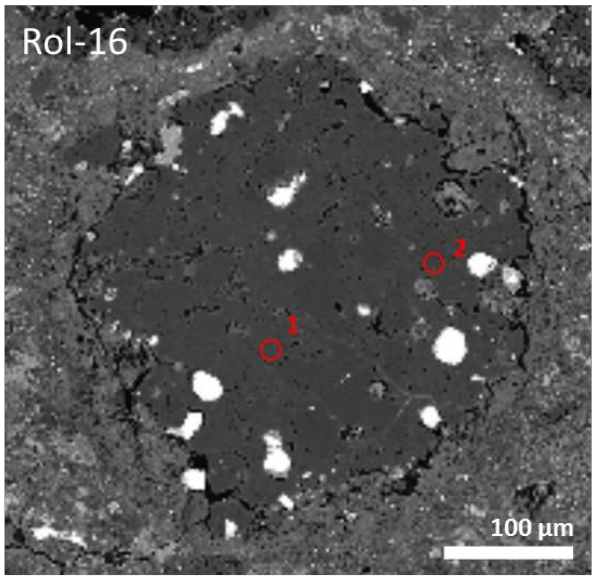
Rol-16
1
2
100 µm

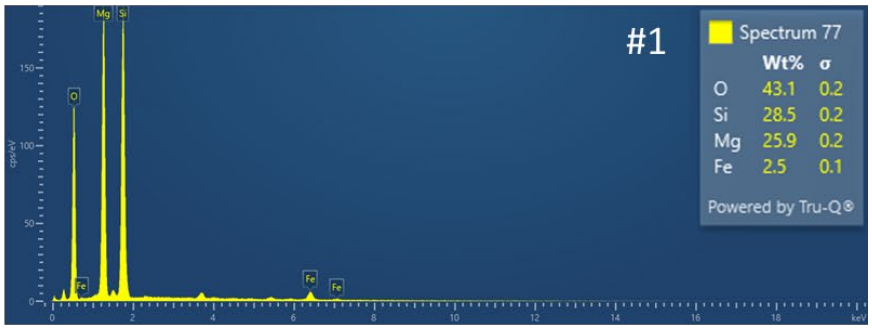
#1
Spectrum 77
Wt% σ
O 43.1 0.2
Si 28.5 0.2
Mg 25.9 0.2
Fe 2.5 0.1
Powered by Tru-Q®

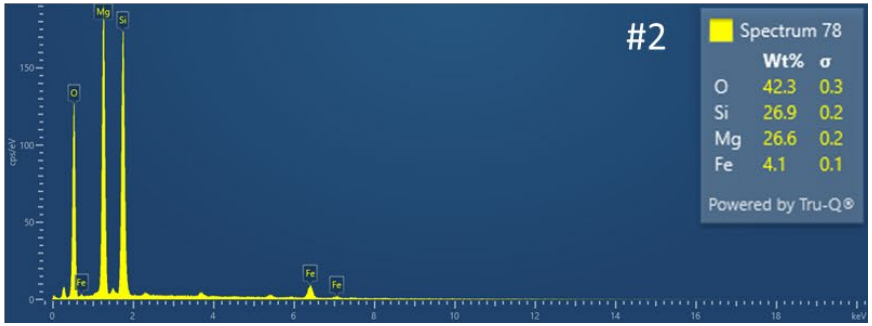
#2
Spectrum 78
Wt% σ
O 42.3 0.3
Si 26.9 0.2
Mg 26.6 0.2
Fe 4.1 0.1
Powered by Tru-Q®

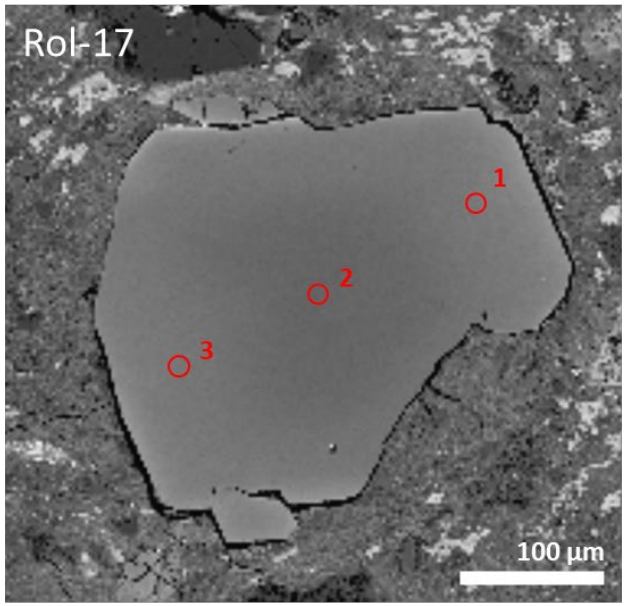
Rol-17
1
2
3
100 µm

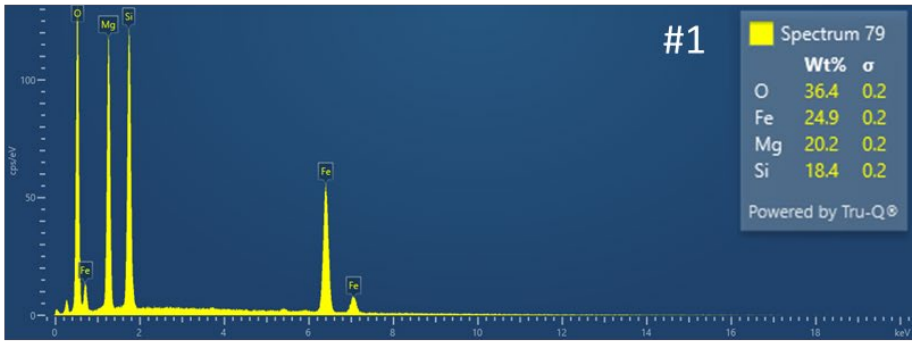
#1
Spectrum 79
Wt% σ
O 36.4 0.2
Fe 24.9 0.2
Mg 20.2 0.2
Si 18.4 0.2
Powered by Tru-Q®

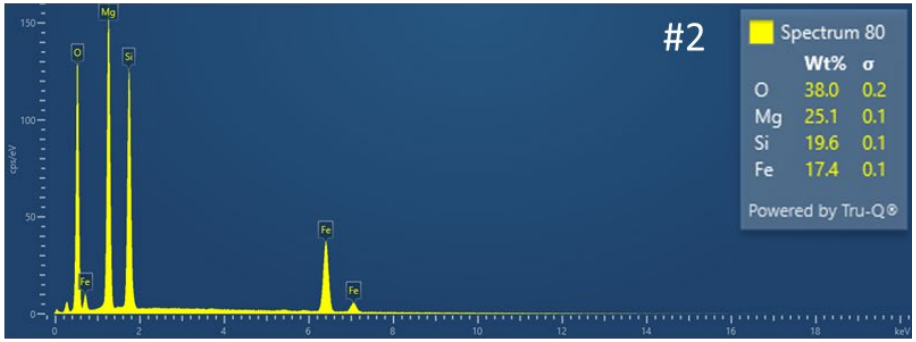
#2
Spectrum 80
Wt% σ
O 38.0 0.2
Mg 25.1 0.1
Si 19.6 0.1
Fe 17.4 0.1
Powered by Tru-Q®

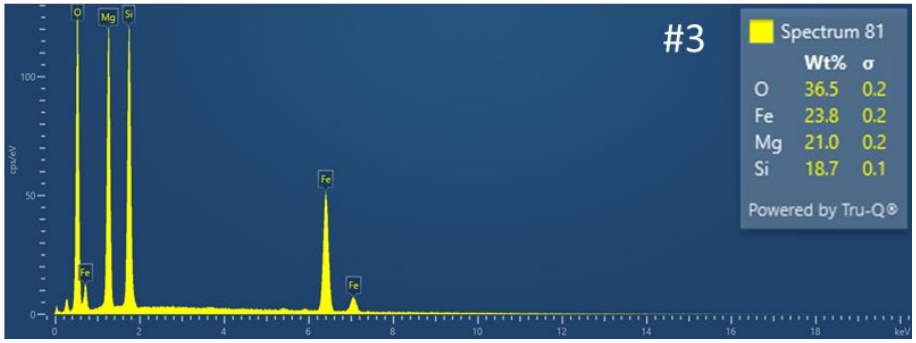
#3
Spectrum 81
Wt% σ
O 36.5 0.2
Fe 23.8 0.2
Mg 21.0 0.2
Si 18.7 0.1
Powered by Tru-Q®

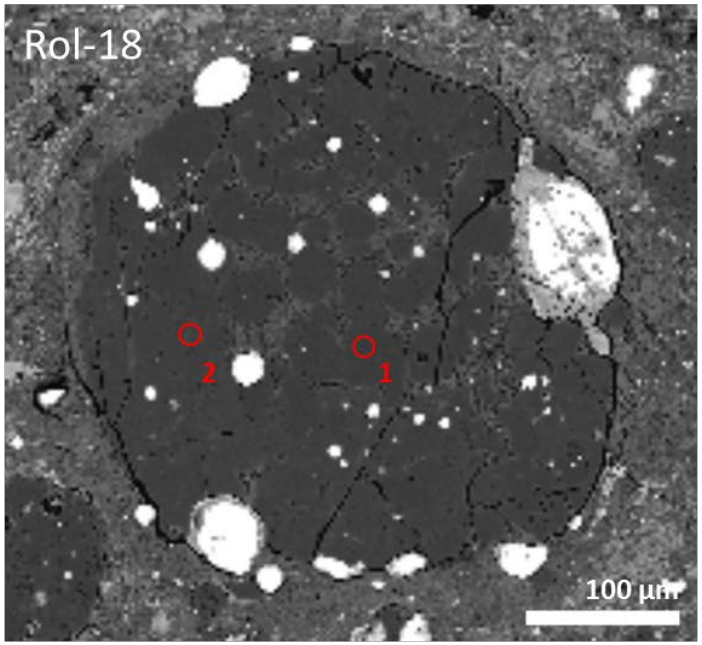
Rol-18
2
1
100 µm

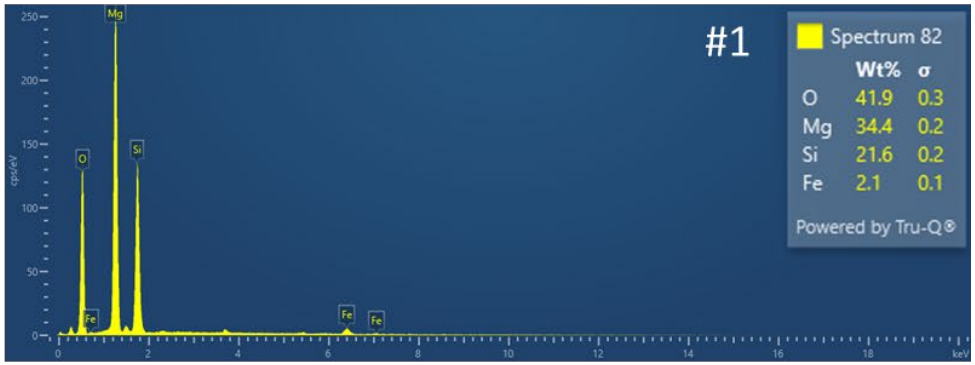
#1
Spectrum 82
Wt% σ
O 41.9 0.3
Mg 34.4 0.2
Si 21.6 0.2
Fe 2.1 0.1
Powered by Tru-Q®
Mg
Si
O
Fe
Fe
Fe
cps/eV
keV

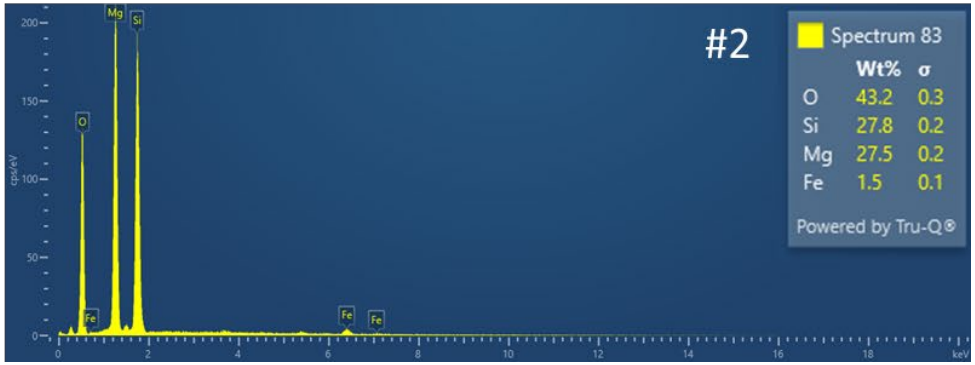
#2
Spectrum 83
Wt% σ
O 43.2 0.3
Si 27.8 0.2
Mg 27.5 0.2
Fe 1.5 0.1
Powered by Tru-Q®
Mg
Si
O
Fe
Fe
Fe
cps/eV
keV

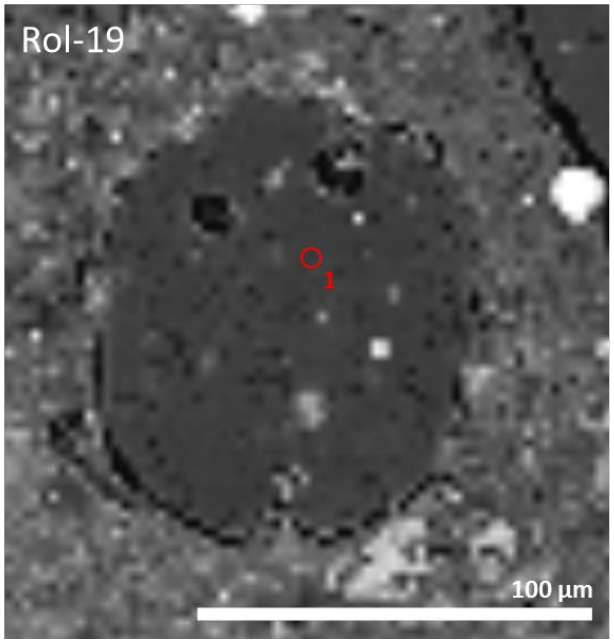
Rol-19
1
100 µm

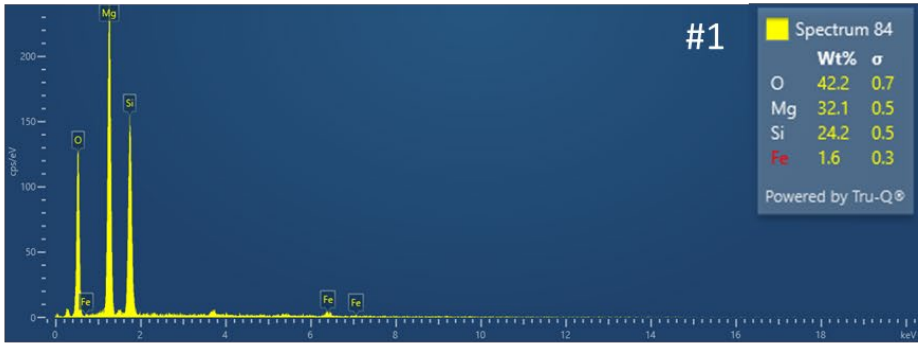
#1
Mg
Si
O
Fe
Fe
Fe
Spectrum 84
Wt% σ
O 42.2 0.7
Mg 32.1 0.5
Si 24.2 0.5
Fe 1.6 0.3
Powered by Tru-Q®
cps/eV
keV

7.8.3 Winchcombe

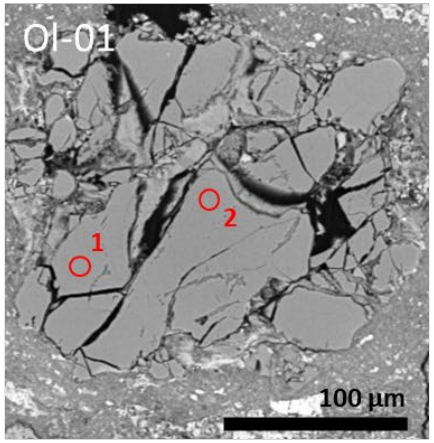

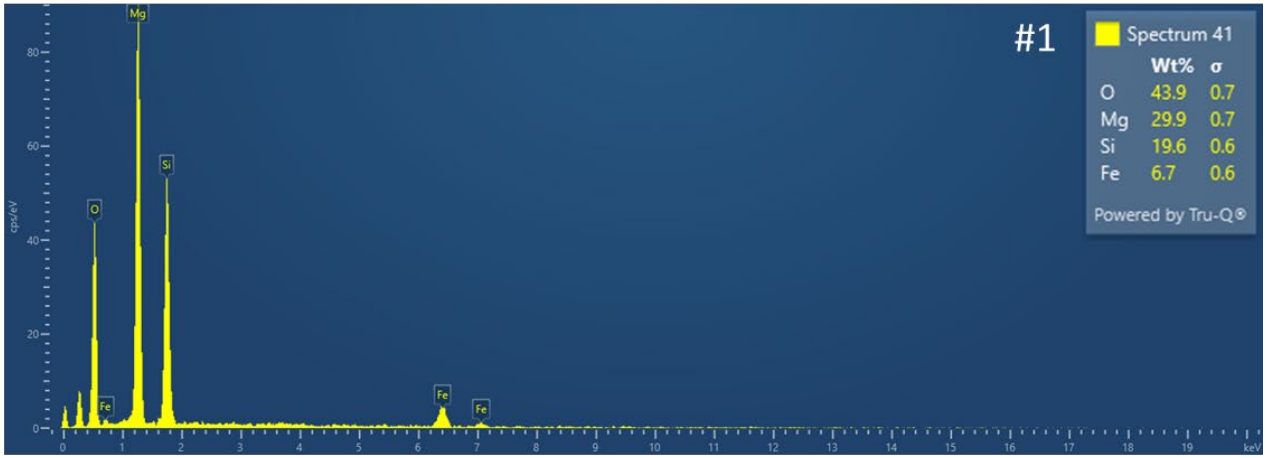

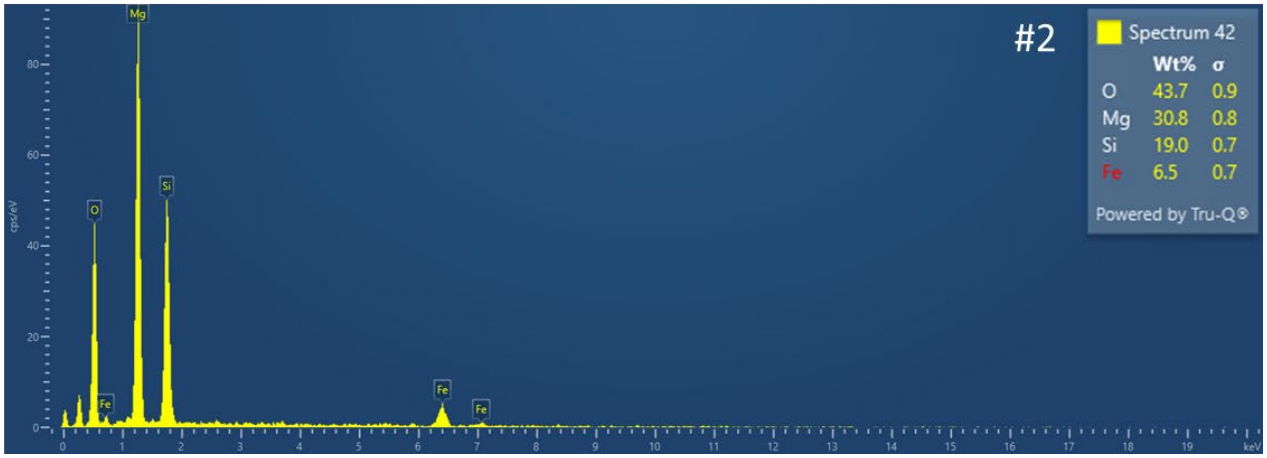

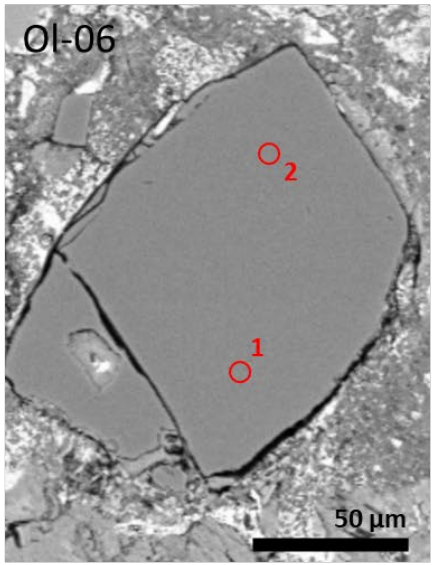
Ol-06
2
1
50 µm

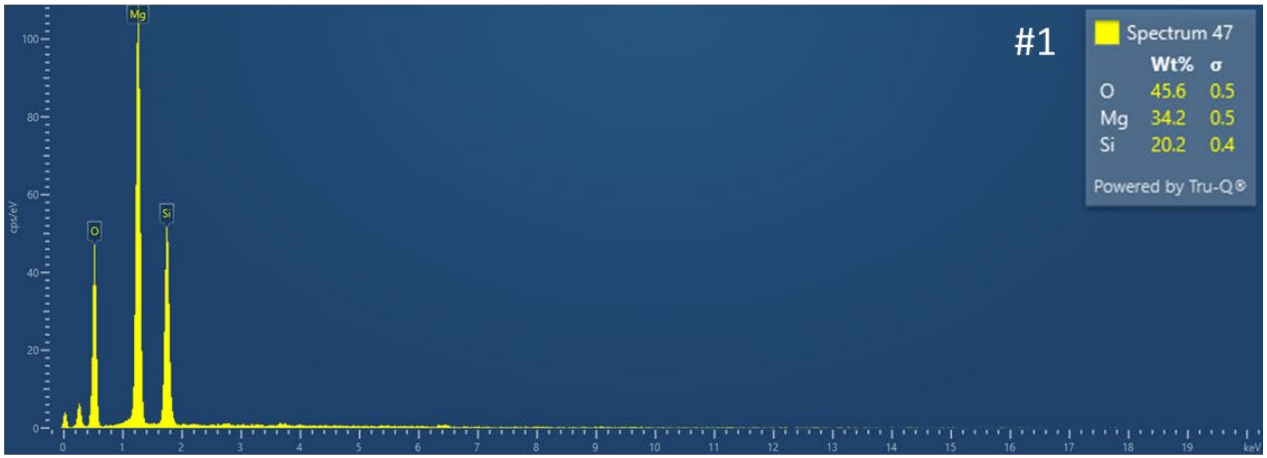
#1
Spectrum 47
Wt% σ
O 45.6 0.5
Mg 34.2 0.5
Si 20.2 0.4
Powered by Tru-Q®
Mg
O
Si
cps/eV
keV

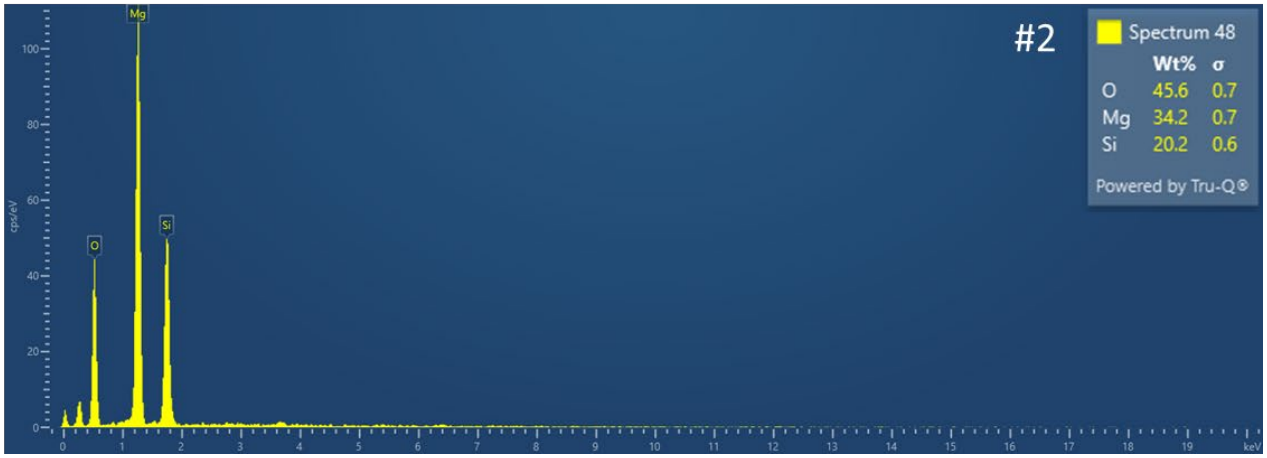
#2
Spectrum 48
Wt% σ
O 45.6 0.7
Mg 34.2 0.7
Si 20.2 0.6
Powered by Tru-Q®
Mg
O
Si
cps/eV
keV

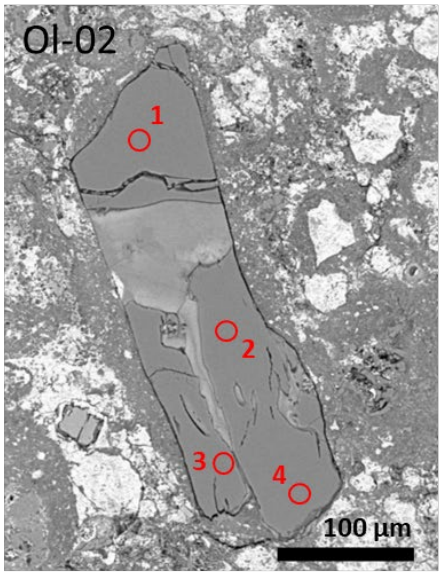
Ol-02
1
2
3
4
100 µm

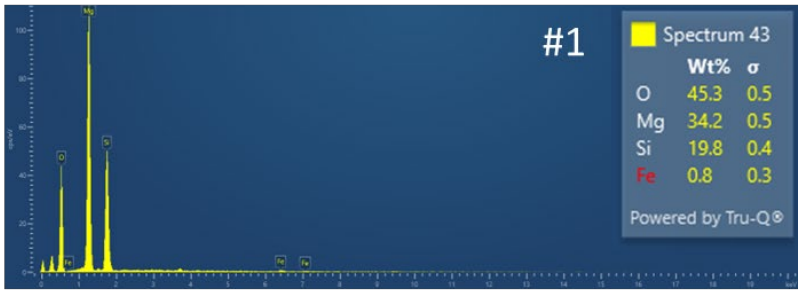
#1
Spectrum 43
Wt% σ
O 45.3 0.5
Mg 34.2 0.5
Si 19.8 0.4
Fe 0.8 0.3
Powered by Tru-Q®


#2
Spectrum 44
Wt% σ
O 45.3 0.4
Mg 33.8 0.4
Si 20.1 0.4
Fe 0.8 0.2
Powered by Tru-Q®


#3
Spectrum 45
Wt% σ
O 45.5 1.4
Mg 34.4 1.3
Si 20.1 1.2
Powered by Tru-Q®

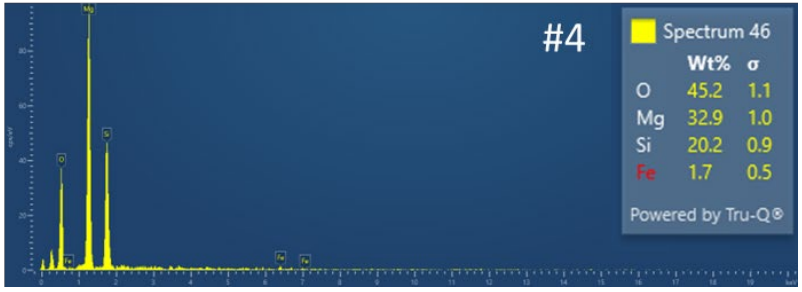
#4
Spectrum 46
Wt% σ
O 45.2 1.1
Mg 32.9 1.0
Si 20.2 0.9
Fe 1.7 0.5
Powered by Tru-Q®

7.9 SIMS Pit Images

BSE and SE images of all CCCAIs, CAIs, and chondrules containing SIMS pits and analyses are presented in the following galleries, organised by meteorite. Since Secondary Electron (SE) imaging is sensitive to surface morphology, high-contrast SE images were used to visualise SIMS pits in greater detail. BSE images are positioned either above or to the left of each pair, marked by the 'Det. SSD' label next to the scale bar. SE images appear below or to the right, identified by the 'Det. ETD' label. In the case of the Winchcombe meteorite, SIMS pits are more visible in SE images with carbon coating; therefore, only SE images are provided for sample P30552. It is also important to note that the images of the Paris meteorite display long dark streaks caused by damage to the carbon coating during postal transport from the CRPG back to the University of Glasgow.

SIMS spot locations are colour-coded according to the targeted mineral phase as follows:

- Spinel (Sp): lavender
- Forsterite (Fo): red
- Fayalite (Fa): aqua
- Diopside (Dio): green
- Data points excluded from study: yellow

Although SIMS data were also acquired for calcite, these points were excluded from this study due to the absence of appropriate standards. Spinel, olivine, and pyroxene measurements were also removed in cases of mistargeting. Common mistargeted phases include hibonite, perovskite, calcite, and Fine-Grained Rims (FGR). If spinel, diopside, or olivine was mistakenly targeted, the analysis was instead retained but reclassified accordingly (with updated colour coding). Objects consisting solely of failed measurements (i.e. those not listed in Table 4.6) are also included to ensure full transparency in the data discrimination and selection process.

7.9.1 Aguas Zarcas

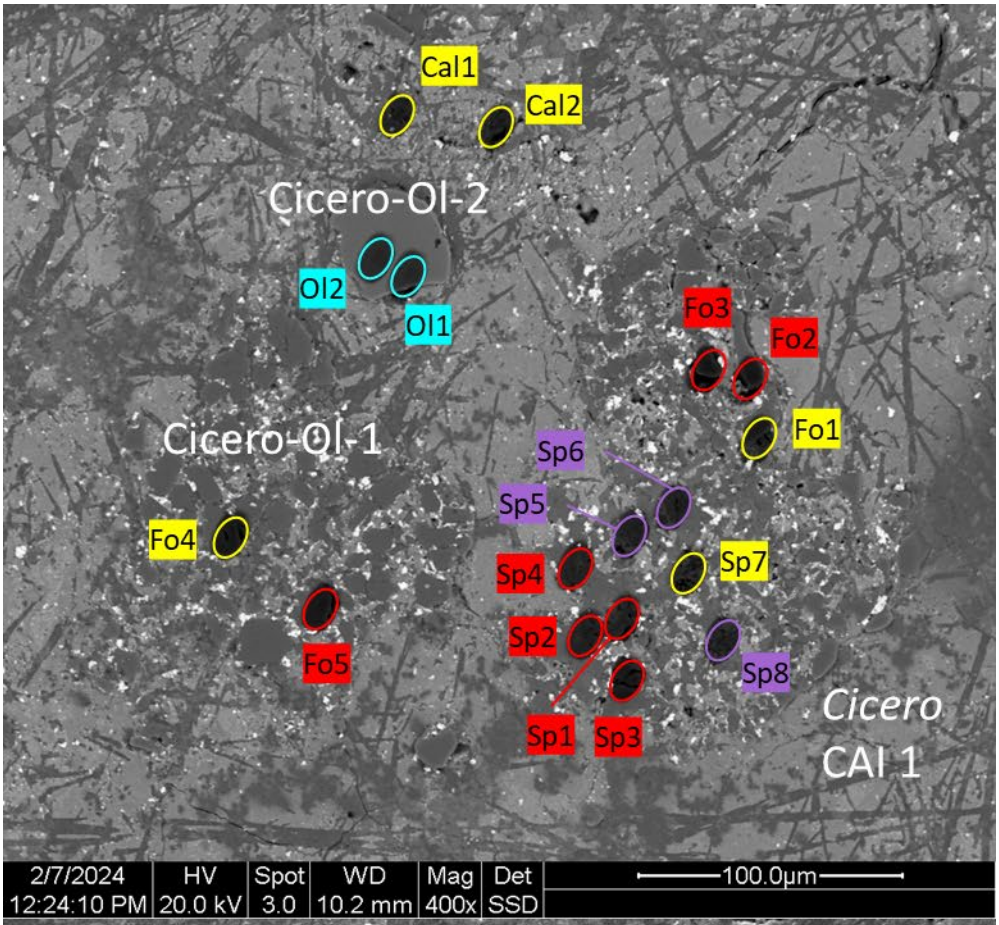

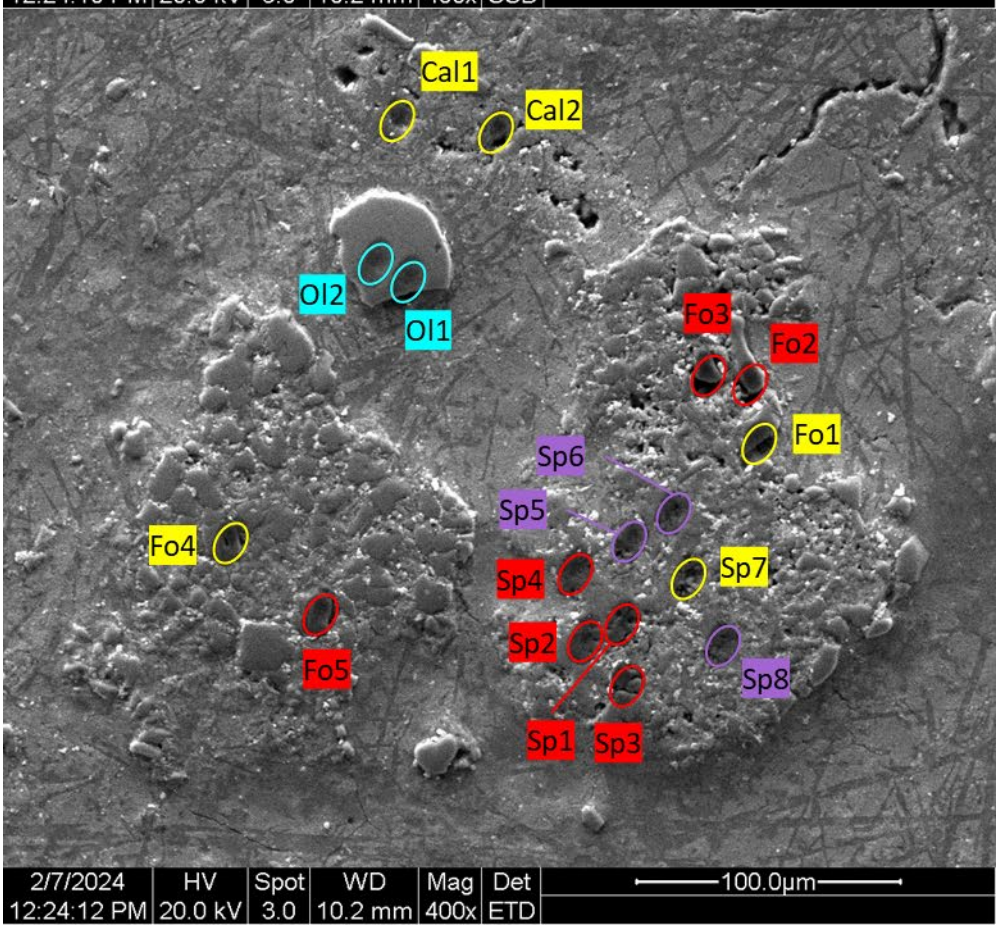

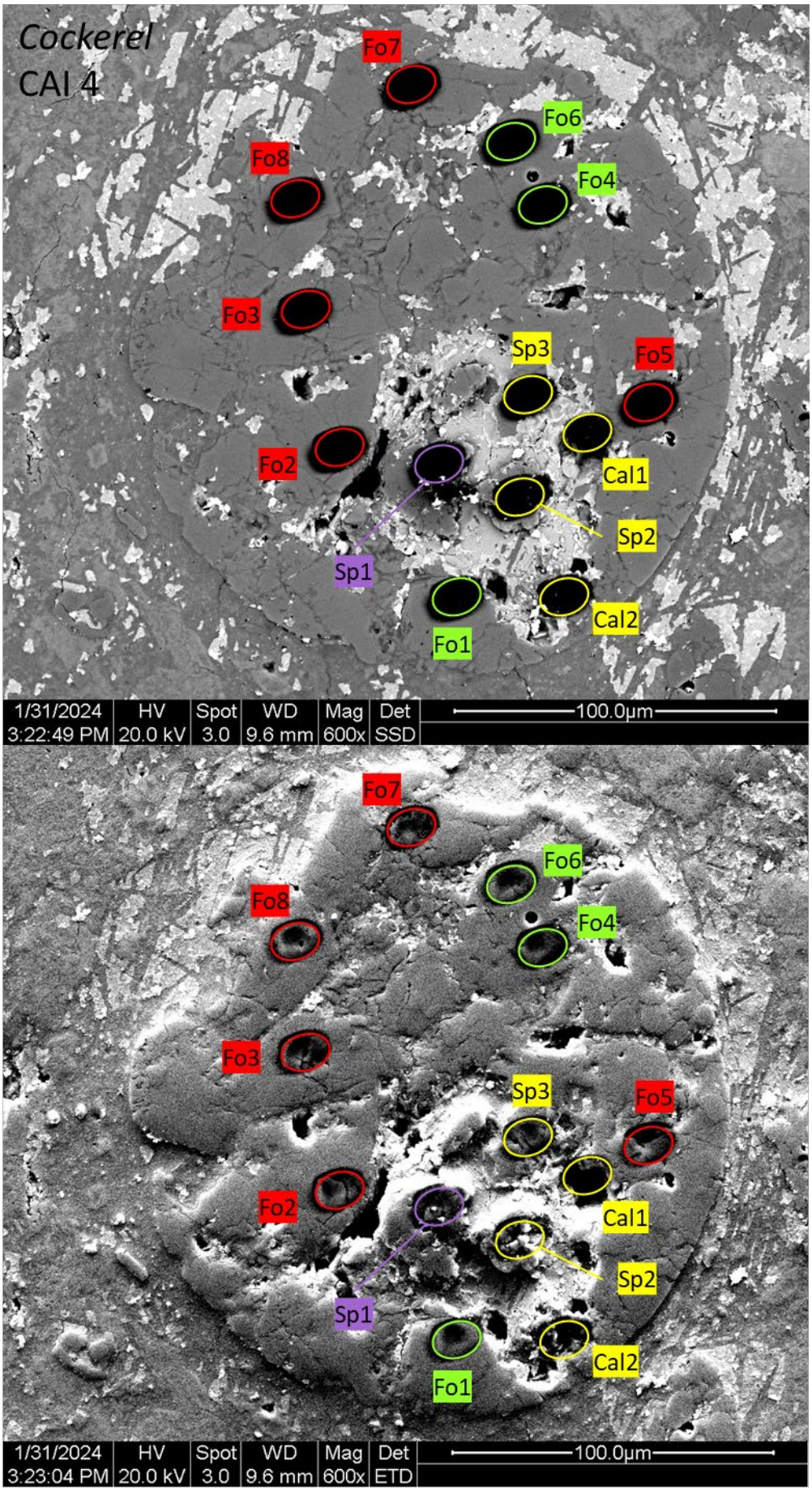
Cockerel
CAI 4
Fo7
Fo6
Fo8
Fo4
Fo3
Sp3
Fo5
Fo2
Cal1
Sp2
Sp1
Cal2
Fo1
1/31/2024 3:22:49 PM
HV 20.0 kV
Spot 3.0
WD 9.6 mm
Mag 600x
Det SSD
100.0µm
Fo7
Fo6
Fo8
Fo4
Fo3
Sp3
Fo5
Fo2
Cal1
Sp2
Sp1
Cal2
Fo1
1/31/2024 3:23:04 PM
HV 20.0 kV
Spot 3.0
WD 9.6 mm
Mag 600x
Det ETD
100.0µm

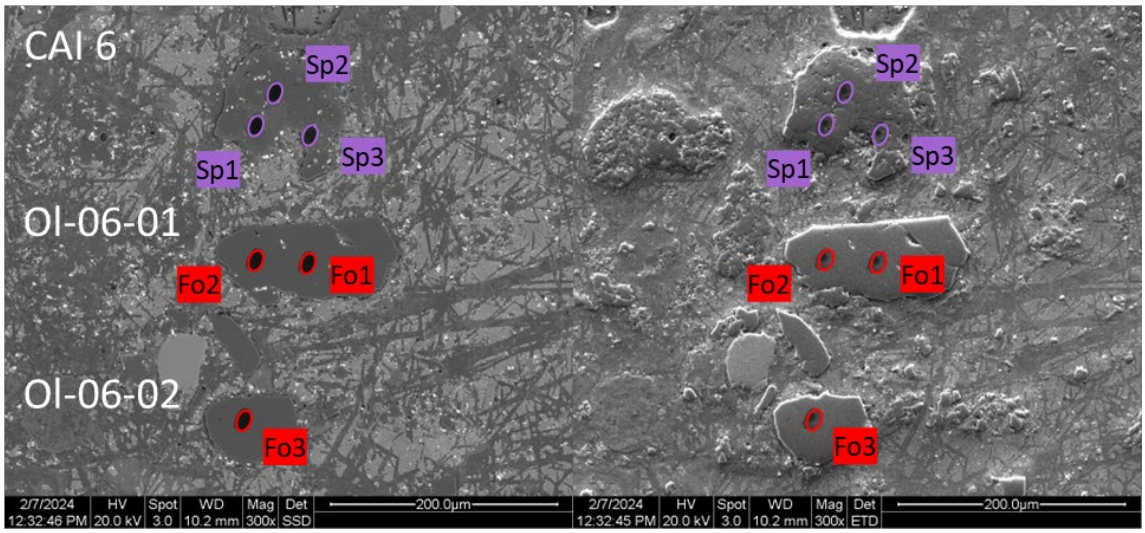
CAI 6
Sp2
Sp1
Sp3
Ol-06-01
Fo2
Fo1
Ol-06-02
Fo3
2/7/2024 12:32:46 PM HV 20.0 kV Spot 3.0 WD 10.2 mm Mag 300x Det SSD 200.0µm
2/7/2024 12:32:45 PM HV 20.0 kV Spot 3.0 WD 10.2 mm Mag 300x Det ETD 200.0µm

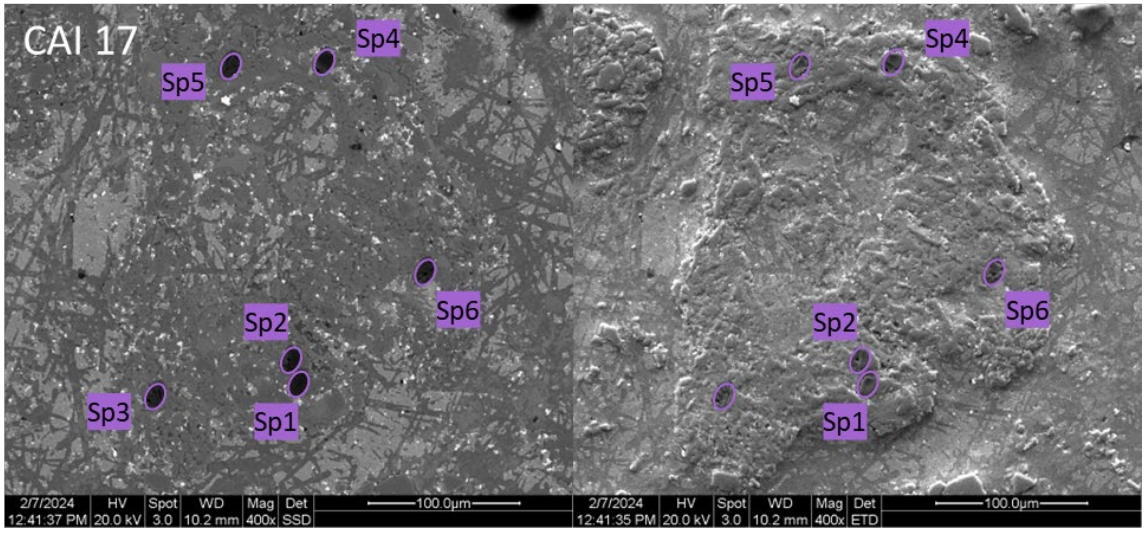
CAI 17
Sp4
Sp5
Sp6
Sp2
Sp3
Sp1
2/7/2024 12:41:37 PM HV 20.0 kV Spot 3.0 WD 10.2 mm Mag 400x Det SSD 100.0µm
2/7/2024 12:41:35 PM HV 20.0 kV Spot 3.0 WD 10.2 mm Mag 400x Det ETD 100.0µm

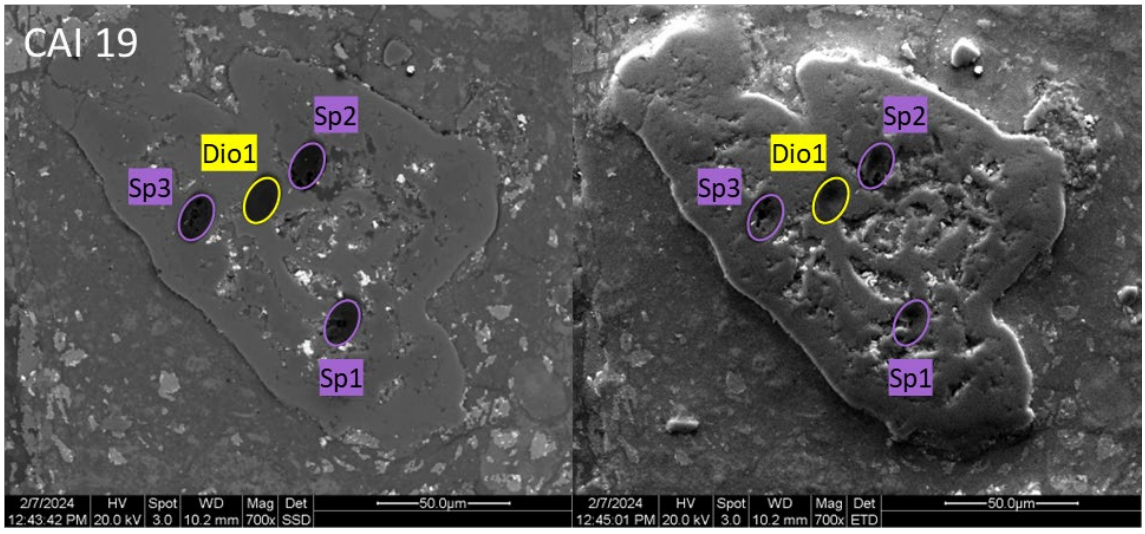
CAI 19
Sp2
Dio1
Sp3
Sp1
2/7/2024 12:43:42 PM HV 20.0 kV Spot 3.0 WD 10.2 mm Mag 700x Det SSD 50.0µm
2/7/2024 12:45:01 PM HV 20.0 kV Spot 3.0 WD 10.2 mm Mag 700x Det ETD 50.0µm

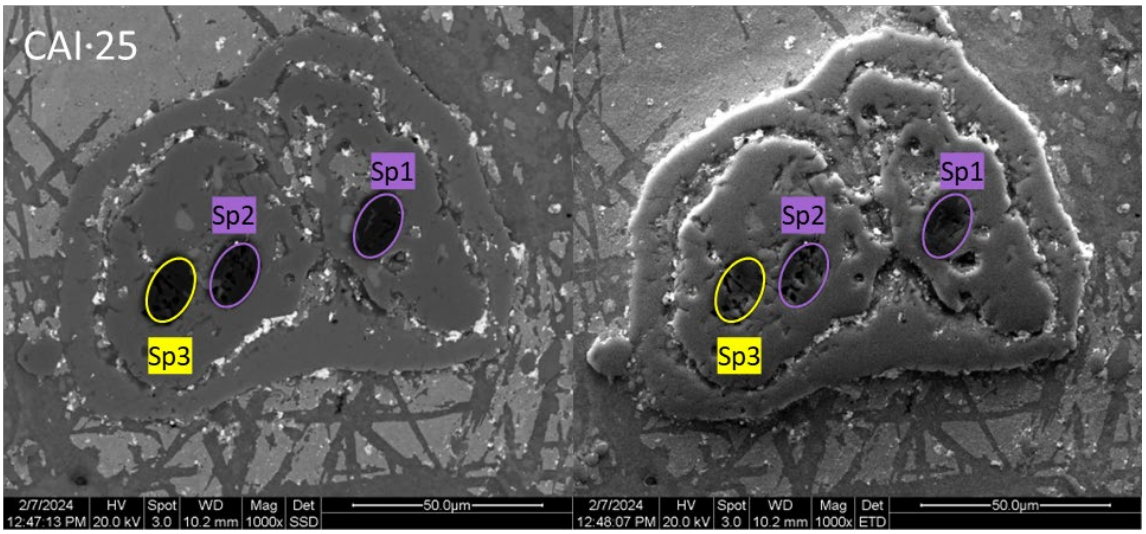
CAI-25
Sp1
Sp2
Sp3
Sp1
Sp2
Sp3
2/7/2024 12:47:13 PM HV 20.0 kV Spot 3.0 WD 10.2 mm Mag 1000x Det SSD 50.0µm
2/7/2024 12:48:07 PM HV 20.0 kV Spot 3.0 WD 10.2 mm Mag 1000x Det ETD 50.0µm

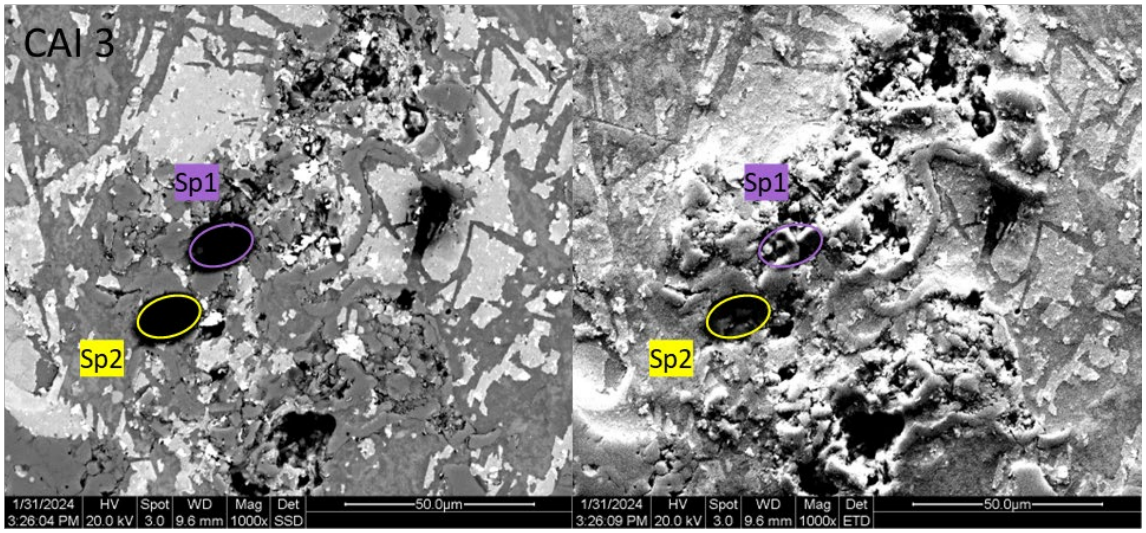
CAI 3
Sp1
Sp2
Sp1
Sp2
1/31/2024 3:26:04 PM HV 20.0 kV Spot 3.0 WD 9.6 mm Mag 1000x Det SSD 50.0µm
1/31/2024 3:26:09 PM HV 20.0 kV Spot 3.0 WD 9.6 mm Mag 1000x Det ETD 50.0µm

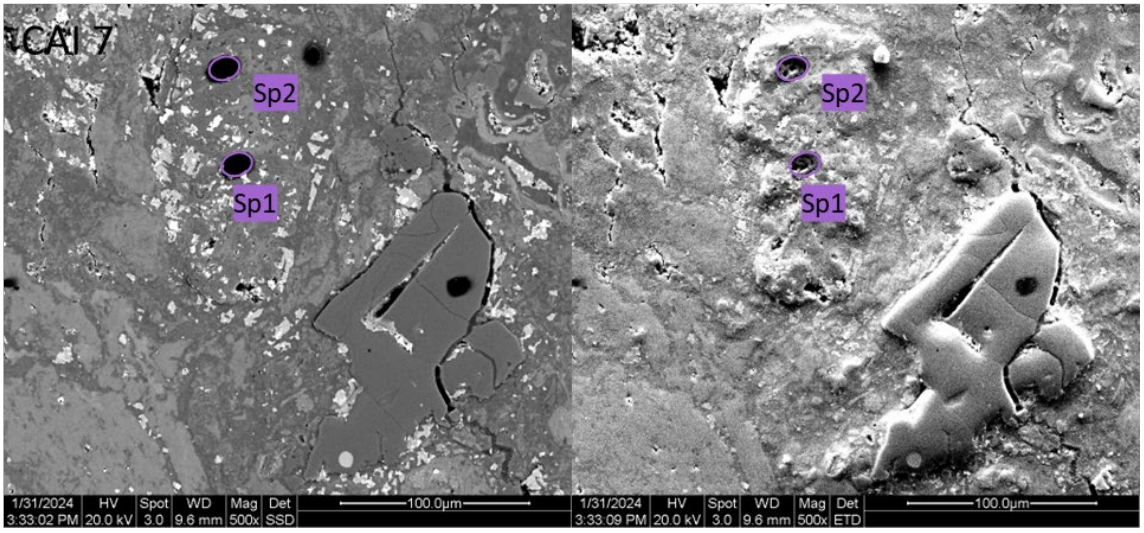
CAI 7
Sp2
Sp1
Sp2
Sp1
1/31/2024 3:33:02 PM HV 20.0 kV Spot 3.0 WD 9.6 mm Mag 500x Det SSD 100.0µm
1/31/2024 3:33:09 PM HV 20.0 kV Spot 3.0 WD 9.6 mm Mag 500x Det ETD 100.0µm

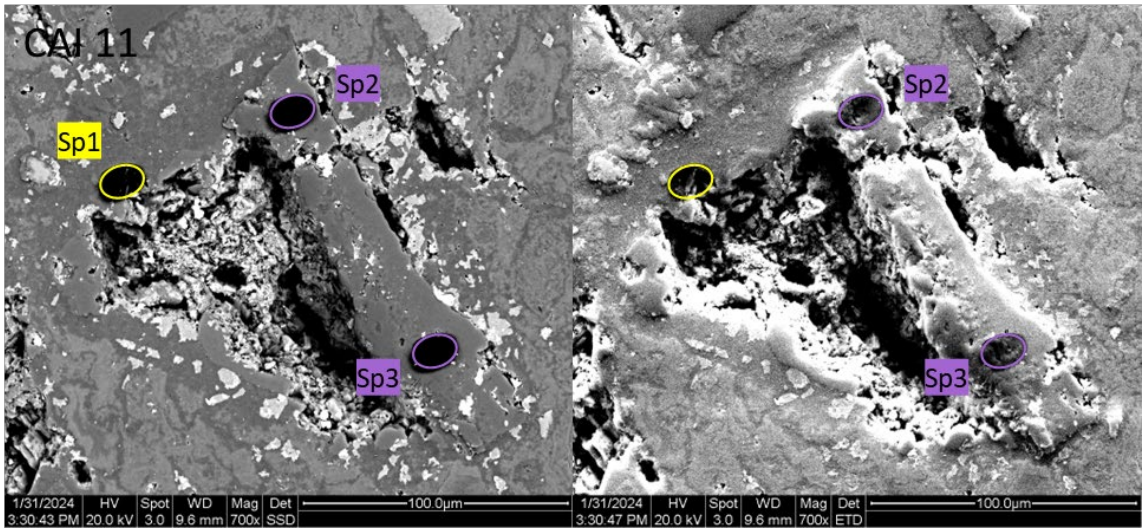
CAI 11
Sp1
Sp2
Sp3
1/31/2024 3:30:43 PM HV 20.0 kV Spot 3.0 WD 9.6 mm Mag 700x Det SSD 100.0µm
Sp2
Sp3
1/31/2024 3:30:47 PM HV 20.0 kV Spot 3.0 WD 9.6 mm Mag 700x Det ETD 100.0µm

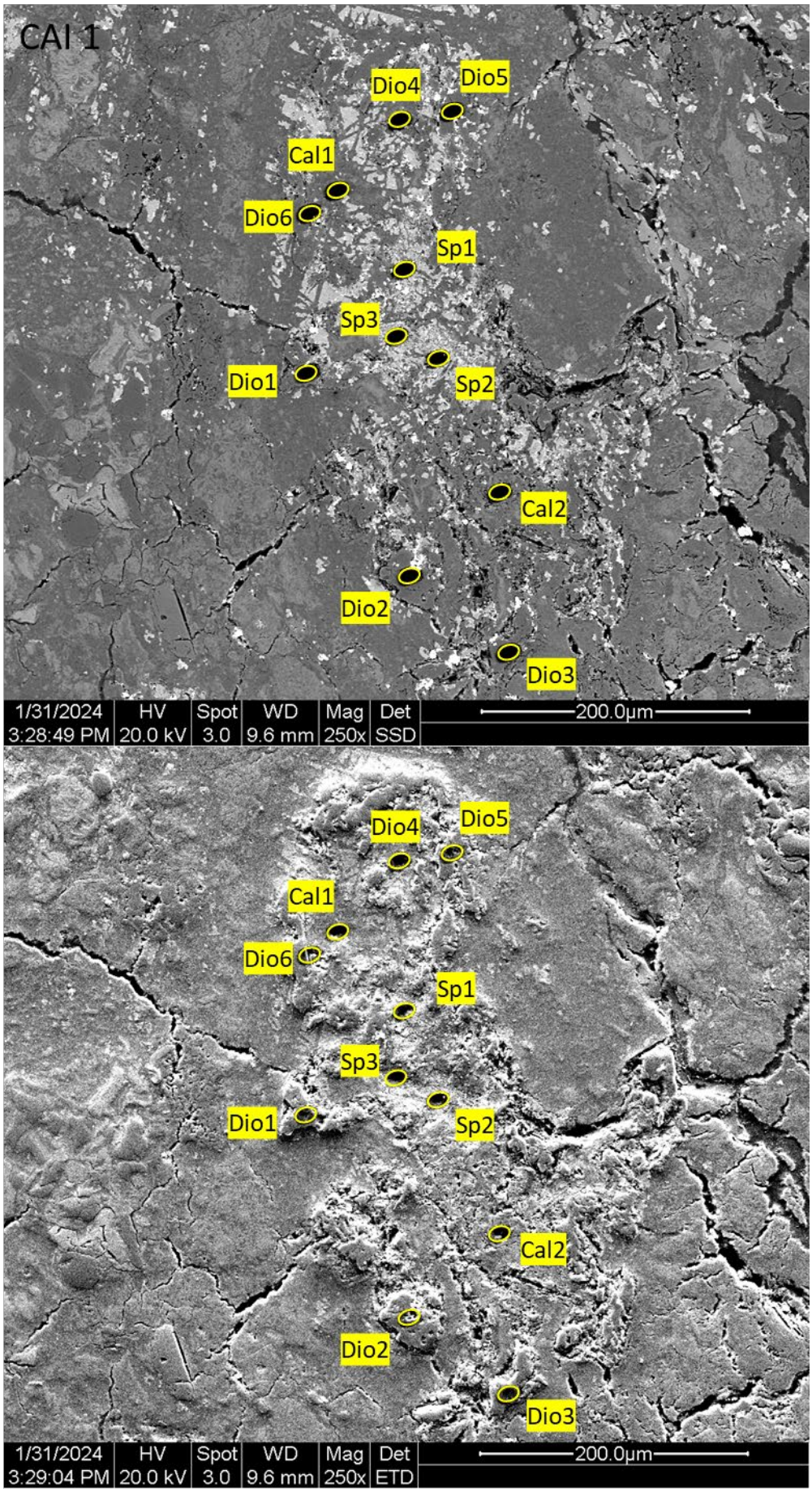
CAI 1
Dio4
Dio5
Cal1
Dio6
Sp1
Sp3
Dio1
Sp2
Cal2
Dio2
Dio3
1/31/2024 3:28:49 PM
HV 20.0 kV
Spot 3.0
WD 9.6 mm
Mag 250x
Det SSD
200.0µm
Dio4
Dio5
Cal1
Dio6
Sp1
Sp3
Dio1
Sp2
Cal2
Dio2
Dio3
1/31/2024 3:29:04 PM
HV 20.0 kV
Spot 3.0
WD 9.6 mm
Mag 250x
Det ETD
200.0µm

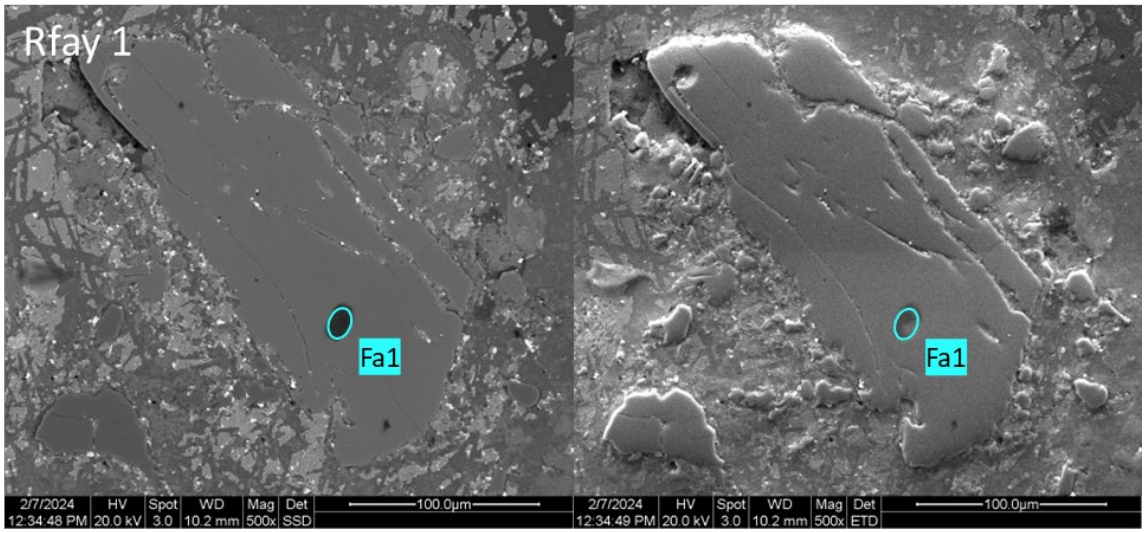
Rfay 1
Fa1
Fa1
2/7/2024 12:34:48 PM HV 20.0 kV Spot 3.0 WD 10.2 mm Mag 500x Det SSD 100.0µm
2/7/2024 12:34:49 PM HV 20.0 kV Spot 3.0 WD 10.2 mm Mag 500x Det ETD 100.0µm

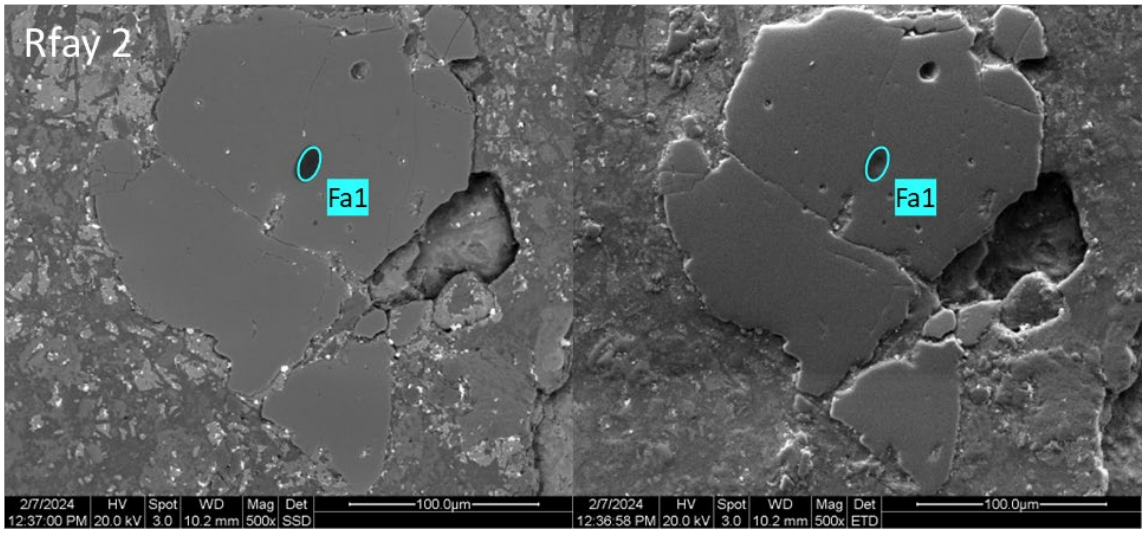
Rfay 2
Fa1
Fa1
2/7/2024 12:37:00 PM HV 20.0 kV Spot 3.0 WD 10.2 mm Mag 500x Det SSD 100.0µm
2/7/2024 12:36:58 PM HV 20.0 kV Spot 3.0 WD 10.2 mm Mag 500x Det ETD 100.0µm

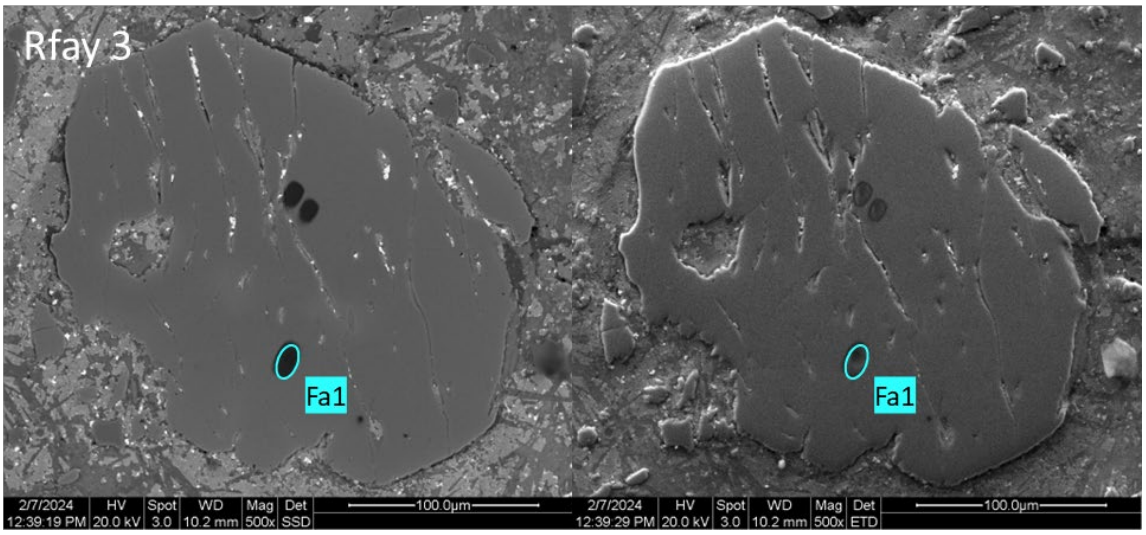
Rfay 3
Fa1
Fa1
2/7/2024 12:39:19 PM HV 20.0 kV Spot 3.0 WD 10.2 mm Mag 500x Det SSD 100.0µm
2/7/2024 12:39:29 PM HV 20.0 kV Spot 3.0 WD 10.2 mm Mag 500x Det ETD 100.0µm

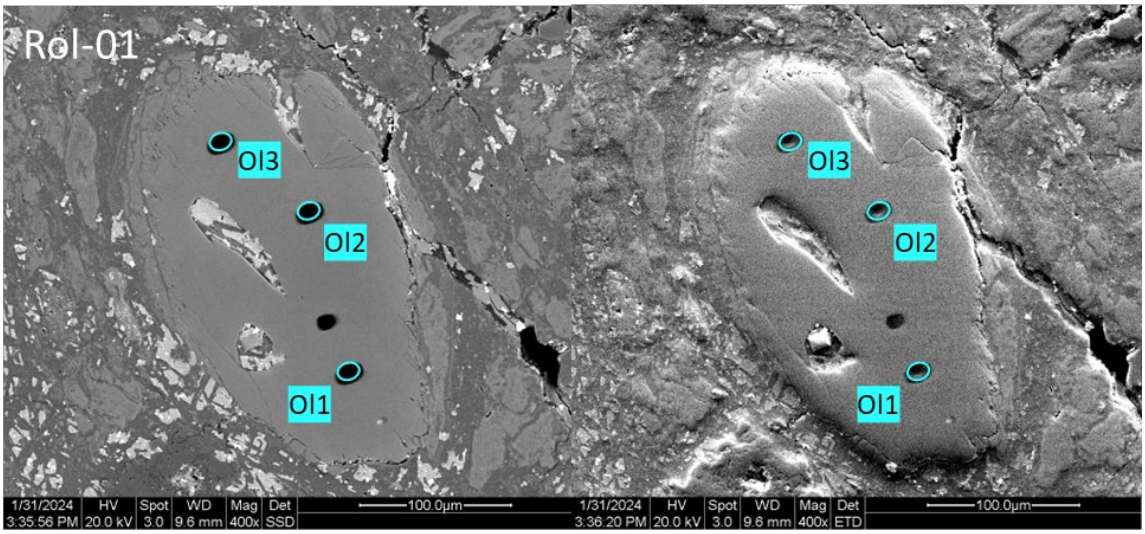
Rol-01
Ol3
Ol2
Ol1
Ol3
Ol2
Ol1
1/31/2024 3:35:56 PM HV 20.0 kV Spot 3.0 WD 9.6 mm Mag 400x Det SSD 100.0µm
1/31/2024 3:36:20 PM HV 20.0 kV Spot 3.0 WD 9.6 mm Mag 400x Det ETD 100.0µm

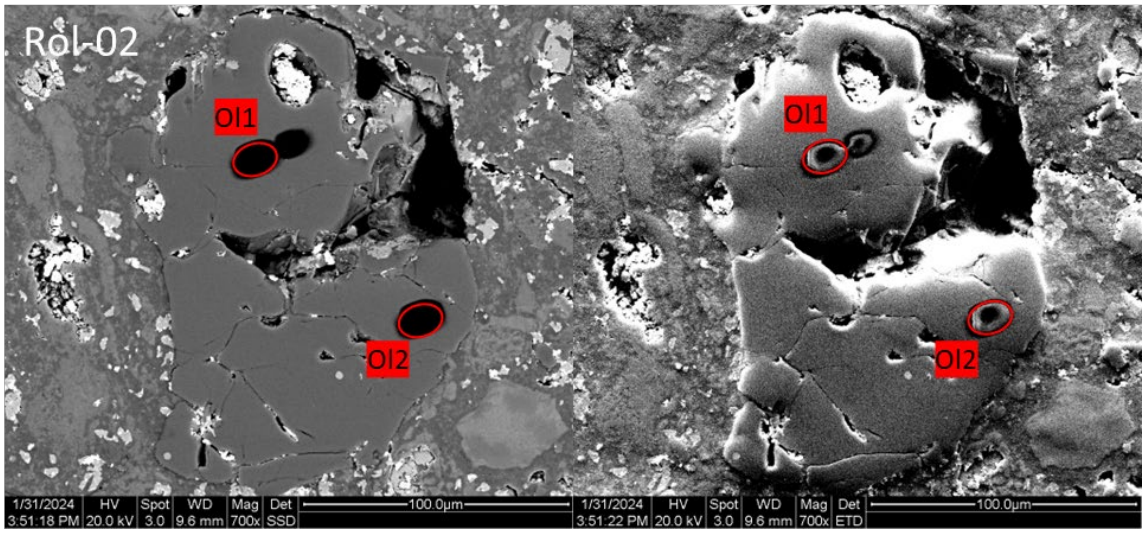
Rol-02
Ol1
Ol2
Ol1
Ol2
1/31/2024 3:51:18 PM HV 20.0 kV Spot 3.0 WD 9.6 mm Mag 700x Det SSD 100.0µm
1/31/2024 3:51:22 PM HV 20.0 kV Spot 3.0 WD 9.6 mm Mag 700x Det ETD 100.0µm

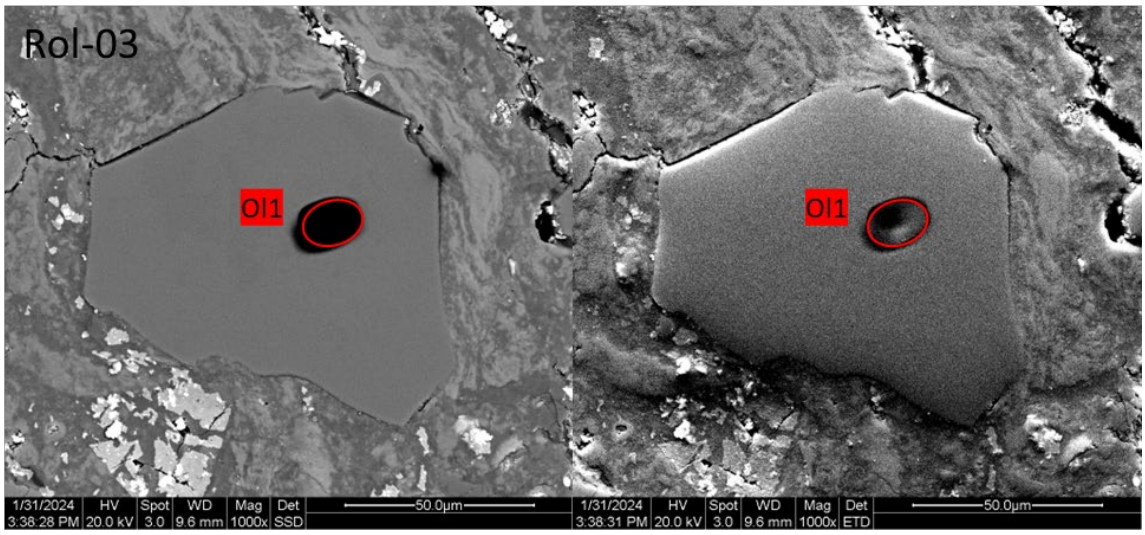
Rol-03
Ol1
Ol1
1/31/2024 3:38:28 PM HV 20.0 kV Spot 3.0 WD 9.6 mm Mag 1000x Det SSD 50.0µm
1/31/2024 3:38:31 PM HV 20.0 kV Spot 3.0 WD 9.6 mm Mag 1000x Det ETD 50.0µm

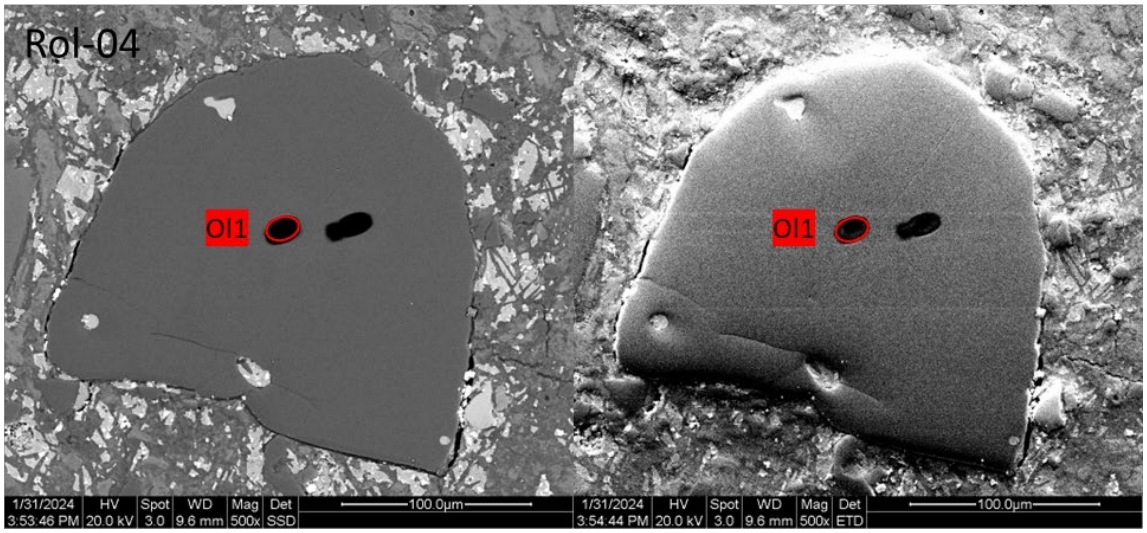
Rol-04
Ol1
Ol1
1/31/2024 3:53:46 PM HV 20.0 kV Spot 3.0 WD 9.6 mm Mag 500x Det SSD 100.0µm
1/31/2024 3:54:44 PM HV 20.0 kV Spot 3.0 WD 9.6 mm Mag 500x Det ETD 100.0µm

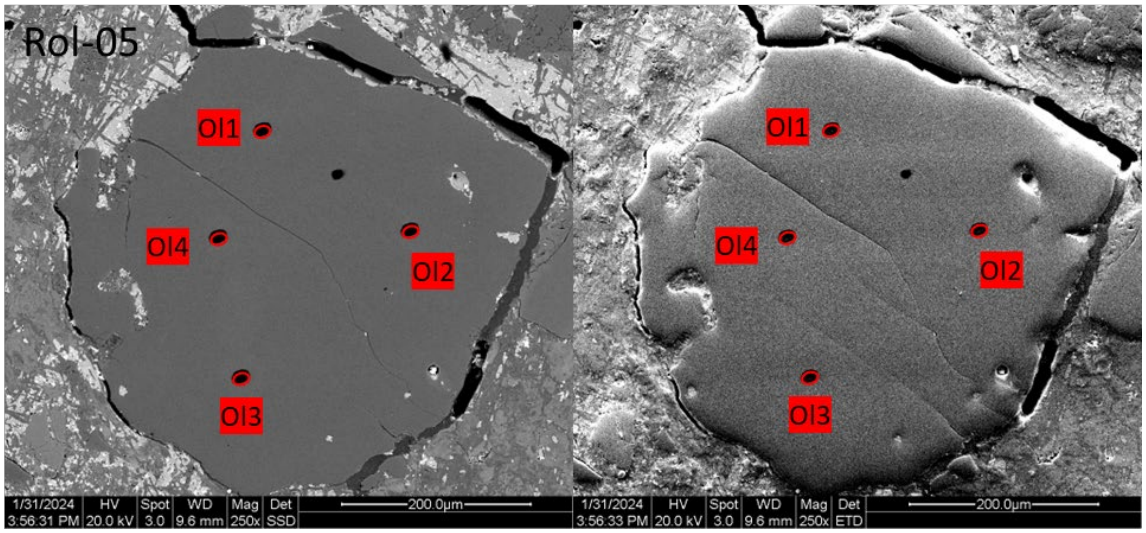
Rol-05
Ol1
Ol4
Ol2
Ol3
Ol1
Ol4
Ol2
Ol3
1/31/2024 3:56:31 PM HV 20.0 kV Spot 3.0 WD 9.6 mm Mag 250x Det SSD 200.0µm
1/31/2024 3:56:33 PM HV 20.0 kV Spot 3.0 WD 9.6 mm Mag 250x Det ETD 200.0µm

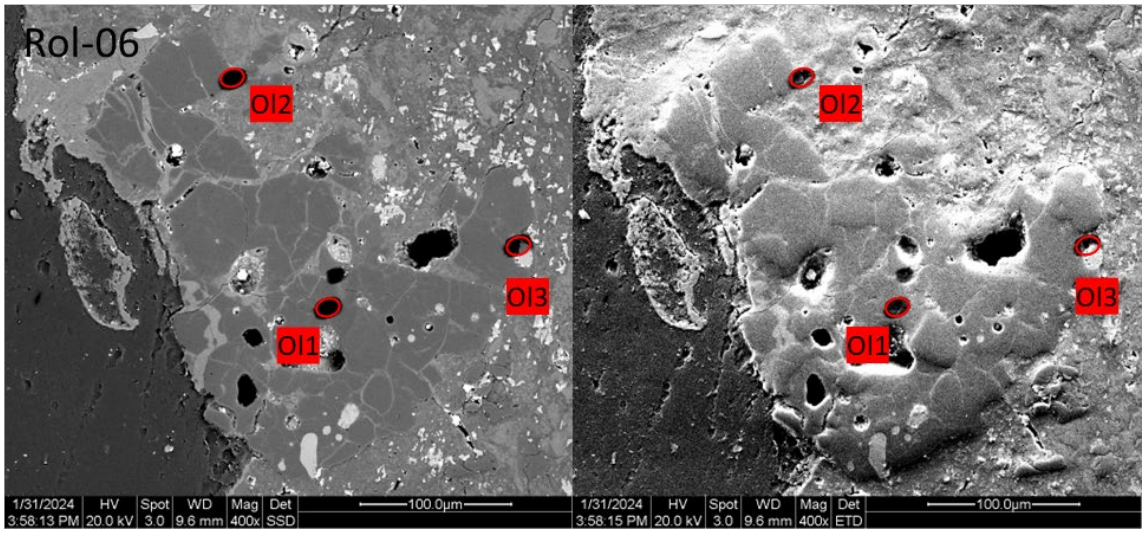
Rol-06
Ol2
Ol3
Ol1
Ol2
Ol3
Ol1
1/31/2024 3:58:13 PM HV 20.0 kV Spot 3.0 WD 9.6 mm Mag 400x Det SSD 100.0µm
1/31/2024 3:58:15 PM HV 20.0 kV Spot 3.0 WD 9.6 mm Mag 400x Det ETD 100.0µm

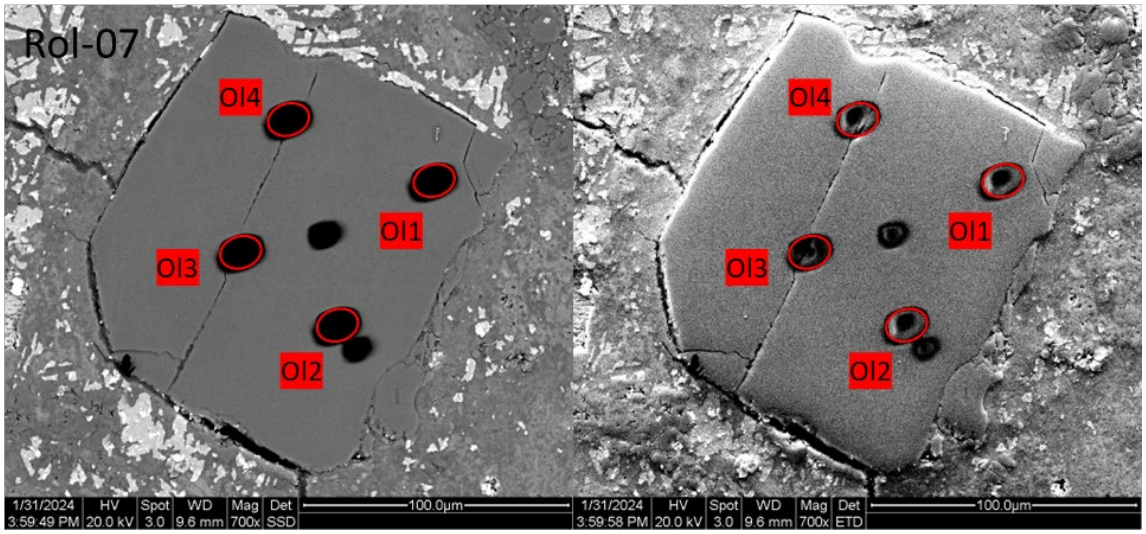
Rol-07
Ol4
Ol1
Ol3
Ol2
1/31/2024 3:59:49 PM HV 20.0 kV Spot 3.0 WD 9.6 mm Mag 700x Det SSD 100.0µm
Ol4
Ol1
Ol3
Ol2
1/31/2024 3:59:58 PM HV 20.0 kV Spot 3.0 WD 9.6 mm Mag 700x Det ETD 100.0µm

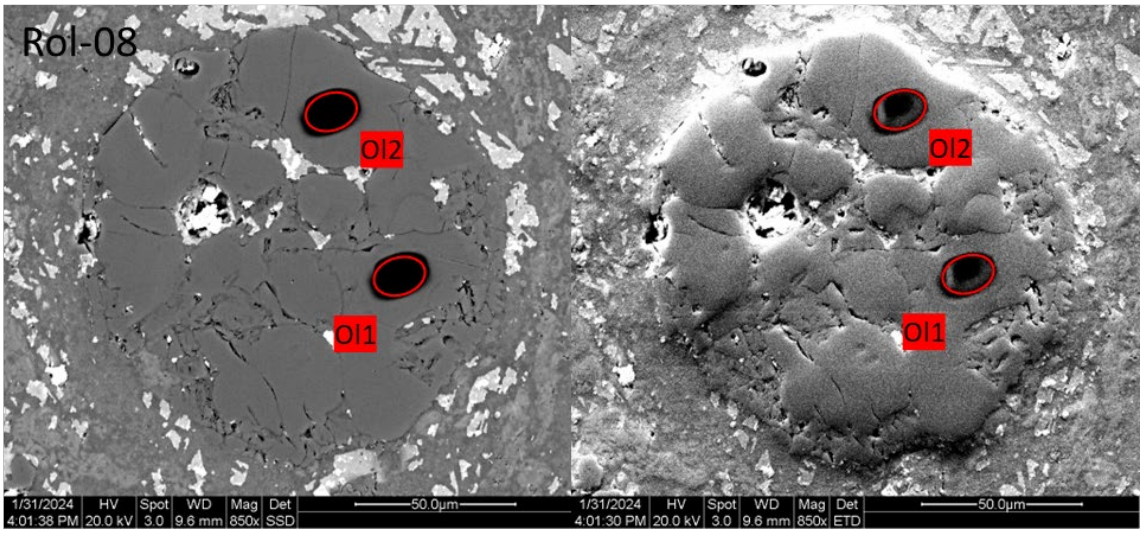
Rol-08
Ol2
Ol1
1/31/2024 4:01:38 PM HV 20.0 kV Spot 3.0 WD 9.6 mm Mag 850x Det SSD 50.0µm
Ol2
Ol1
1/31/2024 4:01:30 PM HV 20.0 kV Spot 3.0 WD 9.6 mm Mag 850x Det ETD 50.0µm

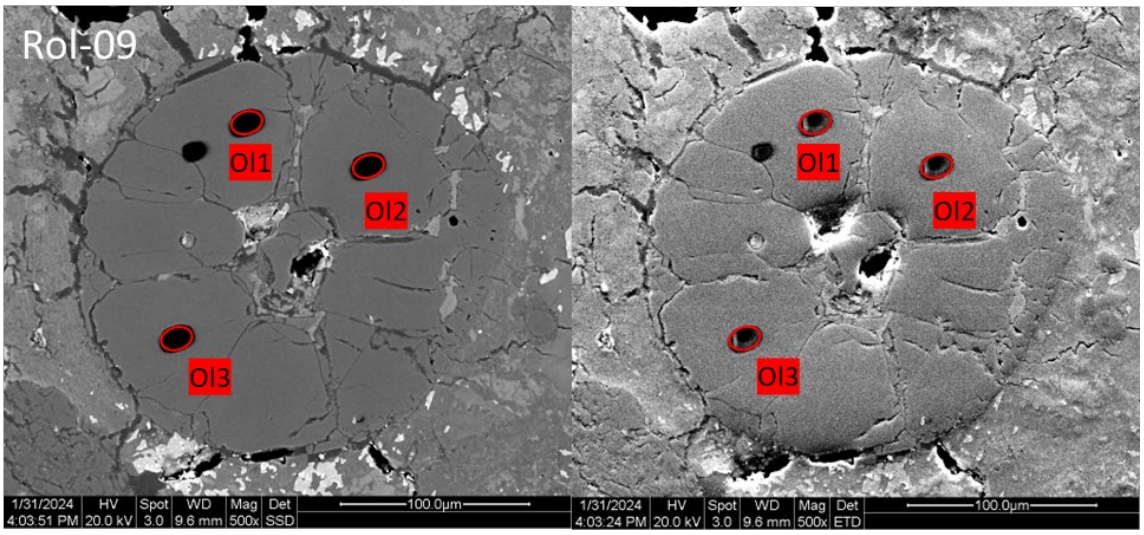
Rol-09
Ol1
Ol2
Ol3
1/31/2024 4:03:51 PM HV 20.0 kV Spot 3.0 WD 9.6 mm Mag 500x Det SSD 100.0µm
Ol1
Ol2
Ol3
1/31/2024 4:03:24 PM HV 20.0 kV Spot 3.0 WD 9.6 mm Mag 500x Det ETD 100.0µm

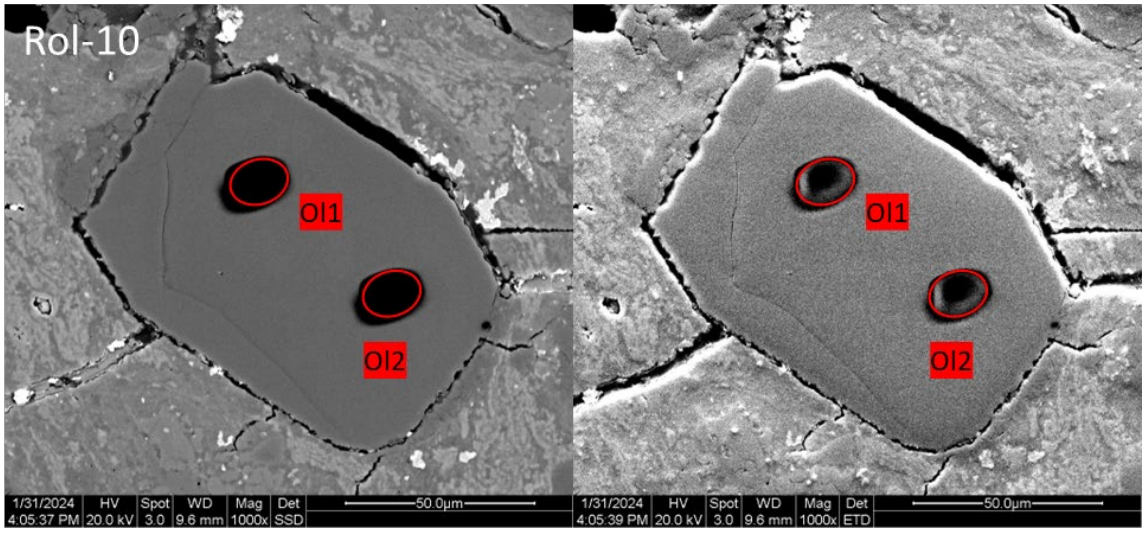
Rol-10
Ol1
Ol2
1/31/2024 4:05:37 PM HV 20.0 kV Spot 3.0 WD 9.6 mm Mag 1000x Det SSD 50.0µm
Ol1
Ol2
1/31/2024 4:05:39 PM HV 20.0 kV Spot 3.0 WD 9.6 mm Mag 1000x Det ETD 50.0µm

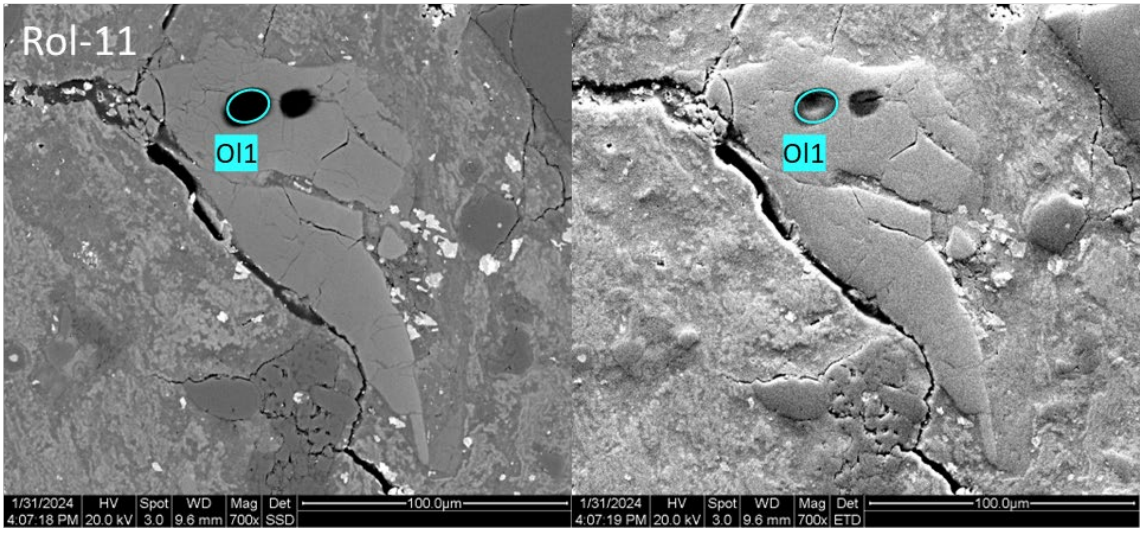
Rol-11
Ol1
1/31/2024 4:07:18 PM HV 20.0 kV Spot 3.0 WD 9.6 mm Mag 700x Det SSD 100.0µm
Ol1
1/31/2024 4:07:19 PM HV 20.0 kV Spot 3.0 WD 9.6 mm Mag 700x Det ETD 100.0µm

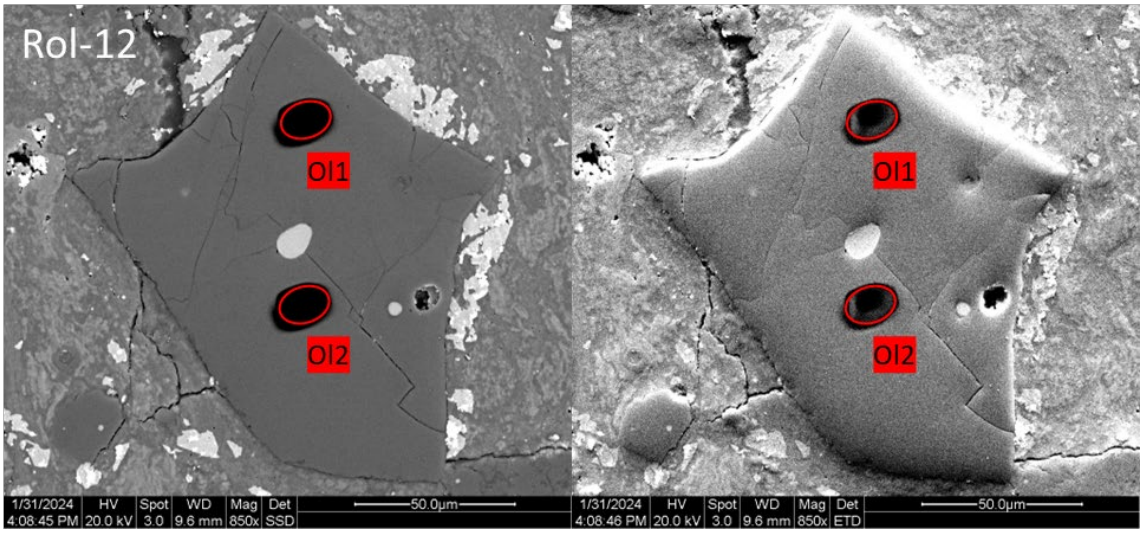
Rol-12
Ol1
Ol2
1/31/2024 4:08:45 PM HV 20.0 kV Spot 3.0 WD 9.6 mm Mag 850x Det SSD 50.0µm
Ol1
Ol2
1/31/2024 4:08:46 PM HV 20.0 kV Spot 3.0 WD 9.6 mm Mag 850x Det ETD 50.0µm

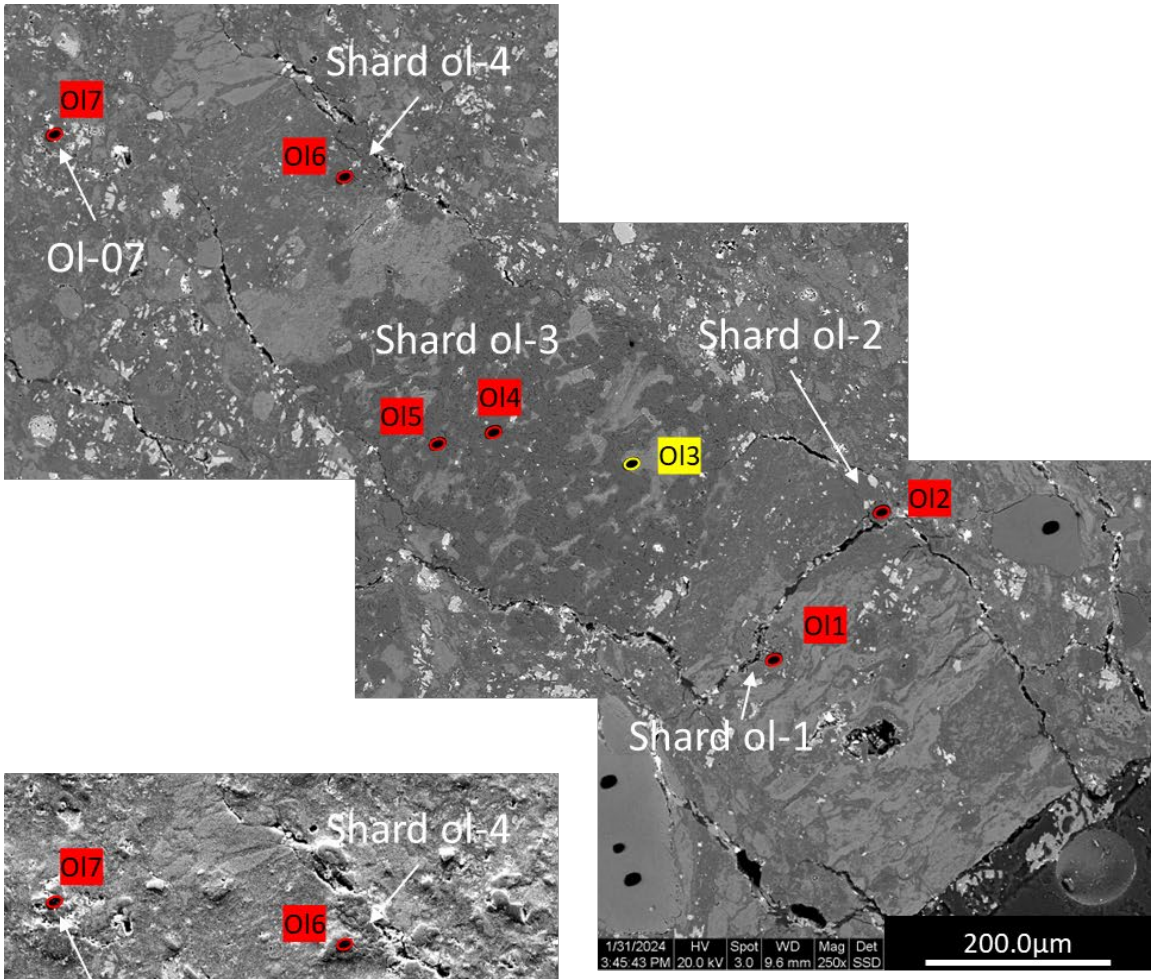
Shard ol-4
Ol7
Ol6
Ol-07
Shard ol-3
Shard ol-2
Ol5
Ol4
Ol3
Ol2
Ol1
Shard ol-1
1/31/2024 3:45:43 PM
HV 20.0 kV
Spot 3.0
WD 9.6 mm
Mag 250x
Det SSD
200.0µm

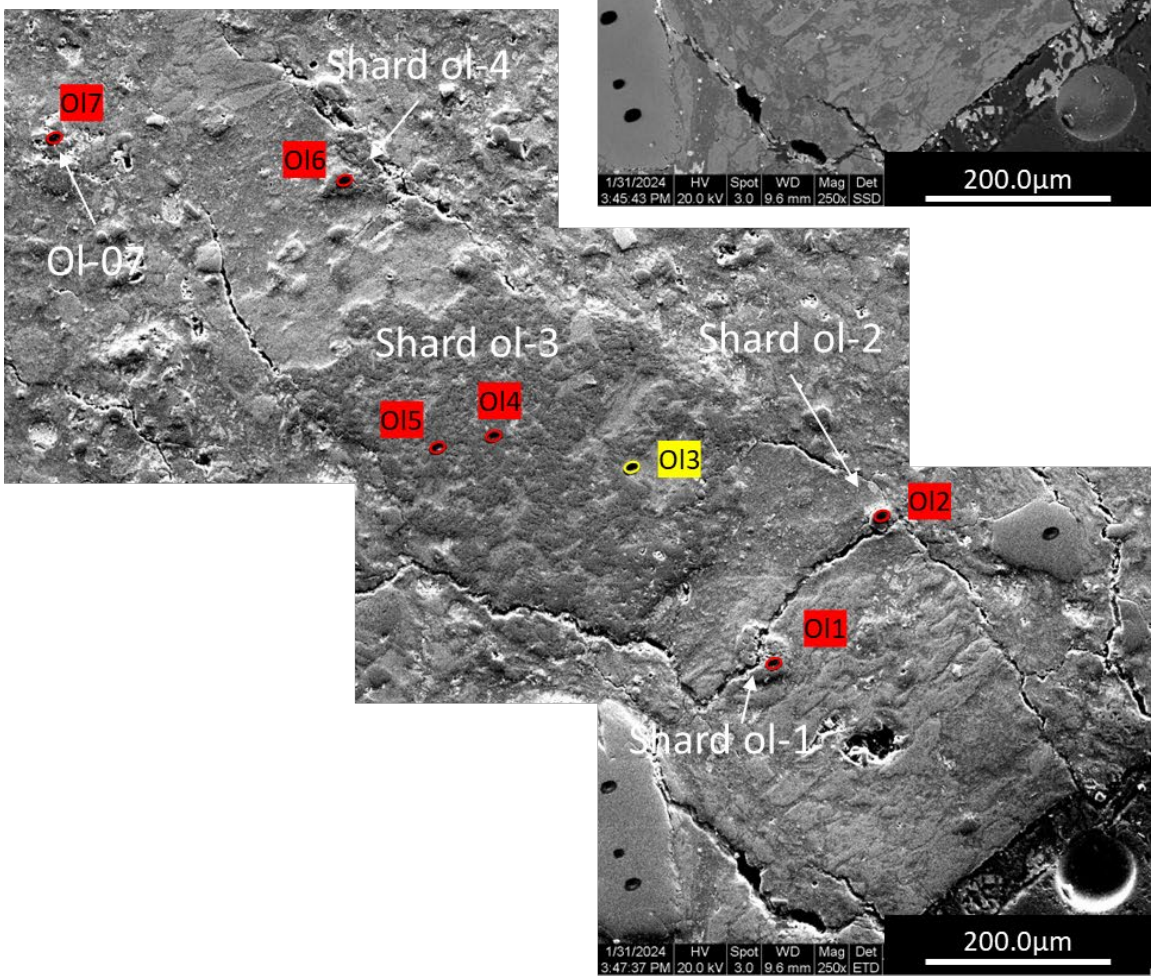
Shard ol-4
Ol7
Ol6
Ol-07
Shard ol-3
Shard ol-2
Ol5
Ol4
Ol3
Ol2
Ol1
Shard ol-1
1/31/2024 3:47:37 PM
HV 20.0 kV
Spot 3.0
WD 9.6 mm
Mag 250x
Det ETD
200.0µm

7.9.2LAP 02239

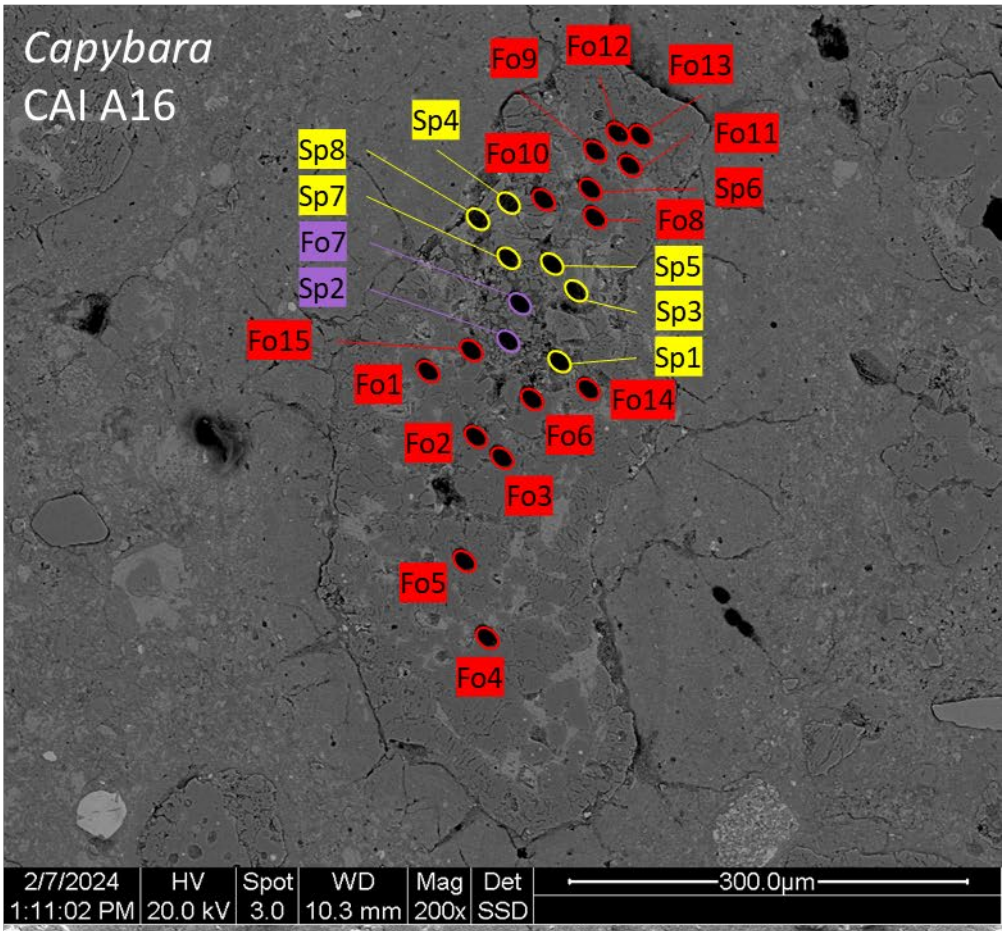

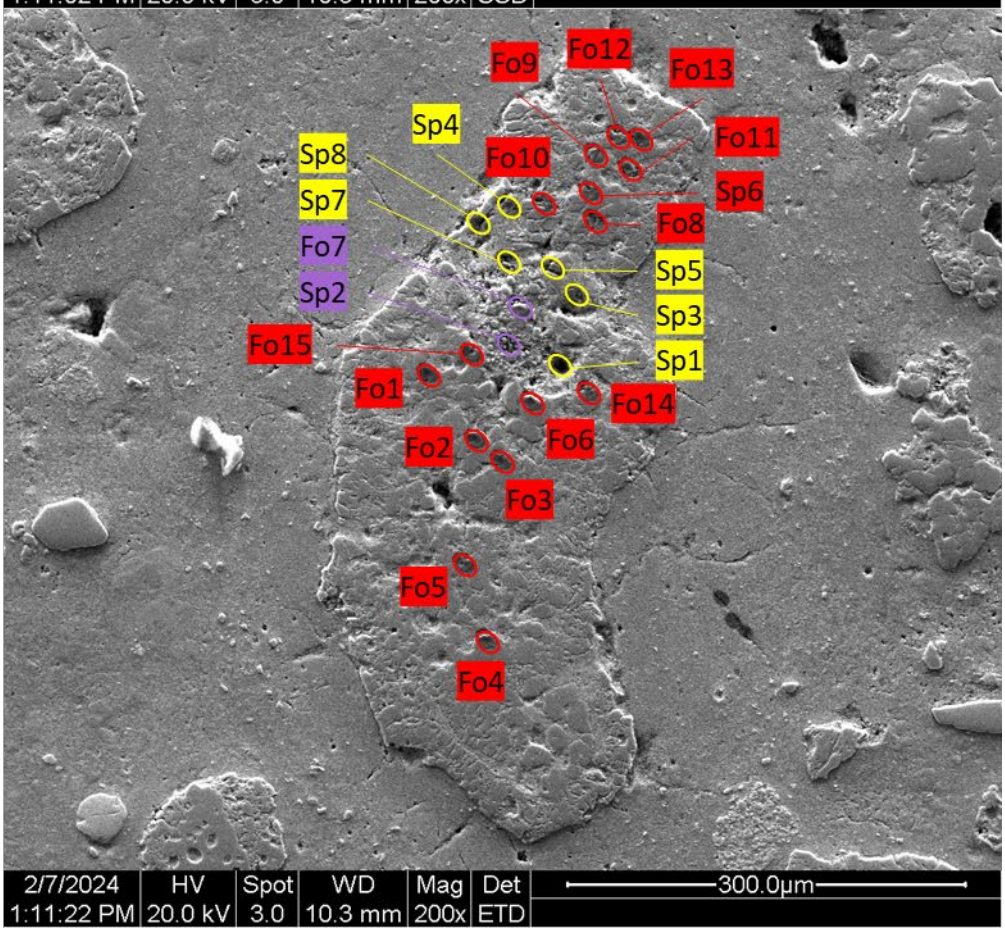

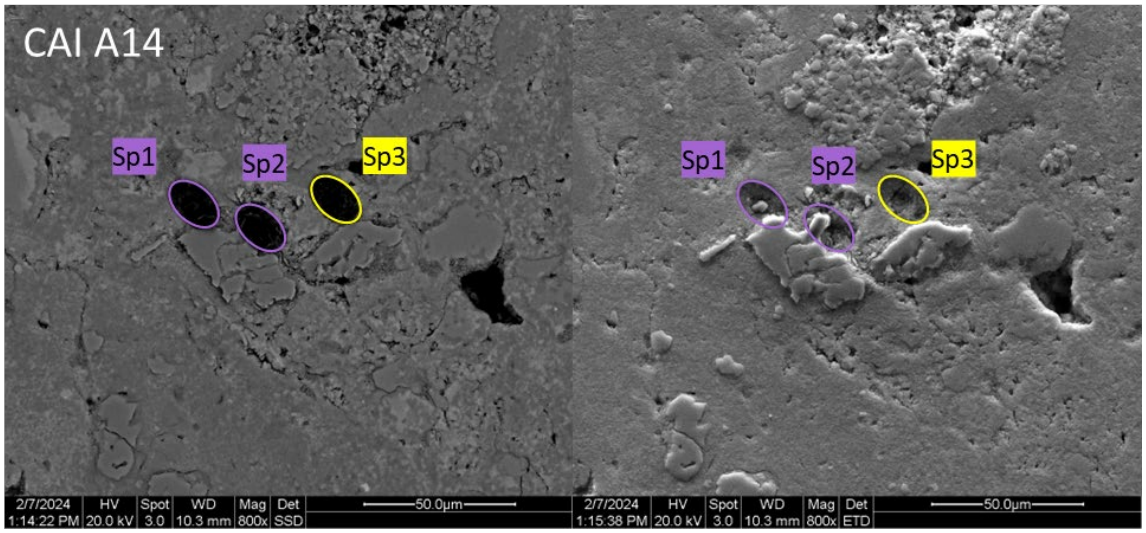
CAI A14
Sp1
Sp2
Sp3
Sp1
Sp2
Sp3
2/7/2024 1:14:22 PM HV 20.0 kV Spot 3.0 WD 10.3 mm Mag 800x Det SSD 50.0µm
2/7/2024 1:15:38 PM HV 20.0 kV Spot 3.0 WD 10.3 mm Mag 800x Det ETD 50.0µm

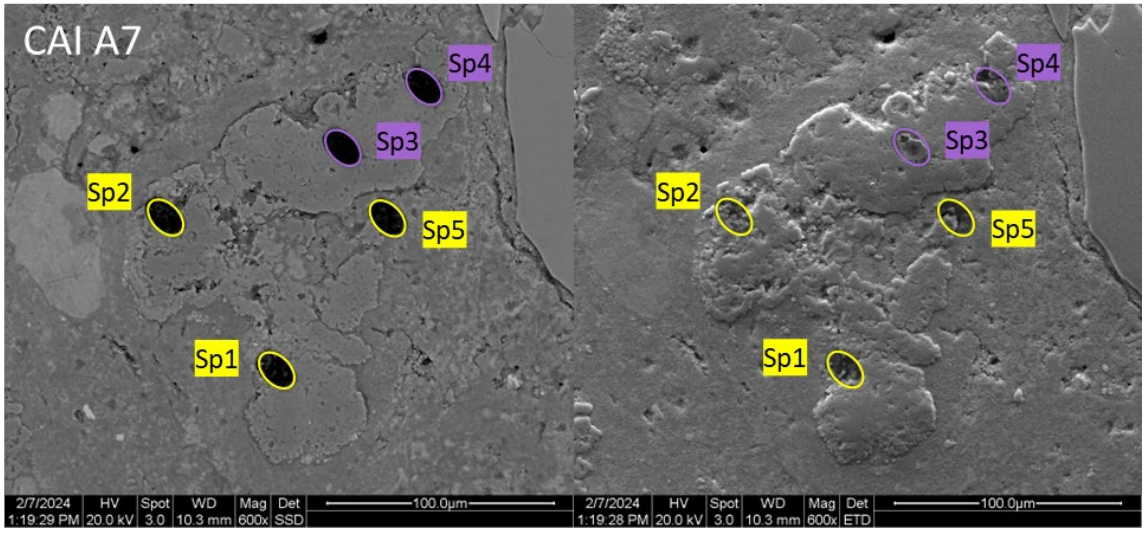
CAI A7
Sp4
Sp3
Sp2
Sp5
Sp1
Sp4
Sp3
Sp2
Sp5
Sp1
2/7/2024 1:19:29 PM HV 20.0 kV Spot 3.0 WD 10.3 mm Mag 600x Det SSD 100.0µm
2/7/2024 1:19:28 PM HV 20.0 kV Spot 3.0 WD 10.3 mm Mag 600x Det ETD 100.0µm

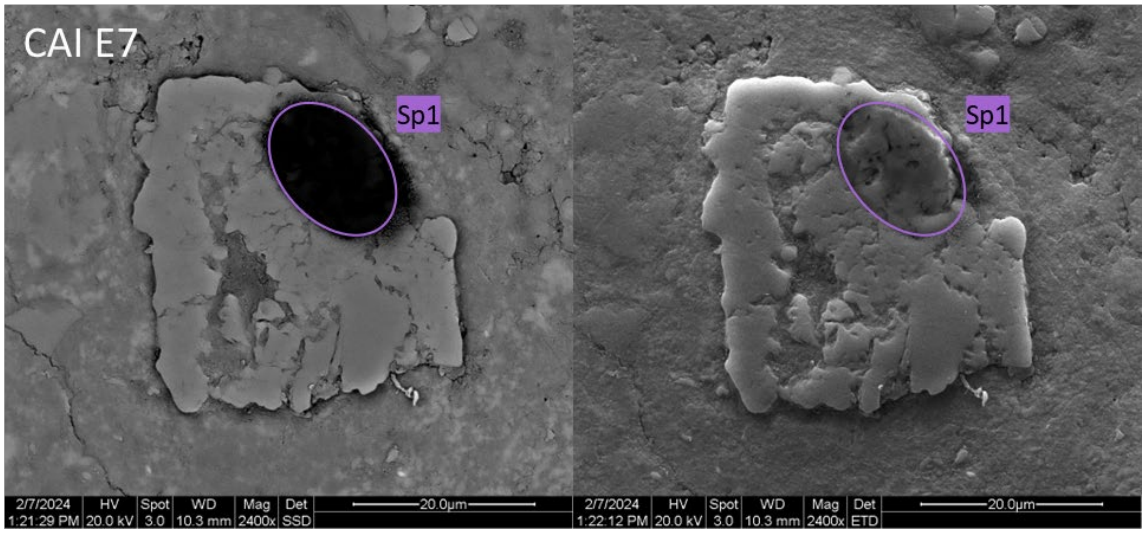
CAI E7
Sp1
Sp1
2/7/2024 1:21:29 PM HV 20.0 kV Spot 3.0 WD 10.3 mm Mag 2400x Det SSD 20.0µm
2/7/2024 1:22:12 PM HV 20.0 kV Spot 3.0 WD 10.3 mm Mag 2400x Det ETD 20.0µm

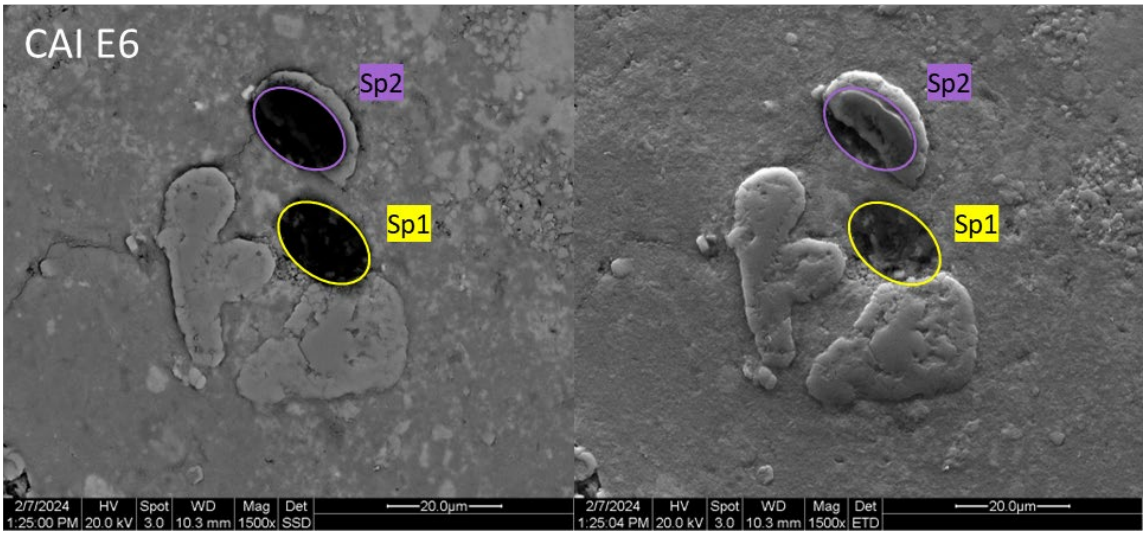
CAI E6
Sp2
Sp1
Sp2
Sp1
2/7/2024 1:25:00 PM HV 20.0 kV Spot 3.0 WD 10.3 mm Mag 1500x Det SSD 20.0µm
2/7/2024 1:25:04 PM HV 20.0 kV Spot 3.0 WD 10.3 mm Mag 1500x Det ETD 20.0µm

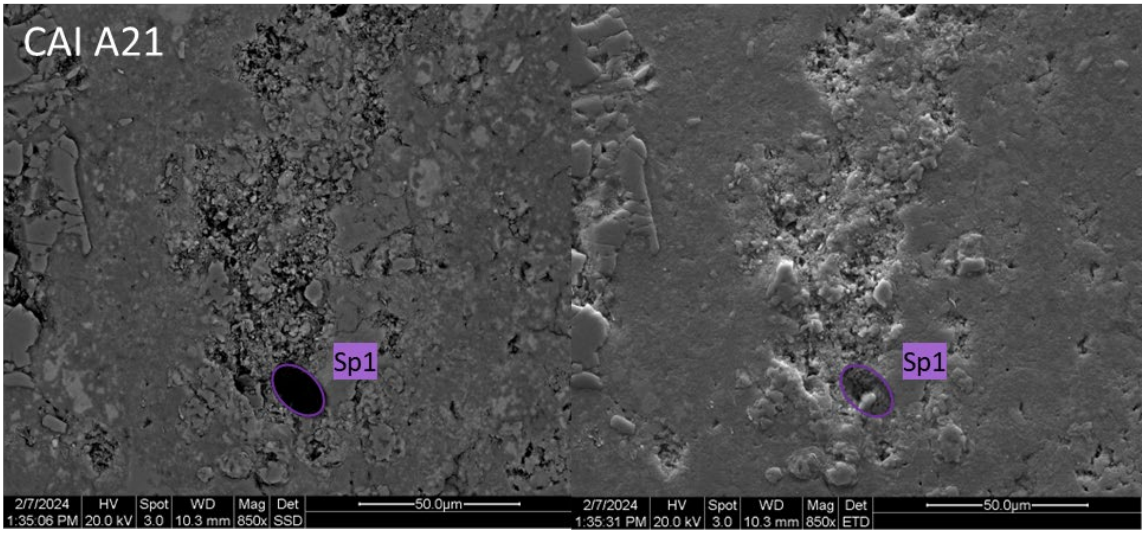
CAI A21
Sp1
Sp1
2/7/2024 1:35:06 PM HV 20.0 kV Spot 3.0 WD 10.3 mm Mag 850x Det SSD 50.0µm
2/7/2024 1:35:31 PM HV 20.0 kV Spot 3.0 WD 10.3 mm Mag 850x Det ETD 50.0µm

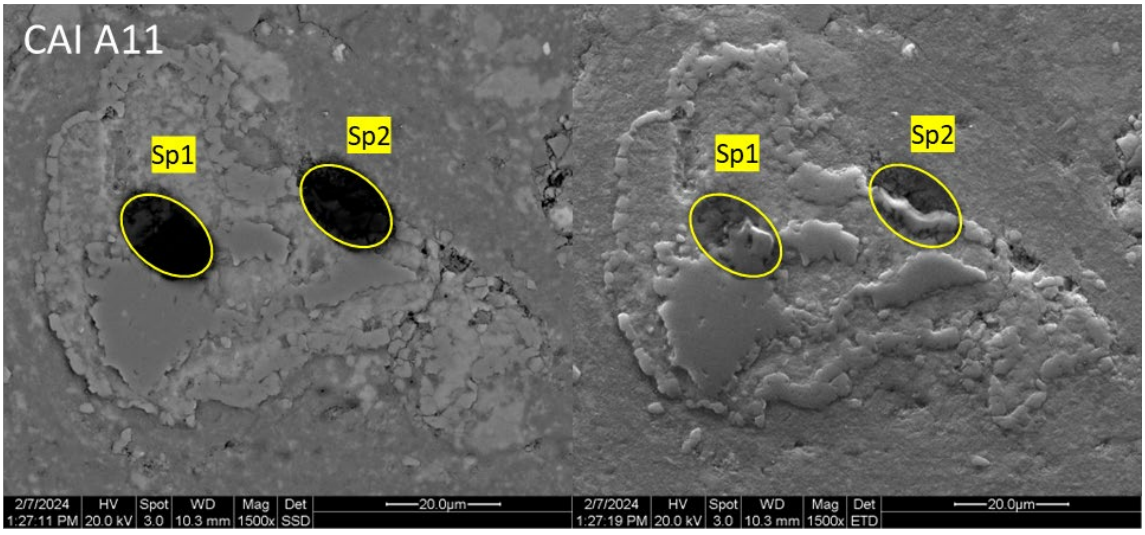
CAI A11
Sp1
Sp2
Sp1
Sp2
2/7/2024 1:27:11 PM HV 20.0 kV Spot 3.0 WD 10.3 mm Mag 1500x Det SSD 20.0µm
2/7/2024 1:27:19 PM HV 20.0 kV Spot 3.0 WD 10.3 mm Mag 1500x Det ETD 20.0µm

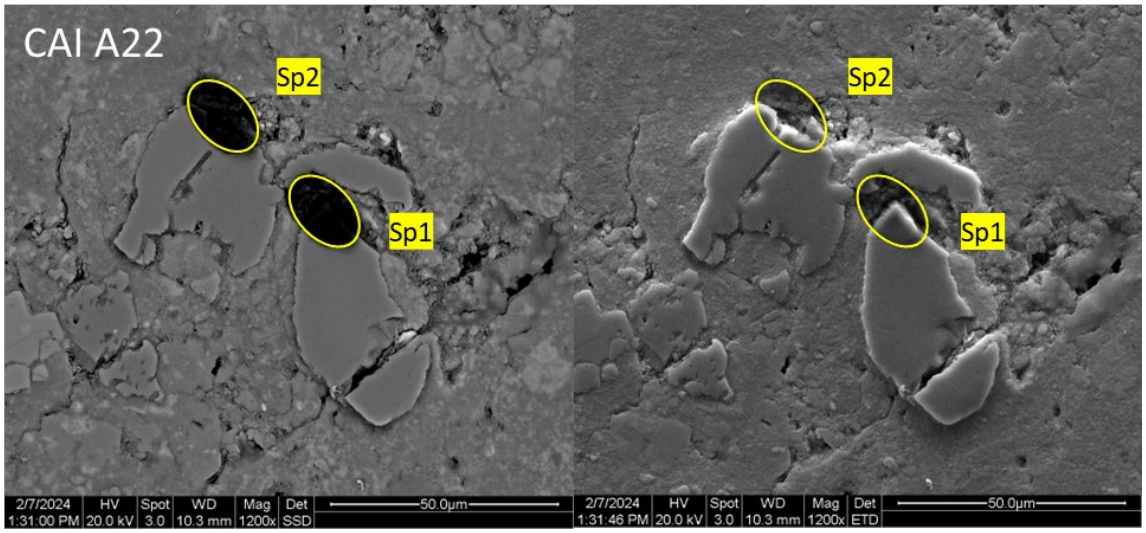
CAI A22
Sp2
Sp1
Sp2
Sp1
2/7/2024 1:31:00 PM HV 20.0 kV Spot 3.0 WD 10.3 mm Mag 1200x Det SSD 50.0µm
2/7/2024 1:31:46 PM HV 20.0 kV Spot 3.0 WD 10.3 mm Mag 1200x Det ETD 50.0µm

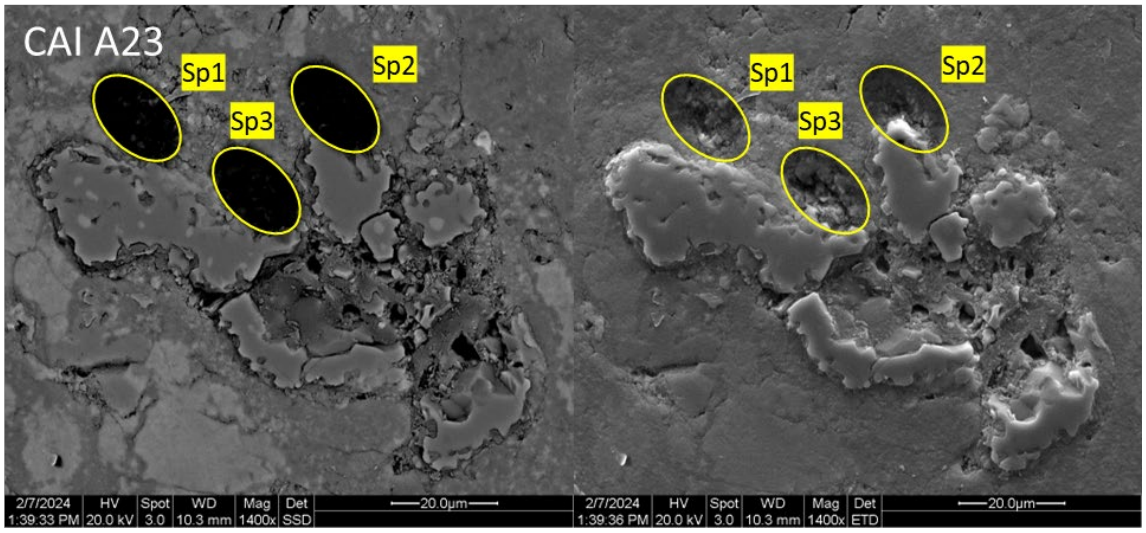
CAI A23
Sp1
Sp3
Sp2
Sp1
Sp3
Sp2
2/7/2024 1:39:33 PM HV 20.0 kV Spot 3.0 WD 10.3 mm Mag 1400x Det SSD 20.0µm
2/7/2024 1:39:36 PM HV 20.0 kV Spot 3.0 WD 10.3 mm Mag 1400x Det ETD 20.0µm

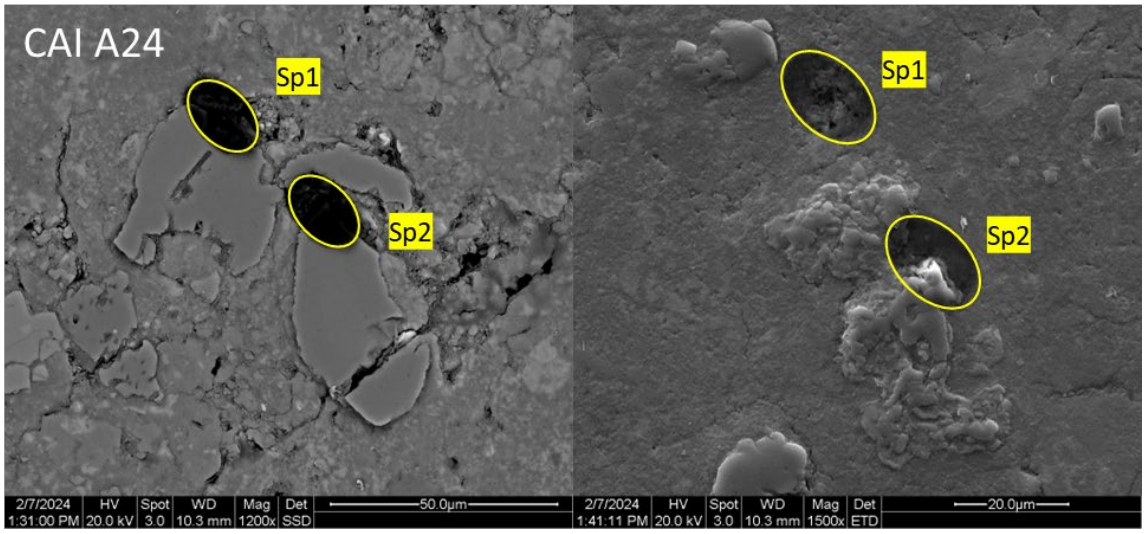
CAI A24
Sp1
Sp2
Sp1
Sp2
2/7/2024 1:31:00 PM HV 20.0 kV Spot 3.0 WD 10.3 mm Mag 1200x Det SSD 50.0µm
2/7/2024 1:41:11 PM HV 20.0 kV Spot 3.0 WD 10.3 mm Mag 1500x Det ETD 20.0µm

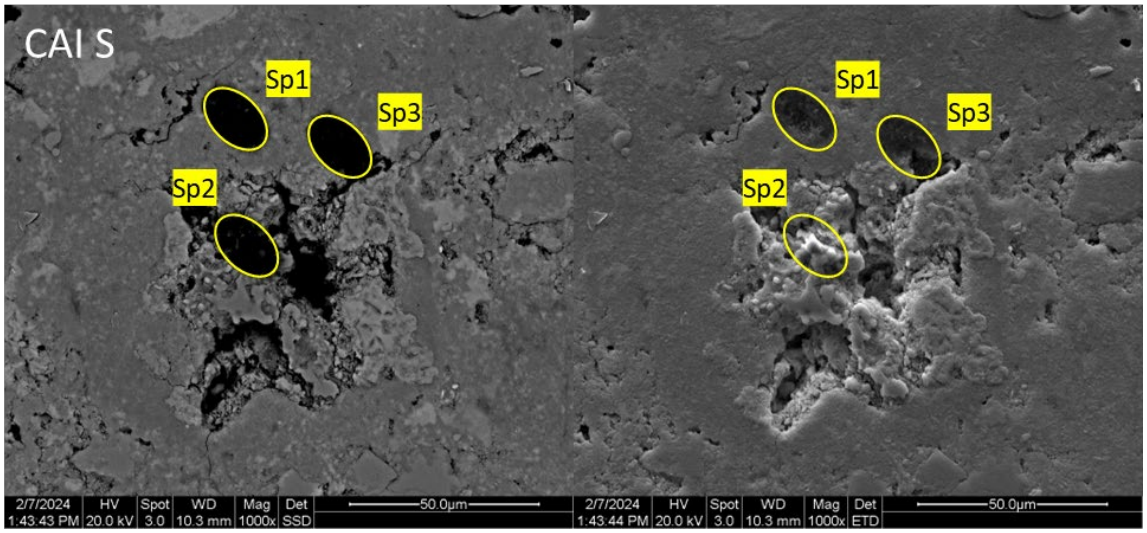
CAI S
Sp1
Sp3
Sp2
Sp1
Sp3
Sp2
2/7/2024 1:43:43 PM HV 20.0 kV Spot 3.0 WD 10.3 mm Mag 1000x Det SSD 50.0µm
2/7/2024 1:43:44 PM HV 20.0 kV Spot 3.0 WD 10.3 mm Mag 1000x Det ETD 50.0µm

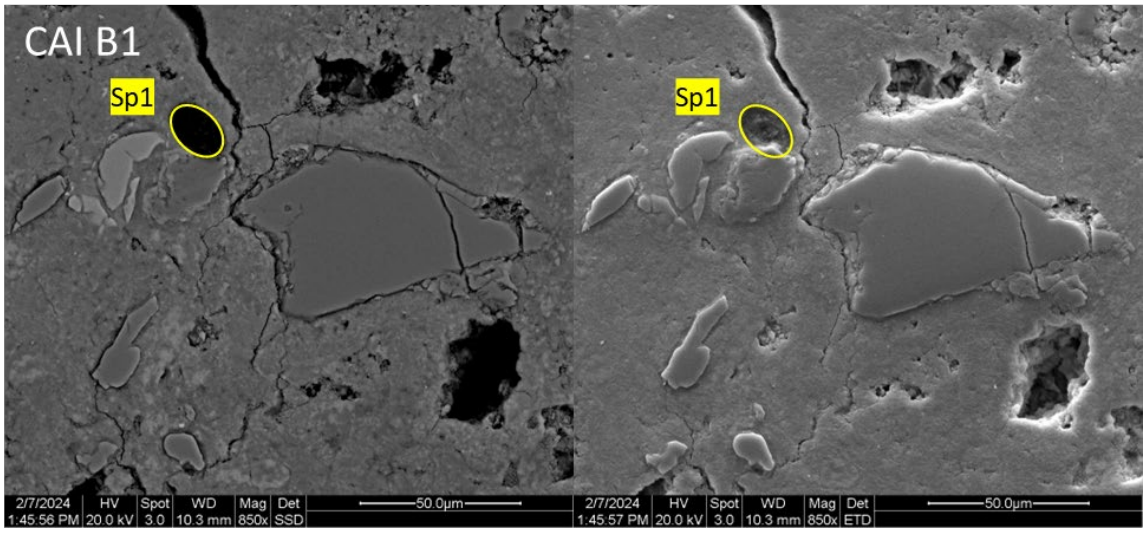
CAI B1
Sp1
Sp1
2/7/2024 1:45:56 PM HV 20.0 kV Spot 3.0 WD 10.3 mm Mag 850x Det SSD 50.0µm
2/7/2024 1:45:57 PM HV 20.0 kV Spot 3.0 WD 10.3 mm Mag 850x Det ETD 50.0µm

7.9.3 DNG 06004

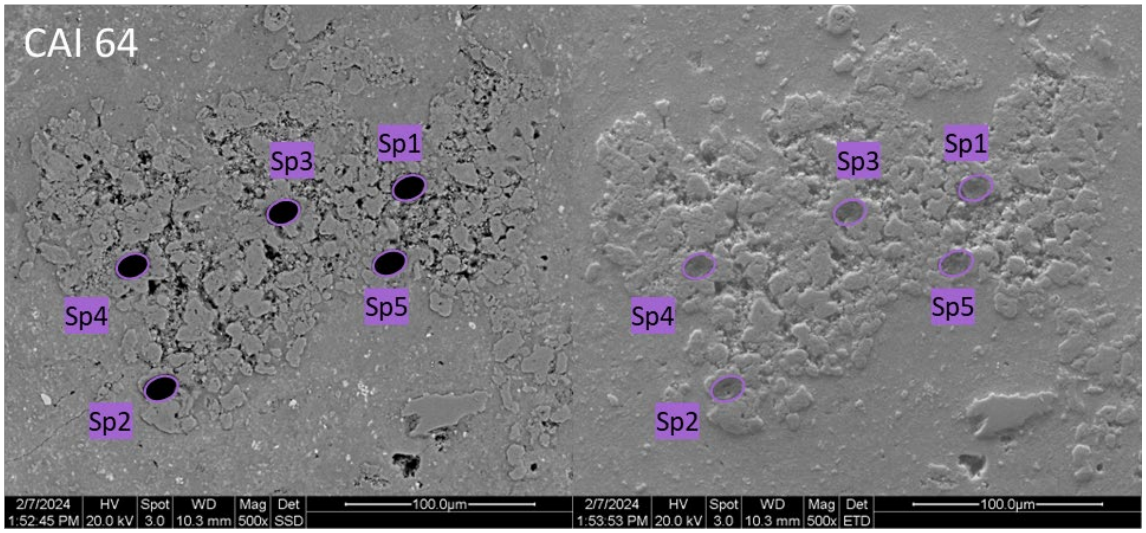

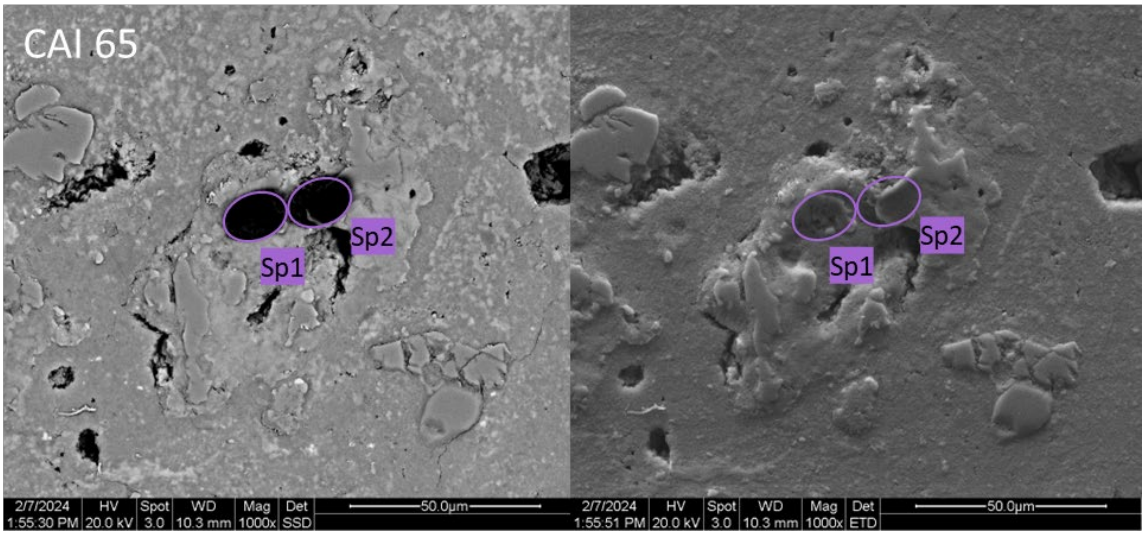

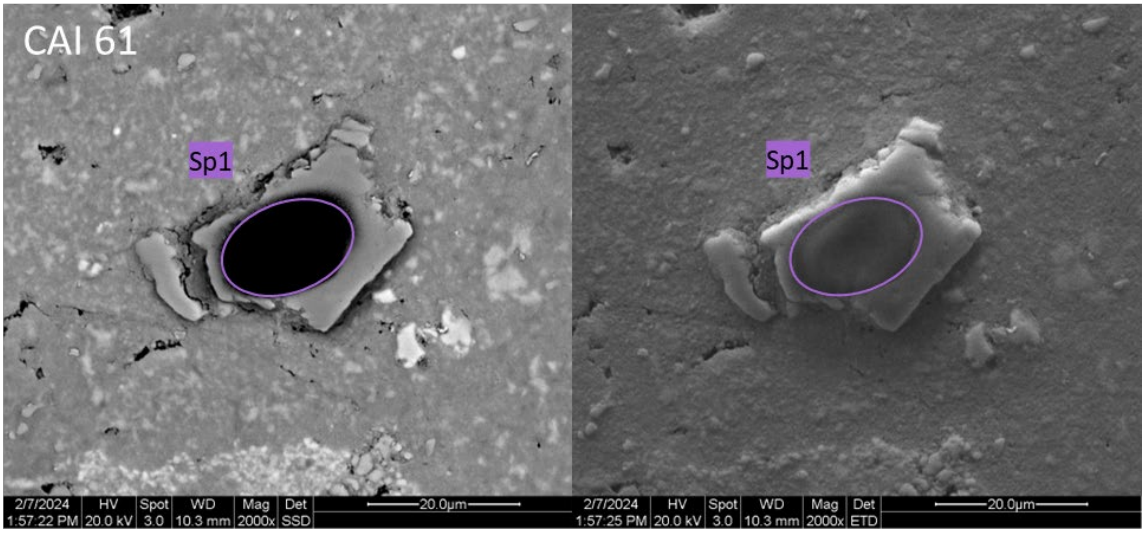

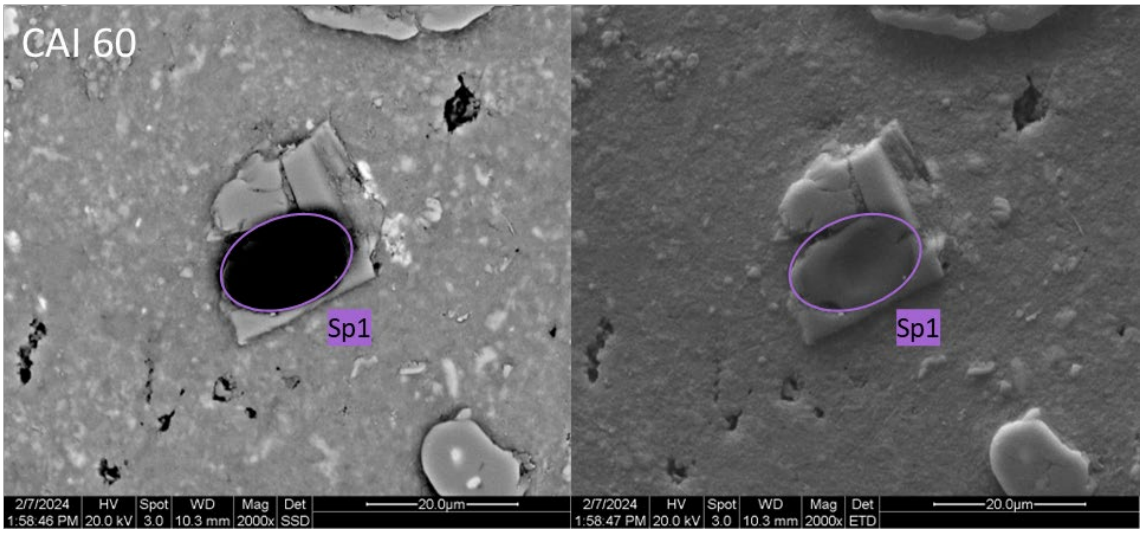
CAI 60
Sp1
Sp1
2/7/2024 1:58.46 PM HV 20.0 kV Spot 3.0 WD 10.3 mm Mag 2000x Det SSD 20.0µm
2/7/2024 1:58.47 PM HV 20.0 kV Spot 3.0 WD 10.3 mm Mag 2000x Det ETD 20.0µm

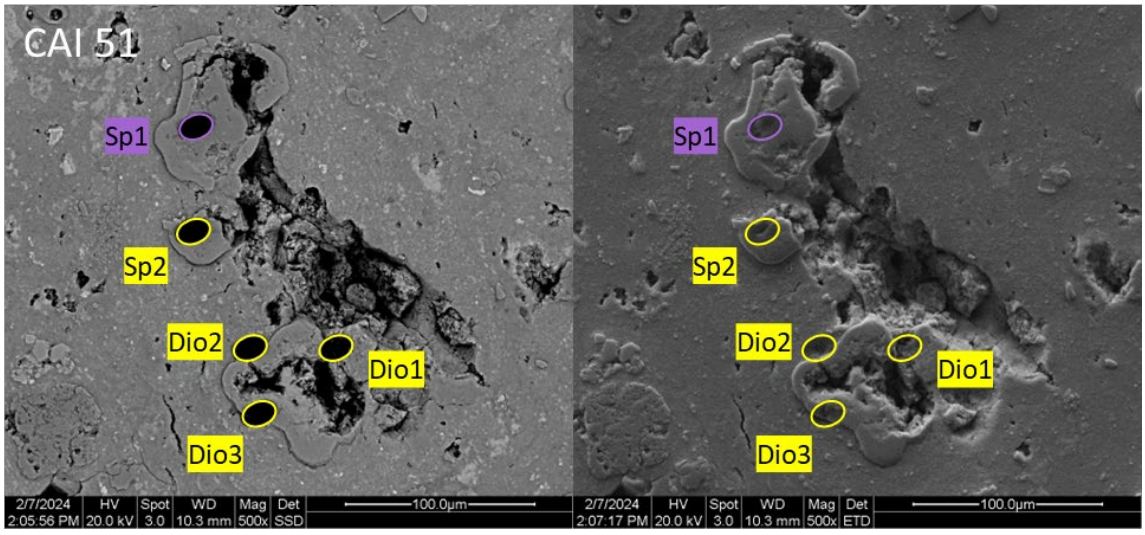
CAI 51
Sp1
Sp2
Dio2
Dio1
Dio3
Sp1
Sp2
Dio2
Dio1
Dio3
2/7/2024 2:05.56 PM HV 20.0 kV Spot 3.0 WD 10.3 mm Mag 500x Det SSD 100.0µm
2/7/2024 2:07.17 PM HV 20.0 kV Spot 3.0 WD 10.3 mm Mag 500x Det ETD 100.0µm

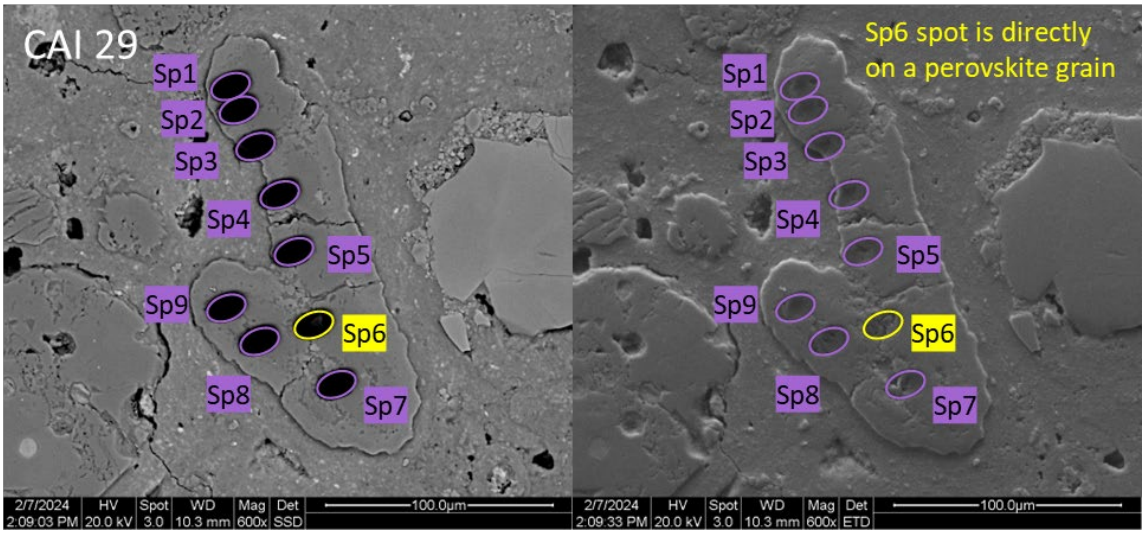
CAI 29
Sp1
Sp2
Sp3
Sp4
Sp5
Sp9
Sp6
Sp8
Sp7
Sp6 spot is directly on a perovskite grain
Sp1
Sp2
Sp3
Sp4
Sp5
Sp9
Sp6
Sp8
Sp7
2/7/2024 2:09.03 PM HV 20.0 kV Spot 3.0 WD 10.3 mm Mag 600x Det SSD 100.0µm
2/7/2024 2:09.33 PM HV 20.0 kV Spot 3.0 WD 10.3 mm Mag 600x Det ETD 100.0µm

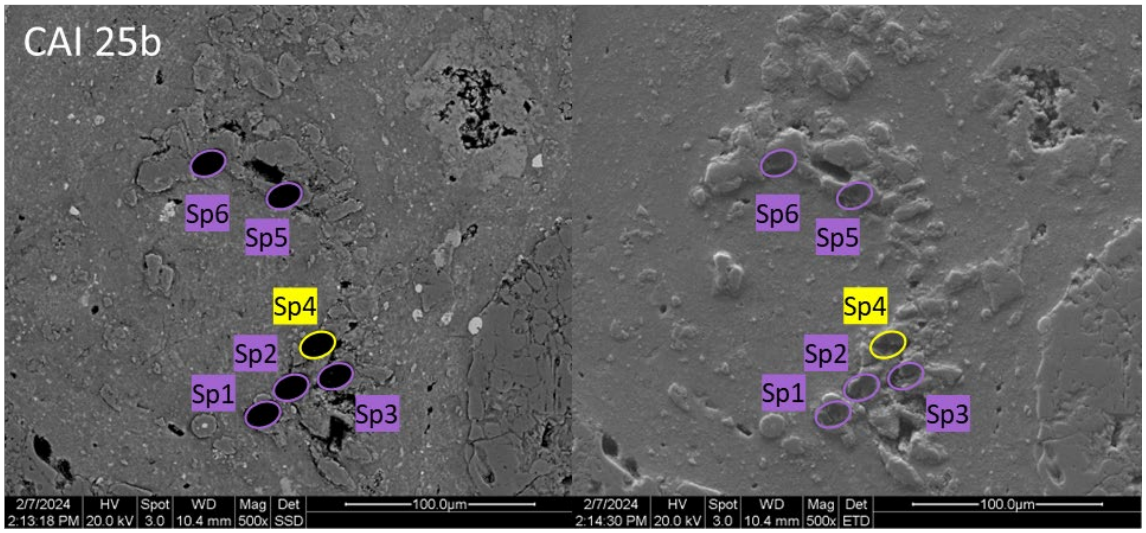
CAI 25b
Sp6
Sp5
Sp4
Sp2
Sp1
Sp3
Sp6
Sp5
Sp4
Sp2
Sp1
Sp3
2/7/2024 2:13.18 PM HV 20.0 kV Spot 3.0 WD 10.4 mm Mag 500x Det SSD 100.0µm
2/7/2024 2:14.30 PM HV 20.0 kV Spot 3.0 WD 10.4 mm Mag 500x Det ETD 100.0µm

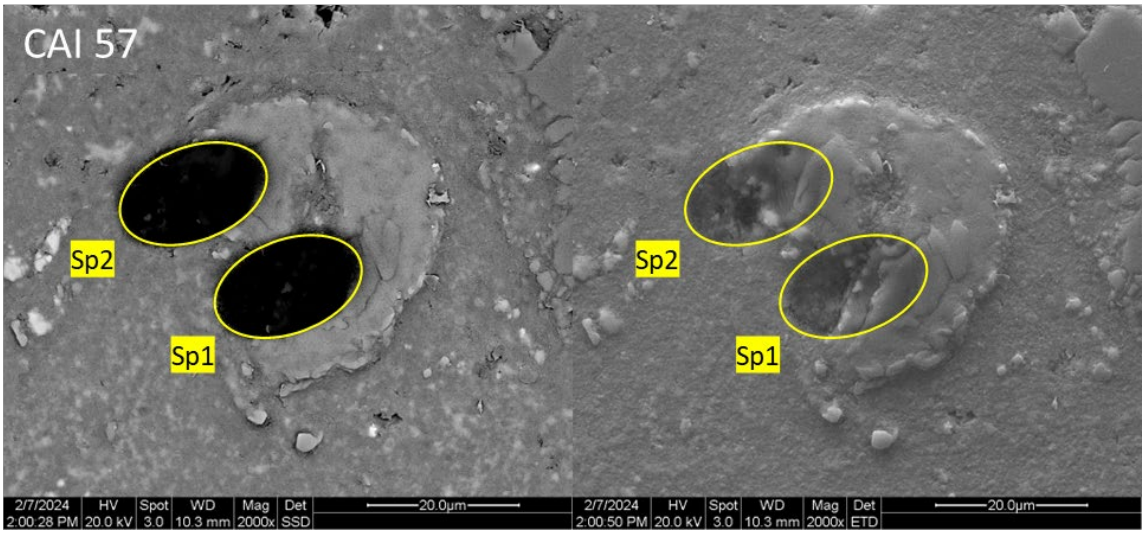
CAI 57
Sp2
Sp1
Sp2
Sp1
2/7/2024 2:00.28 PM HV 20.0 kV Spot 3.0 WD 10.3 mm Mag 2000x Det SSD 20.0µm
2/7/2024 2:00.50 PM HV 20.0 kV Spot 3.0 WD 10.3 mm Mag 2000x Det ETD 20.0µm

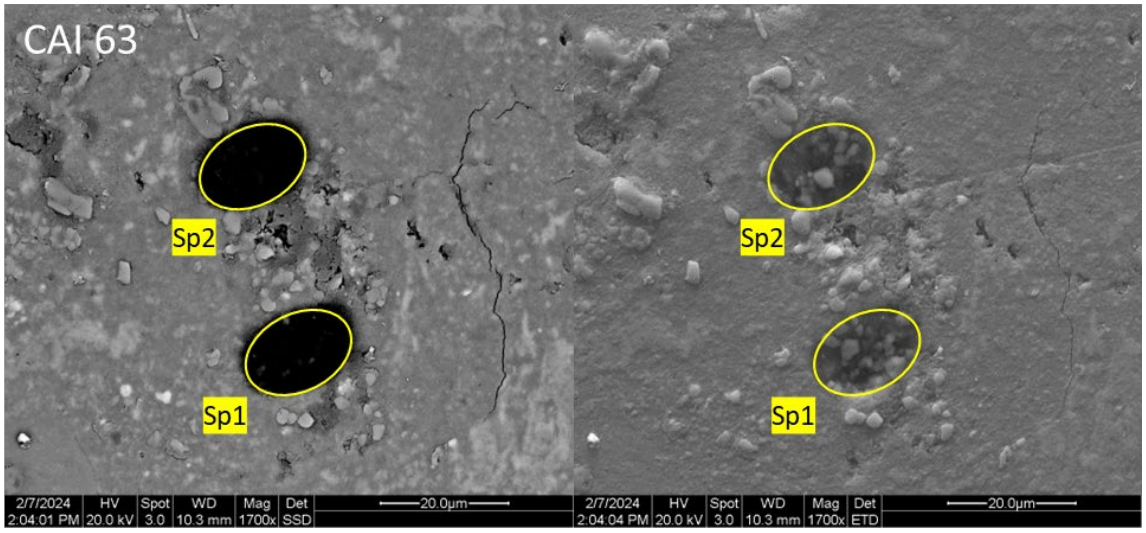
CAI 63
Sp2
Sp1
Sp2
Sp1
2/7/2024 2:04.01 PM HV 20.0 kV Spot 3.0 WD 10.3 mm Mag 1700x Det SSD 20.0µm
2/7/2024 2:04.04 PM HV 20.0 kV Spot 3.0 WD 10.3 mm Mag 1700x Det ETD 20.0µm

7.9.4Paris

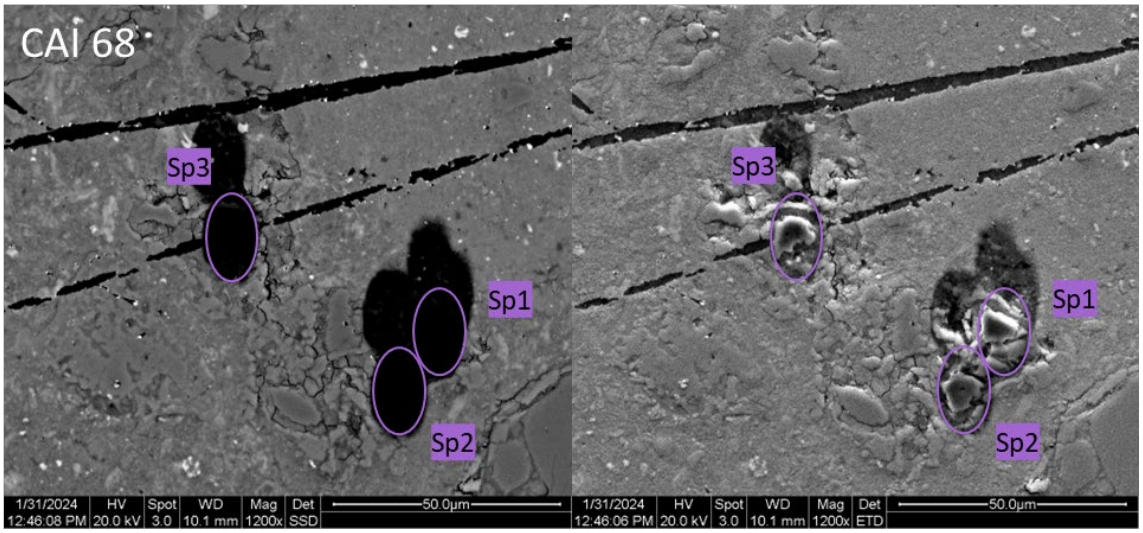
CAI 68
Sp3
Sp1
Sp2
Sp3
Sp1
Sp2
1/31/2024 12:46:08 PM HV 20.0 kV Spot 3.0 WD 10.1 mm Mag 1200x Det SSD 50.0µm
1/31/2024 12:46:06 PM HV 20.0 kV Spot 3.0 WD 10.1 mm Mag 1200x Det ETD 50.0µm

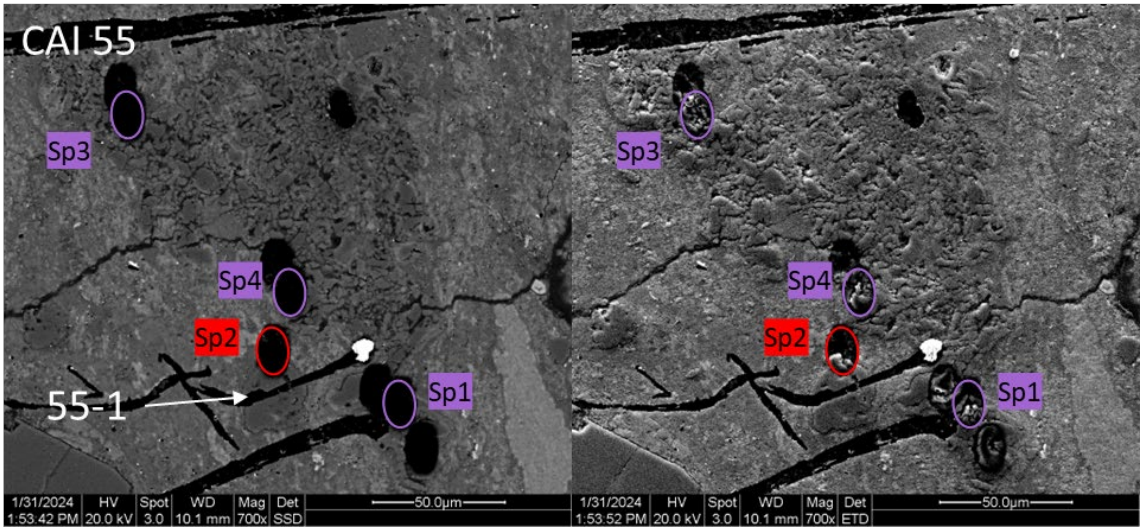
CAI 55
Sp3
Sp4
Sp2
55-1
Sp1
Sp3
Sp4
Sp2
Sp1
1/31/2024 1:53:42 PM HV 20.0 kV Spot 3.0 WD 10.1 mm Mag 700x Det SSD 50.0µm
1/31/2024 1:53:52 PM HV 20.0 kV Spot 3.0 WD 10.1 mm Mag 700x Det ETD 50.0µm

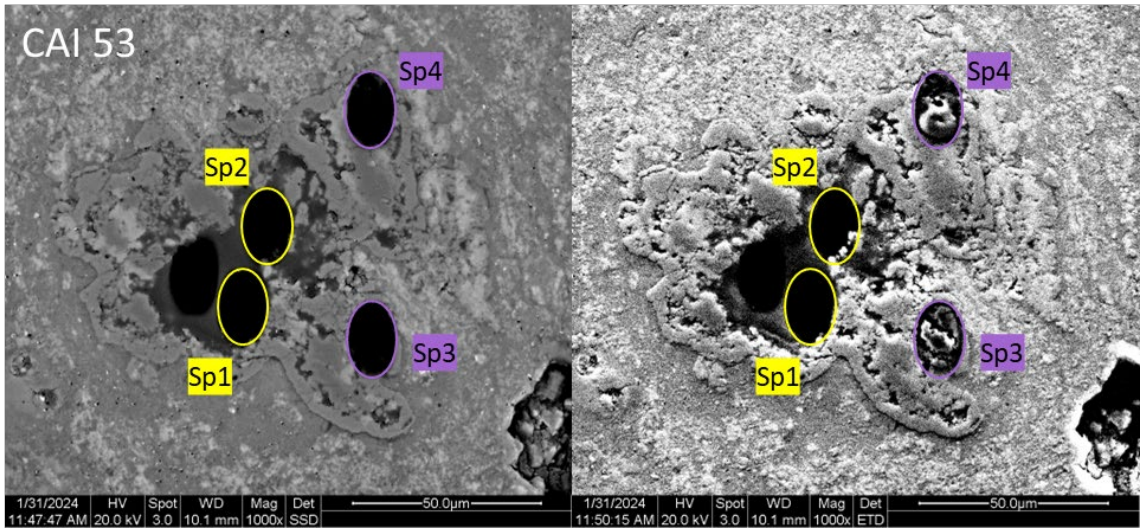
CAI 53
Sp4
Sp2
Sp1
Sp3
Sp4
Sp2
Sp1
Sp3
1/31/2024 11:47:47 AM HV 20.0 kV Spot 3.0 WD 10.1 mm Mag 1000x Det SSD 50.0µm
1/31/2024 11:50:15 AM HV 20.0 kV Spot 3.0 WD 10.1 mm Mag 1000x Det ETD 50.0µm

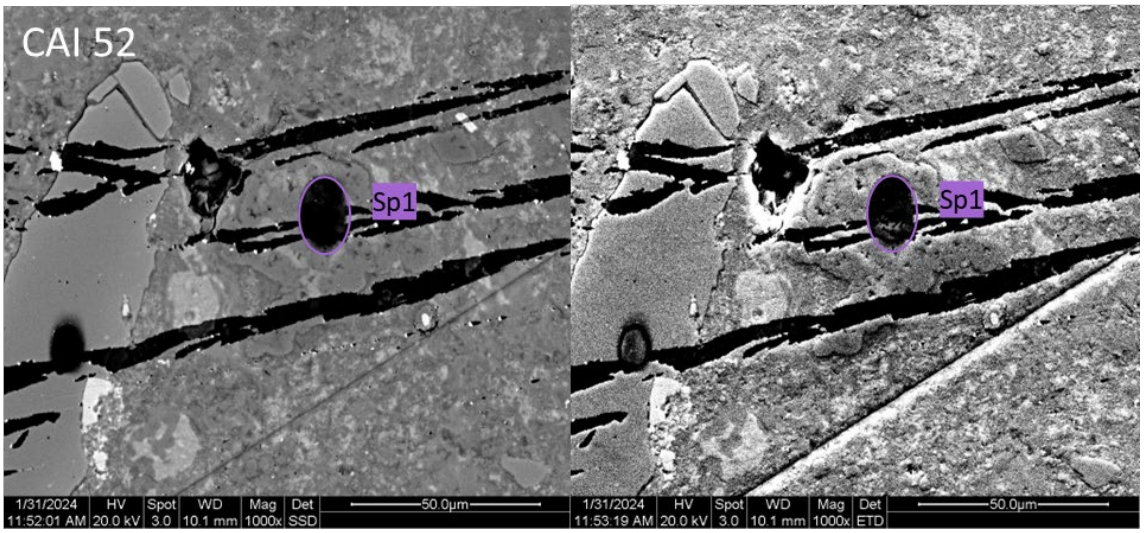
CAI 52
Sp1
Sp1
1/31/2024 11:52:01 AM HV 20.0 kV Spot 3.0 WD 10.1 mm Mag 1000x Det SSD 50.0µm
1/31/2024 11:53:19 AM HV 20.0 kV Spot 3.0 WD 10.1 mm Mag 1000x Det ETD 50.0µm

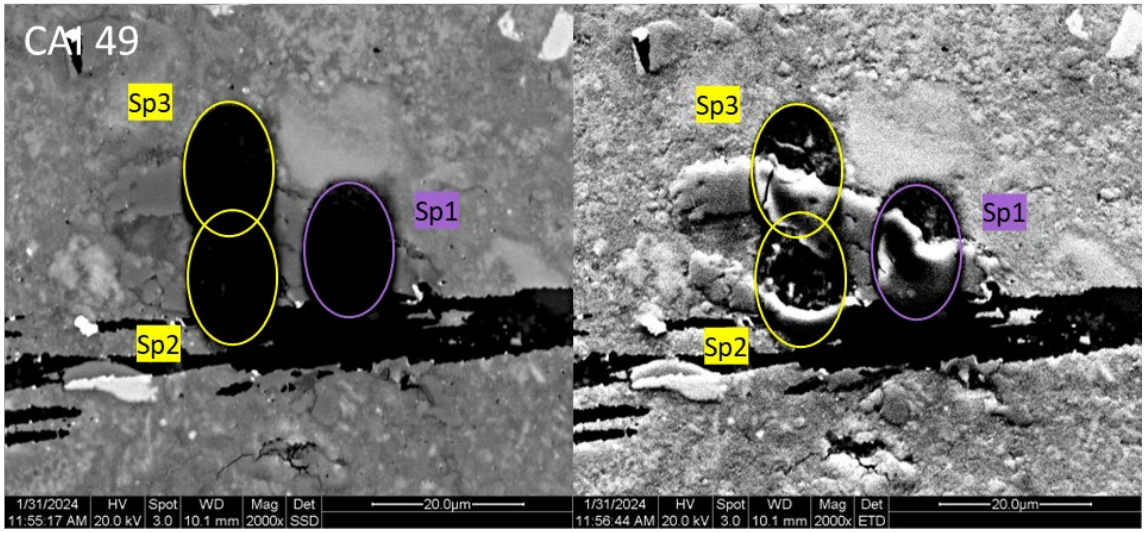
CAI 49
Sp3
Sp1
Sp2
Sp3
Sp1
Sp2
1/31/2024 11:55:17 AM HV 20.0 kV Spot 3.0 WD 10.1 mm Mag 2000x Det SSD 20.0µm
1/31/2024 11:56:44 AM HV 20.0 kV Spot 3.0 WD 10.1 mm Mag 2000x Det ETD 20.0µm

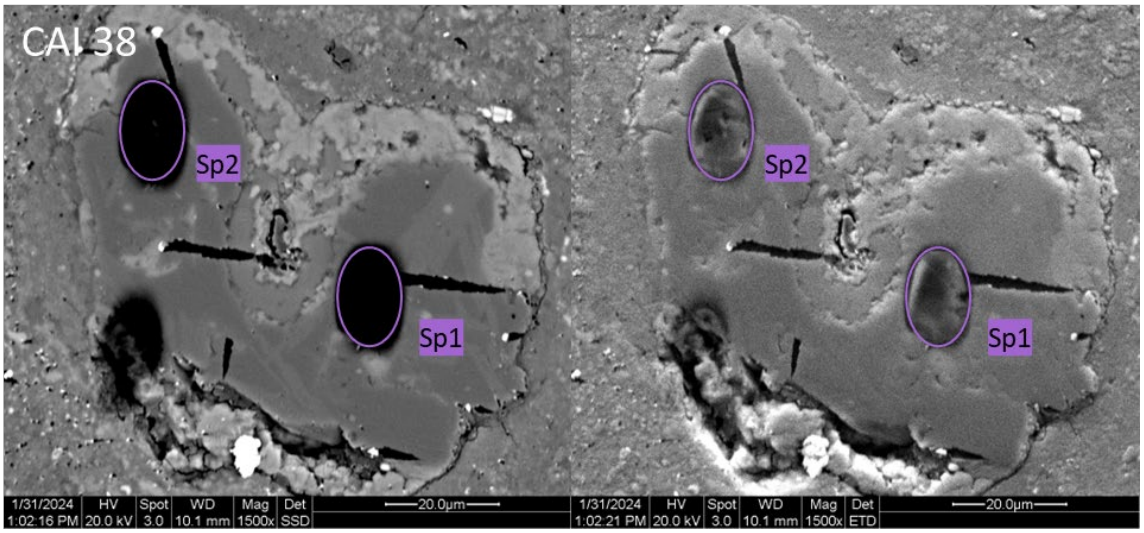
CAI 38
Sp2
Sp1
Sp2
Sp1
1/31/2024 1:02:16 PM HV 20.0 kV Spot 3.0 WD 10.1 mm Mag 1500x Det SSD 20.0µm
1/31/2024 1:02:21 PM HV 20.0 kV Spot 3.0 WD 10.1 mm Mag 1500x Det ETD 20.0µm

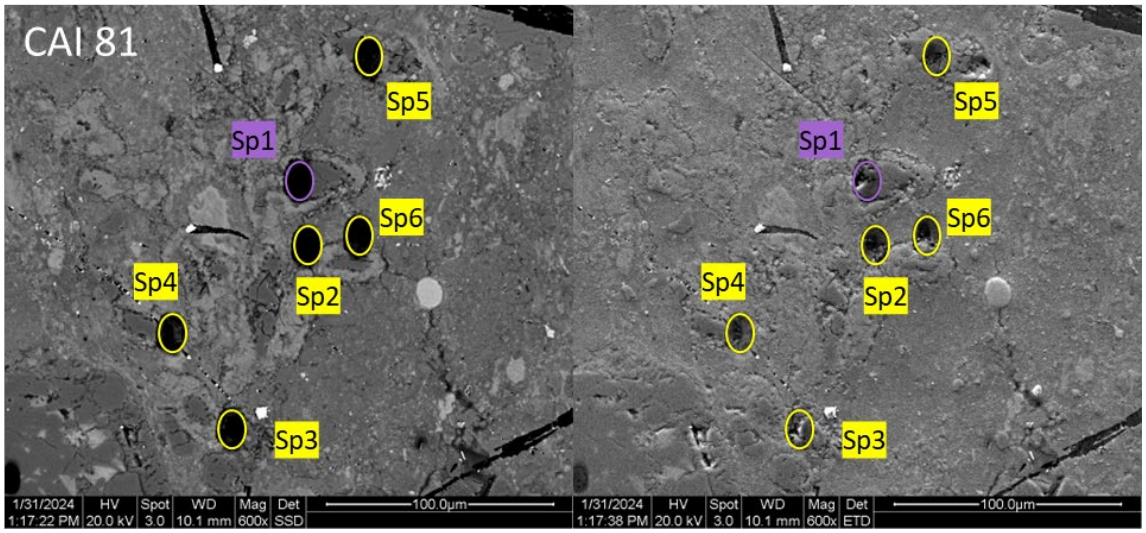
CAI 81
Sp1
Sp2
Sp3
Sp4
Sp5
Sp6
1/31/2024 1:17:22 PM HV 20.0 kV Spot 3.0 WD 10.1 mm Mag 600x Det SSD 100.0µm
1/31/2024 1:17:38 PM HV 20.0 kV Spot 3.0 WD 10.1 mm Mag 600x Det ETD 100.0µm

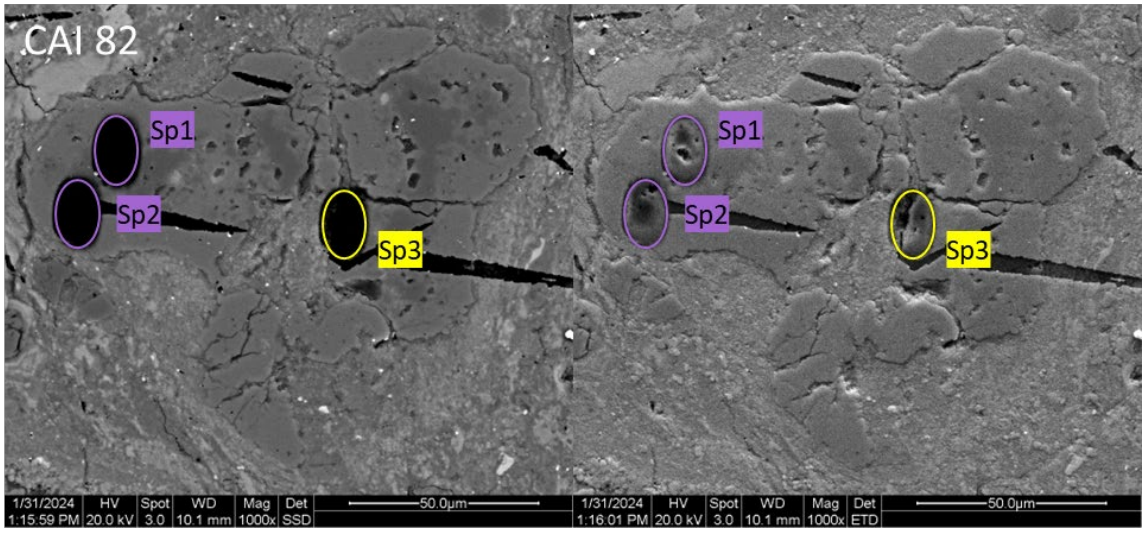
CAI 82
Sp1
Sp2
Sp3
1/31/2024 1:15:59 PM HV 20.0 kV Spot 3.0 WD 10.1 mm Mag 1000x Det SSD 50.0µm
1/31/2024 1:16:01 PM HV 20.0 kV Spot 3.0 WD 10.1 mm Mag 1000x Det ETD 50.0µm

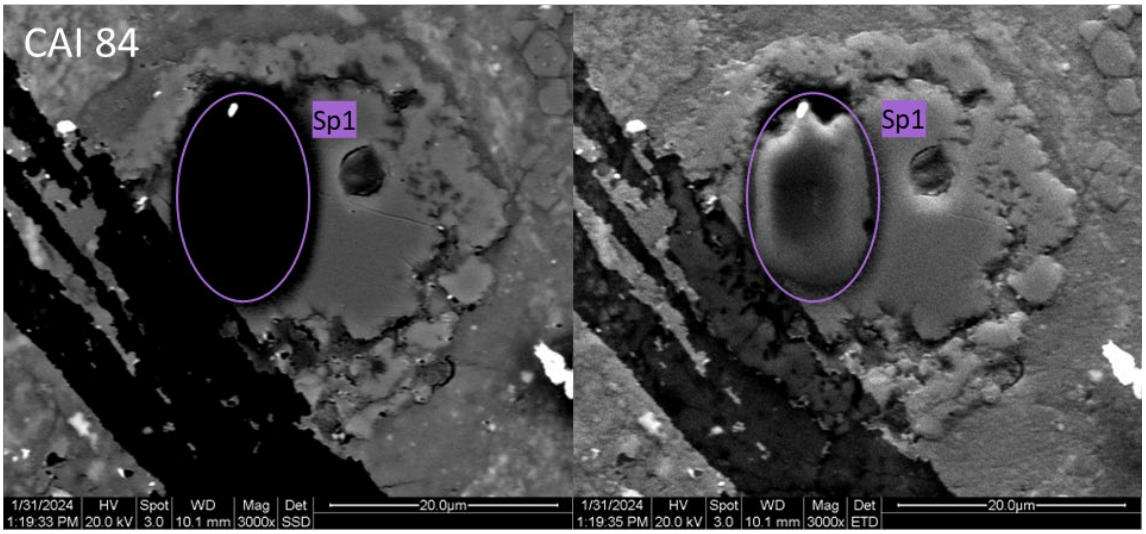
CAI 84
Sp1
1/31/2024 1:19:33 PM HV 20.0 kV Spot 3.0 WD 10.1 mm Mag 3000x Det SSD 20.0µm
1/31/2024 1:19:35 PM HV 20.0 kV Spot 3.0 WD 10.1 mm Mag 3000x Det ETD 20.0µm

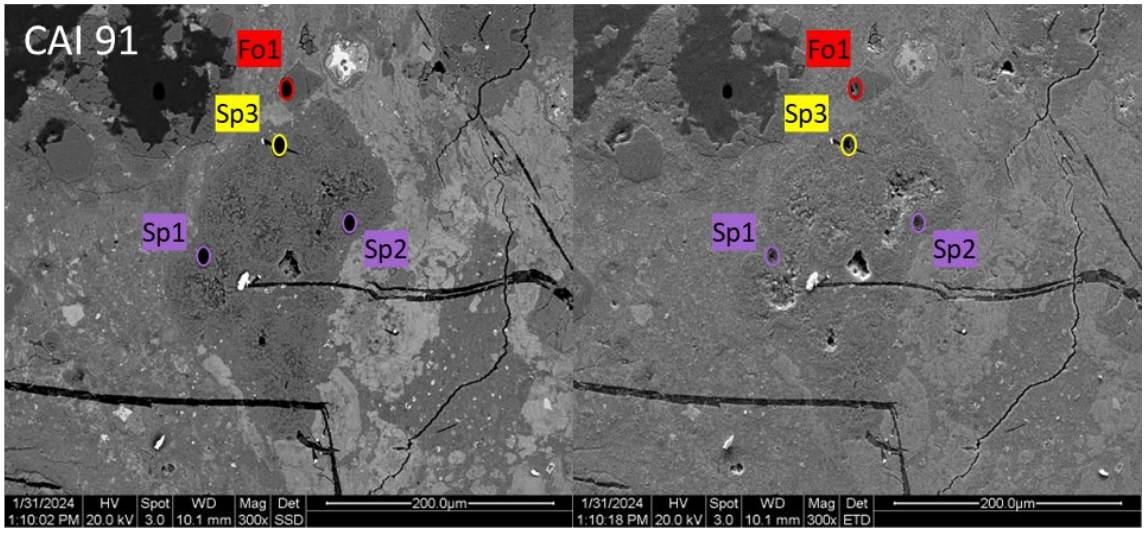
CAI 91
Fo1
Sp3
Sp1
Sp2
1/31/2024 1:10:02 PM HV 20.0 kV Spot 3.0 WD 10.1 mm Mag 300x Det SSD 200.0µm
1/31/2024 1:10:18 PM HV 20.0 kV Spot 3.0 WD 10.1 mm Mag 300x Det ETD 200.0µm

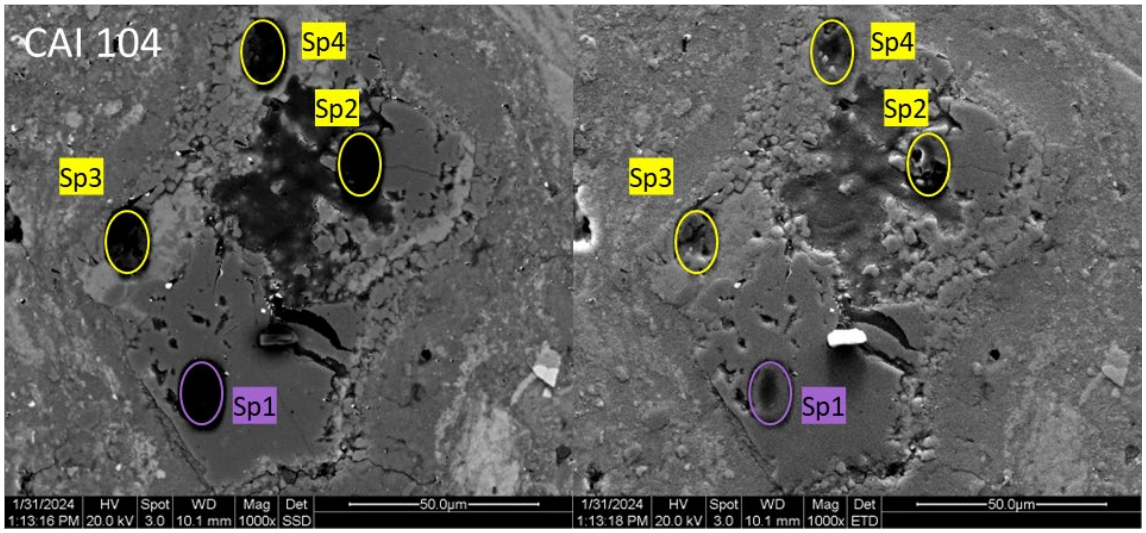
CAI 104
Sp4
Sp2
Sp3
Sp1
1/31/2024 1:13:16 PM HV 20.0 kV Spot 3.0 WD 10.1 mm Mag 1000x Det SSD 50.0µm
1/31/2024 1:13:18 PM HV 20.0 kV Spot 3.0 WD 10.1 mm Mag 1000x Det ETD 50.0µm

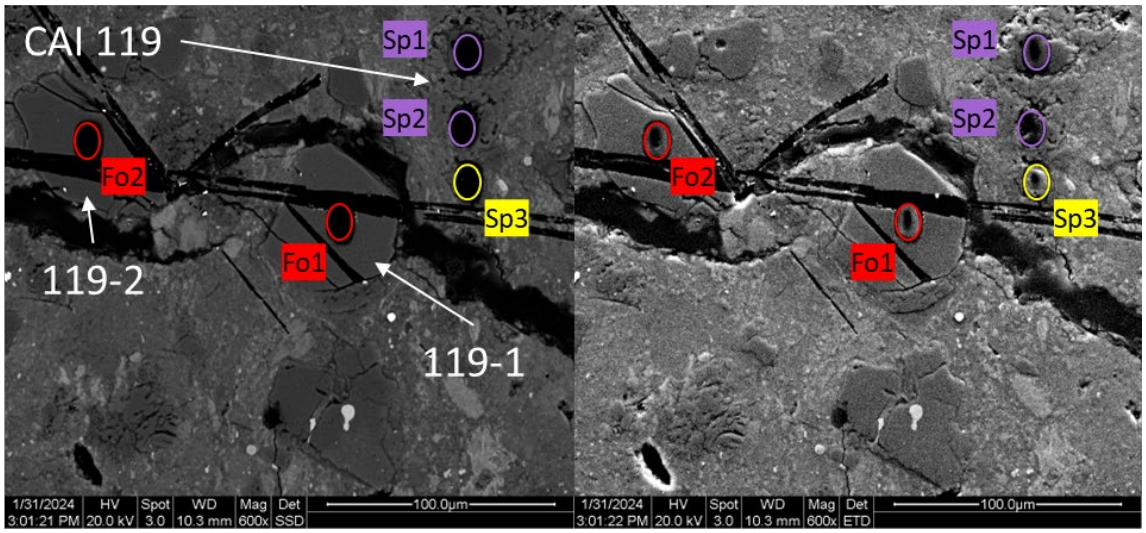
CAI 119
Sp1
Sp2
Fo2
Sp3
Fo1
119-2
119-1
1/31/2024 3:01:21 PM HV 20.0 kV Spot 3.0 WD 10.3 mm Mag 600x Det SSD 100.0µm
1/31/2024 3:01:22 PM HV 20.0 kV Spot 3.0 WD 10.3 mm Mag 600x Det ETD 100.0µm

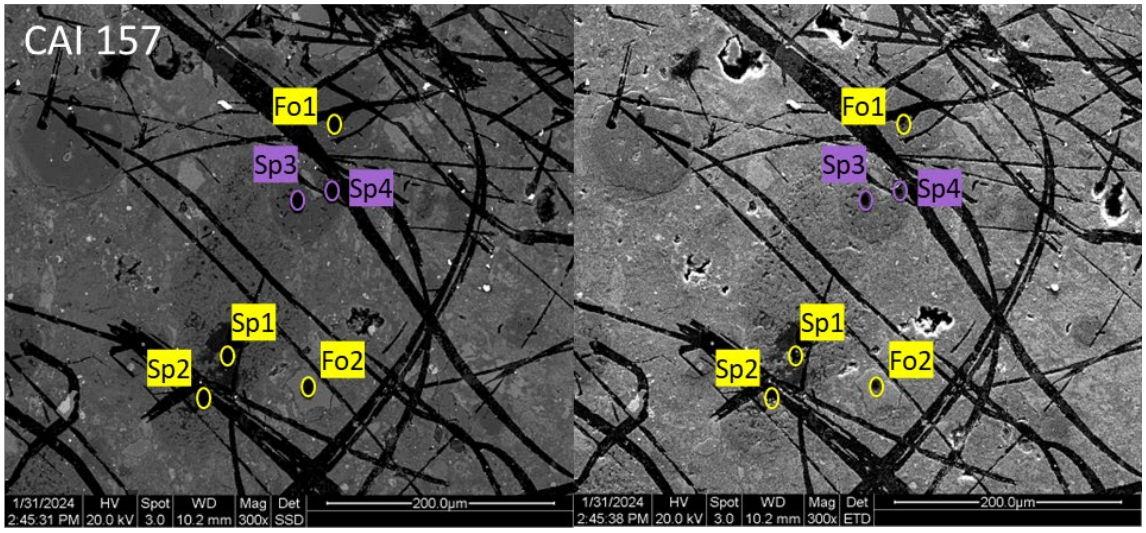
CAI 157
Fo1
Sp3
Sp4
Sp1
Sp2
Fo2
1/31/2024 2:45.31 PM HV 20.0 kV Spot 3.0 WD 10.2 mm Mag 300x Det SSD 200.0µm
1/31/2024 2:45.38 PM HV 20.0 kV Spot 3.0 WD 10.2 mm Mag 300x Det ETD 200.0µm

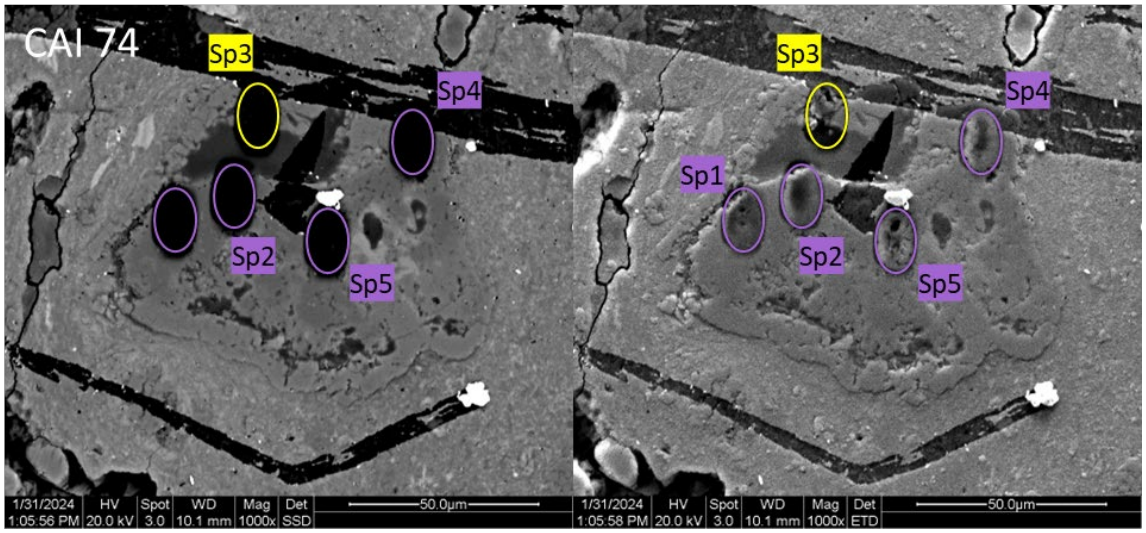
CAI 74
Sp3
Sp4
Sp2
Sp5
Sp1
1/31/2024 1:05.56 PM HV 20.0 kV Spot 3.0 WD 10.1 mm Mag 1000x Det SSD 50.0µm
1/31/2024 1:05.58 PM HV 20.0 kV Spot 3.0 WD 10.1 mm Mag 1000x Det ETD 50.0µm

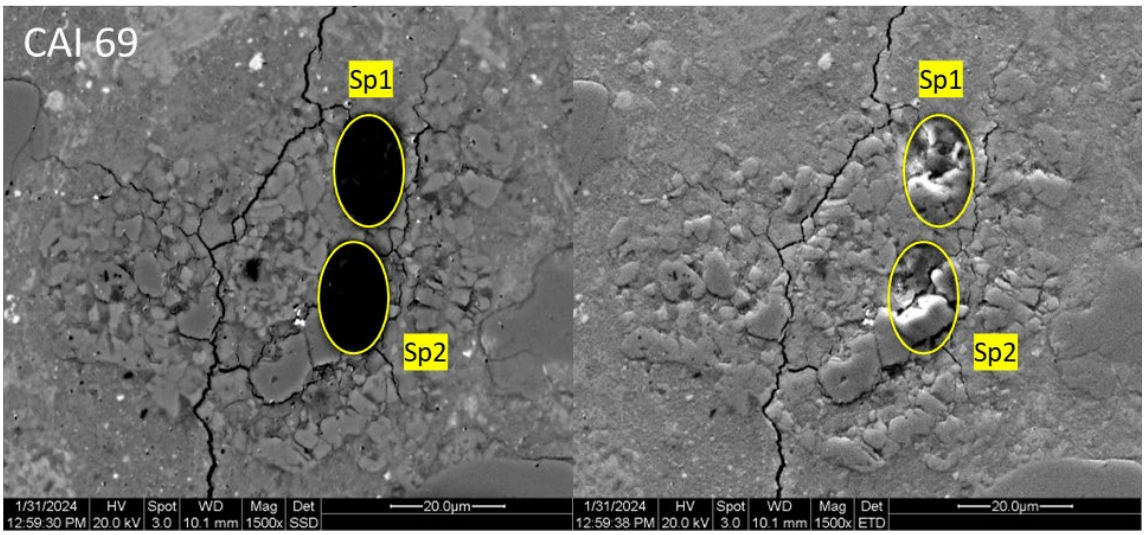
CAI 69
Sp1
Sp2
1/31/2024 12:59.30 PM HV 20.0 kV Spot 3.0 WD 10.1 mm Mag 1500x Det SSD 20.0µm
1/31/2024 12:59.38 PM HV 20.0 kV Spot 3.0 WD 10.1 mm Mag 1500x Det ETD 20.0µm

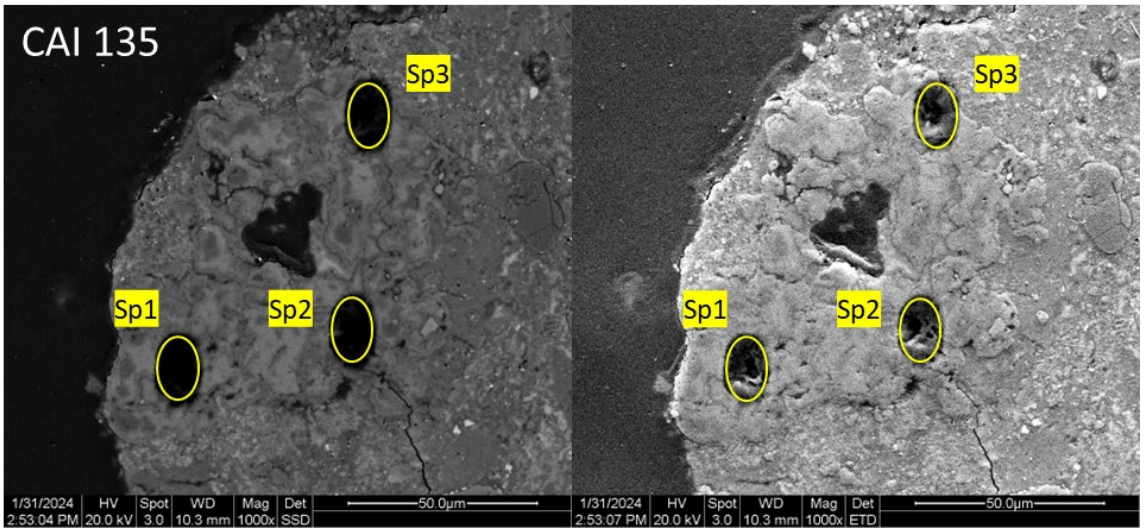
CAI 135
Sp3
Sp1
Sp2
Sp3
Sp1
Sp2
1/31/2024 2:53:04 PM HV 20.0 kV Spot 3.0 WD 10.3 mm Mag 1000x Det SSD 50.0µm
1/31/2024 2:53:07 PM HV 20.0 kV Spot 3.0 WD 10.3 mm Mag 1000x Det ETD 50.0µm

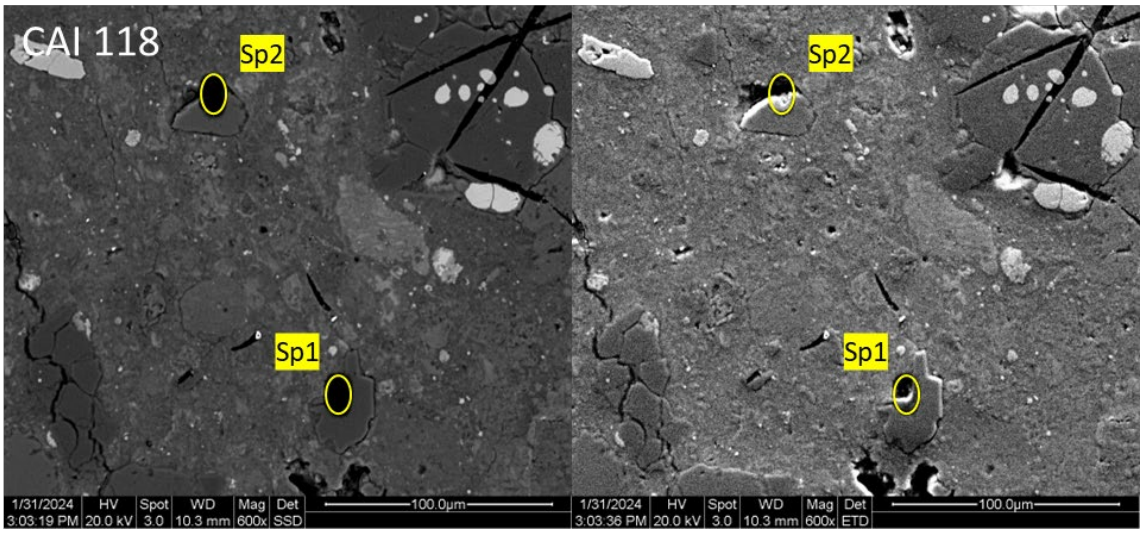
CAI 118
Sp2
Sp1
Sp2
Sp1
1/31/2024 3:03:19 PM HV 20.0 kV Spot 3.0 WD 10.3 mm Mag 600x Det SSD 100.0µm
1/31/2024 3:03:36 PM HV 20.0 kV Spot 3.0 WD 10.3 mm Mag 600x Det ETD 100.0µm

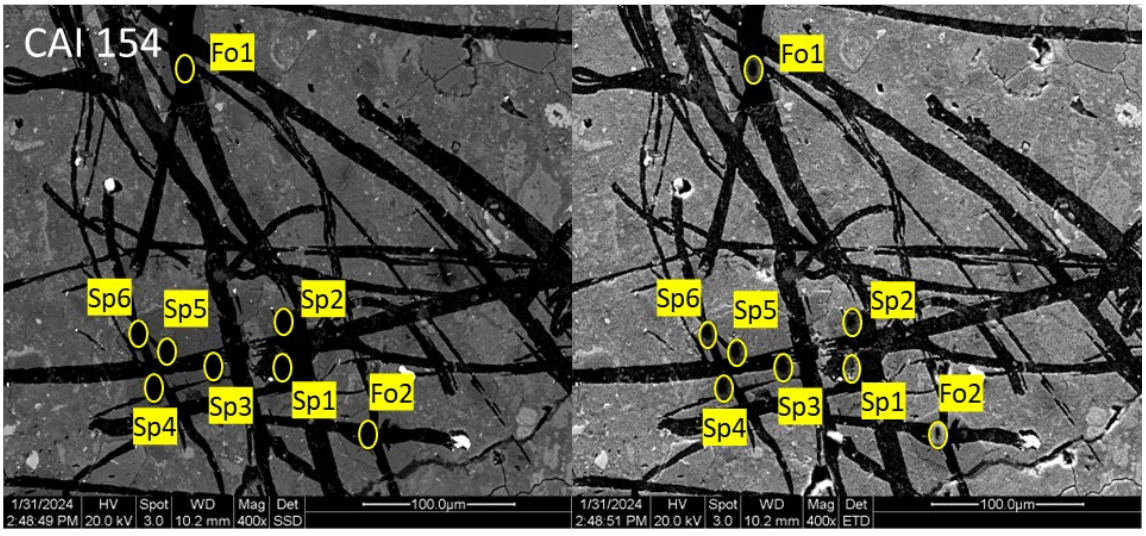
CAI 154
Fo1
Sp6
Sp5
Sp2
Sp4
Sp3
Sp1
Fo2
Fo1
Sp6
Sp5
Sp2
Sp4
Sp3
Sp1
Fo2
1/31/2024 2:48:49 PM HV 20.0 kV Spot 3.0 WD 10.2 mm Mag 400x Det SSD 100.0µm
1/31/2024 2:48:51 PM HV 20.0 kV Spot 3.0 WD 10.2 mm Mag 400x Det ETD 100.0µm

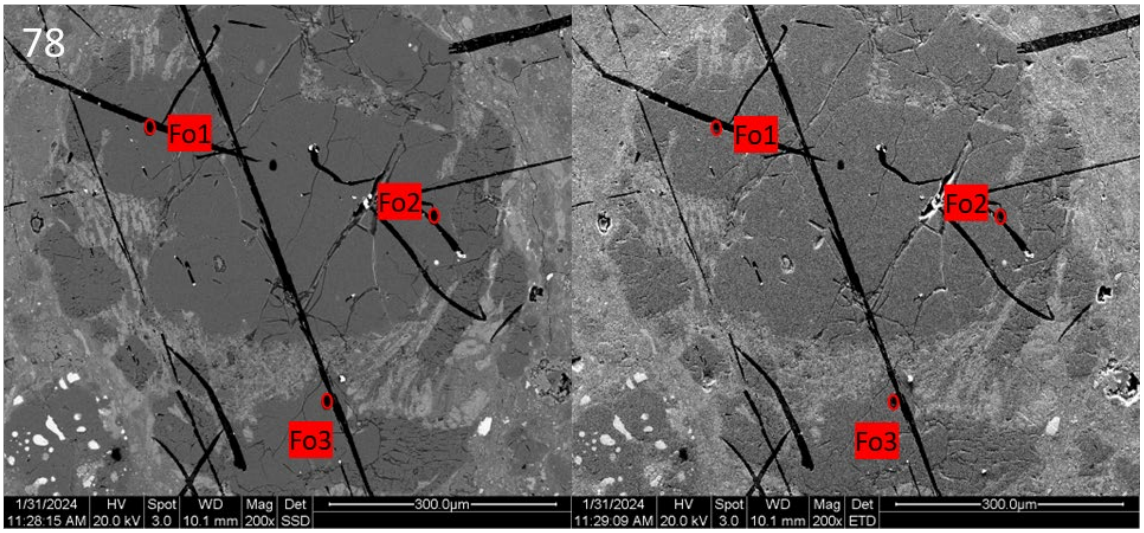
78
Fo1
Fo2
Fo3
1/31/2024 11:28:15 AM HV 20.0 kV Spot 3.0 WD 10.1 mm Mag 200x Det SSD 300.0µm
Fo1
Fo2
Fo3
1/31/2024 11:29:09 AM HV 20.0 kV Spot 3.0 WD 10.1 mm Mag 200x Det ETD 300.0µm

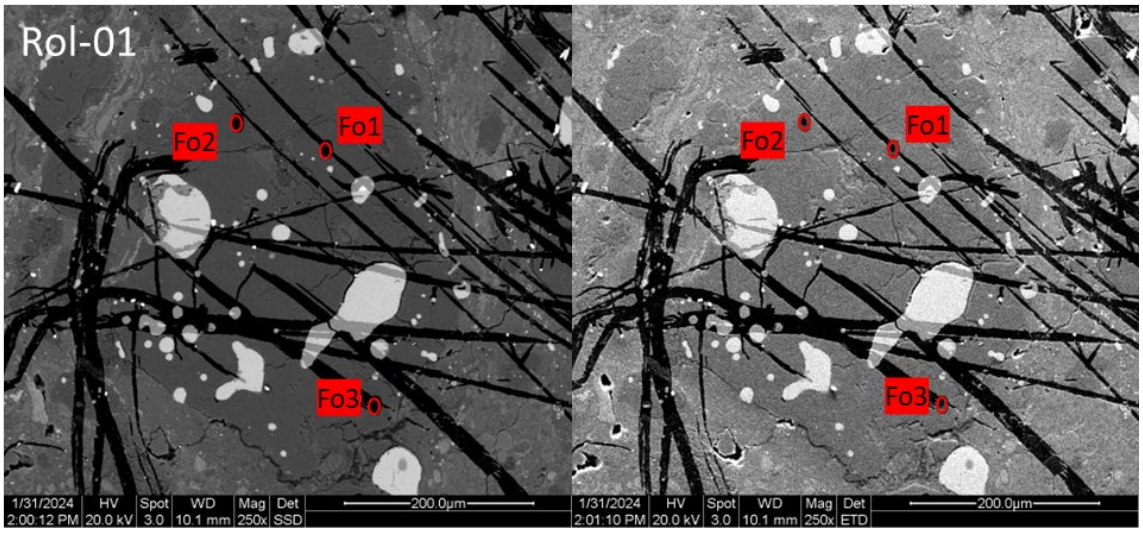
Rol-01
Fo2
Fo1
Fo3
1/31/2024 2:00:12 PM HV 20.0 kV Spot 3.0 WD 10.1 mm Mag 250x Det SSD 200.0µm
Fo2
Fo1
Fo3
1/31/2024 2:01:10 PM HV 20.0 kV Spot 3.0 WD 10.1 mm Mag 250x Det ETD 200.0µm

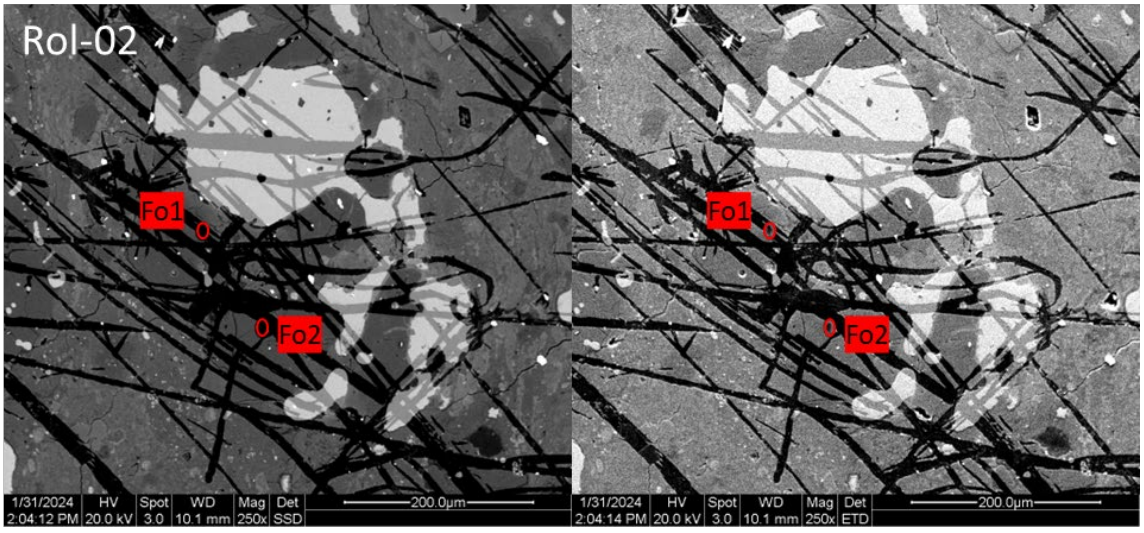
Rol-02
Fo1
Fo2
1/31/2024 2:04:12 PM HV 20.0 kV Spot 3.0 WD 10.1 mm Mag 250x Det SSD 200.0µm
Fo1
Fo2
1/31/2024 2:04:14 PM HV 20.0 kV Spot 3.0 WD 10.1 mm Mag 250x Det ETD 200.0µm

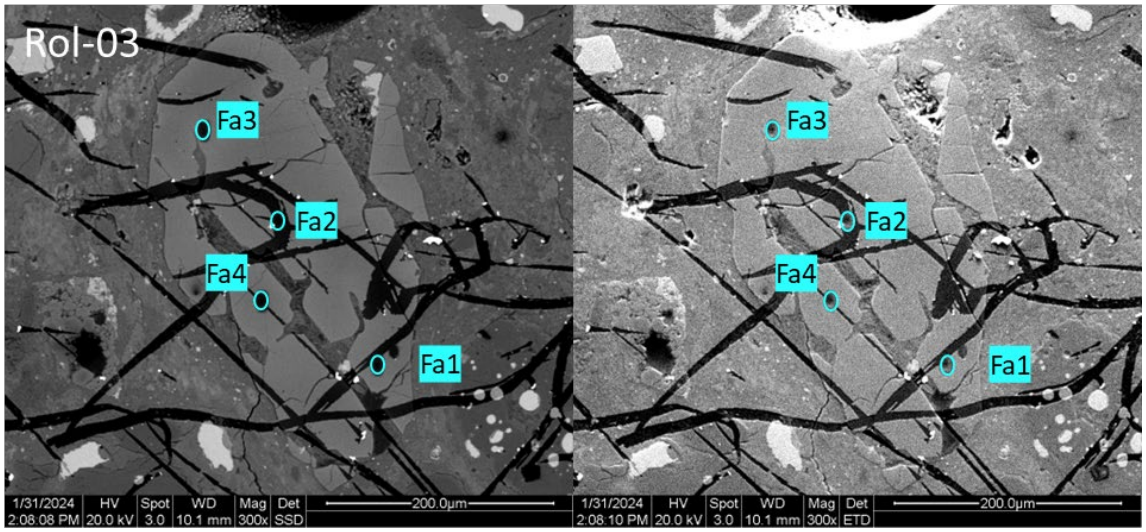
Rol-03
Fa3
Fa2
Fa4
Fa1
1/31/2024 2:08:08 PM HV 20.0 kV Spot 3.0 WD 10.1 mm Mag 300x Det SSD 200.0µm
Fa3
Fa2
Fa4
Fa1
1/31/2024 2:08:10 PM HV 20.0 kV Spot 3.0 WD 10.1 mm Mag 300x Det ETD 200.0µm

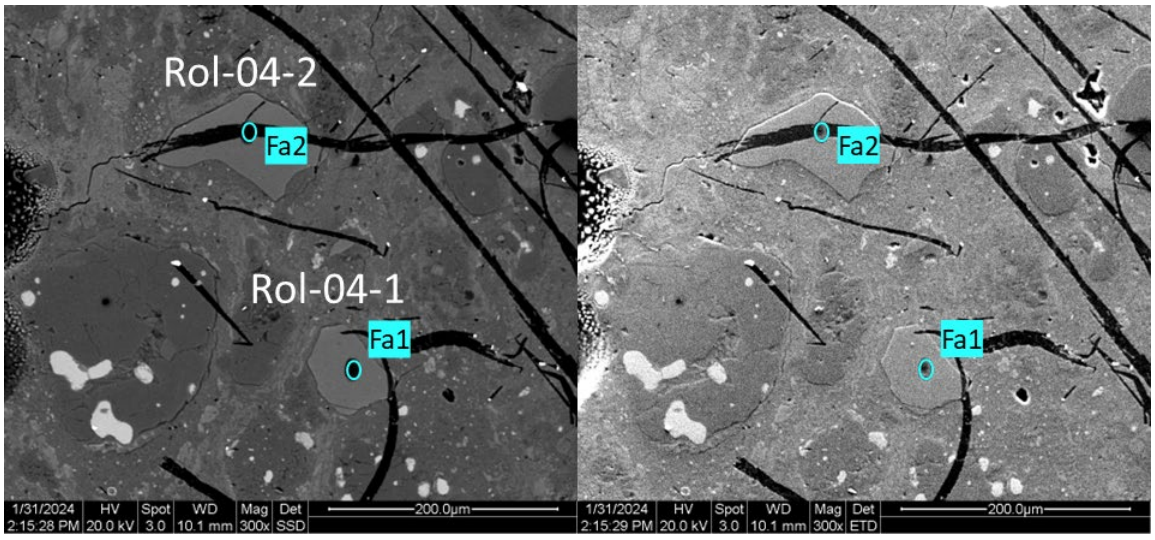
Rol-04-2
Fa2
Rol-04-1
Fa1
1/31/2024 2:15:28 PM HV 20.0 kV Spot 3.0 WD 10.1 mm Mag 300x Det SSD 200.0µm
Fa2
Fa1
1/31/2024 2:15:29 PM HV 20.0 kV Spot 3.0 WD 10.1 mm Mag 300x Det ETD 200.0µm

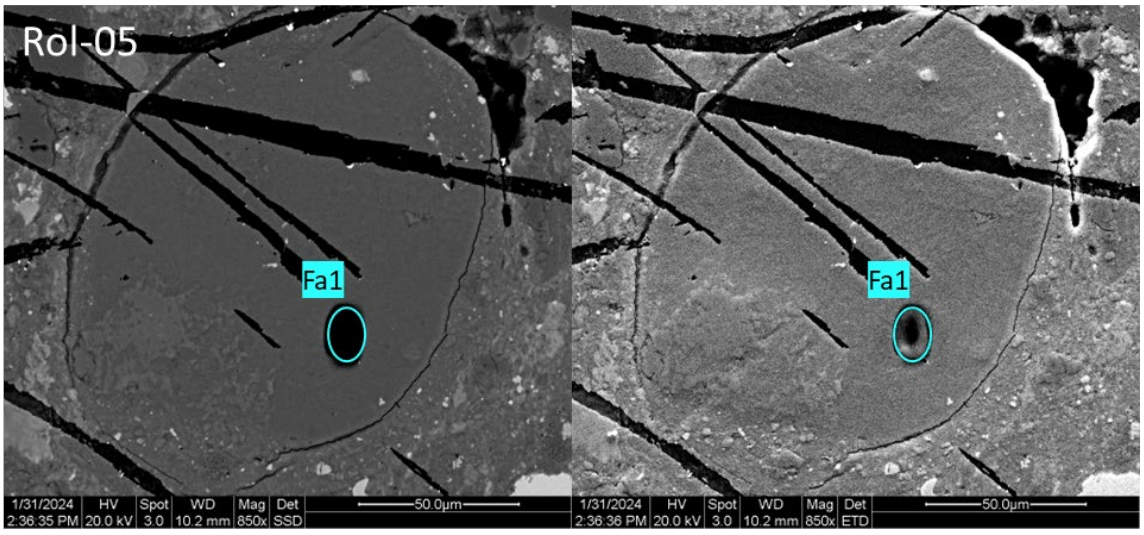
Rol-05
Fa1
1/31/2024 2:36:35 PM HV 20.0 kV Spot 3.0 WD 10.2 mm Mag 850x Det SSD 50.0µm
Fa1
1/31/2024 2:36:36 PM HV 20.0 kV Spot 3.0 WD 10.2 mm Mag 850x Det ETD 50.0µm

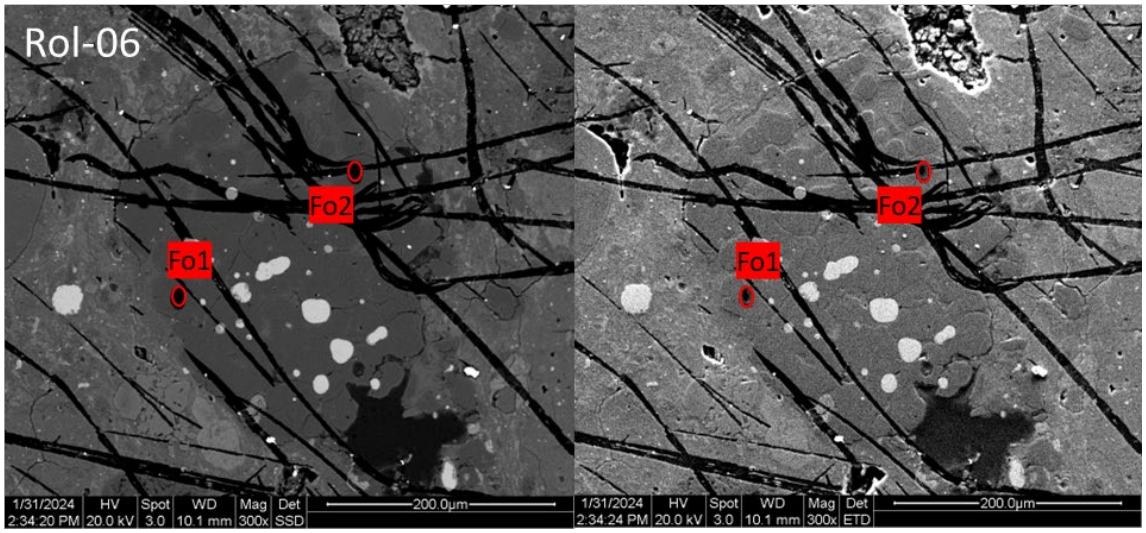
Rol-06
Fo2
Fo1
1/31/2024 2:34:20 PM HV 20.0 kV Spot 3.0 WD 10.1 mm Mag 300x Det SSD 200.0µm
Fo2
Fo1
1/31/2024 2:34:24 PM HV 20.0 kV Spot 3.0 WD 10.1 mm Mag 300x Det ETD 200.0µm

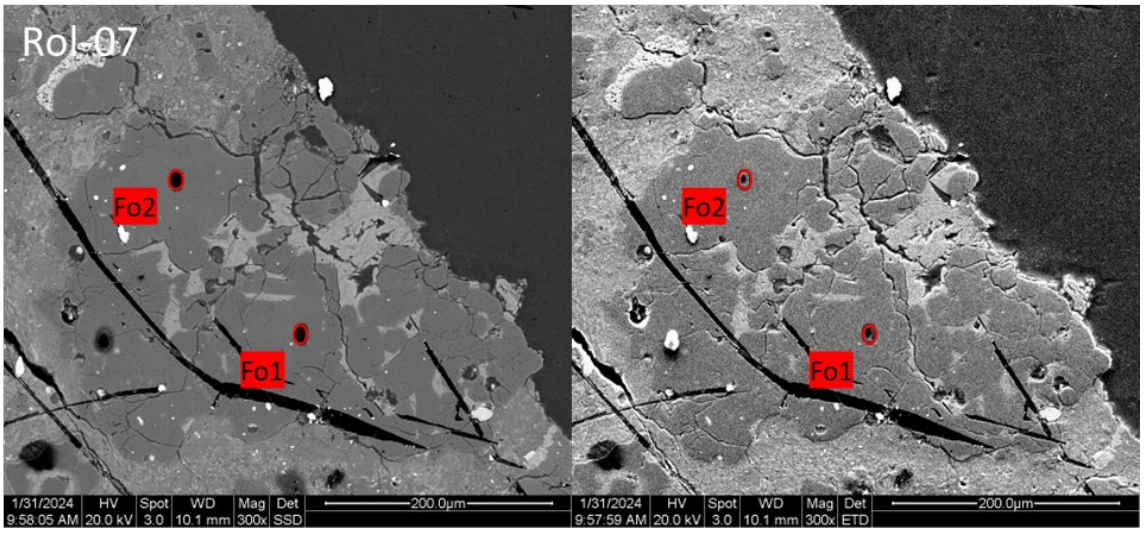
Rol-07
Fo2
Fo1
1/31/2024 9:58:05 AM HV 20.0 kV Spot 3.0 WD 10.1 mm Mag 300x Det SSD 200.0µm
Fo2
Fo1
1/31/2024 9:57:59 AM HV 20.0 kV Spot 3.0 WD 10.1 mm Mag 300x Det ETD 200.0µm

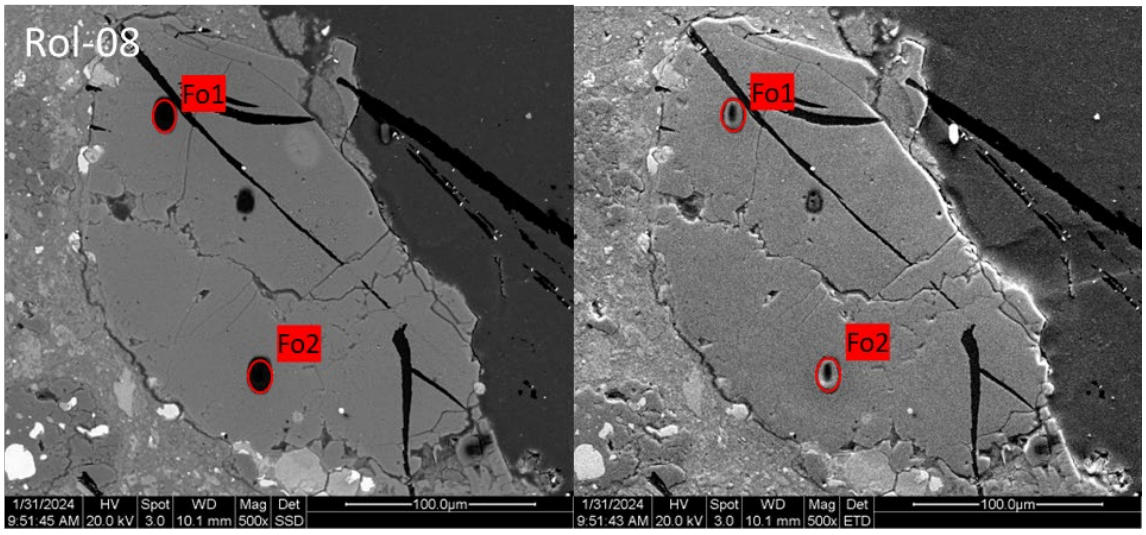
Rol-08
Fo1
Fo2
1/31/2024 9:51:45 AM HV 20.0 kV Spot 3.0 WD 10.1 mm Mag 500x Det SSD 100.0µm
Fo1
Fo2
1/31/2024 9:51:43 AM HV 20.0 kV Spot 3.0 WD 10.1 mm Mag 500x Det ETD 100.0µm

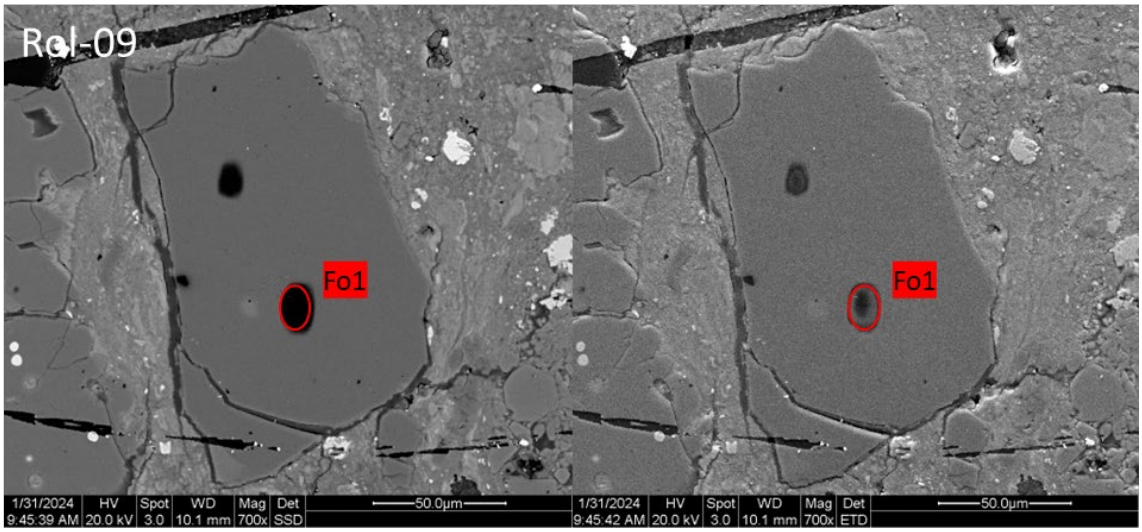
Rol-09
Fo1
Fo1
1/31/2024 9:45:39 AM HV 20.0 kV Spot 3.0 WD 10.1 mm Mag 700x Det SSD 50.0µm
1/31/2024 9:45:42 AM HV 20.0 kV Spot 3.0 WD 10.1 mm Mag 700x Det ETD 50.0µm

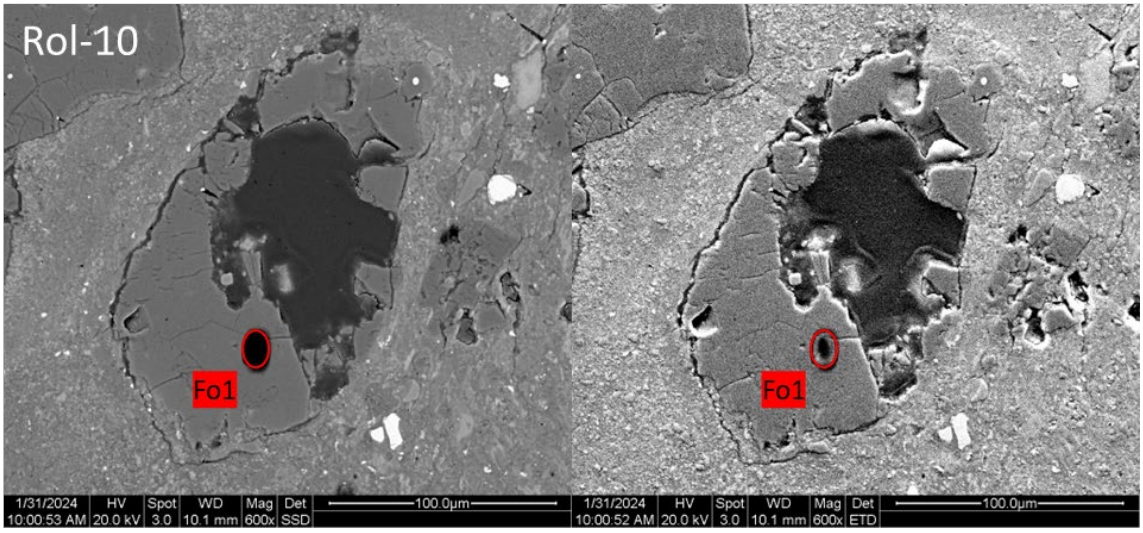
Rol-10
Fo1
Fo1
1/31/2024 10:00:53 AM HV 20.0 kV Spot 3.0 WD 10.1 mm Mag 600x Det SSD 100.0µm
1/31/2024 10:00:52 AM HV 20.0 kV Spot 3.0 WD 10.1 mm Mag 600x Det ETD 100.0µm

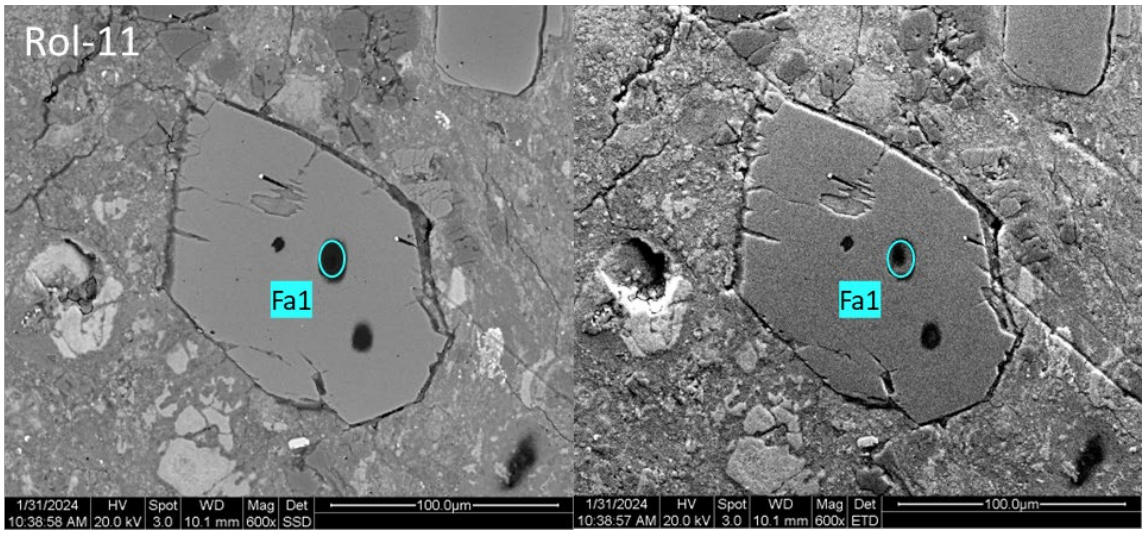
Rol-11
Fa1
Fa1
1/31/2024 10:38:58 AM HV 20.0 kV Spot 3.0 WD 10.1 mm Mag 600x Det SSD 100.0µm
1/31/2024 10:38:57 AM HV 20.0 kV Spot 3.0 WD 10.1 mm Mag 600x Det ETD 100.0µm

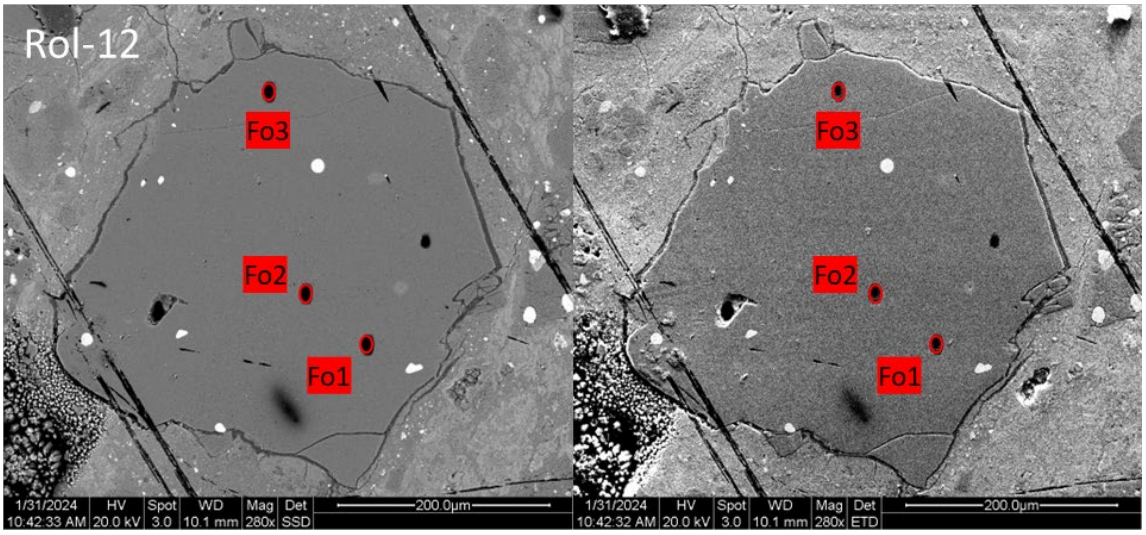
Rol-12
Fo3
Fo2
Fo1
1/31/2024 10:42:33 AM
HV 20.0 kV
Spot 3.0
WD 10.1 mm
Mag 280x
Det SSD
200.0µm
Fo3
Fo2
Fo1
1/31/2024 10:42:32 AM
HV 20.0 kV
Spot 3.0
WD 10.1 mm
Mag 280x
Det ETD
200.0µm

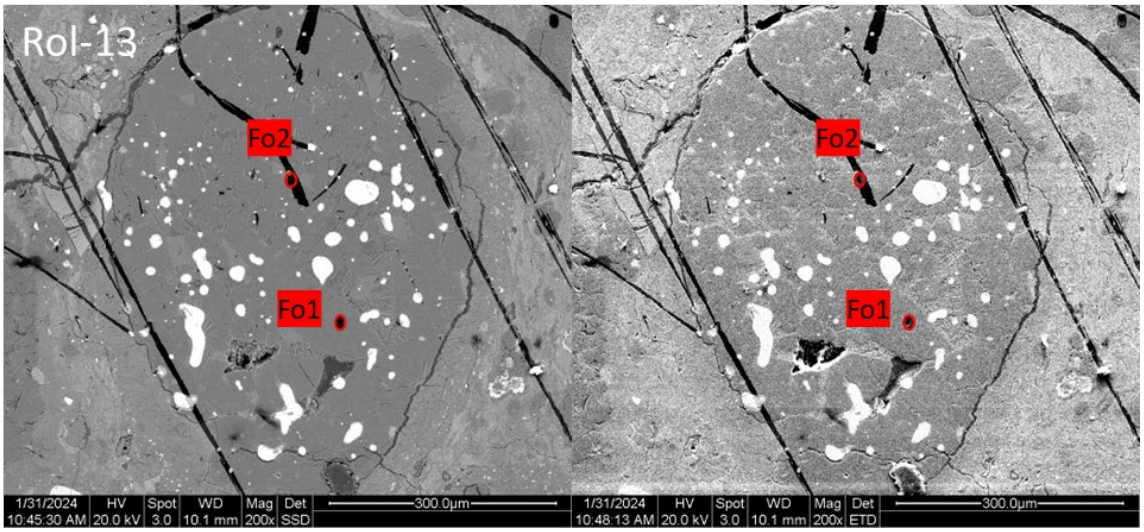
Rol-13
Fo2
Fo1
1/31/2024 10:45:30 AM
HV 20.0 kV
Spot 3.0
WD 10.1 mm
Mag 200x
Det SSD
300.0µm
Fo2
Fo1
1/31/2024 10:48:13 AM
HV 20.0 kV
Spot 3.0
WD 10.1 mm
Mag 200x
Det ETD
300.0µm

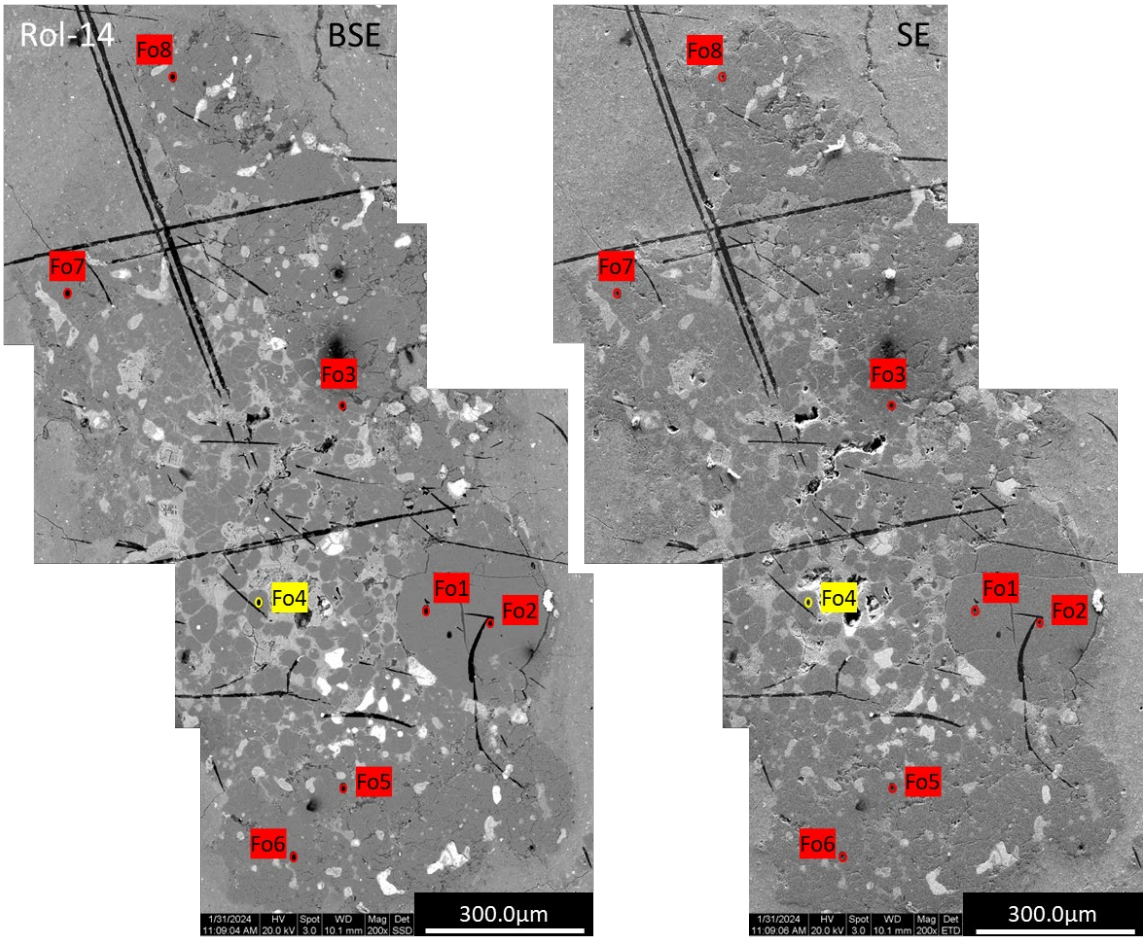
Rol-14
BSE
Fo8
Fo7
Fo3
Fo4
Fo1
Fo2
Fo5
Fo6
300.0µm
SE
Fo8
Fo7
Fo3
Fo4
Fo1
Fo2
Fo5
Fo6
300.0µm

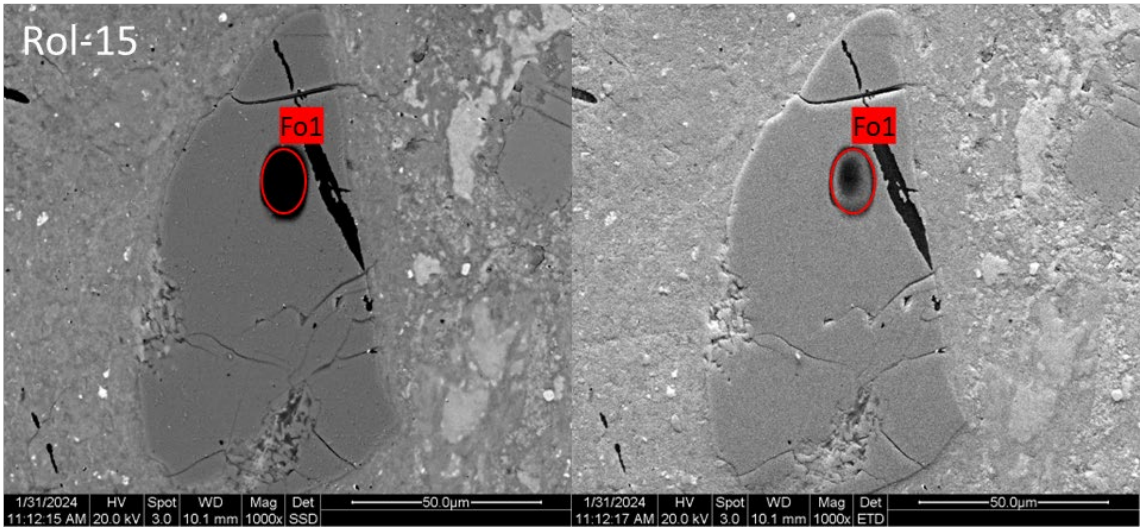
Rol-15
Fo1
50.0µm
Fo1
50.0µm

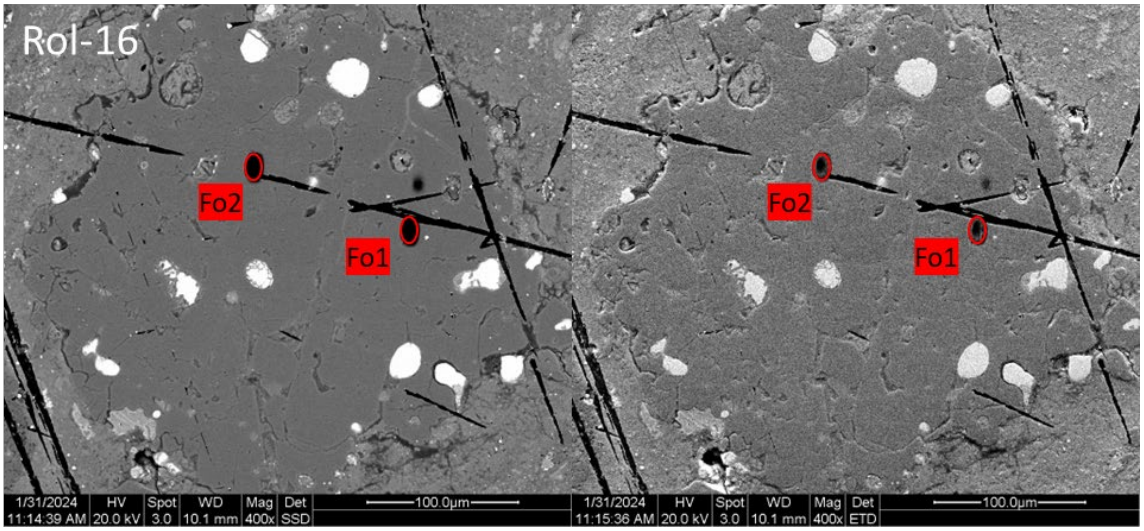
Rol-16
Fo2
Fo1
Fo2
Fo1
1/31/2024 11:14:39 AM HV 20.0 kV Spot 3.0 WD 10.1 mm Mag 400x Det SSD 100.0µm
1/31/2024 11:15:36 AM HV 20.0 kV Spot 3.0 WD 10.1 mm Mag 400x Det ETD 100.0µm

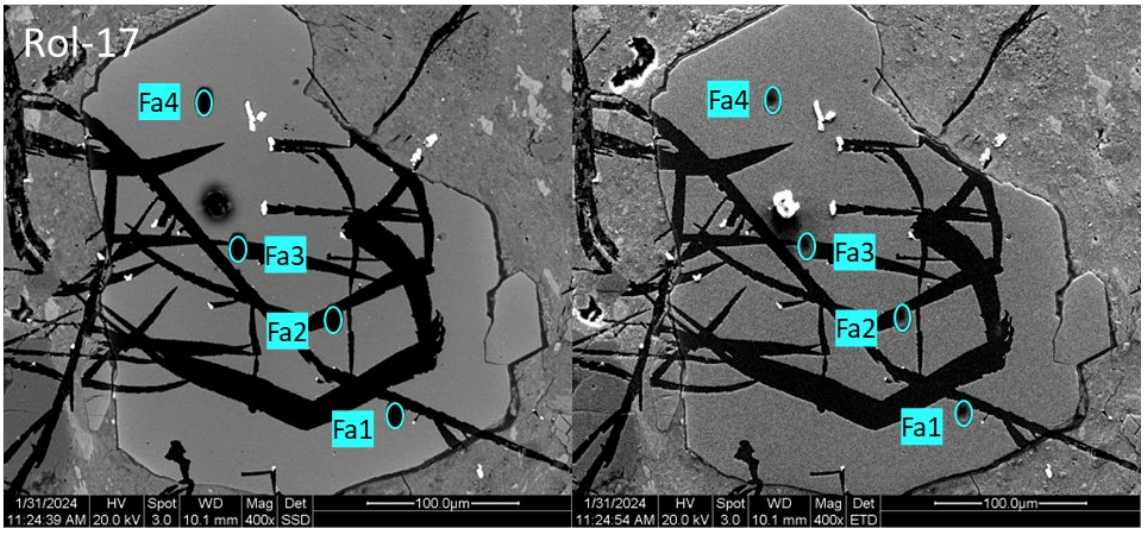
Rol-17
Fa4
Fa3
Fa2
Fa1
Fa4
Fa3
Fa2
Fa1
1/31/2024 11:24:39 AM HV 20.0 kV Spot 3.0 WD 10.1 mm Mag 400x Det SSD 100.0µm
1/31/2024 11:24:54 AM HV 20.0 kV Spot 3.0 WD 10.1 mm Mag 400x Det ETD 100.0µm

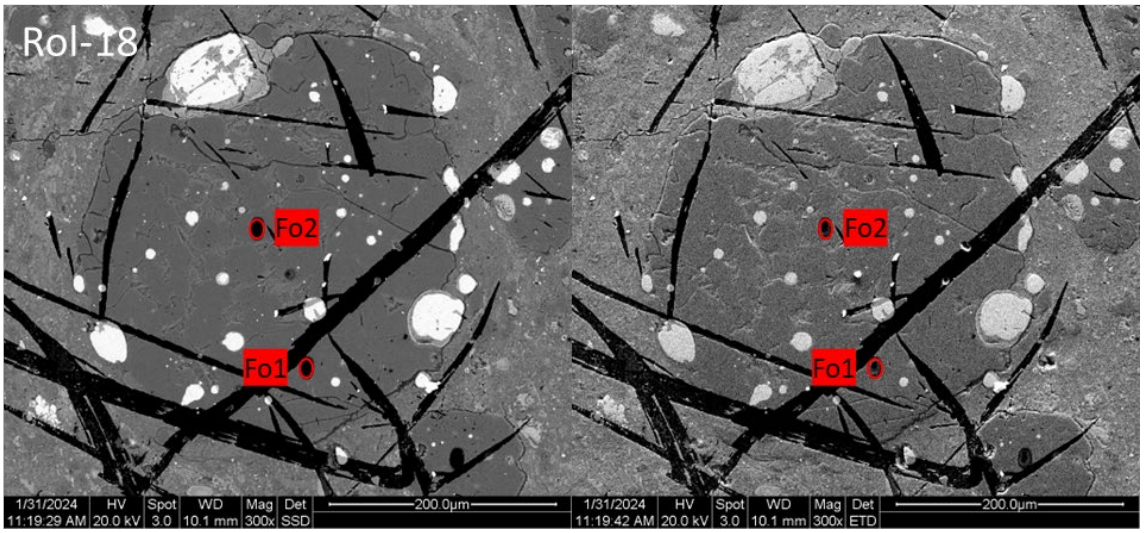
Rol-18
Fo2
Fo1
Fo2
Fo1
1/31/2024 11:19:29 AM HV 20.0 kV Spot 3.0 WD 10.1 mm Mag 300x Det SSD 200.0µm
1/31/2024 11:19:42 AM HV 20.0 kV Spot 3.0 WD 10.1 mm Mag 300x Det ETD 200.0µm

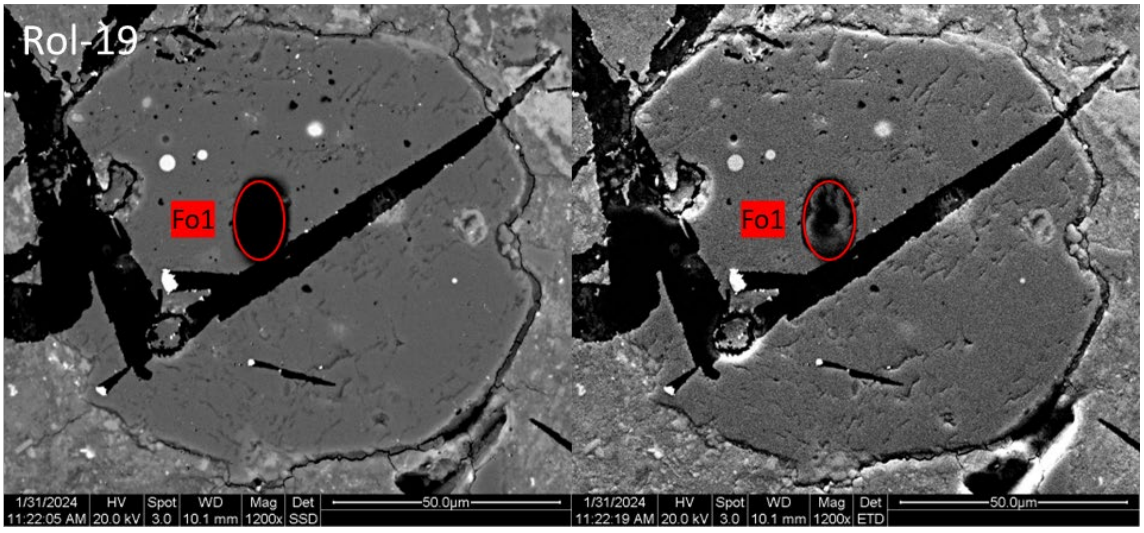
RoI-19
Fo1
Fo1
1/31/2024 11:22:05 AM HV 20.0 kV Spot 3.0 WD 10.1 mm Mag 1200x Det SSD 50.0µm
1/31/2024 11:22:19 AM HV 20.0 kV Spot 3.0 WD 10.1 mm Mag 1200x Det ETD 50.0µm

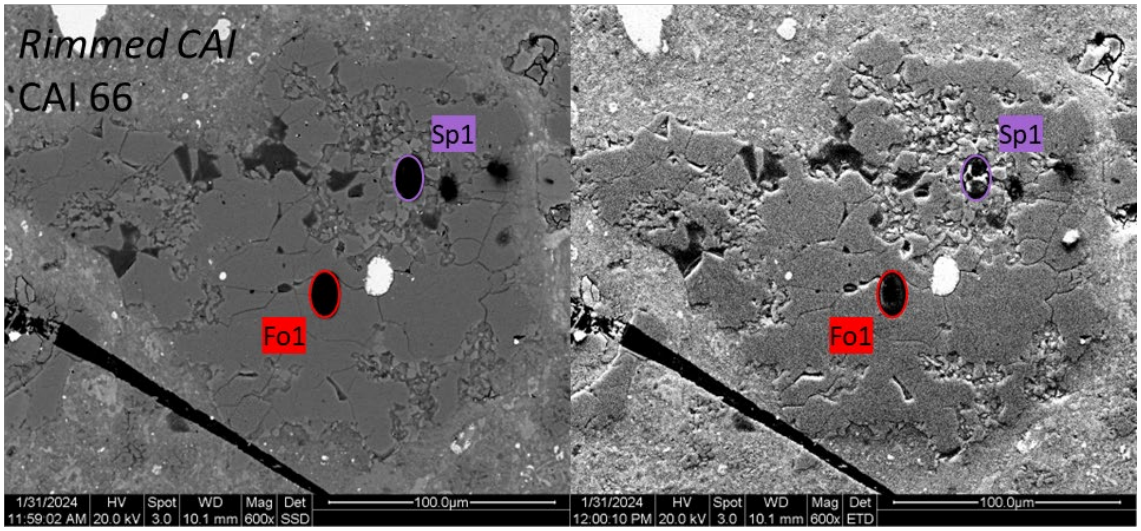
Rimmed CAI
CAI 66
Sp1
Fo1
Sp1
Fo1
1/31/2024 11:59:02 AM HV 20.0 kV Spot 3.0 WD 10.1 mm Mag 600x Det SSD 100.0µm
1/31/2024 12:00:10 PM HV 20.0 kV Spot 3.0 WD 10.1 mm Mag 600x Det ETD 100.0µm

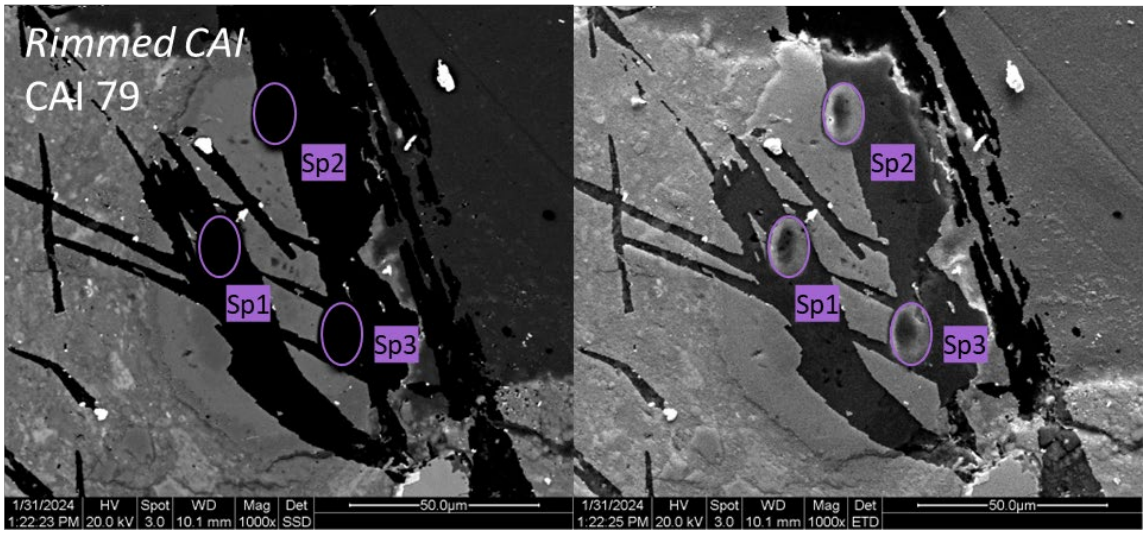
Rimmed CAI
CAI 79
Sp2
Sp1
Sp3
Sp2
Sp1
Sp3
1/31/2024 1:22:23 PM HV 20.0 kV Spot 3.0 WD 10.1 mm Mag 1000x Det SSD 50.0µm
1/31/2024 1:22:25 PM HV 20.0 kV Spot 3.0 WD 10.1 mm Mag 1000x Det ETD 50.0µm

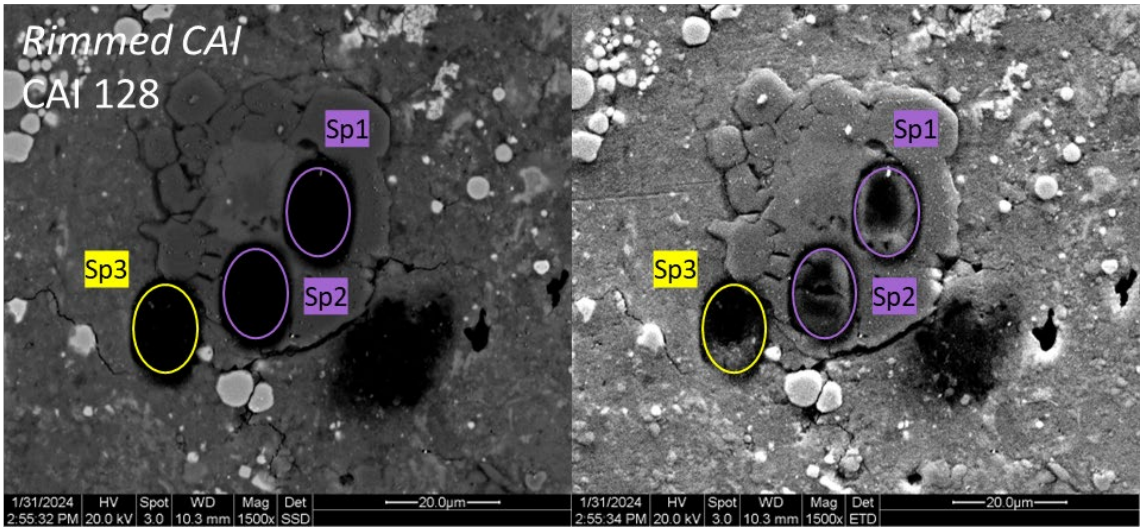
Rimmed CAI
CAI 128
Sp1
Sp3
Sp2
Sp1
Sp3
Sp2
1/31/2024 2:55:32 PM HV 20.0 kV Spot 3.0 WD 10.3 mm Mag 1500x Det SSD 20.0µm
1/31/2024 2:55:34 PM HV 20.0 kV Spot 3.0 WD 10.3 mm Mag 1500x Det ETD 20.0µm

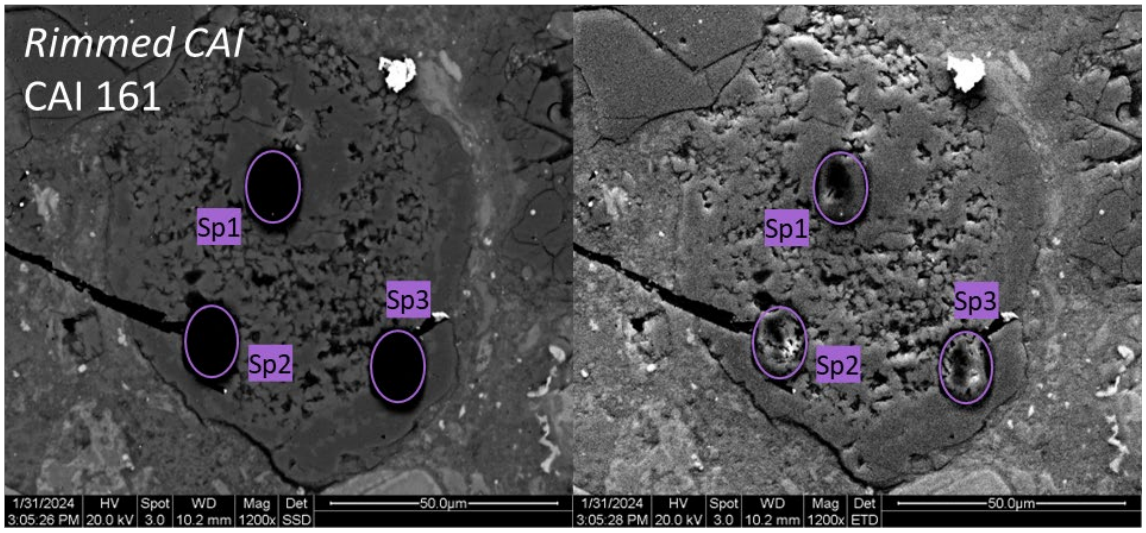
Rimmed CAI
CAI 161
Sp1
Sp3
Sp2
Sp1
Sp3
Sp2
1/31/2024 3:05:26 PM HV 20.0 kV Spot 3.0 WD 10.2 mm Mag 1200x Det SSD 50.0µm
1/31/2024 3:05:28 PM HV 20.0 kV Spot 3.0 WD 10.2 mm Mag 1200x Det ETD 50.0µm

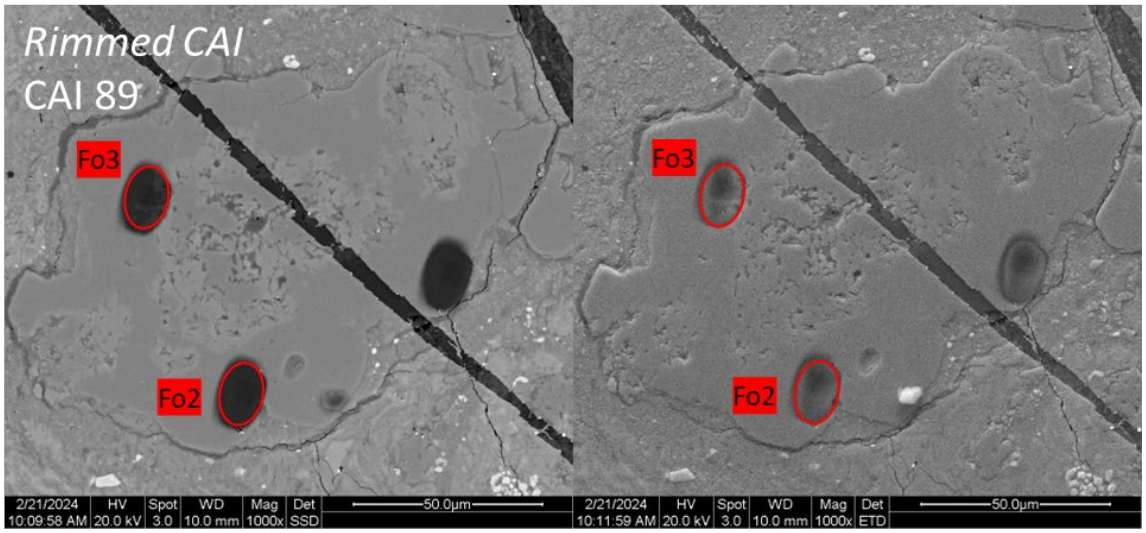
Rimmed CAI
CAI 89
Fo3
Fo2
Fo3
Fo2
2/21/2024 10:09:58 AM HV 20.0 kV Spot 3.0 WD 10.0 mm Mag 1000x Det SSD 50.0µm
2/21/2024 10:11:59 AM HV 20.0 kV Spot 3.0 WD 10.0 mm Mag 1000x Det ETD 50.0µm

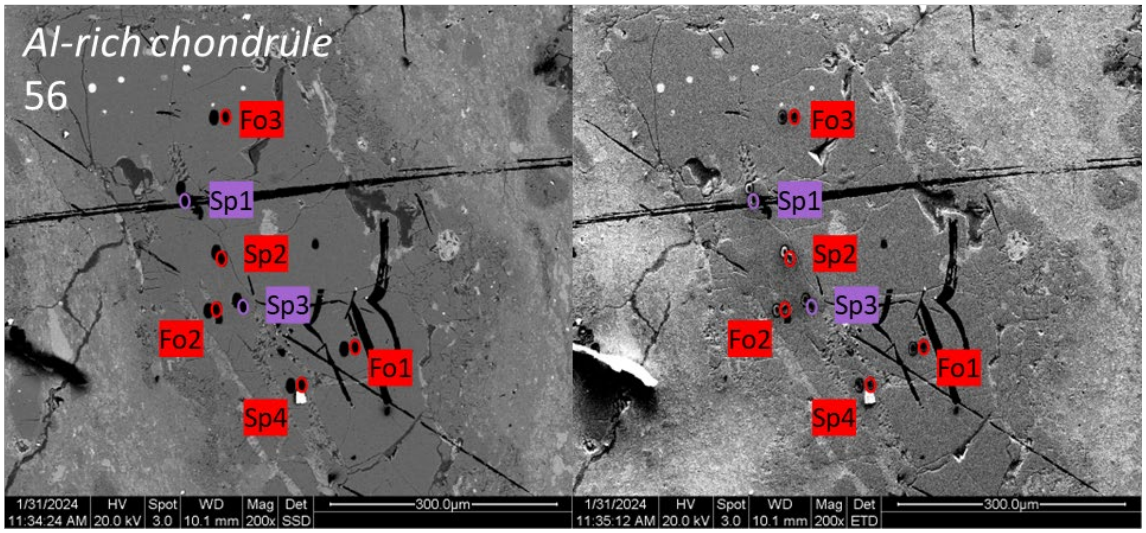
Al-rich chondrule
56
Fo3
Sp1
Sp2
Sp3
Fo2
Fo1
Sp4
1/31/2024 11:34:24 AM HV 20.0 kV Spot 3.0 WD 10.1 mm Mag 200x Det SSD 300.0µm
1/31/2024 11:35:12 AM HV 20.0 kV Spot 3.0 WD 10.1 mm Mag 200x Det ETD 300.0µm

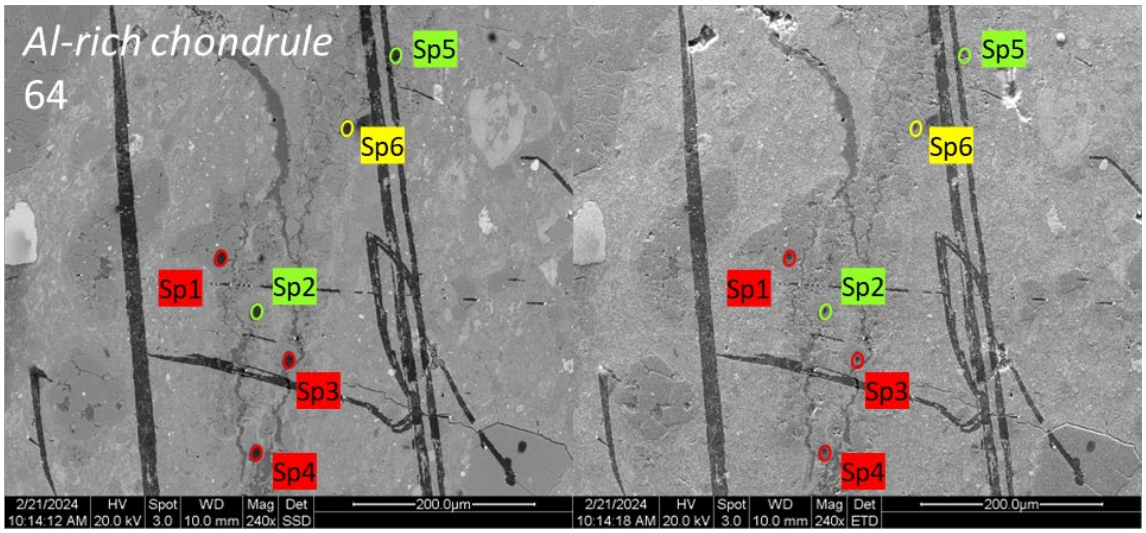
Al-rich chondrule
64
Sp5
Sp6
Sp1
Sp2
Sp3
Sp4
2/21/2024 10:14:12 AM HV 20.0 kV Spot 3.0 WD 10.0 mm Mag 240x Det SSD 200.0µm
2/21/2024 10:14:18 AM HV 20.0 kV Spot 3.0 WD 10.0 mm Mag 240x Det ETD 200.0µm

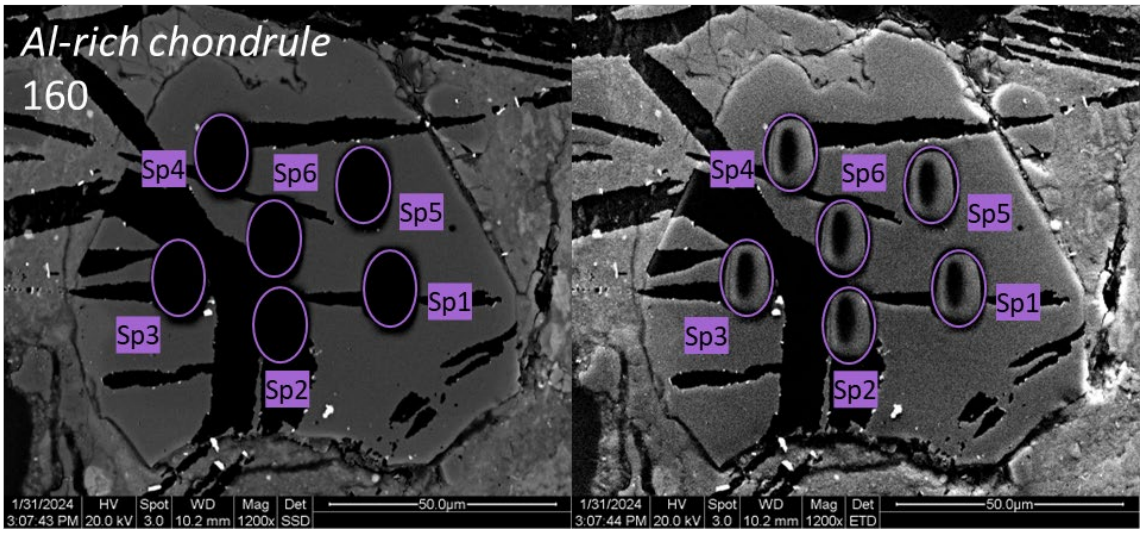
Al-rich chondrule
160
Sp4
Sp6
Sp5
Sp1
Sp3
Sp2
1/31/2024 3:07:43 PM HV 20.0 kV Spot 3.0 WD 10.2 mm Mag 1200x Det SSD 50.0µm
1/31/2024 3:07:44 PM HV 20.0 kV Spot 3.0 WD 10.2 mm Mag 1200x Det ETD 50.0µm

7.9.5 Winchcombe

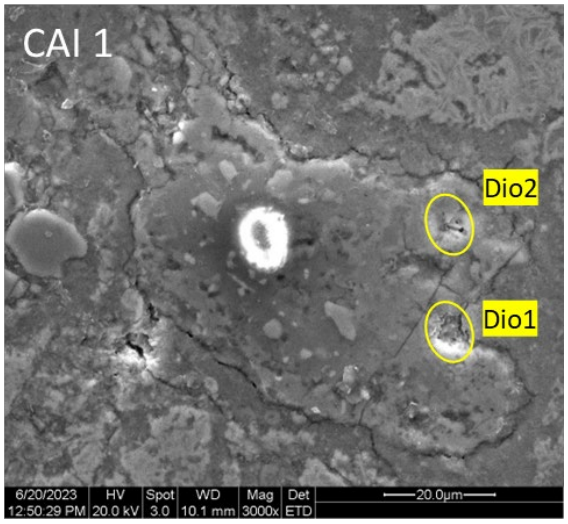

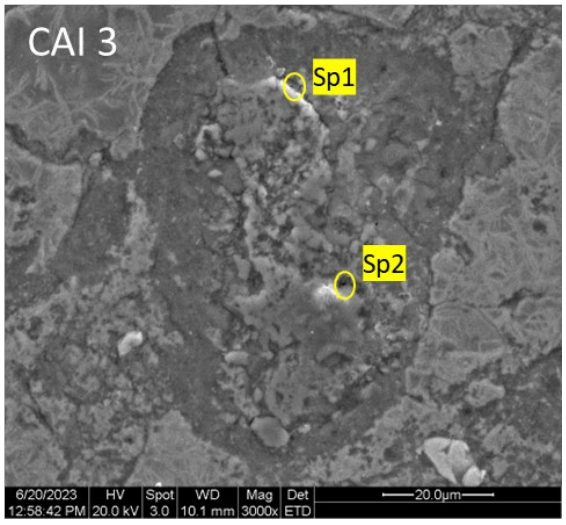

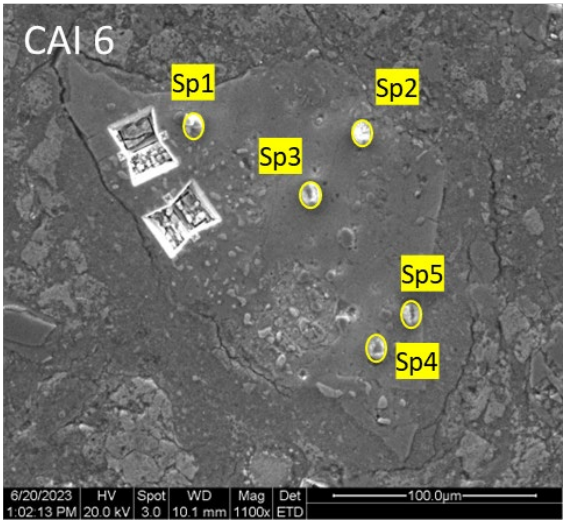

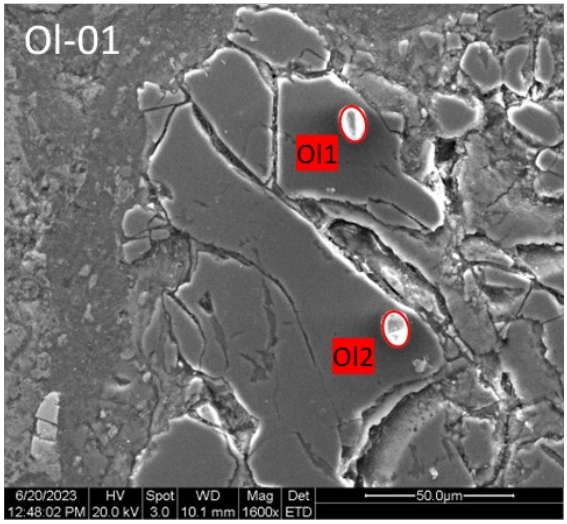

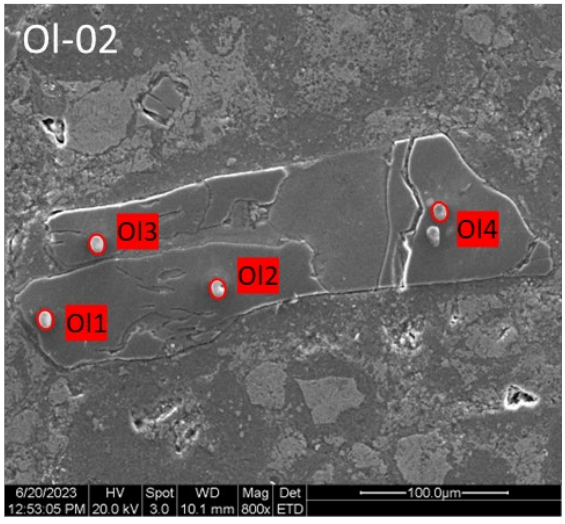

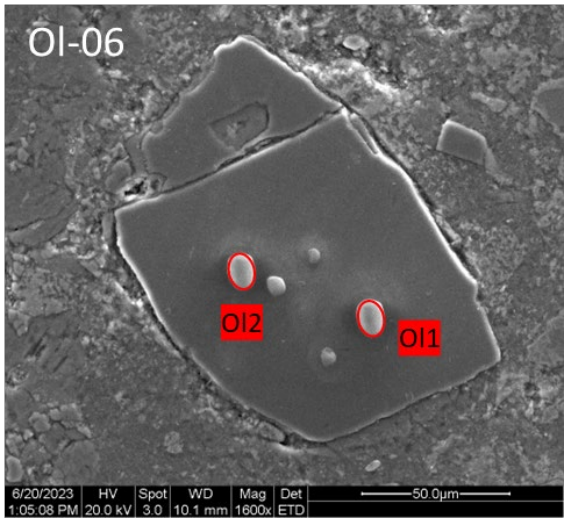

List of References

Aléon J., Krot A. N., McKeegan K. D., 2002. Calcium-aluminum-rich inclusions and amoeboid olivine aggregates from the CR carbonaceous chondrites. Meteoritics & Planetary Science 37, 1729-1755

Amelin, Y., Kaltenbach, A., Iizuka, T., Stirling, C.H., Ireland, T.R., Petaev, M., Jacobsen, S.B., 2010. U-Pb chronology of the Solar System's oldest solids with variable 238U/235U. Earth Planet Sci Lett 300, 343–350. https://doi.org/10.1016/j.epsl.2010.10.015

Amelin, Y., Krot, A.N., Hutcheon, I.D., Ulyanov, A.A., 2002. Lead Isotopic Ages of Chondrules and Calcium-Aluminum-Rich Inclusions. Science (1979) 297, 1678–1683. https://doi.org/10.1126/science.1073950

Armstrong, J.T., Meeker, G.P., Huneke, J.C., Wasserburg, G.J., 1982. The Blue Angel: I. The mineralogy and petrogenesis of from the Murchison meteorite: a hibonite inclusion, Geochimica et Cosmochimica Acta. Pergamon Press Ltd.

Barber, D.J., 1981. Matrix phyllosilicates and associated minerals in CM2 carbonaceous chondrites.

Bates, H.C., King, A.J., Donaldson Hanna, K.L., Bowles, N.E., Russell, S.S., 2020. Linking mineralogy and spectroscopy of highly aqueously altered CM and CI carbonaceous chondrites in preparation for primitive asteroid sample return. Meteorit Planet Sci 55, 77–101. https://doi.org/10.1111/maps.13411

Beckett, J.R., 1986. The origin of calcium-, aluminum-rich inclusions from carbonaceous chondrites: An experimental study. The University of Chicago.

Beckett, J.R., Stolper, E., 1994. The stability of hibonite, melilite and other aluminous phases in silicate melts: implications for the origin of hibonite-bearing inclusions from carbonaceous chondrites. Meteoritics 29, 41–65. https://doi.org/10.1111/j.1945-5100.1994.tb00651.x

Bischoff, A., 1998. Aqueous alteration of carbonaceous chondrites: Evidence for preaccretionary alteration—A review. Meteorit Planet Sci 33, 1113–1122. https://doi.org/10.1111/j.1945-5100.1998.tb01716.x

Bischoff, A., Scott, E.R.D., Metzler, K., Goodrich, C.A., 2006. Nature and origins of meteoritic breccias. Meteorites and the Early Solar System II 679–712.

Bland, P.A., Howard, L.E., Prior, D.J., Wheeler, J., Hough, R.M., Dyl, K.A., 2011. Earliest rock fabric formed in the Solar System preserved in a chondrule rim. Nat Geosci 4, 244–247. https://doi.org/10.1038/ngeo1120

Bollard J., Connelly J. N., Whitehouse M. J., Pringle E. A., Bonal L., Jørgensen J. K., Nordlund Å., Moynier F. and Bizzarro M. (2017) Early formation of planetary building blocks inferred from Pb isotopic ages of chondrules. Science advances 3, e1700407.

Bottke, W.F., Cellino, A., Paolicchi, P., Binzel, R.P., 2021. Bottke et al.: An Overview of Asteroids: The Asteroids III Perspective.

Bouden, N., Villeneuve, J., Marrocchi, Y., Deloule, E., Füri, E., Gurenko, A., Piani, L., Thomassot, E., Peres, P., Fernandes, F., 2021. Triple Oxygen Isotope Measurements by Multi-Collector Secondary Ion Mass Spectrometry. Front Earth Sci (Lausanne). https://doi.org/10.3389/feart.2020.601169

Brearley, A.J., 2006. The action of water. Meteorites and the Early Solar System II 587–624.

Brearley, A.J., Jones, R.H., 1998. INTRODUCTION, in: Planetary Materials. De Gruyter, pp. 125–137. https://doi.org/10.1515/9781501508806-008

Bunch, T.E., Chang, S., 1980. Carbonaceous chondrites. Carbonaceous chondrite phyllosilicates and light element geochemistry as indicators of parent body processes and surface conditions.

Busemann, H., Alexander, C.M.O.D., Nittler, L.R., 2007. Characterization of insoluble organic matter in primitive meteorites by microRaman spectroscopy. Meteorit Planet Sci 42, 1387–1416. https://doi.org/10.1111/j.1945-5100.2007.tb00581.x

Carry, B., 2012. Density of asteroids. Planet Space Sci 73, 98–118. https://doi.org/10.1016/j.pss.2012.03.009

Cashion, M.D., Johnson, B.C., Deienno, R., Kretke, K.A., Walsh, K.J., Krot, A.N., 2025. Chondrule formation indicates protracted growth of giant planet cores. Icarus 429, 116400. https://doi.org/10.1016/j.icarus.2024.116400

Chambers, J.E., 2004. Planetary accretion in the inner Solar System. Earth Planet Sci Lett 223, 241–252. https://doi.org/10.1016/j.epsl.2004.04.031

Chaumard, N., Defouilloy, C., Hertwig, A.T., Kita, N.T., 2021. Oxygen isotope systematics of chondrules in the Paris CM2 chondrite: Indication for a single large formation region across snow line. Geochim Cosmochim Acta 299, 199–218. https://doi.org/10.1016/j.gca.2021.02.012

Chaumard, N., Defouilloy, C., Kita, N.T., 2018. Oxygen isotope systematics of chondrules in the Murchison CM2 chondrite and implications for the CO-CM relationship. Geochim Cosmochim Acta 228, 220–242. https://doi.org/10.1016/j.gca.2018.02.040

Chaussidon, M., Robert, F., McKeegan, K.D., 2006. Li and B isotopic variations in an Allende CAI: Evidence for the in-situ decay of short-lived 10Be and for the possible presence of the short-lived nuclide 7Be in the early solar system. Geochim Cosmochim Acta 70, 224–245. https://doi.org/10.1016/j.gca.2005.08.016

Chizmadia, L.J., Brearley, A.J., 2008. Mineralogy, aqueous alteration, and primitive textural characteristics of fine-grained rims in the Y-791198 CM2 carbonaceous chondrite: TEM observations and comparison to ALHA81002. Geochim Cosmochim Acta 72, 602–625. https://doi.org/10.1016/j.gca.2007.10.019

Clayton, R.N., Mayeda, T.K., 1999. Oxygen isotope studies of carbonaceous chondrites.

Connelly, J.N., Bollard, J., Bizzarro, M., 2017. Pb–Pb chronometry and the early Solar System. Geochim Cosmochim Acta 201, 345–363. https://doi.org/10.1016/j.gca.2016.10.044

Cournede, C., Gattacceca, J., Gounelle, M., Rochette, P., Weiss, B.P., Zanda, B., 2015. An early solar system magnetic field recorded in CM chondrites. Earth Planet Sci Lett 410, 62–74. https://doi.org/10.1016/j.epsl.2014.11.019

Daly, L., Suttle, M.D., Lee, M.R., Bridges, J., Hicks, L., Martin, P.E.M.C., Floyd, C.J., Jenkins, L.E., Salge, T., King, A.J., Almeida, N. V., Johnson, D., Trimby, P.W., Mansour, H., Wadsworth, F.B., Rollinson, G., Genge, M.J., Darling, J., Bagot, P.A.J., White, L.F., Stephen, N.R., Mitchell, J.T., Griffin, S., Willcocks, F.M., Jones, R., Piazolo, S., Einsle, J.F., Macente, A., Hallis, L.J., O'Brien, A., Schofield, P.F., Russell, S.S., Bates, H., Smith, C., Franchi, I., Forman, L. V., Bland, P.A., Westmoreland, D., Anderson, I., Taylor, R., Montgomery, M., Parsons, M., Vasseur, J., van Ginneken, M., Wozniakiewicz, P.J., Burchell, M.J., Hallatt, D., Alesbrook, L.S., Spathis, V., Worden, R., Behnsen, J., Black, K., 2024. Brecciation at the grain scale within the lithologies of the Winchcombe Mighei-like carbonaceous

chondrite. Meteorit Planet Sci 59, 1068–1100. https://doi.org/10.1111/maps.14164
Desch, S.J., Kalyaan, A., Alexander, C.M.O., 2018. The Effect of Jupiter's Formation on the Distribution of Refractory Elements and Inclusions in Meteorites. Astrophys J Suppl Ser 238, 11. https://doi.org/10.3847/1538-4365/aad95f
Doukhan, N., Doukhan, J.C., 1986. Dislocations in perovskites BaTiO3 and CaTiO3. Phys Chem Miner 13, 403–410. https://doi.org/10.1007/BF00309185
Dowty, E., Clark, J.R., 1973. Crystal Structure Refinement and Optical Properties Ti3+ Fassaite from the Allende Meteorite, American Mineralogist.
Dunham, E.T., Sheikh, A., Opara, D., Matsuda, N., Liu, M.C., McKeegan, K.D., 2023. Calcium–aluminum-rich inclusions in non-carbonaceous chondrites: Abundances, sizes, and mineralogy. Meteorit Planet Sci 58, 643–671. https://doi.org/10.1111/maps.13975
Dyl, K.A., Simon, J.I., Young, E.D., 2011. Valence state of titanium in the Wark-Lovering rim of a Leoville CAI as a record of progressive oxidation in the early Solar Nebula. Geochim Cosmochim Acta 75, 937–949. https://doi.org/10.1016/j.gca.2010.09.042
Ebel, D.S., 2021. Condensation Calculations in Planetary Science and Cosmochemistry, in: Oxford Research Encyclopedia of Planetary Science. Oxford University Press. https://doi.org/10.1093/acrefore/9780190647926.013.201
Ebel, D.S., L.D.S., & M.H.Y., 2006. Condensation of rocky material in astrophysical environments, in: Meteorites and the Early Solar System II. pp. 253–277.
Ebel D. D. and Grossman L. (2000) Condensation in dust-enriched systems. Geochim. Cosmochim. Acta 64, 339–366.
Egerton, R.F., 2016. Physical Principles of Electron Microscopy.
Fendrich, K. V., Ebel, D.S., 2021. Comparison of the Murchison CM2 and Allende CV3 chondrites. Meteorit Planet Sci 56, 77–95. https://doi.org/10.1111/maps.13623
Fuchs, L.H., Olsen, E., Jensen, K.J., 1973. Mineralogy, Mineral-Chemistry, and Composition of the Murchison (C2) Meteorite. Smithsonian Contributions to the Earth Sciences 1–39. https://doi.org/10.5479/si.00810274.10.1
Fujiya, W., Sugiura, N., Hotta, H., Ichimura, K., Sano, Y., 2012. Evidence for the late formation of hydrous asteroids from young meteoritic carbonates. Nat Commun 3. https://doi.org/10.1038/ncomms1635
Fukuda, K., Tenner, T.J., Kimura, M., Tomioka, N., Siron, G., Ushikubo, T., Chaumard, N., Hertwig, A.T., Kita, N.T., 2022. A temporal shift of chondrule generation from the inner to outer Solar System inferred from oxygen isotopes and Al-Mg chronology of chondrules from primitive CM and CO chondrites. Geochim Cosmochim Acta 322, 194–226. https://doi.org/10.1016/j.gca.2021.12.027
Gaffey, M.J., Cloutis, E.A., Kelley, M.S., Reed, K.L., 2011. Mineralogy of Asteroids, in: Asteroids III. University of Arizona Press, pp. 183–204. https://doi.org/10.2307/j.ctv1v7zdn4.20
Goldstein, J. ed., 2012. Practical scanning electron microscopy: electron and ion microprobe analysis. Springer Science & Business Media.
Goldstein, J.I., N.D.E., M.J.R., R.N.W., S.J.H.J., & J.D.C., 2017. Scanning electron microscopy and X-ray microanalysis. springer.
Gooding, J.L., Keil, K., 1981. RELATIVE ABUNDANCES OF CHONDRULE PRIMARY TEXTURAL TYPES IN ORDINARY CHONDRITES AND THEIR BEARING ON

CONDITIONS OF CHONDRULE FORMATION. Meteoritics 16, 17–43. https://doi.org/10.1111/j.1945-5100.1981.tb00183.x

Gounelle, M., Chaussidon, M., Rollion-Bard, C., 2013. Variable and extreme irradiation conditions in the early solar system inferred from the initial abundance of 10Be in isheyevo CAIs. Astrophysical Journal Letters 763. https://doi.org/10.1088/2041-8205/763/2/L33

Greenwood, R.C., Lee, M.R., Hutchison, R., Barber, D.J., 1994. Formation and alteration of CAIs in Cold Bokkeveld (CM2). Geochim Cosmochim Acta 58, 1913–1935. https://doi.org/10.1016/0016-7037(94)90424-3

Gröger, R., Holzer, J., Kruml, T., 2023. Twinning and antitwinning in body-centered cubic metals. Comput Mater Sci 216. https://doi.org/10.1016/j.commatsci.2022.111874

Grossman, J.N., MacPherson, G.J., Vicenzi, E.P., Alexander, C.M.O., 2006. A spectacular compound chondrule-CAI in Northwest Africa 2918, a new CO3.1 chondrite.

Grossman, L., Larimer, J.W., 1974. Early Chemical History of the Solar System, REVIEWS OF GEOPHYSICS AND SPACE PHYSICS.

Grossman, L., Simon, S.B., Rai, V.K., Thiemens, M.H., Hutcheon, I.D., Williams, R.W., Galy, A., Ding, T., Fedkin, A. V., Clayton, R.N., Mayeda, T.K., 2008. Primordial compositions of refractory inclusions. Geochim Cosmochim Acta 72, 3001–3021. https://doi.org/10.1016/j.gca.2008.04.002

Halfpenny, A., 2010. Some important practical issues for the collection and manipulation of electron backscatter diffraction (EBSD) data from geological samples. Journal of the Virtual Explorer 35. https://doi.org/10.3809/jvirtex.2011.00272

Halfpenny, A., Prior, D.J., Wheeler, J., 2012. Electron backscatter diffraction analysis to determine the mechanisms that operated during dynamic recrystallisation of quartz-rich rocks. J Struct Geol 36, 2–15. https://doi.org/10.1016/j.jsg.2012.01.001

Hanna, R.D., Hamilton, V.E., Haberle, C.W., King, A.J., Abreu, N.M., Friedrich, J.M., 2020. Distinguishing relative aqueous alteration and heating among CM chondrites with IR spectroscopy. Icarus 346. https://doi.org/10.1016/j.icarus.2020.113760

Hanna, R.D., Ketcham, R.A., 2018. Evidence for accretion of fine-grained rims in a turbulent nebula for CM Murchison. Earth Planet Sci Lett 481, 201–211. https://doi.org/10.1016/j.epsl.2017.10.029

Hanowski, N.P., Brearley, A.J., 2001. Aqueous alteration of the chondrules in the CM carbonaceous chondrite, Alla Hills 81002: Implications for parent body alteration. Geochim Cosmochim Acta 65, 495–518. https://doi.org/10.1016/S0016-7037(00)00552-4

Haugbølle, T., Weber, P., Wielandt, D.P., Benítez-Llambay, P., Bizzarro, M., Gressel, O., Pessah, M.E., 2019. Probing the Protosolar Disk Using Dust Filtering at Gaps in the Early Solar System. Astron J 158, 55. https://doi.org/10.3847/1538-3881/ab1591

Herbst, W., Greenwood, J.P., 2024. Chondrule formation during low-speed collisions of planetesimals: A hybrid splash–flyby framework. Meteorit Planet Sci 59, 895–909. https://doi.org/10.1111/maps.14153

Hertwig A., Defouilloy C., Kimura M. and Kita N. T. (2017) Oxygen isotope systematics of chondrule minerals from the reduced CV3 chondrite NWA 8613. In 48th Lunar and Planet. Sci. Conf. CD-ROM. p. #1227, abstr.

Hertwig A., Defouilloy C. and Kita N. T. (2018) Formation of chondrules in a moderately high dust enriched disk: evidence from oxygen isotopes of

chondrules from the Kaba CV3 chondrite. Geochim. Cosmochim. Acta 224, 116–131.
Hewins R. H. 1997. Chondrules. Annu. Rev. Earth Planet. Sci 25:61–83. www.annualreviews.org (Accessed May 28, 2025).
Hezel, D.C., Russell, S.S., Ross, A.J., Kearsley, A.T., 2008. Modal abundances of CAIs: Implications for bulk chondrite element abundances and fractionations. Meteorit Planet Sci 43, 1879–1894. https://doi.org/10.1111/j.1945-5100.2008.tb00649.x
Hiyagon, H., Hashimoto, A., 1999. 16O Excesses in Olivine Inclusions in Yamato-86009 and Murchison Chondrites and Their Relation to CAIs. Science (1979) 283, 828–831. https://doi.org/10.1126/science.283.5403.828
Howard, K.T., Alexander, C.M.O.D., Schrader, D.L., Dyl, K.A., 2015. Classification of hydrous meteorites (CR, CM and C2 ungrouped) by phyllosilicate fraction: PSD-XRD modal mineralogy and planetesimal environments. Geochim Cosmochim Acta 149, 206–222. https://doi.org/10.1016/j.gca.2014.10.025
Hu, J.Y., Dauphas, N., Tissot, F.L.H., Yokochi, R., Ireland, T.J., Zhang, Z., Davis, A.M., Ciesla, F.J., Grossman, L., Charlier, B.L.A., Roskosz, M., Alp, E.E., Hu, M.Y., Zhao, J., 2021. Heating events in the nascent solar system recorded by rare earth element isotopic fractionation in refractory inclusions.
Hua, X., Wang, J., Buseck, P.R., 2002. Fine-grained rims in the Allan Hills 81002 and Lewis Cliff 90500 CM2 meteorites: Their origin and modification. Meteorit Planet Sci 37, 229–244. https://doi.org/10.1111/j.1945-5100.2002.tb01106.x
Huss, G.R., MacPherson, G.J., Wasserburg, G.J., Russell, S.S., Srinivasan, G., 2001. Aluminum-26 in calcium-aluminum-rich in inclusions and chondrules from unequilibrated ordinary chondrites. Meteorit Planet Sci 36, 975–997. https://doi.org/10.1111/j.1945-5100.2001.tb01934.x
Ireland, T.R., Avila, J., Greenwood, R.C., Hicks, L.J., & Bridges, J.C. (2020) Oxygen Isotopes and Sampling of the Solar System. Space Science Reviews, 216, pp. 25.
Ireland, T.R., 2004. SIMS Measurement of Stable Isotopes.
Ito, M., Nagasawa, H., Yurimoto, H., 2004. Oxygen isotopic SIMS analysis in Allende CAI: details of the very early thermal history of the solar system. Geochim Cosmochim Acta 68, 2905–2923. https://doi.org/10.1016/j.gca.2004.02.001
Itoh, S., Yurimoto, H., 2003. Contemporaneous formation of chondrules and refractory inclusions in the early Solar System. Nature 423, 728–731. https://doi.org/10.1038/nature01699
Ivanova, M.A., Krot, A.N., Nagashima, K., Macpherson, G.J., 2012. Compound ultrarefractory CAI-bearing inclusions from CV3 carbonaceous chondrites. Meteorit Planet Sci 47, 2107–2127. https://doi.org/10.1111/maps.12031
Ivanova, M.A., Lorenz, C.A., Krot, A.N., Macpherson, G.J., 2015. A compound Ca-, Al-rich inclusion from CV3 chondrite Northwest Africa 3118: Implications for understanding processes during CAI formation. Meteorit Planet Sci 50, 1512–1528. https://doi.org/10.1111/maps.12489
Jacquet, E., Marrocchi, Y., 2017. Chondrule heritage and thermal histories from trace element and oxygen isotope analyses of chondrules and amoeboid olivine aggregates. Meteorit Planet Sci 52, 2672–2694. https://doi.org/10.1111/maps.12985
Jaresowich, 1990.

Johnson, C.A., Prinz, M., 1993. Carbonate compositions in CM and CI chondrites, and implications for aqueous alteration, Geochimica et Cosmochimica Acta.

Jones, R.H., 2012. Petrographic constraints on the diversity of chondrule reservoirs in the protoplanetary disk. Meteorit Planet Sci 47, 1176–1190. https://doi.org/10.1111/j.1945-5100.2011.01327.x

Kallemeyn, G.W., Wasson, J.T., 1981. The compositional classification of chondrites-I. The carbonaceous chondrite groups.

Kallemeyn, G.W., Wasson, J.T., 1986. Compositions of enstatite (EH3, EH4,5 and EM) chondrites: Implications regarding their formation.

Kawasaki, N., Wada, S., Park, C., Sakamoto, N., Yurimoto, H., 2020. Variations in initial 26Al/27Al ratios among fine-grained Ca-Al-rich inclusions from reduced CV chondrites. Geochim Cosmochim Acta 279, 1–15. https://doi.org/10.1016/j.gca.2020.03.045

Keller, L.P., Busek, P.R., 1994. Twinning in meteoritic and synthetic peroyskite. American Mineralogist 79, 73–79.

Kerraouch, I., Bischoff, A., Zolensky, M.E., Pack, A., Patzek, M., Hanna, R.D., Fries, M.D., Harries, D., Kebukawa, Y., Le, L., Ito, M., Rahman, Z., 2021. The polymict carbonaceous breccia Aguas Zarcas: A potential analog to samples being returned by the OSIRIS-REx and Hayabusa2 missions. Meteorit Planet Sci 56, 277–310. https://doi.org/10.1111/maps.13620

Kevin D. McKeegan, Laurie A. Leshin, Sara S. Russell, Glenn J. MacPherson, 1998. Oxygen Isotopic Abundances in Calcium-Aluminum–Rich Inclusions from Ordinary Chondrites: Implications for Nebular Heterogeneity.

Kimura, M., Imae, N., Komatsu, M., Barrat, J.A., Greenwood, R.C., Yamaguchi, A., Noguchi, T., 2020. The most primitive CM chondrites, Asuka 12085, 12169, and 12236, of subtypes 3.0–2.8: Their characteristic features and classification. Polar Sci 26. https://doi.org/10.1016/j.polar.2020.100565

King, A.J., Daly, L., Rowe, J., Joy, K.H., Greenwood, R.C., Devillepoix, H.A.R., Suttle, M.D., Chan, Q.H.S., Russell, S.S., Bates, H.C., Bryson, J.F.J., Clay, P.L., Vida, D., Lee, M.R., O'brien, Á., Hallis, L.J., Stephen, N.R., Tartèse, R., Sansom, E.K., Towner, M.C., Cupak, M., Shober, P.M., Bland, P.A., Findlay, R., Franchi, I.A., Verchovsky, A.B., Abernethy, F.A.J., Grady, M.M., Floyd, C.J., Ginneken, M. Van, Bridges, J., Hicks, L.J., Jones, R.H., Mitchell, J.T., Genge, M.J., Jenkins, L., Martin, P.-E., Sephton, M.A., Watson, J.S., Salge, T., Shirley, K.A., Curtis, R.J., Warren, T.J., Bowles, N.E., Stuart, F.M., Di Nicola, L., Györe, D., Boyce, A.J., Shaw, K.M.M., Elliott, T., Steele, R.C.J., Povinec, P., Laubenstein, M., Sanderson, D., Cresswell, A., Jull, A.J.T., Sýkora, I., Sridhar, S., Harrison, R.J., Willcocks, F.M., Harrison, C.S., Hallatt, D., Wozniakiewicz, P.J., Burchell, M.J., Alesbrook, L.S., Dignam, A., Almeida, N. V, Smith, C.L., Clark, B., Humphreys-Williams, E.R., Schofield, P.F., Cornwell, L.T., Spathis, V., Morgan, G.H., Perkins, M.J., Kacerek, R., Campbell, P., Horak, J., Jones, D., James, N., Bosley, S., Shuttleworth, A., Dickinson, P., Mcmullan, I., Robson, D., Smedley, A.R.D., Stanley, B., Bassom, R., Mcintyre, M., Suttle, A.A., Fleet, R., Bastiaens, L., Ihász, M.B., Mcmullan, S., Boazman, S.J., Dickeson, Z.I., Grindrod, P.M., Pickersgill, A.E., Weir, C.J., Suttle, F.M., Farrelly, S., Spencer, I., Naqvi, S., Mayne, B., Skilton, D., Kirk, D., Mounsey, A., Mounsey, S.E., Mounsey, S., Godfrey, P., Bond, L., Bond, V., Wilcock, C., Wilcock, H., Wilcock, R., 2022. The Winchcombe meteorite, a unique and pristine witness from the outer solar system, Gareth S. Collins.

Kita N. T., Ushikubo T., Fu B., Valley J. W., 2009. High precision SIMS oxygen isotope analysis and the effect of sample topography. Chemical Geology 264, 43–57.

Krot, A.N., 2019. Refractory inclusions in carbonaceous chondrites: Records of early solar system processes. Meteorit Planet Sci. https://doi.org/10.1111/maps.13350

Krot, A.N., McKeegan, K.D., Huss, G.R., Liffman, K., Sahijpal, S., Hutcheon, I.D., Srinivasan, G., Bischoff, A., Keil, K., 2006. Aluminum-Magnesium and Oxygen Isotope Study of Relict Ca-Al-rich Inclusions in Chondrules. Astrophys J 639, 1227–1237. https://doi.org/10.1086/498610

Krot, A.N., Nagashima, K., van Kooten, E.M.M., Bizzarro, M., 2017. Calcium-aluminum-rich inclusions recycled during formation of porphyritic chondrules from CH carbonaceous chondrites. Geochim Cosmochim Acta 201, 185–223. https://doi.org/10.1016/j.gca.2016.09.001

Krot, A.N., Petaev, M.I., Nagashima, K., 2021. Infiltration metasomatism of the Allende coarse-grained calcium-aluminum-rich inclusions. Prog Earth Planet Sci 8. https://doi.org/10.1186/s40645-021-00437-4

Krot, A.N., Yurimoto, H., Hutcheon, I.B., MacPherson, G.J., 2005. Chronology of the early Solar System from chondrule-bearing calcium-aluminium-rich inclusions. Nature 434, 998–1001. https://doi.org/10.1038/nature03470

Lauretta, D.S., Hua, X., Buseck, P.R., 2000. PII S0016-7037(00)00425-7 Mineralogy of fine-grained rims in the ALH 81002 CM chondrite.

Lee, M. R., Alexander C. M. O'D., Bischoff A., Brearley A. J., Dobrica E., Fujiya W., Le Guillou C., King A. J., van Kooten E., Krot A. N., Leitner J., Marrocchi Y., Patzek M., Petaev M. I., Piani L., Pravdivtsena O., Remusat L., Telus M., Tsuchiyama A., Vacher L. G., 2025. Low-temperature aqueous alteration of chondrites. Space Science Reviews (2025) 221:11. https://doi.org/10.1007/s11214-024-01132-8

Lee, M.R., Floyd, C., Martin, P.E., Zhao, X., Franchi, I.A., Jenkins, L., Griffin, S., 2023. Extended time scales of carbonaceous chondrite aqueous alteration evidenced by a xenolith in LaPaz Icefield 02239 (CM2). Meteorit Planet Sci 58, 672–687. https://doi.org/10.1111/maps.13978

Lee, M.R., Greenwood, R.C., 1994. Alteration of calcium and aluminium-rich inclusions in the Murray (CM2) carbonaceous chondrite. Meteoritics 29, 780–790. https://doi.org/10.1111/j.1945-5100.1994.tb01093.x

Lee, M.R., Lindgren, P., Sofe, M.R., 2014. Aragonite, breunnerite, calcite and dolomite in the CM carbonaceous chondrites: High fidelity recorders of progressive parent body aqueous alteration. Geochim Cosmochim Acta 144, 126–156. https://doi.org/10.1016/j.gca.2014.08.019

Lee, M.R., Lindgren, P., Sofe, M.R., O'D Alexander, C.M., Wang, J., 2012. Extended chronologies of aqueous alteration in the CM2 carbonaceous chondrites: Evidence from carbonates in Queen Alexandra Range 93005. Geochim Cosmochim Acta 92, 148–169. https://doi.org/10.1016/j.gca.2012.06.005

Lentfort, S., Bischoff, A., Ebert, S., Patzek, M., 2021. Classification of CM chondrite breccias—Implications for the evaluation of samples from the OSIRIS-REx and Hayabusa 2 missions. Meteorit Planet Sci 56, 127–147. https://doi.org/10.1111/maps.13486

Leroux, H., Cuvillier, P., Zanda, B., Hewins, R.H., 2015. GEMS-like material in the matrix of the Paris meteorite and the early stages of alteration of CM chondrites. Geochim Cosmochim Acta 170, 247–265. https://doi.org/10.1016/j.gca.2015.09.019

Li, X., Zhang, Z., Wang, J., 2023. Deformation twinning in body-centered cubic metals and alloys. Prog Mater Sci. https://doi.org/10.1016/j.pmatsci.2023.101160

Libourel G., Nagashima K., Portail M., Krot A. N., 2022. Oxygen isotope variations in Mg-rich olivines from type I chondrules in carbonaceous chondrites. Geochimica et Cosmochimica Acta 319, 73–93.

Lindgren, P., Lee, M.R., Sofe, M.R., Zolensky, M.E., 2013. Clasts in the CM2 carbonaceous chondrite Lonewolf Nunataks 94101: Evidence for aqueous alteration prior to complex mixing. Meteorit Planet Sci 48, 1074–1090. https://doi.org/10.1111/maps.12133

Ma, Chi, Rossman, G.R., 2009. Grossmanite, CaTi3+AlSiO6, a new pyroxene from the Allende meteorite. American Mineralogist 94, 1491–1494. https://doi.org/10.2138/am.2009.3310

Ma, C., Rossman, G.R., 2009b. Davisite, CaScAlSiO6, a new pyroxene from the Allende meteorite. American Mineralogist 94, 845–848. https://doi.org/10.2138/am.2009.3209

Ma, C., Simon, S.B., Rossman, G.R., Grossman, L., 2009. Calcium Tschermak's pyroxene, CaAlAlSiO6, from the Allende and Murray meteorites: EBSD and micro-Raman characterizations. American Mineralogist 94, 1483–1486. https://doi.org/10.2138/am.2009.3231

Macdougall, J.D., 1979. REFRACTORY-ELEMENT-RICH INCLUSIONS IN CM METEORITES, Earth and Planetary Science Letters.

Macpherson, G.J., Davis, A.M., 1994. Refractory inclusions in the prototypical CM chondrite, Mighei, Geochimica et Cosmochimica Acta.

MacPherson, G.J., 2013. Calcium-Aluminum-Rich Inclusions in Chondritic Meteorites, in: Treatise on Geochemistry: Second Edition. Elsevier Inc., pp. 139–179. https://doi.org/10.1016/B978-0-08-095975-7.00105-4

Macpherson, G.J., Grossman, L., 1984. "Fluffy" Type A Ca-, Al-rich inclusions in the Allende meteorite, Geochimica et Cosmochimica Acta.

Macpherson, G.J., Hashimoto, A., Grossman', L., 1985. Accretionary rims on inclusions in the Allende meteorite, Geochimica et Cosmochimica Acta.

MacPherson, G.J., Huss, G.R., 2005a. Petrogenesis of Al-rich chondrules: Evidence from bulk compositions and phase equilibria. Geochim Cosmochim Acta 69, 3099–3127. https://doi.org/10.1016/j.gca.2004.12.022

Macpherson, G.J., Simon, S.B., Davis, A.M., Grossman, L., Krot, A.N., 2005. Calcium-Aluminum-rich Inclusions: Major Unanswered Questions.

Makide, K., Nagashima, K., Krot, A.N., Huss, G.R., Hutcheon, I.D., Bischoff, A., 2009. Oxygen- and magnesium-isotope compositions of calcium–aluminum-rich inclusions from CR2 carbonaceous chondrites. Geochim Cosmochim Acta 73, 5018–5050. https://doi.org/10.1016/j.gca.2009.01.042

Marrocchi, Y., Jones, R.H., Russell, S.S., Hezel, D.C., Barosch, J., Kuznetsova, A., 2024. Chondrule Properties and Formation Conditions. Space Sci Rev 220, 69. https://doi.org/10.1007/s11214-024-01102-0

Marrocchi, Y., Rigaudier, T., Piralla, M., Piani, L., 2023. Hydrogen isotopic evidence for nebular pre-hydration and the limited role of parent-body processes in CM chondrites. Earth Planet Sci Lett 611. https://doi.org/10.1016/j.epsl.2023.118151

Martin, P-E M. C., Daly, L., King, A.J., Spratt, J., Daly, L., Lee, M.R., 2023. Chemical and Crystallographic Characterisation of a Grossmanite-bearing Calcium-Aluminium-rich Inclusion within the Winchcombe CM2 Carbonaceous Chondrite.

Martin, P-E M C, Daly, L., Lee, M.R., 2023. Link Between Calcium-Aluminium-rich Inclusion Abundance and the Degree of Aqueous Alteration of Lithologies within CM Chondritic Breccias.
Martin, P.-E.M.C., Daly, L., Villeneuve, J., Lee, M.R., Marrocchi, Y., 2024. On the Origin of the Compound-Chondrule-CAI Components within CM Chondrites.
Martin, P.-E.M.C., King, A.J., Mitchell, J.T., Stephen, N.R., Trimby, P., Van Ginneken, M., Salge, T., Almeida, N. V, Willcocks, F.M., Daly, L., Lee, M.R., 2022. Calcium-Aluminium-rich Inclusion Populations within the Winchcombe CM2 Meteorite Breccia.
Martin, P.M.C., Lee, M.R., 2021. Clast Populations within the CM2.2 Brecciated Carbonaceous Chondrite Aguas Zarcas: Implications for Understanding Aqueous Alteration on Ryugu.
Martin, P.M.C., Lee, M.R., 2020. Petrological Characterisation of the Carbonaceous Chondrite Aguas Zarcas: Implications for Understanding Asteroid Ryugu.
Mckeegan, K.D., Chaussidon, M., Robert, F., 2000. Incorporation of Short-Lived 10 Be in a Calcium-Aluminum-Rich Inclusion from the Allende Meteorite.
McSween, H.Y.Jr., 1979. Are Carbonaceous Chondrites Primitive or Processed? A Review. Reviews of Geophysics and Space Physics 17, 1059–1078.
Metzler, K., B.A., 1996. Constraints on Chondrite Agglomeration from Fine-Grained Chondrule Rims. Chondrules and the protoplanetary disk 153.
Metzler, K., Bischoff, A., Stöffler, D., 1992. Accretionary dust mantles in CM chondrites: Evidence for solar nebula processes. Geochim Cosmochim Acta 56, 2873–2897. https://doi.org/10.1016/0016-7037(92)90365-P
Misawa, K., Fujita, T., 1994. A relict refractory inclusion in a ferromagnesian chondrule from the Allende meteorite. Nature 368, 723–726. https://doi.org/10.1038/368723a0
Mishra, R.K., Marhas, K.K., 2019. Meteoritic evidence of a late superflare as source of 7Be in the early Solar System. Nat Astron 3, 498–505. https://doi.org/10.1038/s41550-019-0716-0
Morimoto, N., 1988. Nomenclature of Pyroxenes. Mineral Petrol 39, 55–76. https://doi.org/10.1007/BF01226262
Nakamura, T., 2006. Yamato 793321 CM chondrite: Dehydrated regolith material of a hydrous asteroid. Earth Planet Sci Lett 242, 26–38. https://doi.org/10.1016/j.epsl.2005.11.040
Nakashima D., Kimura M., Yamada K., Noguchi T., Ushikubo T. and Kita N. T. (2010) Study of chondrules in CH chondrites – I: Oxygen isotope ratios of chondrules. In 73rd Annual Meteoritical Society Meeting. p. #5288, abstr.
Nakashima D., Ushikubo T., Gowda R. N., Kita N. T., Valley J. and Nagao K. (2011) Ion microprobe analyses of oxygen threeisotope ratios of chondrules from the Sayh al Uhaymir 290 CH chondrite using a multiple-hole disk. Meteorit. Planet. Sci. 46, 857–874.
Nolin, Robert (8 October 2013). "Local expert reveals who really coined the word 'asteroid'". Sun-Sentinel. Archived from original on 30 November 2014. Retrieved 22nd October 2023.
Norton, M.B., Mcsween, H.Y., 2007. Quantifying the Volumetric Abundances of the Components of the Murray CM Chondrite: A Preliminary Investigation.
Oelkers, E.H., Declercq, J., Saldi, G.D., Gislason, S.R., Schott, J., 2018. Olivine dissolution rates: A critical review. Chem Geol 500, 1–19. https://doi.org/10.1016/j.chemgeo.2018.10.008

Pape J., Mezger K., Bouvier A.-S. and Baumgartner L. P. (2019) Time and duration of chondrule formation: Constraints from 26Al-26Mg ages of individual chondrules. Geochimica et cosmochimica acta 244, 416–436.

Pignatelli, I., Marrocchi, Y., Vacher, L.G., Delon, R., Gounelle, M., 2016. Multiple precursors of secondary mineralogical assemblages in CM chondrites. Meteorit Planet Sci 51, 785–805. https://doi.org/10.1111/maps.12625

Prior, D.J., Boyle, A.P., Brenker, F., Cheadle, M.C., Day, A., Lopez, G., Peruzzo, L., Potts, G.J., Reddy, S., Spiess, R., Timms, N.E., Trimby, P., Wheeler, J., Zetterström, L., 1999. The application of electron backscatter diffraction and orientation contrast imaging in the SEM to textural problems in rocks, American Mineralogist.

Prior, D.J., Mariani, E., Wheeler, J., 2009. EBSD in the Earth Sciences: Applications, Common Practice, and Challenges, in: Electron Backscatter Diffraction in Materials Science. Springer US, Boston, MA, pp. 345–360. https://doi.org/10.1007/978-0-387-88136-2_26

Reed, S.J.B., 1995. Electron probe microanalysis, in: Microprobe Techniques in the Earth Sciences. Springer US, Boston, MA, pp. 49–89. https://doi.org/10.1007/978-1-4615-2053-5_2

Richter, F.M., Davis, A.M., Ebel, D.S., Hashimoto, A., 2002. Elemental and isotopic fractionation of Type B calcium-aluminum-rich inclusions: Experiments, theoretical considerations, and constraints on their thermal evolution.

Richter, F.M., Janney, P.E., Mendybaev, R.A., Davis, A.M., Wadhwa, M., 2007. Elemental and isotopic fractionation of Type B CAI-like liquids by evaporation. Geochim Cosmochim Acta 71, 5544–5564. https://doi.org/10.1016/j.gca.2007.09.005

Rubin, A.E., 2015. An American on Paris: Extent of aqueous alteration of a CM chondrite and the petrography of its refractory and amoeboid olivine inclusions. Meteorit Planet Sci 50, 1595–1612. https://doi.org/10.1111/maps.12482

Rubin, A.E., 2007. Petrography of refractory inclusions in CM2.6 QUE 97990 and the origin of melilite-free spinel inclusions in CM chondrites, Meteoritics & Planetary Science.

Rubin, A.E., Trigo-Rodríguez, J.M., Huber, H., Wasson, J.T., 2007. Progressive aqueous alteration of CM carbonaceous chondrites. Geochim Cosmochim Acta 71, 2361–2382. https://doi.org/10.1016/j.gca.2007.02.008

Russell, S.S., Bodenan, J.D., Starkey, N.A., Jeffries, T.E., Kearsley, A., Spratt, J., Armytage, R.M.G., Franchi, I.A., 2017. Relationship between CAIs and chondrules: A case study of a compound chondrule from the Allende (CV3) meteorite. Geochem J 51, 31–43. https://doi.org/10.2343/geochemj.2.0445

Russell, S.S., Huss, G.R., Fahey, A.J., Greenwood, R.C., Hutchison, R., Wasserburg, G.J., 1998. An isotopic and petrologic study of calcium-aluminum-rich inclusions from CO3 meteorites. Geochim Cosmochim Acta 62, 689–714. https://doi.org/10.1016/S0016-7037(97)00374-8

Schrader D. L., Connolly, Jr., H. C., Lauretta D. S., Nagashima K., Huss G. R., Davidson J. and Domanik K. J. (2013) The formation and alteration of the Renazzo-like carbonaceous chondrites II: linking O-isotope composition and oxidation state of chondrule olivine. Geochim. Cosmochim. Acta 101, 302–327.

Schrader D. L., Nagashima K., Krot A. N., Ogliore R. C. and Hellebrand E. (2014) Variations in the O-isotope composition of gas during the formation of chondrules from the CR chondrites. Geochim. Cosmochim. Acta 132, 50–74.

Schrader D. L., Nagashima K., Krot A. N., Ogliore R. C., Yin Q. -Z., Amelin Y., Stirling C. H. and Kaltenbach A. (2017) Distribution of ^{26}Al in the CR chondrite chondrule-forming region of the protoplanetary disk. Geochim. Cosmochim. Acta 201, 275–302.

Schwarzer, R.A., Field, D.P., Adams, B.L., Kumar, M., Schwartz, A.J., 2009. Present State of Electron Backscatter Diffraction and Prospective Developments, in: Electron Backscatter Diffraction in Materials Science. Springer US, Boston, MA, pp. 1–20. https://doi.org/10.1007/978-0-387-88136-2_1

Scott, E.R.D., Krot, A.N., 2014. Chondrites and Their Components, in: Volume 1 of Treatise on Geochemistry. Elsevier, pp. 65–137.

Shahar, A., Young, E.D., 2007. Astrophysics of CAI formation as revealed by silicon isotope LA-MC-ICPMS of an igneous CAI. Earth Planet Sci Lett 257, 497–510. https://doi.org/10.1016/j.epsl.2007.03.012

Shu, F.H., Shang, H., Glassgold, A.E., Lee, T., 1996. X-rays and Fluctuating X-Winds from Protostars.

Simon, S.B., Sutton, S.R., Grossman, L., 2007. Valence of titanium and vanadium in pyroxene in refractory inclusion interiors and rims>. Geochim Cosmochim Acta 71, 3098–3118. https://doi.org/10.1016/j.gca.2007.03.027

Sneddon, G.C., Trimby, P.W., Cairney, J.M., 2016. Transmission Kikuchi diffraction in a scanning electron microscope: A review. Materials Science and Engineering R: Reports. https://doi.org/10.1016/j.mser.2016.10.001

Sossi, P.A., Moynier, F., Chaussidon, M., Villeneuve, J., Kato, C., Gounelle, M., 2017. Early Solar System irradiation quantified by linked vanadium and beryllium isotope variations in meteorites. Nat Astron 1. https://doi.org/10.1038/s41550-017-0055

Stolper, E., 1982. Crystallization sequences of Ca-Al-rich inclusions from Allende: An experimental study, Geochimrca d Cosmochrmrca Aclo.

Stolper, E., Paque, J.M., 1986. Crystallization sequences of Ca-Al-rich inclusions from Allende: The effects of cooling rate and maximum temperature. Geochim Cosmochim Acta 50, 1785–1806. https://doi.org/10.1016/0016-7037(86)90139-0

Sugiura, N., Fujiya, W., 2014. Correlated accretion ages and ε 54 Cr of meteorite parent bodies and the evolution of the solar nebula. Meteorit Planet Sci 49, 772–787. https://doi.org/10.1111/maps.12292

Suttle, M.D., Daly, L., Jones, R.H., Jenkins, L., Van Ginneken, M., Mitchell, J.T., Bridges, J.C., Hicks, L.J., Johnson, D., Rollinson, G., Taylor, R., Genge, M.J., Schröder, C., Trimby, P., Mansour, H., Piazolo, S., Bonsall, E., Salge, T., Heard, R., Findlay, R., King, A.J., Bates, H.C., Lee, M.R., Stephen, N.R., Willcocks, F.M., Greenwood, R.C., Franchi, I.A., Russell, S.S., Harrison, C.S., Schofield, P.F., Almeida, N. V., Floyd, C., Martin, P.E., Joy, K.H., Wozniakiewicz, P.J., Hallatt, D., Burchell, M.J., Alesbrook, L.S., Spathis, V., Cornwell, L.T., Dignam, A., 2024. The Winchcombe meteorite—A regolith breccia from a rubble pile CM chondrite asteroid. Meteorit Planet Sci. https://doi.org/10.1111/maps.13938

Suttle, M.D., King, A.J., Schofield, P.F., Bates, H., Russell, S.S., 2021. The aqueous alteration of CM chondrites, a review. Geochim Cosmochim Acta. https://doi.org/10.1016/j.gca.2021.01.014

Tenner T. J., Ushikubo T., Kurahashi E., Kita N. T. and Nagahara H. (2013) Oxygen isotope systematics of chondrule phenocrysts from the CO3.0 chondrite Yamato 81020: evidence for two distinct oxygen isotope reservoirs. Geochim. Cosmochim. Acta 102, 226–245.

Tenner T. J., Nakashima D., Ushikubo T., Kita N. T. and Weisberg M. K. (2015) Oxygen isotope ratios of Fe-poor chondrules in CR3 chondrites: influence of dust enrichment and H_2O during chondrule formation. Geochim. Cosmochim. Acta 148, 228–250.

Tenner T. J., Kimura M. and Kita N. T. (2017) Oxygen isotope characteristics of chondrules from the Yamato-82094 ungrouped carbonaceous chondrite: further evidence for common O-isotope environments sampled among carbonaceous chondrites. Meteorit. Planet. Sci. 52, 268–294.

Tomeoka, K., Buseck, P.R., 1985. Indicators of aqueous alteration in CM carbonaceous chondrites: Microtextures of a layered mineral containing Fe, S, 0 and Ni.

Trigo-Rodriguez, J.M., Rubin, A.E., Wasson, J.T., 2006. Non-nebular origin of dark mantles around chondrules and inclusions in CM chondrites. Geochim Cosmochim Acta 70, 1271–1290. https://doi.org/10.1016/j.gca.2005.11.009

Trimby, P.W., 2012. Orientation mapping of nanostructured materials using transmission Kikuchi diffraction in the scanning electron microscope. Ultramicroscopy 120, 16–24. https://doi.org/10.1016/j.ultramic.2012.06.004

Trimby, P.W., Cao, Y., Chen, Z., Han, S., Hemker, K.J., Lian, J., Liao, X., Rottmann, P., Samudrala, S., Sun, J., Wang, J.T., Wheeler, J., Cairney, J.M., 2014. Characterizing deformed ultrafine-grained and nanocrystalline materials using transmission Kikuchi diffraction in a scanning electron microscope. Acta Mater 62, 69–80. https://doi.org/10.1016/j.actamat.2013.09.026

Tyra, M.A., Farquhar, J., Guan, Y., Leshin, L.A., 2012. An oxygen isotope dichotomy in CM2 chondritic carbonates-A SIMS approach. Geochim Cosmochim Acta 77, 383–395. https://doi.org/10.1016/j.gca.2011.10.003

Tyra, M.A., Farquhar, J., Wing, B.A., Benedix, G.K., Jull, A.J.T., Jackson, T., Thiemens, M.H., 2007. Terrestrial alteration of carbonate in a suite of Antarctic CM chondrites: Evidence from oxygen and carbon isotopes. Geochim Cosmochim Acta 71, 782–795. https://doi.org/10.1016/j.gca.2006.10.023

Ushikubo T., Kimura M., Kita N. T. and Valley J. W. (2012) Primordial oxygen isotope reservoirs of the solar nebula recorded in chondrules in Acfer 094 carbonaceous chondrite. Geochim. Cosmochim. Acta 90, 242–264.

Vacher, L.G., Marrocchi, Y., Villeneuve, J., Verdier-Paoletti, M.J., Gounelle, M., 2018. Collisional and alteration history of the CM parent body. Geochim Cosmochim Acta 239, 213–234. https://doi.org/10.1016/j.gca.2018.08.006

Van Schmus W. R. and Wood J. A. (1967) A chemical-petrologic classification for the chondritic meteorites. Geochimica et Cosmochimica Acta 31, 747–765.

Verdier-Paoletti, M.J., Marrocchi, Y., Avice, G., Roskosz, M., Gurenko, A., Gounelle, M., 2017. Oxygen isotope constraints on the alteration temperatures of CM chondrites. Earth Planet Sci Lett 458, 273–281. https://doi.org/10.1016/j.epsl.2016.10.055

Vernazza, P., Marsset, M., Beck, P., Binzel, R.P., Birlan, M., Cloutis, E.A., DeMeo, F.E., Dumas, C., Hiroi, T., 2016. COMPOSITIONAL HOMOGENEITY OF CM PARENT BODIES. Astron J 152, 54. https://doi.org/10.3847/0004-6256/152/3/54

Visser, R., John, T., Whitehouse, M.J., Patzek, M., Bischoff, A., 2020. A short-lived ^{26}Al induced hydrothermal alteration event in the outer solar system: Constraints from Mn/Cr ages of carbonates. Earth Planet Sci Lett 547. https://doi.org/10.1016/j.epsl.2020.116440

Wakaki, S., Itoh, S., Tanaka, T., Yurimoto, H., 2013. Petrology, trace element abundances and oxygen isotopic compositions of a compound CAI-chondrule object from Allende. Geochim Cosmochim Acta 102, 261–279. https://doi.org/10.1016/j.gca.2012.10.039

Wall, Mike (10 January 2011). "Who really invented the word 'Asteroid' for space rocks?". Space.com. Retrieved 22nd October 2023.

Wang, Y., Guyot, F., Liebermann, R.C., 1992. Electron microscopy of (Mg, Fe)SiO_3 Perovskite: Evidence for structural phase transitions and implications for the lower mantle. J Geophys Res Solid Earth 97, 12327–12347. https://doi.org/10.1029/92JB00870

Weisberg M. K., McCoy T. J., and Krot A. N. 2006. Systematics and Evaluation of Meteorite Classification. In Meteorites and the early solar system II, edited by Lauretta D. S., and McSween H. Y. University of Arizona Press. pp. 19–52

Weisberg M. K., Prinz M., Clayton R. N., Mayeda T. K., 1992. The CR (Renazzo-type) carbonaceous chondrite group and its implications. Geochimica et Cosmochimica Acta Vol. 57. pp. 1567-1586

Wielandt, D., Nagashima, K., Krot, A.N., Huss, G.R., Ivanova, M.A., Bizzarro, M., 2012. Evidence for multiple sources of ^{10}Be in the early solar system. Astrophysical Journal Letters 748. https://doi.org/10.1088/2041-8205/748/2/L25

Williams, D.B., Carter, C.B., 2009. Phase-Contrast Images, in: Transmission Electron Microscopy. Springer US, Boston, MA, pp. 389–405. https://doi.org/10.1007/978-0-387-76501-3_23

Yang, L., Ciesla, F.J., 2012. The effects of disk building on the distributions of refractory materials in the solar nebula. Meteorit Planet Sci 47, 99–119. https://doi.org/10.1111/j.1945-5100.2011.01315.x

Young, E.D., Dyl, K.A., Simon, J.I., 2012. Response to the Comment by S.B. Simon, L. Grossman, and S.R. Sutton on “Valence state of titanium in the Wark-Lovering rim of a Leoville CAI as a record of progressive oxidation in the early Solar Nebula.” Geochim Cosmochim Acta. https://doi.org/10.1016/j.gca.2012.01.029

Young, E.D., Russell, S.S., 1998. Oxygen reservoirs in the early solar nebula inferred from an Allende CAI. Science (1979) 282, 452–455. https://doi.org/10.1126/science.282.5388.452

Zega, T.J., Buseck, P.R., 2003. Fine-grained-rim mineralogy of the Cold Bokkeveld CM chondrite. Geochim Cosmochim Acta 67, 1711–1721. https://doi.org/10.1016/S0016-7037(02)01172-9

Zanda B. 2004. Chondrules. Earth and Planetary Science Letters 224:1–17.

Zhang, A.C., Itoh, S., Sakamoto, N., Wang, R.C., Yurimoto, H., 2014. Origins of Al-rich chondrules: Clues from a compound Al-rich chondrule in the Dar al Gani 978 carbonaceous chondrite. Geochim Cosmochim Acta 130, 78–92. https://doi.org/10.1016/j.gca.2013.12.026

Zhang, L., 2013. Aspects of rock permeability. Frontiers of Structural and Civil Engineering 7, 102–116. https://doi.org/10.1007/s11709-013-0201-2

Zhang, M., Fukuda, K., Tappa, M.J., Siron, G., Nachlas, W.O., Kimura, M., Kitajima, K., Bauer, A.M., Kita, N.T., 2024. Forging inner-disk Al-rich chondrules by interactions of CAI-like melt and ambient gas. Geochim Cosmochim Acta. https://doi.org/10.1016/j.gca.2024.06.018

Zhang, M., Lin, Y., Tang, G., Liu, Y., Leya, I., 2020. Origin of Al-rich chondrules in CV chondrites: Incorporation of diverse refractory components into the ferromagnesian chondrule-forming region. Geochim Cosmochim Acta 272, 198–217. https://doi.org/10.1016/j.gca.2019.12.011

Zhou, W., Apkarian, R.P., Lin Wang, Z., Joy, D., 2007. Fundamentals of Scanning Electron Microscopy.

Zolensky, M., Barrett, R., Browning, L., 1993. Mineralogy and composition of matrix and chondrule rims in carbonaceous chondrites, Geochimica et Cosmochimica Acta.

Zolensky, M.E., Mittlefehldt, D.W., Lipschutz, M.E., Wang, M.-S., Clayton, R.N., Mayeda, T.K., Grady, M.M., Pillinger, C., Barber, D., 1997. CM chondrites exhibit the complete petrologic range from type 2 to 1, Geochimica et Cosmochimica Acta.